UNIVERSITÀ
DEGLI STUDI
FIRENZE

PhD in
Earth Sciences

CYCLE XXXIII

COORDINATOR Prof. Lorella Francalanci

The active plumbing system of La Fossa (Vulcano, Italy): clues to mafic-silicic magma interactions and the link with the magmatic-hydrothermal environment

Doctoral Candidate

Dr. Costa Simone

Supervisor

Prof. Gioncada Anna

Co-Supervisors

Prof. Masotta Matteo

Prof. Pistolesi Marco

Coordinator

Prof. Francalanci Lorella

Years 2017/2020

UNIVERSITÀ
DEGLI STUDI
FIRENZE

PhD in
Earth Sciences

CYCLE XXXIII

COORDINATOR Prof Lorella Francalanci

The active plumbing system of La Fossa (Vulcano, Italy): clues to mafic-silicic magma interactions and the link with the magmatic-hydrothermal environment

Doctoral Candidate

Dr. Costa Simone

Supervisor

Prof. Gioncada Anna

Co-Supervisors

Prof. Masotta Matteo

Prof. Pistolesi Marco

Coordinator

Prof. Francalanci Lorella

Years 2017/2020

A mia nonna Bettina,
con la speranza di aver "inventato" qualcosa di importante

A mio padre,
per avermi portato per la prima volta sul cratere "a cavalluccio"

Abstract

La Fossa is the active volcanic center of Vulcano Island, the southernmost of Aeolian Islands (Italy). Although the volcano has been the site of many volcanological, petrological and geochemical studies since decades, some questions are still debated. Examples are the genetic relationships between the mafic and rhyolitic magmas, often involved in the same eruptions, and the depth of their storage. An additional limitation to the present knowledge comes from the fact that much of the deposits of La Fossa are ash-sized and, therefore, explosive phases of La Fossa volcanic history are less studied by a petrological point of view with respect to lava and coarse pyroclastic material, exception made for the famous AD 1888–90 last eruption. Further interest in this volcano comes from the fact that La Fossa hosts an acid-sulfate hydrothermal system which has been involved in phreatic eruptions, whose fine ashes are enriched in metals carried by hydrothermal fluids, and metal-bearing sulfide accessories have been found in some recent products. Thus, the plumbing system of this volcano may be an ideal site where studying the evolution of chalcophile metal concentration in magmas.

In this PhD thesis, a study integrating petrography, whole-rock geochemistry, compositional analyses of mineral phases, melt inclusions and high pressure high temperature experimental petrology has been carried out on the products representative of the whole magmatic differentiation path (from basalt to rhyolite) of Vulcano, mostly focusing on the explosive products of the last 1000 years erupted at La Fossa. The main aim was to improve the knowledge of the plumbing system of La Fossa by defining the genetic relationships between the mafic and felsic magmas and their crystallization conditions, modeling their geochemical evolution including the concentration of chalcophile metals, and identifying an appropriate approach for reconstructing magma dynamics along the ash-dominated pyroclastic sequences.

Whole-rock major and trace element analyses, major and trace element compositions of mineral and glass phases of natural and experimental products (temperature gradients experiments that simulate differentiation in a thermal-zoned reservoir), together with thermobarometric calculations and geochemical modelling

allowed to depict the plumbing system of La Fossa as a complex polybaric system where rhyolitic magmas can be generated by extraction from crystal mush regions. The partial melting of the crystal mush by mafic magma inputs is accountable for the chemical and textural variability of the erupted intermediate and evolved products including the genesis of K- and Ba-rich trachytic magma.

The stratigraphic record of La Fossa is mostly characterized by ash-sized deposits, originated by long-lasting low-intensity eruptive phases, that have not been fully employed to gain insights into La Fossa plumbing system dynamics. In this thesis, clinopyroxene phenocrysts were analyzed along the complex explosive sequence of the Palizzi Eruptive Unit (12^{th}-13^{th} century) that represents one of the most important eruptive period of the last 1000 years activity at La Fossa. Major element core to rim chemical profiles of clinopyroxene phenocrysts have been employed to perform a hierarchical cluster analysis that allows to recognize four chemical clusters. The compositional differences between the clusters have been reconciled with variations in the degree of undercooling and in the silicate melt composition towards both a mafic and an evolved end-members. The clusters distribution in the different portions of the crystals (cores, mantles and rims) and thermobarometric calculations, allowed to recognize several cycles of mafic magma input followed by ascent and eruption.

The polybaric nature of the plumbing system together with the evidence of sulfide-silicate melt immiscibility in intermediate and evolved products erupted at La Fossa allowed to investigate the evolution of chalcophile metal concentration in crustal magma reservoirs, thus shedding light on mechanisms at the base of mineralization processes beneath arc volcanoes. Indeed, the mineralization potential of arc magmas depends, among other factors, on the timing of sulfide melt saturation relative to magma differentiation and to exsolution of a magmatic fluid phase. In this thesis, the major and trace element analyses of silicate melt and sulfide inclusions, for the basalt to rhyolite compositional spectrum, have been carried out to understand the evolution of chalcophile metals in the plumbing system and to give insights into magma fertility potential. The obtained results suggest that in case of sulfide-undersaturated arc basalts, metals reach the highest abundances in intermediate lati-trachytic magmas. At the point of sulfide saturation the

chalcophile metal contents in the silicate melt dramatic decrease after fractionation of only 0.2-0.3 wt.% of sulfide in the solid assemblage.

In this thesis the whole-rock Platinum-group elements (PGE) concentrations of the Vulcano magmatic suite have been measured with a Ni-sulfide fire assay method. The PGE are sensitive indicators of sulfide saturation because of their very high partition coefficients into a sulfide phase. The decrease in PGE constrained the onset of the sulfide saturation during magma differentiation at ~ 4 wt.% MgO; by this point magma evolution takes place under sulfide-saturated conditions. The obtained results, together with the high content of Pd comparable to other arc-related igneous suites associated with mineralized deposits, suggest that magmatic evolution in crustal magma reservoirs at an arc-related magmatic system similar to La Fossa, fed by sulfide-undersaturated shoshonitic basalts, has the potential to produce fertile magmas.

Riassunto

La Fossa è l'apparato vulcanico attivo dell'isola di Vulcano, la più meridionale delle Isole Eolie. Per quanto da decenni il vulcano sia stato oggetto di numerosi studi vulcanologici e petrologici, alcune tematiche sono tuttora dibattute. Alcuni esempi sono rappresentati dalle relazioni genetiche tra magmi mafici ed evoluti spesso coinvolti negli stessi eventi eruttivi, così come le loro profondità di stazionamento. Ulteriori limiti alle attuali conoscenze derivano dal fatto che la maggior parte dei depositi di La Fossa sono rappresentati da ceneri fini. Ne consegue che le fasi esplosive della storia eruttiva del vulcano sono poco conosciute da un punto di vista petrologico a differenza dei prodotti di natura effusiva o dei depositi piroclastici più grossolani, eccezion fatta per i prodotti dell'ultima celebre eruzione del 1888–1890. Ulteriore interesse per La Fossa deriva dal fatto che il vulcano è caratterizzato da un sistema idrotermale di tipo "acid sulfate" che è stato coinvolto in eruzioni di tipo freatico. Le ceneri fini relative a questo tipo di eventi sono risultate essere arricchite in metalli trasportati dai fluidi idrotermali, inoltre sono stati osservati solfuri magmatici contenenti metalli in alcuni prodotti recenti. Ne deriva che il sistema di alimentazione di questo vulcano è molto appropriato per studiare l'evoluzione della concentrazione degli elementi calcofili nei magmi.

In questa tesi di dottorato è stato effettuato uno studio che integra petrografia, geochimica di roccia totale, analisi chimiche su fasi minerali, inclusioni silicatiche e tecniche di petrologia sperimentale ad alta pressione e temperatura, su prodotti rappresentativi dell'intero percorso di differenziazione magmatica (da basalto a riolite) di Vulcano; lo studio è principalmente mirato ai prodotti esplosivi eruttati nel corso degli ultimi 1000 anni a La Fossa. L'obiettivo principale è stato quello di incrementare le conoscenze attuali sul sistema di alimentazione, definendo le relazioni genetiche tra magmi mafici ed evoluti e le loro condizioni di cristallizzazione, modellizzandone l'evoluzione geochimica, compresa la concentrazione degli elementi calcofili ed identificando un approccio idoneo per ricostruire processi magmatici lungo sequenze piroclastiche dominate da ceneri.

Analisi chimiche degli elementi maggiori e in tracce su roccia totale, la composizione in elementi maggiori e in tracce delle fasi minerali, inclusioni

silicatiche e vetri sia dei prodotti naturali che sperimentali (esperimenti di gradiente di temperatura atti a replicare differenziazione in un serbatoio magmatico termicamente zonato), insieme a calcoli termo-barometrici e modellizzazioni geochimiche, hanno permesso di dipingere il sistema di alimentazione di La Fossa come un complesso sistema poli-barico dove i magmi riolitici possono essere prodotti a seguito di processi di estrazione da regioni cristalline del sistema (crystal mush). La fusione parziale dei crystal mush causata da ricariche ad opera di magmi mafici è responsabile per la variabilità chimica e tessiturale dei prodotti intermedio-evoluti, compresa la genesi di prodotti trachitici arricchiti in K e Ba.

Il record stratigrafico del vulcano La Fossa è caratterizzato in buona parte da depositi cineritici difficili da analizzare, messi in posto da fasi eruttive di bassa intensità e lunga durata. Questo tipo di depositi è stato solo marginalmente utilizzato per ottenere informazioni sulle dinamiche del sistema di alimentazione di La Fossa. In questa tesi sono stati analizzati cristalli di clinopirosseno lungo la sequenza esplosiva del periodo eruttivo di Palizzi (XII-XIII secolo). Questo periodo rappresenta uno dei periodi eruttivi più importanti dell'attività vulcanica degli ultimi 1000 anni di La Fossa. La composizione degli elementi maggiori del clinopirosseno è stata analizzata attraverso transetti nucleo-bordo che sono stati poi impiegati per effettuare una analisi dei cluster la quale ha permesso di identificare quattro cluster composizionali. Le differenze nella composizione chimica dei cluster sono state interpretate come variazioni del grado di sotto-raffreddamento e della composizione del fuso silicatico da cui i cristalli si sono formati, da un end member mafico a uno più evoluto. I risultati, insieme alla diversa distribuzione dei cluster nelle diverse porzioni dei cristalli (nuclei, porzioni intermedie e bordi) e calcoli termo-barometrici, hanno permesso di riconoscere alcuni cicli di input di magma mafico seguiti da risalita ed eruzione.

La natura poli-barica del sistema di alimentazione, insieme alle evidenze di saturazione in una fase a solfuri nei prodotti intermedio evoluti eruttati a La Fossa, ha permesso di studiare l'evoluzione della concentrazione dei metalli calcofili nei serbatoi magmatici. Ciò ha permesso di far luce sui meccanismi alla base di processi mineralizzanti al di sotto di vulcani di arco, in particolare su quelli che governano la fertilità dei magmi. Il potenziale di mineralizzazione dei magmi dipende infatti,

in maniera importante, oltre che da altri fattori, dal timing della saturazione in solfuri relativamente alla differenziazione magmatica e all'essoluzione di una fase fluida. In questa tesi è stata investigata la composizione degli elementi maggiori e in tracce di inclusioni silicatiche e di solfuri magmatici, per tutto lo spettro composizionale da basalto a riolite. Lo scopo è stato quello di contribuire a capire l'evoluzione dei metalli calcofili nel sistema di alimentazione e dare informazioni circa il potenziale di fertilità del magma. I risultati indicano che, nel caso di basalti di arco sottosaturi rispetto a una fase a solfuri, i metalli raggiungono le concentrazioni più alte con la differenziazione nei magmi intermedi lati-trachitici. Alla saturazione di una fase a solfuri il contenuto in metalli nel magma decresce in maniera significativa, a seguito del frazionamento di circa 0.2-0.3 wt.% di solfuro nel residuo solido.

In questa tesi sono anche state misurate le concentrazioni in elementi del gruppo de Platino (PGE) in roccia totale con il metodo Ni-sulfide fire assay. I PGE sono molto sensibili alla presenza di una fase a solfuri poiché i loro coefficienti di distribuzione per queste fasi sono estremamente elevati. L'andamento della concentrazione dei PGE nei prodotti di Vulcano, da basalto a riolite, ha permesso di riconoscere l'inizio della saturazione in solfuri durante la differenziazione magmatica a circa 4 wt.% MgO. Da questo punto in avanti l'evoluzione magmatica procede in condizioni di saturazione in solfuri. I risultati ottenuti in questa tesi, considerando anche le elevate concentrazioni in Pd dei campioni analizzati, comparabili con quelle di altre serie di arco associate a sistemi mineralizzati, indicano che l'evoluzione magmatica in serbatoi situati nella crosta in sistemi di arco simili a La Fossa, alimentati da basalti shoshonitici sottosaturi rispetto a una fase a solfuri, ha il potenziale di produrre magmi fertili.

Acknowledgements

First of all I would like to express endless gratitude to my supervisors: Anna Gioncada, Matteo Masotta and Marco Pistolesi. Thank you so much for your advices, support, help and patience since the times of my MSc thesis. I would also like to thank Paolo Fulignati for being an extra supervisor during these years. You encouraged me up the whole way, and I will always be grateful for everything that you've done and all the incredible effort that you put in. Many thanks also to Mauro Rosi for his assistance, discussions and suggestions during fieldworks. Thank to Delphine Bosch and Olivier Bruguier for the good times spent in Montpellier. Thank to Luca Caricchi and Costanza Bonadonna for the hospitality at Geneva. Many thanks to Ian Campbell for welcoming me to Canberra even if in difficult times. All these people have taught me teachings that I will never forget. Thank also to Piergiorgio Scarlato for giving me access to the HP-HT laboratory at INGV in Rome and to Luca Ziberna and Kurt Roggensack for the constructive review of this thesis.

I want to thank all the people and friends who have accompanied and supported me through this journey. Thanks to Arianna for her support, patience, love and for having that beer with me on the beach at Vulcano. Thanks to Alessandro for being a colleague, flat mate and a friend since our firsts steps in the world of geology. Thanks to Stefano, Fabrizio and Gilda for these years. Thanks to the "Magicians" for their lifelong friendship and support. Thanks to the guys of the petrology and volcanology group at Geneva, in particular to Stefano and Allan for hosting me in their house and to Ollie and Tom for help during analyses. Thanks to the people at the RSES in Canberra, especially to Carlos, Monika, Zhijie and Yamila for their help in the lab.

Finally, I wish to conclude expressing incalculable gratitude to my parents and my brother for their support, for letting me to cultivate my passions, for teaching me to pursue my dreams and for their boundless love.

The author has benefited from financial support from a Tuscany Regional "Pegaso" doctoral grant POR CRO Toscana FSE 2014/2020.

Table of Contents

1 Introduction, aims and thesis structure

The physical and chemical characterization of the eruptive products of active volcanoes is one of the main challenges in volcanology, as it provides essential elements for the definition of the plumbing system and for the assessment of future eruptive scenarios. The estimate of the pre-eruptive conditions of magmas emplaced during past eruptions is possible either through the thermobarometric calculations based on the phase compositions of eruptive products (e.g. Putirka, 2008) or via direct comparison of the natural products with laboratory experiments performed under constrained physical conditions (Scaillet et al., 2008; Pichavant et al., 2014). Clues on the chemical composition of magmas can be also obtained through the direct petrologic study of the erupted products (e.g. Blundy et al., 2006; Blundy and Cashmamn, 2008). Such information, combined with data acquired from the geochemical and geophysical monitoring, are critical for assessing the physico-chemical parameters of magmas beneath active volcanoes and, ultimately, for the volcanic hazard assessment and for designing risk mitigation plans (Neri et al., 2008). In such a scenario, the La Fossa volcano, the active volcanic center of the Island of Vulcano (Italy), has been one of the archetypes locations where petrological and volcanological investigations have been successfully carried out thanks both to the great variability of erupted products reflecting several eruptive styles, and the wide range of erupted magma composition (e.g. De Astis et al., 2013).

Since ancient times, classical mythology inspired several legends about this land whose main leading character was Hephaestus, the Greek god of blacksmiths who worked in its forge located below the island. Given its nature, Vulcano has always been an ideal natural laboratory for volcanologist. It can be said, indeed, that part of modern volcanology was born here. As an example, the renowned volcanologist Giuseppe Mercalli, who described the last eruption occurred in the island in AD 1888–1890, coined the term *"Vulcanian"* eruption, still used in modern volcanology. The natural phenomena occurring on the island make it a very popular place for tourists, especially during summer season, when the population

grows to several thousands. This ranks Vulcano as a high volcanic risk area in case of renewal of eruptive activity (Selva et al., 2020).

Several times since the last eruption La Fossa volcano underwent important variations of the monitored parameters, such as seismicity, CO_2 flux and changes in the chemical composition and temperature of fumaroles (Chiodini et al., 1995). These volcanic "crises", although not culminated into an eruptive event, underlined that the volcanic area is still very active.

1.1 Motivations and aims

The petrological complexity of the plumbing system of La Fossa has been the object of many studies in the past three decades, mainly aimed at investigating the intensive variables and the magmatic processes governing the evolution of parental magmas (De Astis et al., 1997; Del Moro et al., 1998; Gioncada et al., 1998), the pre- and syn-eruptive interaction of magmas at different degrees of evolution (De Fino et al., 1991; Clocchiatti et al., 1994; Piochi et al., 2009; Bullock et al., 2019) and the dynamics and time scales of pre-eruptive magma ascent, mixing and eruption (Vetere et al., 2015; Nicotra et al., 2018; Rossi et al., 2019). Although there is a general consensus for the pre-eruptive temperature estimates and mixing processes of the erupted magmas (Clocchiatti et al., 1994; Gioncada et al., 1998; Vetere et al., 2015), uncertainty in the determination of pressure of magma storage and volatile content and in the overall genetic relationships among these magmas still exists. Indeed, for example, contrasting petrogenetic models have been proposed to explain the relationships between the crystal-rich latitic to trachytic magmatic enclaves and their rhyolitic hosts (Perugini et al., 2007; Piochi et al., 2009; Vetere et al., 2015; Bullock et al., 2019).

The uncertainty of the proposed petrologic models are in part explained by the fact that these studies are focused on lava flows and on the youngest products, which are more easily accessible and better constrained from a chrono-stratigraphic point of view. This inevitably leads to underestimating the significance of the pyroclastic component (e.g. fallout deposits) that constitutes the largest fraction of the volume of erupted magmas (De Astis et al., 2013; Di Traglia et al., 2013; Selva

et al., 2020). Only through the analysis of the entire spectrum of erupted products, including pyroclastic ones, and their distribution in the eruptive sequence it is thus possible to obtain a broader picture of the plumbing system and to place constraints on magma dynamics and evolution in similar arc volcanoes.

The main aim of this PhD thesis is to constrain magma storage conditions and petrogenesis in the last 1000 years of activity of La Fossa volcano. Particular effort was dedicated to better define the genesis and evolution of intermediate and evolved products (latites, trachytes and rhyolites) in the shallow plumbing system, defining their mutual genetic relationships, such as the genesis of crystal-poor rhyolitic melts and of anomalous K- and Ba-rich trachytic magma, the occurrence of magmatic enclaves in rhyolitic products and the role of mafic recharge pulses.

The stratigraphic record of many arc volcanoes worldwide, including La Fossa, is often related to small explosive eruptions associated to long-lasting episodes of low intensity activity (e.g. Sparks et al., 1997) resulting in the emplacement of volcanic successions mainly constituted by fine-grained materials difficult to analyze, by a chemical point of view, with respect to lava samples or lapilli-sized pyroclasts. The consequence is that many petrological works did not focus on such types of products potentially omitting information that could be crucial in the study of a magmatic system of an active volcano. At La Fossa, where fine grained materials constitute the majority of erupted products (Di Traglia et al., 2013), such types of volcanic deposits have only been investigated to define quantitative hazard maps based on physical parameters (e.g. Dellino et al., 2011), but never in order to provide clues on the plumbing system and magma dynamics. In this thesis, an approach suitable for ash-sized to coarse pyroclastic successions, based on a data-driven approach of clinopyroxene chemical profiles, allows to associate variations of distinct magmatic processes (e.g. magmatic recharge, ascent and eruption) in such type of complex volcanic successions.

Advances in understanding of the La Fossa plumbing system act also as launching point to investigate the magmatic processes controlling the composition of fluids exsolved at shallow depth, at the magmatic-hydrothermal transition. Indeed, the polybaric nature of the plumbing system, where some of intermediate products show clear evidences of sulfide-silicate melt immiscibility (Fulignati et

al., 2018), is suitable to study the effect of the saturation of magma in a sulfide phase during differentiation on the chalcophile metal fertility of magmas. Indeed, the mineralization potential of arc magmas depends, among other factors, on the timing of sulfide melt saturation relative to magma differentiation and to the exsolution of a magmatic fluid phase (Richards, 2015). In fossil mineralized or barren systems, understanding the evolution of metals along the magma differentiation path is often hindered by late magmatic processes and hydrothermal alteration. In this thesis the occurrence of sulfide saturation in the La Fossa magmas, the timing related to volatile exsolution, together with the chalcophile metals content in the melt are explored with the aim to better understand magmatic processes relevant to the development of mineralization at arc-related systems.

The eruptive products are examined with the purpose of: i) depict their petrological and geochemical characteristics, through whole-rock, melt inclusions and mineral phases major and trace elements composition; ii) provide, through an experimental study, information about the conditions of crystallization and differentiation of latitic, trachytic and rhyolitic magmas; iii) explore an alternative model for the genesis of crystal-poor rhyolitic magmas and define their genetic relationships with less evolved products emitted during same eruptive events; iv) provide, through a data-driven approach applied to the study of clinopyroxene chemical profiles, a first petrological investigation of a long-lasting, fine-grained explosive sequence otherwise difficult to analyze; v) track, through the study of sulfide accessory minerals, melt inclusions and whole-rock Platinum Group elements (PGE) geochemistry, the sulfur and chalcophile elements evolution in the magmatic system and constrain the possible magmatic contribution to ore-forming fluids in arc systems.

The thesis is mainly focused on the volcanic products of the eruptive sequence of the Palizzi Eruptive Unit (~13th century) since this period represents a fundamental moment in the recent life of the volcano. Indeed, during this period, a large volume of volcanic materials was erupted with a great variety of eruptive styles and magma chemistry (latite, trachyte and rhyolite) and abrupt changes of the composition of eruptive products even in a same sequence. Moreover, it emerges that the behavior of La Fossa changed after that period, both in terms of volumes of

erupted material and eruptive styles (Di Traglia, 2011; Di Traglia et al., 2013; De Astis et al., 2013; Selva et al., 2020).

Some of the samples employed in this research belong also to the most recent eruptions (e.g. Pietre Cotte and AD 1888–1890; see De Astis et al., 2013; Di Traglia et al., 2013) and to older volcanic units as well (e.g. La Sommata, Quadrara, Spiaggia Lunga; see alo Pinarelli et al., 2019; Nicotra et al., 2020; Palummo et al., 2020). These samples have been employed together with the ones associated to the Palizzi Eruptive Unit, in order to have a broader picture of the magmatic processes, in terms of magma composition and differentiation.

1.2 Thesis structure

This thesis is organized in ten chapters:

- Chapter 1 is the introduction to the aim of the thesis and its structure;
- Chapters 2 is an introduction to the Aeolian Islands arc magmatism and a summary of the magma chemistry and structural features of Vulcano island;
- Chapter 3 is a state of the art of La Fossa volcano magmatic and hydrothermal systems in the last 1000 years;
- Chapter 4 describes the analytical and experimental methods employed in this thesis, including samples collection and preparation;
- Chapter 5 is a summary of the field and stratigraphic observations of the main investigated products;
- Chapter 6 examines the differentiation of latitic, trachytic and rhyolitic magmas at La Fossa. In this chapter a series of representative rock samples, with a special regard to explosive products, encompassing the entire compositional range of erupted magmas during the recent (last 1000 years) activity of La Fossa volcano has been selected. The main objective is to reconstruct the physical conditions at which magmas evolved, interacted and erupted. At this purpose, new whole-rock major and trace element analyses and micro-chemical analyses of mineral phases of natural samples have been combined with temperature gradient experiments run in a non-end loaded piston cylinder (QUICKpress type) and geochemical modelling;

- Chapter 7 explores the role of the magmatic inputs of recharging magmas in the La Fossa plumbing system. In this chapter the potential links between magma chemistry and plumbing system dynamics, during the emplacement of a long-lasting eruptive sequence, mainly characterized by ash emissions, are investigated. New major element analyses along core-to-rim profiles in clinopyroxene crystals collected along the stratigraphy of the Palizzi Eruptive Unit are used to perform a hierarchical cluster analysis. By using this method, the chemical complexity of the pyroxene profiles are reduced to sequences of clusters that are reconciled with several cycles interpreted as progressive replenishment of the magma reservoir, ascent and eruption;
- Chapter 8 is a combined study of major and trace element compositions of sulfide accessories, melt inclusions and mineral phases of several products of Vulcano Island for the whole basalt to rhyolite magma composition. The main results allowed to track sulfur and chalcophile elements evolution in the magmatic system and demonstrate that the mechanisms governing metal evolution inferred for the magmatic stage in porphyry Cu environments can be also tracked at an active arc volcano;
- Chapter 9 illustrates the behavior of the PGE in Vulcano magmas. Whole-rock trace elements and, for the first time at Vulcano, new PGE analyses, are employed to constrain the timing of sulfide saturation during magma evolution. Indeed, PGE are sensitive indicator of the saturation of a sulfide phase in the magma, thanks to their extremely high partition coefficients between sulfide and silicate melt. This study highlights the fact that Vulcano magmas have high Pd content, comparable to magmatic suites associated with porphyry Au-Cu system;
- Chapter 10 contains the final conclusions.

Chapters from 4 to 9 are accompanied by supplementary appendices containing supplementary information and or data tables. The nomenclature of appendices follows an alphabetical order.

2 The Aeolian Islands volcanic arc and Vulcano Island

2.1 Geodynamic context and structural framework

The Aeolian Island archipelago is located on the southern edge of the Tyrrhenian Abyssal Plain and lies on a continental crust 20–25 km thick (Beccaluva et al., 1985). The arc is formed by seven islands (Alicudi, Filicudi, Salina, Lipari, Vulcano, Panarea and Stromboli) and several seamounts that form a roughly annular structure around the Marsili back-arc basin (Fig. 2.1a) (Ventura et al., 1999; De Astis et al., 2000; Francalanci et al., 2004, 2007; Blanco-Montenegro et al., 2007). The volcanism in the area, both sub-aerial and submarine, is active since ~1.3 Ma. The genesis of the volcanism in the area has been related to the rapid subduction of the Ionian slab toward NW (Fig. 2.1b) (Barberi et al., 1973; Ellam et al., 1988). The focal mechanisms of earthquakes allows to estimate a subduction angle of about 50–70° at the depth of ~500 km (Fig. 2.1c) (Chiarabba et al., 2008; Ventura et al., 2013). Ellam et al. (1988) suggest the volcanic activity of the area is due to the processes of partial melting of the mantle linked with the subduction of the Ionian oceanic crust. Other authors relate the magmatism of the arc to the passive subduction of a detached portion of the slab and to the thermal rise due to the opening of the southern Tyrrhenian sea, in a post-subduction extensional regime (Wang et al., 1989; Crisci et al., 1991; Esperança et al., 1992).

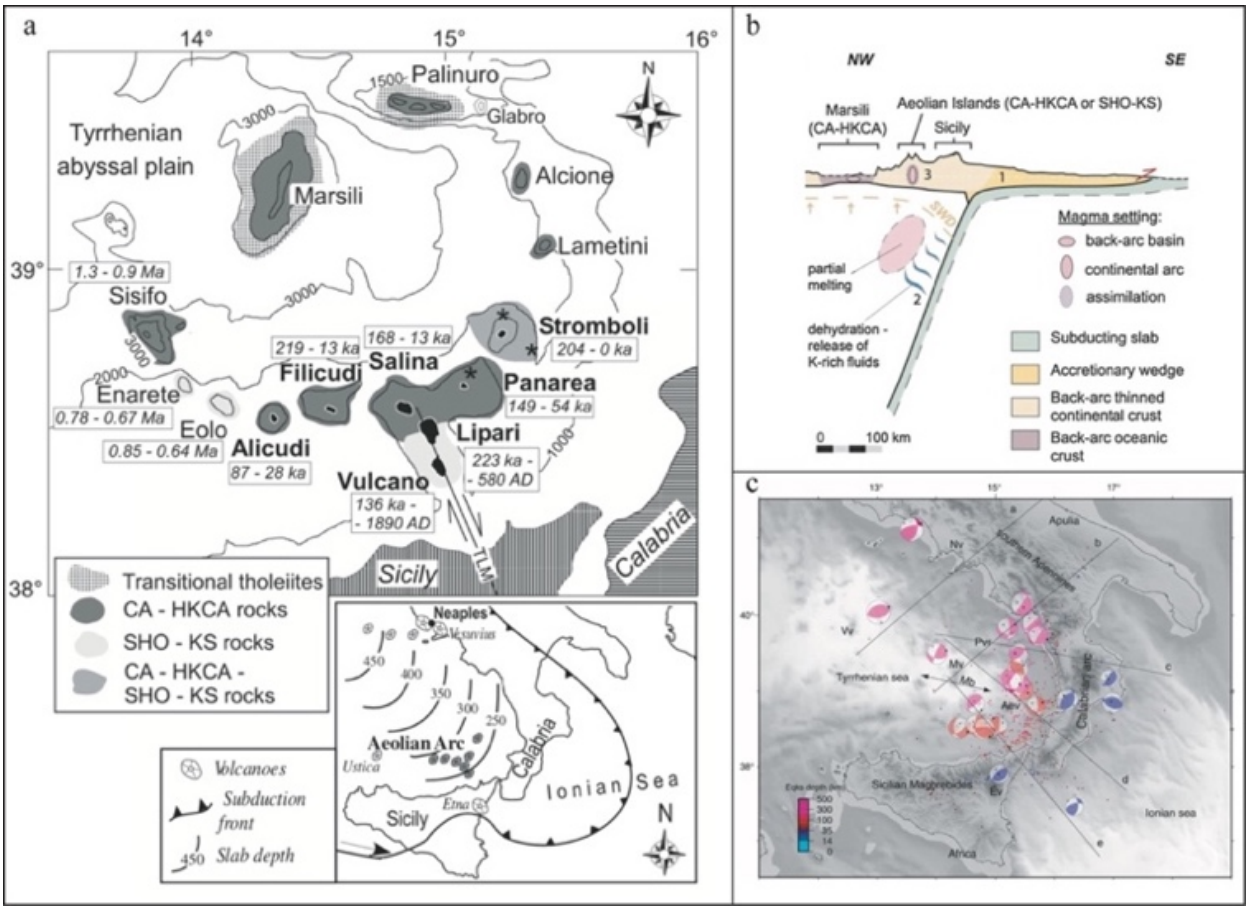

Figure 2.1 – a: General sketch map of Aeolian Islands and seamounts with the associated age and magmatic series (Francalanci et al., 2007); b: simplified profile showing the Ionian subduction below the Aeolian Arc (Beerman et al., 2017); c: subduction of the Ionian lithosphere highlighted by the focal mechanisms of earthquakes (Chiarabba et al., 2008).

The tectonic framework is simplified in three active tectonic zones: a NW-SE trending extensional zone in the western Calabria and in the north-eastern Sicily related to the roll-back of the Ionic slab, a compression zone in the southern Tyrrhenian sea, and the NNW-SSE trending dextral strike slip of the Tindari-Letojanni fault system that joins up the first two zones (Fig. 2.2). This important structure influences the magmatic evolution of the arc, that is usually divided in three sectors: western (Alicudi and Filicudi), central (Salina, Lipari and Vulcano) and eastern (Panarea, Stromboli) sectors (Ruch et al., 2016).

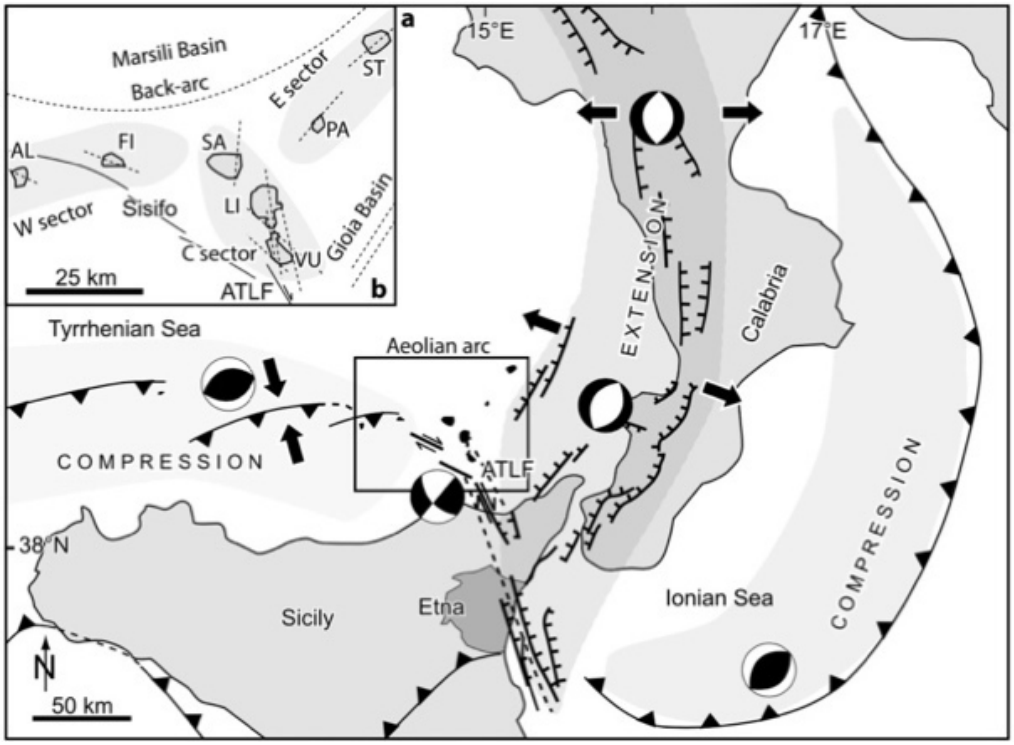

Figure 2.2 – Simplified structural scheme of southern Italy; ATLF: Aeolian Tindari-Letojanni fault (Ruch et al., 2016).

2.2 Geochemistry and petrogenesis of Aeolian volcanic rocks

The Aeolian volcanic rocks mostly belong to the series related to orogenic magmatism: tholeiitic (only in seamounts), calc-alkaline (CA), high-K calc-alkaline (HKCA) and shoshonitic (SHO) series (Fig. 2.1a). There is a large variation in K_2O within the shoshonitic rocks with similar content in SiO_2, and a potassic series (KS) has been defined to distinguish the younger high-K rocks of Stromboli and Vulcano (Fig. 2.3). (Ellam et al., 1988; Crisci et al., 1991; De Astis et al., 2000; Francalanci et al., 2004, 2007; Peccerillo, 2005; Peccerillo et al., 2013). Since the KS rocks are also the youngest erupted among the whole archipelago, some authors suggest that the subduction may be in its senile evolutionary stage (Barberi et al., 1973). Many authors agree that the large compositional range of erupted magmas is due to various processes such as the occurrence of different mantellic sources (e.g. MORB- vs. OIB-like mantle) below the arc, variation of the amount and type of metasomatizing agents in the mantle source (e.g. fluids vs. sediments) (Ellam et al., 1988; De Astis et al., 2000; Francalanci et al., 2007), or to shallow level processes

of magmatic evolution such as fractional crystallization and crustal assimilation (AFC) of magmas derived from heterogeneous mantle (Ellam and Harmon, 1990).

The erupted rocks show a large compositional variability, even within the same magmatic series (Fig. 2.3). In the western sector, erupted magmas are mainly basaltic to andesitic (rhyolites have been erupted at Salina), while in the central sector, the erupted products show a wider compositional range, ranging from basalt to rhyolite (Peccerillo et al., 2013).

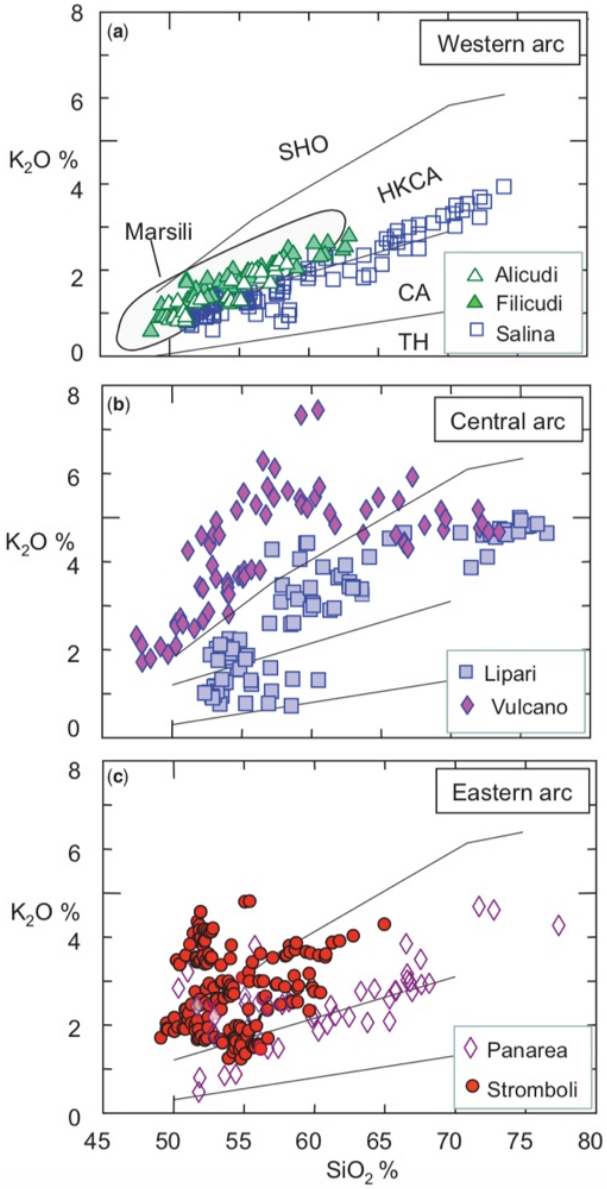

Figure 2.3 – K_2O vs. SiO_2 of Aeolian Islands rocks (Peccerillo et al., 2013).

2.3 Vulcano Island: geological and structural background

Vulcano is the southernmost island, and the third for extension (21.2 km^2) of the Aeolian archipelago (Fig. 2.1a). The island is the emerged part of a complex volcanic edifice whose base is approximately 1000 m below sea the level (Fig. 2.4a) (Beccaluva et al., 1985; Ventura et al., 1999; Romagnoli et al., 2013).

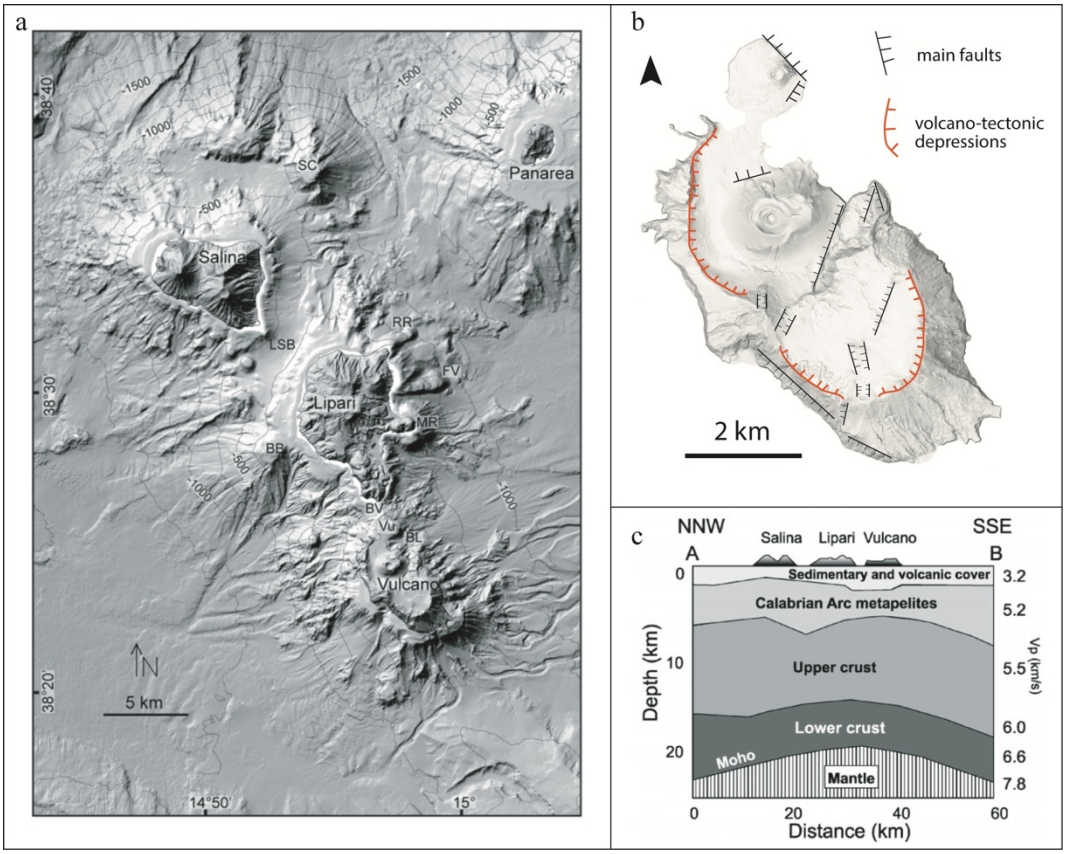

Figure 2.4 – a: Shaded relief map of the central sector of Aeolian Islands (Romagnoli et al., 2013); b: simplified structural map of Lipari and Vulcano islands (modified from Gioncada et al., 2003); c: crustal velocity model and crustal structure below of the central sector of Aeolian Islands (Peccerillo et al., 2006).

Together with Salina and Lipari, Vulcano forms an NNW-SSE trending structure that intersects the arc in his central sector along the Tindari-Letojanni strike slip fault system (Figs. 2.2 and 2.4b) (Ventura et al., 1999; De Ritis et al., 2005). As a consequence, the tectonic structure of the island is controlled by main NW-SE trending fault systems (Frazzetta et al., 1982; Mazzuoli et al., 1995; Ventura et al., 1999; Ruch et al., 2016) which, together with subordinated NNE-

SSW trending normal fault systems, represent the surface expression of the Tindari-Letojanni fault (Fig. 2.4b). Mazzuoli et al. (1995) and Ventura et al. (1999) suggest that these lineaments can have a role in the formation of the morpho-tectonic depressions of Lipari and Vulcano islands, such as the volcano-tectonic depression of La Fossa caldera (see section 2.4), that have been interpreted as pull-apart type structures.

The tectonic framework of the central sector of Aeolian Islands probably plays a key role in the location of eruptive vents, which at Lipari and Vulcano are mainly aligned NW-SE and become younger from S toward N, especially during the latest stages (<55 ka) of development of these two islands (Gioncada et al., 2003; Ruch et al., 2016). To better define the tectonic-magmatic relations in a context dominated by a strike-slip system, Ruch et al. (2016) carried out a detailed stratigraphic-structural survey. Most of the identified structures are NNE-SSW to NNW-SSE oriented, eastward dipping, and show an almost dip-slip movement consistent with a E-W extension. Following these observations, a model has been proposed in order to explain the magmatic-structural evolution of the central sector of the arc. This model suggests that magmatic events generate the stress necessary to create the observed structures, instead of considering the magma pathways conditioned by the strike-slip fault systems (Mazzuoli et al., 1995; Ventura et al., 1999). Briefly, the stress field would vary from pure strike-slip type movements oriented NW-SE along the Tindari-Letojanni, to an extensional regime associated with faulting with NNW-SSE to N-S structures observed at Lipari and Vulcano islands. These structures, which appear to have a spatial and temporal relationships with the magmatic events, support the hypothesis that most of them derive from short eruptive episodes (Ruch et al., 2016). The same authors also suggest that the main stress would changes from horizontal (regional tectonic stress) to vertical (dominant magmatic stress) thank to the presence of a stable magmatic system below Lipari and Vulcano capable to modify the local stress field. This would therefore explain the general N-S orientation of many structures as well as their progressive migration to NE of the eruptive vents in both islands (Fig. 2.5). This

would reinforce the hypothesis that consider these two islands as part of a single volcanic complex, the Lipari-Vulcano complex (LVC, Gioncada et al., 2003).

As suggested by geophysical data, Vulcano island lies on a 20–25 km thick crustal structure made up by three main horizons: mafic and felsic granulites of the lower and upper crust, respectively, and metapelites of the Calabrian Arc (Fig. 2.4c) (Ventura et al., 1999; Peccerillo et al., 2006).

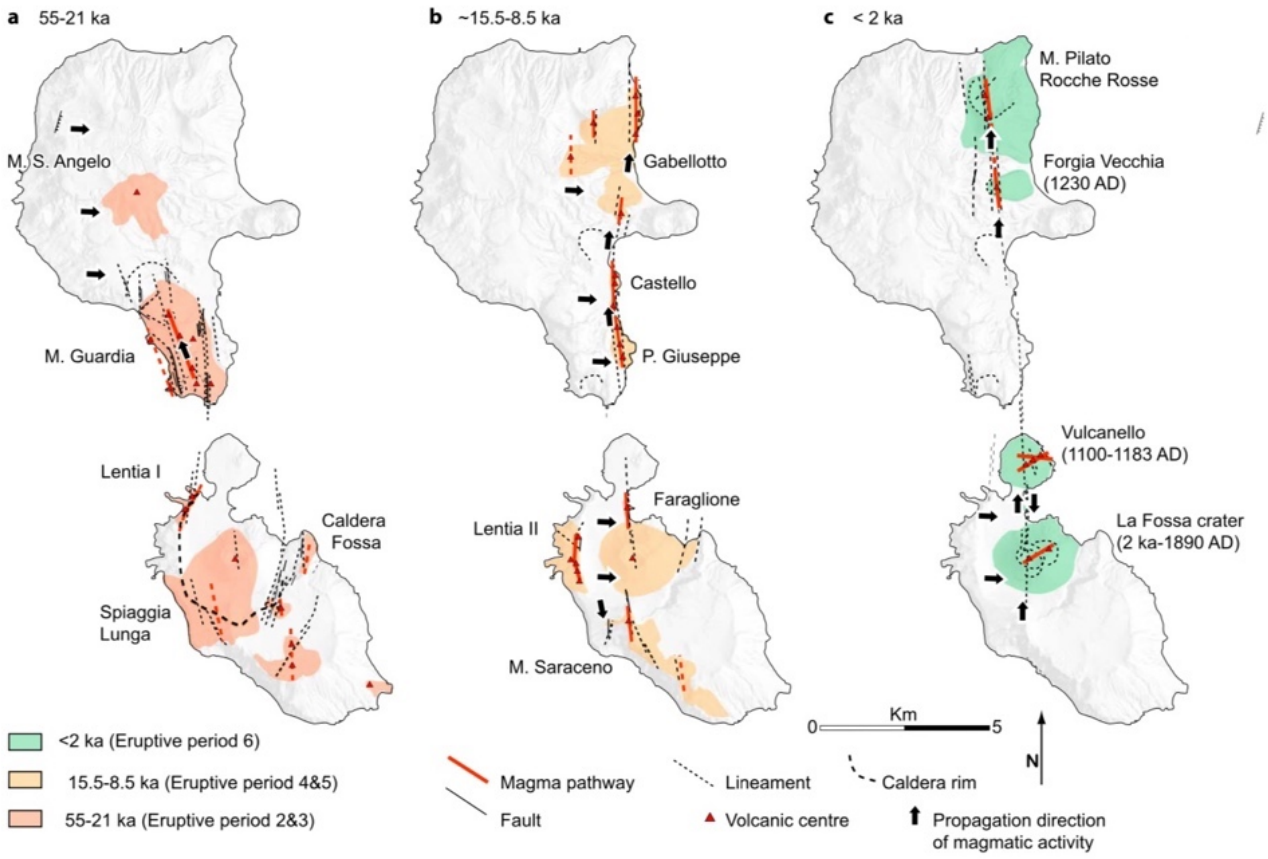

Figure 2.5 – Tectono-magmatic evolution of the Lipari-Vulcano complex (Ruch et al., 2016).

2.4 Eruptive history of Vulcano Island

The eruptive history of Vulcano has been divided in 8 eruptive epochs (Fig. 2.6) (De Astis et al., 2013 and reference therein). The volcanic activity started in the southern part of the island in a period between ~130 and 99 ka with the formation of Vulcano Primordiale stratovolcano. The Vulcano Primordiale was affected by a collapse that formed the Piano Caldera, a sub-circular volcano-

tectonic structure of about 2.5 km in diameter. The Piano Caldera was progressively filled by lava flows emitted between ~78 and 42 ka and by more recent pyroclastic units, with mostly mafic compositions belonging to the HKCA and SHO series, erupted from the centers of Monte Aria, Piano di Luccia, Monte Rosso and La Sommata. The products of La Sommata are particularly important by a geochemical point of view, being the less evolved of the entire magmatic series of Vulcano (De Astis et al., 1997; Gioncada et al., 1998; Lanzo et al., 2016; Palummo et al., 2020). Between 50 and 20 ka the volcanic activity moved outside the Piano Caldera, resulting in the centers of Monte Luccia, Spiaggia Lunga, Gelso and Quadrara (De Astis et al., 1997; Pinarelli et al., 2019; Nicotra et al., 2020; Palummo et al., 2020). Since ~28 ka, the volcanic activity shifted toward NW with the formation of the Mastro Minico-Lentia complex, made up by lava flows and domes ranging from latite to rhyolite in composition (De Astis et al., 1997; Gioncada et al., 2003). The Lentia complex marks the western border of the second main volcano-tectonic collapse happened on the island, the La Fossa Caldera, located in the NW sector of Vulcano (De Astis et al., 2013; Casalbore et al., 2019). The eruptive activity occurred in the last ~15 ka is related to the La Fossa Caldera system. Effusive and explosive eruptions occurred between ~15 and 8 ka, associated with vents located in the southern border (Tufi di Grotte dei Rossi, Monte Saraceno) or inside (e.g. Lave della Roja) the La Fossa Caldera, and consisted of different volcano-stratigraphic units from shoshonitic to latitic composition (Gioncada and Sbrana, 1991; De Astis et al., 1997; Meschiari et al., 2020). Latitic submarine lavas and minor pyroclastics filled the depression (Gioncada and Sbrana, 1991). The volcanic center of La Fossa cone has grown during the last 6 ka in the middle of La Fossa Caldera. La Fossa consists of lavas and pyroclastic products ranging from latite to rhyolite in composition, and last erupted in AD 1888–1890 (Mercalli and Silvestri, 1891; Keller, 1980; Frazzetta et al., 1983; De Astis et al., 1997; Dellino, 1997; Arrighi et al., 2006; Di Traglia et al., 2013). The migration of volcanic activity toward N in the northern border of La Fossa Caldera, eventually originated the Vulcanello peninsula, that represents the most recent volcanic structure of the island (Arrighi et al., 2006; Di Traglia et al., 2013; Fusillo et al., 2015). Vulcanello consists of three partially overlapped cones and a lava platform, with volcanic

products ranging from shoshonite to trachyte in composition (Davì et al., 2009; Fusillo et al., 2015).

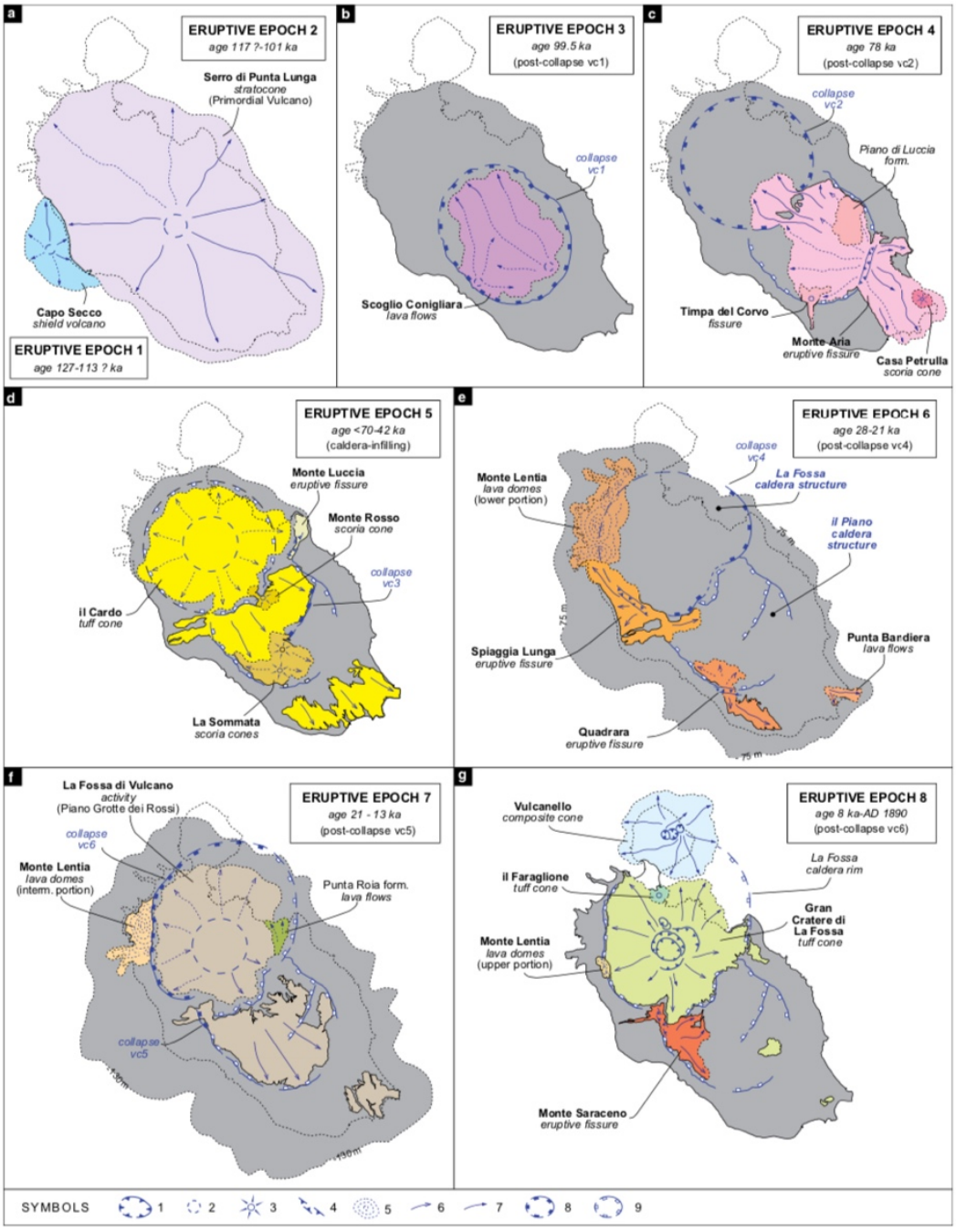

Figure 2.6 – Sketch map showing the eruptive history and the building of Vulcano Island (De Astis et al., 2013).

2.5 Geochemistry and petrogenesis of Vulcano magmas

The eruptive products emplaced at Vulcano cover the entire compositional spectrum from basalt to rhyolite and show prevalently shoshonitic affinity (SHO) and at a lesser extent high-K calc-alkaline affinity (HKCA) and potassic (KS). Shoshonitic rocks show a wide degree of K_2O content (up to 7.5 wt.%). These rocks are classified as trachytes (if the TAS, Total alkali versus Silica diagram, is considered) or latites (when considering the K_2O vs. SiO_2 diagram of Peccerillo and Taylor, 1976) (Fig. 2.7). In several cases the mafic-intermediate products of Vulcano are slightly silica undersaturated, as common in the SHO series. Part of the mafic rocks in the last eruptive epoch are more silica-undersaturated and they have been included in the potassic series (KS) (De Astis et al., 2000). Figure 2.7 shows that the rocks representative of the first eruptive epochs (EE 1–7 of De Astis et al., 2013) fall between the HKCA and SHO fields with composition ranging from basalt to basaltic andesite and shoshonite, to rhyolite. The last eruptive epoch, mainly represented by the complex system of La Fossa and Vulcanello, embraces those ascribable to the KS series (Fig. 2.7).

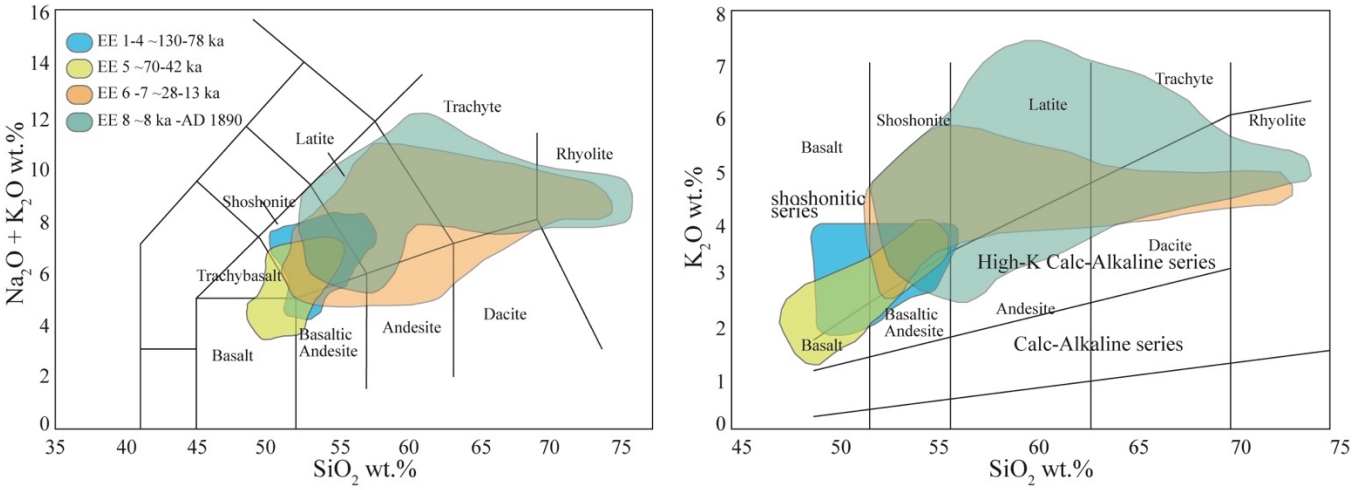

Figure 2.7- Total alkali versus silica diagram (TAS) and K_2O versus SiO_2 diagram for the whole eruptive products of Vulcano Island (modified from De Astis et al., 2013).

Major elements show negative correlations of MgO, FeO, Fe_2O_3, CaO and TiO_2 with SiO_2 and positive correlation of K_2O, Na_2O, Al_2O_3 and P_2O_5 up until 55-60% wt.% SiO_2. At about 60 wt.% SiO_2, the alkali contents as well as Al_2O_3 and

P_2O_5 tend to decrease. This is in accord with the fractionation of a mineral assemblage constituted by olivine, clinopyroxene, Ti-magnetite and plagioclase up to intermediate compositions and then fractionation of alkali feldspar, biotite and apatite in evolved magmas (Del Moro et al., 1998; Gioncada et al., 1998). The involvement of feldspars fractionation in the genesis of the most silicic products is also testified by the REE patterns that show marked Eu anomalies in the most evolved rocks (Clocchiatti et al., 1994; De Astis et al., 1997; Del Moro et al., 1998; Gioncada et al., 1998; Piochi et al., 2009).

Patterns of incompatible trace elements of the erupted mafic rocks (MgO < 3.8 wt.%) show the typical signature of subduction related magmas with negative anomalies in Nb, Ta and Ti (Fig. 2.8). Moreover, these patterns display how the mafic HKCA rocks of the older eruptive epochs show lower concentrations of incompatible trace elements than the younger KS rocks (Fig. 2.8) (De Astis et al., 1997; Del Moro et al., 1998; Gioncada et al., 1998). The transition (at ~ 30-28 ka) between the older HKCA series and the younger SHO to KS series coincides with the emplacement of the products belonging to the Spiaggia Lunga eruption (Pinarelli et al., 2019). These variations have been explained by several authors with a complex interplay of various processes, such as change in primary melt compositions, different mantle sources (fertile asthenospheric or residual lithospheric), mantle source heterogeneities (OIB-like or MORB-type), different amount and type of metasomatizing contaminant (sediment and/or fluid), various degree of partial melting of the source, assimilation of different crustal material (upper crust versus lower crust) and lower pressure processes of magmatic differentiation (e.g. assimilation and fractional crystallization or pure fractional crystallization) (Ellam et al., 1988; Ellam and Harmon, 1990; De Astis et al., 1997; Del Moro et al., 1998; Gioncada et al., 1998; De Astis et al., 2000; Frezzotti et al., 2004; Pinarelli et al., 2019). In figure 2.8, the change in the incompatible trace element content of the melt inclusions hosted in Fo_{90} olivine crystals found in the La Sommata basalt and in the products of the AD 1888–1890 eruption, representing the primitive melts related to the two different evolutive series (Gioncada et al., 1998), is shown.

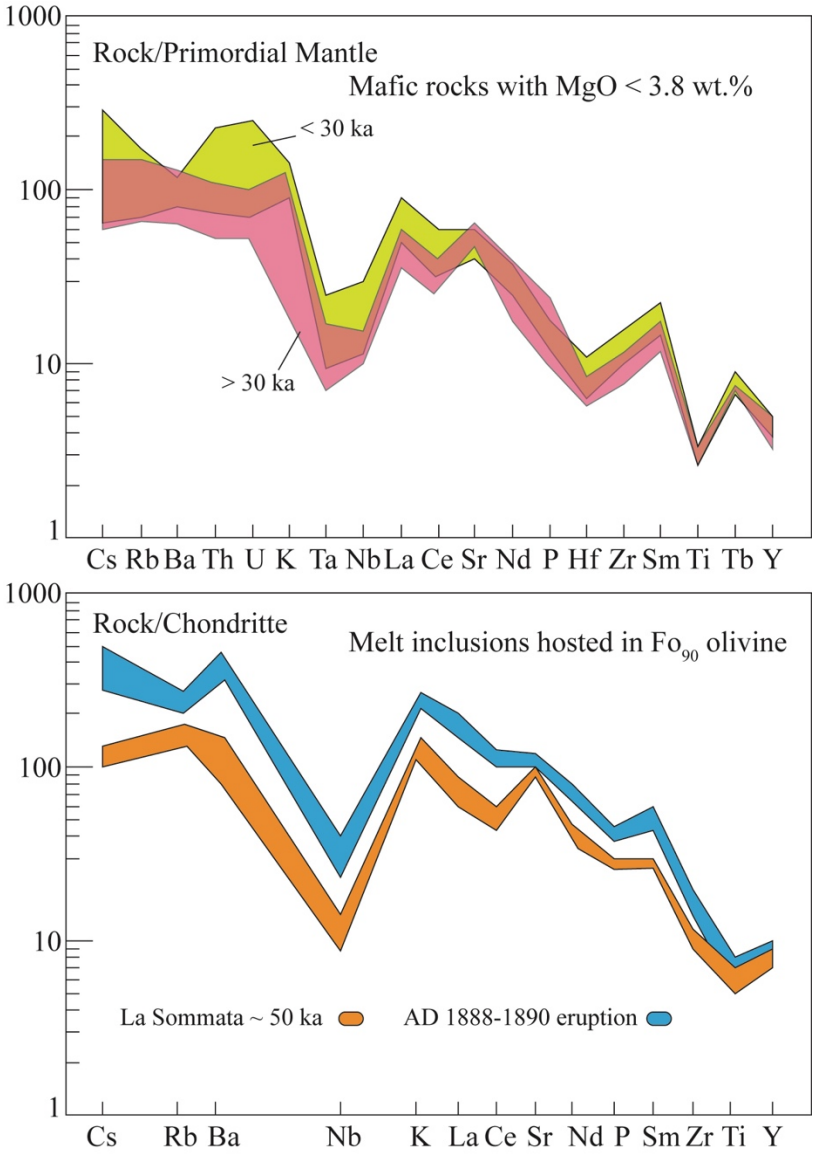

Figure 2.8 – Incompatible trace element contents for the mafic rocks of Vulcano (modified from De Astis et al., 2013) and for the La Sommata and AD 1888–1890 eruption melt inclusions (modified from Gioncada et al., 1998).

As regards the models concerning the evolution of the plumbing system of Vulcano, several geochemical petrological works have been carried out (De Astis et al., 1997; Del Moro et al., 1998; Gioncada et al., 1998; Zanon et al., 2003; Frezzotti et al., 2004; Nicotra et al., 2018, 2020; Palummo et al., 2020). De Astis et al. (1997), on the basis of petrological and geochemical data including isotopic data, suggest that magma differentiation processes occur in various reservoirs located at several depths. The HKCA and SHO magmas of the older eruptive epochs (EE 1–5, De Astis et al., 2013), evolved at depth, probably at the transition between lower

and upper crust, thanks to continuous processes of crustal assimilation and fractional crystallization (AFC) and mixing with primary melts originated in the mantellic source (De Astis et al., 1997). This process is commonly called RAFC (AFC in a continuously refilled and tapped magma chamber, De Astis et al., 1997). According to fluid inclusions trapping pressure data, a stable 19–16 km depth reservoir associated to a shallower (5–3 km) reservoir is present during this time (Zanon et al., 2003; Palummo et al., 2020). The higher degree of evolution of the products of the eruptive epochs 6–7 (e.g. rhyolites of Lentia complex), reveals a change in the magma differentiation process, with a major role of the AFC of shoshonitic magmas with respect to RAFC process of the previous epochs and mixing processes between evolved and intermediate magmas at shallow levels (De Astis et al., 1997). The textural and compositional characteristics of the products erupted during the most recent epoch (EE 8; De Astis et al., 2013) emphasize a higher complexity of the plumbing system. Indeed, La Fossa, in a relatively small time interval, erupted a great variability of products with abrupt, irregular, compositional variations with time (Clocchiatti et al., 1994; De Astis et al., 1997; Davì et al., 2009; Piochi et al., 2009). De Astis et al. (1997) and Del Moro et al. (1998) explain the geochemical and isotopic characteristics of the products emplaced during this period with a two-stage model: the first one dominated by RAFC process of shoshonitic magmas in the lower crust (~21 km; Zanon et al., 2003) and the second, at lower pressure, dominated by AFC and mixing between melts at various degree of evolution in small reservoirs in the upper crust (5–2 km). A general scheme of the petrologic evolution of Vulcano is shown in figure 2.9. Since the main focus of this thesis is the magmatic system of the active center of La Fossa in the last 1000 years, a more detailed review of its products, as well as the current understandings of the recent plumbing system, will follow in the next chapter.

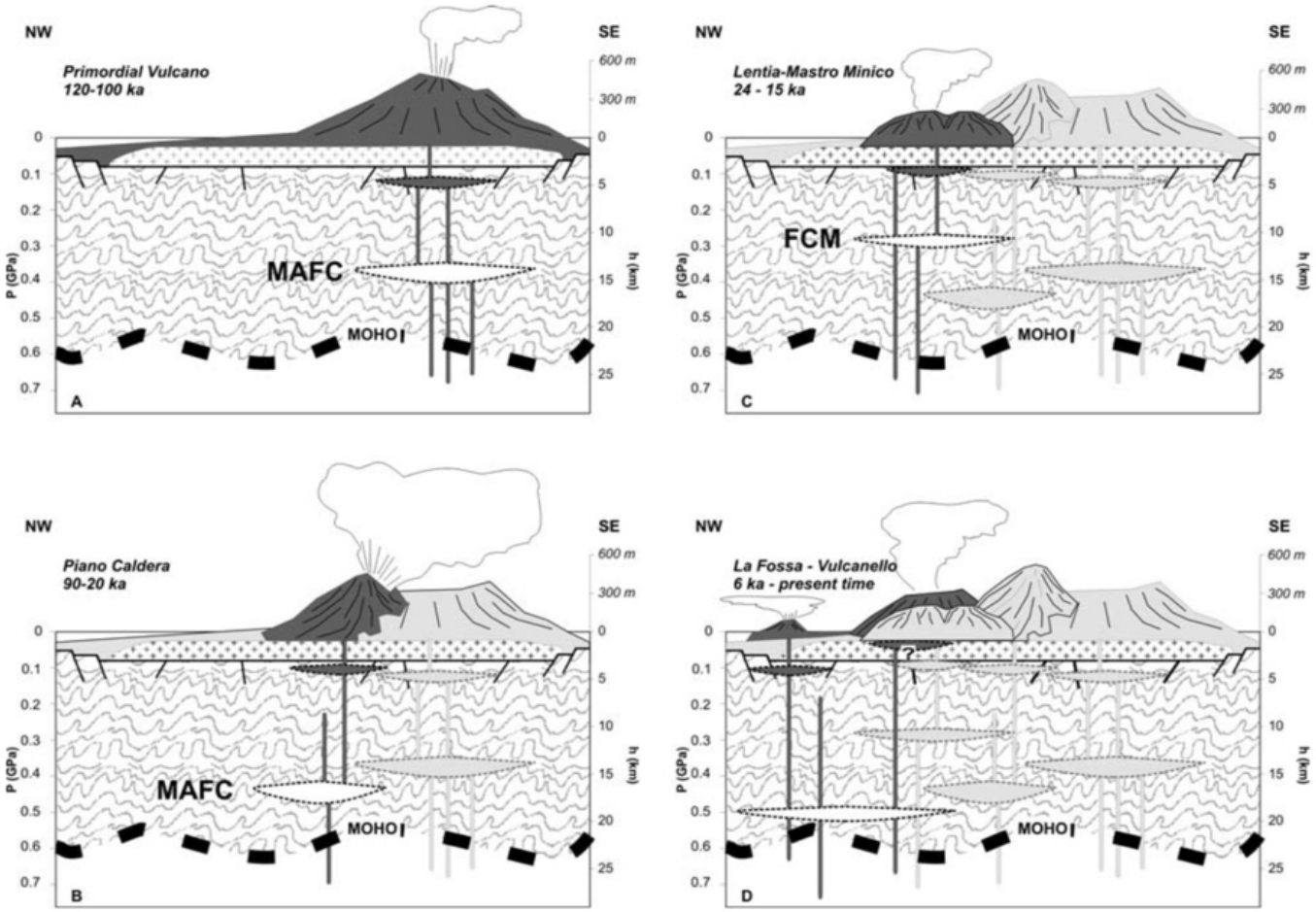

Figure 2.9 – Schematic model of the magma plumbing system evolution of Vulcano (Zanon et al., 2003); MAFC: mixing with mafic magmas plus crustal assimilation and fractional crystallization; FCM: high rates of fractional crystallization and minor mixing with mafic magmas.

3 La Fossa volcano in the last 1000 years: state of the art

3.1 Introduction

In the middle of La Fossa Caldera, during the last ~6000 years, the 391 m-high composite volcano of La Fossa has grown (Fig. 3.1) (Keller, 1980; Frazzetta et al., 1983, 1984; De Astis et al., 2013; Di Traglia et al., 2013). The edifice has a conical shape with an elliptical base and the summit area is characterized by a general NE-SW trending direction resulted by the overlapping of several structures (Fig. 3.1) (Di Traglia et al., 2013). The volcano erupted both with explosive (sub-plinian, long lasting vulcanian eruption and ash emissions) and effusive styles resulting in the emplacement of pyroclastic fallout deposits (ash layer, pumices, blocks and breadcrust bombs), minor pyroclastic density current deposits, lava flows and breccia deposits from phreatic/phreatomagmatic explosions (Clocchiatti et al., 1994; Piochi et al., 2009; Dellino et al., 2011; Gurioli et al., 2012; De Astis et al., 2013; Rosi et al., 2018; Selva et al., 2020). Since the last eruption in AD 1888–90, the volcano is in state of rest characterized by an intense fumarolic activity and moderate seismicity (Selva et al., 2020). At least in five episodes of unrest occurred between 1985 and 2009, the temperature of the fumaroles, mainly found in a fumarolic field located in the northern border of the present day crater, raised up to 700°C, in association to ground deformation of the area interested by gas emissions and of the CO_2 flux (Chiodini et al., 1995; Granieri et al., 2006; Paonita et al., 2013; Inguaggiato et al., 2018).

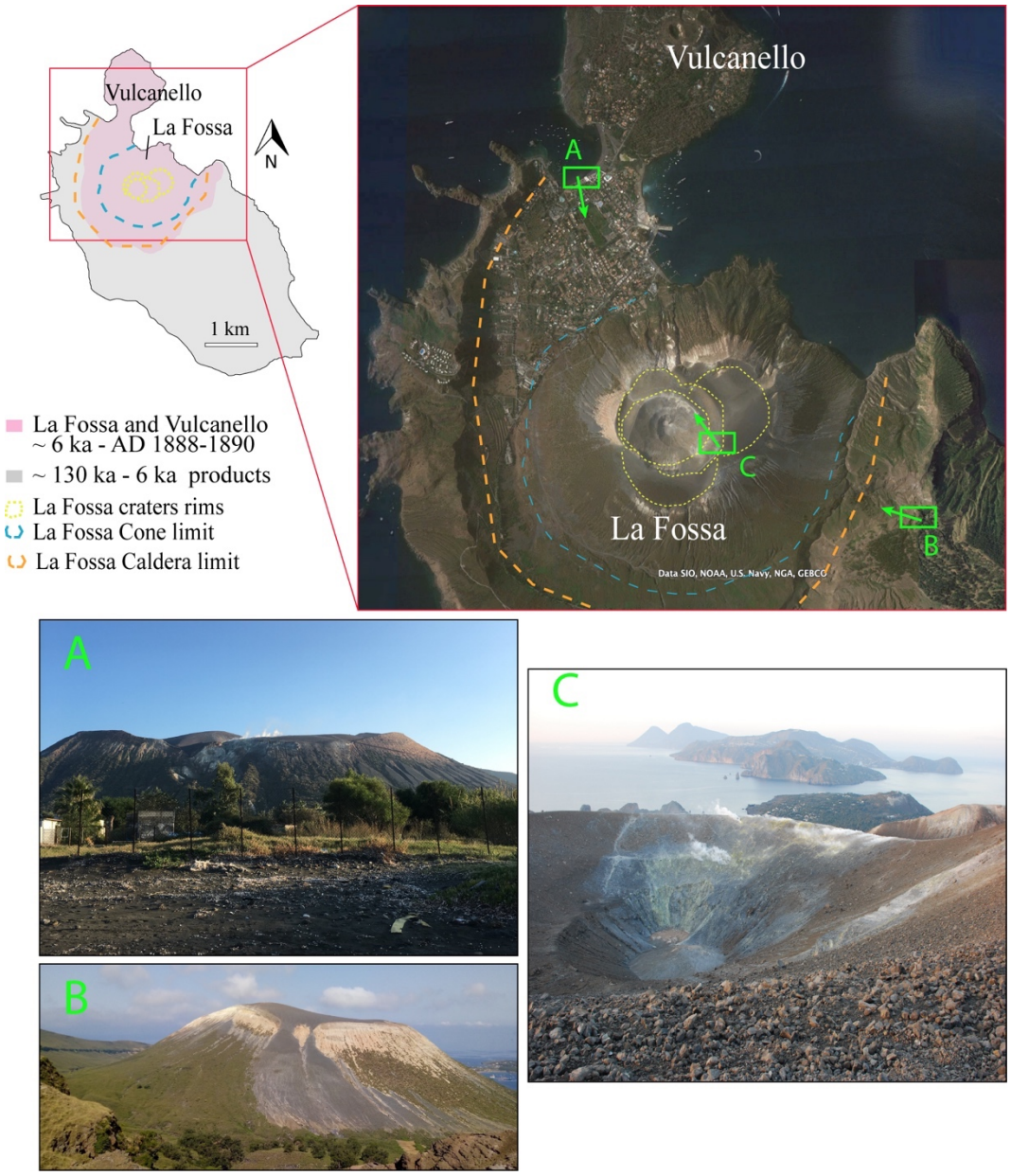

Figure 3.1 – Simplified geological map of Vulcano with the location of La Fossa volcano inside the La Fossa Caldera (from Google Earth) and panoramic views of the volcanic edifice, of the present day crater and the fumarolic field.

3.2 Deposit stratigraphy of the last 1000 years

The main works concerning the stratigraphy of La Fossa volcano have been carried out by Keller (1980), Frazzetta et al. (1983), La Volpe et al. (1997), De Astis et al. (2013) and Di Traglia et al. (2013). Since this thesis mainly focuses on the recent plumbing system of La Fossa, in the following the stratigraphic reconstruction for the last 1000 years activity proposed by Di Traglia et al. (2013)

is summarized and the corresponding nomenclature of the volcanic units is adopted. This reconstruction employs the Unconformity-Bounded Stratigraphic Units for volcanic terrains (De Rita et al., 1998) and uses the expression "eruptive cluster" for grouping the eruptions close in time that form a stratigraphic unit hierarchically higher than an eruptive unit but lower than an eruptive epoch. In this framework, the eruptive cluster is bounded by unconformities identifiable over a wide area (Di Traglia et al., 2013). Following this reconstruction, the eruptive history of the last 1000 years is summarized in two main eruptive clusters: the Palizzi-Commenda eruptive cluster (PCEC), developed during the 12–13th centuries, and the Gran Cratere eruptive cluster (GCEC, 15th century-1890 AD) (Fig. 3.2). The stratigraphic sequence of PCEC displays a large variety of eruptive products and a wide spectrum of magma compositions, ranging from latite to trachyte and rhyolite (Figs. 3.2 and 3.3, see also section 3.3). It encompasses the products belonging to the Palizzi eruptive unit (PEU) and of the Commenda eruptive unit (CEU): i) latitic and trachytic cross-stratified and parallel-bedded ash layers (Pal A and Pal C); ii) pumiceous fallout layers of rhyolitic and trachytic composition (Pal B and Pal D, respectively); iii) lava flows, including the rhyolitic obsidian Commenda lava and the trachytic lava flows of Palizzi, Campo Sportivo and Punte Nere; iv) ash layers and widely dispersed pyroclastic density currents deposits associated to the hydrothermal eruption of Breccia di Commenda (Gurioli et al., 2012; Rosi et al., 2018). The GCEC includes the products of the Lower and Upper Pietre Cotte eruptive units, consisting of: i) latitic ash and lapilli layers; ii) rhyolitic pumiceous fallout layers iii) the rhyolitic AD 1739 Pietre Cotte lava flow (Piochi et al., 2009; Vetere et al., 2015; Bullock et al., 2019). The uppermost part of the GCEC is represented by the products of the AD 1888–1890 eruption, consisting of latitic spatters, trachytic and rhyolitic ash and lapilli layers and the characteristic breadcrust bombs, trachytic and rhyolitic in composition (Clocchiatti et al., 1994).

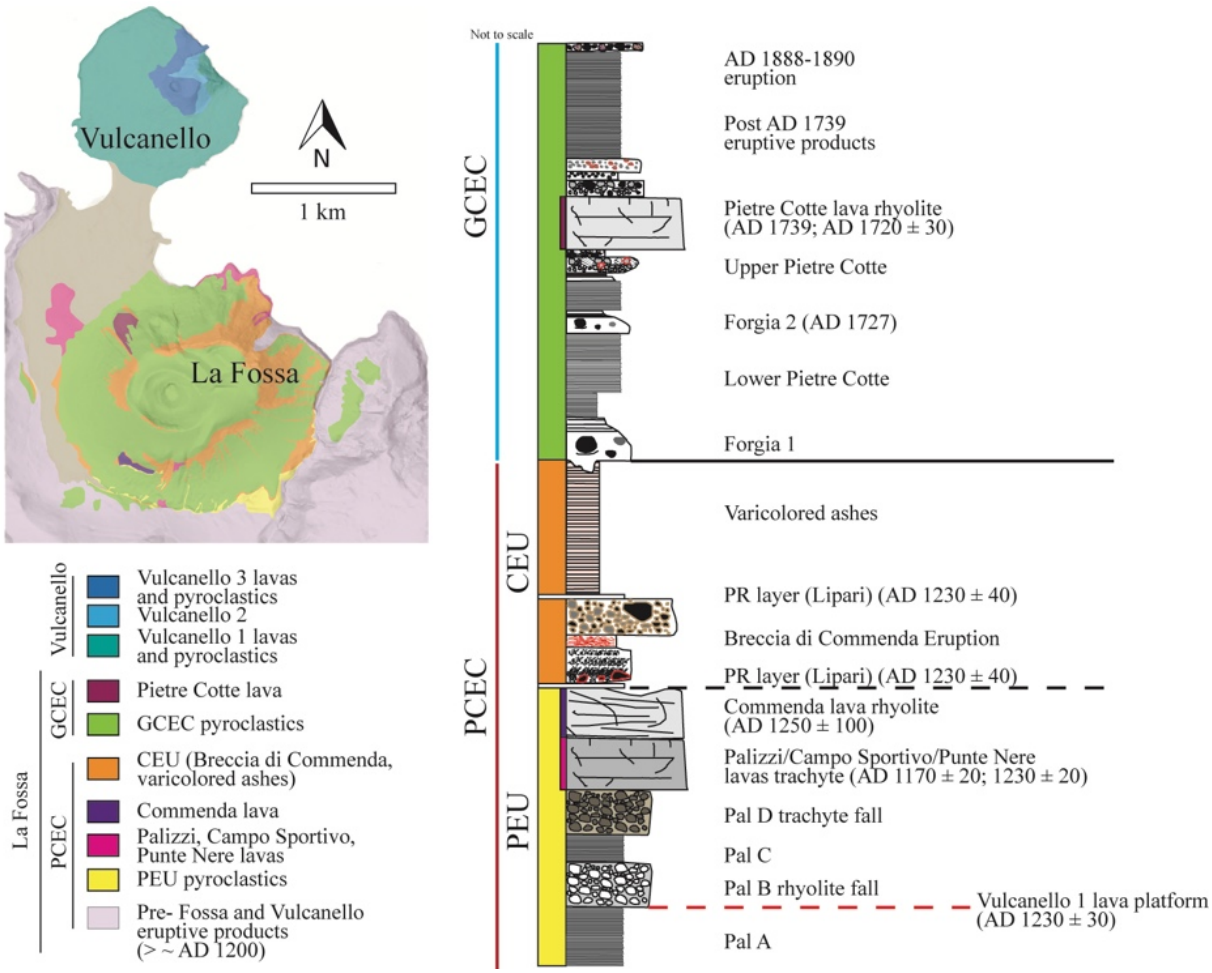

Figure 3.2 – Simplified geological sketch map and stratigraphy for the products of the last 1000 years of La Fossa and Vulcanello (modified from Di Traglia et al., 2013). Ages are from Arrighi et al., 2006. See the review of Selva et al (2020) for a complete chronological framework. PCEC (Palizzi Commenda eruptive cluster); PEU (Palizzi eruptive unit); CEU (Commenda eruptive unit); GCEC (Gran Cratere eruptive cluster).

The Palizzi Eruptive Unit

The products investigated in this work mainly belong to the Palizzi eruptive unit (Fig. 3.2) (PEU, Di Traglia et al., 2013). The sequence is variably exposed in several outcrops on the southern flanks of La Fossa, in the Palizzi valley and in the neighboring ring plain at the base of the volcanic cone (Fig. 3.2). The products of the PEU are particularly relevant in the framework of the last 1000 years of activity of La Fossa. Indeed, during this period, a large volume of volcanic materials was erupted, resulting in a substantial growth of the volcanic edifice (Di Traglia et al., 2013). Following this phase of the volcanic history of La Fossa, there is a sharp

decrease in the volume of the erupted material (De Astis et al., 2013; Selva et al., 2020). Given its importance, this eruptive sequence has been chosen as a reference event for short terms eruptive scenarios in the evaluation of volcanic hazard at Vulcano island (Dellino et al., 2011; Selva et al., 2020). The products emitted during the PEU are the results of: i) long lasting vulcanian activity with associated pyroclastic density currents; ii) lava flows; iii) high intensity, short-lived sustained explosive eruptions (Dellino et al., 2011; Biass et al., 2016; Selva et al., 2020). With the exception of Pal A, for which there is a lack of direct stratigraphic and chronological constraints, the PEU products were emplaced after the formation of Vulcanello 1 lava platform dated back to AD 1050 ± 70 to 1230 ± 30 (Fig. 3.2) (Arrighi et al., 2006; Di Traglia et al., 2013; Fusillo et al., 2015), given the presence of the Pal B layer directly on top of it (see the review of Selva et al., 2020 for a complete chronostratigraphic framework). The stratigraphic position of the Commenda lava is uncertain, and considered older (De Astis et al., 2013) or younger (Di Traglia et al., 2013) than the Palizzi, Punte Nere, Campo Sportivo lavas, which are grouped by Di Traglia et al. (2013) in the same eruptive period

3.3 Major and trace element geochemistry of volcanic products

The products of La Fossa and Vulcanello of the last 1000 years are classified in the TAS diagram and in the K_2O versus SiO_2 diagram of Peccerillo and Taylor (1976) and grouped following the stratigraphic units (Fig. 3.3). The products emplaced during this time span belong to the shoshonitic series and range from shoshonite to rhyolite in composition. The alkali behavior in the eruptive products is noteworthy. In the trachytic field the samples branch out essentially in two arrays, with the majority of them that describe a linear trend that reaches rhyolitic compositions with an almost constant K_2O content (Fig. 3.3). The other group, that basically correspond to the trachytic pumice of Pal D (see chapter 6), show a K_2O content higher than the all products of the entire volcanic succession of the island (Figs. 2.7 and 3.3). The products that maintain a constant alkali content show linear trends in all the other variation diagrams (Fig. 3.3). These products are essentially represented by the pyroclastic products of Upper Pietre Cotte and of the AD 1888–

1890 eruption (De Fino et al., 1991; Clocchiatti et al., 1994; Del Moro et al., 1998; Rossi et al., 2019). When the petrographic features of these products are considered, it is evident how their compositions is determined by mixing processes between a latitic and a rhyolitic end members (De Fino et al., 1991; Clocchiatti et al., 1994; De Astis et al., 1997; Del Moro et al., 1998; Gioncada et al., 1998) (see also section 3.4 and chapter 6). Interestingly, if the products originated by mixing are not considered, there is a marked compositional gap between the erupted intermediates magmas (latites) and rhyolites. Trace elements compositions suggest that the evolved rhyolitic magmas derive through substantial feldspars fractionation by intermediate ones. Indeed, rhyolites always display very low concentration of Ba, Sr and Eu indicative of intense feldspar removal under relatively low fO_2 conditions (Clocchiatti et al., 1994; De Astis et al., 1997; Del Moro et al 1998; Gioncada et al., 1998; Piochi et al., 2009) (Fig. 3.4). All these features, including the genesis of the K-rich trachytic composition and of rhyolites will be quantitively discussed in chapter 6.

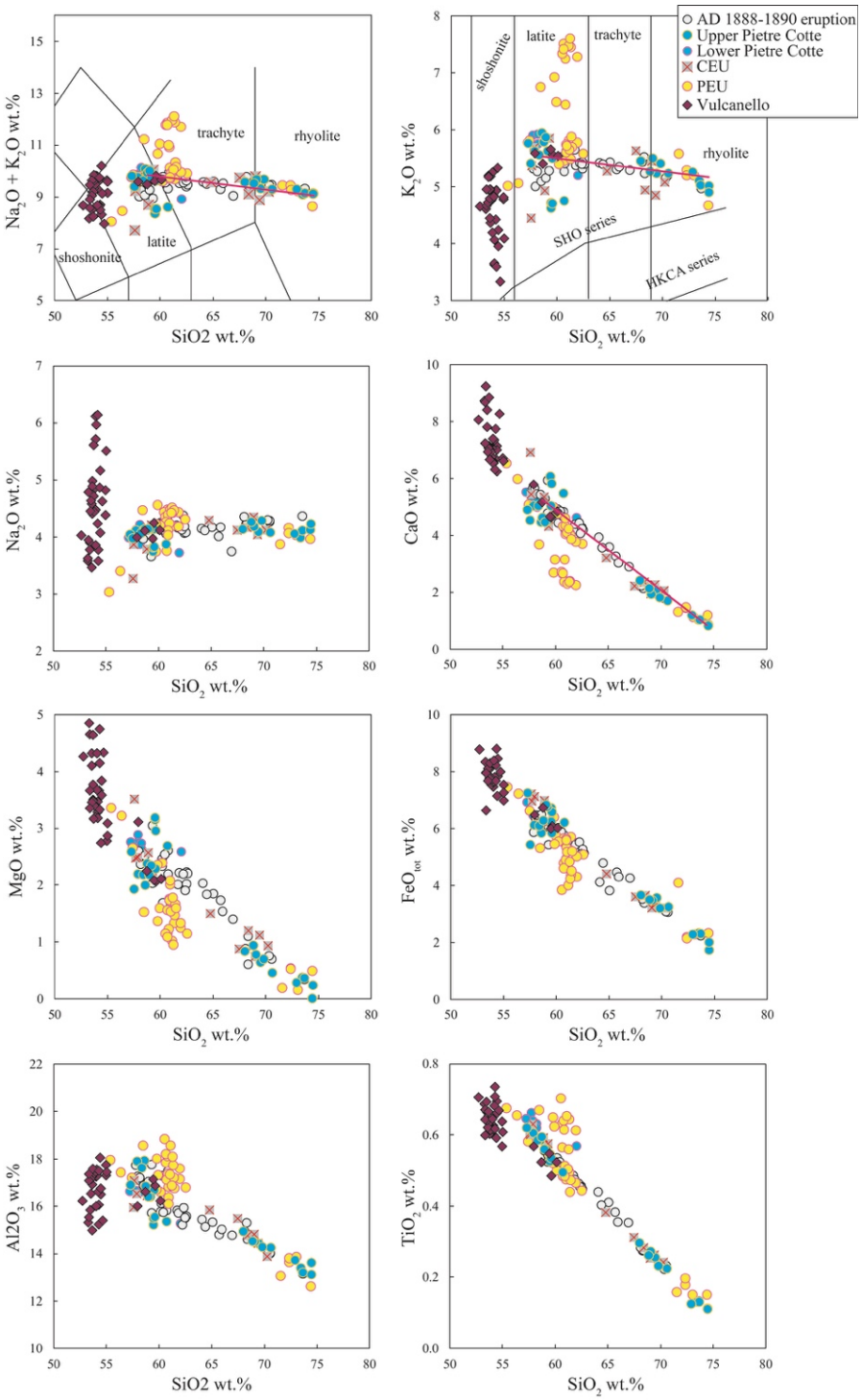

Figure 3.3 – Major element variation diagrams for the products erupted at La Fossa and Vulcanello in the last 1000 years. The red line shows the suggested mixing trend between latites and rhyolites (Clocchiatti et al., 1994; Del Moro et al., 1998). Major elements are recalculated to 100% on anhydrous basis. Data are from Clocchiatti et al. (1994), Gioncada (1997), Del Moro et al. (1998), Davì et al. (2009), De Astis et al. (2013), Fusillo et al. (2015), Nicotra et al. (2018), Pinarelli et al. (2019) and this work.

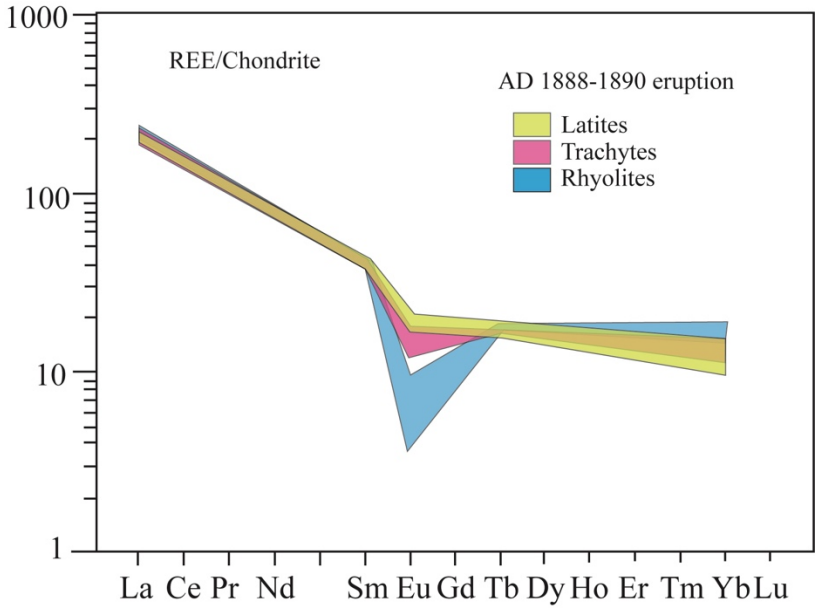

Figure 3.4 – REE patterns for the products involved in the AD 1888–1890 eruption (modified from Clocchiatti et al., 1994).

3.4 La Fossa plumbing system

Crystallization pressure, temperature and water content of magmas

The plumbing system of La Fossa cone has been object of several studies that reported petrological evidences of magma mixing processes, such as the occurrence of magmatic enclaves and banding of latitic and trachytic compositions within rhyolitic lava flows and pyroclastic products (Frazzetta et al. 1983; De Fino et al. 1991; Clocchiatti et al. 1994; Piochi et al. 2009; De Astis et al. 2013; Bullock et al. 2019; Rossi et al. 2019). The combination of petrological and geochemical data, including melt, fluid inclusions and gas geochemistry (Clocchiatti et al. 1994; Gioncada et al. 1998; Zanon et al. 2003; Peccerillo et al., 2006; Paonita et al. 2013; Mandarano et al. 2016), contributed to envisage the plumbing system of La Fossa as a complex polybaric system, represented by multiple reservoirs that have been variably involved during the activity of both La Fossa and Vulcanello (Fig. 3.5) (Peccerillo et al. 2006; Davì et al. 2009; De Astis et al. 2013; Nicotra et al. 2018). The deepest reservoir (basaltic to shoshonitic) is presumably located between 21 and 18 km (Zanon et al., 2003). This reservoir directly fed the emission of mafic

magmas at Vulcanello through the border fault systems of the northern sector of La Fossa Caldera (Vetere et al., 2007; Davì et al., 2009). A shoshonitic to latitic storage level has been recognized between ~17 and 12 km (De Astis et al. 2013 and reference therein). The shallow crustal reservoirs hosting latitic to trachytic magmas are presumably located at depths comprised between 5 and 2 km (Zanon et al., 2003; Fulignati et al., 2018). A reservoir hosted at similar depth has been also suggested below Vulcanello (Zanon et al., 2003). An uppermost rhyolitic reservoir located at depth of about 1–2 km has been suggested by Clocchiatti et al. (1994) and Zanon et al. (2003) based on the study of secondary fluid inclusions found in metamorphic xenoliths, yielding to equilibration pressure and temperature of 30–60 MPa and ~1000 °C, respectively (Fig. 3.5).

Based on thermodynamic modelling, Vetere et al. (2015) estimated the pre-eruptive temperature of latitic and rhyolitic magmas involved in the mixing process leading to the effusion of the AD 1739 Pietre Cotte lava flow, obtaining temperature of about 1010 °C for the latite and 950 °C for the rhyolite at the time of the mixing. Thermometric analyses on melt inclusions by Clocchiatti et al. (1994) indicate crystallization temperatures of 1080 ± 10 and 1050 ± 10 °C respectively for the latite and trachyte involved in the AD 1888–1890 eruption. For what concerns the trachytes, these values are in agreement with the temperature range 1000–1130 °C inferred by Bullock et al. (2019) by mineral-melt thermometers for lati-trachytic magmas of Pietre Cotte, but are in excess compared to other recent temperature estimates by mineral-melt geo-thermometry for trachytic magmas of the recent activity (Palizzi, Pietre Cotte and AD 1888–1890) that indicate temperatures between ~950 and 1000 °C (Fulignati et al., 2018; Masotta and Mollo, 2019).

Based on a recent calibration of a plagioclase-liquid hygrometer, Masotta and Mollo (2019) estimated H_2O contents ranging from 2.5 to 3.5 wt.% for the latitic and trachytic magmas, respectively. Gioncada et al. (1998) measured values of H_2O between 0.3–0.6 and between 0.8–1.9 wt.% in the melt inclusions of shoshonitic and latitic composition respectively.

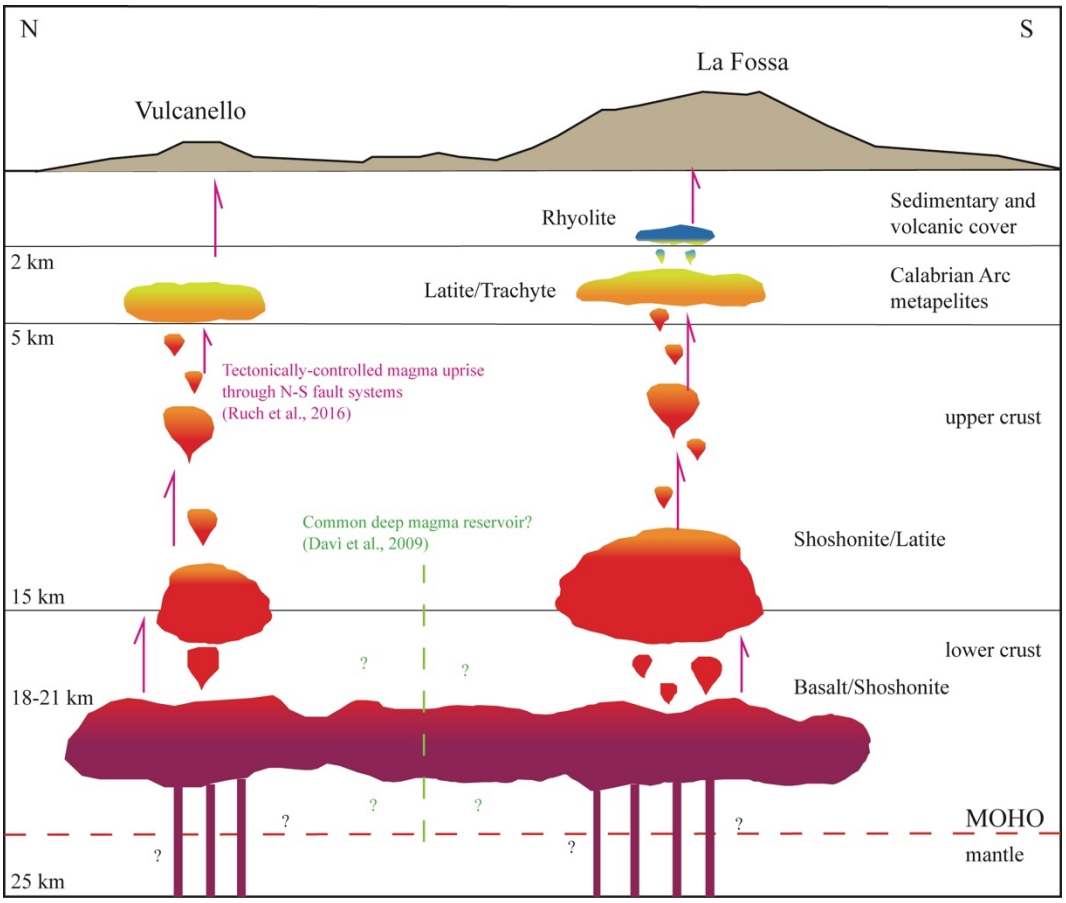

Figure 3.5 – Sketch model of the inferred plumbing system of La Fossa and Vulcanello during the last 1000 years (modified from Nicotra et al., 2018).

Magma differentiation and mixing processes

The great variability of petrographic and chemical characteristics of the products of La Fossa and Vulcanello raises many questions on the processes acting in the recent and still active magmatic system of the island. The widespread evidences of mixing processes and the relatively small volumes of the erupted magmas, suggest that several magmatic bodies evolved independently at various depth below the La Fossa-Vulcanello system (De Astis et al., 2013 and reference therein). Therefore, the plumbing system consists most likely of multiple storage levels with magma batches undergoing mutual interactions (Peccerillo et al., 2006; Piochi et al., 2009; De Astis et al., 2013; Vetere et al. 2015; Nicotra et al., 2018; Bullock et al., 2019). As previously written, De Astis et al. (1997) and Del Moro et al. (1998) explain the geochemical and isotopic characteristics of the products

emplaced during this period, with a two-stage model. In the first stage the basaltic SHO-KS magmas differentiates up to shoshonitic and latitic compositions with RAFC process in the lower crust (~21 km, Zanon et al., 2003). Then the second stage, at lower pressure, is dominated by AFC and mixing between evolved and intermediate magmas in several small reservoirs in the upper crust (5–2 km). This view implies that all the magma bodies feeding La Fossa and Vulcanello eruptions reasonably originated by a similar parental magmas and then evolved independently in various batches at several depths (De Astis et al., 2013). The least evolved magma emplaced in the last eruptive period is represented by the shoshonitic products of Vulcanello, but these are not considered the primary magmas of the system due to their isotopic composition ($^{87}Sr/^{86}Sr$ ~ 0.7046), their SiO_2 content (52–54 wt.%) and relatively low Mg# (45–50) (De Astis et al., 1997; Del Moro et al., 1998). Davì et al. (2009) suggest that the Vulcanello shoshonites differentiated by the parental shoshonitic basalts represented by the melt inclusions hosted in olivine (Fo_{90}) and reported in Gioncada et al. (1998) (Fig. 2.8). Moreover, the transition from undersaturated shoshonite to slightly silica saturates latites of La Fossa is likely accompanied by low rates of crustal assimilation (Davì et al., 2009). As regards the rhyolitic products erupted at La Fossa, the isotopic ratios suggest the assimilation of crustal material in their petrogenesis. Indeed, the mafic to intermediate rocks of La Fossa and Vulcanello have $^{87}Sr/^{86}Sr$ ~ 0.7046–0.7048, while the rhyolites reach values of $^{87}Sr/^{86}Sr$ ~0.7052–0.7056 (De Astis et al., 1997; Del Moro et al., 1998). The isotopic variations are thus correlated with the degree of evolution of the rocks with the most contaminated composition occurring in the most differentiated rocks that are consequently interpreted as the result of AFC processes (Fig. 3.6). Repeated oscillatory variations with time of the isotopic composition of the products of La Fossa testifies to frequent arrivals of mafic magmas, consequent AFC processes and syn-eruptive mixing (Del Moro et al., 1998). The crustal contaminant is more likely to be the upper crust material ascribable to the metamorphic rocks of the Calabrian Arc, as suggested by the high $^{207}Pb/^{204}Pb$ that characterize in general the post ~25 ka products (Del Moro et al., 1998). This is also in accordance with the study of Si-rich melt inclusions hosted in quartz-rich xenoliths in the products of Vulcano island carried out by Frezzotti et

al. (2004), which shows that those inclusions are the result of partial melting of the metamorphic rocks of the Calabro Peloritano basement.

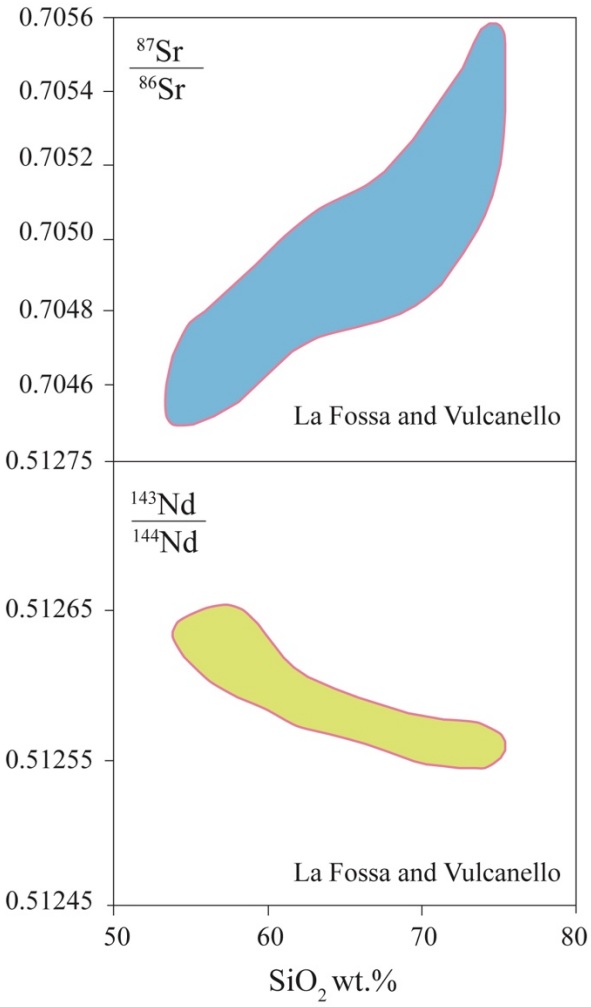

Figure 3.6 – $^{87}Sr/^{86}Sr$ and $^{143}Nd/^{144}Nd$ versus SiO_2 for the products of La Fossa and Vulcanello (modified from Del Moro et al., 1998).

In general, all the rhyolitic lavas and pyroclastic products of La Fossa exhibit evidences of mixing and mingling with less differentiated magmas. These occur in the form of magmatic enclaves, xenocrysts in chemical disequilibrium with the host rock, resorbed phenocrysts, reaction rims, bimodal mineral compositions and lati-trachytic variably porphyritic domains (e.g. bandings) in lavas and pyroclastic products (Fig. 3.7) (Frazzetta et al., 1983; De Fino et al., 1991; Clocchiatti et al. 1994; Piochi et al. 2009; De Astis et al. 2013; Bullock et al. 2019). More in detail, the petrographic features of the samples that define the straight line in figure 3.3

(e.g. trachytic lava flows of the PEU and pyroclastic products of GCEC), testify to disequilibrium conditions such as: i) coexistence of K-feldspar, olivine and clinopyroxene, ii) opacified biotite, iii) orthopyroxene reaction rim in olivine and plagioclase with sanidine rim overgrowth, iv) lati-trachytic bandings, from glassy to variable porphyritc texture, in evolved products, v) crystals (mainly clinopyroxene and plagioclase) embedded in a microlitic groundmass in a glassy host (De Fino et al., 1991; Clocchiatti et al., 1994; Gioncada et al., 1998; Del Moro et al., 1998; Piochi et al., 2009). It is thus evident that the chemical composition of these products is the result of mixing processes between a latitic and a rhyolitic end members (De Fino et al., 1991; Clocchiatti et al., 1994; Del Moro et al., 1998; Gioncada et al., 1998; Rossi et al., 2019).

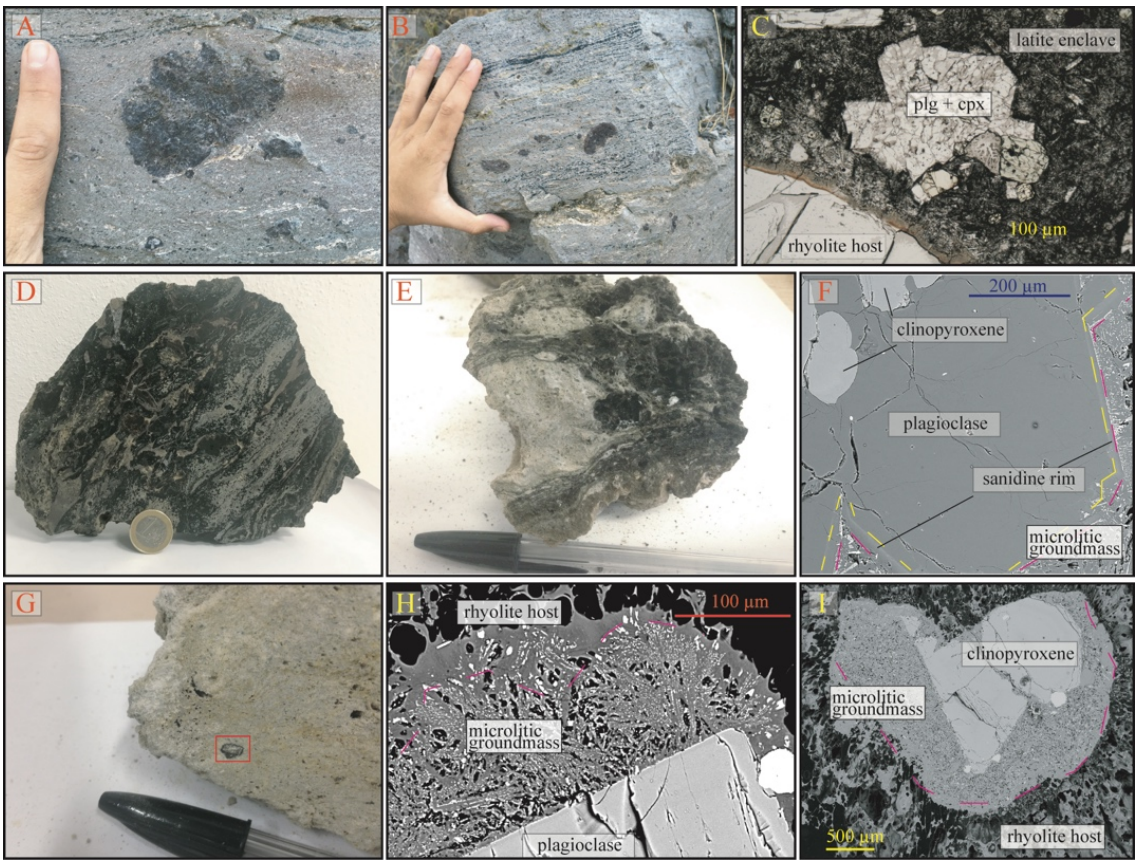

Figure 3.7 – A,B: magmatic enclaves in the obsidianaceous Pietre Cotte lava flow; C: microphotograph of a crystal-rich enclave and the contact with the rhyolite host of Pietre Cotte lava; D: banding in the Commenda obsidian lava; E: banding in the Upper Pietre Cotte pumice; F: BSE (backscattered electron) image showing a sanidine rim overgrowth in a plagioclase (magmatic enclave in Upper Pietre Cotte pumice); G,H,I: Pal B pumice with a plagioclase (G,H) and a clinopyroxene (I) wrapped in a microlitic groundmass; the purple dashed line highlights the contact with the host rhyolitic vesiculated groundmass.

3.5 The magmatic-hydrothermal system

Since the last eruption of AD 1888–1890, the most relevant manifestations at Vulcano are represented by a high-temperature (up to 700 °C during the volcanic unrests) fumarole field located in the inner part and on the northern edge of La Fossa crater, and a lower temperature (< 100 °C) degassing area located at Levante Bay (Fig. 3.8) (Chiodini et al., 1995; Capasso et al., 1997). The existence of several hot water wells in the area confirms the presence of a thermal boiling aquifer (Capasso et al., 2014). Diffusive degassing of CO_2 occurs in the whole area of Vulcano Porto village and from La Fossa volcano (Inguaggiato et al., 2012; Di Martino et al., 2020). All these characteristics testify to the presence of an active magmatic-hydrothermal system (Fulignati et al., 1998). By combining ground and satellite-based thermal infrared remote sensing Mannini et al. (2019) constrained the thermal flux of La Fossa hydrothermal system between the years 2000 and 2019, confirming that Vulcano is in the top 20 most active hydrothermal systems in the world.

The origin of magmatic fluids is to be sought in the shallow magmatic system of the volcano at ~3.5–3 km depth. Here, the degassing phase of magmatic bodies of intermediate composition, fed by volatile rich mafic magma at depth, mainly composed by H_2O, CO_2, H_2S, Cl and N_2, mixes with groundwaters (Fulignati et al., 1998; Paonita et al., 2013; Chiaradia et al., 2018). The interactions between these fluids and the rocks of the subsoil and of the volcanic edifice itself result in high temperature alteration typical of an acid-sulfate hydrothermal alteration (Fulignati et al., 1998; Boyce et al., 2007). The presence of a similar hydrothermal system, active at least in the last 1000 years, is testified by the occurrence of hydrothermally-altered lithic clasts similar to the current alteration in the eruptive products of the Breccia di Commenda and AD 1888–1890 eruption (Figs. 3.2 and 3.8) (Clocchiatti et al., 1994; Fulignati et al., 1998; Gurioli et al., 2012; Rosi et al., 2018). This implies that the fluids of the hydrothermal system were previously involved in phreatic-hydrothermal eruptions at La Fossa. Indeed, in the case of Breccia di Commenda eruption, the emplacement of highly dispersed, altered lithic-rich, blast-like pyroclastic density currents suggests that the explosion mostly

involved the fluid-saturated hydrothermally altered rocks in the shallower portion of the volcanic conduit (Gurioli et al., 2012; Rosi et al., 2018).

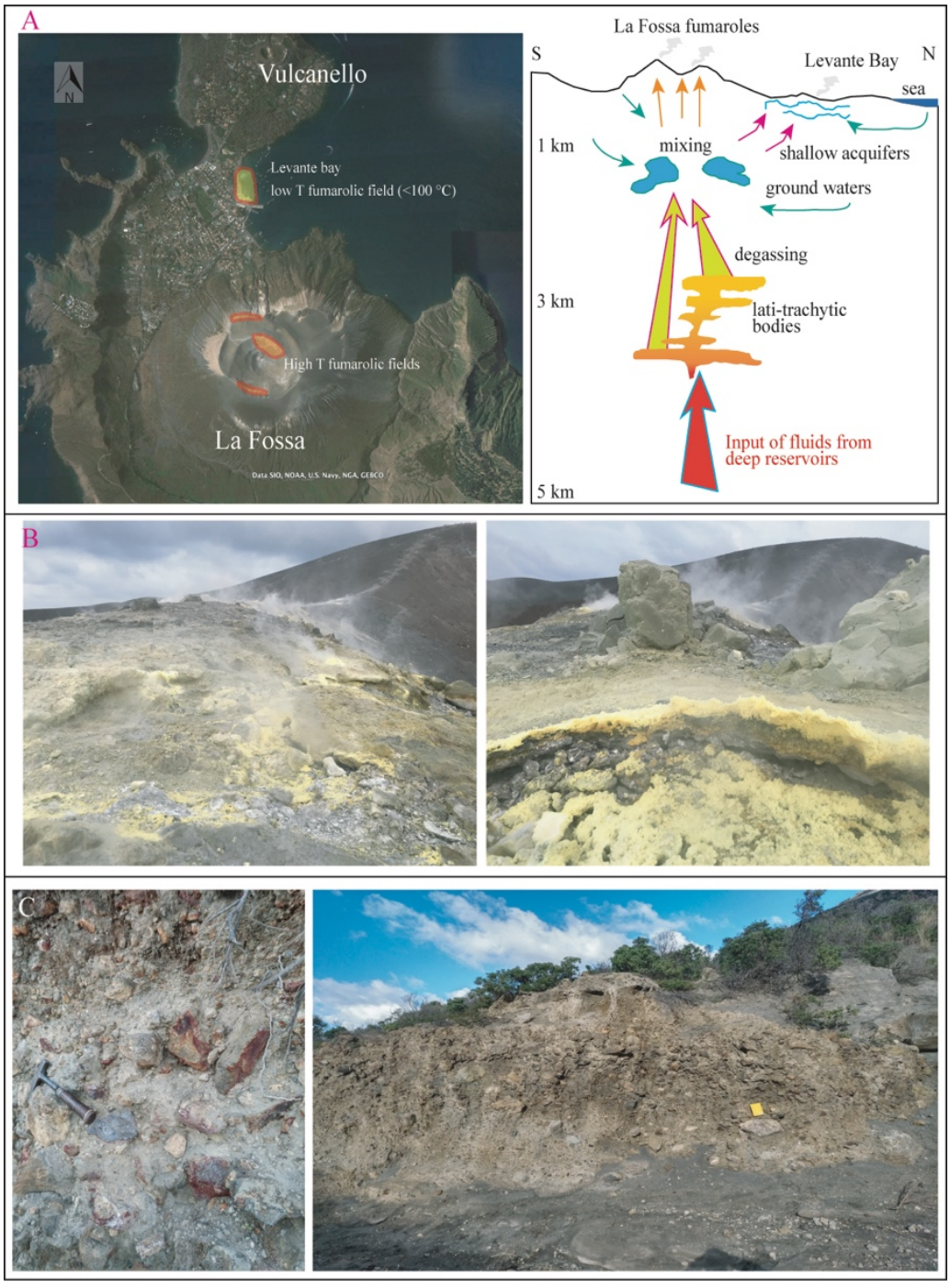

Figure 3.8 – A: Location of the fumarole fields at La Fossa and in the Levante Bay area and schematic sketch map of the active magmatic-hydrothermal system (modified from Selva et al., 2020, after Paonita et al., 2013); B: Hydrothermally altered rocks and sulfur sublimates in the high temperature fumarolic field located inside the crater of La Fossa; C: hydrothermally altered lithics and outcrops of the Breccia di Commenda eruption.

4 Materials and Methods

4.1 Sampling and samples preparation

Samples were collected during several fieldwork campaigns carried out at Vulcano island. Samples mainly came from the last 1000 years eruptive products of La Fossa and the eruptive unit to which they refer are those proposed by Di Traglia et al. (2013). The PEU is entirely represented by the samples collected for this thesis. They are the ash layers of Pal A and Pal C, the rhyolitic and trachytic pumices from the fallout layers (Pal B and Pal D, respectively) and the trachytic Palizzi lava flow. Samples from GCEC include the latitic enclaves contained in the obsidian of Pietre Cotte, the Pietre Cotte lava and the spatter of the AD 1888–1890 eruption. In addition, in order to cover the entire range of evolution from basalt to rhyolite of Vulcano Island, samples erupted from other volcanic centers and belonging to older eruptive epochs have been selected for the sake of completeness and comparison (see Chapter 8 and 9). They include the scoriaceous lapilli of La Sommata, the pumiceous lapilli of Quadrara eruption, the welded scoriae of Spiaggia Lunga, the scoriaceous lapilli of Mt. Saraceno and the lava flow and the scoriaceous lapilli of Vulcanello 1 formation (see Gioncada et al., 1998; De Astis et al., 2013; Fusillo et al., 2015; Nicotra et al., 2020; Palummo et al., 2020 for further information on the chemistry and stratigraphy of these products). In Appendix A is reported a list of the investigated samples together with their geographical coordinates.

The samples were prepared in polished thin and thick sections for petrography and microanalysis. The pumiceous and scoriaceous lapilli were crushed and crystals were manually separated under a stereomicroscope, embedded in epoxy mounts and polished. Slices of lava flow samples were also prepared in epoxy resin. Sample powders were prepared by selecting aliquots of samples that did not show mixing features (e.g. compositional banding and enclaves), crushed and pulverized using a planetary mill with agate jars at the Dipartimento di Scienze della Terra at the Università di Pisa and used for whole-rock chemical analyses.

4.2 Experimental methods

Temperature gradient experiments were performed at the High Pressure High Temperature Laboratory at Istituto Nazionale di Geofisica e Vulcanologia (Rome, Italy) in a non-end loaded piston cylinder (QUICKpress type). Temperature gradient experiments take advantage of the intrinsic temperature gradient of piston cylinder furnaces. This experimental strategy has been adopted by several authors to investigate the effect of temperature gradient on melt differentiation, isotopic fractionation and fluid transport in magmas (Huang et al., 2009; Masotta et al., 2012a, b; Rodriguez et al., 2015, 2017; Laumonier et al., 2019). Experiments were performed using a NaCl-borosilicate glass-graphite 19–25 mm assembly designed for experiments at pressure between 150 and 300 MPa, and calibrated using the NaCl melting method (Masotta et al. 2012a)

The temperature profile in the experiments was measured following the procedure described in Masotta et al. (2012b), through several calibration experiments in which the thermocouple was placed each time at a different position along the axis of the assembly (9, 14 and 19 mm). Current, voltage and temperature were recorded at different output conditions and then regressed into equations specific for each position of the thermocouple. Temperature gradient curves were then obtained at different conditions of output and used to reconstruct the temperature zoning in the experiments.

Experiments were performed using 5 mm outer diameter and Pt capsules, at both anhydrous and hydrous (H_2O= 2 and 4 wt.%) conditions. Deionized H_2O was added in the hydrous charge using a micro-syringe, yielding to a precision of about 0.1 wt.%. The weight of the capsule was checked before and after welding, and after 30 min at 110 °C to ensure that water did not escape during capsule preparation. As starting materials, a glass obtained by melting at 1400 °C for 1 hour a latitic rock obtained from a magmatic enclave hosted in the AD 1739 Pietre Cotte rhyolitic lava flow has been used. The starting glass was crushed into a fine powder, inserted in the capsule and manually pressed using a die. The latitic composition represents one of the least evolved magma compositions erupted at La Fossa during

the last 1000 years and is taken as representative of the latitic magma of La Fossa plumbing system (see Chapters 3, 5 and 6). Experiments were performed at the pressure of 150 MPa, at a temperature of 1050 °C (hot spot) and with a duration of 24 hours. While the bottom of the capsule is located in the furnace hot spot, the temperature at the top of the capsule depends on the height of the capsule and the gradient curves, being as low as 900 °C. The temperature of the hot spot was constantly monitored using a C-type thermocouple, with a precision of 5 °C. At the beginning of the experiments, the temperature was increased to 1300 °C at a rate of 80 °C/min and held 30 minutes at this temperature, in order to anneal the crystal nuclei formed during the heating and to allow melt homogenization (Masotta et al. 2020). The temperature was then decreased to the experimental resting temperature with the same rate of 80 °C/min. After the experiment, both the position of the capsule in the assembly and the final height of the capsule after compression was checked to correctly asses the temperature distribution along the capsule profile.

4.3 Petrography and scanning electron microscopy

The polished thin sections and resin mounts of natural and experimental products were firstly inspected with a petrographic microscope under both transmitted and reflected light in order to check for the occurrence of magmatic sulfides and melt inclusions and to investigate their overall petrographic characteristics. Then, the samples were carbon-coated and analyzed with a Quanta 450 Field Emission-Scanning Electron Microscope (FE-SEM) equipped with Bruker microanalytical EDS system QUANTAX, installed at the Centro Interdipartimentale di Scienza e Ingegneria dei Materiali (CISIM) at Università di Pisa. Backscattered electron (BSE) images were obtained using a 20 kV filament voltage, 10 mm working distance and 0.1 nA. The same instrumentation has been used to perform part of the major element analyses of mineral phases, sulfide and melt inclusions using a 15 kV accelerating voltage, 10 mm working distance and 0.1 nA.

4.4 Whole-rock chemical analyses

Major elements analyses

The chemical composition of selected samples was determined by X-ray Fluorescence (XRF) on pressed powder pellets using an ARL 9400 XP+ sequential X-ray spectrometer under the instrumental conditions reported in Lezzerini et al. (2013) at Dipartimento di Scienze della Terra (Università di Pisa). The loss on ignition (LOI) was determined at 950°C. Major element were also analyzed by lithium metaborate/tetraborate fusion ICP-OES (inductively coupled plasma optical emission spectrometry) at Actalabs (Activation Laboratories Ltd., QOP WRA analytical package) in Ancaster (Canada). The LOI was determined by gravimetric method. The samples were run for major oxides on a combination simultaneous/sequential Thermo Jarrell-Ash ENVIRO II ICP or a Varian Vista 735 ICP. Calibration was performed using 14 prepared USGS and CANMET certified reference materials (Appendix B). The complete data set of whole-rock major element is reported in Appendix C.

Trace elements analyses

The trace element content of the whole-rock samples was determined by Inductively Coupled Plasma-Mass Spectrometry (ICP-MS) using a Perkin-Elmer NexION 300x. About 50 mg of each powdered sample was dissolved in a mixture of Suprapur HF and HNO_3 inside perfluoroalkoxy (PFA) vessels on a hot plate at 150 °C. The obtained solutions were properly diluted with Mill-Q purified water (18.2 M cm) and mixed online, before reaching the nebulizer, with an internal standard solution containing 20 ng/mL of Rh, Re and Bi to correct for signal fluctuations and matrix effect. External calibration was used to determine the concentration of each selected isotope by means of a solution of the BE-N (alkaline basalt) geochemical reference sample. The geochemical reference sample WS-E was dissolved and analyzed along with the unknown samples to check the accuracy

of the results (Appendix B). The complete data set of whole-rock trace element analyses is reported in Appendix C.

Platinum Group Elements and Rhenium analyses

Platinum Group Elements (PGE), Re and Au concentrations of whole-rock samples were determined using the Ni-sulfide fire assay dilution method, described by Park et al. (2012a). Five grams of rock powder, 0.5 g of Ni, 0.25 g of S and 5 g of sodium borax were mixed, placed in a porcelain crucible and weighted. A mixed spike solution of PGE and Re (~0.06 g) was weighted and added to each crucible. Samples were prepared in 3 different batches, including 1 batch of duplicate analyses, along with the standards TDB-1 CCRMP-CANMET diabase and the CRM olivine tholeiitic basalt Oreas30a, which were prepared in the same way as the unknown samples. A procedure blank, consisting of the same amount of 0.5 g of Ni, 0.25 g of S plus 10 g of sodium borax (5 g representing the sample), was run with each batch of analyses. A second crucible, containing ~0.1 g of cooking flour was placed outside each crucible containing the samples, to provide reducing conditions at the beginning of the fusion. The crucibles were dried in a furnace for 60 minutes at 100 °C to remove moisture. Then the mixtures were melted in a preheated furnace at 1100 °C for 10 minutes, shaken and returned to the furnace for another 20 minutes. N_2 gas was introduced in the furnace with a constant flow rate of ~0.03 m^3/min to maintain reducing conditions during the fusion. The samples then were quenched at room temperature by removing the crucible from the furnace. After quenching crucibles were broken and NiS beads handpicked. Thus, the beads were dissolved in 150 ml of 6 M HCl on a hot plate, the solutions were filtered with a Millipore filter paper and washed with Milli-Q water. The resulting filter papers, containing the samples, were digested in 1 ml of 14 M HNO_3 and 3 ml of 8 M HCl. After completing the digestion, the solutions were dried in a hot plate down to ~0.1 ml of remaining solution. The solutions were then diluted with 4 ml of 2% HNO_3 and allowed to cool at room temperature. Samples were then analyzed with an Agilent 7700x quadrupole ICP-MS at Research School of Earth Sciences at the Australian National University. The potential molecular

interferences of Ni, Cu, Zn, Co, Hf, Mo, Zr and Ta argides on the analyzed isotopes were checked and the effects of the interferences were subtracted using measured oxide and argide production rates. Concentrations of PGE and Re were determined by isotope dilution using the $^{191}Ir/^{193}Ir$, $^{99}Ru/^{101}Ru$, $^{191}Ir/^{193}Ir$, $^{195}Pt/^{194}Pt$, $^{105}Pd/^{108}Pd$ and $^{185}Re/^{187}Re$ ratios, respectively. Concentrations of Rh were obtained using the method described by Meisel et al. (2003) and Park et al. (2012a), by using count rates of ^{103}Rh and ^{106}Pd, assuming that the loss of Rh was similar to the loss of Pd during analyses. Average procedural blanks determined by sample free analyses (n= 3) were 0.004 ppb for Ir, 0.021 ppb for Ru, 0.005 ppb for Rh, 0.46 ppb for Pt, 0.24 ppb for Pd, 0.06 ppb for Re and 0.016 ppb for Au. The method detection limits (m.d.l.), taken to be three standard deviations of the procedural blanks after subtraction of average procedural blank values (Park et al., 2012a), are reported in Appendix B. To assess the accuracy and precision of the analyses, replicate analyses of the reference materials TDB-1 and Oreas30a were carried out, results are consistent with values reported in literature within the stated error (Appendix B).

4.5 Electron microprobe analyses

The major element chemical composition of the experimental starting material glass, the experimental products, the mineral phases and melt inclusions of natural products was obtained using an electron probe microanalyzer (EPMA) JEOL JXA-8200 superprobe, operating in wavelength dispersive mode at the Dipartimento di Scienze della Terra at the Università di Milano (operative conditions were 15 kV accelerating voltage, 10 nA beam current for mineral phases and 5 nA for melt inclusions). Glasses in both natural and experimental products were analyzed with a defocused electron beam of 5 μm and counting time of 5 s on background and 15 s on peak. For minerals, a beam size of 2 μm and counting time of 20 s on peaks and 10 s in background were used. Chemical profile of clinopyroxene crystals were also collected using a using a JEOL JXA-8200 superprobe at the University of Geneva using 15 keV acceleration voltage, 10 nA beam current with a 1 μm beam size and 20 μm steps. The following standards have

been adopted: jadeite (Si and Na), labradorite (Al and Ca), forsterite (Mg), andradite (Fe), rutile (Ti), orthoclase (K), barite (Ba), apatite (P) and spessartine (Mn). Na and K were analyzed as first elements to minimize alkali loss. For the glasses the standards VG-2 (Jarosewich et al., 1980) and SMN49 (Marshall et al., 1998) have been used (Appendix B). In Appendix D major element composition of experimental products (glass and mineral phases, including Fe-SEM analyses) are reported. In Appendix E is reported the complete major elements analyses data set of mineral phases (including Fe-SEM analyses). In Appendix F and G the major element composition of melt inclusions and sulfide inclusions are reported, respectively (including Fe-SEM analyses).

4.6 In situ trace elements analyses

Trace elements analyses of mineral phases, melt and sulfide inclusions were performed in situ by laser ablation inductively coupled plasma mass spectrometry (LA-ICPMS) at Géosciences Montpellier (Université de Montpellier, AETE-ISO regional facility of the OSU OREME), with a pulsed 193 nm ArF excimer laser (Analyte G2 from Teledyne) coupled to a Thermofinnigan Element XR mass spectrometer. For the analyses of mineral phases, the laser was operated at a repetition rate of 8 Hz using spot sizes of 85 and 110 μm and a 6 J/cm^2 energy density. Total analysis time was 120 s with the first 80 s used for background measurement and last 40 s for sample ablation. Synthetic glass NIST 612 was used for external calibration. For melt inclusions the laser was operated at a repetition rate of 6Hz using spot sizes of 10 to 20 μm and a 6 J/cm^2 energy density. Total analysis time was 120 s with the first 80 s used for background measurement and last 40 s for sample ablation. Synthetic glass NIST 610 was used for external calibration. For minerals and melt inclusions the accuracy of the analyses was monitored using the standard glass BIR-1 and SiO_2 of each mineral/glass, used as internal standard. For sulfide inclusions, only those where their exposed diameter was >15 μm were analyzed. The beam spot sizes were 5 to 10 μm. Only two non-homogeneous (polymineralic sulfide inclusions, see Chapter 8) sulfide inclusions were sufficiently large to be analyzed; the laser spot was tuned to approximate the

"bulk" composition of the sulfide inclusion, without distinguishing among the single sulfide phases. The laser was operated at a repetition rate of 6 Hz using and a 6 J/cm^2 energy density with a total analysis time of 240 s (200 s for background measurement and 40 s of sample analysis). The Synthetic standard MASS-1 was used for external calibration. Measured FeO, in the case of homogeneous sulfide inclusions, and reconstructed bulk FeO (see image analyses method in the next section), in the case of non-homogeneous polymineralic sulfide inclusions, was used as an internal standard. Data reduction for the mineral, melt and sulfide inclusions was performed with the software package Glitter (http://www.glitter-gemoc.com). Results of reference materials and control standard analysis are provided in Appendix B. Trace elements analyses of mineral phases are reported in Appendix E. The trace elements analyses of melt inclusions are reported in Appendix F, and the trace element analyses of sulfide inclusions in Appendix G.

4.7 Image analyses

The freeware software package ImageJ (Image Processing and Analysis in Java, http://rsb.info.nih.gov/ij/) was used for image analysis of experimental products obtained at different temperatures to determine the glass/crystalline phases ratio and mineral phases abundance on BSE images of experimental products (Chapter 6). The same technique was adopted to calculate the original bulk major element compositions of the texturally non-homogeneous sulfide inclusions (Chapter 8). Their bulk composition were reconstructed using spot analyses on the various sulfide phases present within each exposed sulfide inclusion. The reconstructed bulk composition was calculated dependent on the relative area percent of each sulfide phase in the BSE images. Area percentages were determined using the image ImageJ and the 2D images were segmented by manual thresholding. The uncertainty on the reconstructed bulk composition, involving both instrumental analytical error and manual image thresholding error, was evaluated to be <10%. (Chapter 8).

5 Field and stratigraphic observations

The products mainly investigated in this work belong to the Palizzi Eruptive Unit (PEU) (the ash layers of Pal A and Pal C, the pumiceous fallout of Pal B and Pal D and the Palizzi lava Flow) and to the Upper Pietre Cotte unit of the Gran Cratere Eruptive Cluster (GCEC) (Pietre Cotte lava and its magmatic enclaves). The explosive sequence of the pyroclastic products of the PEU is variably exposed in several outcrops on the southern flanks of La Fossa Cone, in the Palizzi Valley and in the neighboring ring plain at the base of the volcanic cone (Di Traglia et al., 2013 (Figs. 5.1 and 3.2). In addition to the study of natural outcrops, giving the nature itself of the majority of the PEU products (easily erodible ashes highly susceptible to reworking processes, Di Traglia et al., 2013), the stratigraphic record of the entire explosive sequence (total thickness up to 4 m) has been also studied and sampled, in a 13 x 6 m and 2 to 7 m deep machine excavated trench (in a collaboration with the University of Geneva) located in the SE flank of La Fossa cone (Figs. 5.1 and 5.2).

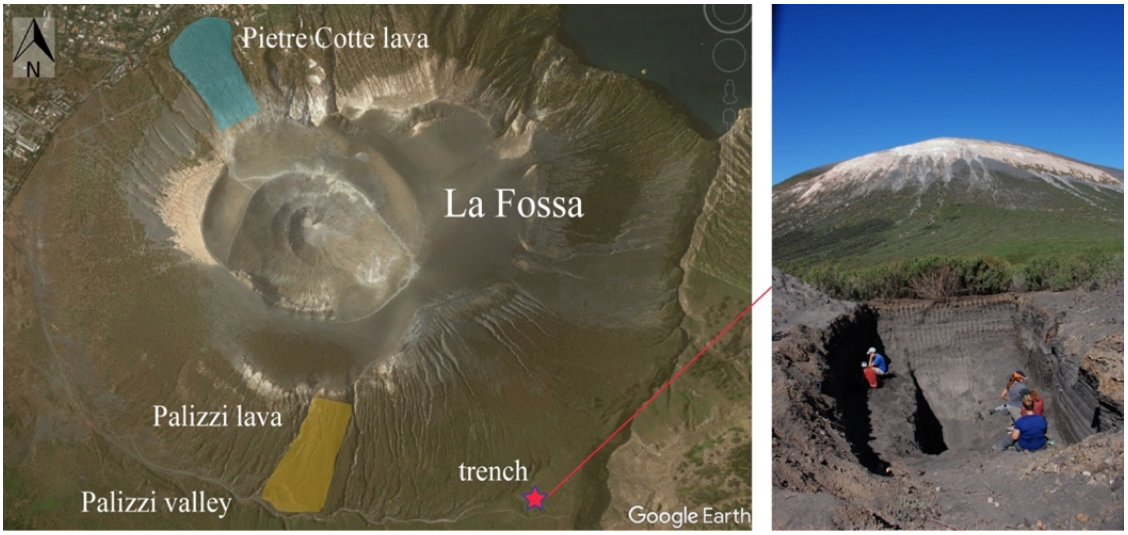

Figure 5.1 – Location of the investigated lava flows of Palizzi and Pietre Cotte and of the excavated trench in the Palizzi valley area.

The PEU explosive products

Pal A, the lowermost part of the PEU sequence, is constituted by a metric series of cross-stratified to parallel-bedded coarse-ash to fine-ash dark grey layers overlying a ~4 cm thick grey-brown massive fine ash layer (Fig. 5.2a, c, d). The Pal A sub-unit is bounded at the base by a grey-brown hard-ground, corresponding to the S1 unconformity of Di Traglia et al. (2013), that separates the products erupted in the last 1000 years at La Fossa from the older units. The sequence is abruptly interrupted by the pumiceous fallout layer of Pal B. In the excavated trench, Pal B is a ~5 cm thick coarse pale-grey ash layer containing white vesiculated pumiceous lapilli (Fig. 5.2a, c, d). The same level, in other outcrops, consists of a massive, grain-supported deposits made up by high vesiculated white pumiceous bombs and lapilli. The Pal B layer reaches a maximum thickness up to ~1.5 m at the base of the Lentia Dome Complex at NW of the Fossa Cone (Fig. 5.2e) (Di Traglia et al., 2013; Biass et al., 2016). The Pal C sub-unit has been divided into 3 portions on the basis of textural features (Fig. 5.2). Pal C1, that lies directly above Pal B, consists of several millimetric to centimetric layers made up by parallel bedded fine dark-grey ash, for a total thickness of ~144 cm (Fig. 5.2a, c, d). Pal C2 is about 65 cm thick and is made up by embedded fine ash layers alternating with thin layers of fine pinkish ash and minor unconformities with associated reworked material (Fig. 5.2a, f, g). Pal C3 is dominated by reworked material that is present in two main intervals of 30–40 cm thick each at the base and the top, separated by a thin (~5 cm) layer of grey stratified primary tephra (Fig. 5.2a, f, g). Pal D represents the upper portion of the explosive PEU sequence and consists of a massive, grain-supported deposit bearing pumiceous bombs and lapilli with a thickness up to 2-3 m in medial outcrops in the southern flanks of La Fossa (Fig. 5.2a, b) (Di Traglia et al., 2013; Biass et al., 2016; Fulignati et al., 2018).

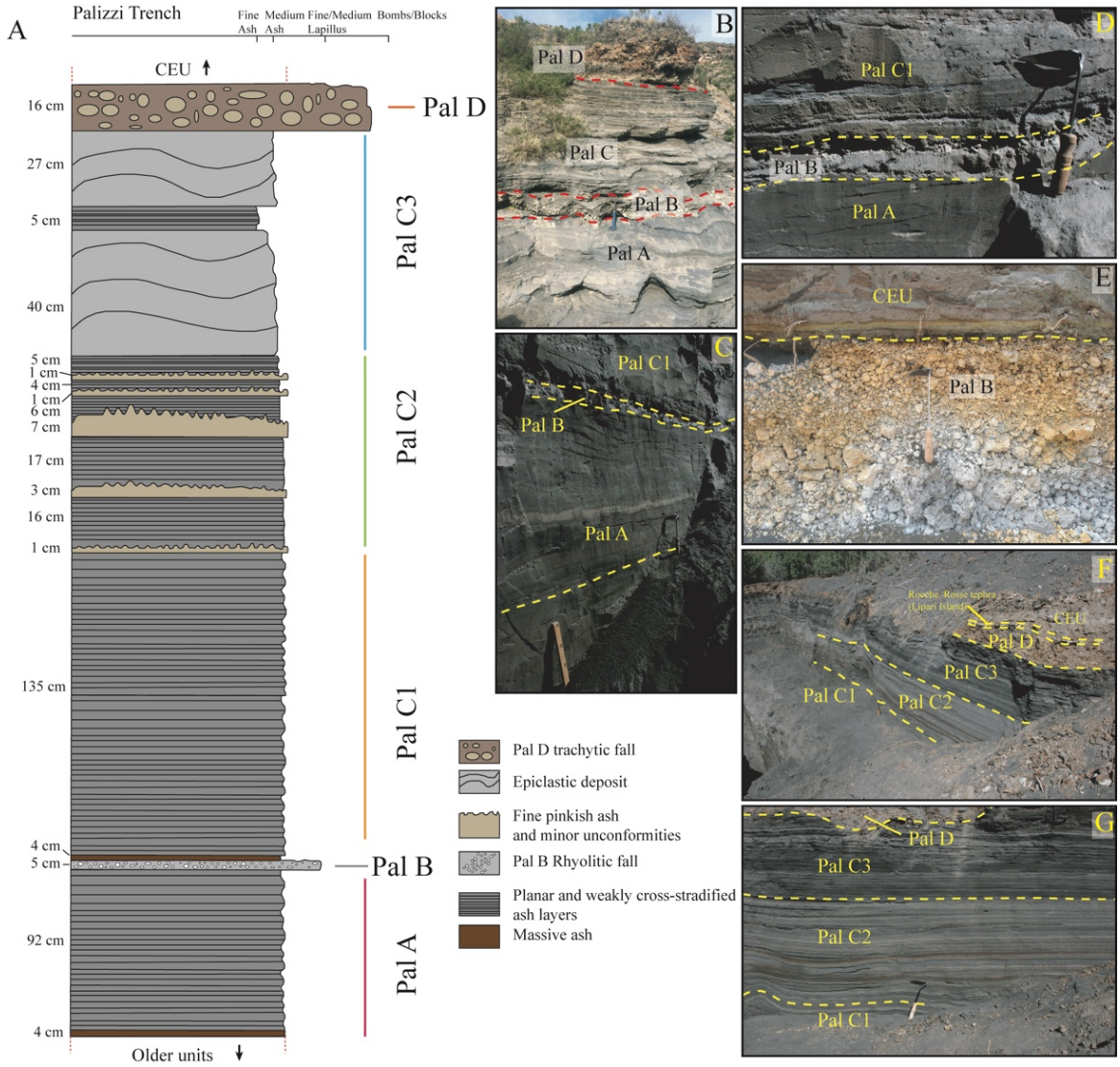

Figure 5.2 – A: Schematic stratigraphic log of the PEU explosive products; B: PEU explosive sequence exposed in an outcrop on the southern flank of La Fossa Cone; C,D,F,G: PEU explosive products in the machine excavated trench; E: Pal B fallout at the base of Lentia dome complex.

Palizzi lava flow

The Palizzi lava flow is exposed on the southern flank of La Fossa, covering an area of about 0.04 km^2 with a maximum thickness up to 8–10 m at the footwall of the flow (De Fino et al., 1991). It is characterized by a massive texture in the basal and central portions of the flow while becomes variably scoriaceous showing also clinker features typical of aa lava type at the top (Figs. 5.1 and 5.3a).

Pietre Cotte lava flow

The tongue-like obsidianaceous lava flow of Pietre Cotte is located in the north-western flank of La Fossa and is up to 20 m thick at the flow front. With an archaeomagnetic age of AD 1720, is the last lava effusion emitted at La Fossa (Arrighi et al., 2006; De Astis et al., 2013) (Figs. 5.1 and 5.3b). Frazzetta (1991) estimated a volume of 2.4 x 10^6 m^3 for the flow. The Pietre Cotte lava is characterized by viscous flow banding, foliations, folding and self-brecciated portions and by the occurrence of abundant mafic magmatic enclaves from few mm up to 30 cm in diameter (Figs. 5.3c,d and 3.7) (Perugini et al., 2007; Piochi et al., 2009; Vetere et al., 2015; Bullock et al., 2019).

Figure 5.3 – A: Palizzi lava flow front; B: Pietre Cotte lava flow front; C,D: magmatic enclaves contained in the Pietre Cotte lava.

6 New insights on magma storage and evolution at La Fossa in the last 1000 years

6.1 Introduction

The eruptive products of La Fossa volcano embrace a wide range of magma compositions, ranging from latite to trachyte and rhyolite (see previous chapters). The eruptive products of the PCEC and GCEC are characterized by abrupt changes of the chemical composition both at the scale of the eruptive sequence and also within a single eruptive unit (e.g. Clocchiatti et al., 1994; Del Moro et al., 1998; De Astis et al., 2013). Crystal-rich lati-trachytic magmatic enclaves in rhyolitic lavas and compositionally heterogeneous banded pumices are common in the recent activity of La Fossa volcano, testifying to syn-eruptive mixing and/or mingling processes (e.g. Piochi et al., 2009; De Astis et al., 2013; Rossi et al., 2019). Most of the petrogenetic models that have been proposed focused on the relationships and mixing processes between mafic and rhyolitic melts. Piochi et al. (2009) suggested a mingling process between an uprising rhyolitic magma and a shallower less evolved plug, followed by separation of latitic enclaves in the rhyolite to explain the textural features of the Pietre Cotte lava flow (AD 1739). Perugini et al. (2007) and Vetere et al. (2015) proposed instead that the crystal-rich enclaves occurring in the Pietre Cotte rhyolitic lava are due to the injection of the latitic magma into the more evolved magma. Forni et al. (2015), and more recently Bullock et al. (2019), suggested that crystal-rich enclaves occurring in the Pietre Cotte lava are the result of re-mobilization of crystal-rich cumulates. Following this latter interpretation, the association between crystal-poor rhyolites and crystal-rich enclaves at La Fossa can provide evidence of the importance of crystal-melt separation processes leading to the generation of evolved melts. Additionally, significant variations of the magma chemistry at same SiO_2 content occur in the PCEC sequence, whose Pal D trachytic fallout has the highest concentration in K_2O and Ba of the entire eruptive history of Vulcano. Such features make La Fossa an ideal site to investigate plumbing system dynamics leading to the generation of

evolved magmas in shallower reservoirs and their mutual relationships with mafic to intermediate melts.

In this chapter, the magmatic products erupted during the recent (last 1000 years) activity of La Fossa volcano are investigated. The main aim is to constrain the physical conditions at which magmas evolved, interacted and erupted and to reconstruct their geochemical differentiation. At this purpose, a series of representative rock samples, encompassing the entire compositional range of erupted magmas, have been selected. Whole-rock major and trace element analyses and micro-chemical analyses of mineral phases of natural samples have been combined with temperature gradient experiments. Thermobarometric calculation indicate that the K-rich trachytic magma of Pal D crystallized at lower pressure compared to latitic and trachytic ones. Magma differentiation modelling by mean of mass balance calculations and assimilation plus fractional crystallization, based both on major and trace element composition of eruptive products, suggests that the evolved trachytic and rhyolitic magma compositions cannot be fully explained through fractional crystallization from a latitic magma. The obtained results instead suggest that the formation of crystal-poor rhyolitic products that characterize the products of the last 1000 years can be explained and modeled through melt segregation from a lati-trachytic crystal mush. Thus, the obtained results contribute to envisage a complex polybaric storage system, which can be ascribed as a vertically developed plumbing system where crystal-poor differentiated melts are periodically extracted from variably crystallized crystal mushes. Finally, the partial melting of low temperature phases of the crystal mush due to periodic new magmatic inputs is here suggested to play a critical role in the petrogenesis of latitic and trachytic magmas in the shallow system.

6.2 Petrographic features and whole-rock major elements chemistry of La Fossa latitic, trachytic and rhyolitic products

The recent activity of the PCEC and GCEC is characterized by the eruption of magmas that encompass a broad range of composition from latite to trachyte and rhyolite (Fig. 3.3). Selected samples have been analyzed in this study and

considered as representative of these three types of magmas erupted at La Fossa: the enclaves of Pietre Cotte obsidian as representative of the latite, the Palizzi lava flow and Pal D fallout for the trachyte and the Pal B pumice for the rhyolite (Figs. 3.2 and 6.1). Their petrography and geochemistry is summarized here below.

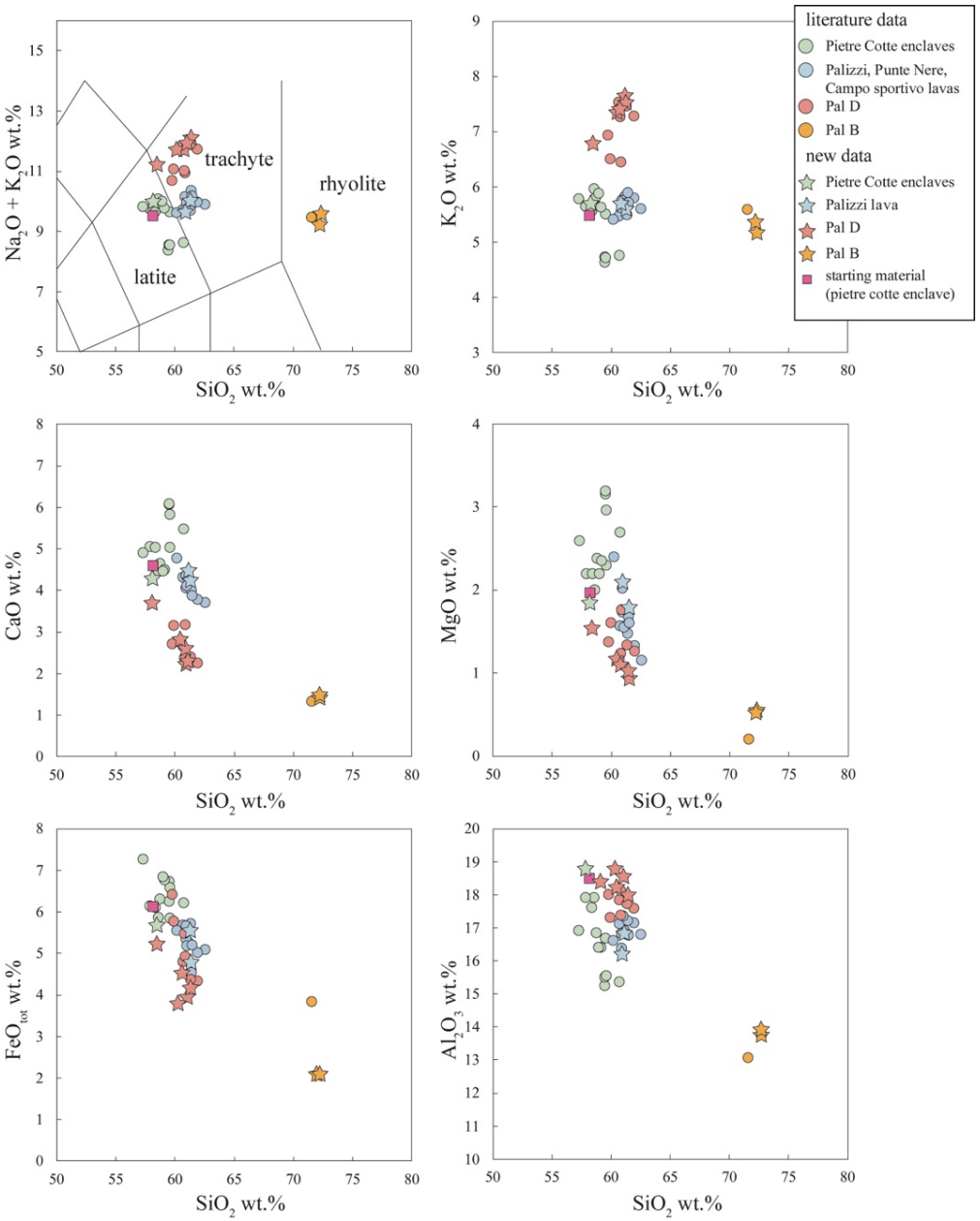

Figure 6.1 - Total alkali vs SiO_2 and major elements variation diagrams showing whole-rock data of La Fossa products investigated in this work. Major elements are recalculated to 100% on anhydrous basis. Literature data from Clocchiatti et al. (1994), Del Moro et al. (1998), De Astis et al. (2013), Nicotra et al. (2018). (Modified after Costa et al., 2020).

Latitic magma

The latitic magma occurs both as the juvenile component of several spatter and ash layers of PCEC (Pal A, Pal C) and GCEC (lower Pietre Cotte and AD 1888–1890), and as magmatic enclaves in the rhyolitic pumices of Pal B, Upper Pietre Cotte and in the rhyolitic obsidian lava flows of Commenda and Pietre Cotte (Figs. 3.7 and 5.3) (Perugini et al., 2007; Piochi et al., 2009; De Astis et al., 2013). The Commenda lava and the pyroclastic products of Upper Pietre Cotte contain latitic magma both as vitrophyric bands stretched and mingled with the rhyolitic glass, and as rounded to blocky porphyritic enclaves with a microcrystalline groundmass (Fig. 3.7). The latitic magma constituting the juvenile fraction of the pyroclastic deposits and that occurring as mingled bands is variably porphyritic (porphyritic index, P.I., ranging from 3 to 30%), whilst the one constituting the enclaves in both lavas and pumices is crystal-rich (P.I. = 25–30%). The latitic enclaves sampled within the Pietre Cotte obsidian exhibit a mineral assemblage consisting of abundant euhedral to subeuhedral plagioclase (29%) and clinopyroxene (15%), olivine (3%) and rare sanidine (< 1%). Apatite and Ti-magnetite are common accessories (Figs. 3.7 and 6.2a, b). The groundmass is constituted by microlites of plagioclase and sanidine, and intergranular clinopyroxene and opaque minerals. Plagioclase and clinopyroxene phenocrysts often occur in glomerophyric texture (Figs. 3.7 and 6.2a, b). The bulk composition has SiO_2 ranging from 57 to 59 wt.% and Na_2O+K_2O ranging from 8.5 to 10 wt.% (Tab. 6.1 and Fig. 6.1).

Trachytic magma

The trachytic magma is represented by the lava flows of Punte Nere, Palizzi, Campo Sportivo of the PCEC and by pyroclastic products of the PCEC and GCEC, as well as by some coarse ash layers and some lapilli and bombs of the AD 1888–1890 eruption of GCEC (Clocchiatti et al. 1994). The trachytic magma also occurs as mingled bands within the rhyolitic pumices of the Upper Pietre Cotte (Rossi et al. 2019). The Palizzi lava flow exhibits a porphyritic texture (P.I. ~20%) and a mineral assemblage made up of, in order of abundance, euhedral to subhedral

plagioclase (12%), sanidine (10%), clinopyroxene (6%) and scarce (~1%) olivine (Fig. 6.2c). Glomerocrysts of plagioclase and clinopyroxene are also present (Fig. 6.2d). Ti-magnetite, apatite and Cu-rich sulfide inclusions are the accessory minerals (see Chapter 8). The groundmass is holocrystalline and made up by sanidine and minor amounts of plagioclase and clinopyroxene (Fig. 6.2c, d). The whole-rock composition of Palizzi lava is trachytic with SiO_2 from 60 to 61 wt.% and Na_2O+K_2O from 9.5 to 10.4 wt.% (Tab. 6.1 and Fig. 6.1). The pumices of Pal D fallout layer belonging to the PEU are highly vesiculated (~80 vol.%) and low porphyritic (P.I. is less than 5 %). Scarce phenocrysts of plagioclase, clinopyroxene, sanidine, biotite and olivine occur in a glassy groundmass (Fig. 6.2e, f), whilst Ti-magnetite, apatite and pyrrhotite are common accessories (Fulignati et al. 2018 and Chapter 8). A K-rich trachytic composition is exclusive of the Pal D fallout layer. The SiO_2 content of these pumices ranges from 56 to 61 wt.%, with a K_2O content as high as ~7.6 wt% and to a total alkali content up to 12 wt.% (Tab. 6.1; Fig. 6.1).

Rhyolitic magma

The rhyolitic magma constitutes the juvenile fraction of both pyroclastic products (Pal B pumices, Upper Pietre Cotte fallout and AD 1888–90 eruption breadcrust bombs) and lava flows (Commenda and Pietre Cotte) of both PCEC and GCEC (Fig. 3.3). All the rhyolitic products exhibit evidence of mingling with either latitic or trachytic magmas, with the rhyolitic magma constituting the main fraction of the magma erupted during these eruptions (Fig. 3.7). Rhyolitic products range from aphyric, with common xenocrysts of plagioclase and clinopyroxene (i.e. Pietre Cotte lava and pumices, AD 1888–90 eruption bread crust bombs; Clocchiatti et al., 1994; Piochi et al., 2009; De Astis et al., 2013) to weakly porphyritic (i.e., Pal B pumices). The pumices from the Pal B fallout deposit consist of white lapilli and bombs containing magmatic enclaves and showing a low porphyricity (P.I. is less than 5%) with a glassy groundmass (Fig. 6.2g). Phenocrysts are, in order of abundance, plagioclase, sanidine, clinopyroxene and biotite. Accessory Ti-magnetite and apatite occur as inclusions within phenocrysts. The latitic and trachytic enclaves are constituted by phenocrysts of plagioclase and clinopyroxene

that are surrounded by a dark microlitic matrix (Fig. 6.2h). The composition of these rhyolites range in SiO_2 from 71 % to 72 wt.% and in Na_2O+K_2O from 9.1 to 9.4 wt.% (Tab. 6.1 and Fig. 6.1).

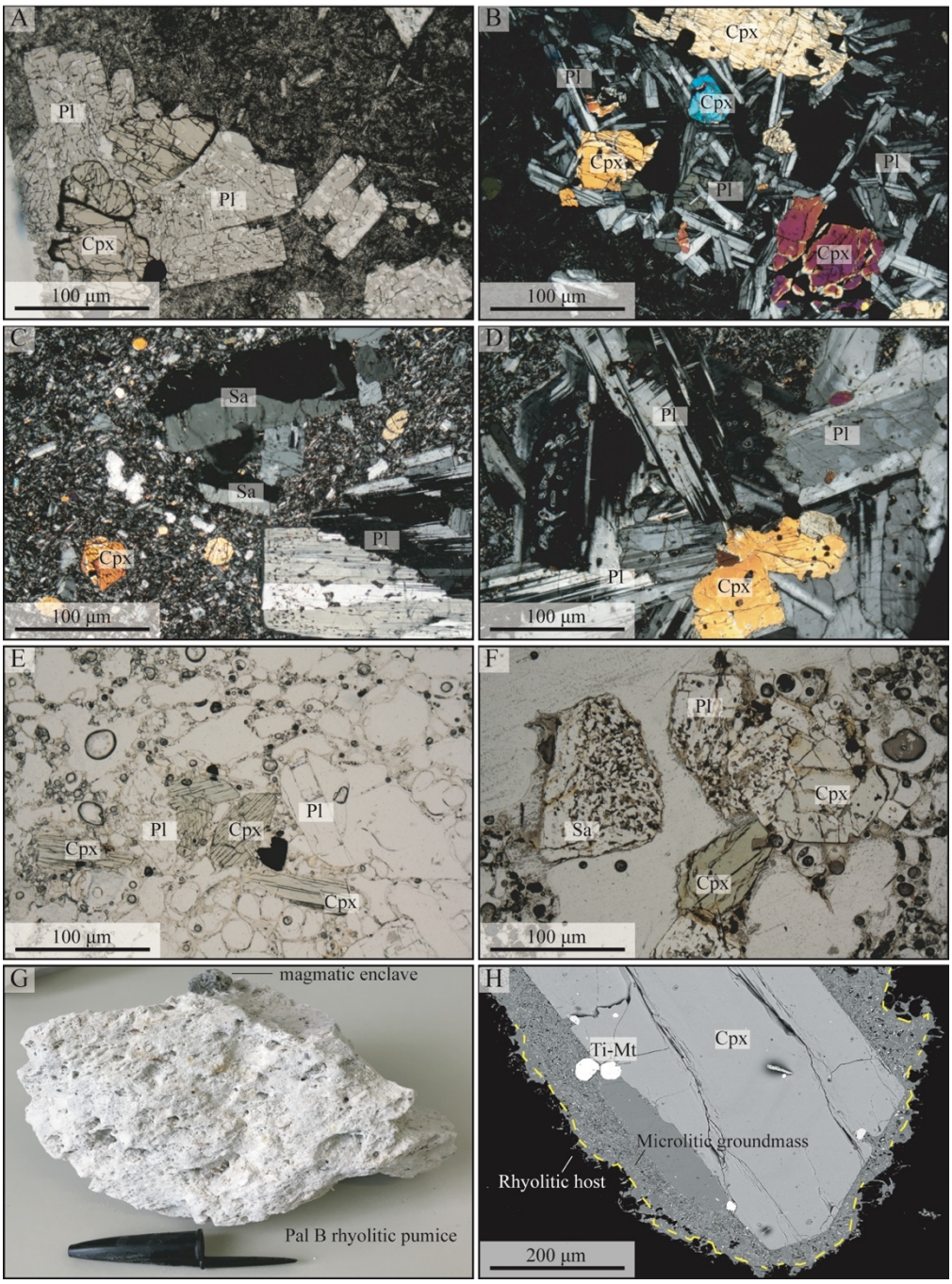

Figure 6.2 – a,b: Microphotographs of latitic crystal rich enclaves of Pietre Cotte; c,d: the Palizzi trachytic lava; e,f: the K-rich Pal D pumice; g: Pal B rhyolitic pumice hosting a magmatic enclave; h: BSE image of a clinopyroxene in the rhyolitic pumice of Pal B, the crystal is wrapped by a microlitic corona isolating it from the rhyolitic groundmass glass (yellow line). Mineral abbreviations: Cpx, clinopyroxene; Pl, plagioclase; Sa, sanidine; Ti-Mt, Ti-magnetite. (Modified after Costa et al., 2020).

Table 6.1 – Whole-rock major elements analyses by XRF and ICP-OES , trace elements analyses by ICP-MS of the investigated products of La Fossa and EPMA analysis of the glass used as starting material for the experiments. See Appendix C for the complete data set.

Eruptive Unit	Pal D	Pal D	Pal D	Pal D	Pal D	Pal B	Pal B	Palizzi	Palizzi	Pietre Cotte	^Starting Material	
Sample	S33b 60-90	S33b 90-110	SC-18-20	SC-20-31	SC-20-31b	Pal-L 18-01	Pal-L 18-02	SC-18-24	VGPl3	VPCl8i^	VPCl8i	
Composition	K-rich Trachyte	K-rich Trachyte	K-rich Trachyte	K-rich Trachyte	K-rich Trachyte	Rhyolite	Rhyolite	Trachyte	Trachyte	Latite	Latite	
Type	Pumice	Pumice	Scoriae	Pumice	Pumice	Pumice	Pumice	Lava	Lava	Enclave	glass	σ (10)
wt.% SiO_2	57.58	59.52	60.00	59.15	61.10	69.21	70.03	60.89	60.70	57.21	56.60	0.47
TiO_2	0.66	0.69	0.64	0.55	0.56	0.17	0.19	0.48	0.50	0.70	0.72	0.04
Al_2O_3	18.27	18.52	18.22	17.75	18.04	13.06	13.36	16.08	16.73	18.40	17.98	0.49
Fe_2O_3*	5.89	4.25	4.37	4.99	4.70	2.33	2.31	6.22	4.80	5.53	5.95	0.22
MnO	0.11	0.10	0.09	0.10	0.11	0.07	0.07	0.12	0.15	0.13	0.12	0.02
MgO	1.50	1.13	1.00	1.06	0.95	0.51	0.51	2.08	1.77	1.83	1.90	0.07
CaO	3.63	2.68	2.27	2.60	2.38	1.40	1.44	4.60	4.20	4.18	4.48	0.21
Na_2O	4.41	4.37	4.40	4.25	4.50	3.98	3.94	4.03	4.39	4.23	3.92	0.12
K_2O	6.65	7.22	7.34	7.23	7.58	5.07	5.04	5.72	5.60	5.63	5.32	0.22
P_2O_5	0.43	0.32	0.26	0.28	0.25	0.09	0.10	0.32	0.30	0.31	0.28	0.05
Total	99.13	98.80	98.59	97.96	100.16	95.89	96.99	100.54	99.14	98.15	97.26	
L.O.I.	0.87	1.2	1.41	1.32	0.46	4.11	3.01	0.09	0.86	1.85		
ppm V	94.32	59.05	50.98	68.64	52.24	13.95	17.85	118.98				
Cr	4.17	1.05		1.64		2.02	2.81	19.40				
Co	10.51	6.32	5.01	6.80	5.35	2.39	2.84	14.20				
Ni	2.53	1.26	1.59	1.50	0.91	1.86	2.32	10.26				
Rb	205.68	224.59	241.37	223.09	233.87	270.36	270.03	210.22				
Sr	1404.20	936.23	778.37	1032.56	772.31	110.39	134.36	863.89				

Y	24.17	25.09	21.02	23.78	22.98	37.49	38.95	29.65
Zr	201.11	220.42	229.18	208.75	232.87	171.22	175.63	254.56
Nb	24.96	28.17	28.51	27.76	31.63	32.35	32.94	28.28
Mo	4.17	4.45	4.47	4.79	4.76	5.65	5.82	5.51
Cs	9.49	10.38	10.43	10.80	11.28	15.48	15.68	3.51
Ba	3101.87	1909.28	1452.48	2165.52	1528.66	110.35	129.64	806.59
La	67.80	68.08	63.55	74.33	71.40	60.47	63.61	82.25
Ce	121.03	120.51	107.80	128.22	125.57	113.56	118.98	146.93
Pr	12.69	12.34	11.66	13.05	12.87	12.15	12.69	15.26
Nd	43.68	41.88	38.63	43.71	43.24	40.64	42.33	51.95
Sm	7.63	7.02	6.24	7.45	7.27	7.83	8.08	8.65
Eu	1.79	1.60	1.43	1.64	1.59	0.28	0.31	1.39
Gd	5.73	5.49	4.49	5.50	5.30	6.39	6.57	6.49
Tb	0.84	0.80	0.65	0.80	0.77	1.04	1.07	0.92
Dy	4.46	4.34	3.55	4.37	4.14	6.18	6.34	5.00
Ho	0.83	0.84	0.69	0.83	0.79	1.24	1.29	1.00
Er	2.37	2.44	2.03	2.43	2.30	3.73	3.85	2.91
Tm	0.36	0.37	0.31	0.37	0.34	0.59	0.60	0.43
Yb	2.33	2.43	1.99	2.40	2.24	3.83	3.94	2.78
Lu	0.35	0.36	0.32	0.36	0.34	0.58	0.61	0.44
Hf	4.81	5.33	5.35	5.26	5.58	6.03	6.18	6.33
Ta	1.48	1.67	1.60	1.66	1.91	2.23	2.31	1.68
Pb	24.83	25.67	30.04	38.53	26.95	34.57	34.09	31.64
Th	32.36	35.05	35.11	34.74	36.96	45.74	47.87	41.74
U	8.84	9.60	9.39	9.49	10.13	13.18	13.74	11.14

*$Fe_2O_{3\,tot}$ for XRF and ICP-OES bulk rock analyses, FeO_{tot} for electron microprobe analyses of the starting glass

6.3 Whole-rock trace elements geochemistry

Representative trace element compositions of the investigated products are reported in table 6.1. The spider diagrams of incompatible trace elements (Fig. 6.3) are characteristic of a subduction-related magmatism, with negative anomalies in Nb and Ta. The Pal B rhyolite, coherently with the other rhyolitic products erupted at La Fossa, shows markedly lower contents of Sr and Ba and higher Rb compared to latitic and trachytic magmas. Interestingly, the Ba content of the Pal D K-rich trachyte is higher with respect to the others trachytic and latitic products, up to ~3100 ppm (Fig. 6.4). The Cr content decreases as the degree of evolution increases, except for the K-rich compositions, showing Cr content even lower than the rhyolites (Fig. 6.4). Rare Earth Elements (REE) patterns (Fig. 6.3) show fractionation between Light-REE (LREE) and Heavy-REE (HREE) with the latitic enclaves of Pietre Cotte showing slightly higher enrichments in LREE (Fig. 6.4) and the rhyolites showing an increase in HREE. The Eu anomaly becomes markedly negative with the increasing degree of evolution from latite to rhyolite, with the exception of the Pal D K-rich trachyte that shows slightly negative Eu/Eu* (0.79-0.83, with $Eu/Eu^* = Eu_N/(Sm_N * Gd_N)^{1/2}$, compared to the Palizzi lava and the Pietre Cotte enclaves.

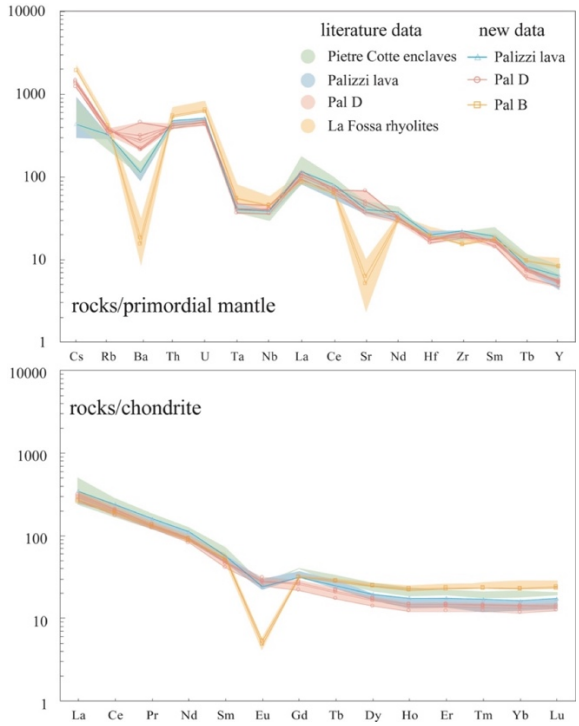

Figure 6.3 – Incompatible trace elements and REE patterns of the investigated products normalized to the Primordial Mantle and Chondrites values respectively (Sun and McDonough, 1989). Literature data are from Del Moro et al. (1998), De Astis et al. (2013), Nicotra et al. (2018) and Bullock et al. (2019).

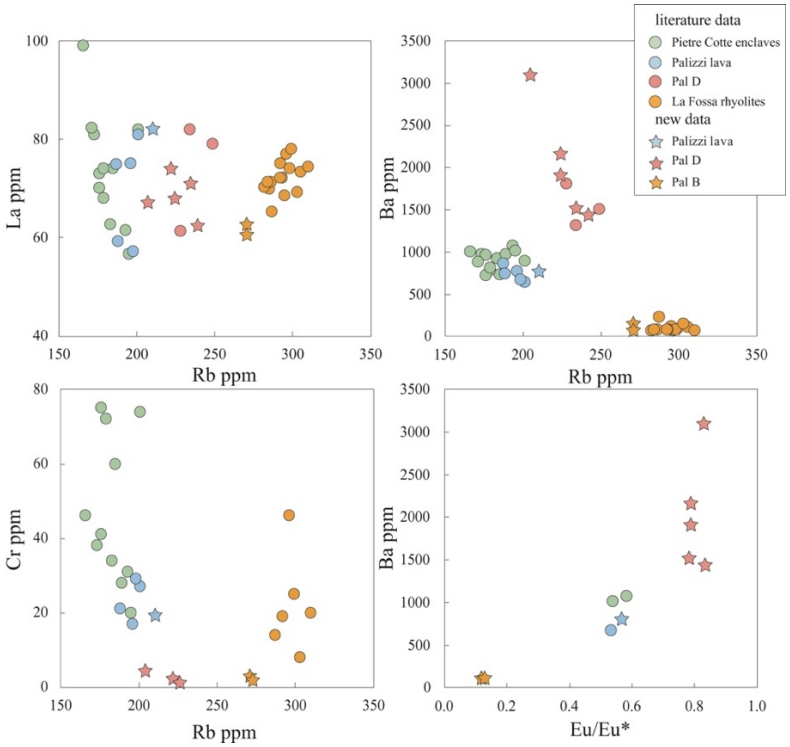

Figure 6.4 – Trace elements variation diagrams of the investigated products. Literature data sources as in figure 6.3.

6.4 Mineral chemistry

In the products of La Fossa, plagioclase composition ranges from labradorite to andesine and oligoclase, with a significant overlap of latitic and trachytic products (Fig. 6.5a). In the latitic enclaves of Pietre Cotte plagioclase is $An_{39-57}Ab_{37-48}Or_{5-13}$, whilst in the trachytic lava of Palizzi and in the K-rich trachytic pumices of Pal D plagioclase is $An_{39-61}Ab_{34-50}Or_{3-9}$ and $An_{37-55}Ab_{39-54}Or_{6-13}$, respectively. In the rhyolitic pumices of Pal B, plagioclase is $An_{25-59}Ab_{33-66}Or_{3-11}$. Alkali feldspar shows a rather homogeneous composition in trachytic and rhyolitic products ($An_{1-6}Ab_{3-44}Or_{5-67}$), with the exception of the K-rich trachytic pumices that are evidently enriched in the Or component ($An_{3-5}Ab_{22-36}Or_{59-72}$).

Clinopyroxene has augitic composition in all products ($Wo_{42-47}En_{37-42}Fs_{12-19}$), with the Diopside-Hedembergite (DiHd, calculated following the method presented in Putirka et al., 1996) component ranging from 0.76 to 0.86 (Fig. 6.5b). Clinopyroxene in the K-rich trachytic pumices of Pal D is enriched in the DiHd component (DiHd = 0.83–0.84) with respect to other latitic and trachytic products (DiHd = 0.76–0.82). In the Pal B pumices, clinopyroxene displays a very large compositional variation (DiHd = 0.77–0.86). Biotite in the K-rich trachytic pumices of Pal D has $Mg/(Mg + Fe_{tot})$ = 0.65–0.67 (Fulignati et al., 2018). Olivine composition in the latitic and trachytic products varies from Fo_{72} to Fo_{55} (Gioncada et al., 1998; Fuignati et al., 2018).

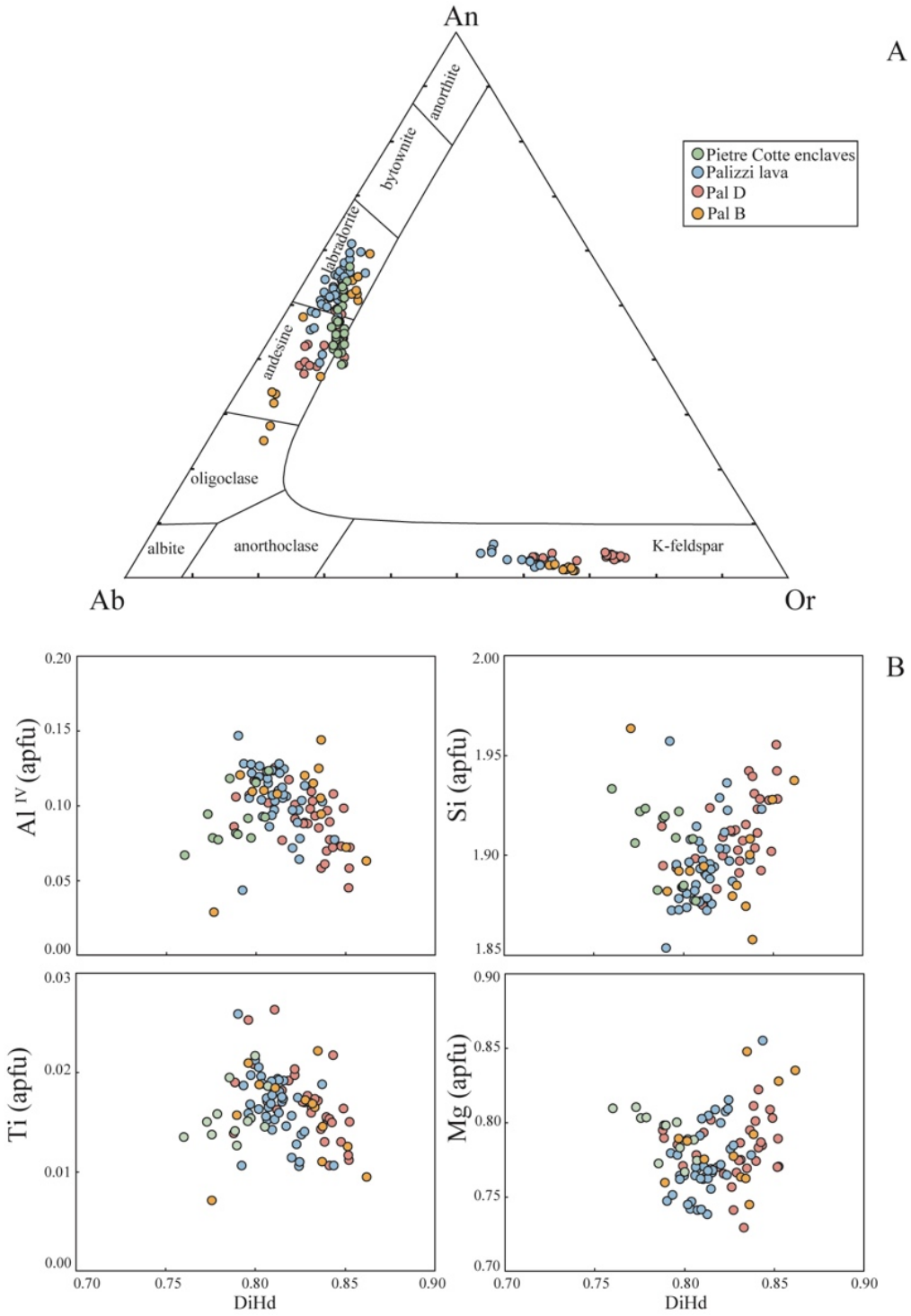

Figure 6.5 – a: Feldspar ternary diagram showing the composition of feldspar phenocrysts in the investigated products. Data of plagioclase occurring in the latitic enclaves of Pietre Cotte are from Piochi et al. (2009) and this work; b: diagrams showing Al^{IV}, Si, Ti, Mg cations (apfu, atom per formula unit) vs. the DiHd component of clinopyroxene in the investigated products. Data of clinopyroxene occurring in the latitic enclaves of Pietre Cotte are from Piochi et al. (2009) and this work (modified after Costa et al., 2020).

Rare Earth Elements patterns in plagioclase reveal that the plagioclase of the K-rich trachytic pumices of Pal D has lower concentrations of HREE with respect to plagioclase of the latitic enclaves of Pietre Cotte and the trachytic lava of Palizzi (Fig. 6.6). Sr and Ba abundances in plagioclase are higher in the Pal D K-rich trachyte compared to the other latitic and trachytic magmas (Ba up to 2536 ppm and Sr up to 6869 ppm) and display also higher Eu anomaly with respect to the plagioclase of the latitic enclaves and Palizzi lava (Pal D plagioclase Eu/Eu*= 22-37) (Fig. 6.7). Clinopyroxene phenocrysts of Pal D show higher REE concentration compared to clinopyroxene of the latitic enclaves and the trachytic lava of Palizzi (Fig. 6.6). The Sr content of clinopyroxene is variable (70–206 ppm), with the lowest values observed for the K-rich trachytic pumices of Pal D and a positive correlation with the Eu anomaly (0.48–0.74) (Fig. 6.7). The complete dataset (major and trace elements) of mineral phase is reported in Appendix E.

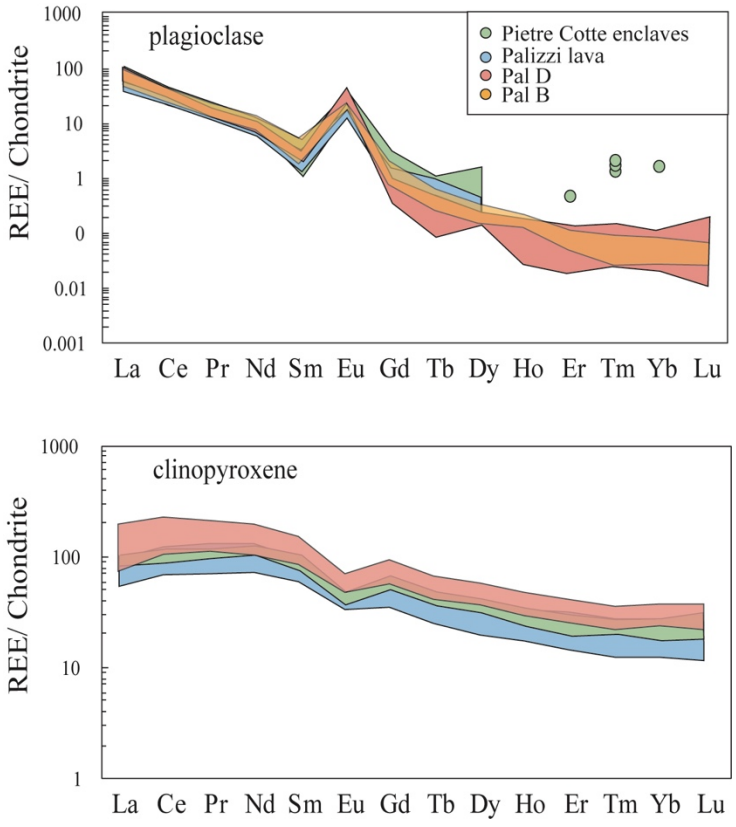

Figure 6.6 - Chondrite-normalized Rare Earth Element (REE) patterns for plagioclase and clinopyroxene. Data of plagioclase in the latitic enclaves of Pietre Cotte and Palizzi lava flow are from Piochi et al. (2009), Nicotra et al. (2018) and this work. Data of clinopyroxene in the latitic enclaves of Pietre Cotte are from Piochi et al. (2009) (modified after Costa et al., 2020).

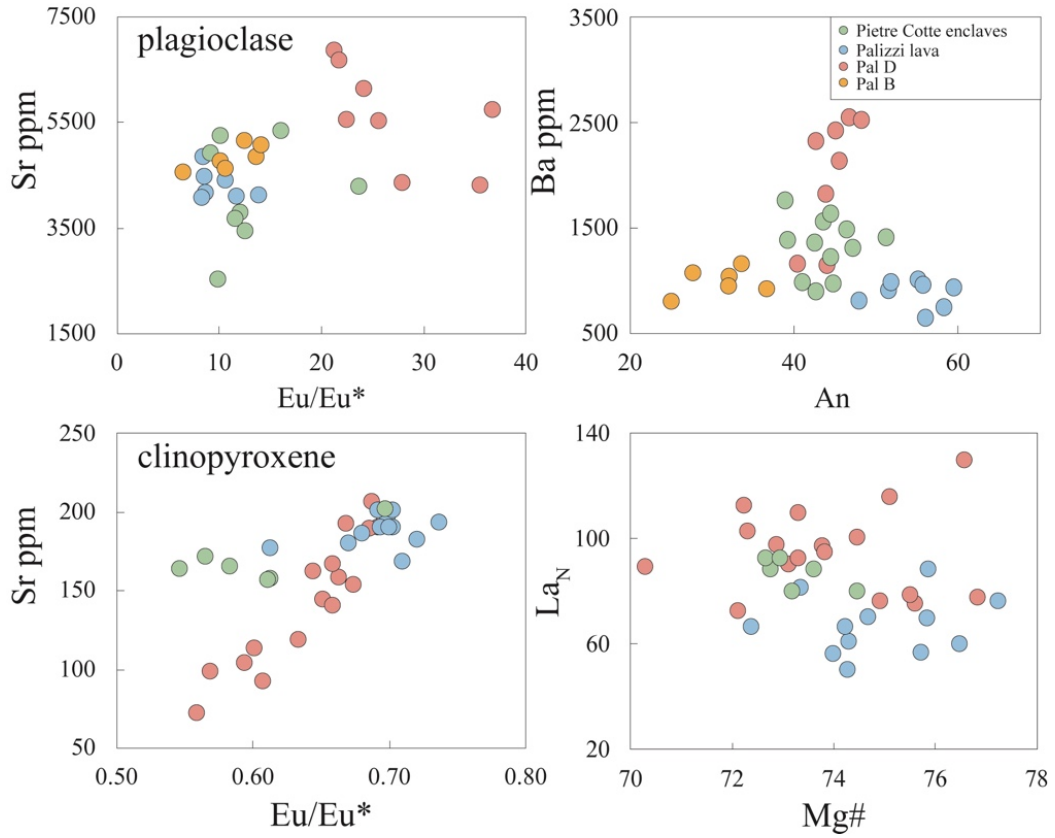

Figure 6.7 – Sr vs. Eu/Eu and Ba vs. An content for plagioclase and Sr vs. Eu/Eu* and La_N vs. Mg# for clinopyroxene. Data of plagioclase in the latitic enclaves of Pietre Cotte and Palizzi lava flow are from Piochi et al. (2009), Nicotra et al. (2018) and this work. Data of clinopyroxene in the latitic enclaves of Pietre Cotte are from Piochi et al. (2009) (modified after Costa et al., 2020).*

6.5 Temperature gradient experiments results

Temperature gradient experiments produced variable phase relationships and crystal-melt proportion in response to the temperature variation along the charge (Tab. 6.2, Fig. 6.8). In all the experiments, clinopyroxene is the most abundant mineral phase, forming large (200–1000 μm) skeletal crystals in the hotter region of the capsule and small (20–200 μm) and increasingly euhedral crystals at lower temperatures. Such variability of crystal size and shape can be attributed to the effect of undercooling upon cooling from superliquidus (Shea and Hammer 2013; Pontesilli et al. 2019; Masotta et al. 2020).

*Table 6.2 – Phase proportions in experimental samples obtained through image analyses (ImageJ); *Alkali feldspar and plagioclase counted together because of the similar backscattered electrons intensity. Mineral abbreviations: Cpx: clinopyroxene; Afs: alkali feldspar; Pl: plagioclase; Ox: oxide; Bt: biotite.*

	Temperature along the capsule (°C)					
Phase (vol.%)	1050-1025	1025-1000	1000-975	975-950	950-925	925-900
H_2O = 0 wt.%						
Glass	86	84	61	45	30	20
Cpx	14	16	14	24	26	24
Afs+Pl*	0	0	24	30	42	54
Ox	0	0	1	1	2	2
H_2O = 2 wt.%						
Glass	90	87	82	77	68	50
Cpx	8	11	14	17	19	24
Afs+Pl*	0	0	0	0	0	15
Ox	1	1	1	1	2	2
Bt	0	0	2	2	8	6
Vesicles	1	1	1	3	3	3
H_2O = 4 wt.%						
Glass	80	78	72	69	65	60
Cpx	6	7	13	13	13	15
Ox	1	1	1	2	2	2
Bt	9	10	10	12	15	18
Vesicles	4	4	4	4	5	5

At anhydrous conditions (H_2O = 0 wt.%), clinopyroxene is the only mineral in the temperature range 1050–1000 °C. Fe-oxide and feldspars start to crystallize at 1000 °C. The same mineral assemblage constituted by clinopyroxene, Fe-oxide and alkali feldspar is maintained up to the top of the capsule, where the crystal fraction increases up to 80 vol.% at about 900 °C (Tab. 6.2, Fig. 6.8). Upon increasing crystallization, the composition of the interstitial glass enriches in K_2O from 6.0 to 7.3 wt.% with only a slight variation in SiO_2 from 58 to 59 wt.% (Fig. 6.9 and Appendix D). It is worth noting that the glass in the anhydrous experiment is slightly enriched in FeO compared to the starting material, as result of the extensive crystallization of feldspar (Fig. 6.9). At hydrous conditions with H_2O = 2 wt.% and at the temperature of 1050 °C, clinopyroxene and Fe-oxide co-saturate

the melt. Biotite crystallization starts at 1000 °C and is followed by the crystallization of plagioclase and alkali feldspar at 925 °C. At the top of the capsule, the temperature decreases to 900 °C and the crystallinity reaches ~50 vol.% (Tab. 6.2, Fig. 6.8). The composition of interstitial glasses along the experimental charge varies with the increasing crystallization, with SiO_2 increasing from 58 to 62 wt.% and K_2O increasing from 5.7 to 6.7 wt.% (Fig. 6.9 and Appendix D). In the hydrous experiment with H_2O = 4 wt.%, clinopyroxene biotite and Fe-oxide co-saturate the melt in the temperature range 1050–1000 °C and the same mineral assemblage is maintained up until the temperature of 900 °C, where the crystallinity is ~40 vol. % (Tab. 6.2 and Fig. 6.8). The composition of interstitial glass varies in SiO_2 from 62 to 67 wt.%, with a rather small increase in K_2O from 5.4 to 6.1 wt.% and a marked depletion in FeO, CaO and MgO due to extensive crystallization of biotite and clinopyroxene (Fig. 6.9 and Appendix D). In Appendix D the analyses of interstitial glass in the experimental capsules and of mineral phases are reported respectively.

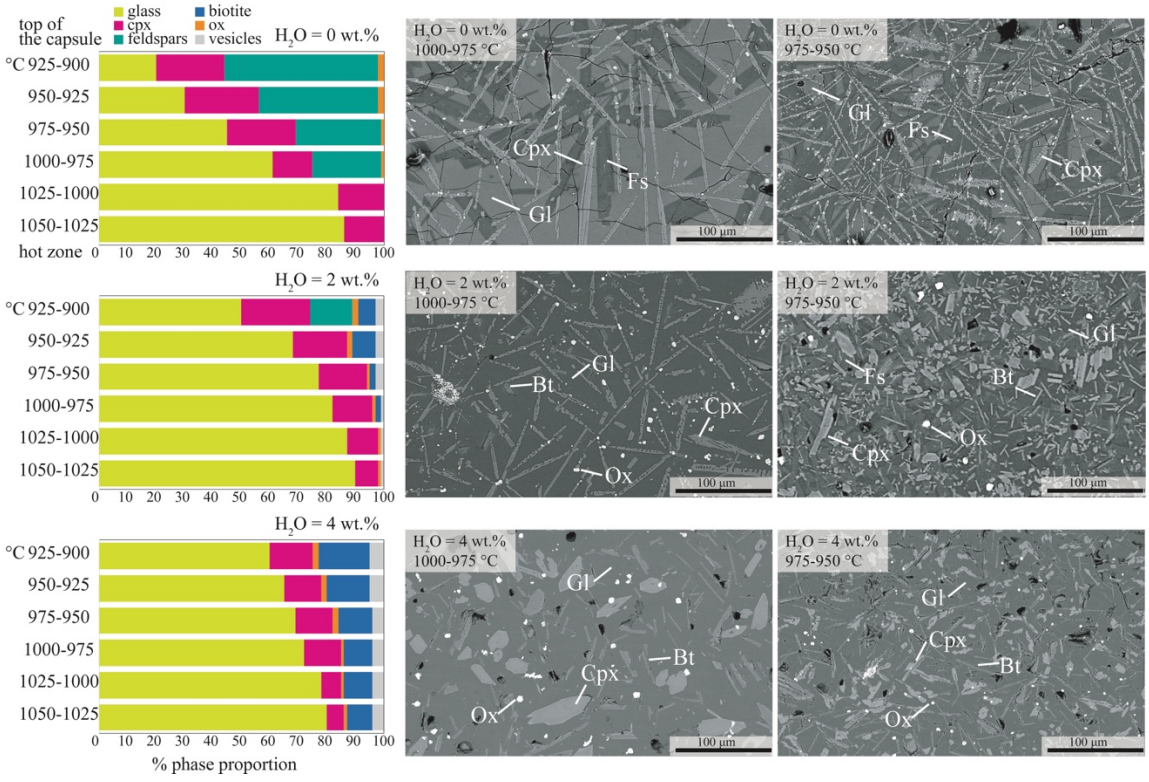

Figure 6.8 – Phase proportions along the temperature gradient of the experiments and BSE images of experimental products at two different temperature ranges (1000–975 °C and 975–950 °C) and H_2O content (modified after Costa et al., 2020). Phase abbreviations: Gl: glass; Cpx, clinopyroxene; Fs: feldspars; Bt, biotite; Pl, plagioclase; Ox, oxide.

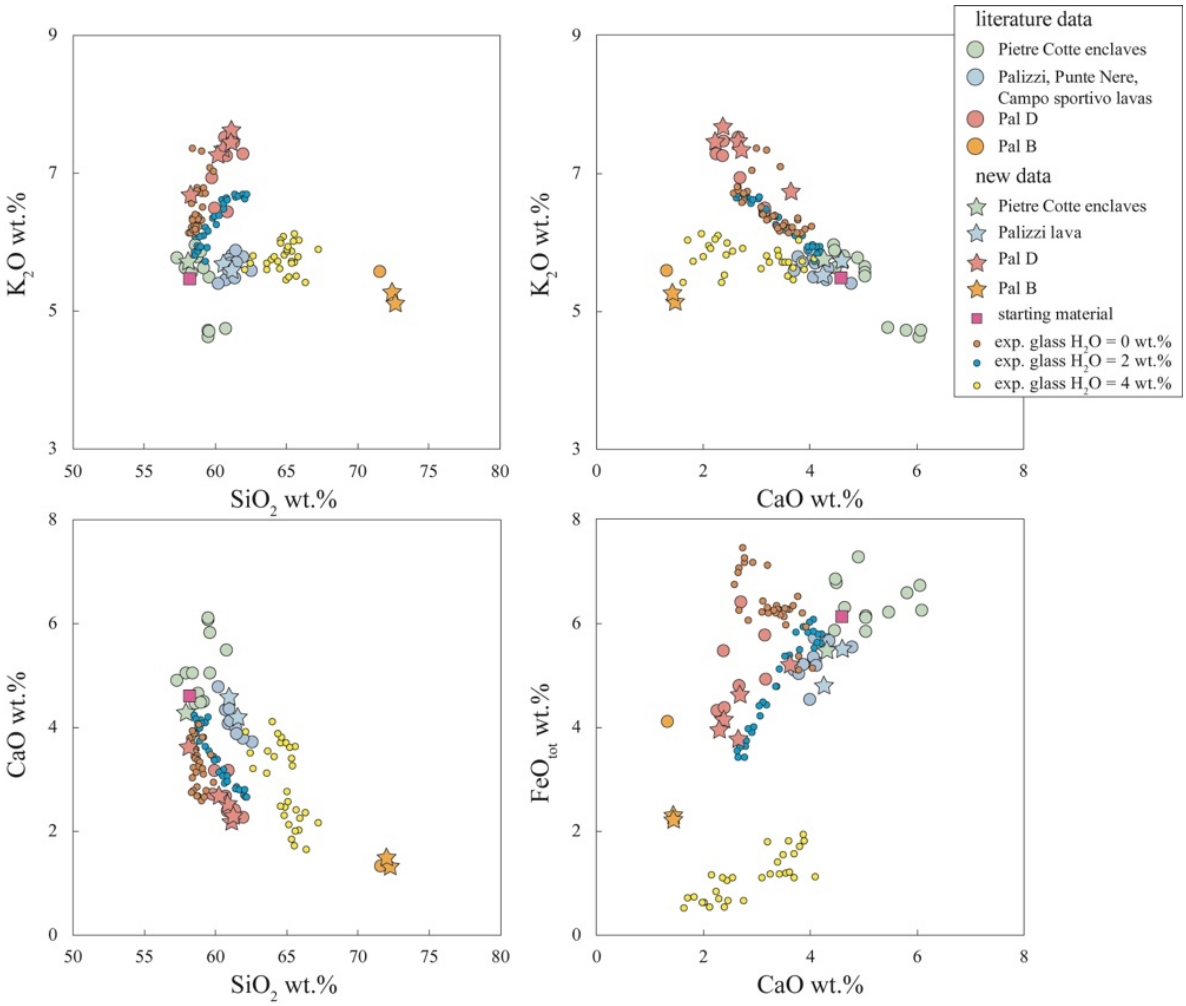

Figure 6.9 - Major elements variation diagrams for the investigated products (literature data as reported in Fig. 6.1) and experimental glasses. Major elements are recalculated to 100% on anhydrous basis (modified after Costa et al., 2020).

6.6 Mineral-melt equilibrium, thermobarometry and hygrometry

Crystallization temperature and pressure of the investigated products were estimated using the clinopyroxene-liquid thermobarometer of Masotta et al. (2013) (model errors on temperature and pressure estimates are ± 18 °C and 115 MPa respectively, Masotta et al., 2013). This model is specific to alkaline differentiated magmas and includes in the calibration dataset experiments performed with the trachytic composition of the Palizzi lava flow. The use of this model theoretically yields to the highest accuracy for the estimates of the intensive variables of magmas erupted at La Fossa. Before the calculation with the thermobarometer, clinopyroxene-melt pairs in equilibrium were selected on the basis of the predicted

vs. calculated clinopyroxene DiHd component (Mollo et al., 2013a), assuming at equilibrium the pairs with $\Delta DiHd < 0.1$ (Mollo and Masotta, 2014) (Fig. 6.10). Most of the clinopyroxene crystals resulted in equilibrium with the latitic and trachytic magmas, with the exception of clinopyroxene in the rhyolitic pumices of Pal B, not used for the calculation of the intensive variables with this method (Fig. 6.10). In particular, given the similarity between the whole-rock and the melt inclusions compositions (see Fulignati et al., 2018 and Chapter 8) of the K-rich trachytic pumices of Pal D, the clinopyroxene cores of Pal D were paired both with the whole-rock and melt inclusions data (data of melt inclusions from Fulignati et al., 2018). The crystal rims of clinopyroxene belonging to Pal D were paired with matrix glass analyses (data from Fulignati et al., 2018). Given the lack of melt inclusions and matrix glass in the trachytic lava flow (Palizzi lava) and in the latitic enclaves hosted in the Pietre Cotte lava, the bulk-rock composition was assumed as representative of the liquid in equilibrium with both clinopyroxene cores and rims for these samples. The H_2O value used as input for the thermobarometer was assumed between 2.0 and 3.5 wt.%, as determined through iterative solution by combining the plagioclase-liquid hygrometer of Masotta and Mollo (2019) and the clinopyroxene-liquid thermobarometer of Masotta et al. (2013). It should be noted that an increase of the H_2O content by 1 wt.% corresponds to an increase of the temperature estimates of less than 10 °C.

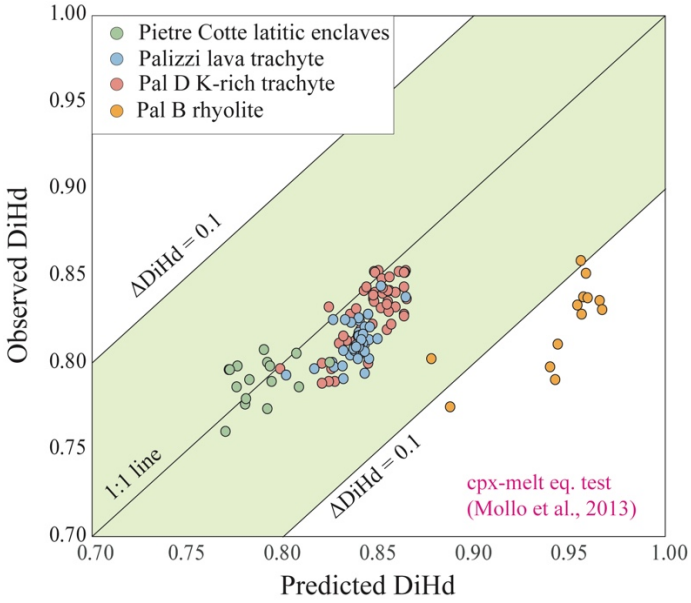

Figure 6.10 – Clinopyroxene-melt equilibrium test comparing the observed and predicted values for the DiHd component in clinopyroxene of Mollo et al. (2013a) (modified after Costa et al., 2020).

Pressure and temperature values calculated for the trachytic K-rich Pal D pumices are based on 30 core-liquid pairs and 20 rim-liquid pairs. The cores indicate crystallization temperature and pressure of 1004±14 °C and 160±54 MPa, while crystal rims show slightly lower values of temperature and pressure, although identical within the error of the model, of 996±13 °C and 132±33 MPa respectively (Fig. 6.11). Clinopyroxene core-liquid pairs (20 pairs) from the trachytic lava flow of Palizzi indicate temperature and pressure of 1007±9 °C and 199±39 MPa, whereas rim-liquid pairs (20 pairs) give temperature and pressure of 1005±8 °C and of 208±30 MPa (Fig. 6.11). Notably, the estimates obtained using both core and rim analyses are identical within the error. Compared to the trachytic products, the clinopyroxene-liquid pairs of the latitic enclaves of Pietre Cotte lava flow indicate higher temperature and pressure, with core-liquid pairs (10 pairs) giving values of 1027±5 °C and 307±47 MPa and rim-liquid pairs (10 pairs) yielding to values of 1025± 6 °C and 294±38 MPa (Fig. 6.11). As for the trachytic lava of Palizzi, core and rim analyses give results that are identical within the error. Overall, the temperature and pressure distribution inferred using clinopyroxene-liquid thermobarometry (Fig. 6.11) is consistent with the polybaric nature of the plumbing

system of La Fossa, with latitic magmas evolving at greater depth compared to trachytic ones (see Chapter 3).

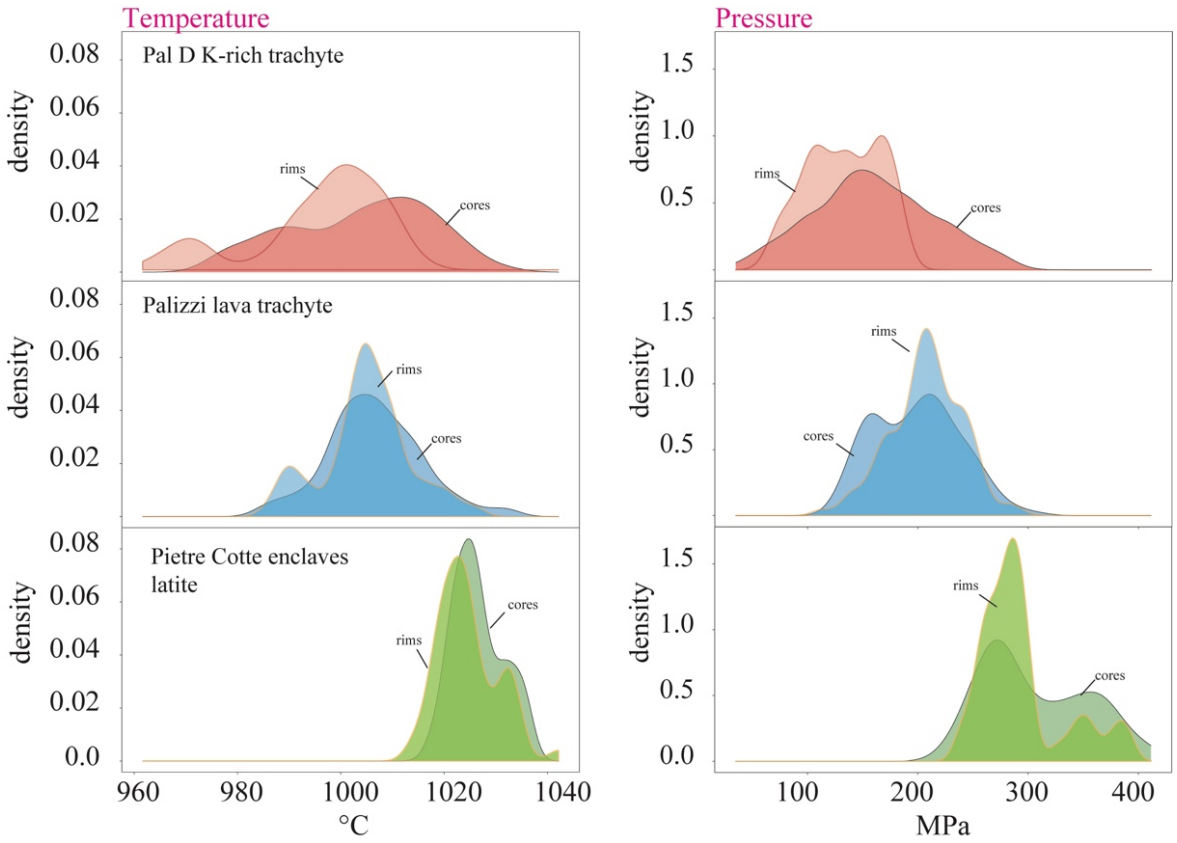

Figure 6.11 – Kernel density plots showing pressure and temperature estimates for the latitic and trachytic magmas at La Fossa obtained through clinopyroxene-liquid thermobarometer of Masotta et al. (2013). The model errors on temperature and pressure estimates are ± 18 °C and 115 MPa respectively (Masotta et al., 2013).

Further calculation of the crystallization temperatures for the latitic and trachytic magmas have been performed using the REE-in-plagioclase-clinopyroxene thermometer (Sun and Liang, 2017). This thermometer is based on REE + Y exchange between plagioclase and clinopyroxene. Calculations have been performed assuming pressures of 150 and 300 MPa, and H_2O contents of 2.5 and 3.0 wt.%, for the K-rich trachytic pumices of Pal D and the latitic enclaves of Pietre Cotte obsidian, respectively. The results, based on 42 clinopyroxene-plagioclase pairs (14 pairs for each magma composition), indicate average temperatures of 991±31 °C and 1037±8 °C for the Pal D K-rich trachytic pumices and the Pietre Cotte latitic enclave, respectively (Fig. 6.12). These values are consistent with those

inferred using the clinopyroxene-liquid thermobarometer. In contrast, the average temperature obtained for the Palizzi trachytic lava is slightly higher (1057±8 °C), probably testifying to a higher co-saturation temperature for clinopyroxene and plagioclase.

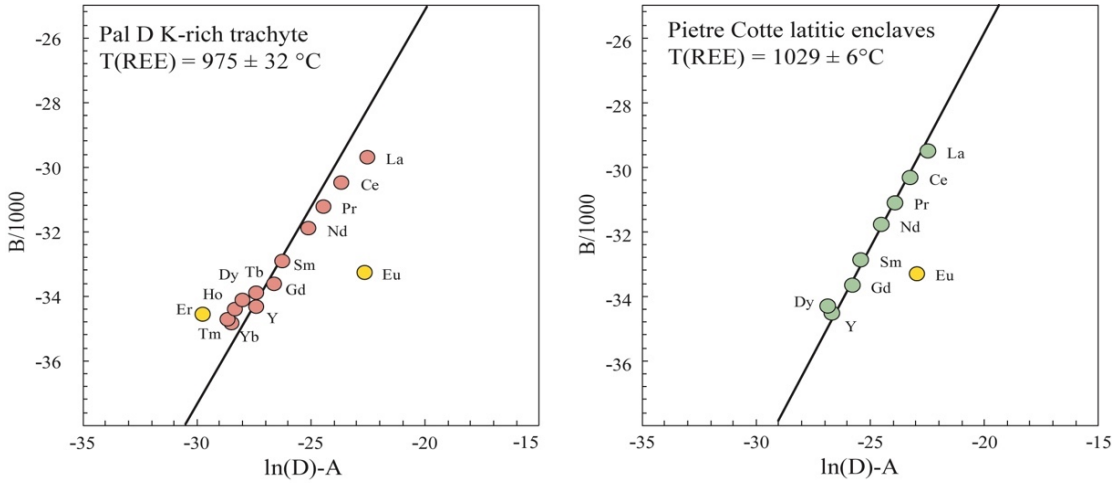

Figure 6.12 - temperature inversion diagrams showing the linear least squares regression analyses of the REE partitioning data calculated for plagioclase-clinopyroxene pairs from Pal D K-rich pumice and Pietre Cotte latitic enclave using the REE-exchange thermometer of Sun and Liang (2017). D is the partition coefficient of a given element in the geochemical group of REE. A and B are coefficients corresponding to the changes of entropy and enthalpy. At the thermodynamic equilibrium, all elements in the same geochemical group define a straight line (best fit line passing through the origin) in a plot of ln(D)-A vs. B/1000, where temperature corresponds to the slope. Yellow dots are the data excluded from the regression analysis (Costa et al., 2020).

The crystallization temperature of the Pal B rhyolite was estimated using the plagioclase-liquid thermometer of Putirka (2008) (eq. 24a calibration error ± 36 °C, Putirka, 2008). Calculations have been performed by the plagioclase (oligoclase) occurring in the Pal B pumices and the bulk rock analyses as representative of the liquid in equilibrium. According to the estimated pressure for the rhyolitic reservoir at La Fossa (Clocchiatti et al., 1994; Zanon et al., 2003), pressures from 50 to 200 MPa were used for the calculation, yielding to increasing but comparable crystallization temperatures within the errors, from 948±7 °C to 957±8°C. All the considered plagioclase-liquid pairs provide values of K_D(Ab-An) of 0.06–0.12, consistent with the equilibrium value of K_D(Ab-An) 0.10±0.05 for T < 1050 °C (Fig. 6.13) (Putirka, 2008).

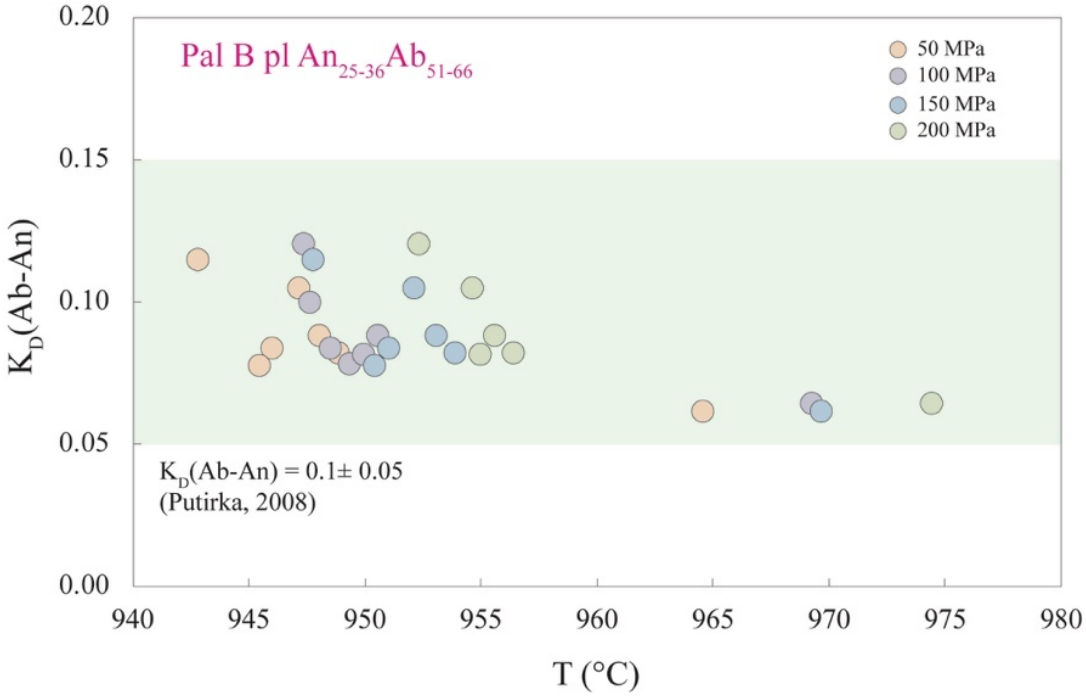

Figure 6.13 – Equilibrium test based on the K_D(Ab-An) and temperature estimates for the Pal B rhyolite using the plagioclase-melt thermometer of Putirka (2008); (eq. 24a calibration error ± 36 °C, Putirka, 2008)

Plagioclase-liquid pairs have been used to determine the H_2O content of the K-rich trachytic magma of Pal D eruption at crystallization, through the plagioclase-liquid hygrometer of Masotta and Mollo (2019) (Fig. 6.14). Plagioclase core analyses coupled with the whole-rock compositions yield a H_2O content of 2.54±0.57 wt.%, whilst rim analyses coupled with the average composition of the matrix glass indicate a water content of 2.42±0.52 wt.%. These values are in accordance with those proposed for the latitic and trachytic magmas at La Fossa by Masotta and Mollo (2019), and with the highest water content measured in melt inclusions hosted in the Pal D phenocrysts (ranging from 1.01 to 2.52 wt.%, with the low measured values interpreted as hourglass inclusions re-equilibrated with magma degassing; Fulignati et al., 2018). Plagioclase-liquid pairs of Pal B rhyolitic pumice, along with the inferred temperatures, have been used in the hygrometer of Masotta and Mollo (2019) to determine the H_2O content of the rhyolitic magma, obtaining values of 1.99±0.30 wt.% H_2O (Fig. 6.14). In table 6.3 the intensive variables obtained in this work for the investigated products are summarized.

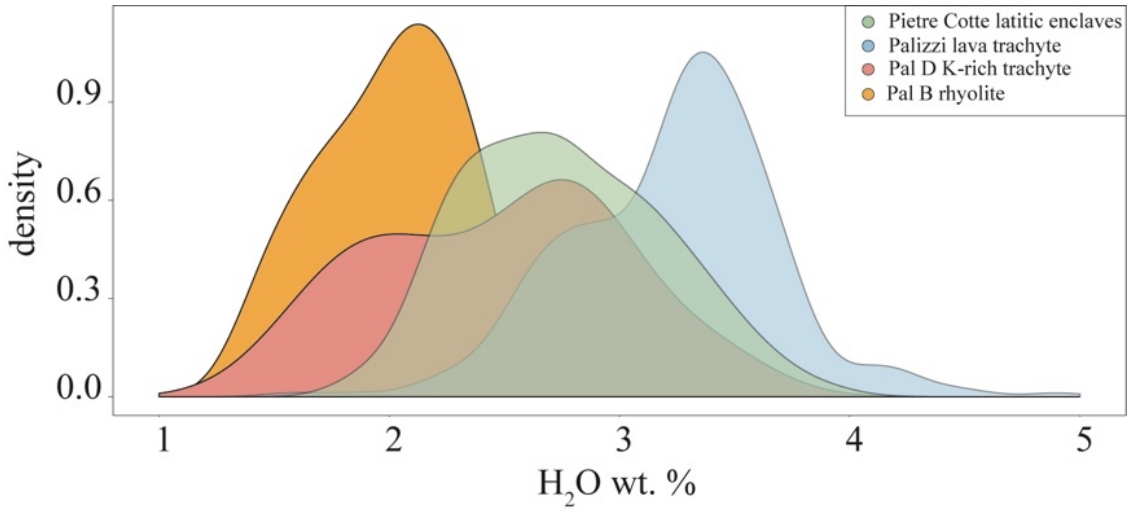

Figure 6.14 – Kernel density plot showing the range of H_2O content determined for the Pal B and Pal D products (this work) together with those obtained for the Palizzi trachytic lava and Pietre Cotte latitic enclaves (data from Masotta and Mollo, 2019) through the plagioclase-liquid hygrometer of Masotta and Mollo (2019).

*Table 6.3 - Temperature, pressure and H_2O estimates for the investigated products of La Fossa. Model: [a]Masotta et al. (2013); [b]Sun and Liang (2017); [c]Putirka (2008); [d]Masotta and Mollo (2019); [e]minimum water saturation pressure obtained with VolatileCalc2.0 (Newman and Lowenstern, 2002); *Data from Masotta and Mollo (2019)*

Eruptive Unit		Pietre Cotte	Pal D	Palizzi	Pal B
Magma composition		Latite	K-rich Trachyte	Trachyte	Rhyolite
Product		Enclave	Pumice	Lava	Pumice
T (°C)	Cpx-liq (cores)[a]	1027±5	1004±14	1007±9	-
	Cpx-liq (rims)[a]	1025±6	996±13	1005±8	-
	REE in Cpx-Pl[b]	1037±8	991±31	1057±8	-
	Pl-liq[c]	-	-	-	948±7 – 957±8
P (MPa)	Cpx-liq (cores)[a]	307±47	160±54	199±39	-
	Cpx-liq (rims)[a]	294±38	132±33	208±30	-
	Min. H_2O sat. P.[e]	-	-	-	27 – 44
H_2O (wt.%)	Pl-liq[d]	2.50-3.50*	2.54±0.57	2.50-3.50*	1.99±0.30

6.7 Magma crystallization conditions

A polybaric plumbing system consisting of multiple storage levels with magma batches undergoing mutual interactions has been invoked to explain the broad range of magma composition and the variety of mixing and mingling features

observed in the eruptive products at La Fossa volcano (Piochi et al., 2009; De Astis et al., 2013; Vetere et al. 2015; Mandarano et al., 2016; Nicotra et al., 2018). In spite of the number of petrological studies, a large uncertainty of crystallization pressure and temperature estimates of magmas erupted at La Fossa volcano still exists. This is mostly related to the reduced accuracy of several thermobarometric models applied to alkaline magma compositions and the lack of equilibrium selection criteria. Indeed, it has been demonstrated that thermobarometric and hygrometric models that are based on calibration specific to a restricted range of magma compositions have lower uncertainties compared to models based on global regressions (Masotta et al., 2013; Mollo et al., 2015; Perinelli et al., 2016; Brugman and Till, 2019). Coherently with previous works, the estimates obtained in this thesis envisage a polybaric storage system below La Fossa cone. In addition, for the first time, they allow to define the difference in the crystallization pressure between the K-rich trachytic magma of Pal D and the other trachytic magmas (Fig. 6.11). The K-rich trachytic magma of Pal D pumices equilibrated at a lower pressure (160±54 MPa) compared to other trachytic (208±30 MPa) and latitic (307±47 MPa) magmas (Fig. 6.11). The lowermost pressure estimates obtained for the K-rich trachytic magma of Pal D (30-50 MPa) is consistent with the minimum H_2O saturation pressure estimated by Fulignati et al. (2018) based on the H_2O content in melt inclusions. It is therefore possible to suggest that the K-rich trachytic magma feeding the Pal D eruption was erupted from a reservoir located at shallower depth (2-5 km) compared to those feeding the other latitic and trachytic eruptions (3-8 km).

As regarding the rhyolitic magma of Pal B, the inferred temperature of ~950±8 °C is fully consistent with the temperature estimate of 950 °C inferred for the GCEC rhyolites (Vetere et al. 2015). The lack of clinopyroxene in equilibrium with the rhyolite (Fig. 6.10) did not allow a crystallization pressure estimate based on cpx-melt equilibrium for the rhyolitic magma, however, based on the lower H_2O content of the rhyolite (~2 wt.%) obtained with plagioclase-liquid hygrometer, a H_2O-saturation pressure below 100 MPa could be supposed. The obtained H_2O range allows to estimate a minimum water saturation pressure range that spans between ~27 and ~44 MPa, calculated using the solubility model VolatileCalc 2.0

of Newman and Lowenstern (2002) at 950°C (temperature obtained for Pal B through the use of the plagioclase-liquid thermometer) (Fig. 6.15). The calculated range of pressure is in good agreement with the estimates for the rhyolite erupted at La Fossa, constraining the rhyolites (including Pal B pumice) within the shallower portions of the plumbing system of La Fossa (Clocchiatti et al., 1994; Gioncada et al., 1998; Zanon et al., 2003; Paonita et al., 2013).

The crystallization conditions obtained in this thesis provide evidence of the capability of the shallow magma system of La Fossa to feed also significant sustained explosive eruptions. Indeed, the rhyolitic Pal B and K-rich trachytic Pal D eruptions constitute the main explosive events occurred at La Fossa volcano during the studied period, being characterized by similar plume height (7-8 km a.s.l.) and erupted volume (3.6-4.0 x 10^6 m^3) (Di Traglia, 2011; Biass et al. 2016; Selva et al., 2020).

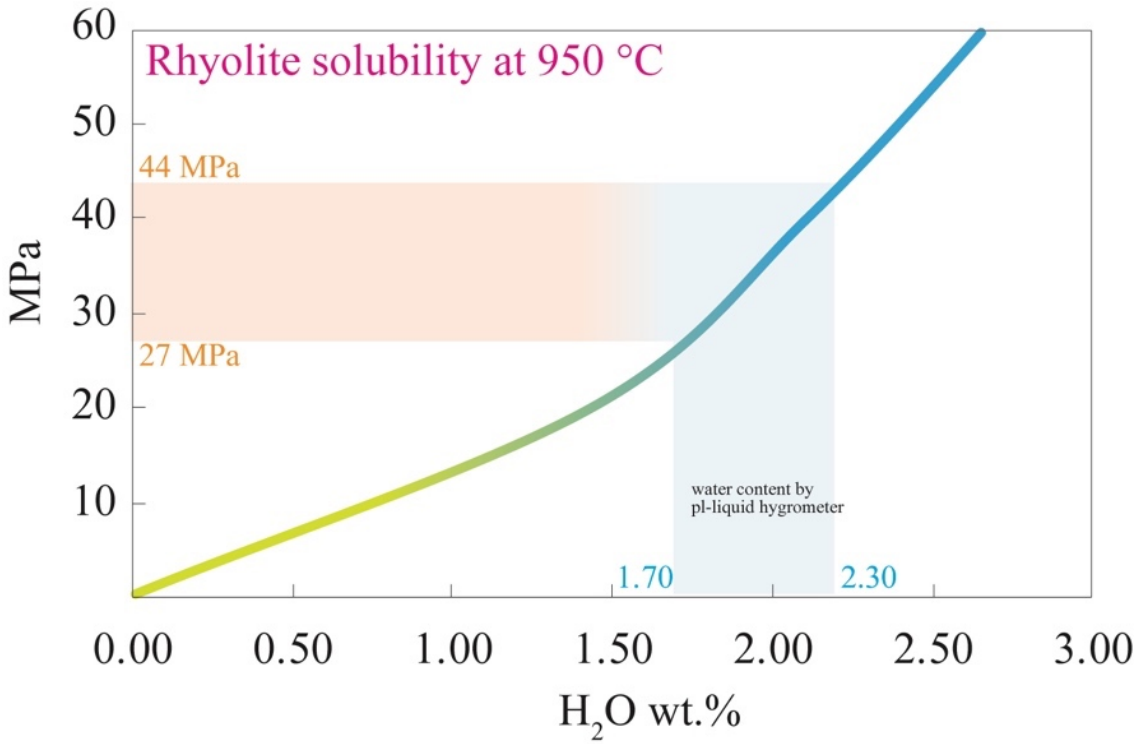

Figure 6.15 – H_2O solubility curve for a rhyolitic melt at 950 °C obtained through VolatileCalc 2.0 of Newman and Lowenstern (2002). The H_2O range measured with the plagioclase-liquid hygrometer allows to constraint a range of minimum water saturation pressure.

6.8 Magmatic differentiation at La Fossa

Mass balance modelling using major elements

One of the most interesting features at la Fossa volcano is the twofold differentiation path followed by intermediate magmas during their late evolution, leading to the formation of either K-rich trachytes (Pal D pumices) or trachytes (the trachytic lava flows of Palizzi, Punte Nere and Campo Sportivo) and then rhyolites (represented by the obsidian lava flows of Commenda and Pietre Cotte or by the pumices of Pal B) (Figs. 3.3 and 6.1). A combination of fractional crystallization and crustal assimilation (AFC) processes has been invoked in order to explain the formation of the rhyolitic magmas starting from the less differentiated latitic ones (Clocchiatti et al., 1994; De Astis et al., 1997; Del Moro et al., 1998; Gioncada et al., 1998; Piochi et al., 2009; Bullock et al., 2019). The low content of Ba and Sr, and the negative Eu anomaly of the Pal B rhyolitic pumice and in general of all the rhyolites erupted at La Fossa (Fig. 6.3), testifies to a process of fractional crystallization with a significant involvement of plagioclase and K-feldspar under relatively low fO_2 conditions. In this framework, the processes that determined the enrichment in K_2O that produced the K-rich trachytic magma and the differentiation to trachytes and rhyolites have been here explored. Mass balance calculations using major element composition of bulk rocks and mineral phases have been carried out. Calculations have been also implemented with GeoBalance (Li et al., 2020), an excel VBA program for least square regression analysis based on major element composition, giving the mineral assemblage required to reproduce a target composition from a starting composition. GeoBalance includes a Monte Carlo simulation (1000 iterations per simulation) to evaluate the uncertainties of the calculated phase proportions that propagated from the error of input data, expressed as standard deviations. The starting composition is represented by the latitic magma (latitic enclave of Pietre Cotte obsidian) and the targeted compositions are represented by both the trachytic (i.e., the K-rich trachyte of Pal D pumices and the trachyte of the Palizzi lava) and the rhyolitic (i.e, Pal B pumice) magmas. The choice of the latite as starting point for the differentiation modelling is supported

by the fact that this composition represents: i) one of the least evolved magma erupted at La Fossa and ii) the point in the differentiation line where two distinct evolutionary trends branch out (Figs. 3.3 and 6.1). The results obtained through mass balance calculations and those obtained with GeoBalance are quite similar and are reported in Appendix H. Four possible differentiation segments are thus modelled (Fig. 6.16):

1. Latite to K-rich trachyte: the K-rich trachytic composition of Pal D pumices is obtained through fractionation (fractionated solid ~30%) of a mineral assemblage made up by plagioclase (~17%), clinopyroxene (~7%), sanidine (~3%), Fe-Ti oxide (~2%), olivine (~0.5%) and biotite (~0.5%);

2. Latite to trachyte: the trachytic composition of the Palizzi lava is obtained through fractionation (fractionated solid ~37%) of a mineral assemblage made up by sanidine (~13%), plagioclase (~15%), clinopyroxene (~4%), biotite (~3%), Fe-Ti oxide (~2%) and olivine (~0.5%);

3. K-rich trachyte to rhyolite: the rhyolitic composition of Pal B pumices is obtained through fractionation (fractionated solid ~70%) of a mineral assemblage made up by sanidine (~41%), plagioclase (~17%), biotite (~6%), Fe-Ti oxide (~4%) and clinopyroxene (~2%);

4. Trachyte to rhyolite: the rhyolitic composition of Pal B pumices is obtained through fractionation of a mineral assemblage (fractionated solid ~66%) made up by sanidine (~32%), plagioclase (~21%), clinopyroxene (~6%), Fe-Ti oxide (~4%) and biotite (~3%).

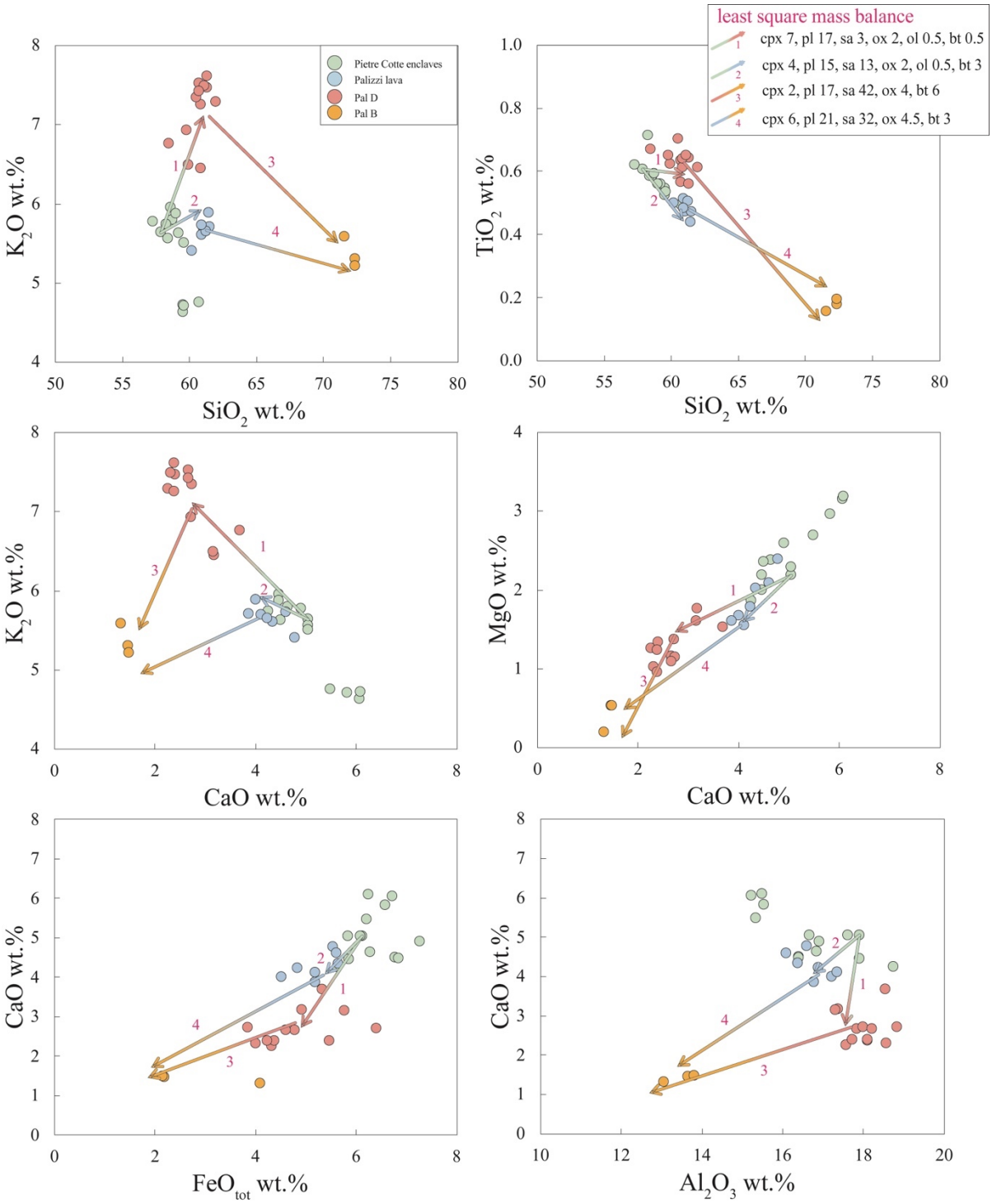

Figure 6.16 - Fractional crystallization modelling based on least square mass balance calculation using major element of bulk rocks and minerals of the investigated eruptive products of La Fossa (literature data references as reported in Fig. 6.1; modified after Costa et al., 2020). The starting composition is represented by the latitic enclaves of Pietre Cotte, whereas the target compositions are the K-rich trachyte of Pal D (segment 1), the trachyte of the Palizzi lava (segment 2) and the rhyolite of Pal B (segment 3 and 4). Only results displaying a regression sum of squares (SSR)<2, and error sum of squares (SSE) <0.6 were considered (see Appendix H).

Concerning the differentiation toward the two trachytic terms, segments 1 and 2 differ substantially in the proportions of fractionated mineral phases. The plagioclase/sanidine ratio varies from about 5:1 to about 1:1, determining the evolution of the melt toward either K-rich (Pal D) (segment 1) or other (segment 2) trachytes (Palizzi lava) (Fig. 6.16). The two contrasting trends can be associated to the different pressures inferred from thermobarometric calculation, suggesting a lower pressure for the K-rich trachyte compared to normal trachyte. This is because the higher fractionation of plagioclase would be favored at a lower pressure due to the lower activity of H_2O in the melt. The formation of the rhyolite has been modelled by considering differentiation paths starting from the two different trachytes (segments 3 and 4, respectively; Fig. 6.16). Segment 3 differs from segment 4 because of the higher sanidine/plagioclase ratio the higher biotite/clinopyroxene ratio. The compositional variability of magmas erupted at La Fossa, with the K-rich trachytic composition being erupted only during a single eruptive event (Pal D pumices), overall suggests that rhyolitic magmas could originate through differentiation from trachytic magmas represented by the composition of the Palizzi lava.

Effect of H_2O on magma differentiation: evidences from temperature gradient experiments

Temperature gradient experiments explored the effect of the H_2O melt content (0, 2 and 4 wt.%) on the differentiation of the latitic magma. Experiments designate different paths of melt differentiation that overall indicate an increase of the SiO_2/K_2O ratio with the increasing H_2O in the system (Fig. 6.9). The interstitial glasses analyzed in the two experiments with 0 and 2 wt.% H_2O better approximate the K_2O enrichment trend modelled by segment 1 (high K trachyte of Pal D) whereas the most hydrous experiment with 4 wt.% H_2O approximates the SiO_2 enrichment trend modelled by segments 2 and 4 (trachytes and rhyolites). Overall, the divergence of these trends is explained by the different proportions of feldspars, clinopyroxene and biotite that crystallize at different H_2O content (Fig. 6.8). Therefore, the experimental results confirm what inferred from the crystal

fractionation modelling and from thermobarometric and hygrometric analyses, that the K-rich trachytic magma of Pal D originated at lower pressure and at lower H_2O concentration compared to other trachytic magmas erupted at La Fossa volcano (Figs 6.11 and 6.14). The H_2O content in the melt (in turn related to the storage depth of the magma), by varying the clinopyroxene/feldspar+biotite ratio, exerts a primary control on phase stability and determines the differentiation trend towards either K-rich composition (segment 1) or trachytes and rhyolites (segments 2 and 4). The higher H_2O content of both latitic and trachytic magmas, compared to the K-rich trachytic of Pal D, is in accordance with the H_2O estimates of 2.5–3.5 wt.% inferred using the plagioclase-liquid hygrometer (Masotta and Mollo, 2019). This finding is also in accordance with experimental results by Beermann et al. (2017), reproducing the crystallization of basaltic andesite of the 24 ka Lower Pollara eruption (Salina, Aeolian Islands) and demonstrating that a strong increase of K_2O relative to SiO_2 can be reproduced at higher temperatures and relatively low H_2O content.

Trace elements geochemical modelling

A combination of fractional crystallization and crustal assimilation (AFC) processes has been invoked to explain the formation of the rhyolitic magmas at La Fossa starting from the less differentiated shoshonitic and latitic ones (Clocchiatti et al., 1994; Del Moro et al., 1998; Piochi et al., 2009; Bullock et al. 2019). The low content of Ba and Sr, and the marked negative Eu anomaly of La Fossa rhyolites (Figs 6.3 and 6.4) testifies to a process of fractional crystallization with a significant involvement of plagioclase and K-feldspar. In addition to the mass balance calculations performed using major elements composition, the evolution of latitic, trachytic and rhyolitic magmas has been investigated with FC and AFC trace elements modelling using the equations proposed by DePaolo (1981). The crustal contaminant used in the model is represented by the average composition of the Calabro Peloritano metapelites (Frezzotti et al., 2004). The used bulk partition coefficients (D_{bulk}) have been estimated using modal mineral assemblages of the relative proportions of crystallizing phases obtained through the least square mass

balance calculations and a series of mineral/melt partition coefficients ($k_d^{min\text{-}melt}$). The $k_d^{min\text{-}melt}$ have been selected among those available in the literature (Germ database) specific for latitic, trachytic and rhyolitic magmas, including those estimated for La Fossa products (Appendix I). Thus, each step of magmatic differentiation (latite-trachytes, trachytes-rhyolite) has been modelled using a minimum (low) and a maximum (high) calculated D_{bulk}, and modelled via pure FC and AFC with *r* between 0.2 and 0.5 (*r*, rate of assimilation/rate of fractional crystallization) (De Astis et al., 1997; Del Moro et al., 1998; Frezzotti et al., 2004; Piochi et al., 2009), in order to embrace a series of initial trace elements concentration (Figs. 6.17 and 6.18). See Appendix I for additional details of FC and AFC models.

Starting from the same latitic composition and assuming the same phase assemblage obtained through mass balance calculations, the model shows that the trachytic products (both the K-rich composition of Pal D and the Palizzi lava) are not entirely reproduced by simple FC or AFC processes. Indeed, after 30–40% of crystal removal, ideally corresponding to the paths 1 and 2 showed in figure 6.16, and considering either a low or high D_{bulk}, the modelled fractionated liquids plot in a region where none of the intermediate-evolved samples of Vulcano occur. The origin of the K-rich trachytic magma of Pal D could be only in part explained by 30 to 40% crystal fractionation involving a higher plagioclase/sanidine ratio (as inferred from mass balance calculations and experiments) in the fractionated solid and leading to a slight increase in Ba and Rb compared to the other latitic and trachytic products (Fig. 6.17). It is worth noting that the two different modal assemblages responsible for both the latite to K-rich trachyte and trachyte, do not reproduce significant differences in the fractionated liquids via trace element modelling (Fig. 6.17).

The AFC process for the genesis of the rhyolitic magma (Fig. 6.18) has been modeled starting from the ending points of the latite-trachyte fractionation of figure 6.17 and thus considered as the parental intermediate liquid compositions of the rhyolite.

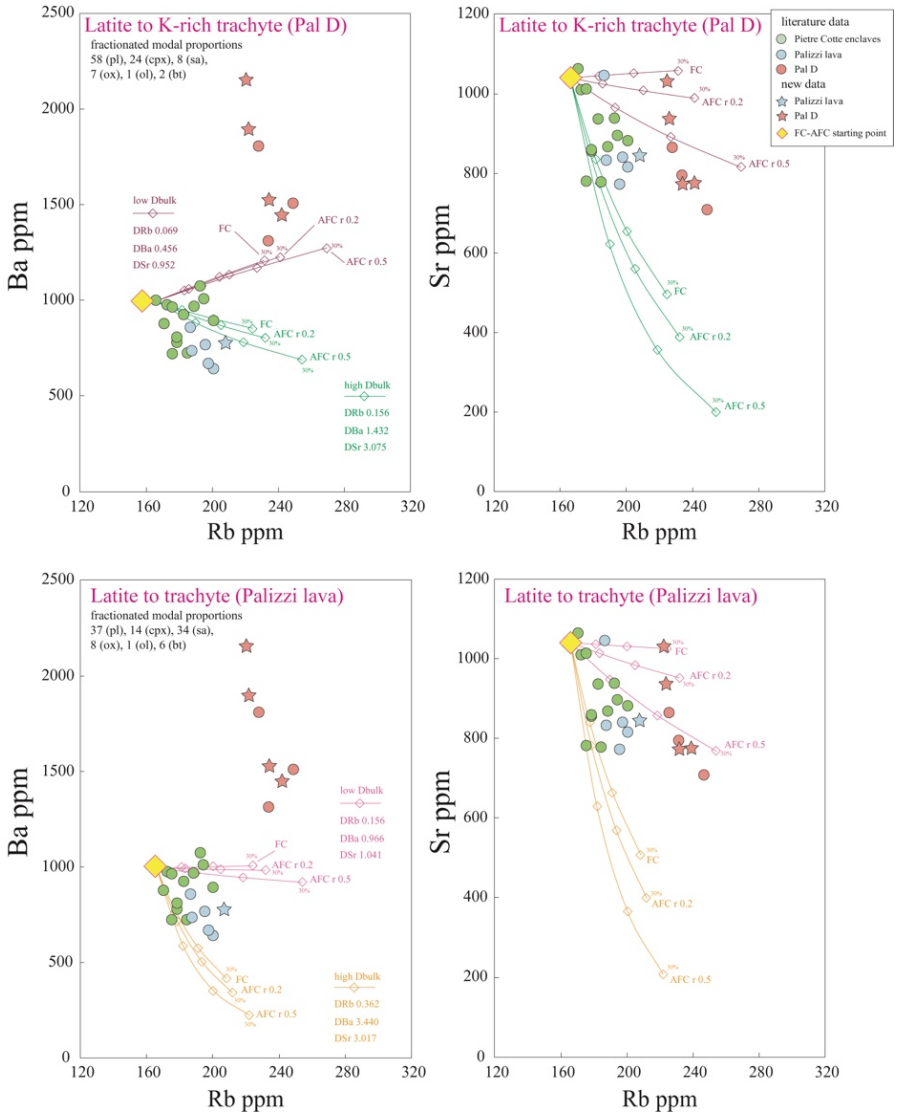

Figure 6.17 – FC and AFC modelling for the latite to trachyte magmatic differentiation. The used D_{bulk} have been estimated using modal mineral assemblages of the relative proportions of crystallizing phases obtained through the mass balance calculations and selected $k_d^{min/melt}$ (see Appendix I and the test for further explanations). The numbers along the differentiation paths refer to the crystal fractions. Literature data are from De Astis et al. (1997), Del Moro et al (1998), Nicotra et al. (2018), Bullock et al. (2019). (Modified after Costa et al. 2020).

Modelling the trachyte-rhyolite differentiation from two distinct starting points (obtained with low and high D_{bulk}), allows to cover a range of starting trace element concentrations plotting between this compositional field and the erupted rhyolites. By these points, rhyolites are possibly explained by 40–50 % crystal fractionation with an assimilation rate between 0.2 and 0.5. The high fraction of sanidine involved in the fractionated assemblage drives the liquid evolution toward depletion in Sr and Ba (Fig. 6.18).

Compared to mass balance calculations with major elements, the AFC model indicates a lower amount of crystal fractionation (40–50% instead of ~66–70 %, path 3 and 4 in Fig. 6.16). This discrepancy could be symptomatic of the fact that, to model the evolution from trachyte to rhyolite, the partition coefficients may need to be varied during differentiation or other mechanisms of liquid fractionation may be accounted. Furthermore, the crystal-poor or even aphyric nature of the rhyolitic magmas erupted at La Fossa is in contrast with the results obtained by both mass balance calculations and AFC modelling. These findings are in accordance with the thermodynamic simulations carried out by Palummo et al. (2020), that fail to reproduce the trachytic and rhyolitic melt compositions erupted at Vulcano between 50 and 8 ka, after about 50% of fractionated solid. Bearing in mind these considerations, and also the fact that the trachytic magmas are not fully explained by trace elements modelling, other possibilities regarding the formation of the trachytic and crystal-poor differentiated magmas at La Fossa must be considered.

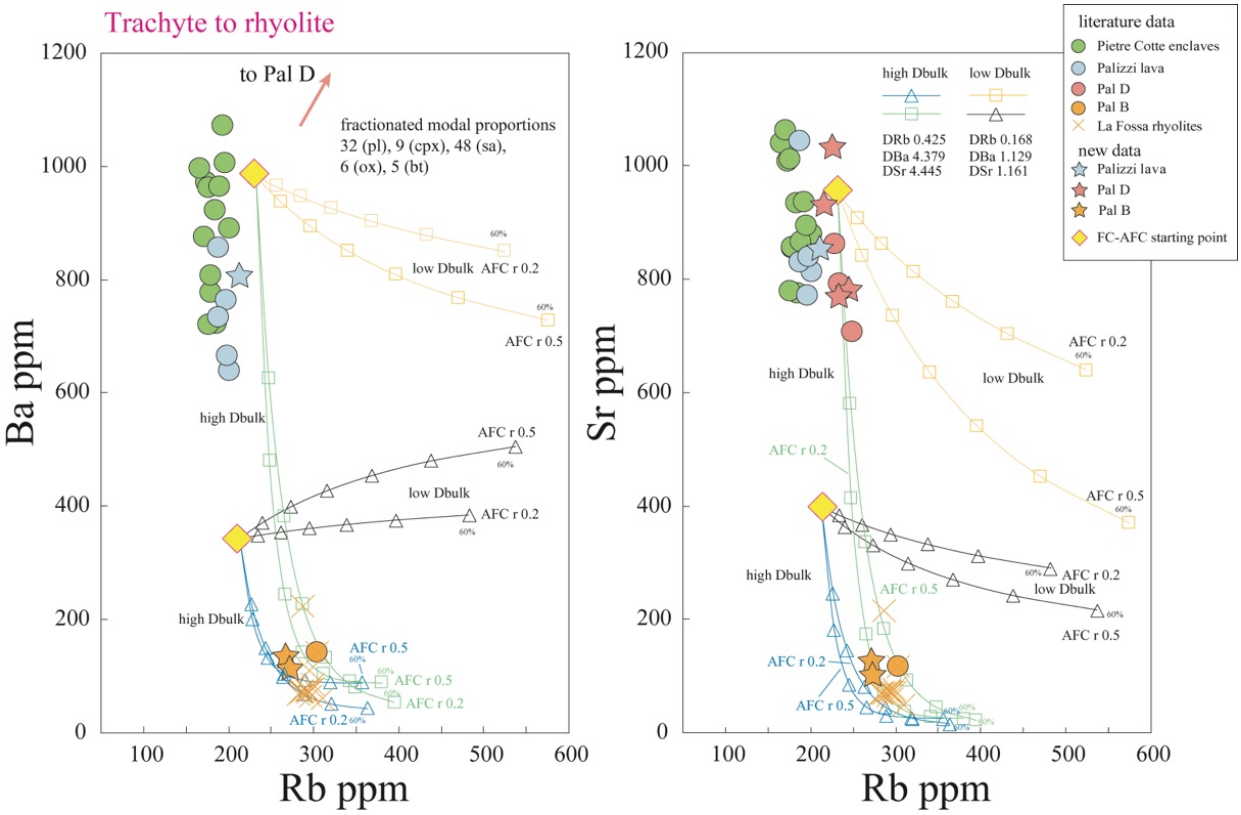

Figure 6.18 – AFC modelling for the trachyte to rhyolite magmatic differentiation. The numbers along the differentiation paths refer to the crystal fractions. Literature data as in figure 6.17. (Modified after Costa et al. 2020). (see Appendix I and the text for additional details on the models).

6.9 The role of the crystal mushes in the La Fossa plumbing system

Genesis of the rhyolitic magmas

One possible explanation of the origin of the crystal-poor rhyolites is the partial melting of crustal and subvolcanic rocks favored by the intrusion of hotter magmas at depth. This process has been invoked at Lipari island by Crisci et al. (1991) and Esperança et al. (1992) and more recently by Masotta et al. (2018) for the formation of rhyolitic melts at Krafla volcano (Iceland). The anatectic origin for the La Fossa rhyolites can be ruled out, since the lithology of the subvolcanic rocks are inconsistent with the formation of the La Fossa rhyolitic melts. Even if the perforations carried out for geothermal exploration within the La Fossa Caldera at 1000 m and 2000 m revealed the presence of rhyolitic-latitic-shoshonitic subvolcanic bodies, and a monzogabbroic body, respectively (Faraone et al., 1986; Gioncada and Sbrana, 1991), the homogeneous composition of the rhyolitic magmas erupted at La Fossa contrasts with the heterogeneity of the lithotypes revealed by the perforations. Indeed, partial melting of latitic and trachytic lithologies is inconsistent with the isotopic composition of the rhyolites and with the low content of Ba, Sr and the marked negative Eu anomaly that, in turn, are better explained by processes of crystal fractionation plus a small amount of crustal assimilation (Fig. 6.18).

As alternative to partial melting of shallow crustal rocks, the crystal-poor rhyolites could be explained in the light of efficient crystal-melt separation processes. It is widely accepted that the architecture of magmatic systems should be envisaged in a “mush-dominating” perspective, where the melts and exsolved fluids are distributed within a crystalline network, in vertically developed systems (Forni et al., 2015; Cashman et al., 2017; Edmonds et al., 2019; Sparks et al., 2019; Di Stefano et al., 2020). In this scenario, crystal-poor evolved melts can be generated by the extraction from crystal mushes of intermediate composition favored by efficient crystal-melt separation processes. These models include: i) compaction-induced segregation of melt and subsequent extrusion of interstitial melt in response to deformation and settling of a crystalline framework (Bachmann

and Bergantz, 2004, 2008), ii) segregation of evolved liquid induced by gravitational instability of the upper solidification front (Marsh, 2002; Masotta et al., 2012b), iii) filter-press induced by volatile exsolution (Pistone et al., 2015) and iv) melt extraction during shear (Petford et al., 2020). Thermo-mechanical modelling suggests that melt extraction is more efficient at high crystal content between 50 and 70% (Bachmann and Bergantz, 2004; Dufek and Bachmann 2010; Gelman et al., 2014). In this context, volatile exsolution plays a fundamental role on the physical and rheological properties of melts produced within mush-dominated regions of such systems (Parmigiani et al., 2014; Edmonds et al., 2019; Hartung et al., 2019). When the fluid exsolution is reached, in a system largely dominated by a high crystal fraction (50–70%), the volatile phase is concentrated in narrow channels (Oppenheimer et al., 2015) that may favor the segregation of melt locked in the crystal network, through gas-driven filter pressing (Sisson et al., 1999; Pistone et al., 2015). A similar process was also observed in temperature gradient experiments by Rodriguez et al. (2017), who described the migration through the crystal mush of a fluid phase exsolved through second boiling (i.e. volatile exsolution induced by isobaric crystallization).

Extraction of rhyolitic melt from intermediate crystal mushes has been therefore explored with the help of the model proposed by Gelman et al. (2014). Through this model, consisting of equations for the conservation of mass, it is possible to simulate the evolution of a trace element in a magma mush environment simultaneously undergoing crystallization and extraction of interstitial melt. In the model, the bulk partition coefficients, as well as the starting composition already used in the AFC model for the trachyte-rhyolite differentiation step, have been selected as input parameters and melt extraction starting points, respectively. An additional starting point of melt extraction, plotting in the middle of the gap region outlined by the differentiation of trachytic magmas has been tested (Fig. 6.19). Although these starting compositions do not usually occur in the erupted products of La Fossa, the presence of crystal mushes of intermediate compositions from which rhyolite may be extracted can be envisaged thank to the occurrence of sanidine-rich enclaves (sanidine-rich mush rock, classified as alkali-syenite) composed by idiomorphic medium-grained K-feldspar with minor femic minerals,

and augitic clinopyroxene. These types of magmatic enclaves have been found in the rhyolitic products of the AD 1888–1890 eruption and interpreted as fragments of the wall-rock (Clocchiatti et al., 1994). In trace and major (not shown) elements variation diagrams the sanidinite plots in the region of compositional gap highlighted by magmatic differentiation with its composition being not so dissimilar from the starting points of melt extraction (Fig. 6.19).

The model of Gelman et al. (2014) allows extraction of interstitial melt when the system reaches a mid-crystallinity peak of 50–70%, in accord with the crystal fraction required by the trachyte to rhyolite differentiation modelled through mass balance calculations and AFC modelling (Fig. 6.19). The modeled liquid match with the rhyolite composition erupted at La Fossa if low amounts (0.1 to 0.3 of the total initial mass of the system (i.e. crystal mush plus interstitial liquid) are extracted. The rhyolitic melts at La Fossa, that are enriched in Rb, Zr and depleted in Eu, Sr, and Ti, are thus explained by extraction of interstitial melts from crystal mushes of intermediate composition largely dominated by K-feldspar. These findings are in strong accordance with the model proposed by Palummo et al. (2020), who suggest that also the older (50–8 ka) differentiated trachytic and rhyolitic products of Vulcano can be obtained by in-situ crystallization starting from intermediate magmas.

At La Fossa volcano, pre-eruptive volatile exsolution is likely to occur at the rhyolite stage in the shallow system (Gioncada et al., 1998; Fulignati et al., 2018; see also Chapter 8). The rhyolitic magmas at La Fossa could be therefore generated by differentiation processes within crystal mushes. Melt extraction can be favored by the exsolved fluid phase, which contributes in rejuvenating the crystal mush through the increase of the melt fraction (Ardia et al., 2008; Pistone et al., 2013; Pistone et al., 2017; Hartung et al., 2019). These processes can be even more effective in the case of a mush system that approaches the second boiling upon late solidification (Edmonds et al., 2019).

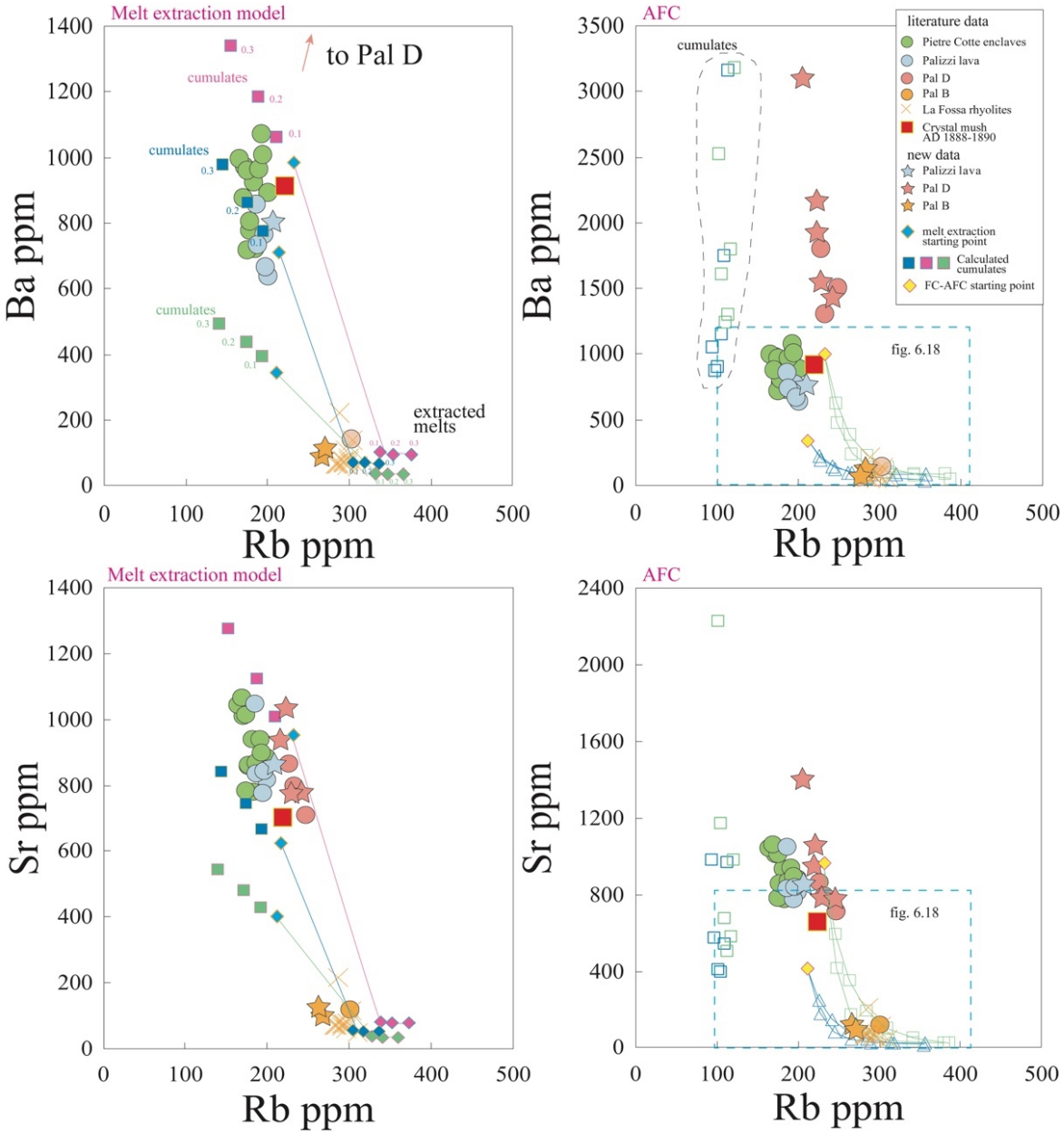

Figure 6.19 – Trace element modelling of rhyolitic melt extraction using the model of Gelman et al. (2014) and comparison with AFC modelling. Numbers along the extracted melts and calculated leftover cumulate composition after melt extraction, refer to the total amount of extracted melt (0.1-0.3). Note the difference between the calculated cumulate compositions between the melt extraction model and the AFC model. Literature data as in figure 6.17.

Crystal mush-recharging melts interaction and the origin of magmatic enclaves

Assuming that the rhyolitic magma originated through melt extraction from intermediate crystal mushes, it is important to consider also the genetic relationship between the rhyolite and the crystal-rich latitic-trachytic enclaves occurring in the rhyolitic samples, previously seen as evidence of simple magma mingling/mixing

processes (Piochi et al., 2009; Vetere et al., 2015). In the similar context of the nearby Lipari island, Davì et al. (2010) demonstrated that the rhyolitic magma feeding the Rocche Rosse lava flow was produced through AFC processes, starting from the latitic magma compositions represented by magmatic enclaves contained in the rhyolitic lava. According to Forni et al. (2015), these enclaves represent remobilized and partially melted portions of the crystal mush from which the rhyolitic melt originated. A similar origin for the crystal-rich latitic enclaves found in the Pietre Cotte obsidian lava has been proposed (Forni et al., 2015; Bullock et al., 2019).

In the case of the products erupted at La Fossa in the last 1000 years, the coexistence of latitic-trachytic and rhyolitic magmas in the eruptive products testifies to the presence of magmas belonging to the same liquid line of descent, but yielding to different types of interaction. The contrasting rheological behavior of the crystal-rich latitic-trachytic enclaves and the host rhyolitic magma, as for example in the case of the Pietre Cotte obsidian, suggests that very different rheology characterized the two magma domains before the mixing process (Fig. 3.7) (i.e., the entrained enclaves were crystal-rich; P.I. = 25–30%). In contrast, in the case of the mafic banding in the Pietre Cotte pumices and the Commenda lava, the trachytic-latitic domain had similar rheological behavior. Consistently, the crystal content of the latitic-trachytic domain (P.I. ranging from 3 to 30%) overlaps only in part the crystallinity range that defines the magma as a crystal mush (25-50%; Marsh, 1996) and that, in turn, allows to classify the magmatic enclaves of Pietre Cotte as a whole constituted by partially remobilized fragments of the crystal mush and a mafic recharging magma. Indeed, the remobilization of the crystal mush could have been caused by the arrival of a new batch of hotter magma that reduced the crystallinity of the mush (Deering et al., 2011; Wolff et al., 2015; Zou and Ma, 2020). Part of this magma was erupted (e.g. evidence for the eruption of a latitic magma is the banding in the Upper Pietre Cotte pumices and Commenda lava, Fig. 3.7) and the remaining part interacted with the crystal mush at depth. The melting of mineral phases such as alkali feldspar and biotite, almost absent in magmatic enclaves but necessary to form rhyolitic magma, reduced the crystallinity and caused the hydration and remobilization of the crystal mush. The previously

extracted rhyolitic melt, the remobilized portions of the crystal mush (i.e., enclaves and glomerocrysts) and the newly arrived latitic magma were thus erupted together.

In order to verify this hypothesis, partial melting simulations of the modeled cumulates leftover by the extracted rhyolitic melt, has been carried out using the equation for aggregated non-modal fractional melting (Shaw, 1970). The thermal modification of the mush could be favored by periodical arrival of relatively mafic melts from depth, that in the case of the recent (last 1000 years) plumbing system of La Fossa-Vulcanello, may be represented by shoshonitic composition (Fig. 6.20) (erupted directly only at Vulcanello, Vetere et al., 2007; Davì et al., 2009; De Astis et al., 2013; Fusillo et al., 2015). Calculated mixing lines between shoshonitic samples and melts originated by the partial melting of the mush show that the latitic enclaves of Pietre Cotte and other trachytic composition (e.g. Palizzi lava), are explained by variable degree of mixing between mafic melts and liquids produced by the partial melting of the crystal mush and cumulate crystals (Fig. 6.20). This process explains the geochemical and textural characteristics of the magmatic enclaves of Pietre Cotte, that show isotropic microlitic groundmass indicative of a rapid growth in a latitic melt and where high-Sr plagioclase (Piochi et al., 2009; Bullock et al., 2019) is often surrounded by an overgrowth of sanidine, related to the crystallization from a melt originated by partial melting of a feldspar-rich crystal mush (Forni et al., 2015). The texture of magmatic enclaves and, more in general, of the lati-trachytic magmas that exhibit a broad range of crystal size, shape and textures (including glomerocrysts; Figs. 3.7 and 6.2) supports this hypothesis. This variability may be caused not only by the repeated episodes of recharge by a more mafic magma composition, magma ascent and mixing in short time scales (1–10 years, Nicotra et al., 2018), but mainly by the variable degree of interaction of the recharging magmas with the crystal mushes. Mixing processes in variable proportion between shoshonitic to latitic recharging magmas, partial melted crystal mushes and the extracted rhyolites, account also for the compositional and textural features of trachytic products that show evidence of mixing, plotting in straight lines in major and trace elements variation diagrams connecting the rhyolites with the crystal-rich enclaves (Fig. 6.20).

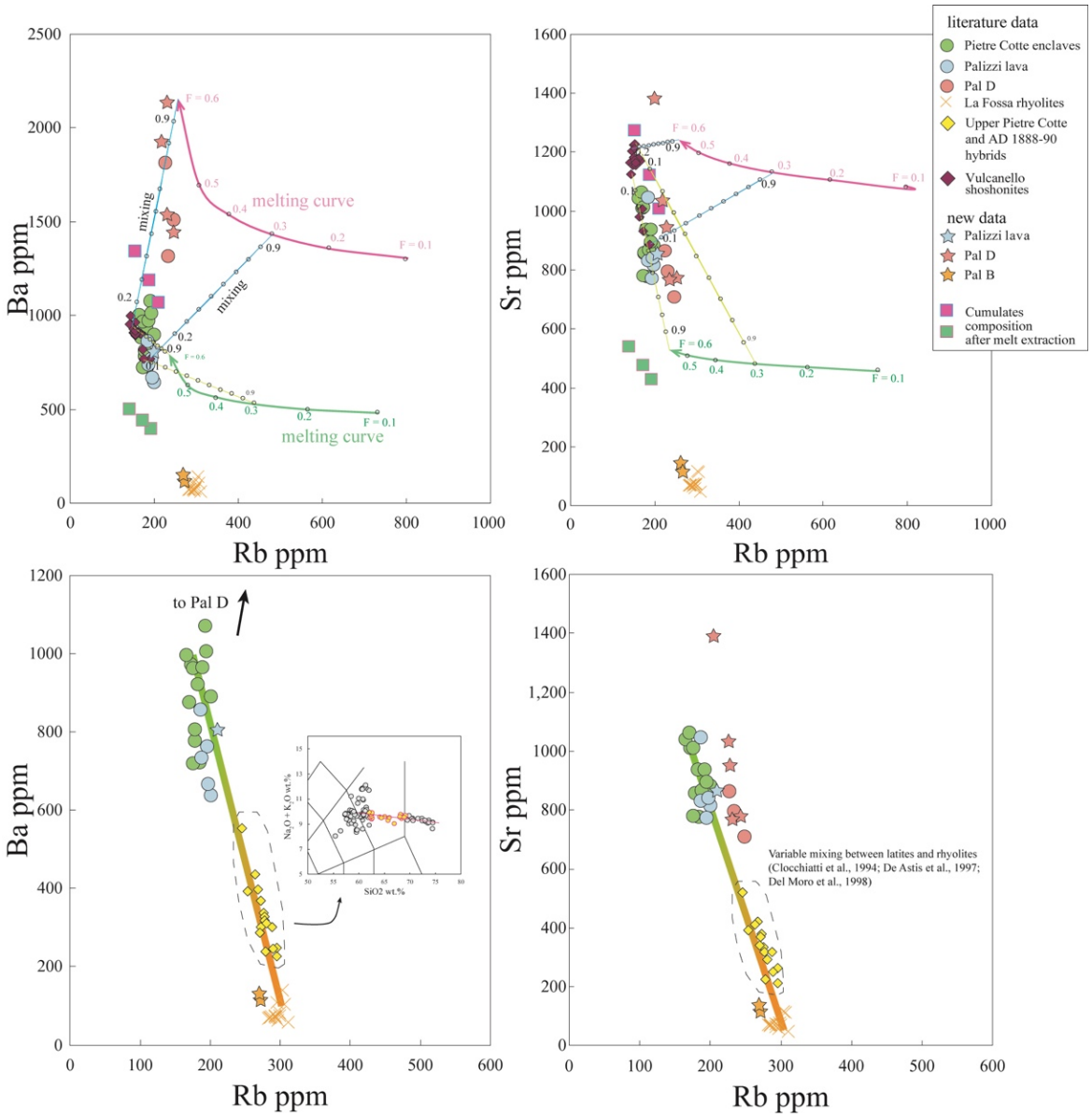

Figure 6.20 – Non-modal aggregative fractional melting modelling (Shaw, 1970) of cumulates leftover from rhyolitic melt extraction and calculated mixing lines between mush-melts and recharging magmas represented by Vulcanello shoshonites. Mixing in variable proportion between recharging magmas, partial melted crystal mushes and the extracted rhyolites, accounts for the compositional and textural features of trachytic products that show evidence of mixing and for the K_2O, Ba-rich Pal D eruption. Literature data as in figure 6.17.

In this multifaceted framework, the "unique" composition of Pal D find its precise explanation. Variable interactions between a shoshonitic-latitic magma undergoing differentiation at low P (~150 MPa) and H_2O content (~2 wt.%), as inferred from clinopyroxene thermobarometry and plagioclase-liquid hygrometry, and a higher amount of melts coming from the partial melting of the crystal mush is able to explain the enrichment not only in K_2O, but also in Al_2O_3, TiO_2, Ba and

Sr that characterize the Pal D eruption. The slightly negative Eu anomaly (0.79-0.83) of Pal D pumice, together with marked enrichment in Ba and to a less extent in Sr suggest the assimilation by recharging magmas of melts derived by partial melting of K-feldspar-rich mush (Forni et al., 2018a; Forni et al., 2018b; Wolff et al., 2020). The origin from a melt strongly modified by the interaction with this type of melt is also supported by the composition of plagioclase, enriched in Sr and Ba, with respect to plagioclase from other latitic and trachytic magmas, and by the sanidine enriched in the Or component.

6.10 Conclusions

The complex relationships among latitic, trachytic and rhyolitic magmas erupted at La Fossa volcano in the last 1000 years are unveiled by mineral-liquid thermobarometry and hygrometry, geochemical modelling and temperature gradient experiments. By combining these information with the petrographic analysis of explosive and effusive products, a new model for the polybaric magmatic system is obtained (Fig. 6.21)

In this framework, the latitic magma represents the least differentiated composition erupted at La Fossa volcano in the last 1000 years and the closest parental magma for both K-rich (Pal D) and “normal” trachytes (Palizzi lava flow). The polybaric differentiation of this magma leads to the formation of several vertically distributed crystal mushes. Geochemical modelling highlights the fact that the rhyolitic melts are originated within the latitic-trachytic crystal mush and eventually segregated into crystal-poor batches. Repeated episodes of melt extraction are possibly linked to increased volatile concentration in the melt up to exsolution of a fluid phase (i.e. second boiling of mushy magmas).

The latitic-trachytic enclaves and mingled bands in rhyolites, as well as glomerocrysts, testify to disrupted portions of the crystal mush (i.e. highly porphyritic enclaves) carried by the mafic (shoshonitic to latitic) magma responsible for the mush remobilization into the rhyolitic body. In such system, the geochemistry of the erupted products testifies to complex histories that is interactions between cumulates and recharging magmas, including mush

remobilization, partial melting of the mush regions and interactions between recharging magmas, mush-derived melts and extracted rhyolitic magmas. The K-rich trachytic magma of Pal D is a consequence if this complexity. The differentiation at slightly lower depth (corresponding to 160 ± 54 MPa) of a latitic magma, and the interaction with melts derived from the partial melting of a feldspar-rich mush explain its origin and geochemical features.

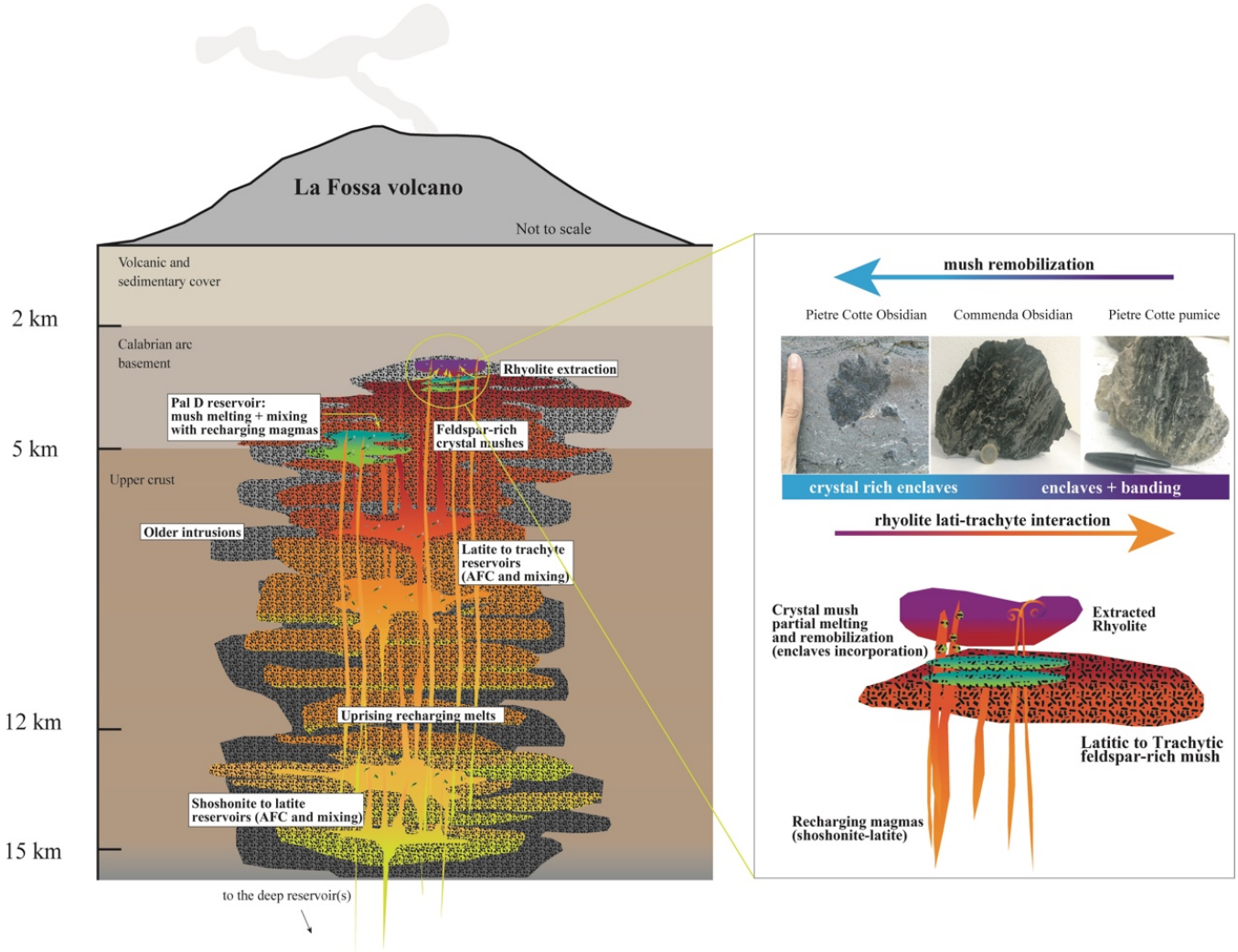

Figure 6.21 - Sketch representation showing the depth of the reservoirs that have been active at La Fossa volcano in the last 1000 years (depths and crustal structure after Peccerillo et al., 2006) and of the extraction of crystal-poor rhyolite from the crystal mush. The different interactions between the recharging magmas and the rhyolite explains the petrologic features of the recent eruptive products of La Fossa. Modified after Costa et al. (2020).

7 Hierarchical clustering of clinopyroxene composition for the study of complex explosive sequences: the case of the Palizzi Eruptive Unit

7.1 Introduction

Fine-grained beds in pyroclastic volcanic successions, even when their stratigraphic record and eruptive physical parameters are well characterized, may suffer from scarce petrological data collection with respect to lapilli-sized material or lava samples. This is mainly due to the limitations in having representative chemical data. Many petrological studies that focused on products of explosive volcanism often underestimated information coming from deposits related to small explosive eruptions, that are predominant in the life span of many stratovolcanoes and are associated to long-lasting episodes of low intensity activity (Sparks et al., 1997; Davidson and De Silva, 2000; Taddeucci et al 2004; Cioni et al., 2008; Nemeth and Cronin, 2008, 2009; D'Oriano et al., 2011). Problems arising from the petrological study of such type of products are essentially due to the small size of the volcanic material, which may prevent the traditional bulk rock chemistry approach for reconstructing the evolution of erupted magma. This problem is emphasized when complex stratigraphic sequences of long lasting, low-intensity small explosive eruptions are investigated. Indeed, the glass composition of juvenile fragments may deviate significantly from the bulk composition due to a large variability in crystallinity, hampering the use of glass composition for detailed chemical variations of the erupted magma. Additional obstacles to understanding successions of ash deposits are: i) the intrinsic nature of tephra deposits that may lack of erosional surfaces or discontinuities particularly when the activity lasts in time (D'Oriano et al., 2011); ii) the low rate of volcanic sedimentation due to the simultaneous effect of deposition and reworking of the ash (Di Traglia, 2011; Di Traglia et al., 2013); iii) the effects of magma fragmentation and selective

atmospheric transport of pyroclasts in modifying bulk tephra deposits and thus chemistry (Wolff, 1985). Hence, in order to fully investigate the evolution of an active volcanic plumbing system, and contribute to understand the complex dynamics of pre-eruptive processes, it is crucial to consider the whole spectrum of eruptive products, including ash-sized tephra successions.

A valuable allied in this kind of investigation is the use of crystals and the study of their zoning patterns, that can provide insights into the time scales and processes that occur in a plumbing system (Morgan and Blake, 2006; Turner and Costa, 2007; Costa and Morgan, 2011; Costa et al., 2020b). Indeed, crystals record the evolution and variation of the melt chemistry and changes of the intensive parameters of magmas (Wallace and Bergantz, 2002; Kahl et al., 2011; Cashman and Blundy, 2013). In recent years, the advancement in analytical methods increased the use of petrologic data for the definition of the time scales of magmatic processes and the monitoring of unrest signals (Cheng et al., 2017; Probst et al., 2018; Petrone et al., 2018; Cheng and Costa, 2019; Cheng et al., 2020; Weber et al., 2020). Additionally, recent studies demonstrated the efficacy of machine or unsupervised learning approaches in the solution of petrological and volcanological problems (Bolton et al., 2020; Caricchi et al., 2020; Itano et al., 2020; Li et al., 2020b; Petrelli and Perugini, 2016; Petrelli et al., 2017, 2020; Ren et al., 2019; Ueki et al., 2020).

In this chapter, the potential link between magma chemistry and magma dynamics are investigated through a data driven approach. Major element analyses across core-to-rim transects in clinopyroxene crystals collected along the stratigraphy of the explosive products of the Palizzi Eruptive Unit (PEU, see Chapter 5). Clinopyroxene analyses have been used to perform a hierarchical cluster analysis, applied for the first time in a sequence dominated by ash layers, in order to reduce the chemical complexity of the pyroxene profiles to sequence of clusters (Caricchi et al., 2020). The main point is the definition of an approach sufficiently suitable for ash-sized to coarse tephra deposits that allows to associate chemical variations to distinct magmatic processes. The explosive sequence of the PEU is taken as a case study because it represents one of the most important periods of La Fossa, being characterized by variable eruptive dynamics that produced a

large spectrum of tephra deposits that resulted in a substantial growth of the volcanic edifice (Di Traglia et al., 2013).

Hierarchical clustering of chemical analyses of mineral phases has been already used to detect magma mixing and mixed crystal population of lava samples at Stromboli volcano (Cortés et al., 2007), and to study the evolution of the effusive Bardarbunga-Holuhraun eruption (Iceland) which lasted approximately six months between 2014 and 2015 (Caricchi et al., 2020). However, hierarchical clustering has never been used for the study of a complex, long-lasting explosive sequence producing mostly fine-grained material (Di Traglia et al., 2013; Selva et al., 2020). In order to perform such type of analysis, clinopyroxene is preferred among other crystals because it is stable over the entire volcanic plumbing systems and thus offers a complete record of the changing P-T-H_2O conditions (Armienti et al., 2007; Armienti et al., 2013; Mollo et al., 2010; Mollo et al., 2013a, 2013b; Mollo and Masotta, 2014; Giacomoni et al., 2016; Putirka, 2008; Masotta et al., 2013; Neave and Putirka, 2017). In the case of Vulcano magmas, clinopyroxene is a stable phase from mafic to intermediate and evolved (up to trachyte) compositions from deep to shallower reservoirs (Gioncada et al., 1998; De Astis et al., 2013; Palummo et al., 2020).

7.2 Materials and methods

Selection of samples and chemical analyses

Clinopyroxene crystals were picked from eleven selected samples of the sequence of the PEU pyroclastic products (Fig. 7.1 and Chapter 5). The samples have been selected in order to at least cover the base and the top of each sub-unit of Pal A (two samples), Pal C1 (two samples), Pal C2 (three samples) and Pal C3 (two samples). Samples were selected also from the two main pumiceous fallout layers of Pal B and Pal D (one sample each). A total of 130 clinopyroxene crystals in the grain-size range of 500–1000 μm, that represents the most frequent size of phenocrysts in PEU deposits of the PEU crystals (Folzani, 2019), devoid of alteration and coated in juvenile glass, were hand-picked under a stereomicroscope,

embedded in resin epoxy mounts and polished. Crystals were preferentially mounted in order to have the *c* crystallographic axis parallel to the section of the resin mount and polished in order to expose a section through the core of the crystal. After carbon-coating of the resin mounts, backscattered electron images (BSE) were collected with a Quanta 450 Field Emission-Scanning Electron Microscope (FE-SEM) at the Centro Interdipartimentale di Scienza e Ingegneria dei Materiali (CISIM) at the Università di Pisa (see also Chapter 4). Major elements core to rim profiles of clinopyroxene were collected using a JEOL JXA 8200 superprobe at the University of Geneva using 15 keV acceleration voltage, 20 nA beam current and a beam diameter of 1 μm and a 20 μm step between two analytical spots in a profile. The analytical profiles were obtained by systematically moving from the core to the rim of each crystal, in transect as more perpendicular as possible to the *c* crystallographic axis. 130 profiles were collected for a total of 1896 analytical spots (mean analytical total of 100.04 wt.% ± 0.46, see Appendix E and Chapter 4). In Appendix E only selected chemical profiles are reported, the complete data set is available upon request to the author of this thesis.

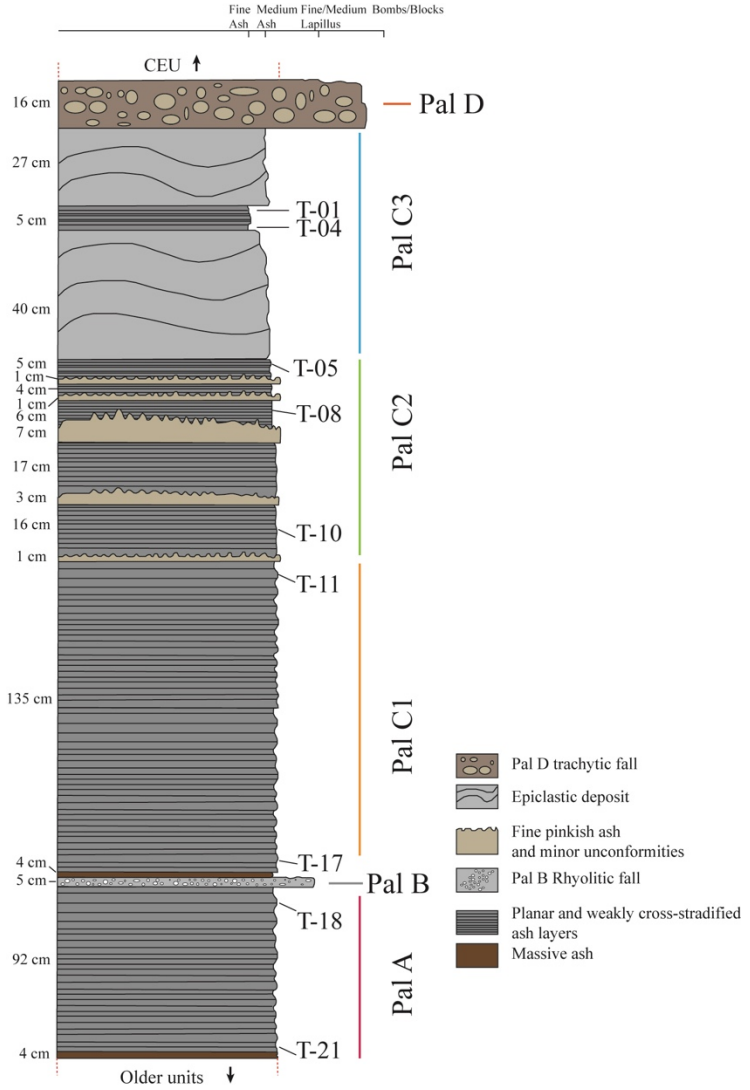

Figure 7.1 - Simplified stratigraphic log of the Palizzi Eruptive Unit PEU (only explosive products), showing the sampled levels.

Hierarchical cluster analysis

The hierarchical cluster analysis was conducted using the 10 major oxides (SiO_2, TiO_2, Al_2O_3, MnO, MgO, FeO, CaO, Na_2O, K_2O, Cr_2O_3) composition of clinopyroxene analyzed along core-rim profiles, following the procedure described in Caricchi et al. (2020). The method was performed using the *"cluster"* library in the freeware software R (R core team, 2017). To cluster the data, the Ward linkage method (Ward, 1963) has been used. Briefly, for a given dataset representable in a Euclidean space, the measurement of variability is calculated using the Euclidean

distance of each data point from all the other points. Clinopyroxene analyses were first normalized for each element, considering all analyses simultaneously, to values between 0 and 1 to give them the same weight and avoid false results. The normalized values were used to calculate the Euclidean distance between each analytical spot. With this method, pairs of clusters are gradually identified considering the smallest value of Euclidean distance and combined together. By default, the exact number of clusters able to explain a specific problem (in that case the exact number of clusters representative of the geochemical variance of clinopyroxene profiles) is *a priori* unknown. Ideally, the data can be grouped in as many clusters as the data points or in a single cluster that includes all of them. To evaluate the exact number of clusters that can better explain the dataset object of this work, the cluster analysis has been implemented by using the R package *Nbclust* (Charrad et al., 2014). This package applies 24 indices for determining the number of clusters and suggests the best clustering scheme for a given dataset, by varying all possible combinations of the number of clusters, distance measures, and clustering methods (see also Caricchi et al., 2020).

7.3 Results

Petrographic features of the ash layers of the PEU

The petrographic study of thin sections of the PEU ash layers highlighted the presence of five main categories of components: juvenile vesiculated glass (both transparent light brown in color and opacified), lithic fragments (fresh and altered), euhedral to subhedral loose crystals of clinopyroxene, plagioclase and minor amount of olivine (Fig. 7.2). The petrographic features of the Pal B and Pal D pumiceous fallout layers have been already described in Chapter 6.

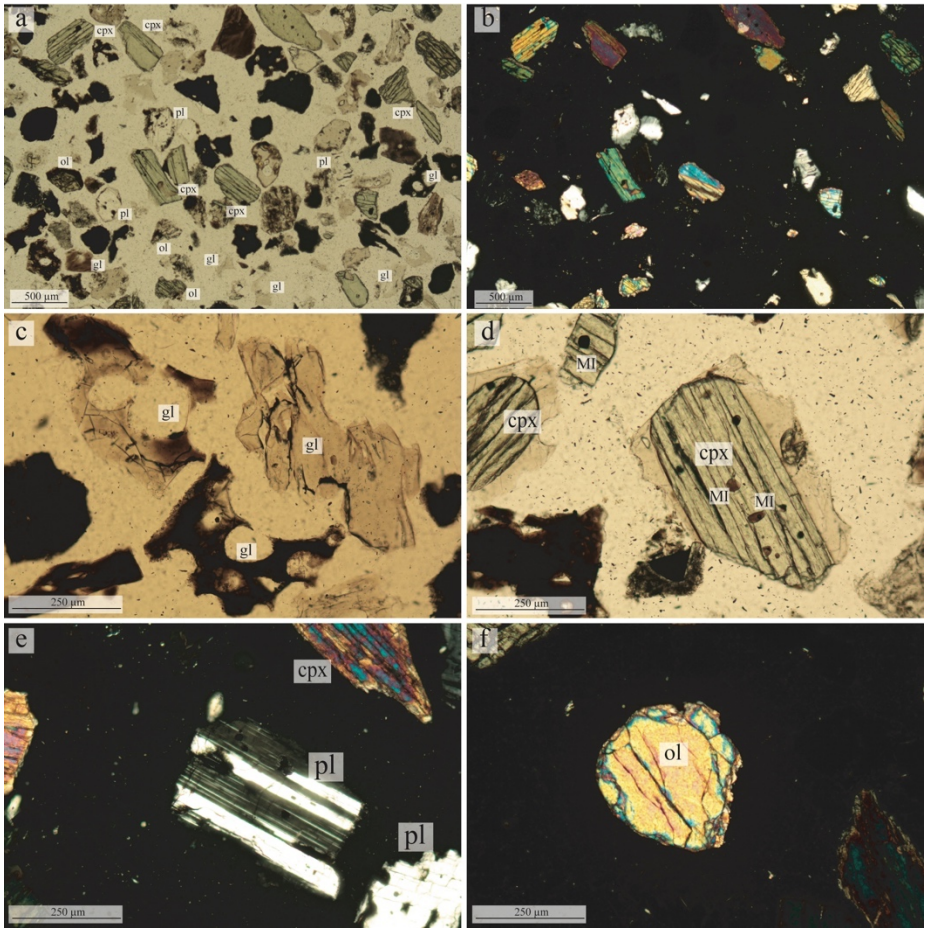

Figure 7.2 – microphotographs showing the petrographic features of the investigated ash layers; cpx: clinopyroxene, pl: plagioclase, ol: olivine, gl: glass, MI: melt inclusion.

Major element composition of whole-rock and glass of the PEU explosive products

The nature itself (ash layers) of the pyroclastic products collected from the PEU prevented the possibility to obtain bulk rock analyses representing the composition of the erupted magma. Only the composition of the juvenile glass for the different tephra layers is reported. When the TAS diagram is considered, the majority of the juvenile glasses of the Pal A and Pal C1, Pal C2 and Pal C3 sub-units lies in the field of the tephriphonolite. In the K_2O versus SiO_2 diagram, the juvenile glass crosses the boundary between latite and shoshonite having SiO_2 contents between 53.2 and 57.6 wt.% and K_2O between 6.3 and 8.6 wt.% (Fig. 7.3) and do not show significant variations from the base to the top of the sequence. Only the juvenile glass of one sample (T-17), belonging to the Pal C1 sub-unit, the first level after the emplacement of the Pal B rhyolite, is trachytic with SiO_2 between

59.5 and 66.1 wt.% and K_2O between 6.0 and 8.0 wt.% (Figs. 7.1 and 7.3). Whole-rock data are available for the coarsest-grained layers. Pal B pumices show rhyolitic composition with SiO_2 contents of ~72.3 wt.% and K_2O of ~5.3 wt.%, while glasses of the groundmass show slightly greater variations (SiO_2 67.6–71.1 wt.% and K_2O 5.8–6.3 wt.%). Among the intermediate magmas, Pal D pumices show the highest K_2O content of the Vulcano products (up to ~7.6 wt.%, see also Chapter 6) and SiO_2 contents comparable to other latitic and trachytic magmas emitted at La Fossa (~58–61 wt.% SiO_2), being classified as trachytic in the TAS diagram and latitic in the K_2O versus SiO_2 diagram (Fig. 7.3). The groundmass glasses of Pal D pumices show only slight variations when compared to the whole-rock analyses (Fig. 7.3) (Fulignati et al., 2018).

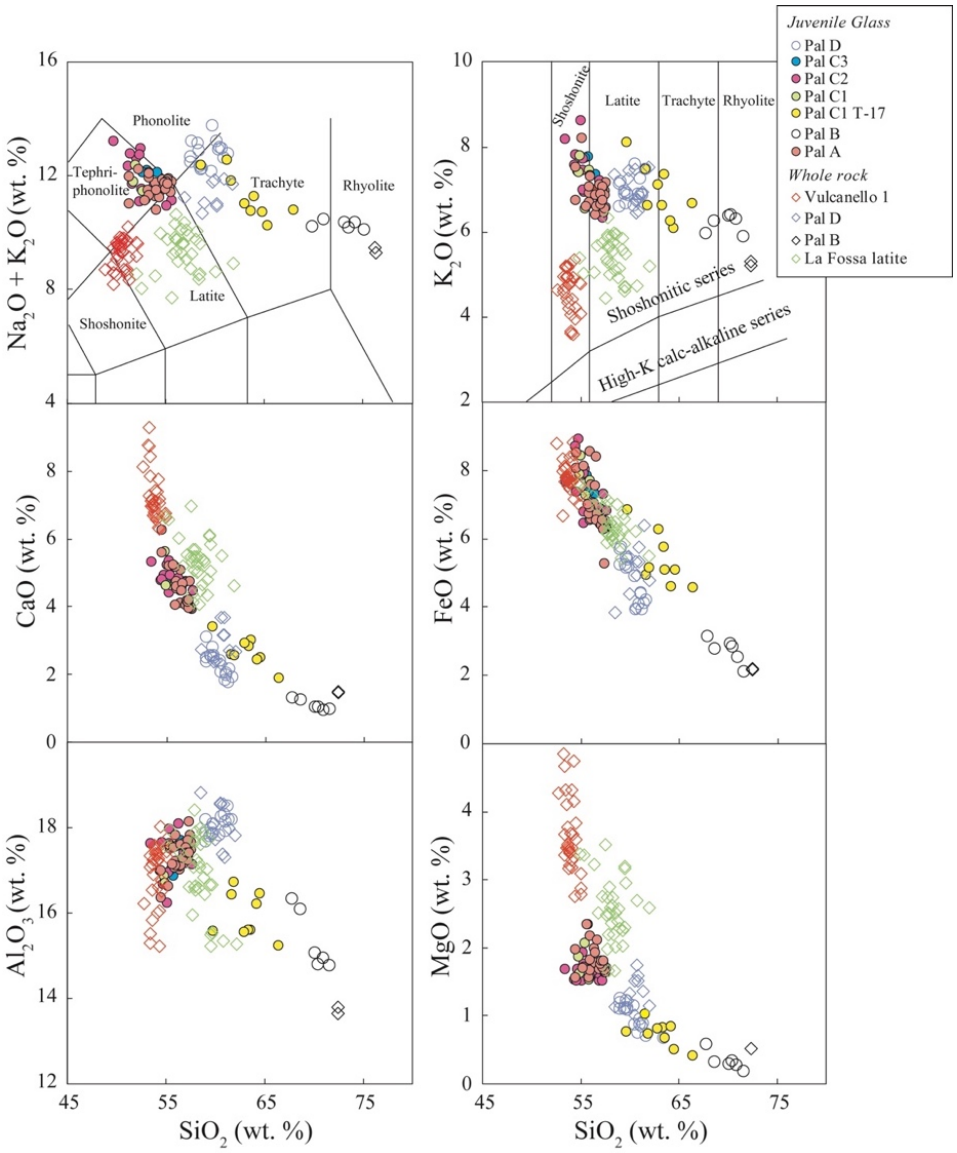

Figure 7.3 - Total alkali vs SiO2, K_2O vs. SiO_2 and major elements variation diagrams showing whole-rock data of Pal B and Pal D sub-units (data from this work), Vulcanello shoshonites (data from Davì et al., 2009 and Fusillo et al., 2015) and juvenile glass fragment analyses of the PEU levels (EPMA data from Fulignati et al., 2018; EDS data from Costa, 2017 MSc thesis and Folzani, 2019 MSc thesis). Major elements are recalculated to 100% on anhydrous basis.

Textural features of clinopyroxene

The BSE images of clinopyroxene belonging to the PEU explosive products show that crystals range from un-zoned (Fig. 7.4 a-c) to weakly concentrically zoned (Fig. 7.4d, e). Oscillatory zoning is sometimes observed (Fig. 7.4f) and in several cases cores are characterized by a darker zone and darker concentric bands in BSE images (Fig. 7.4g, h). Inclusions of Ti-magnetite, apatite and glassy melt

inclusions are commonly observed at the cores or in concentric layers (Fig. 7.4d, f). No sector zoning has been observed in clinopyroxene of the PEU.

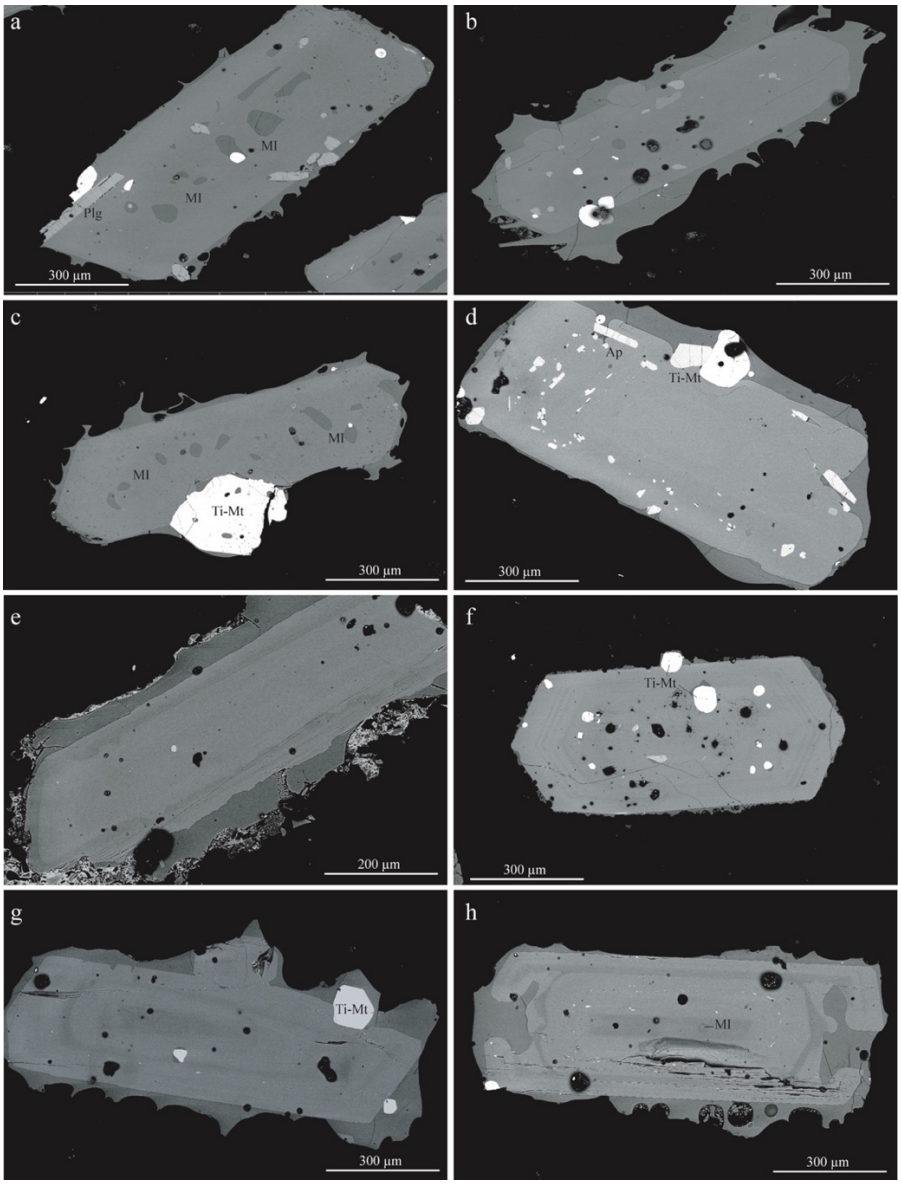

Figure 7.4 – BSE images of clinopyroxene crystals occurring in: a) Pal D, b) Pal C2, c) Pal D, d) Pal A, e) Pal C1, f) Pal B, g) Pal A, h)Pal A; MI: melt inclusion, plg: plagioclase, ap:apatite, Ti-mt: Ti-magnetite.

Clinopyroxene composition

The composition of clinopyroxene in the investigated samples is Wo_{41-49}, En_{35-47}, Fs_{6-19} covering a narrow band parallel to the augite-diopside line (Fig. 7.5), being thus comparable with the clinopyroxene composition of shoshonitic and lati-

trachytic magmas emitted in the last 1000 years at Vulcano (De Fino et al., 1991; Gioncada et al., 1998). The compositional variability is nearly the same for the different samples along the sequence and the variation diagrams do not show any evident trend. Thus, taken as a whole, clinopyroxene chemical composition alone does not help to decipher magmatic processes during the emplacement along the stratigraphy of the PEU.

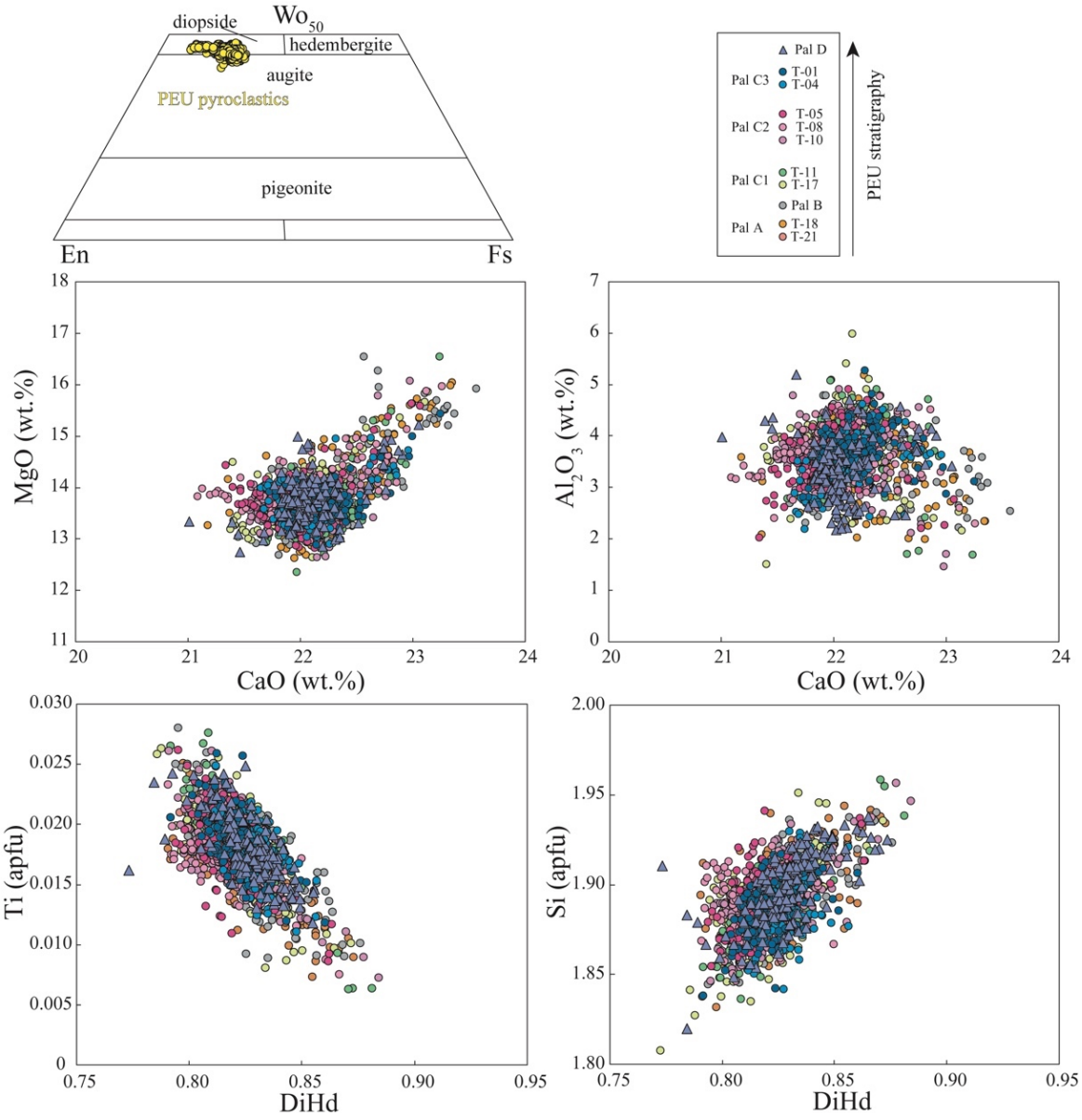

Figure 7.5 – Quadrilateral classification scheme of pyroxene (Morimoto, 1988) and variation diagram showing the composition of clinopyroxene of the PEU sequence.

Hierarchical clustering of clinopyroxene composition

The hierarchical cluster analysis was conducted by using the 10 major oxides of all the collected clinopyroxene profiles of the sub-units of Pal A, Pal B, Pal C1, Pal C2, Pal C3 and Pal D. The results show that the chemical profiles of the PEU clinopyroxene are best represented by four compositional clusters (Fig. 7.6).

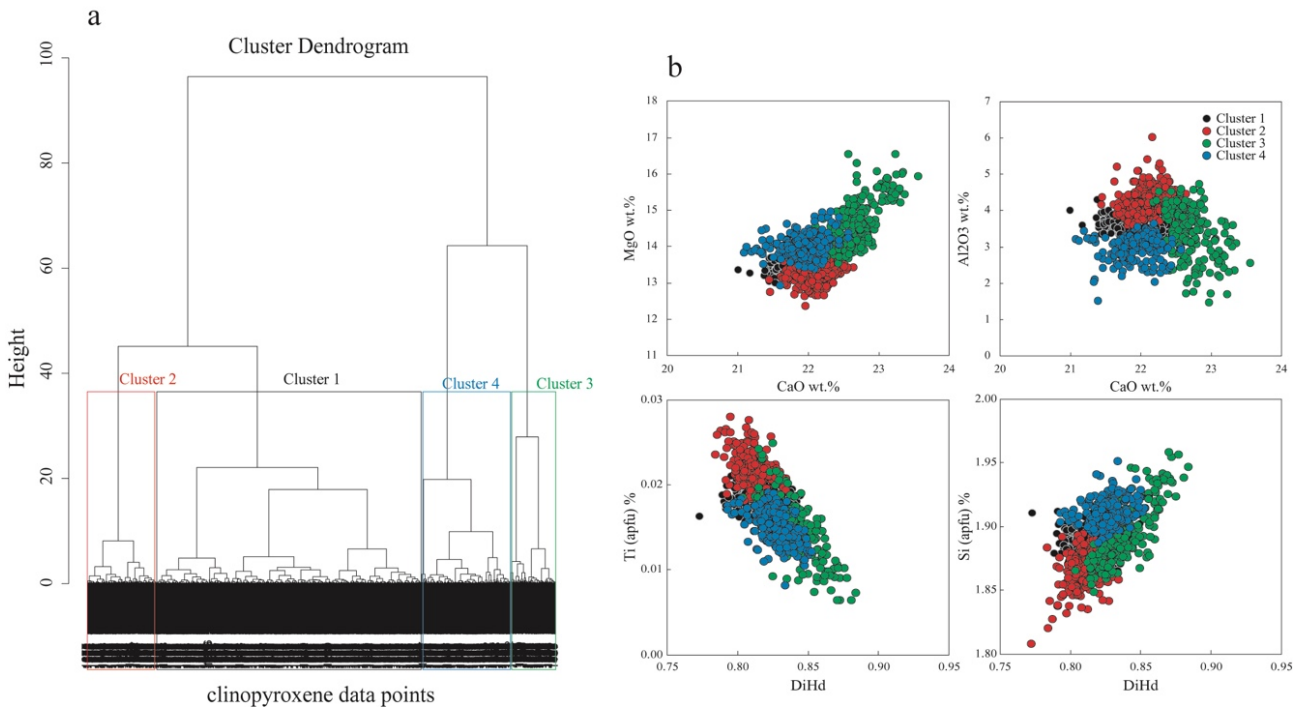

Figure 7.6 – a): Dendrogram obtained by the Euclidean distance linkage clustering method (Ward, 1963). The colored squares show the groups of analyses associated with each cluster. The height represents the compositional difference required to merge two clusters together; b) results of cluster analysis as it appears in variation diagrams of clinopyroxene composition (same diagrams as in Fig. 7.5)

Clusters 1 (black) and 2 (red) are chemically similar, with the exception of Al and Ti, that are higher in cluster 2, which in turn shows lower Mg with respect to cluster 1 (Figs. 7.6 and 7.7). Cluster 2 shows higher content of Ti and Al among all clusters. The cluster 3 (green) shows the largest chemical differences with respect to the other three clusters being enriched in Ca, Mg, Cr and having lower Fe, Al, Ti and Na. The Cluster 4 (blue) shows in general an intermediate chemical composition between cluster 1 and cluster 3, with the exception of Al, Ca and Cr that are lowest among all clusters (Figs. 7.6 and 7.7). The clinopyroxene profiles

are thus simplified into a sequence of clusters with each analytical spot assigned to a cluster (Figs. 7.8 and 7.9).

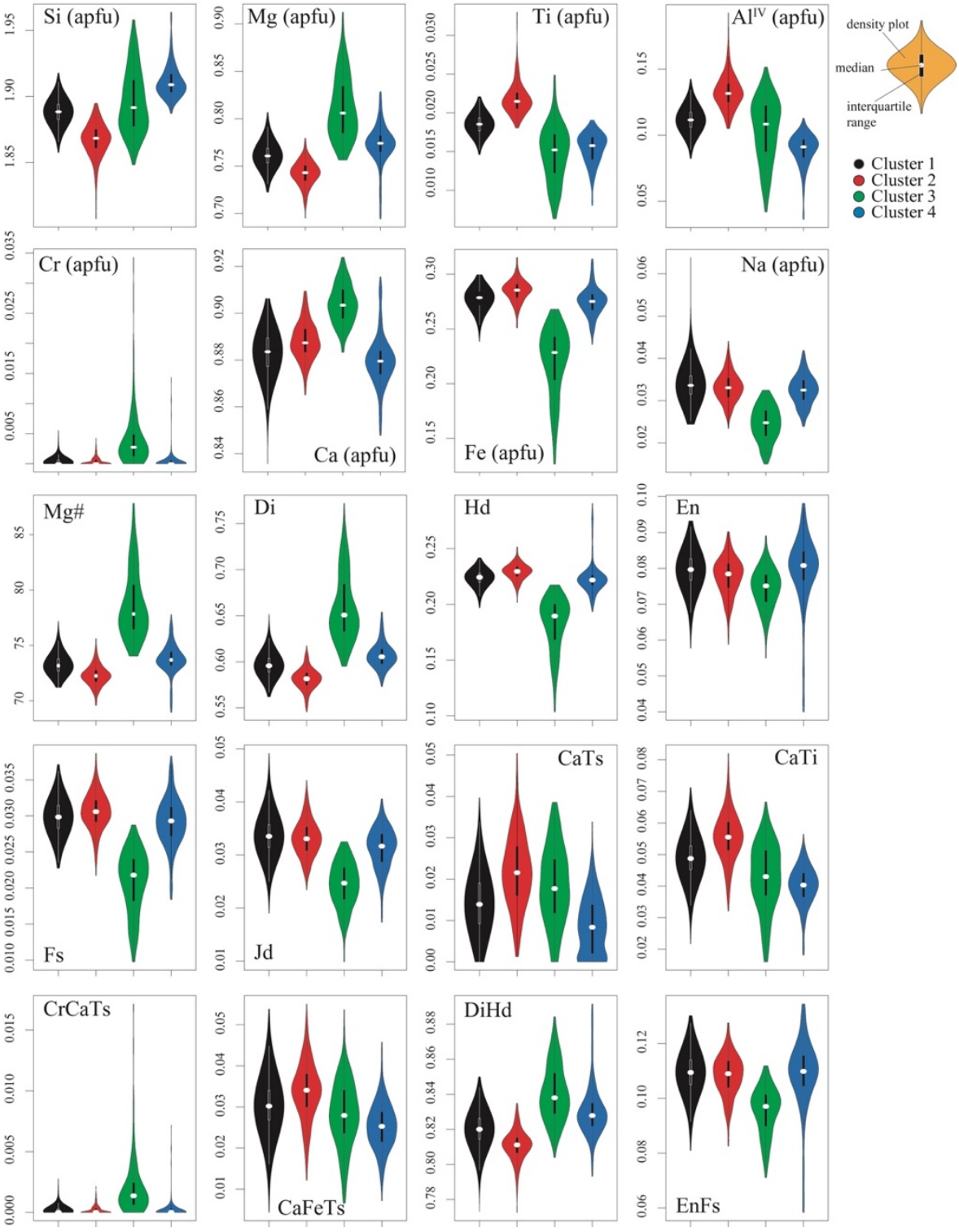

Figure 7.7 – Violin plots showing the density distribution of each cluster.

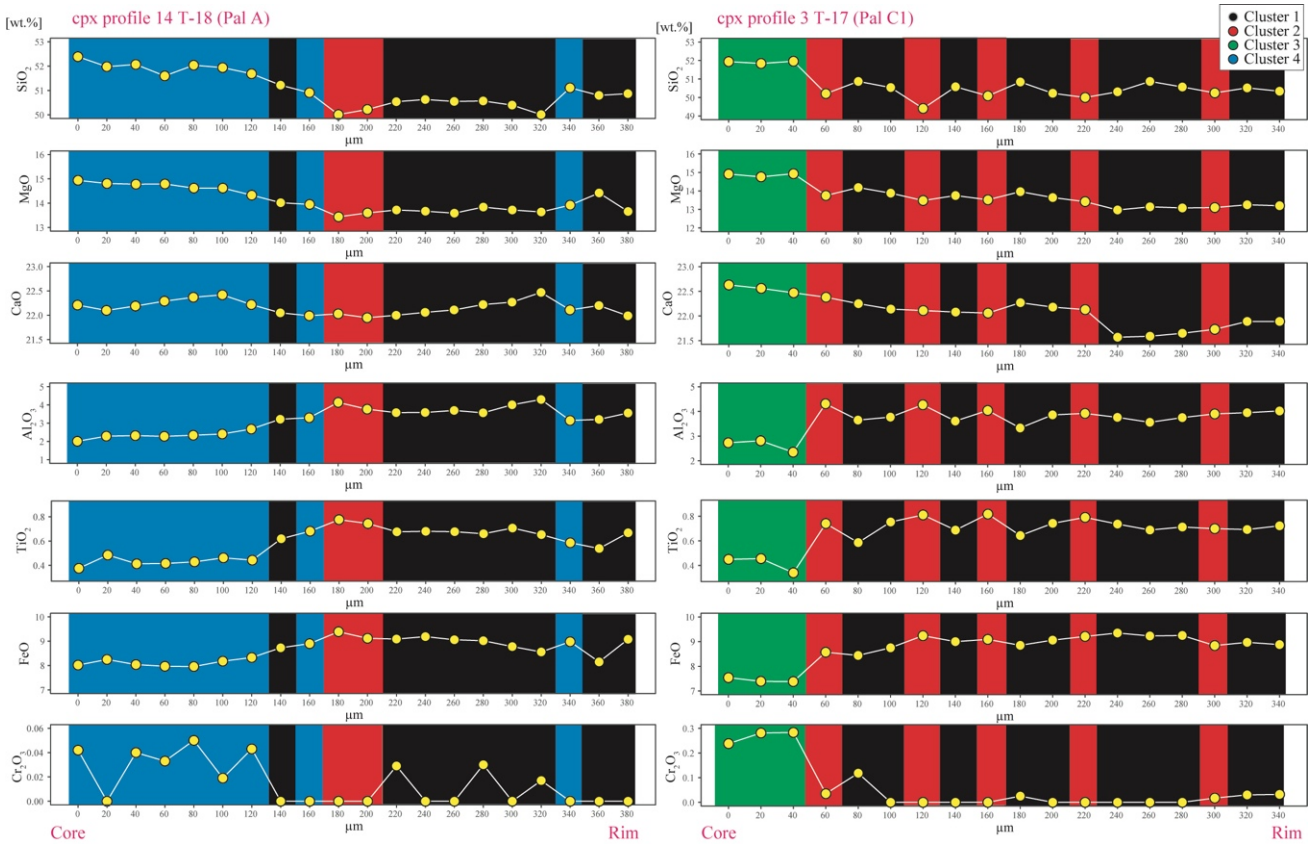

Figure 7.8 – Example of two core to rim chemical profiles of clinopyroxene with each point marked with the corresponding cluster.

By considering the total number of clustered analyses, the distribution of the analyses is represented for the 56% by the cluster 1, for the 19% by the cluster 4, for the 15% by the cluster 2 and only the 10% belongs to cluster 3 (Fig. 7.10). The relative abundance of the four clusters varies along the stratigraphy of the PEU (Fig. 7.10). The cluster 1 maintains steady abundances (~63–73%) in each level, cluster 2 reaches is maximum in correspondence to the Pal C1 sub-unit (~18–20%), the less abundant cluster 3 passes from a minimum of 2% at the base of the sequence (Pal A sub-unit), reaching its maximum at the top of Pal A and Pal B sub-units (15–16%) and then is constant at 7–8% up until the middle of Pal C2 sub-units, when increases again up to 12% and decreases again toward Pal C3 sub-unit (Fig. 7.10). Cluster 4 reaches two maximum peaks at the top of Pal A sub-unit (22%) and in Pal D where it dominates (53%) (Fig. 7.10) and maintains steady abundances in the whole sequence reaching its minimum in the Pal C1 sub-unit (Fig. 7.10).

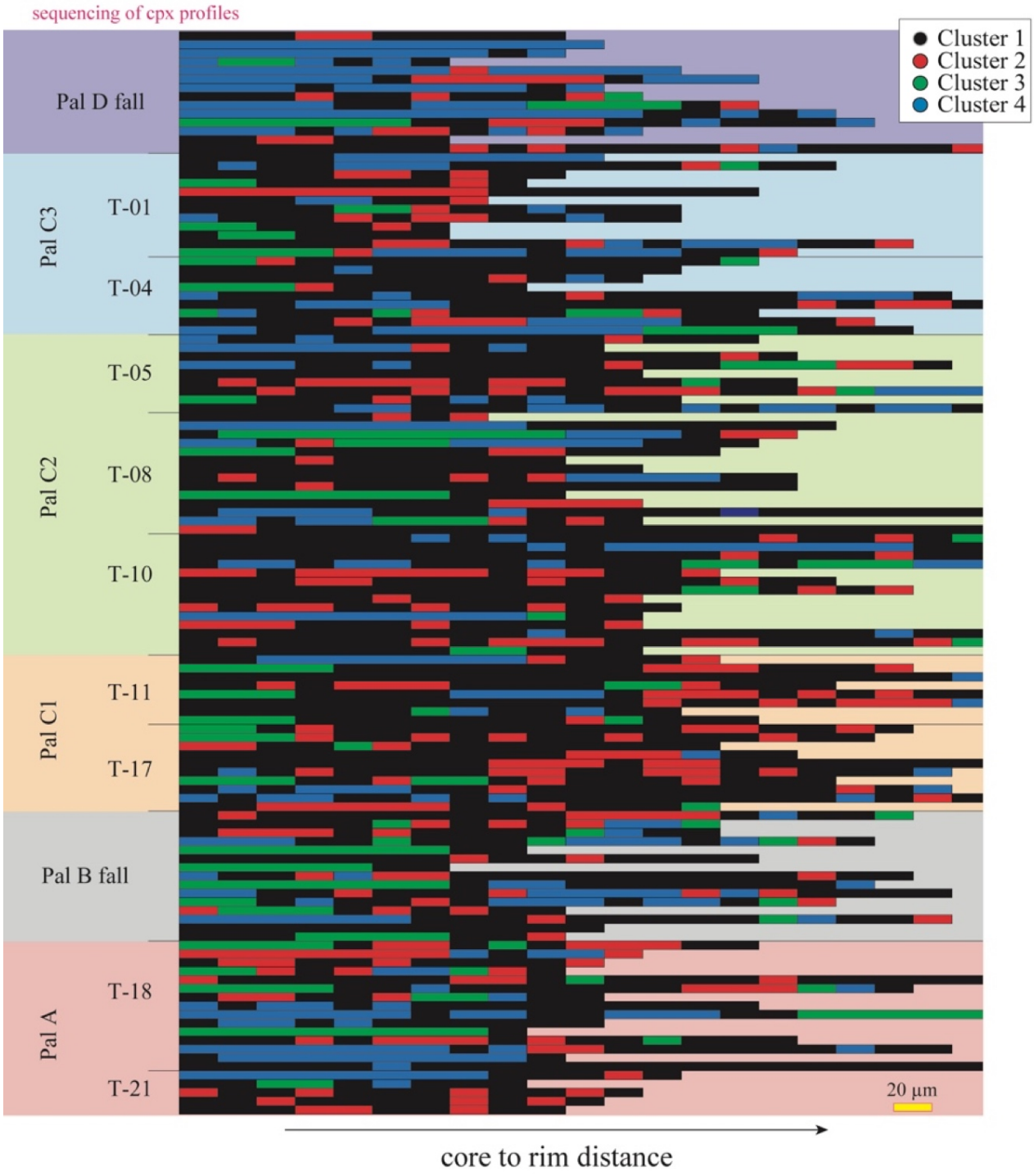

Figure 7.9 – Barplot showing the total sequence of clusters for each collected chemical profile. Each segment represents an analytical spot spaced 20 µm.

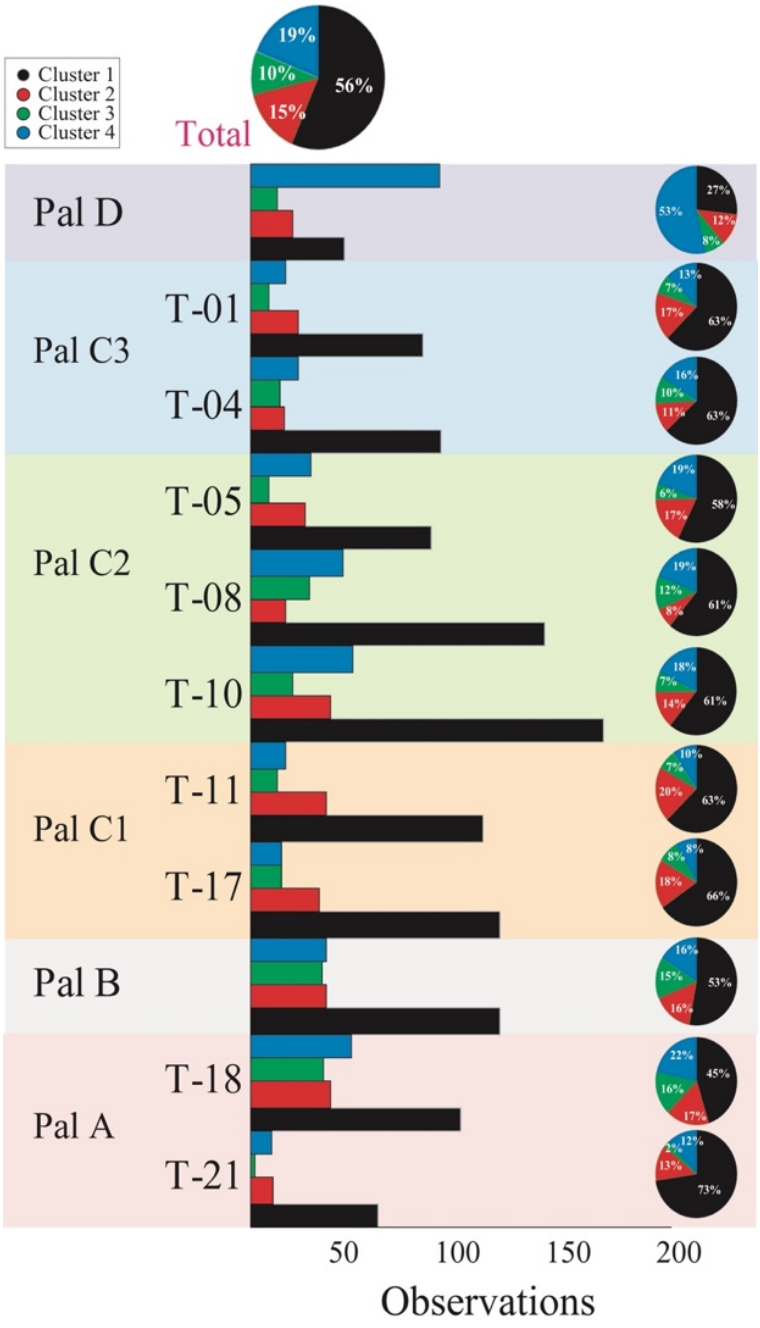

Figure 7.10 – Total distribution of clusters and total distribution for each stratigraphic level.

As the proportion of clusters varies along the stratigraphy, their relative abundances changes when looking at the different position occupied by each cluster along the analytical profiles (cores, mantles and rims of clinopyroxene). Each profile has been thus divided in equal portions (33% each) with each part representing the core, the mantle and the rim. The cluster 1 is equally distributed between the cores, mantles and rims of clinopyroxene crystals, while the cluster 2

is most abundant (40%) in the mantles (Fig. 7.11). The cluster 3 is more present in clinopyroxene cores (48%) as well as the cluster 4 (41%) (Fig. 7.11). Some interesting features are also observed when considering the cluster distribution, normalized for the number of observations of each sample, among cores, mantles and rims along the stratigraphic sequence (Fig. 7.11). The mantles and the rims belonging to cluster 2 increase in number only when the cores belonging to cluster 3 start to decrease and vice versa. To a general increase of cores of cluster 3, corresponds a general decrease of cores belonging to cluster 1 and 2 (Fig. 7.11). The increase of the spots relative to cluster 4 (cores, mantles and rims) follows the increase of mantles and rims of cluster 3 (Fig. 7.11).

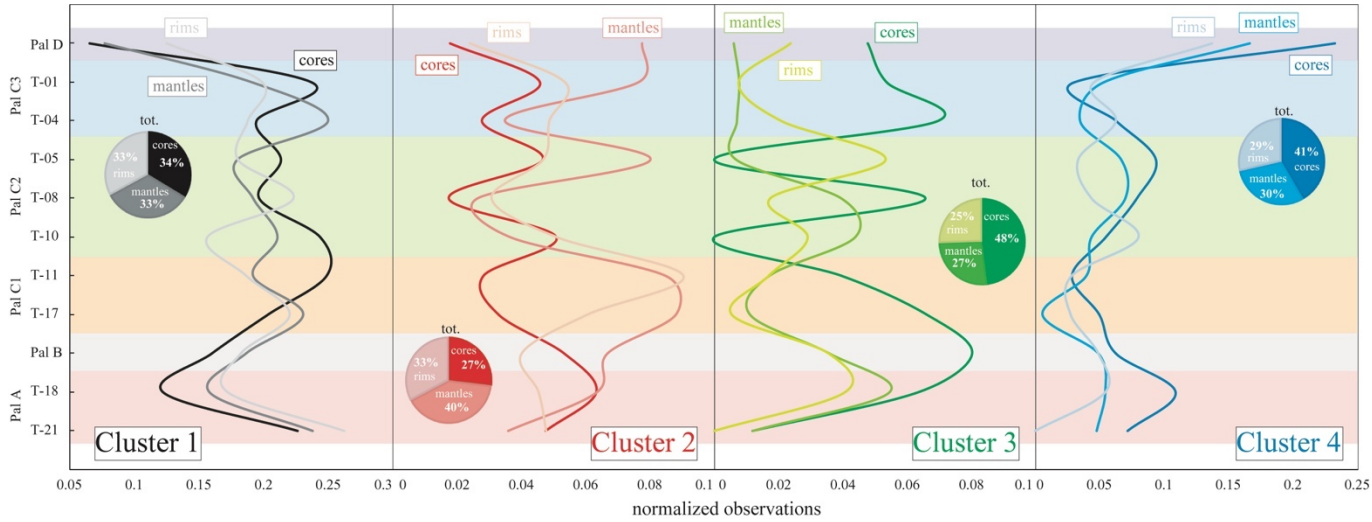

Figure 7.11 – Distribution of each clusters along the PEU divided for core, mantles and rims.

Clinopyroxene-melt equilibrium

In order to investigate the range of temperature and pressure of crystallization of the magmas of the PEU from which clinopyroxene crystals grew, clinopyroxene-melt equilibrium has been used for thermobarometry. The four compositional clusters have been combined with the mean compositions representative of the melt in equilibrium with clinopyroxene for the mafic-intermediate magmas erupted at Vulcano in the same time span. Since one of the main problems occurring in the study of fine ash volcanic layers is the lack of whole-rock data that could be assumed as representative of the erupted magma, the clinopyroxene analyses have

been combined with the mean of whole-rock compositions of Vulcanello shoshonites and La Fossa latites and Pal D trachyte (Tab. 7.1). This choice is dictated by the fact that: i) petrographic observation suggests that the main mineral assemblage of the ash layers (clinopyroxene + plagioclase + olivine) is consistent with that of latitic and shoshonitic magmas erupted at La Fossa; ii) the composition of juvenile glass fragments of the PEU could reflect a residual (lacking of mineral phases) of a shoshonitic to latitic magmas (whole-rock) (Fig. 7.2).

Table 7.1 – Mean of whole rock data used in clinopyroxene-melt equilibrium test and thermobarometric calculations (see text).

Unit	Vulcanello 1	Pietre Cotte enclaves	AD 1888-1890	Pal D
Type	Whole-rock	Whole-rock	Whole-rock	Whole-rock
Composition	Shoshonite	Latite	Latite	Trachyte
SiO2	53.95	59.00	58.50	60.21
TiO2	0.64	0.56	0.57	0.65
Al2O3	16.84	16.52	17.30	17.93
FeOt	7.85	6.40	6.11	5.10
MnO	0.15	0.13	0.12	0.11
MgO	3.67	2.51	2.38	1.45
CaO	7.27	5.13	5.38	2.97
Na2O	4.60	4.02	4.05	4.31
K2O	4.60	5.38	5.24	6.97
P2O5	0.42	0.35	0.36	0.31

To verify the chemical equilibrium between the four clinopyroxene clusters and melt compositions, the test for equilibrium based on the Fe-Mg exchange coefficient ($K_{dFe\text{-}Mg}^{cpx\text{-}liq}$) with an equilibrium range of 0.28 ± 0.08 (Putirka, 2008) (Fig. 7.12a) and the equation of Wood and Blundy (1997) to calculate the Mg# of the melt in equilibrium with each clinopyroxene (Fig. 7.12b) have been considered. Additionally, the equilibrium test of Mollo et al. (2013a), based on the difference between measured and predicted diopside + hedenbergite clinopyroxene components (ΔDiHd), assuming in equilibrium clinopyroxene-melt pairs with a ΔDiHd < 0.1 (Mollo and Masotta, 2014), has been also used (Fig. 7.13).

In all the equilibrium tests, each cluster has been alternately paired with whole-rock data representative shoshonitic (Vulcanello 1 formation) and latitic (AD 1888–1890 eruption, Pietre Cotte latitic enclaves) compositions (whole-rock data from Gioncada et al., 1998, Davì et al., 2009, Fusillo et al., 2015). Additionally, cluster 4 has been also paired with the whole-rock composition of Pal D trachyte (data presented in Chapter 6). The latter choice is dictated by the fact that cluster 4

predominantly occurs in clinopyroxene found in the Pal D pumice. The test for equilibrium based on the $K_{dFe\text{-}Mg}^{cpx\text{-}liq}$ (Putirka, 2008) in Figure 7.12a shows that all the clusters are in equilibrium with latitic melts except cluster 3 that is more in equilibrium with a shoshonitic composition. The cluster 4 is also in large part with a trachytic melt. However, it must be noted that the ranges of Mg# of shoshonitic to latitic magmas of the La Fossa-Vulcanello system partially overlap (Fig. 7.12a). The Mg# of the melt in equilibrium with clinopyroxene obtained with the equation of Wood and Blundy (1997) (Fig. 7.12b) highlights that cluster 3 is characterized by a wider range of Mg# compared to the other three clusters, being mostly in equilibrium with shoshonitic melts. Instead clusters 1, 2 and 4 show a narrower range of Mg#, being thus in equilibrium with intermediate lati-trachytic melts.

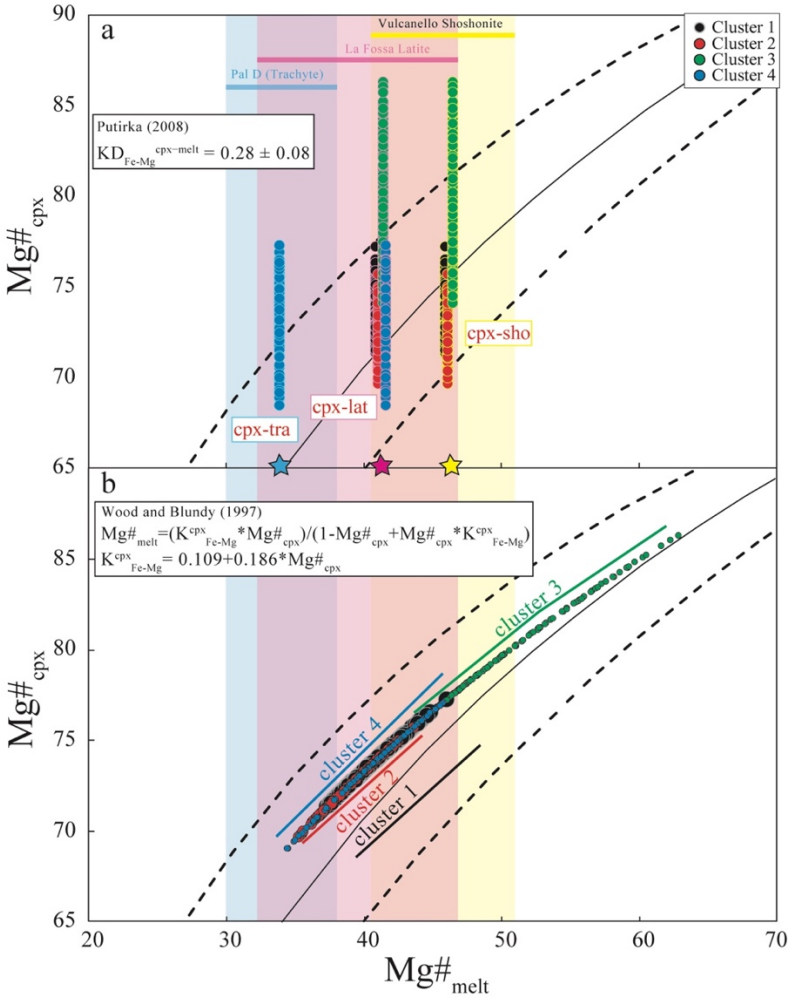

Figure 7.12 – a: equilibrium test based on the Fe-Mg exchange coefficient ($K_{DFe\text{-}Mg}^{cpx\text{-}liq}$) with an equilibrium range of 0.28 ± 0.08 (Putirka, 2008); b: Mg# of the melt in equilibrium with clinopyroxene clusters obtained with the equation of Wood and Blundy (1997). Stars indicate the melt composition used for the equilibrium (means of Mg# of shoshonitic, latitic and trachytic products). The colored bands represent the Mg# range of latitic, shoshonitic and trachytic products erupted at La Fossa and Vulcanello in the last 1000 years (data from Del Moro et al., 1998; Gioncada et al., 1998; Davì et al., 2009; De Astis et al., 2013; Fusillo et al., 2015; Costa et al., 2020).

The equilibrium test of Mollo et al. (2013a) shows that all the clinopyroxene analyses of the four clusters are in equilibrium with shoshonitic to latitic (clusters 1, 2, 3 and 4) and trachytic (cluster 4) compositions showing always a ΔDiHd < 0.1 (Fig. 7.13). In particular, clusters 1 and 2 are more in equilibrium with a latitic melt having ΔDiHd = 0.007 ± 0.05 and ΔDiHd = 0.014 ± 0.07 respectively. The same clusters, paired with a shoshonitic melt, result still in equilibrium but show slightly higher ΔDiHd of 0.033 ± 0.07 and 0.023 ± 0.07, respectively. Cluster 3 shows virtually the same ΔDiHd if paired with a shoshonitic (ΔDiHd of 0.015 ± 0.012) or

latitic (ΔDiHd = 0.013 ± 0.010) composition (Fig. 7.13). The cpx-melt equilibrium test for cluster 4 yields decreasing ΔDiHd from shoshonite (ΔDiHd of 0.043 ± 0.011) to latite (ΔDiHd of 0.009 ± 0.020) and trachyte (ΔDiHd of 0.008 ± 0.007), resulting more in equilibrium with latitic and trachytic compositions. The analyses of the clinopyroxene belonging to the rhyolitic Pal B pumice, if paired with a rhyolitic composition get out of the equilibrium range having a ΔDiHd >1, thus confirming that clinopyroxene occurring in the Pal B pumices are xenocrysts belonging to mafic-intermediate magmas, as already discussed in previous chapters (Fig. 7.13).

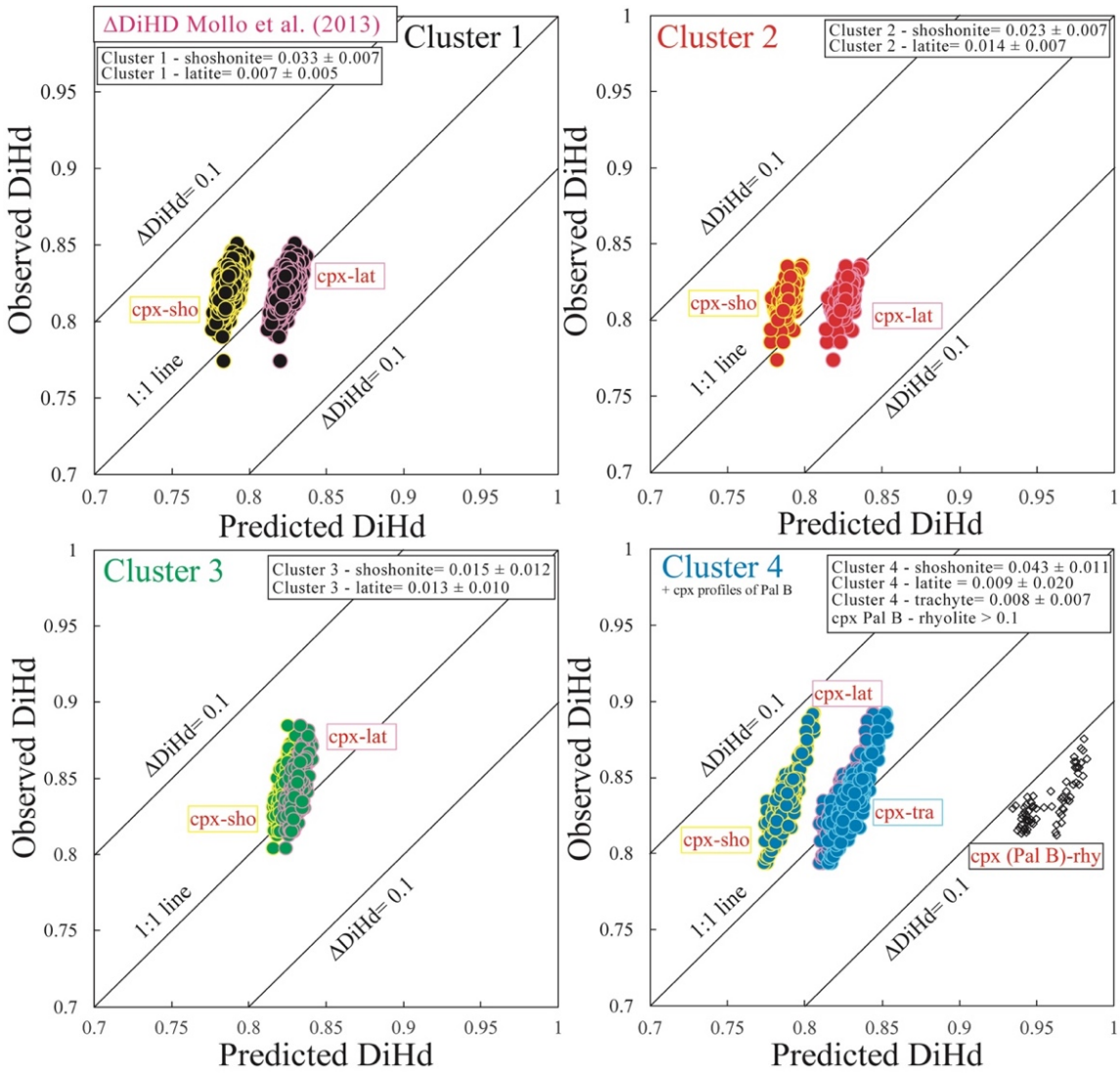

Figure 7.13 - Test of equilibrium of clinopyroxene clusters comparing the observed and predicted values for the DiHd component in clinopyroxene (Mollo et al., 2013a)

7.4 Discussion

The hierarchical cluster analysis applied to the major element composition of clinopyroxene profiles along the PEU stratigraphy recognized four compositional clusters (Fig. 7.6). In the following section, thermobarometric estimates and compositional variations of clinopyroxene are discussed in the light of hierarchical clustering and in the frame of the stratigraphy of the PEU sequence. The main aim is to unravel potential links between the composition of the clinopyroxene clusters and magmatic processes responsible of the observed compositional variability.

Thermobarometry of clinopyroxene clusters

Crystallization pressure and temperature of clinopyroxene have been determined with the clinopyroxene-liquid thermobarometer of Masotta et al. (2013) (see also Chapter 6) (Fig. 7.14). Based on the cpx-melt equilibrium tests, clusters 1, 2 have been paired with a melt of latitic composition, cluster 3 with both latitic and shoshonitic melt compositions, while cluster 4 has been paired with latitic and trachytic compositions. The H_2O content required as input data for the thermobarometer for the clinopyroxene-shoshonite pairs has been made to vary between 0.3 and 0.6 wt.% (range in shoshonitic melt inclusions measured by Gioncada et al., 1998). For clinopyroxene-latite pairs H_2O in the range of 2.5–3.5 wt.% (Masotta and Mollo, 2019 and Chapter 6) and H_2O between 1.5 and 2.5 wt.% for trachyte-clinopyroxene pairs (Fulignati et al., 2018 and Chapter 6) have been used respectively. It is important to note that for an increase in H_2O content of 1 wt.% correspond a maximum variation of temperature estimates of ~10 °C, such value is however lower than the error of ± 18 °C of the thermometer (Masotta et al., 2013).

Crystallization temperature and pressure estimates for clinopyroxene of clusters 1 and cluster 2 latitic pairs are identical within the error, respectively 1014 ± 4 °C and 382 ± 31 MPa for cluster 1 and 1014 ± 5 °C and 386 ± 35 MPa for cluster 2. Clinopyroxene from cluster 3 paired with a latitic melt composition yielded temperature of 1033 ± 8 °C and pressure of 380 ± 48 MPa, whereas, coupled

with a shoshonitic melt yielded temperature of 1024 ± 7 °C and pressure of 458 ± 48 MPa. Finally, clinopyroxene of cluster 4 paired with a latitic composition show similar temperature and slightly lower pressure compared to the other clusters, respectively 1017 ± 5 °C and 351 ± 34 MPa, whereas paired with a trachytic composition show the lowest temperature and pressure ranges among all clusters, of 1010 ± 3 °C and 151 ± 23 MPa respectively (Fig. 7.14). Given the results of the equilibrium tests, thermobarometric estimates obtained through clinopyroxene-shoshonitic and clinopyroxene-trachytic pairs are preferred.

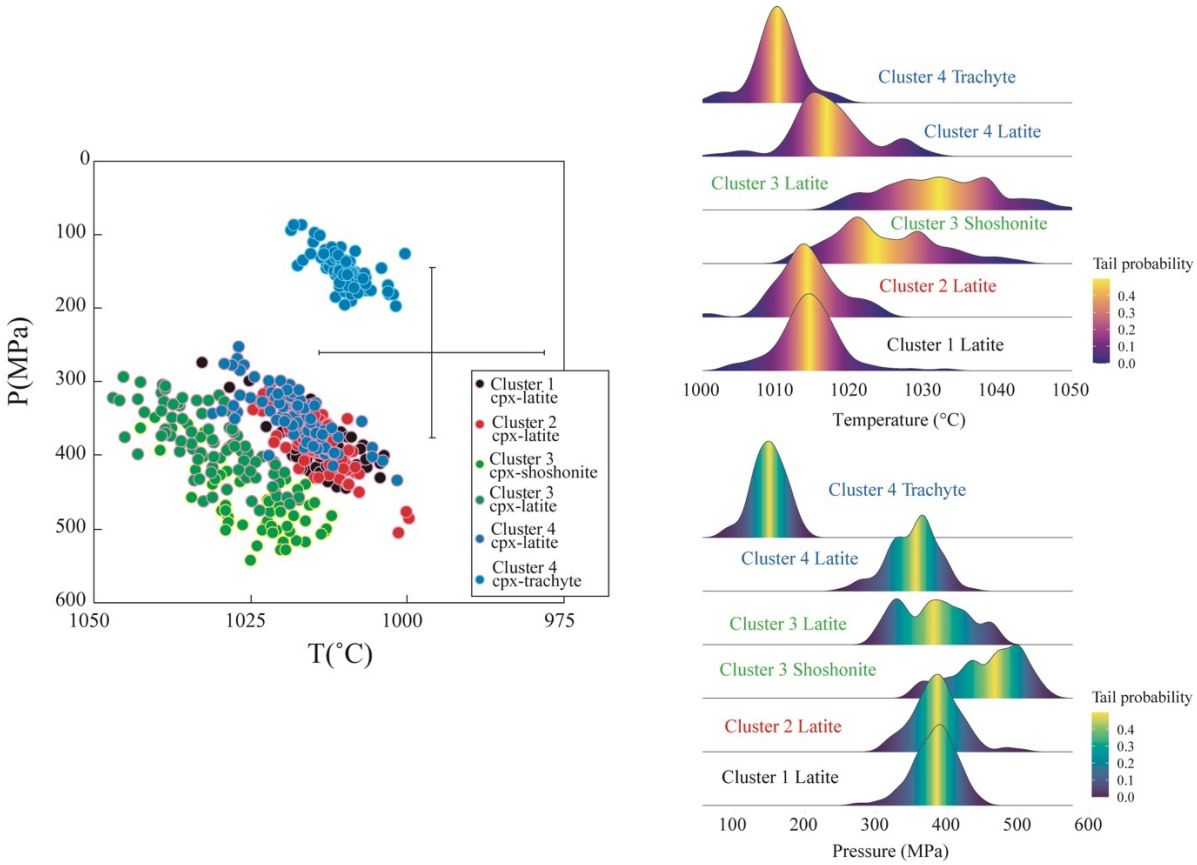

Figure 7.14 – Pressure and temperature estimates obtained for the clinopyroxene clusters using the clinopyroxene-melt thermobarometer of Masotta et al. (2013) (the cross represents the errors of the thermobarometer) and Kernel density distributions showing the pressure and temperature estimates. Color gradient in density distributions represents the probability of distribution. Bright yellow represents the median (i.e. lower/upper 50%). Darker zones represent the extreme tails, e.g. 0.1 represents 10% of the lower/upper distribution.

The obtained pressure estimates allow to give estimates on the crystallization depth of the analyzed clinopyroxene clusters. Assuming a mean density value of 2.7 g/cm^3 for the crust, clinopyroxene-latite melt pressures for cluster 1, 2 and 4,

indicate crystallization depths between 13 and 16 km. Analogue depths are inferred for clinopyroxene of cluster 3 paired with a latite melt. In general, the inferred pressures for the clinopyroxene clusters-latitic melt pairs are in accordance with those inferred for the shoshonitic to latitic reservoir (17–12 km) of La Fossa plumbing system, that has been always active at least in the last 1000 years (De Astis et al., 2013 and reference therein; Mandarano et al., 2016; Nicotra et al., 2018, see also Chapter 6). As regards to clinopyroxene crystals of the cluster 3 coupled with shoshonitic melts, the estimated pressure of 458 ± 48 MPa are in accordance with the deepest reservoirs of basaltic to shoshonitic melts inferred for both La Fossa and Vulcanello system, estimated between 21 and 18 km (Zanon et al., 2003; Peccerillo et al., 2006; Davì et al., 2009; De Astis et al., 2013). Finally, the pressure obtained for the clinopyroxene of cluster 4 paired with a trachytic melt composition, yielding to 151 ± 23 MPa, confirms a possible shallower storage conditions of clinopyroxene belonging to the Pal D trachytic magma (see also Chapter 6). It should be noted that, with the exception of cluster 4-trachytic melt pairs, the inferred thermobarometric conditions for cluster 1, 2 and 3 (coupled with both latitic and shoshonitic compositions) fall within the errors of prediction of the thermobarometric models (Fig. 7.14, error on temperature and pressure estimates are ± 18 °C and 115 MPa; Masotta et al., 2013).

Factors governing the chemical composition of clinopyroxene clusters

The chemical differences of the clinopyroxene clusters can be the result of changes in pressure and temperature conditions and/or change in the melt chemistry during crystal growth (Putirka, 2008; Armienti et al., 2013; Perinelli et al., 2016; Mollo et al., 2018). However, the effect of crystallization kinetics on the clinopyroxene composition should be also evaluated. Indeed, many works demonstrated that the clinopyroxene morphology and composition are strongly dependent on crystallization kinetics (Skulski et al., 1994; Lofgren et al., 2006; Mollo et al., 2010, 2013b; Pontesilli et al., 2019). Particularly, crystal growth and compositional zoning largely depend on the degree of undercooling of the system (expressed as the difference between the *liquidus* temperature of the magma and

the actual crystallization temperature; cfr. Mollo and Hammer, 2017). A characteristic textural feature of clinopyroxene is that the type of compositional zoning (concentric, sector or dendritic zoning) is primarily affected by the degree of undercooling (Welsch et al., 2016; Mollo and Hammer, 2017; Ubide et al., 2019a, 2019b; Masotta et al., 2020). The most characteristic textural feature that characterize clinopyroxene crystals that are subjected to low degrees of undercooling and slow growth rates is the development of the sector zoning or hourglass sector {-111}, that grows along the *c* crystallographic axes (Downes et al., 1974; Welsch et al., 2016; Mollo and Hammer, 2017; Ubide et al., 2019a, 2019b; Masotta et al., 2020). However, such feature has not been observed in the clinopyroxene of the PEU sequence.

The differences observed in the chemistry of the four clusters might be related with the compositional variation associated to the compositional zoning of clinopyroxene (Fig. 7.4). Clusters 1 and 2 result in fact enriched in Ti and Al compared to cluster 3 and 4 that, in turn, result slightly enriched in Si and Mg (Figs. 7.6 and 7.7). Furthermore, the cluster 3 is also enriched in Cr (Fig. 7.15).

As revealed by trace element high resolution mapping studies, compatible transition metals such as Cr, Ni and Sc, indicate either growth in less evolved melt or processes of mafic magma recharge, that in the case of Cr are even detectable with EPMA analyses (Ubide and Kamber, 2018; Ubide et al., 2019a; Magee et al., 2020). It is thus possible to infer that cluster 3, which preferentially occurs in cores and mantles of analyzed crystals (48%, Fig. 7.11), is related to crystallization in a less evolved magma.

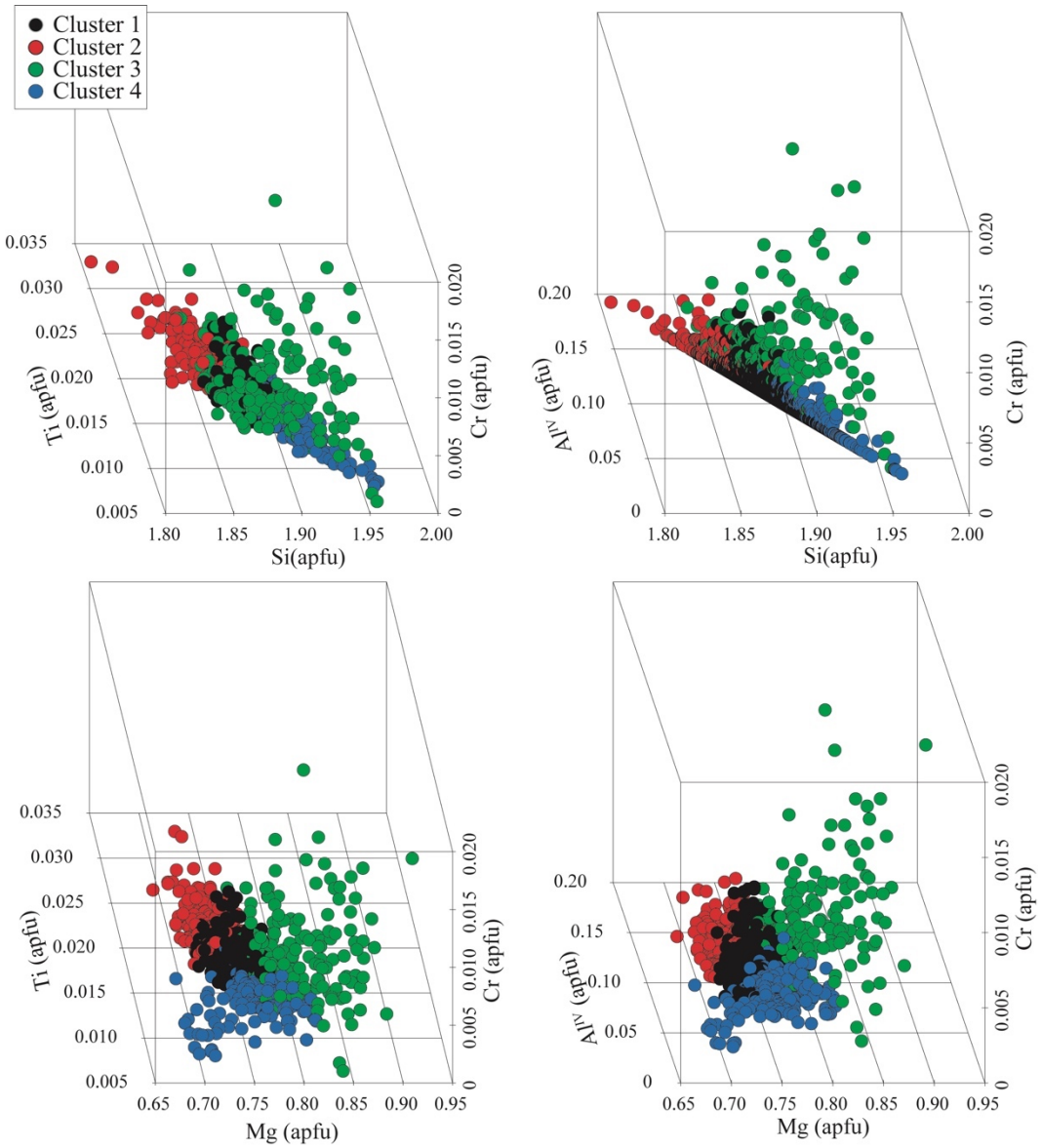

Figure 7.15 – 3D plots of Ti, Al^{IV},Mg, Si and Cr of the four compositional clusters. Cluster 2 is enriched in Ti and Al, cluster 3 in Cr and Mg.

Thermobarometric calculation showed that analytical points of cluster 3 could represent crystallization in a slightly hotter and even deeper (when considering cluster 3 spots paired with a shoshonitic melt), with respect to clusters 1, 2 and 4 (Fig. 7.14). However, the observed chemical variations within the clinopyroxene clusters may be also explained as the result in changes of the degree of the undercooling. Following an increase of the undercooling, clinopyroxene becomes depleted in Mg and Si and enriched in Al^{IV} and Ti (Fig. 7.15) (Mollo et al, 2010; Masotta et al., 2020). Part of the compositional features of the four clusters can thus be viewed as the result of the varying degree of undercooling, with the cluster 2

showing the highest undercooling (Figs. 7.7 and 7.15). Specifically, the occurrence of cluster 2 in the 73% of the cases in mantles and rims of the analyzed clinopyroxenes, could testify to episode of overgrowth of existing crystals following magma ascent towards the surface (decompression-induced crystallization). Clinopyroxene belonging to cluster 4 are enriched in Si, Na, Fe and depleted in Ca, Al and Cr. Considering thermobarometric constraints for this cluster, this chemical evidence could suggest the growth in a slightly evolved, cooler and shallower latitic to trachytic melt possibly with concurrent crystallization of feldspars and biotite (as observed in Chapter 6 by petrographic features of the trachytic magma of Pal D, in which clinopyroxene is mostly represented by cluster 4), which depleted the magma in Ca, Al and Cr.

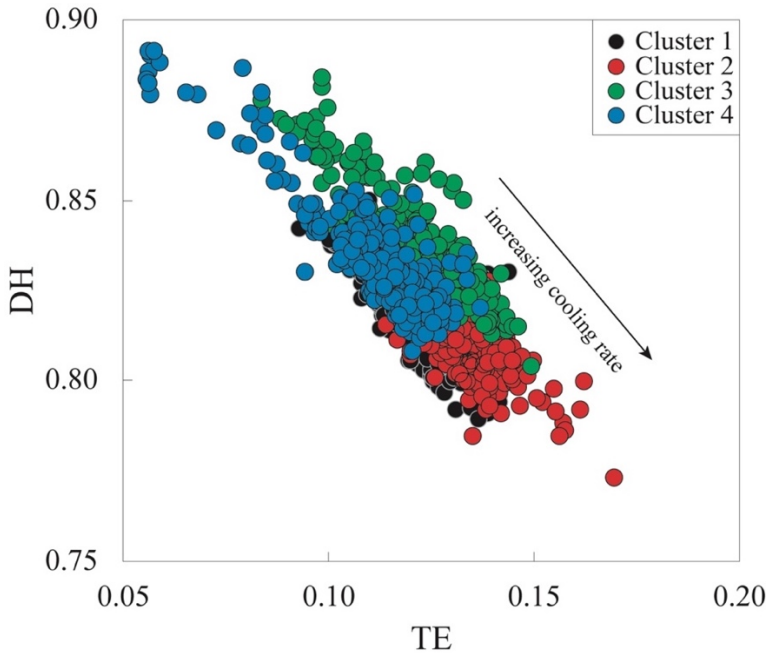

Figure 7.16 – DH (Di + Hd) vs. TE (CaTs + CaFeTs + En) of clinopyroxene clusters. DH decreases and TE increases with increasing undercooling (Mollo et al., 2010; Masotta et al., 2020).

Exploring magma dynamics along the PEU stratigraphy

Enrichments in Al and Ti are typical of crystallization under increasing degree of undercooling and are likely related to magma ascent towards the surface, while Cr reflects growth in a more primitive melt or recharge by new magma into reservoir (Ubide and Kamber, 2018; Mollo et al., 2010, 2013b; Magee et al., 2020).

In order to explore potential links between the chemistry of clinopyroxene clusters and magma dynamics along the stratigraphy of the PEU, the variation of the concentration variance of those elements that indicate either growth or recharge by more mafic magmas (Cr, Mg) and higher degree of undercooling (Al, Ti) has been examined.

The changes in chemical composition of clinopyroxene that are attributable to magma dynamics can be inferred by measuring the magnitude of the concentration variance along the PEU stratigraphy. The concentration variance, for a given chemical element, calculated on all individual spots for each level, is expressed as:

$$\sigma^2 = \frac{\sum_{i=1}^{N}(C_i - \mu_i)^2}{N}$$

Where *Ci* is the concentration of the element *i*, μi the mean of the element *i* and *N* the number of analyses. The decay of the concentration variance and with time has been used as a proxy to evaluate the degree of melt homogenization during magma mixing (Perugini et al., 2013; Perugini et al., 2015; Morgavi et al., 2013). The chemical variance has been calculated for Cr, Mg, Al^{IV} and Ti for each sample. The values of the concentration variance were then normalized to the concentration variance of the sample T-21 of the Pal A sub-unit. The reasons to normalize to this sample are essentially two: i) T-21 is at the base of the stratigraphy of the PEU sequence and likely represents the initial phase of the whole eruptive sequence (Fig. 7.1); ii) it shows the lowest value of concentration variance for all the considered chemical elements (Fig. 7.17a). In Figure 7.17a it emerges that, along the stratigraphy of the PEU, Al and Ti vary together in an opposed way compared to Mg and Cr (Fig. 7.17a). Indeed, in the stratigraphic levels in which the chemical variance of Al and Ti increases, that of Cr and Mg decreases and vice versa, probably testifying to alternating moments of recharging pulses and magma ascent.

Along with the study of the changes in magnitude of the chemical variance, the magma dynamics through the PEU have been investigated focusing on the relative relationships among the four clusters. Particularly, the changes in the fraction of a cluster over the total have been considered for each stratigraphic level

(Fig. 7.17b). For example, the fraction of a cluster x relative to the sample j (stratigraphic level) over the total has been calculated through the relation:

$$frx(j) = n.clust\ x(j)/(n.clust\ 1(j) + n.clust\ 2(j) + n.clust\ 3(j) + n.clust4(j))$$

Where *n.* represents the number of spots relative to a cluster x (with x= cluster 1, 2, 3 or 4) in a level (j) (Fig. 7.17b). The fraction of cluster 3 increases when the fractions of clusters 1, 2 and 4 decrease (7.17b). Conversely, the fractions of clusters 1 and 2 increase only when the cluster 3 starts to decrease (Fig. 7.17b). The fraction of cluster 4 systematically increases before that of the fraction of cluster 3.

The changes in the chemical variance along the stratigraphy can be thus correlated to variations of the cluster fractions. The changes in the concentration variance of Al and Ti indeed track the increase of the fraction of cluster 2. Instead covariation of Cr and Mg systematically follows the increase of the fraction of cluster 3 along the stratigraphy (Fig. 7.17a, b).

It is thus possible to recognize at least three cycles of magmatic (mafic) recharge within the crustal magma reservoir, followed by ascent and eruption (Figs. 7.17c and 7.18). The beginning of each cycle is characterized by the eruption of clinopyroxene that record crystallization in a lati-trachytic magma (i.e., increase of cluster 4; Figs. 7.11 and 7.17b). Magmatic input by shoshonitic melts during these phases is firstly recorded by the mantles and rims of clinopyroxene (mantles and rims of cluster 3, Fig. 7.11). The increase of the fraction of cluster 4 is accompanied by the increase of cluster 3 (increase of Cr) in mantles and rims of crystals, suggesting the arrival (recharge) of new magma. Then, the positions of the cluster 3 inside the crystal zones changes three times along the stratigraphy from the more peripheral portions (mantles and rims) of the crystals at the beginning of each magmatic input to the cores of clinopyroxene (Figs. 7.11 and 7.17c). This could indicate a process of repeated cycles of eruption of slightly evolved, cooler and shallower magma (cores with cluster 4 and mantles and rims of cluster 3) at the beginning of each cycle and progressive replenishment of the subvolcanic magma reservoir and clinopyroxene growth in a more mafic (hotter) melt (Figs. 7.17c and

7.18). The increase of cluster 2 (mostly occurring in mantles and rims, Fig. 7.11) follows immediately the decrease of cluster 3 (Fig. 7.17b). This process is consistent with an increase of the degree of undercooling, likely caused by the ascent of magma to a shallower depth and exsolution of a volatile phase provoking the increase of the *liquidus* temperature. The alternance between cluster 1 and cluster 2, could represents feeble oscillatory zoning caused by small change in the P-T conditions of magma (Fig. 7.18).

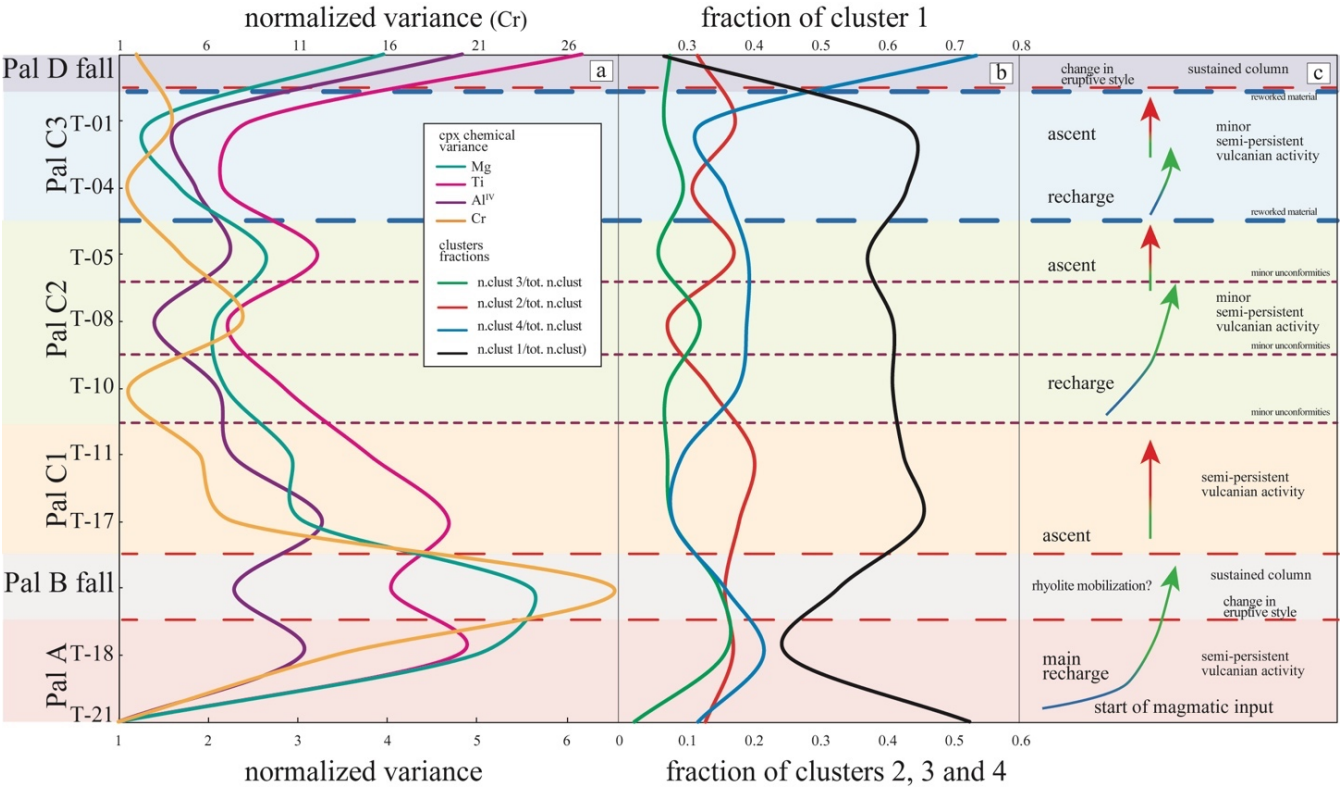

Figure 7.17 – a) Normalized chemical variance of Cr, Mg, Al^{IV} and Ti; b) fractions of cluster changes (see text for explanation); c) simplified sketch of the identified cycles of magmatic recharge with the main textural features of the investigated outcrops and associated eruptive style.

The three moments of magmatic recharge are recognized at the top of the Pal A sub-unit (including Pal B), toward the middle of the Pal C2 sub-unit (T-10, T-08 samples) and at the beginning of Pal C3 sub-unit (Fig. 7.17c). These magmatic inputs are followed by ascent, as recorded by the increase of cluster 2 (Fig. 7.17b, c). The main magmatic input is recorded at the base of the sequence (top of Pal A sub-unit and Pal B). Accordingly, the products belonging to Pal A are mainly constituted by a continuous series of ash layers (Figs. 7.1 and 7.17, see also Chapter

5) without any signs of a pause in the eruptive activity. During this phase, the magmatic input could have played also a major role in the abrupt change in the eruptive style recorded by the emplacement of Pal B fallout. Petrologic, geochemical and petrographic features of the Pal B rhyolite, such as the occurrence of magmatic enclaves and xenocrysts (see also Chapters 3 and 6) strongly support the hypothesis that a mafic input could have triggered the Pal B eruption. After the eruption of Pal B, the recharge is immediately followed by a period of steady state activity characterized by the emplacement of the layers of Pal C1 sub-unit, that, like Pal A, do not record pauses in the eruptive activity (Figs. 7.1 and 7.17, see also Chapter 5). After this moment, there is a decrease in the frequency of the eruptive activity caused by a decrease in the magmatic supply, testified by the beginning of a series of unconformities in the stratigraphic succession. In this moment, a minor recharge is identified in the middle of Pal C2 sub-unit (Figs. 7.1 and 7.17, see also Chapter 5). Finally, after a major pause chronicled by the presence of reworked material, a minor reappraisal of the activity is recorded by the emplacement of the primary ash layers of the Pal C3 sub-unit (Figs. 7.1 and 7.17, see also Chapter 5). The emplacement of Pal D occurred after a period of stasis in eruptive activity with a substantial change of eruptive style. The majority of clinopyroxene of Pal D belongs to cluster 4, that is associated to growth in an evolved magma (Figs. 7.9 and 7.11). This, together with the different behavior of the chemical variance in this level (Fig. 7.17a) and by the clearly different composition of whole-rock, pumice matrix glass, mineral phases and melt inclusions (Fig. 7.3, see also Chapters 6 and 8), could be symptomatic that other processes occurred in the petrogenesis and eruption of the Pal D magma. In chapter 6, it has been proposed that the origin of the Pal D magma is related to a mixing between shoshonitic recharging magmas and liquids derived by melting of crystal mush. Such process, together with the stratigraphic position of the Pal D eruption at the top of the explosive portion of the PEU, could be consistent with a prolonged period of melts interaction and homogenization due to recharge events.

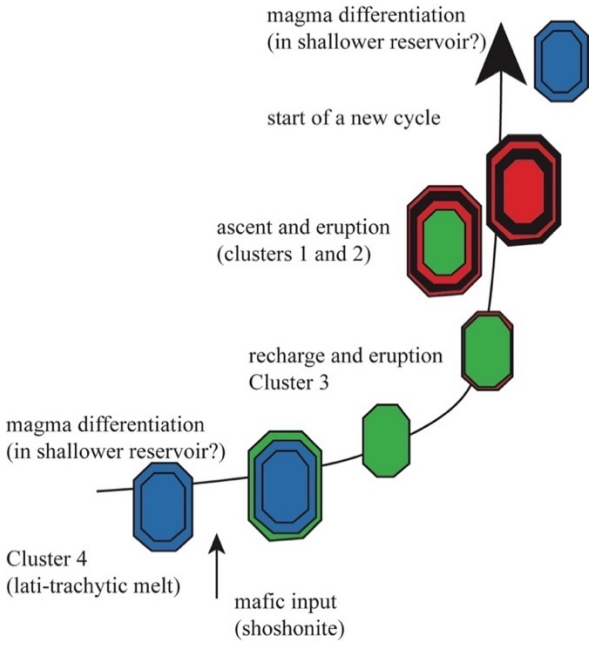

Figure 7.18 – Simplified sketch of the occurrence of clinopyroxene clusters during each cycle of magmatic input and eruption.

7.5 Conclusions

In this chapter, a hierarchical cluster analysis applied to major element core-rims profiles of clinopyroxene belonging to the PEU explosive sequence, has been performed and four chemical clusters have been identified. This allowed to recognize magma dynamics through the stratigraphic sequence of the PEU and to identify the different processes responsible for the chemical variability of clusters. By combining thermobarometric calculations with the study of the relationships occurring among the chemical clusters and the chemical variance of clinopyroxene composition, at least three cycles of magmatic recharge are recognized in the eruptive sequence. The petrological interpretation is thus corroborated by the deposit features observed at the scale of natural outcrops. The approach presented here may can be helpful for understand similarly complex volcanic successions worldwide constituted by fine-grained material, where only mineral phases may hold crucial information on the magma dynamics and plumbing systems evolution.

8 The role of sulfide saturation at La Fossa volcano for the evolution of chalcophile elements concentration during magmatic differentiation and implications for the magmatic-hydrothermal system

8.1 Introduction

Sulfur in magmas plays a key role in the control of metal enrichments leading to magma fertility and genesis of magmatic-hydrothermal ore deposits and high-sulfidation epithermal systems (Halter et al., 2005; Nadeau et al., 2010; Wilkinson, 2013; Jenner et al., 2010, 2015; Richards, 2015). Most mineralized systems are usually associated to relatively oxidized mafic arc mafic magmas (Sillitoe, 2010). The decrease of the fO_2 in the magma allows the conversion of high soluble oxidized sulfate (S^{6+}) to less soluble sulfide (S^{2-}) (Carroll and Rutherford, 1985; O'Neill and Mavrogenes, 2002; Jugo et al., 2010; Ricards, 2015; Edmonds and Mather, 2017). This process is one of the most important factors triggering the sulfide saturation with the production of an immiscible sulfide phase. In this framework, evolution of metal concentration in arc magmas is difficult to investigate due to the loss of volatiles and metals during crystallization and saturation of a sulfide phase at some stage during their evolution (Audétat and Simon, 2012). Indeed, due to the strong affinity of chalcophile and siderophile elements (e.g. PGE, Fe, Cu, Au, and Ag) for the sulfide phase (Mungall and Brenan, 2014), sulfides exsolved from silicate magmas lead to severe metal depletion in the residual silicate melt (Park et al., 2015). Thus, metal evolution in arc magmas is controlled by several factors such as: i) the timing of sulfide saturation relative to magmatic differentiation and volatile exsolution; ii) the amount of metal segregated into magmatic sulfides; iii) the amount of sulfide formed; iv) and whether sulfides are 'irretrievably lost' or may instead release metals again at later stages (Halter et al., 2005; Wilkinson, 2013; Mungall et al., 2015; Zhang and Audétat, 2017; Chang

and Audétat, 2018; Hao et al., 2019; Park et al., 2015, 2019; Bai et al., 2020). In the case of a sulfide saturation occurring in the first stages of magmatic differentiation (early sulfide saturation), magmas ascending to shallower reservoirs may be depleted in ore metals and therefore unable to produce fertile ore-deposits (Wilkinson, 2013). On the other hand, the occurring of sulfide saturation late in the evolution of a magmatic suite (late sulfide saturation) would let incompatible ore metals to become concentrated in the magma. The exsolution of an aqueous fluid phase from magma that undergo sulfide saturation, implies ore metals partitioning into the exsolved fluid (Pokrovski et al., 2013; Cocker et al., 2016; Hao et al., 2017; Lowczak et al., 2018), with a consequent production of a potential mineralizing aqueous solution. The combined role of these factors has been always difficult to investigate, largely because of the complexity in measuring the metal content of the magmas during their evolution (Park et al., 2019). Information mostly derives from the "roots" (e.g. sulfide-bearing cumulates) of the plumbing systems or from mineralized bodies (Chang and Audétat, 2018, Chen et al., 2020).

Several studies focused on the role of sulfide saturation in generating porphyry Cu-Au and related epithermal systems in magmatic rocks associated with mineralized or barren areas (Halter et al., 2002, 2005; Park et al., 2015; Cocker et al., 2016; Hao et al., 2017; Zhang and Audetat, 2017; Lowczak et al., 2018). As magmatic-hydrothermal ore deposits can be considered the extinct equivalent of active magmatic systems (Hedenquist and Lowenstern, 1994), the investigation of these processes in the "fresh" products of active arc volcanoes, particularly with the support of data from silicate melt inclusions, can provide essential information on metal budget and ore genetic models associated with arc-related magmas. A significant advantage in studying active volcanic systems is the lack of hydrothermal alteration or overprinting mineralization, as shown by recent works for magmatic sulfide saturation studies (Nadeau et al., 2010; Fulignati et al., 2018; Georgatou et al., 2018; Zelenski et al., 2018; Georgatou and Chiaradia, 2020). Despite that, very few works have undertook the investigation of metal evolution through the processes of magma differentiation, sulfide exsolution and fluid exsolution at active volcanoes or across the wide compositional spectra of magma types (Timm et al., 2012; Park et al., 2013a, 2013b, 2015; Cox et al., 2019).

La Fossa volcano is an ideal site to study potentially mineralizing processes beneath arc volcanoes, being characterized by an active magmatic-hydrothermal system (Fulignati et al., 1998; Boyce et al., 2007, see Chapter 3) and providing evidence of sulfide melt-silicate melt immiscibility (Fulignati et al., 2018). In this chapter, through the study of melt inclusions, magmatic sulfides and host minerals, the evolution of metals has been tracked for the entire basalt to rhyolite compositional spectrum of Vulcano magmas. The subduction related shoshonitic-potassic magmatic series of Vulcano, is similar to part of the magma types found in association with porphyry Cu deposits (Sillitoe, 2010; Audétat and Simon, 2012). Finally, the obtained results are compared with metal content in sulfides from magmatic systems associated with ore deposits, showing that strong analogies exist between metal evolution in active arc volcanoes and those reported for porphyry Cu environments.

8.2 Sulfide melt saturation in the La Fossa plumbing system

By studying the sulfide inclusions (SIs) occurring in the trachytic products of the Pal D eruption, Fulignati et al. (2018) reported the first evidence of sulfide/silicate melt immiscibility at Vulcano. The occurrence of SIs within crystals and in the glass matrix clearly indicates that sulfide saturation and exsolution from silicate melt occurred during crystallization shortly before the eruption (Fulignati et al., 2018). The absence of sulfide inclusions in the products of basaltic and shoshonitic composition, and the newly found SIs in latites (rare) and other trachytes (Palizzi lava) reported in this thesis (see next sections), suggest that sulfide melt saturation occurred late in magmatic evolution, at the latite-trachyte stage of magmatic differentiation. The late sulfide saturation is a common feature in arc settings (Jenner et al., 2010, 2015; Park et al., 2015). Vulcano basaltic melts are undersaturated with respect to sulfide phases, despite their high sulfur content (up to ~2700 ppm measured in melt inclusions, Métrich and Clocchiatti, 1996; Gioncada et al., 1998; Scaillet and Pichavant, 2005). This high sulfur content is in agreement with the relatively high oxygen fugacity of the Vulcano primitive melts (ΔNNO +0.72, Métrich and Clocchiatti, 1996) (Fig. 8.1a) and with the consequent

stabilization of more soluble sulfate complexes in the silicate melt. The negative correlation between sulfur content and degree of evolution observed in the transition from basalts to shoshonites and latites has been ascribed to a loss of sulfur by degassing to a volatile phase (Clocchiatti et al., 1994; Gioncada et al., 1998).

Fulignati et al. (2018) by using the biotite composition occurring in the Pal D products as an oxybarometer, constrained the fO_2 value of Pal D trachyte around ΔNNO -1/-2 (Fig. 8.1a). The occurrence of late sulfide melt saturation in the Pal D trachyte matches with the calculated sulfur content at sulfide saturation (SCSS, calculated with the model of Fortin et al., 2015), between 200-250 ppm, in agreement with the measured sulfur content in the Pal D melt inclusions (Fig. 8.1b) (Fulignati et al., 2018).

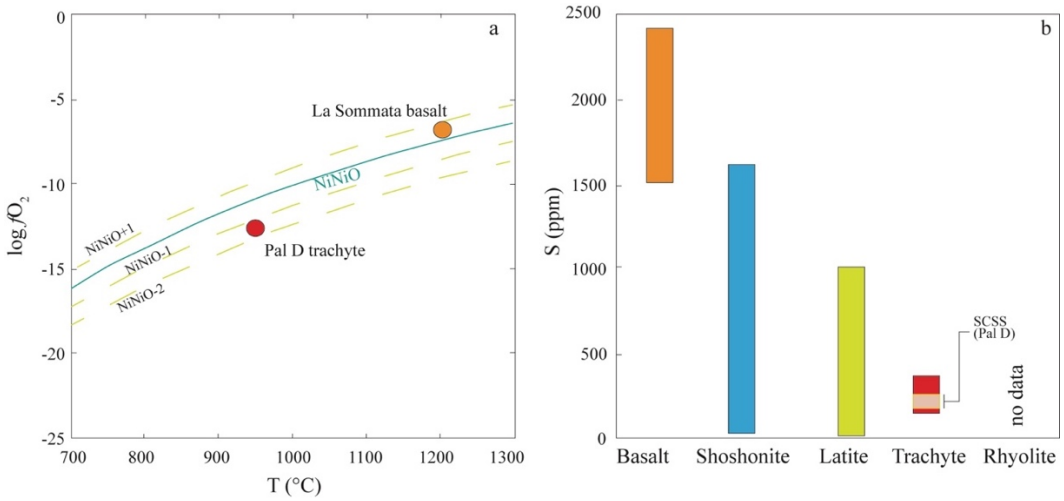

Figure 8.1 – a): Log fO_2 vs. temperature, showing the fO_2 values of La Sommata basalts (from Metrich and Clocchiatti, 1996) and Pal D trachyte (Fulignati et al., 2018). Ni- NiO buffer (Huebner and Sato, 1970) is plotted for comparison (modified from Fulignati et al., 2018); b): Range of sulfur content in Pal D trachyte melt inclusions (Fulignati et al., 2018) with the calculated sulfur concentration at sulfide saturation (SCSS, Fortin et al., 2015), compared to the sulfur content measured in melt inclusions of basalt shoshonites and latites (data from Gioncada et al., 1998 and Fusillo et al., 2015) (modified from Fulignati et al., 2018).

A mechanism invoked to explain the triggering of sulfide saturation, by reducing the silicate melt, is the sudden crystallization of magnetite (the "magnetite crisis" of Jenner et al., 2010). This process, is able to lower the fO_2 value by decreasing the Fe^{3+}/Fe^{2+} ratio of the melt. However, for Vulcano products, magnetite joins the crystallization assemblage much earlier (Gioncada et al., 1998) as testified by the constant decrease of Fe_2O_3 with MgO since the basaltic products

(Fig. 8.2). As a consequence, the late sulfide saturation at the latite-trachyte stage does not appear to be related to the "magnetite crisis". Differentiation by fractional crystallization of a magnetite-bearing assemblage and assimilation of crustal material (De Astis et al., 1997; Del Moro et al., 1998) could, however, lower the fO_2, triggering late sulfide saturation and leading to sulfide melt-silicate melt immiscibility (Park et al., 2015).

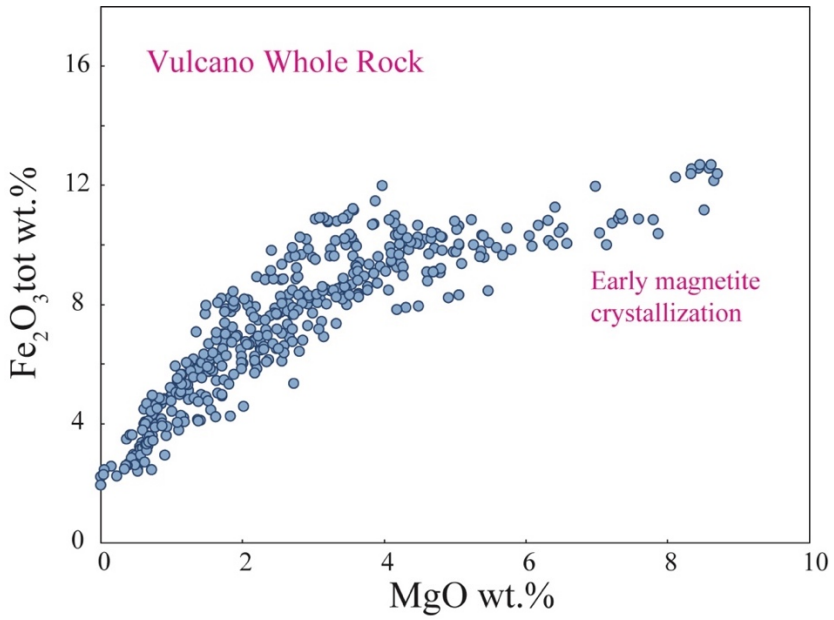

Figure 8.2 - Fe_2O_3 tot. vs MgO diagram of whole-rock Vulcano products. Data are re-calculated to 100 wt.% on anhydrous basis; literature data are from Clocchiatti et al. (1994), De Astis et al. (1997), Del Moro et al. (1998), Gioncada et al. (1998), Davì et al. (2009), Fusillo et al. (2015) and this thesis.

8.3 Samples and melt inclusions selection criteria

Samples were selected in order to include the entire range of magma types from basalt to rhyolite. The samples were analyzed for the occurrence and composition of sulfide (SIs) and melt (MIs) inclusions hosted within phenocrysts. Samples were preferentially selected from explosive eruptions, targeted to ensure quenching of melt inclusions to a glass with the eruption. This minimizes the potential for post-entrapment crystallization of microlites in the trapped melt or crystallization of the host mineral on the inclusion walls. They include the

scoriaceous lapilli of La Sommata and Vulcanello, of basaltic and shoshonitic composition, respectively. The latitic, trachytic and rhyolitic samples are represented by the products of the PEU and GCEC of La Fossa and consist of dark grey coarse ash of Pal A (latite) and Pal C (latite, trachyte), pumiceous lapilli of Pal D (K-rich trachyte) and Pal B and Upper Pietre Cotte (rhyolite), and the Palizzi lava flow (trachyte) (see also previous chapters).

To avoid post-entrapment modifications of the melt composition due to melt crystallization or leakage, the selected melt inclusions are entirely glassy (no microlites) and lack of large vapor bubbles or other evidences of only partial enclosing by the host crystal. Shrinkage bubbles are absent or small in Vulcanello MIs while they are common in La Sommata basalt and in Palizzi trachyte; bubbles may host traces of volatile elements escaped from melt, but the observation that they are apparently empty means that their metal content can be considered negligible. Based on the inspection of MIs under back-scattered electron (BSE) microscopy and on their major element composition, post-entrapment crystallization of the host on the inclusion walls can also be considered negligible with respect to chalcophile metals. This is in agreement with previous estimates (<2 wt%) of olivine host crystallization for Vulcanello MIs (Fusillo et al., 2015), corresponding to a variation of the Cu content within analytical uncertainty.

8.4 Results

Magmatic sulfide occurrence and composition

Based on their textures, two types of sulfide inclusions (Type 1 polymineralic SIs, and Type 2 homogenous SIs) were identified in the Vulcano products. Both types are spherical when found in glass, and spherical or ovoid to elongated in shape when enclosed in host phenocrysts, with shape partially defined by surrounding crystal growth (Fig. 8.3).

Type 1 SIs (17 inclusions) are between 1 and 20 μm in diameter (mostly <10 μm) and consist of two or three Cu-rich sulfide phases each (Fig. 8.3). These SIs are hosted in clinopyroxene, magnetite and feldspars (Fig. 8.3). The composition of

Type 1 sulfides (Tab. 8.1 and Appendix G), when plotted in a Cu-Fe-S diagram at 1000°C (Fig. 8.4), spans from bornite solid solution (bnss) to the sulfide liquid field (SL). The reconstructed bulk composition of these unmixed SIs ranges from 66 wt% to 34 wt% Cu in the Cu-Fe-S diagram (Fig. 8.4, see Chapter 4 for reconstruction method based on image analysis). Trace elements were measured up to 493 ppm Ni, 131 ppm Co, 1145 ppm Zn, 397 ppm As, 208 ppm Se, 354 ppm Ag and 2020 ppm Pb (Tab. 8.2 and Appendix G) within the two Type 1 SIs analyzed (which contained 65 and 46 wt% Cu).

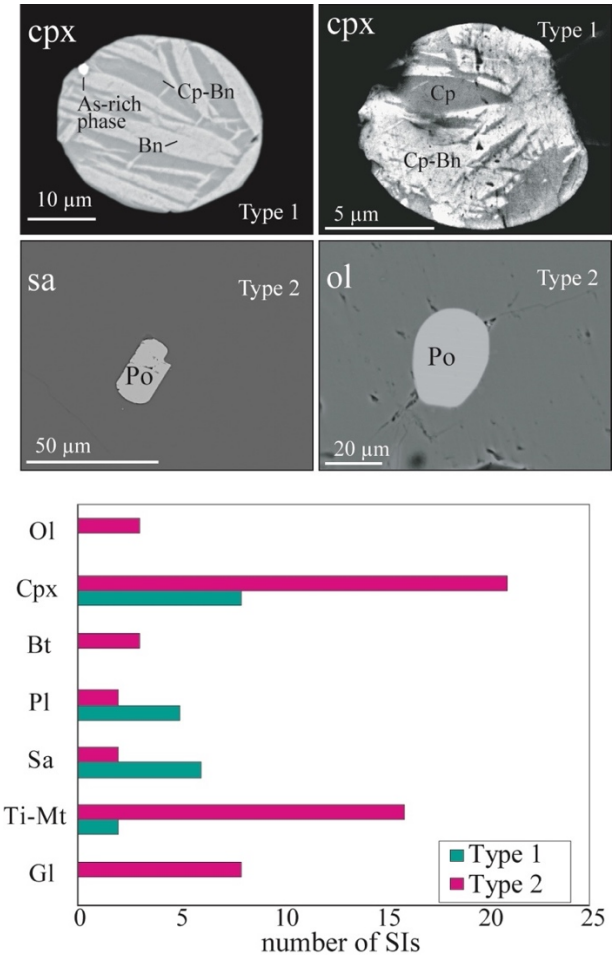

Figure 8.3 - BSE images of Type 1 SIs consisting of unmixed chalcopyrite (Cp)-bornite (Bn) and Type 2 SIs represented by homogeneous pyrrhotite (Po); abundance of SIs in the various mineral phases and groundmass glass of eruptive products (Ol: olivine; Cpx: clinopyroxene; Bt: biotite; Pl: plagioclase; Sa: sanidine; Mt: magnetite; Gl: groundmass glass); modified after Costa et al. (2021).

Type 2 SIs (59 inclusions) are 5-60 µm in diameter with a mean size of 20 µm and homogeneous textures (Fig. 8.3); they occur in clinopyroxene, olivine, Ti-

magnetite, plagioclase, sanidine, biotite and glass and prevail in mafic phases and glass (Fig. 8.3). Type 2 SIs plot, at 1000°C, in the pyrrhotite field (mss, monosulfide solid solution), with Cu content up to 2.6 wt% (Fig. 8.4 and Tab. 8.1, see also Fulignati et al., 2018 and Appendix G). If compared to Type 1 SIs, they show markedly higher Ni and Co contents, up to 3495 ppm and 4248 ppm, respectively, similar Zn and lower Pb (up to 385 ppm), with Ag and Se, in the tens of ppm range (Tab. 8.2). The only SI found in a rhyolite is pyrrhotite with 0.4 wt% Cu, characterized by very low Zn, Pb and Ag and higher Mo contents (Tab. 8.2).

Type 1 and Type 2 SIs are common accessories in trachytes, whereas they are extremely rare in latites (only Type 1 SIs) and in rhyolites (only Type 2 SIs), where just a couple of SIs were found after the inspection of several dozens of crystals. They are absent in basalt-shoshonite rocks. The two types of SIs never coexist in the samples of the same eruption. The entire dataset of analyses of the sulfides inclusions is reported in tables 8.1 and 8.2 and in Appendix G.

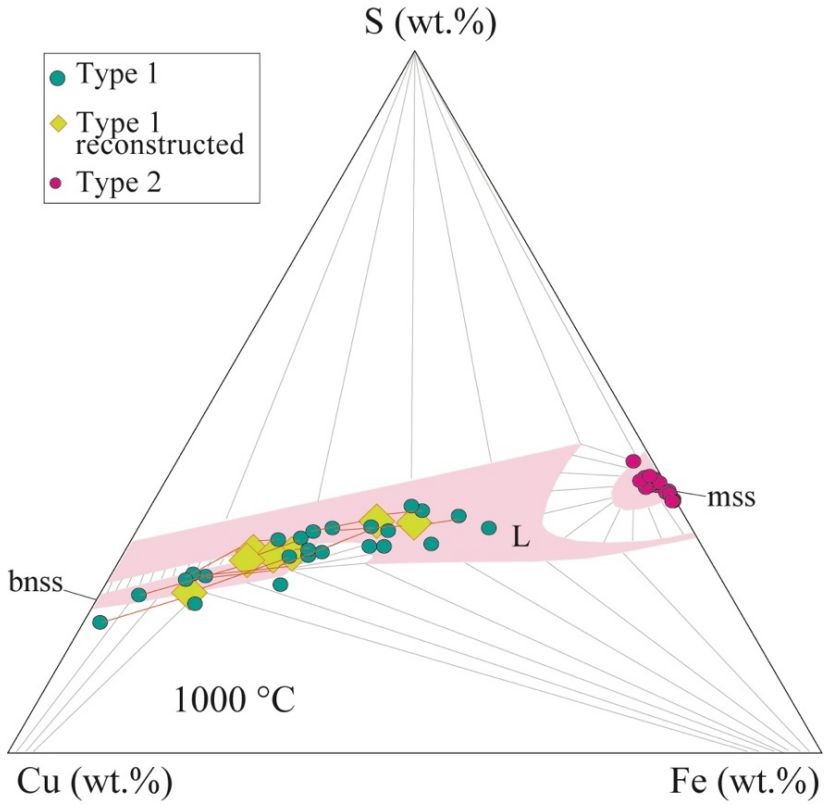

Figure 8.4 - Composition of SIs in the Cu-Fe-S system at 1000°C (Craig and Kullerud, 1969), for Type 1 SIs analyses of unmixed phases and the correspondent reconstructed composition are shown and joined by red lines. Modified after Costa et al. (2021).

*Table 8.1 - Major element composition (wt.%) of selected Type 1 and Type 2 SIs (see appendix G for the complete dataset); Ol: olivine; Cpx: clinopyroxene; Bt: biotite; Pl: plagioclase; Sa: sanidine; Ti-Mt: Ti-magnetite. *: reconstructed bulk composition calculated with image analysis (see Chapter 4 for details); bdl: below detection limit; source: a Fulignati et al. (2018) EPMA analyses; b This thesis. FE-SEM-EDS analyses.*

Host rock	Unit	Host mineral	Sulfide ID	Sulfide type	source	Fe	S	Co	Mn	Ni	Zn	Cu	total
Trachyte	Pal D	sa	PAL-90 sulf1	2	a	58.48	37.19	0.09	0.08	0.06	bdl	1.44	97.33
Trachyte	Pal D	cpx	PAL-90 sulf2	2	a	59.12	38.05	0.03	0.09	0.03	0.10	1.19	98.60
Trachyte	Pal D	cpx	PAL-90 sulf2	2	a	59.89	38.08	0.07	0.12	0.05	0.03	0.42	98.65
Trachyte	Pal D	ol	pal90solf3	2	a	57.19	37.24	0.14	0.18	0.07	0.07	1.62	96.52
Trachyte	Pal D	gl	pal90solf4	2	a	58.01	37.24	0.16	0.11	0.09	bdl	2.32	97.93
Trachyte	Pal D	ol	pal90solf5	2	a	58.94	37.60	0.10	0.12	0.10	bdl	1.67	98.53
Trachyte	Pal D	ol	pal90solf5	2	a	59.19	38.08	0.09	0.18	0.04	bdl	1.29	98.88
Trachyte	Pal D	gl	pal90sulf8	2	a	57.09	38.05	0.07	0.10	0.04	0.11	1.34	96.80
Trachyte	Pal D	Ti-mt	pal90sulf10	2	a	58.72	38.24	0.05	0.16	0.05	0.05	0.97	98.23
Trachyte	Pal D	cpx	pal90sulf13	2	a	58.38	37.99	0.13	0.12	0.00	0.03	1.54	98.18
Trachyte	Pal D	cpx	pal90sulf13	2	a	58.25	37.70	0.07	0.04	0.01	0.06	1.46	97.58
Trachyte	Pal D	cpx	pal90sulf14a	2	a	53.30	39.64	0.14	0.09	0.06	bdl	2.16	95.39
Trachyte	Palizzi lava	cpx	sc1824 4-5-6	1	b	20.42	28.20	bdl	bdl	bdl	bdl	51.38	100.00
Trachyte	Palizzi lava	cpx	sc1824 4-5-6	1	b	2.27	18.68	bdl	bdl	bdl	bdl	79.05	100.00
Trachyte	Palizzi lava	cpx	*sc1824 4-5-6	1	b	10.89	23.21	bdl	bdl	bdl	bdl	65.90	100.00
Trachyte	Palizzi lava	cpx	sc1824 7-8	1	b	29.89	29.63	bdl	bdl	bdl	bdl	40.48	100.00
Trachyte	Palizzi lava	cpx	sc1824 7-8	1	b	22.97	28.30	bdl	bdl	bdl	bdl	48.73	100.00
Trachyte	Palizzi lava	cpx	*sc1824 7-8	1	b	25.18	28.73	bdl	bdl	bdl	bdl	46.09	100.00
Latite	Pal C	Ti-mt	sulf n4	1	b	28.65	32.34	bdl	bdl	bdl	bdl	39.01	100.00
Latite	Pal C	Ti-mt	solf n4	1	b	11.75	25.37	bdl	bdl	bdl	bdl	62.88	100.00
Latite	Pal C	Ti-mt	*solfn4	1	b	18.51	28.15	bdl	bdl	bdl	bdl	53.34	100.00
Rhyolite	Pal B	sa	pallentiasulf1	2	a	59.58	36.72	0.03	0.03	0.04	0.09	0.33	96.81
Rhyolite	Pal B	sa	pallentiasulf1	2	a	58.57	36.56	0.04	0.07	0.01	bdl	0.42	95.67

Table 8.2 - Major and trace elements (ppm) of Type 1 and Type 2 SIs analyzed by LA-ICP-MS; Ol: olivine; Cpx: clinopyroxene; Sa: sanidine; Ti-Mt: Ti-magnetite.

Host rock	Unit	Host	Sulfide ID	Sulfide type	S	V	Mn	Fe	Co	Ni	Cu	Zn	As	Se	Mo	Ag	Cd	Sn	Sb	Te	Pt	Au	Tl	Pb	Bi
Trachyte	Pal D	sa	PAL-90 sulf1	2	371919	bdl	671	676629	823	269	17048	241	bdl	25.84	0.47	3.98	1.16	2.05	0.18	bdl	0.08	0.01	0.07	3.90	bdl
Trachyte	Pal D	cpx	PAL-90 sulf2	2	380658	8.80	275	249572	362	111	6626	378	bdl	2.21	bdl	3.46	bdl	3.47	bdl	bdl	0.48	bdl	0.01	4.38	0.08
Trachyte	Pal D	ol	pal90solf5	2	378390	1.39	493	454061	1406	690	35369	150	bdl	183.55	1.67	3.43	3.85	bdl	0.06	bdl	0.02	0.14	60.27	4.50	0.13
Trachyte	Pal D	Ti-mt	pal90sulf10	2	382459	170	762	690365	593	85	17666	314	34.08	bdl	26.79	2.21	1.16	bdl	0.12	1.67	0.51	bdl	4.06	194	78.4
Trachyte	Pal D	cpx	pal90sulf13	2	378456	24.98	1202	533044	1701	380	20826	157	3.19	bdl	2.78	4.13	0.46	1.41	1.00	1.23	bdl	0.26	1.35	3.27	0.14
Trachyte	Pal D	cpx	pal90sulf14a	2	396402	6.23	795	695233	1334	354	29342	230	bdl	bdl	3.81	3.22	0.50	1.07	bdl	bdl	0.08	0.10	0.07	3.08	0.17
Trachyte	Pal D	Ti-mt	PAL90 u293sulf1	2	379924	85.56	797	445303	1107	153	11738	294	3.32	78.58	2.31	2.28	0.16	2.77	bdl	bdl	bdl	0.04	1.09	35.01	0.71
Trachyte	Pal D	Ti-mt	PAL90 u293sulf1	2	379924	32.83	746	459804	869	185	10467	243	8.76	bdl	7.57	2.19	3.60	0.94	bdl	0.37	bdl	bdl	0.49	19.60	10.8
Trachyte	Pal D	cpx	PAL-15D sulf1	2	149585	1068	39728	582983	1438	1145	6334	1664	bdl	84.77	0.20	17.52	bdl	16.35	bdl	2.31	bdl	bdl	bdl	12.81	0.85
Trachyte	Pal D	cpx	PAL-15D sulf2	2	341034	119	6800	582983	2627	2917	13900	603	2.11	4.71	2.09	3.68	4.18	0.48	bdl	2.00	0.13	0.18	0.03	4.15	0.30
Trachyte	Pal D	cpx	sulf5	2	346344	206	12951	582983	2412	375	10979	1445	bdl	107	2.36	9.86	10.95	4.96	0.99	bdl	0.29	0.04	0.20	6.64	0.38
Trachyte	Pal D	cpx	Pal 15 D sulf 6	2	370083	1.66	3026	582983	4248	3495	24755	433	bdl	48.50	1.68	1.87	1.31	0.93	bdl	0.48	0.18	0.18	0.35	14.51	7.60
Trachyte	Pal D	cpx	Pal 15 D sulf 6	2	232691	132	2413	582983	1550	2145	12373	644	50.61	15.36	22.58	13.36	6.27	bdl	1.82	1.52	0.34	0.46	7.18	384.56	166
Trachyte	Pal D	Ti-mt	Pal 15 D sulf 7	2	422053	712	3501	582983	3248	2661	15932	1006	bdl	bdl	2.12	6.36	1.07	1.29	bdl	bdl	0.10	0.11	0.45	4.66	0.23
Trachyte	Pal D	Ti-mt	Pal 15 D sulf 8	2	349260	314	2605	582983	3377	3397	16455	830	bdl	11.01	1.72	3.74	1.60	3.16	bdl	bdl	0.12	0.07	0.32	3.72	0.12
Trachyte	Palizzi lava	cpx	sc1824 4-5-6	1	595243	117	1505	173263	59	47	1193582	1145	397.31	208	6.46	354.05	0.64	14.27	4.93	0.50	0.07	bdl	0.03	34.41	3.31
Trachyte	Palizzi lava	cpx	sc1824 7-8	1	148141	0.05	682	108824	131	493	248441	607	0.47	15.66	0.02	9.07	16.64	3.95	0.11	1.14	bdl	0.04	0.03	2020	32.6
Rhyolite	Pal B	sa	pallentiasulf1	2	362456	bdl	1616	582983	1216	1979	8003	44	bdl	45.77	76.36	1.85	2.14	1.83	bdl	3.41	bdl	0.03	0.12	0.80	0.23

Melt inclusions composition and sulfide/silicate melt partition coefficients

The composition of glassy MIs in olivine, clinopyroxene, plagioclase, sanidine and biotite found in the products of explosive eruptions of basaltic, shoshonitic, latitic, trachytic and rhyolitic magmas is assumed to be representative of the magmas spanning the whole magmatic differentiation path (Fig. 8.5 and Tab. 8.3 and Appendix F). The differentiation trend involves the fractionation of olivine, clinopyroxene, Ti-magnetite, labradorite to andesine plagioclase and, in evolved magmas, sanidine, minor oligoclase and biotite. Ti-magnetite joins the fractionating assemblage early, while apatite joins later in intermediate terms (Gioncada et al., 1998, see also Chapter 6).

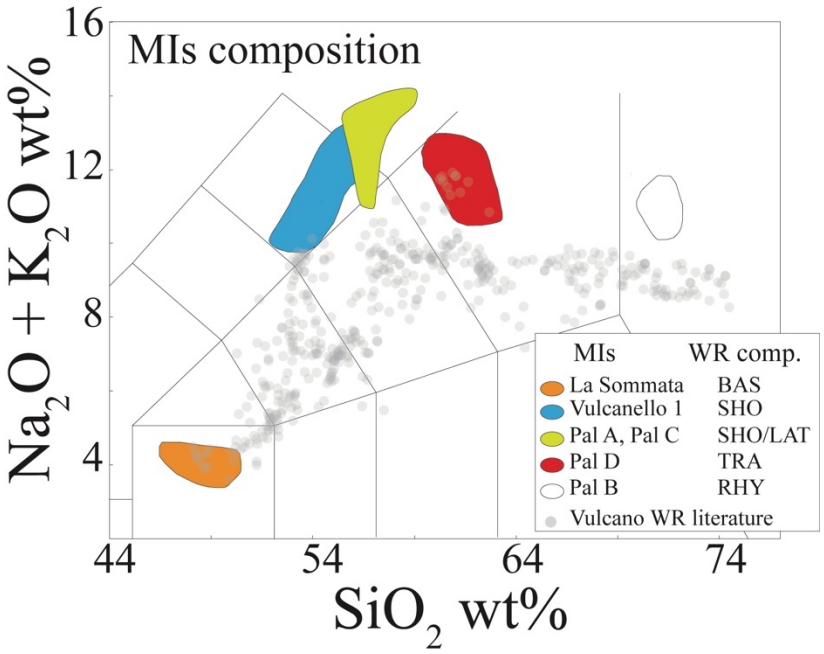

Figure 8.5 - TAS (total alkali vs SiO_2) diagram showing the composition of MIs of the selected samples. Data are re-calculated to 100 wt.% on anhydrous basis; literature data are from Gioncada et al. (1998), Le Voyer et al. (2014), Fusillo et al. (2015), Fulignati et al. (2018) and this work. Modified after Costa et al. (2021).

Table 8.3 - Mean composition and standard deviation (SD) for major elements (wt.%) of MIs in the Vulcano products. Literature EPMA data: Gioncada et al. (1998), Le Voyer et al. (2014) for La Sommata basalt; Fusillo et al. (2015) for Vulcanello 1 shoshonite; Fulignati et al. (2018) for Pal D trachyte. Pal A and Pal C latite and Pal B rhyolite are FE-SEM-EDS analyses from this work.

Composition	Unit		SiO_2	TiO_2	$Al2O_3$	FeO_{tot}	MnO	MgO	CaO	Na_2O	K_2O	P_2O5	Cl
Basalt	La Sommata	mean (15)	45.91	0.62	10.99	8.93	0.17	8.76	14.34	1.99	1.85	0.31	0.29
		SD	0.80	0.06	0.40	0.49	0.02	1.36	0.49	0.17	0.28	0.20	0.05
Shoshonite	Vulcanello 1	mean (33)	54.34	0.63	17.31	7.05	0.15	2.16	4.51	4.57	6.83	0.66	0.30
		SD	1.44	0.09	0.63	0.90	0.04	0.59	0.89	0.34	0.66	0.12	0.03
Latite	Pal A, Pal C	mean (5)	56.55	0.86	18.08	6.18	0.14	1.10	3.39	4.94	7.93	0.40	0.42
		SD	1.09	0.15	0.80	1.59	0.13	0.24	0.77	0.39	1.01	0.15	0.09
Trachyte	Pal D	mean (22)	60.00	0.58	17.38	4.41	0.14	1.01	2.49	4.59	6.82	0.20	0.38
		SD	0.86	0.12	0.56	0.57	0.06	0.32	0.54	0.54	1.04	0.08	0.06
Rhyolite	Pal B	mean (18)	70.44	0.13	14.87	2.02	0.11	0.13	0.95	4.53	6.64	0.06	0.51
		SD	0.79	0.05	0.62	0.29	0.05	0.11	0.16	0.48	0.51	0.00	0.08

The Cu content of MIs reaches the highest values at intermediate compositions (Mg# around 15-10 and Zr around 160-200 ppm, at the latite-trachyte transition) and, when the highest Cu contents are considered, defines a trend that increases with magmatic differentiation from basalt (<50 ppm) to latite (~250 ppm), and then abruptly drops to <50 ppm (Fig. 8.6 and Tab. 8.4, see also next sections and Appendix F). Low Cu values have been also measured in some intermediate MIs composition. Conversely, Pb concentration in MIs increases from basalt (~5 ppm) to trachyte (~35 ppm) and remains constant in rhyolite (Tab. 8.4 and Appendix F).

The average metal concentrations measured in Type 2 SIs (Tab. 8.2) and in coexistent MIs (Tab. 8.4) allow the sulfide phase/silicate melt partition coefficients for Cu (1184), Ni (352), Zn (1.25), V (3.17), Pb (1.77) to be calculated. The sulfide phase/silicate melt partition coefficients for the same metals in Type 1 sulfides, mostly lacking coexistent melt inclusions, are determined assuming the average composition of latitic-trachytic melt inclusions of the other selected samples (Tab. 8.4) and are 1538 for Cu, 154 for Ni, 1.32 for Zn, 1.8 for V and 76 for Pb.

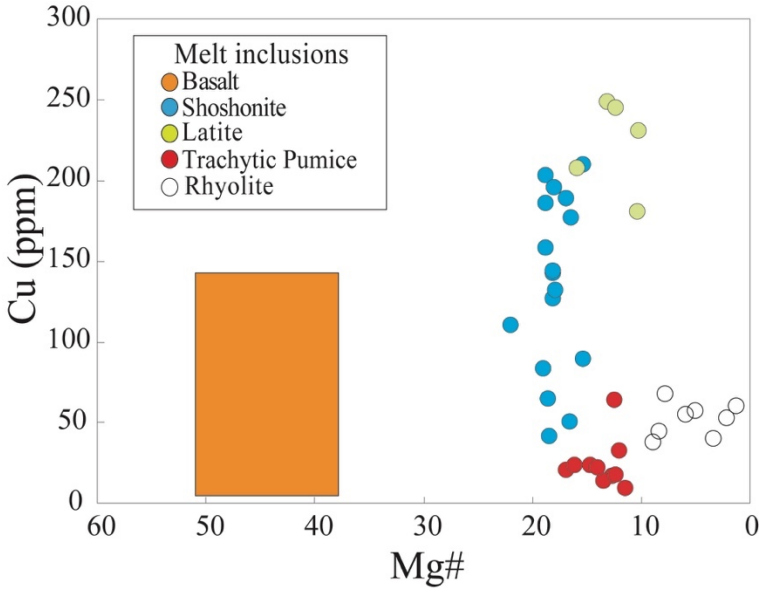

Figure 8.6 – Copper versus Mg# for the glassy MIs representative of the basalt to rhyolite suite at Vulcano. The orange rectangle shows the range in Cu content (this work) and Mg# data (Gioncada et al., 1998; Le Voyer et al., 2014) for La Sommata MIs since data are not from the same inclusions.

Table 8.4 - Trace elements mean composition (ppm) and SD of MIs analyzed by LA-ICP-MS; Ol: olivine; Cpx: clinopyroxene; Sa: sanidine.

Composition	Basalt		Shoshonite		Latite		Trachyte		Rhyolite	
Unit	La Sommata		Vulcanello 1		Pal A, Pal C		Pal D		Pal B	
Host	Ol		Cpx		Cpx,Ol		Cpx, Ol		Sa	
	mean (8)	SD	mean (16)	SD	mean (14)	SD	mean (10)	SD	mean (15)	SD
V	226.46	67.76	153.81	34.59	124.21	36.51	57.44	15.15	1.27	0.54
Cr	235.66	195.39	38.70	68.39	36.07	25.00	29.06	24.55	15.05	1.79
Ni	146.02	218.42	12.97	14.02	21.30	34.48	11.71	6.02	13.94	5.52
Cu	51.80	51.69	140.75	51.83	172.02	57.45	24.15	15.38	46.97	10.04
Zn	100.96	30.76	98.83	17.00	103.98	38.78	91.88	31.24	nd	-
Rb	49.98	30.91	169.85	55.52	208.74	46.37	227.31	18.91	341.59	38.74
Sr	867.73	358.72	771.73	257.41	783.81	162.22	756.76	138.22	15.53	7.43
Y	10.27	3.76	20.85	4.31	18.55	3.02	18.95	3.67	28.97	3.79
Zr	44.29	19.46	149.74	35.05	170.95	26.99	177.05	18.95	264.92	87.56
Nb	3.57	1.53	18.45	6.05	22.42	5.02	21.35	2.78	29.35	3.33
Cs	3.33	6.39	7.05	2.28	8.60	1.85	9.42	1.53	16.92	2.49
Ba	455.47	258.65	872.21	298.24	1016.64	246.81	1614.09	330.76	5.10	2.96
La	20.12	7.17	60.10	15.62	66.34	12.00	60.15	10.61	99.67	12.52
Ce	38.42	12.94	107.68	24.28	113.39	17.68	104.89	16.89	164.24	20.92
Pr	4.42	1.57	11.28	2.16	11.31	1.48	10.26	1.94	15.42	2.09
Nd	18.62	6.41	42.83	7.47	41.36	5.61	36.17	6.24	51.13	7.83
Sm	3.68	1.22	7.89	1.41	7.14	1.18	6.64	1.22	7.91	1.22
Eu	1.04	0.35	1.74	0.26	1.51	0.32	1.42	0.42	0.32	0.14
Gd	2.78	1.07	5.55	1.13	4.73	1.08	5.47	1.76	5.17	1.11
Tb	0.38	0.14	0.77	0.17	0.65	0.14	0.54	0.19	0.88	0.20
Dy	2.26	0.64	4.16	0.89	3.63	0.76	3.69	1.00	5.14	0.91
Ho	0.40	0.15	0.79	0.17	0.70	0.17	0.67	0.27	1.08	0.16
Er	1.09	0.28	1.98	0.46	1.82	0.45	2.02	0.73	3.02	0.53
Tm	0.15	0.06	0.30	0.07	0.28	0.06	0.36	0.11	0.45	0.08
Yb	0.96	0.40	2.06	0.45	1.89	0.39	2.16	0.78	3.44	0.89
Lu	0.14	0.05	0.30	0.06	0.28	0.04	0.25	0.12	0.56	0.13
Hf	1.19	0.43	3.98	0.73	4.28	0.68	4.21	0.94	7.96	1.84
Ta	0.16	0.07	0.94	0.30	1.14	0.24	1.18	0.15	1.91	0.32
Pb	5.50	3.62	22.24	7.26	28.57	6.67	28.32	6.82	34.41	4.07
Th	3.92	1.74	23.59	7.83	29.03	6.49	27.68	4.11	57.21	8.11
U	1.30	0.57	7.54	2.45	9.10	2.08	9.16	1.54	17.12	2.02

8.5 Tracking metal evolution in arc magmas: the case of La Fossa

Evolution of metal concentration: clues from melt inclusions

The petrographic features and the chemical compositions of MIs and SIs found in Vulcano eruptive products allow to track the evolution of metals in the magmatic system of an active arc volcano from basalt to rhyolite. This system is fed by sulfide-undersaturated, H_2O-rich and oxidized basaltic magmas. The first appearance of SIs indicates that sulfide saturation occurs late, during magma evolution, at the latite-trachyte transition. Accordingly, the fO_2 value decreases basalts (NNO - ΔNNO+1) to intermediate magmas (Pal D trachyte magma ΔNNO -1 to -2, Fig. 8.1a; Fulignati et al., 2018). This is potentially due to the combined effects of lower temperatures, the fractionation of minerals with high Fe^{3+}/Fe^{2+}, crustal assimilation and the volatile loss during differentiation (Scaillet and Pichavant, 2005; Scaillet and MacDonald, 2006; Richards, 2015).

Magmatic sulfide inclusions could be trapped either as a liquid (SL) or as a solid, which can be either a monosulfide solid solution (mss) or an intermediate solid solution (iss), having a composition close to pyrrhotite and chalcopyrite, respectively (Parat et al., 2011). For most metals, the partition coefficient between sulfide and silicate melt strongly depends on the nature of the sulfide phase (mss, iss, or SL; Li and Audetat, 2015). Thus, determining the nature of the sulfide phases at the time of trapping is important to constraint the metal budget of the magmatic system (Rottier et al., 2020 and references therein). By plotting both Type 1 and Type 2 SIs analyses on the ternary diagram of the Cu-Fe-S system (at 1000°C), the reconstructed Type 1 SIs compositions fall in the liquid field, whereas Type 2 SIs fall in the pyrrothite (mss) field, suggesting that the latter were trapped as a solid phase (Fig. 8.4). This evidence is supported by comparing their sulfide phase-silicate melt partition coefficients (for Cu, Ni, Pb, Zn), calculated from measured concentrations and predicted according with the equations for $D^X_{SL/SM}$, $D^X_{mss/SM}$ of Li and Audetat (2015) for a trachyte melt with 950°C, ΔFMQ -0.77 and FeO 4.4 wt% (Fig. 8.7) (Fulignati et al., 2018). The comparison shown in figure 8.7 indicates

good match for both the Type 1 and the Type 2 SIs (these elements were selected because they could be reliably quantified in both magmatic sulfide and silicate melt inclusions, and because their partition coefficient is markedly different for *mss* versus SL). The different partition coefficients SL/SM and mss/SM are also in agreement with the measured Ag and Pb contents, which are considerably higher in Type 1 SIs than in Type 2 SIs (Tab. 8.2).

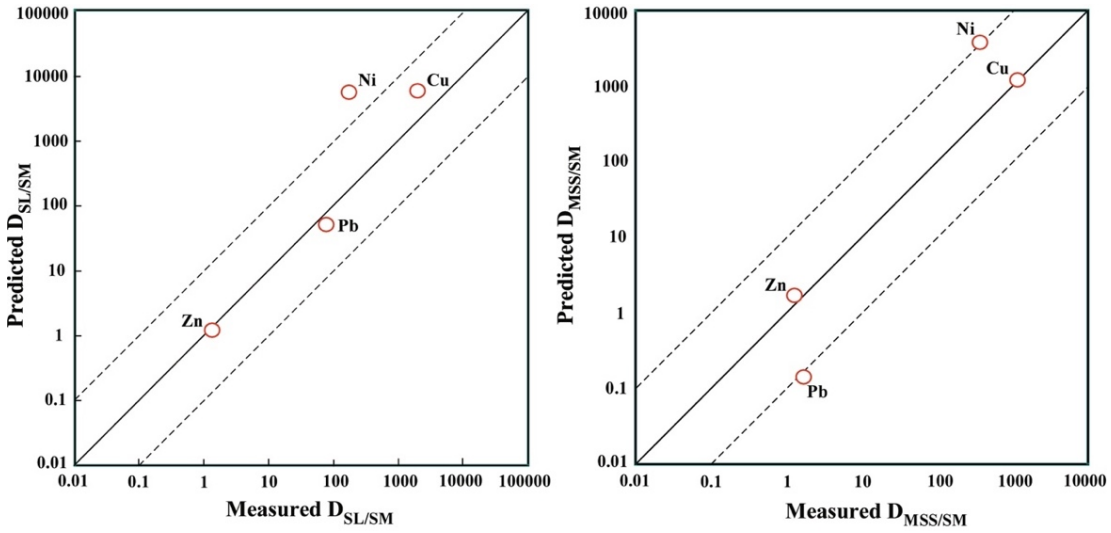

Figure 8.7 - Comparison of measured sulfide/silicate melt partition coefficients with values predicted by the model of Li and Audetat (2015); sulfide liquid (Type 1 SIs)/silicate melt and monosulfide solid solution (Type 2 SIs)/silicate melt. T of 950°C, ΔFMQ= - 0.77 and FeO in the melt = 4.4 wt.% estimated for La Fossa trachyte by Fulignati et al. (2018) have been used in the model. Modified after Costa et al. (2021).

The Cu behavior in the silicate melt confirms late sulfide saturation (Fig. 8.8a). In fact, Cu concentration in MIs increases from basalt to latite MIs, which are sulfide-undersaturated, and then rapidly decreases within a narrow compositional interval (Zr 180-200 ppm; SiO_2 58-60 wt%) once sulfide saturation is reached, due to the stripping of Cu-rich sulfide melt. The scattered Cu concentrations, including very low values in the intermediate composition MIs range, might suggest that: i) incipient sulfide saturation was achieved in some parts of the reservoir (at the contact with wall rock thanks to temperature decrease, fractional crystallization or silica assimilation?) although not revealed by sulfide trapping; ii) Cu was episodically lost to a S-rich vapor phase from mafic magmas. Events of refilling by Cu-poor, S-rich and sulfide undersaturated magma could furthermore enhance the heterogeneity in the Cu content of an intermediate

composition reservoir. This is particularly crucial because, in order to represent the entire basalt to rhyolite differentiation range, the analyzed samples do not necessarily represent the evolution in a single reservoir but rather come from multiple, possibly independent magma batches with variable age (see also Chapter 6).

The evolution of Cu and Pb in the silicate melt has been modeled by simple fractional crystallization, starting from a mean value of the La Sommata basaltic MIs and including a sulfide phase in the fractionating assemblage at the latite-trachyte stage (Fig. 8.8). For this model, for the sake of simplicity, the crustal assimilation processes has been neglected. The model employs bulk distribution coefficient (D) for Zr, Cu and Pb, calculated for each step of the differentiation process using partition coefficients derived from the literature (Germ database and Gioncada, 1997) and the relative proportions of crystallizing phases for Vulcano (Gioncada, 1997; Del Moro et al., 1998; see also Chapter 6) (in Appendix I are reported the details of the model). The sulfide phase/silicate melt partition coefficients for Pb and Cu were calculated according to Li and Audetat (2015) (see Appendix I).

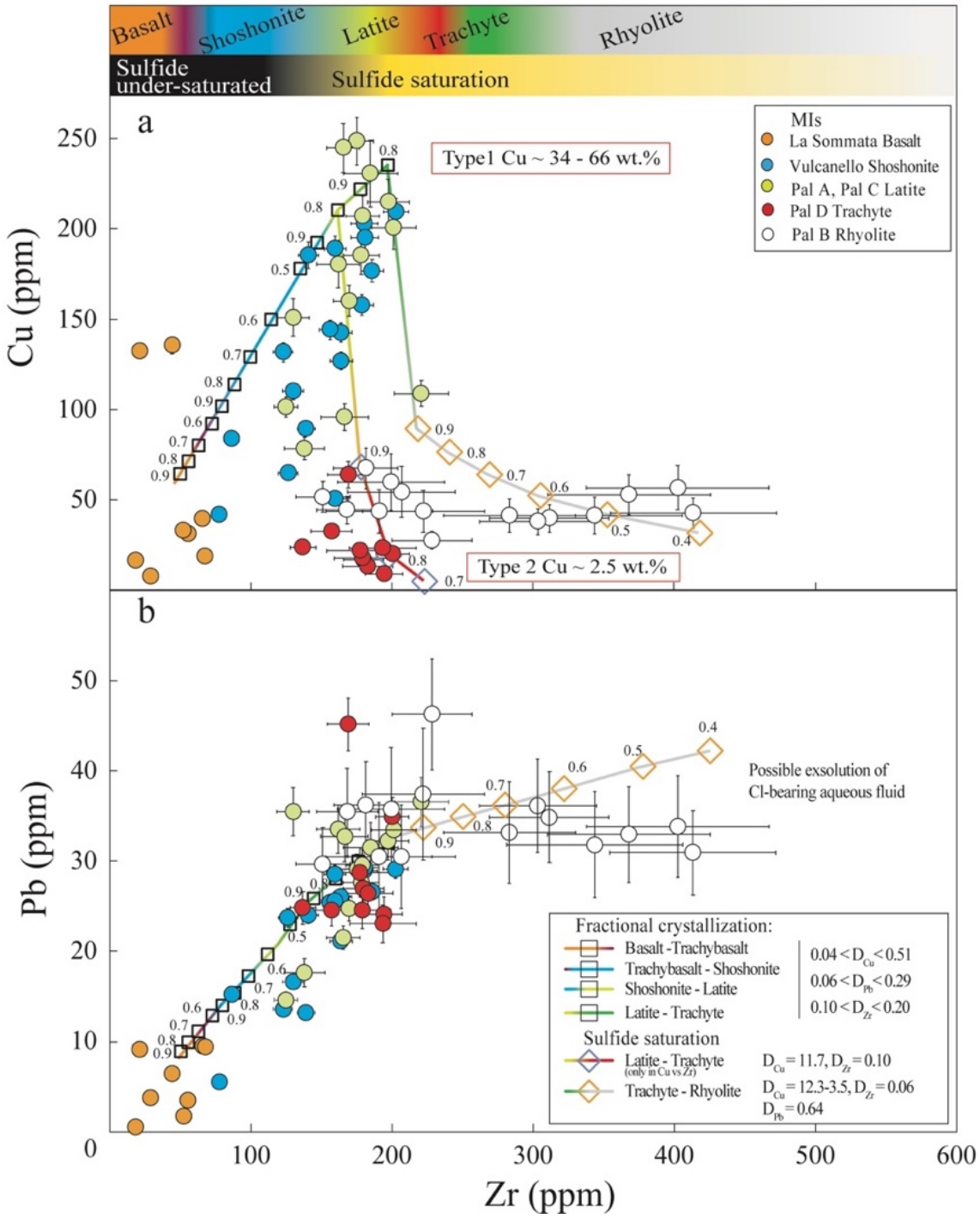

Figure 8.8 - Quantitative fractional crystallization model for the evolution of Cu (a) and Pb (b) vs. Zr in the silicate melt. Bulk partition coefficients (D) for Cu, Pb and Zr have been calculated using minerals/silicate melt partition coefficients from literature and sulfide/silicate melt partition coefficients calculated with the model of Li and Audetat (2015). See Appendix I for additional details. 1sigma error for each analysis is shown as error bars, which if not visible, is smaller than the symbol. Symbols and numbers along the fractionation paths indicate melt fraction. Modified after Costa et al. (2021). The different Cu contents in latitic MIs compared to those showed in Fig. 8.6 is due to the largest amount of trace elements analyses with respect to major element analyses.

The model provides a robust explanation of the Cu behavior in the silicate melt. The fractional crystallization models predict that 0.2–0.3 wt% of sulfide melt, fractionated along with clinopyroxene + plagioclase + Ti-magnetite + olivine + biotite + sanidine, is sufficient to cause a sharp drop in the Cu content of silicate melt at the latite to trachyte transition. Because Type 1 and Type 2 SIs were never found to coexist, it is possible to suggest the first sulfides formed at the highest Cu content are correspondingly Cu-rich (Type 1 SIs), whereas those exsolved from the Cu-depleted trachytic magma are the Cu-poor Type 2 SIs (Cu-bearing mss) found in trachyte and rhyolite (Fig. 8.8a). This reconstruction is in agreement with the composition of clinopyroxene crystals in the latites and trachytes. Clinopyroxene composition testifies that, in the latite-to-trachyte transition, the Cu-depleted trachytic magma is slightly more evolved (that is, having a lower Cr, V and Ni content in clinopyroxenes) than the Cu-rich trachyte and latite (Fig. 8.9). The trachyte-rhyolite step requires a high percentage (60 vol%) of fractionated solid (Chapter 6), strongly increasing the final concentration of incompatible elements and possibly explaining the large spread in Zr values measured in rhyolites.

The evolution of Pb shows an increase with differentiation up to rhyolite (Fig. 8.8b). This agrees well with the low sulfide melt/silicate melt partition coefficient for this element, which is orders of magnitude lower than that of Cu (this thesis and Li and Audétat, 2015). The modeled Pb trend in rhyolites (Zr >200 ppm), despite the higher D_{Pb}, slightly deviates from the measured data. This may be ascribed to the partitioning of Pb in an exsolved Cl-bearing aqueous fluid.

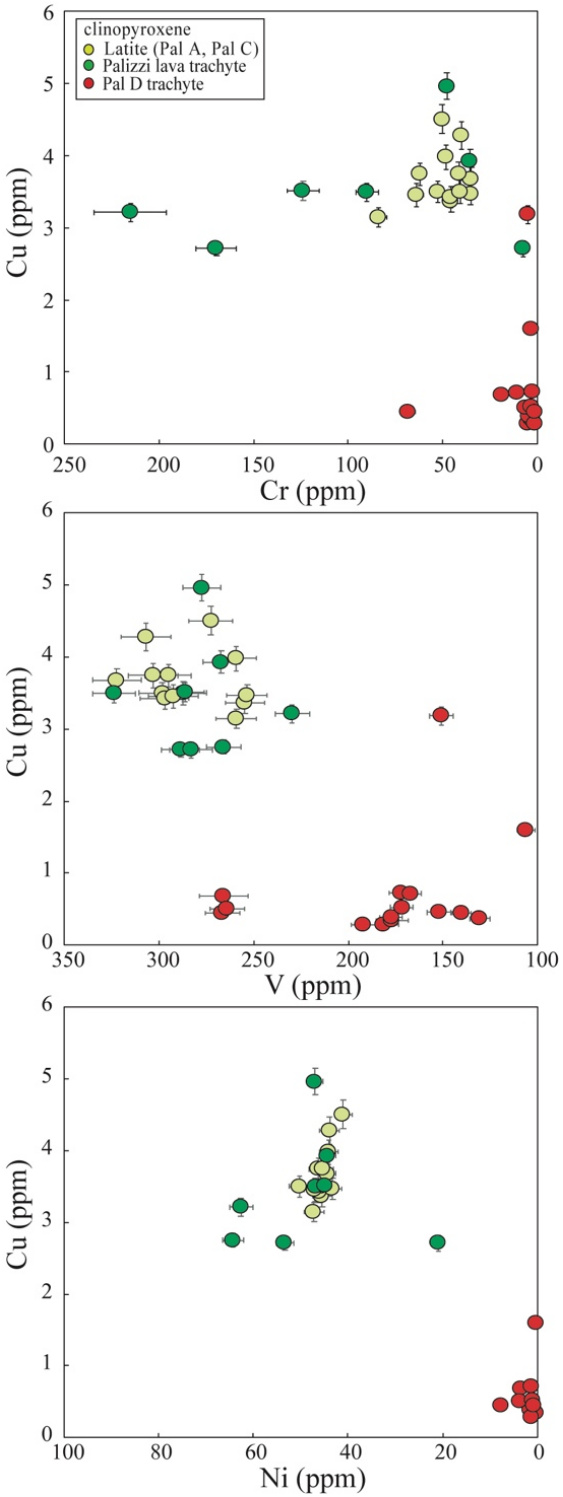

Figure 8.9 - Cu versus Cr, V and Ni (ppm) for clinopyroxene crystals in the latitic and trachytic products of La Fossa hosting the type 1 (Pal A, Pal C and Palizzi lava) and type 2 (Pal D) SIs. 1sigma error for each analysis is shown as error bars, which if not visible, is smaller than the symbol (Costa et al., 2021).

The effect of fluid saturation

Tracking metal evolution in magmas cannot overlook the effect of fluid-saturation along differentiation. While Vulcano basalts are H_2O-, S-, Cl-rich, the shoshonitic magmas have lower volatile contents (Gioncada et al., 1998), suggesting that H_2O, S and Cl may be lost to an exsolved aqueous fluid phase at the basalt-shoshonite transition. The results obtained in this thesis suggest that, despite mafic magmas may degass during ascent, Cu and Pb increase with differentiation (Fig. 8.8). This suggests that the evolution of these metals is not significantly affected by decompression degassing of mafic magmas as they refill crustal reservoirs. Indeed, Cu scarcely partitions into a hydrosaline fluid phase exsolved from mafic magmas according to the experimental results of Zajacz et al. (2012).

In trachytes and rhyolites, the Cu-normalized abundances of S, Mo, Zn, Ag, Pt, Au, Pb in Type 1 (trachyte) and Type 2 (trachyte and rhyolite) SIs show different patterns (Fig. 8.10). While Mo/Cu ratio in the rhyolite Type 2 SIs is higher than that of Type 2 SIs in trachyte, Zn/Cu and Pb/Cu are distinctly lower (Fig. 8.10). This is in agreement with the exsolution of a Cl-rich magmatic fluid phase from the rhyolitic magma at La Fossa (Gioncada et al., 1998; Fulignati et al., 2018), causing Pb and Zn to preferentially partition with respect to Mo (Zajacz et al., 2008). Mo, which is not efficiently partitioned in a Cl-rich magmatic fluid phase (Candela and Holland, 1984; Zajacz et al., 2008), tends to also increase in the rhyolite SIs.

At Vulcano, previous data suggest that metal bearing fluids can be involved in phreatic-phreatomagmatic eruptions as in the case of the Breccia di Commenda eruption, a violent explosive event occurred at La Fossa volcano during 13th century (Gurioli et al., 2012; Rosi et al., 2018, see also Chapter 3). This eruption produced a high amount of lithics which showed acid-sulfate alteration (Gurioli et al., 2012). Interestingly, S/Cu, Zn/Cu, Pb/Cu ratios measured on the fine ash of the Breccia di Commenda deposits are higher than the same ratios measured in the trachytic and rhyolitic SIs (Fig. 8.10). This suggests that Cl-rich fluids carrying Pb and Zn from the magmatic-hydrothermal system were involved in the Breccia di Commenda eruption.

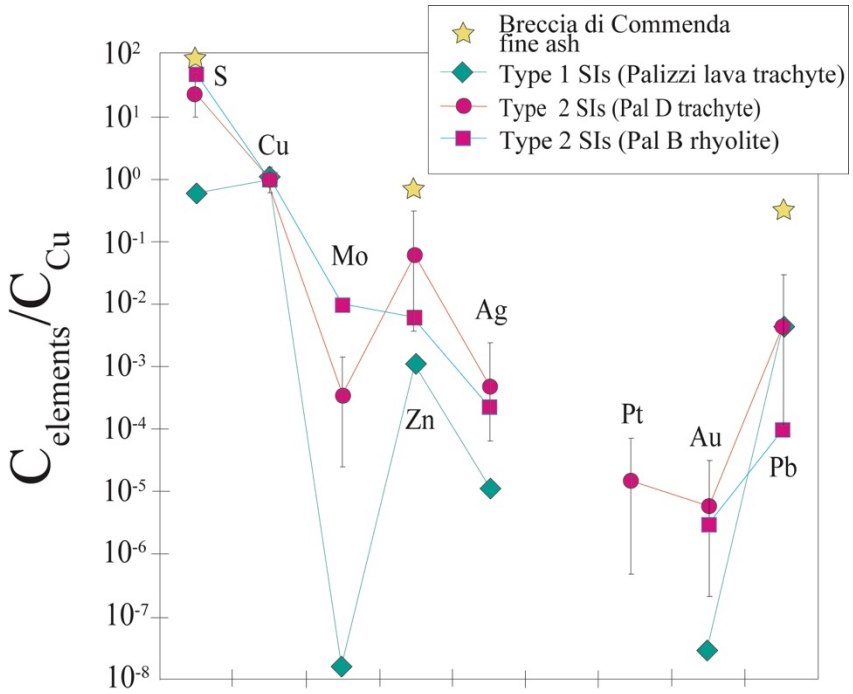

Figure 8.10 - Cu-normalized composition of La Fossa SIs and Breccia di Commenda fine ash (Data from Gurioli et al., 2012). Modified after Costa et al. (2021).

8.6 Inferences on magma fertility and comparison with mineralized systems

With the aim to compare the SIs composition in the products of La Fossa with that of SIs from magmas associated with porphyry mineralization, absolute and Cu-normalized metal concentrations from La Fossa are compared with those found in well-preserved SIs of ore-related igneous rocks. The metal ratios and absolute concentrations in Vulcano SIs (either in Type 1 and Type 2 SIs) match well with those of mineralized systems (Fig. 8.11). This suggests that, at Vulcano, the late attainment of sulfide saturation during fractionation in mid-upper crustal reservoirs prevents the early depletion in S and chalcophile metals and produces sulfide melts with compositions comparable to those found in several porphyry systems. Once formed, the sulfides may be stored in crystal mushes of intermediate to evolved crustal reservoirs (see Chapter 6), re-melted by mafic sulfide-undersaturated recharges or eventually cannibalized by aqueous fluids exsolving at the rhyolite stage, thereby producing highly mineralizing solutions (Keith et al., 1997; Halter et al., 2002; Nadeau et al., 2010; Audétat and Simon, 2012; Wilkinson, 2013).

The results obtained in this thesis indicate that the processes governing metal evolution through silicate melt differentiation in active arc magmatic systems share similarities to those inferred for magmas associated to porphyry Cu systems. Bearing in mind that the magmatic stage is arguably pivotal in the evolution of porphyry Cu systems (Audétat and Simon, 2012), arc volcanoes such as La Fossa can thus be viewed as active analogues and ideal sites for studying the critical early stages of porphyry Cu genesis. Their possibility to evolve towards mineralized systems will, of course, depend also on other factors (magma chamber size and depth, duration of magmatic and hydrothermal activity, and the efficiency of magmatic fluid focusing; Richards, 2011; Wilkinson, 2013) that can either promote or inhibit porphyry Cu formation.

8.7 Conclusions

In this chapter, a combined compositional data (major and trace elements) on melt inclusions, magmatic sulfides and host minerals from the eruptive products of La Fossa, has been carried out to track the evolution of metals along the magma differentiation path of an active magmatic system. In the case of sulfide-undersaturated, volatile-rich arc basalts, metals are scarcely subtracted by degassing during ascent to shallow crustal reservoirs and thus reach their highest abundances in intermediate magmas. Further evolution results in sulfide saturation where Cu and chalcophile metals strongly partition into the sulfide melt, causing an abrupt decrease in abundance from the silicate melt. The evolution of Cu in the silicate melts was modeled with quantitative fractional crystallization, and the results are in close agreement with experimental data. The model shows that fractionation of only 0.2–0.3 wt% of sulfide is sufficient to deplete the silicate melt in Cu down to the values recorded by MIs in trachytic and rhyolitic products. Metals that do not partition in sulfides (Pb, Zn) increase their concentrations with magmatic evolution until they are scavenged by a Cl-rich aqueous fluid phase possibly exsolved at the rhyolitic stage. The comparison of metal ratios and absolute concentrations of the Vulcano magmatic sulfides shows strong similarities with those of sulfides found in magmatic rocks associated with world-class porphyry Cu systems. This suggests

that the processes governing metal evolution through silicate melt differentiation in active arc magmatic systems are similar to those processes inferred for magmatic stage of porphyry Cu environments. These results thus suggest that the investigation of metal evolution in active arc volcanoes such as La Fossa can help to understand the genetic mechanisms of porphyry Cu deposit formation.

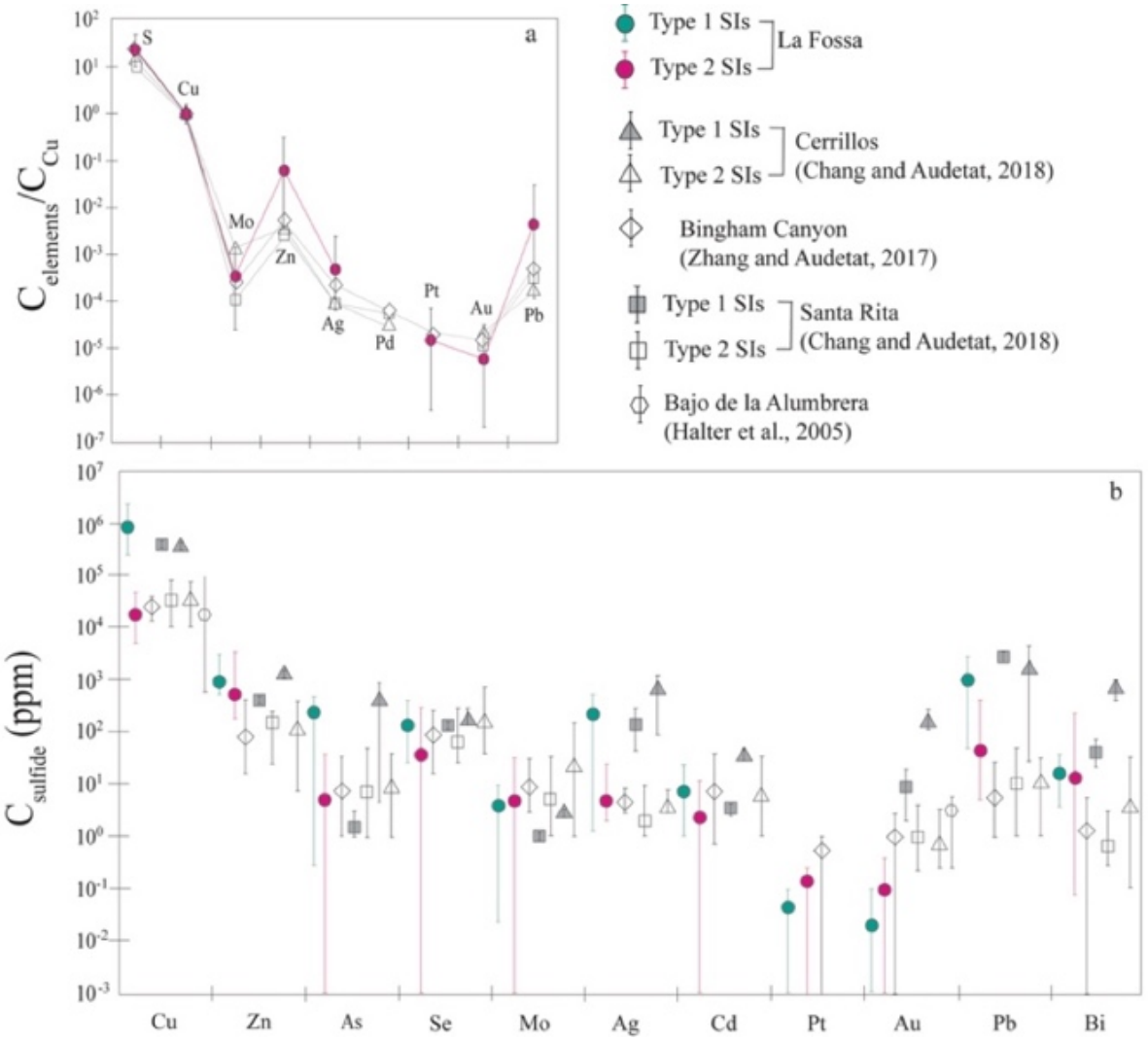

Figure 8.11 – a): Cu-normalized composition (average and range) of Type 2 SIs compared to SIs of ore-related latitic magma at Bingham and at Santa Rita and Cerrillos; b): Absolute metal concentrations in Type 1 and Type 2 La Fossa SIs compared with those found in mineralized systems (Bingham Canyon, Santa Rita, Cerrillos and Bajo de la Alumbrera). Modified after Costa et al. (2021).

9 Platinum-group element (PGE) geochemistry of the Vulcano igneous suite: implications for chalcophile element fertility of magmas

9.1 Introduction

Among the critical factors invoked to play a role in the formation of economic porphyry-style mineralization, the chalcophile metal content in a magma at the point of fluid exsolution (the chalcophile metal fertility) has been considered to be one of the key elements (Park et al., 2015, 2019; Cocker et al., 2016; Hao et al., 2017, 2019; Lowczak et al., 2018). The evolution of chalcophile metal content in arc magmas is primarily controlled by sulfide saturation (Wilkinson, 2013; Park et al., 2015, 2019; Zhang and Audétat, 2017; Chang and Audétat, 2018; Rottier et al., 2020; see also Chapter 8). This is due to the strong affinity of chalcophile elements for the sulfide phase that cause them to be stripped from the silicate melt once sulfide saturation is reached. As a consequence, the timing of sulfide saturation relative to aqueous fluid saturation is a fundamental factor in determining whether a magmatic suite is barren or mineralized (Park et al., 2015, 2019; Cocker et al., 2016; Hao et al., 2017; Hao et al., 2019; Lowczak et al., 2018). In case of early sulfide saturation, the sulfide melt will sequester chalcophile elements (e.g. Cu, Au, PGE) from the silicate melt, which will become depleted in these elements. As a consequence, a lower amount of chalcophile elements will be available to enter the magmatic fluid when the magma becomes volatile-saturated. Conversely, if sulfide saturation occurs late, after, or shortly before volatile saturation, or if the sulfide melt fraction is small, the chalcophile elements are concentrated by fractional crystallization and are available to enter the fluid phase when the magma eventually becomes fluid-saturated (Park et al., 2019 and reference therein). Early sulfide saturation and metal segregation within sulfide melts, however, may be positive for magma fertility if the ore metals, pre-concentrated at crustal levels, are later remobilized either by sulfur-undersaturated silicate melts or by magmatic fluids

(Halter et al., 2002, 2005; Nadeau et al., 2010; Wilkinson, 2013; Zhang and Audétat, 2017; Du and Audétat , 2020).

In this framework, the necessity to detect and evaluate the importance of sulfide saturation has recently prompted several studies, which have demonstrated that Platinum-group elements (PGE), with their extreme partition coefficients into sulfide melts, are particularly sensitive in tracking the chalcophile element evolution and in identifying the onset of sulfide saturation in magmas (Park et al., 2013a, 2013b, 2015, 2019; Cocker et al., 2016; Hao et al., 2017; Lowczak et al., 2018; Huang et al., 2020; Park and Campbell, 2021). The PGEs are preferred to other chalcophile element such Cu o Au for two reasons: (i) because their partition coefficients into an immiscible sulfide phase are one and two orders of magnitude higher than Cu and Au respectively, making them sensitive indicators of sulfide saturation (Mungall and Brenan, 2014); (ii) because they are less mobile than Cu and Au during hydrothermal alteration (Crocket, 2000).

As highlighted in chapter 8, La Fossa volcano provides an excellent opportunity to investigate mineralizing processes beneath active arc volcanoes, being characterized by an active magmatic-hydrothermal system (Fulignati et al., 1998; Boyce et al., 2007) and providing evidence of sulfide melt-silicate melt immiscibility during magma evolution (Fulignati et al., 2018; Chapter 8). In this chapter, the results of major and trace elements analyses, including the first PGE data on the Aeolian Arc, Au and Re data in the magmatic suite (from basalt to rhyolite) of Vulcano island, are reported. The main aim is to better define the evolution of chalcophile elements in arc-related volcanic systems. Special attention was dedicated in identifying the onset of sulfide saturation and documenting how it influenced the geochemistry of the chalcophile elements and the possible implications for magma fertility. The PGE content are finally compared to those from other igneous suites and used to infer the mineralization potential of the magmatic system of La Fossa volcano.

9.2 Selection of samples

Samples were selected in order to bracket the whole range of magma evolution at Vulcano Island, from basalt to rhyolite (Appendix C). Most samples belong to the active La Fossa volcano and have been already presented and discussed in previous chapters. The scoriaceous lapilli of La Sommata are representative of basaltic composition. Shoshonitic magma is represented by scoriaceous lapilli from Vulcanello and Mt. Saraceno, and by welded scoriae from Spiaggia Lunga Formation. The latitic, trachytic and rhyolitic samples are represented by the products of the PEU and GCEC of La Fossa. They include the latitic spatter deposit of the AD 1888–1890 eruption, the pumiceous lapilli fall deposit from Pal D (K-rich trachyte) and Pal B (rhyolite), the Palizzi lava flow (trachyte) and the Pietre Cotte lava flow (rhyolite) (see also chapter 6). A further trachytic sample is added to this study and is represented by the scoriae of the Quadrara formation.

9.3 Results

Whole-rock major and trace element

Whole-rock major and trace element compositions of the selected samples are reported in Appendix C and some of these (trachytes and rhyolites) have been presented in chapter 6. The analyzed samples are plotted on TAS and MgO vs. SiO_2 diagrams, together with the whole spectrum of Vulcano erupted products (Fig. 9.1). SiO_2 ranges from 48 to 72 wt.% and MgO from 8.5 to 0.5 wt.%. Total alkali content varies from ~4 to ~12 wt.%, with a wide range in trachytic products (see also Chapter 6).

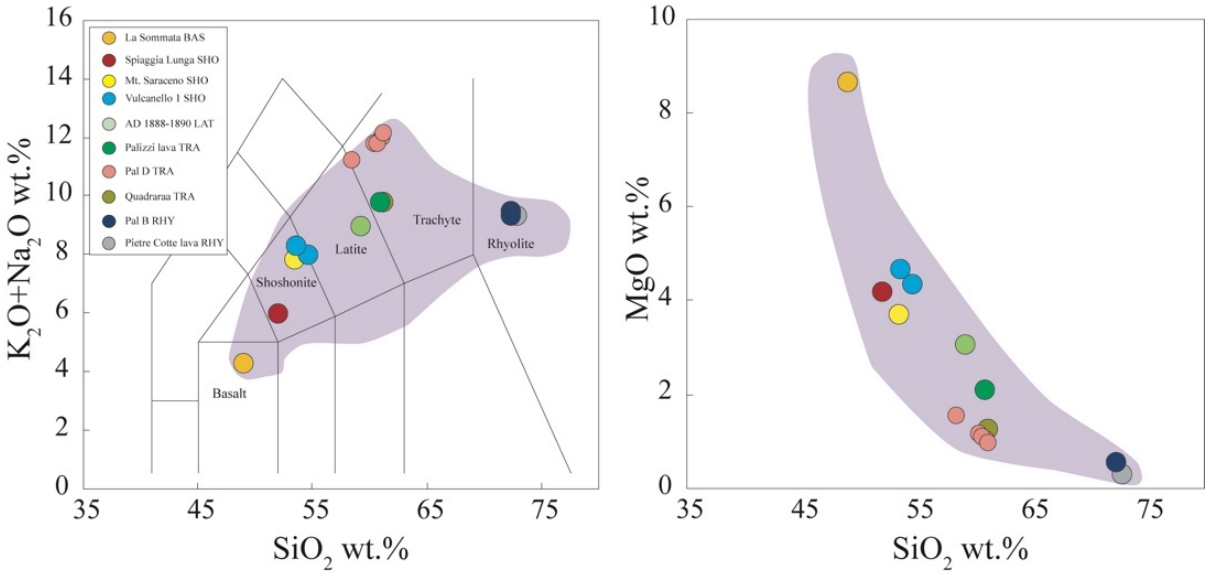

Figure 9.1 – Total alkali vs SiO_2 (TAS) and MgO vs. SiO_2 diagrams of the investigated samples. Analyses are re-calculated to 100 on anhydrous basis. Literature data (purple fields) are from De Astis et al. (2013) and reference therein.

Whole-rock trace element (Appendix C) compositions are in agreement with the data available in literature. Selected compatible trace elements vs. MgO and chondrite normalized REE patterns are shown in figure 9.2. REE patterns show fractionated LREE and modest fractionation of HREE, with the concentration of all REE that increases through the overall fractionation sequence of basalt to rhyolite. Europium anomaly large in rhyolites (Fig. 9.2a, see also Chapter 6), as a consequence of the high fraction of K-feldspar in the fractionating assemblage. Compatible trace elements such as Ni, V, Sc are positively correlated with MgO. In particular, V and Fe_2O_3 (and alsto Ti, see also Gioncada et al., 1998; De Astis et al., 2013; Fulignati et al., 2018; Chapter 8) confirm that Ti-magnetite significantly contributes to the fractionating assemblage at about 4 wt.%, although petrographically it saturates early, at 7–8 wt.% MgO. Cr-spinel fractionate only in basaltic magma (Gioncada et al., 1998).

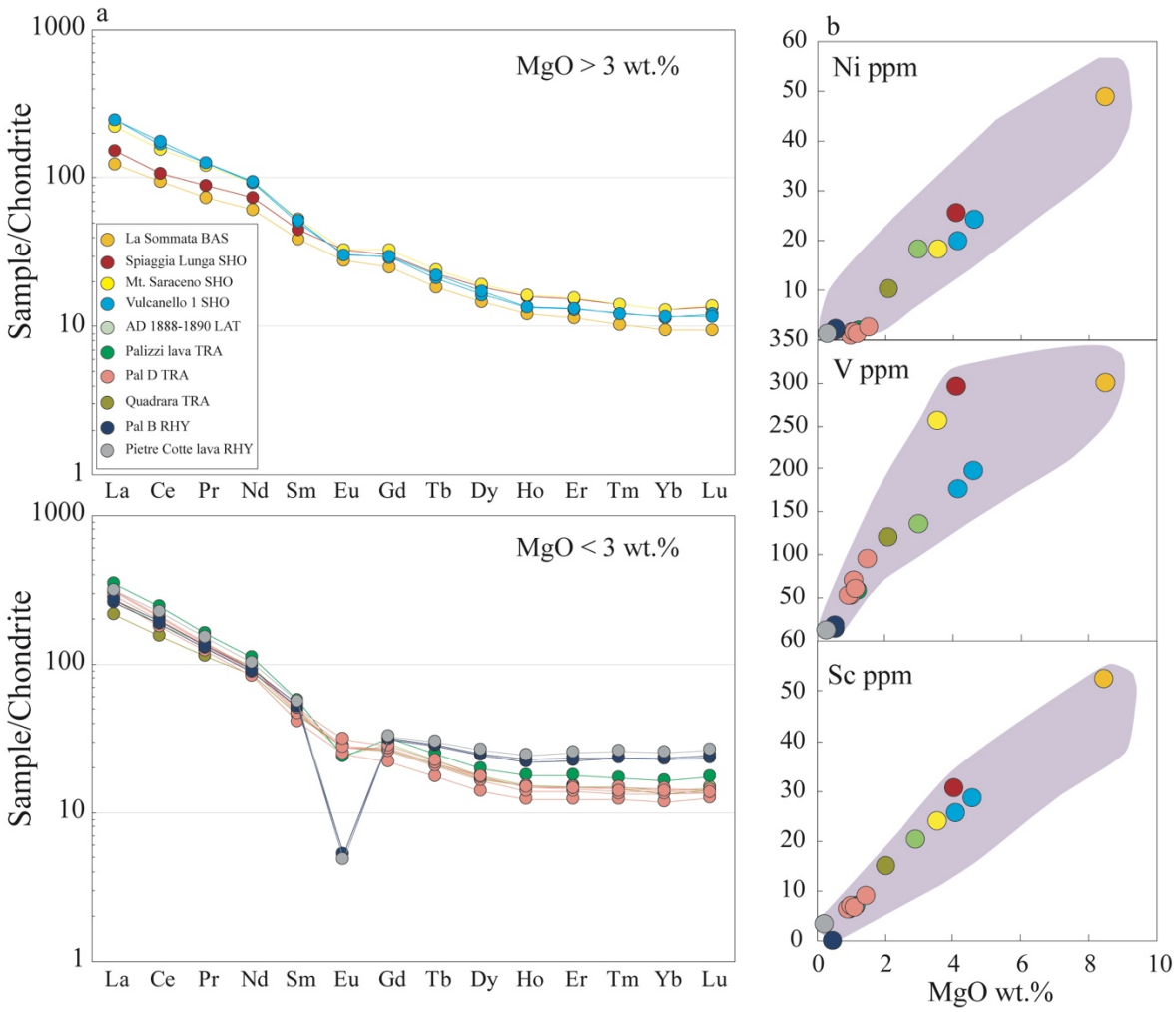

Figure 9.2 – a):Chondrite-normalized REE patterns of investigated samples; b): Ni, V and Sc content vs. MgO. Literature data (purple fields) are from De Astis et al. (2013) and reference therein. Normalizing values are from Sun and McDonough (1989).

Copper concentrations increase with decreasing MgO until MgO reaches ~ 4 wt.%, which corresponds to the shoshonitic samples. These show a wide range of Cu content from ~100 up to ~350 ppm. Copper then decreases reaching a minimum of 15 ppm in the most evolved rhyolite (Fig. 9.3; Tab. 9.1).

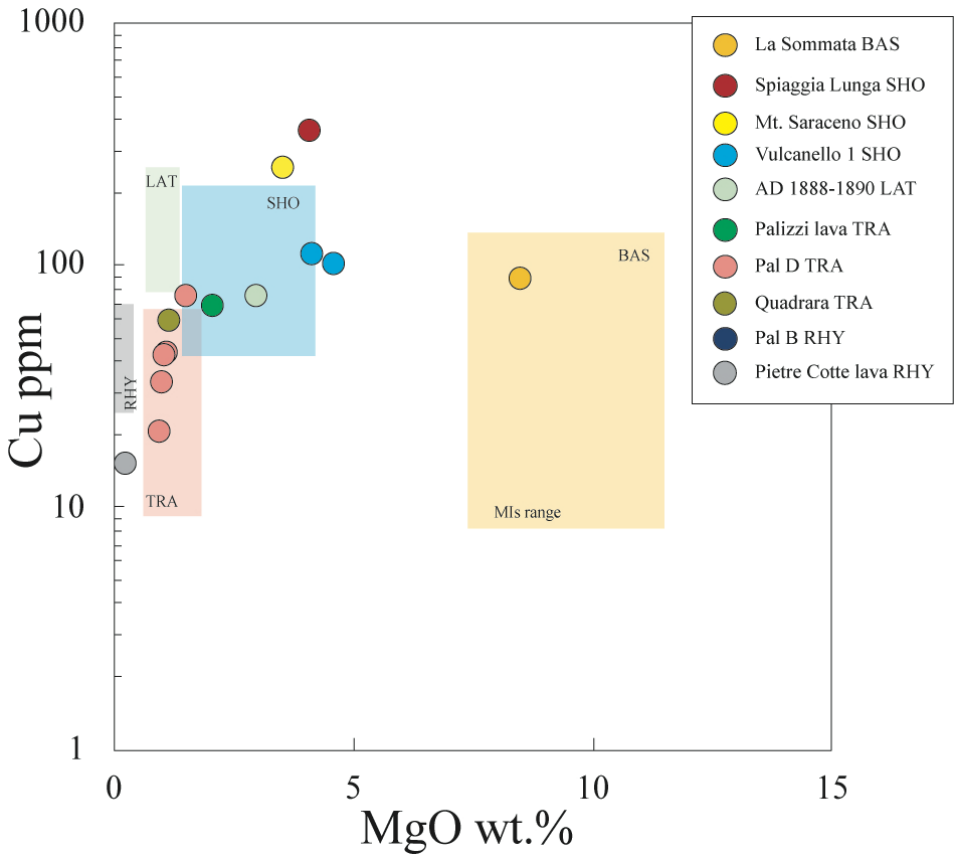

Figure 9.3 – Cu vs. MgO diagram of the investigated samples. Rectangles represent the melt inclusions data (Chapter 8)

Whole-rock PGE, Re and Au analyses

Whole-rock PGE, Re and Au abundances are reported in table 9.1. Iridium was below the detection limit in all samples, with the exception of La Sommata basalt (Ir, 0.15–0.30 ppb). Ruthenium was below the detection limit in all samples. Rhodium, Pt and Pd data are above the detection limit except for most of trachytic and rhyolitic samples and range from 0.02 to 0.2 ppb Rh, 1.2 to 5.2 ppb Pt and 0.6 to 7.8 ppb Pd. Rhenium content vary between 0.3 and 1.4 ppb but the results are below the detection limit in several samples. Au ranges from 0.04 to 1.4 ppb (Tab. 9.1). Abundances of Au, Rh, Pt and Pd are plotted against whole-rock MgO contents (Fig. 9.4). Gold shows a similar trend to Cu, but with appreciable more scatter and it is below the detection limit in the most evolved samples. Pt and Rh decrease with decreasing MgO (Fig. 9.4) and fall below the detection limit in the most evolved samples. Palladium remains constant within uncertainty until MgO

falls to 4 wt.%, then decreases steadily from 4 to 2 wt.% MgO and finally abruptly to the trachytic and rhyolitic samples, where it is below the detection limit (Fig. 9.4).

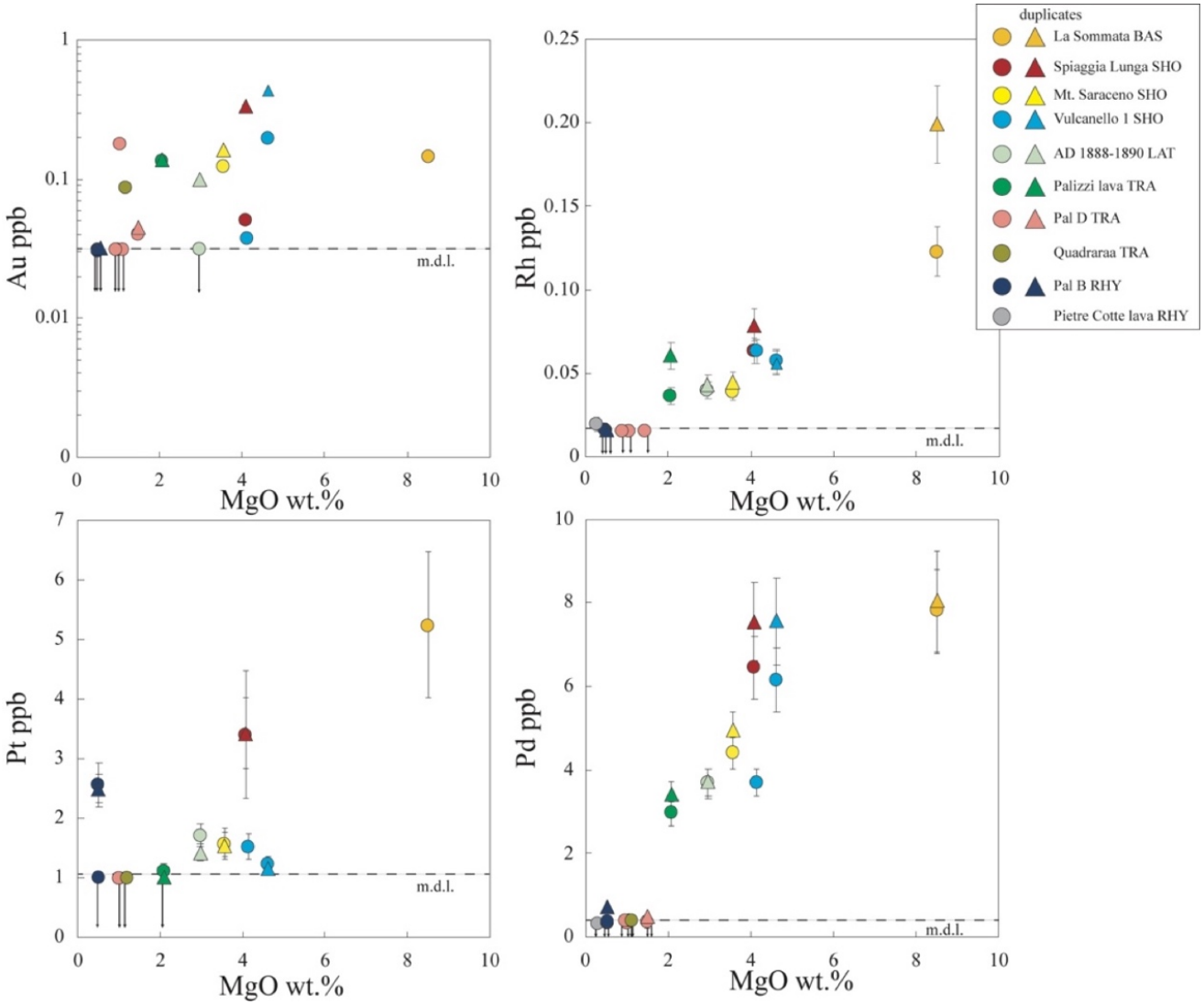

Figure 9.4 – PGE and Au variation diagrams plotted against MgO content. Black arrows indicate samples below the method detection limit (m.d.l., see Chapter 4). 2 sigma error for each analysis is shown as error bars, which if not visible, is smaller than the symbol.

The primitive mantle-normalized PGE, Ni, Au and Cu patterns of the mafic samples of Vulcano (basalt and shoshonites) are reported in figure 9.5, and compared with data from MORB (Mungall and Brenan, 2014) and other arc basalts (Pual Ridge, Park et al., 2013b). The Vulcano samples show higher PGE concentrations with respect to the MORB values (Fig. 9.5), and are characterized

by PGE patterns in which Ir-group PGE (IPGE, including Os, Ir, Ru) are fractionated with respect to Pd-group PGE (PPGE, including Rh, Pt, Pd). These patterns, and the absolute PGE concentration values, are similar to those of the Pual Ridge arc basalts (Park et al., 2013b). Copper content increases from basalt to shoshonites with differentiation. Platinum is slightly fractionated with respect to Pd, and all samples are depleted in Au by ca. x10 compared with the Pual Ridge arc basalts and MORB.

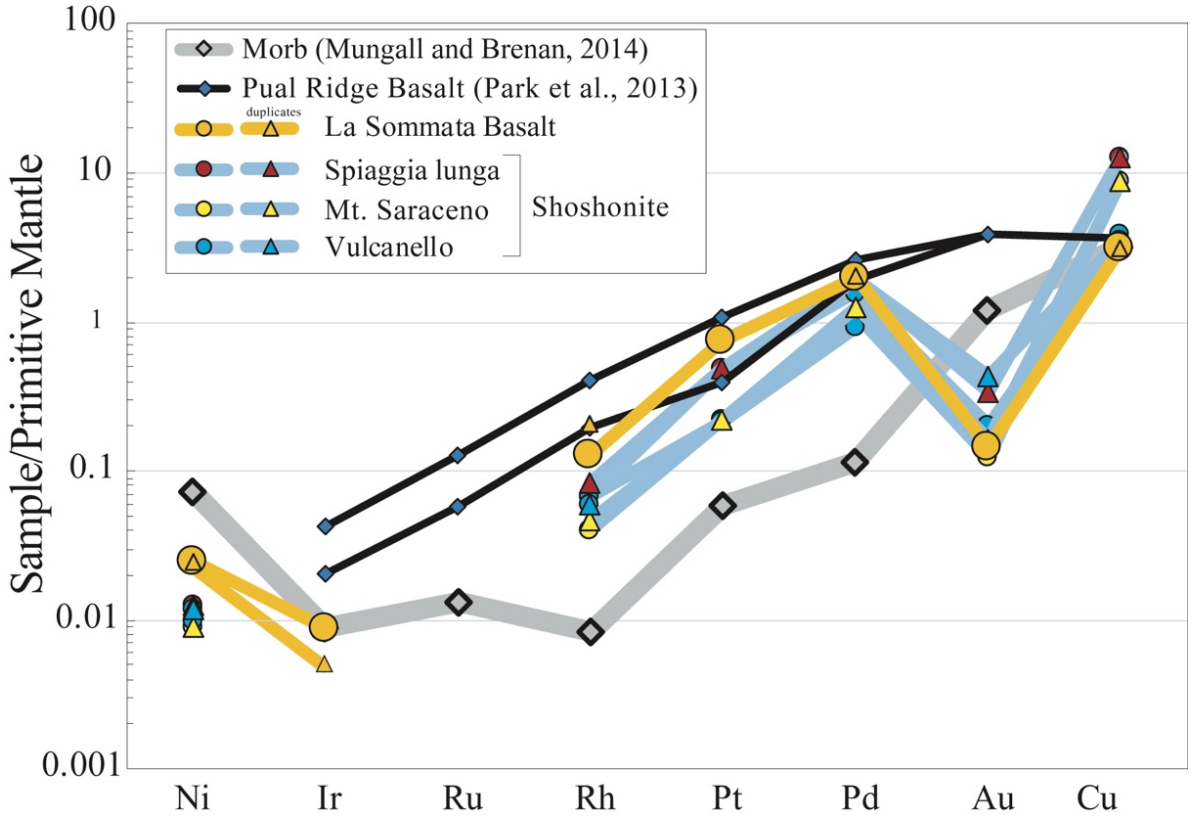

Figure 9.5 – Primitive mantle-normalized PGE, Au, Cu and Ni concentrations of the mafic (Basalt and shoshonites) Vulcano samples. Normalizing values are from Barnes and Meier (1999).

*Table 9.1 - Concentrations of MgO (wt.%), Cu (ppm), PGE, Re and Au (ppb) in the analyzed samples; * duplicates samples; bdl: below detection limit; nd:not determined; errors expressed as 2SD. All values are blank subtracted with an uncorrected sample values to blank average ratio >3 , see also Chapter 4.*

Unit	Comp.	Sample	MgO	Cu	Ir	2σ	Ru	2σ	Rh	2σ	Pt	2σ	Pd	2σ	Au	2σ	Re	2σ
La Sommata	Bas	SC_18_5	8.50	88.00	0.0300	0.0016	bdl		0.1229	0.0146	5.2349	1.2281	7.7978	1.0083	0.1438	0.0034	bdl	
Spiaggia Lunga	Sho	VUL_06	4.08	355.00	bdl		bdl		0.0632	0.0078	3.3975	1.0705	6.4422	0.7360	0.0501	0.0035	bdl	
Mt Saraceno	Sho	SC_18_4	3.57	251.00	bdl		bdl		0.0384	0.0051	1.5646	0.2668	4.4075	0.3826	0.1220	0.0039	0.2845	0.0148
Vulcanello	Sho	SC_20_28	4.14	110.00	bdl		bdl		0.0632	0.0078	1.5202	0.2099	3.6982	0.3131	0.0374	0.0030	bdl	
Vulcanello	Sho	SC_18_13	4.62	100.00	bdl		bdl		0.0571	0.0072	1.2295	0.1311	6.1432	0.7605	0.1972	0.0063	bdl	
88-90 eruption	Lat	SC_20_29B	2.97	74.00	bdl		bdl		0.0394	0.0052	1.7135	0.1955	3.6755	0.3536	bdl		bdl	
Quadrara	Tra	SC_18_08	1.19	59.00	bdl		bdl		bdl		bdl		bdl		0.0862	0.0031	0.3767	0.0180
Palizzi lava	Tra	SC_18_24	2.08	68.00	bdl		bdl		0.0361	0.0049	1.0761	0.1062	2.9532	0.2993	0.1336	0.0043	bdl	
Pal D	Tra	SC_18_20	1.00	33.00	bdl		bdl		bdl		bdl		bdl		bdl		bdl	
Pal D	Tra	S33B_60_90	1.50	74.00	bdl		bdl		bdl		bdl		bdl		0.0397	0.0025	bdl	
Pal D	Tra	S33B_60_110	1.13	43.00	bdl		bdl		bdl		bdl		bdl		bdl		bdl	
Pal D	Tra	SC_20_31	1.06	42.00	bdl		bdl		bdl		bdl		bdl		0.1780	0.0068	0.3204	0.0153
Pal D	Tra	SC_20_31B	0.95	20.30	bdl		bdl		bdl		bdl		bdl		bdl		bdl	
Pietre Cotte	Rhy	SC_20_30	0.28	15.00	bdl		bdl		0.0195	0.0043	bdl		bdl		bdl		bdl	
Pal B	Rhy	PAL_L_18_01	0.51	nd	bdl		bdl		bdl		2.5611	0.3688	bdl		bdl		bdl	
Pal B	Rhy	PAL_L_18_02	0.51	nd	bdl		bdl		bdl		bdl		bdl		bdl		bdl	
La Sommata*	Bas	SC_18_5	8.50	88.00	0.0152	0.0009	bdl		0.1991	0.0234	bdl		8.0342	1.2109	bdl		bdl	
Spiaggia Lunga*	Sho	VUL_06	4.08	355.00	bdl		bdl		0.0786	0.0097	3.4249	0.5973	7.5473	0.9256	0.3320	0.0079	0.2772	0.0171
Mt Saraceno*	Sho	SC_18_4	3.57	251.00	bdl		bdl		0.0449	0.0058	1.5450	0.2023	4.9520	0.4488	0.1620	0.0056	0.6354	0.0290
Vulcanello*	Sho	SC_18_13	4.62	100.00	bdl		bdl		0.0560	0.0070	1.1558	0.0953	7.5560	1.0480	0.4294	0.0099	0.4239	0.0189
88-90 eruption*	Lat	SC_20_29B	2.97	74.00	bdl		bdl		0.0432	0.0056	1.4242	0.1382	3.7169	0.3226	0.0998	0.0025	0.8355	0.0444
Palizzi lava*	Tra	SC_18_24	2.08	68.00	bdl		bdl		0.0604	0.0079	bdl		3.4182	0.3004	0.1391	0.0038	0.9462	0.0351
Pal D*	Tra	SC_33B_60_90	1.50	43.00	bdl		bdl		bdl		bdl		bdl		0.0449	0.0023	1.4064	0.0865
Pal B*	Rhy	PAL_L_18_01	0.51	nd	bdl		bdl		bdl		2.4998	0.2333	0.6665	0.0378	bdl		0.9865	0.0305

9.4 Discussion

Inferences on the PGE abundance of primitive arc magmas

Detailed petrological studies have shown that the Fo-rich (Fo_{91-87}) olivines of La Sommata basalt, hosting Cr-spinel (Cr# 76–81), trapped a mantle-equilibrated primary melt of Mg#66 as melt inclusions (Gioncada et al., 1998; Palummo et al., 2020). The crystallization temperatures of these Fo-rich olivines are estimated in the range 1186–1207 °C (Palummo et al., 2020), in good agreement with the homogenization temperature of their melt inclusions, ranging from 1190 °C to 1250 °C (Gioncada et al., 1998). The equilibrium pressure of these mantle-derived olivine crystals was in the range 620–740 MPa (in accordance with the Moho inferred depth of 21-25 km below Vulcano, Peccerillo et al., 2006). The high Ca/Al ratio of melt inclusions and the diopside-forsterite-Cr-spinel mineral assemblage of La Sommata basalt indicate partial melting of a depleted peridotitic mantle source, in the chromite field, veined by metasomatic, clinopyroxene-rich regions (Kamenetsky and Clocchiatti, 1996; Gioncada et al., 1998).

Most mantle-derived arc basalts show fractionated primitive mantle-normalized PGE patterns with concentrations increasing in the order Ir < Ru < Rh < Pt < Pd, which indicates that the PPGE (Rh, Pt and Pd) are more incompatible during partial melting and magma differentiation with respect to IPGE (Ir, Os, and Ru) (Park et al., 2013b). The Primitive Mantle-normalized spider diagrams for Vulcano mafic rocks shown in figure 9.5 displays the expected depletion in the IPGE relative to the PPGE. Park et al. (2013b) suggest that the initial enrichment in Pt over Ir (i.e. high Pt/Ir) is a characteristic that differentiate arc-type mafic magmas from other primary melts such OIB-like (Barnes and Fiorentini, 2008; Ireland et al., 2009; Pitcher et al., 2009; Barnes et al., 2015). Platinum/Iridium ratios in the Pual Ridge mafic rocks lie between 40 and 316, and those of the Tonga arc lavas between 24 and 270, whereas Hawaiian OIB-type mafic magma have lower Pt/Ir (~14) (Dale et al., 2012; Park et al., 2013b). The La Sommata basalt has a Pt/Ir of 174, within the range expected for subduction-related primary melts and appreciably higher than that found in OIB-type magmas.

Park et al. (2013b) suggest that the main factor controlling the fractionation of IPGE is the presence of Cr-spinel in the magma source region. The partition coefficients for the IPGE, between silicate melt and Cr-spinel, increases with oxidation state (Brenan et al., 2012; Park et al., 2012b). This may explain the difference between arc-type magmas and OIB-type if, as generally accepted, the former are more oxidized than the latter. The compatibility of Ir, Ru and Rh in Cr-spinel is well documented in the literature, with the partition coefficient of Ru in Cr-spinel being generally higher ($kd^{Cr\text{-}spinel/Silicate\ melt}$ 10^3) than those of Ir and Rh ($kd^{Cr\text{-}spinel/Silicate\ melt}$ 10^2) (Righter et al., 2004; Brenan et al., 2012; Park et al., 2012b). However, this cannot explain the depletion of Pt relative to Pd, because neither enters Cr-spinel. Indeed, IPGE and Rh are compatible to Cr-spinel, instead Pt and Pd are incompatible and are enriched in fractionating melt ($k_d^{Cr\text{-}spinel/Silicate\ melt} \sim 2x10^{-1}$ and $\sim 3x10^{-2}$, respectively; Righter et al., 2004; Brenan et al., 2012; Park et al., 2012b).

Another phase must thus be involved in the fractionation, and the most likely candidate is a metal alloy, which can sequester Pt, Rh, Ru and Ir, but importantly, not Pd. Evidence for Pt-rich alloy crystallization are described for ultramafic and mafic rocks and primitive arc lavas (Spandler et al., 2000, 2003; Garuti et al., 2002, 2003; Augé et al., 2005; Zaccarini et al., 2011; Park et al., 2012b). Moreover, magmatic Pt-rich alloy inclusions were frequently observed in Cr-spinel (Capobianco and Drake, 1990; Capobianco et al., 1994; Park et al., 2012b; Pushkarev et al., 2014) indicating that co-saturation of Pt-rich alloy and Cr-spinel is a common process. As a consequence, it is possible suggest that the most primitive of the Vulcano samples was also saturated with a Pt-rich alloy.

Gold is depleted by an order of magnitude relative to adjacent Cu and Pd on the chalcophile element spider diagram (Fig. 9.5). This behavior has been reported only once, in andesites associated with the Kelian epithermal gold deposit In Indonesia (Setiabudi et al., 2007). It has been already discussed that Vulcano magmas may have lost S (and moderately Cl) from a very early stage during their evolution (Gioncada et al., 1998). If this argument is correct the S-rich gas may have stripped Au from the evolving Vulcano magma system and transported it to higher levels in the volcanic pile. Gold depletion, due to its partitioning in an early

S-rich gas phase, and the decoupling between Au and Cu behavior in Vulcano basalts are consistent with the results of Zajacz et al. (2012), showing that the solubility of Au in silicate melts is primarily controlled by the sulfur concentration in the melt at fO_2 < NNO+1 (fO_2 of Vulcano basalt is NNO+0.72, Metrich and Clocchiatti, 1996), and that Cl concentration enhances Au solubility. The effect of S and Cl on Cu solubility is instead much more moderate than in the case of Au. Therefore, early S and minor Cl exsolution from Vulcano basalts is likely to explain the observed Au negative anomaly shown in figure 9.5.

Constraints on sulfide saturation from PGE geochemistry

Recent studies have shown that PGE behavior can be used as a sensitive indicator of sulfide saturation in evolving magmatic systems (Park et al., 2013b; Cocker et al. 2016; Hao et al. 2017). Palladium is the element of choice because it behaves incompatibly prior to sulfide saturation, but is highly compatible into immiscible sulfide melts so that its concentration decreases rapidly once the magma becomes sulfide-saturated (Park and Campbell, 2021 and reference therein). Indeed, the sulfide phase-silicate melt partition coefficients for Pd (10^5–10^6) are much higher than those of Au (10^3–10^4) and Cu (10^2–10^3) (Campbell and Barnes, 1984; Ripley et al., 2002; Fonseca et al., 2009; Mungall and Brenan, 2014). Furthermore, Pd, in contrast to the other PGE, does not partition into metal alloys and is much less affected by hydrothermal fluids than Cu or Au (Park et al., 2013b, 2015, 2019). In Vulcano rocks, the Pd/Pt ratio rises with decreasing MgO content, until it decreases significantly when MgO wt% content of the magma falls below about 4 wt%, revealing the fractionation of an immiscible sulfide melt (Fig. 9.5a). The initial increase of Pd/Pt ratio can be explained by the highly incompatible behavior of Pd whereas Pt is sequestered by Pt-alloys (Fig. 9.5a) (Park et al., 2013b). The involvement of Pt-alloys, sequestering Pt and Rh, is confirmed by the analogous behavior of these elements from the start of fractionation (Fig. 9.4). Once the magma becomes sulfide saturated, the Pd/Pt ratio begins to fall because Pd is more chalcophile than Pt (Park et al. 2013b, 2015; Hao et al. 2017).

Palladium, Au and Cu whole-rock concentrations decrease significantly with decreasing MgO in the Vulcano samples once the MgO content of the magma fall below ca. 4 wt. % (Figs. 9.3 and 9.4). A plot of Pd/Cu against MgO (Fig. 9.6b) provides further evidence for sulfide saturation starting at around 4 wt.% MgO. Samples with MgO > 3–4 wt. % display a relatively flat Pd/Cu trend with decreasing MgO (Fig. 9.6b) because both Cu and Pd are incompatible, but at MgO < 3–4 wt. % (sulfide saturation), Pd falls faster than Cu due to its higher sulfide melt–silicate melt partition coefficient and the Pd/Cu ratio decreases with decreasing MgO (Fig. 9.6b).

The initial increase in whole rock Cu content, with decreasing of MgO, follows a similar pattern to that observed in silicate melt inclusions discussed in chapter 8, that is an increase of Cu content in the inclusions with decreasing MgO until sulfide saturation, at which point Cu drops markedly (Fig. 9.4). However, the point at which the two chalcophile elements start to fall is different: the decline in Pd starts at 4 wt.% MgO whereas Cu starts to decline when MgO falls below 2 wt.%. This difference can be explained if only a small amount of sulfide were formed at the sulfide melt saturation as observed in Skaergaard (Keays and Tegner, 2015), with the fraction of sulfide to precipitate increasing with increasing fractionation. Under these conditions, Pd with its high partition coefficient becomes compatible before Cu. This interpretation is consistent with the evidence that sulfide inclusions have only been observed in latites, trachytes and rhyolites, with MgO < ~3 wt.% (Fulignati et al., 2018; Chapter 8). The lack of sulfide blebs in the less evolved shoshonitic volcanic rocks is probably due to the amount of sulfide in these rocks being so small and rare that they were not detected by petrographic surveys.

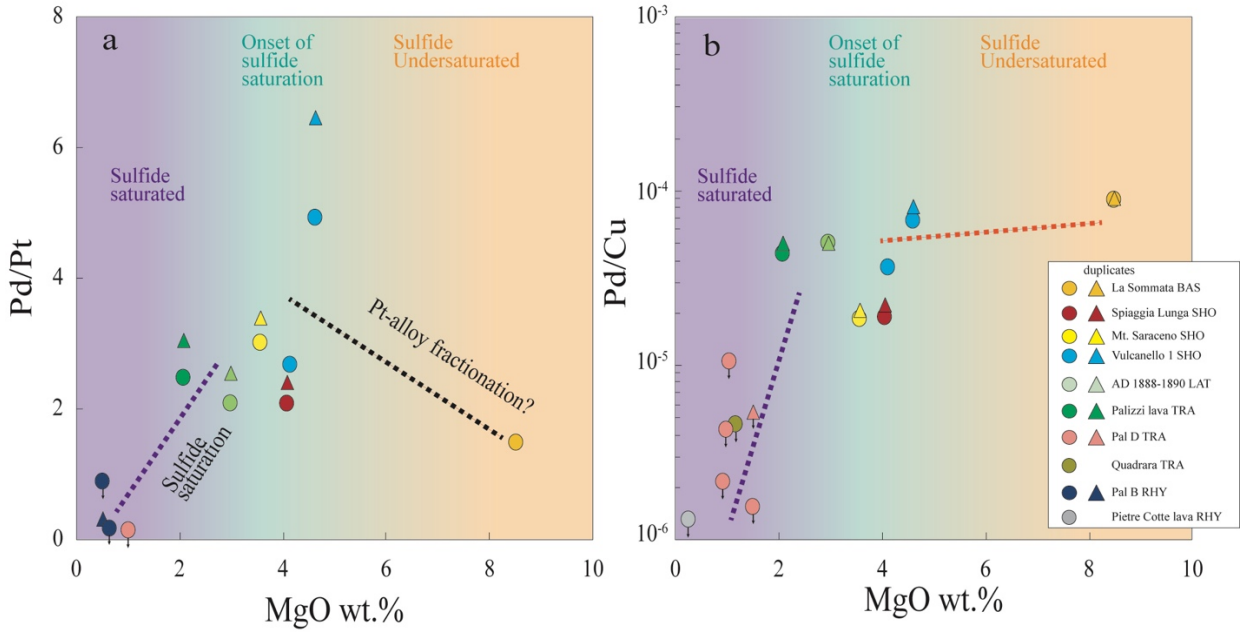

Figure 9.6 – a) Pd/Pt vs. MgO of the investigated samples. The initial increase of the Pd/Pt ratio is attributable to saturation of Pt-alloy, at sulfide saturation both Pd and Pt are compatible in the sulfide phase; b) Pd/Cu plotted against MgO content. The onset of sulfide saturation is recognized at ~4 wt.% MgO. Black arrows indicate samples below the method detection limit (m.d.l., see Chapter 4).

Inferences on chalcophile element fertility of Vulcano magmas

Recent studies of the PGE geochemistry of porphyry systems (Cocker et al. 2016; Hao et al. 2017, 2019; Lowczak et al. 2018; Park et al. 2019) suggested that the PGE contents of volcanic and sub-volcanic rocks can be used as indicators of Cu and Au prospectivity. They showed that the sub-volcanic or volcanic suites associated with porphyry Cu and Cu-Au deposits are significantly enriched in PGE at a given level of fractional crystallization compared to the barren suites (Park and Campbell, 2021). The Pd concentration of Vulcano samples are comparable to the highest values found in other arc-related igneous suites that are associated with porphyry copper systems, and in particular to those associated with Au-Cu deposits (Fig. 9.7). Furthermore, the Pd contents of Vulcano samples are higher than those of magmatic suites that lack associations with mineralized systems (barren suites), at comparable MgO levels (Fig. 9.7).

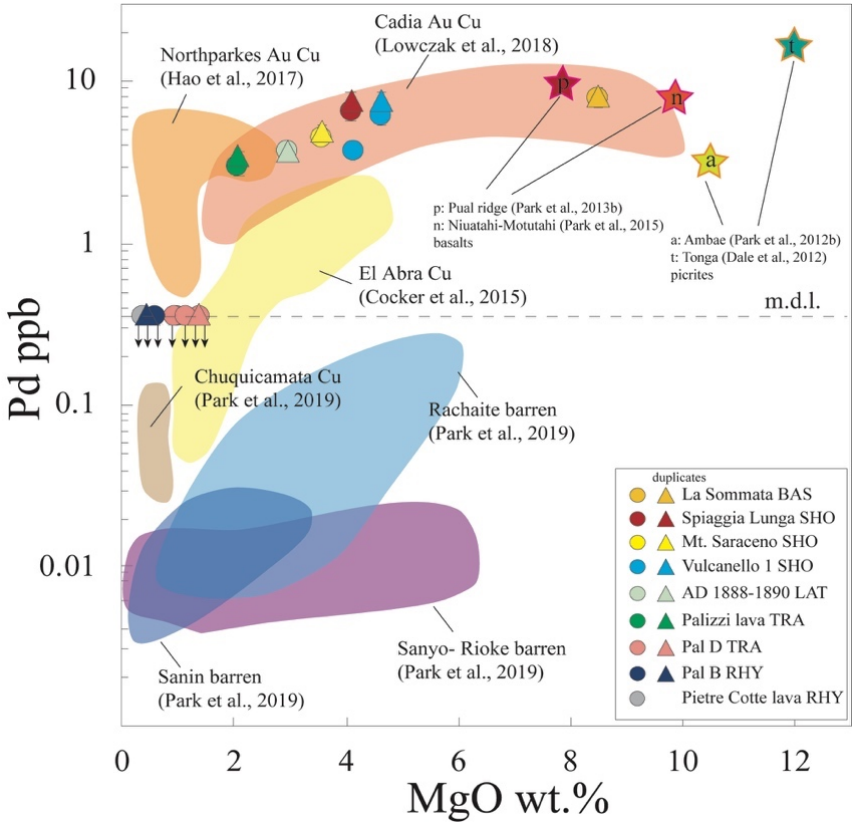

Figure 9.7 - Plot of Pd against MgO for the ore-bearing and barren suites (modified after Park et al., 2019). The Pd content of Vulcano magmas is comparable to magmatic suites associated to Au Cu porphyry systems. The basaltic La Sommata magma has Pd values comparable to other arc-related mafic rocks. Black arrows indicate samples below the method detection limit (m.d.l., see Chapter 4).

Park et al. (2019) proposed that the Pd content of samples normalized to MgO (to correct the discrepancies caused by fractional crystallization), plotted against Pd/Pt (a measure of the amount of fractional crystallization before sulfide saturation) can be used to distinguish between barren, Cu-only and Au-Cu deposits. Figure 9.8 shows the studied volcanic rocks (with MgO < 3 wt.%) plotted on the fertility diagram proposed by Park et al. (2019). The diagram highlights the high Pd values of the analyzed samples. The investigated samples with MgO < 3 wt.% plot in Au-Cu deposits field, suggesting that Vulcano magmas could produce an Au-Cu or Au deposit.

However, the fertility potential of evolving magmas is heavily influenced by other factors such as the timing between sulfide saturation relative to volatile exsolution (Park et al., 2019), which conditions the availability of the chalcophile metal magmatic budget for transfer to the hydrothermal fluids. If sulfide saturation

occurs late in magmatic evolution, closely in time with volatile exsolution, chalcophile elements become concentrated in the melt by Rayleigh fractionation prior to volatile saturation, and the small time difference between the sulfide and volatile saturation may results in only some depletion of chalcophile elements in the magma, which keeps its fertility. Thus, fluid phase that evolves from this silicate melt will be enriched in chalcophile elements. Nevertheless, if sulfide saturation occurs early during magmatic differentiation and before volatile saturation, the chalcophile elements are sequestered from the magma and are stored within cumulate rocks (Chen et al., 2020; Du and Audétat , 2020). In that case, Cu, Au, and PGE will be unable to partition into the ore-forming hydrothermal fluid (Cocker et al., 2016; Hao et al., 2017; Park et al., 2019) unless magmatic sulfides successively interact with an exsolved aqueous fluid phase, in which chalcophile elements are released, generating ore-forming solutions (Halter et al., 2002, 2005; Richards, 2009; Nadeau et al., 2010, 2016; Nadeau, 2015; Audétat and Simon, 2012; Wilkinson, 2013; Park et al., 2015). The mineralization potential of a magmatic system is also dependent on the amount of sulfide melt that forms at sulfide saturation (Cocker et al., 2016). As an example, if a small amount of sulfide melt forms at sulfide saturation, it will be able to deplete the evolving silicate melt in PGE and Au, but not significantly in Cu, resulting in a Cu-only porphyry mineralized system (Cocker et al., 2016). A small amount of sulfide separation can even have no influence in the chalcophile elements budget (Lowczak et al., 2018). If sulfide saturation does not occur or occurs late during magma evolution, then a Cu-Au or Cu-Au-Pd porphyry system could develop (Hao et al., 2017; Lowczak et al., 2018; Park et al., 2019; Park and Campbell, 2021).

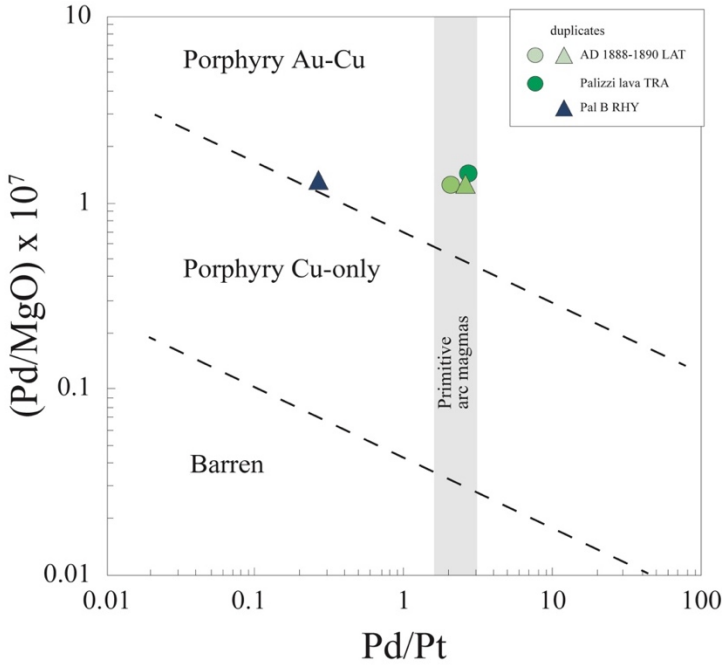

Figure 9.8 – Chalcophile element fertility diagram of Park et al. (2019) showing the difference between barren, Cu- only, and Cu-Au suites. The Vulcano magmas with MgO < 3 wt.% have the fertility potential the develop an Cu-Au system.

In chapter 8 it has been suggested that, at Vulcano, late fractionation of only 0.2–0.3 wt.% of sulfide is sufficient to deplete the silicate melt in Cu down to the values recorded by melt inclusions in trachytic and rhyolitic products. Such amount of fractionated sulfide is in agreement with previous estimates inferred for other felsic systems (0.15 to 0.3 wt.%, Park et al., 2013b, 2015; Cocker et al., 2016; Hao et al., 2017). Cocker et al. (2016) suggested that if the sulfide melt represents the 0.3% of the fractionating phases (at 70% of fractional crystallization) as in the case of late sulfide saturation, most of the Au and PGE will be removed from the silicate melt whilst Cu only for 50%. If fluid saturation occurs after sulfide saturation (at 80% fractionation), the exsolved fluid would be Cu-rich and Au-poor producing a Cu-only deposit. If sulfide fractionation is reduced to 0.1%, the Au content continues to be negligible. The same authors found that a Au-Cu deposit will form only if the amount of sulfide melt formed is below 0.03%, or if fluid saturation occurs just before or very soon after sulfide saturation. Accordingly, Hao et al. (2017) suggest that intrusion-related ores are likely formed if sulfide saturation occurs late at 85% fractional crystallization with the ~0.002 % of sulfide formed. At Vulcano there are evidence that exsolution Cl-rich aqueous fluid phase is likely

to occur at rhyolitic stage of magma differentiation (Fulignati et al., 2018; see also chapter 8) thus after the inferred sulfide saturation at intermediate stages of magmatic differentiation.

All these considerations allow to suggest that magmatic evolution at La Fossa volcano has the potential to lead to fertile magmas. The concurrence of several factors is necessary to form a mineralized system: i) magmatic evolution with continuous magma recharges; ii) fractionation processes to reach evolved compositions; iii) sulfide saturation in intermediate-evolved magma; iv) saturation of volatile phases just before or soon after sulfide saturation.

9.5 Conclusions

In this study the whole-rock PGE geochemistry of the basalt to rhyolite magmatic suite of Vulcano has been presented. The obtained results confirm that PGEs are a powerful tool to identify the occurrence of sulfide saturation in intermediate to felsic rocks. The case of Vulcano is similar to that of magmatic suites associated with Au-Cu mineralization and allows the investigation of similar igneous suites in relatively young and active magmatic systems. Platinum group element analysis show sharp decrease in Pt and Rh trends since early stage of magmatic differentiation with decreasing MgO, suggesting early saturation of Pt-rich alloy and Cr-spinel in basalts. Samples with lower MgO concentrations show decreasing PGE, Au and Cu with decreasing MgO. The abrupt changes in PGE concentrations at ~4 wt. % MgO suggest that the onset of sulfide saturation has occurred at the intermediate stage of magmatic differentiation. Platinum and Pd concentrations of the Vulcano samples are similar to those of other arc-related suites that are associated with hydrothermal mineralization. Pd content are significantly higher than those of suites that have no associated mineralization. The potential of magmas similar to those of Vulcano to produce Au-Cu or Au deposit may be influenced by other factors such as the timing between sulfide saturation relative to volatile exsolution, the nature of the exsolved fluid, the amount of sulfide melt that forms at sulfide saturation.

10 Conclusive remarks

The characterization of the eruptive products emplaced at La Fossa in the last 1000 years carried out in this PhD thesis allowed to gain new interpretations of the active plumbing system of the volcano. The obtained results confirm the complexity of magma dynamics working at La Fossa and envisage a plumbing system characterized by interconnected melt ponding zones forming a vertically-extended mush column. In this frame, latitic, trachytic and rhyolitic magmas, show abrupt shifts in composition through time, and represent the activation of magma batches that differentiate, coexist and interact at shallow crustal depths (15-2 km). The polybaric differentiation of latitic and trachytic magmas is responsible for the formation of several crystal mushes that are periodically perturbated by the arrival of less evolved magmas. Furthermore, as suggested by geochemical modelling, the crystal mushes are accountable for the genesis of the rhyolitic magma through segregation of highly differentiated residual melts. In such a system, the geochemical and petrological variability of the erupted products reflect the complexity of the magmatic processes and the interaction among mush-derived magmas and recharging magmas.

The role of recharging magmas at La Fossa is also investigated in the complex explosive sequence of the Palizzi Eruptive Unit that represents an important eruptive period in the recent (post-1000 years AD) history of the volcano, characterized by a steady-state explosive activity interrupted by two higher intensity explosive events. The hierarchical cluster analysis of clinopyroxene profiles allowed to unveil magma dynamics through the whole stratigraphic sequence and to identify at least three main cycles of magmatic recharge, followed by magma ascent and eruption. The reliability of this analysis is supported by the characteristics of the deposits of the pyroclastic succession. For this reason, the approach presented in this thesis may be applied to the study of complex volcanic successions dominated by fine-grained pyroclastic material.

La Fossa volcano is a perfect place for investigating magmatic processes that may have consequences on the transition between magmatic and hydrothermal systems, in particular on magma fertility with respect to chalcophile metals. The complex differentiation processes involve episodes of sulfide saturation occurring in the intermediate and evolved magmas. In this thesis, the study of different types of sulfide inclusions and chalcophile metal contents in melt inclusions allowed to track the evolution of metal concentration during the magma differentiation path from basalt to rhyolite. When sulfide saturation is reached at the stage of intermediate magma compositions, Cu and chalcophile metals strongly partition in the sulfide melt and their concentration in the silicate melt dramatically decreases even for small amounts of sulfide fractionation (0.2-0.3 wt.%). This is also suggested by the behavior of the Platinum-group elements, which decreases in concentration starting at intermediate stage of magma differentiation (~4 wt.% MgO). Moreover, the Pd content of magmas erupted at Vulcano, as well as the trace element measured in sulfide inclusions, are comparable to those of other arc-related suites that are associated with hydrothermal mineralization, suggesting that early stages of mineralization processes potentially at the base of porphyry Cu deposit formation can be investigated at active arc volcanoes.

This PhD thesis thus combined major and trace elements analyses both on whole-rock samples, mineral phases, melt and sulfide inclusions on a large variability of products (both pyroclastic and effusive) covering a wide spectrum of compositions. The case study of La Fossa, and the multidisciplinary approach, including high-pressure high temperature experiments and a data-driven hierarchical cluster analysis, allowed to propose a model able to explain the genesis of crystal-poor rhyolites and K- rich trachyte, to unveil magma dynamics along a fine-grained ash sequence such as the Palizzi Eruptive Unit, and providing important information on magma fertility and on magmatic processes leading to the development of mineralization in hydrothermal systems.

References

Ardia, P., Giordano, D., & Schmidt, M. W. (2008). A model for the viscosity of rhyolite as a function of H_2O-content and pressure: a calibration based on centrifuge piston cylinder experiments. *Geochimica et Cosmochimica Acta*, *72*(24), 6103-6123.

Armienti, P., Perinelli, C., & Putirka, K. D. (2013). A new model to estimate deep-level magma ascent rates, with applications to Mt. Etna (Sicily, Italy). *Journal of Petrology, 54*, 795-813.

Armienti, P., Tonarini, S., Innocenti, F., & D Orazio, M. (2007). Mount Etna pyroxene as tracer of petrogenetic processes and dynamics of the feeding system. *SPECIAL PAPERS-GEOLOGICAL SOCIETY OF AMERICA*, *418*, 265.

Arrighi, S., Tanguy, J. C., & Rosi, M. (2006). Eruptions of the last 2200 years at Vulcano and Vulcanello (Aeolian Islands, Italy) dated by high-accuracy archeomagnetism. *Physics of the Earth and Planetary Interiors*, *159*(3-4), 225-233.

Audétat, A., Simon, A. C., in Hedenquist, J. W., Harris, M., & Camus, F. (2012). Magmatic controls on porphyry copper genesis. *Geology and genesis of major copper deposits and districts of the world-A tribute to Richard H. Sillitoe*, 553-572.

Augé, T., Genna, A., Legendre, O., Ivanov, K. S., & Volchenko, Y. A. (2005). Primary platinum mineralization in the Nizhny Tagil and Kachkanar ultramafic complexes, Urals, Russia: a genetic model for PGE concentration in chromite-rich zones. *Economic Geology*, *100*(4), 707-732.

Bachmann, O., & Bergantz, G. W. (2008). Rhyolites and their source mushes across tectonic settings. *Journal of Petrology*, *49*(12), 2277-2285.

Bachmann, O., & Bergantz, G. W. (2004). On the origin of crystal-poor rhyolites: extracted from batholithic crystal mushes. *Journal of Petrology*, *45*(8), 1565-1582.

Bai, Z. J., Zhong, H., Hu, R. Z., & Zhu, W. G. (2020). Early sulfide saturation in arc volcanic rocks of southeast China: Implications for the formation of co-magmatic porphyry–epithermal Cu–Au deposits. *Geochimica et Cosmochimica Acta*, *280*, 66-84.

Barberi, F., Gasparini, P., Innocenti, F., & Villari, L. (1973). Volcanism of the southern Tyrrhenian Sea and its geodynamic implications. *Journal of Geophysical Research*, *78*(23), 5221-5232.

Barnes, S. J., & Fiorentini, M. L. (2008). Iridium, ruthenium and rhodium in komatiites: evidence for iridium alloy saturation. *Chemical Geology*, *257*(1-2), 44-58.

Barnes, S. J., & Maier, W. D. (1999). The fractionation of Ni, Cu and the noble metals in silicate and sulphide liquids. *Short Course Notes-Geological Association of Canada*, *13*, 69-106.

Barnes, S. J., Mungall, J. E., & Maier, W. D. (2015). Platinum group elements in mantle melts and mantle samples. *Lithos*, *232*, 395-417.

Beccaluva, L., Gabbianelli, G., Lucchini, F., Rossi, P. L., & Savelli, C. (1985). Petrology and K/Ar ages of volcanics dredged from the Eolian seamounts: implications for geodynamic evolution of the southern Tyrrhenian basin. *Earth and Planetary Science Letters*, *74*(2-3), 187-208.

Beermann, O., Holtz, F., & Duesterhoeft, E. (2017). Magma storage conditions and differentiation of the mafic Lower Pollara volcanics, Salina Island, Aeolian Islands, Italy: implications for the

formation conditions of shoshonites and potassic rocks. *Contributions to Mineralogy and Petrology*, *172*(5), 37.

Biass, S., Bonadonna, C., Di Traglia, F., Pistolesi, M., Rosi, M., & Lestuzzi, P. (2016). Probabilistic evaluation of the physical impact of future tephra fallout events for the Island of Vulcano, Italy. *Bulletin of Volcanology*, *78*(5), 37.

Blanco-Montenegro, I., De Ritis, R., & Chiappini, M. (2007). Imaging and modelling the subsurface structure of volcanic calderas with high-resolution aeromagnetic data at Vulcano (Aeolian Islands, Italy). *Bulletin of Volcanology*, *69*(6), 643-659.

Blundy, J., & Cashman, K. (2008). Petrologic reconstruction of magmatic system variables and processes. *Reviews in Mineralogy and Geochemistry*, *69*(1), 179-239.

Blundy, J., Cashman, K., & Humphreys, M. (2006). Magma heating by decompression-driven crystallization beneath andesite volcanoes. *Nature*, 443(7107), 76-80.

Bolton, M. S., Jensen, B. J., Wallace, K., Praet, N., Fortin, D., Kaufman, D., & De Batist, M. (2020). Machine learning classifiers for attributing tephra to source volcanoes: an evaluation of methods for Alaska tephras. *Journal of Quaternary Science*, *35*(1-2), 81-92.

Boyce, A. J., Fulignati, P., Sbrana, A., & Fallick, A. E. (2007). Fluids in early stage hydrothermal alteration of high-sulfidation epithermal systems: A view from the Vulcano active hydrothermal system (Aeolian Island, Italy). *Journal of Volcanology and Geothermal Research*, *166*(2), 76-90.

Brenan, J. M., Finnigan, C. F., McDonough, W. F., & Homolova, V. (2012). Experimental constraints on the partitioning of Ru, Rh, Ir, Pt and Pd between chromite and silicate melt: the importance of ferric iron. *Chemical Geology*, *302*, 16-32.

Brugman, K. K., & Till, C. B. (2019). A low-aluminum clinopyroxene-liquid geothermometer for high-silica magmatic systems. *American Mineralogist: Journal of Earth and Planetary Materials*, *104*(7), 996-1004.

Bullock, L. A., Gertisser, R., O'Driscoll, B., & Harland, S. (2019). Magmatic evolution and textural development of the 1739 CE Pietre Cotte lava flow, Vulcano, Italy. *Journal of Volcanology and Geothermal Research*, *372*, 1-23.

Campbell, I. H., & Barnes, S. J. (1984). A model for the geochemistry of the platinum-group elements in magmatic sulfide deposits. *The Canadian Mineralogist*, *22*(1), 151-160.

Candela, P. A., & Holland, H. D. (1984). The partitioning of copper and molybdenum between silicate melts and aqueous fluids. *Geochimica et Cosmochimica Acta*, *48*(2), 373-380.

Capasso, G., Favara, R., & Inguaggiato, S. (1997). Chemical features and isotopic composition of gaseous manifestations on Vulcano Island, Aeolian Islands, Italy: an interpretative model of fluid circulation. *Geochimica et Cosmochimica Acta*, *61*(16), 3425-3440.

Capasso, G., Federico, C., Madonia, P., & Paonita, A. (2014). Response of the shallow aquifer of the volcano-hydrothermal system during the recent crises at Vulcano Island (Aeolian Archipelago, Italy). *Journal of volcanology and geothermal research*, *273*, 70-80.

Capobianco, C. J., & Drake, M. J. (1990). Partitioning of ruthenium, rhodium, and palladium between spinel and silicate melt and implications for platinum group element fractionation trends. *Geochimica et Cosmochimica Acta*, *54*(3), 869-874.

Capobianco, C. J., Hervig, R. L., & Drake, M. J. (1994). Experiments on crystal/liquid partitioning ruthenium, rhodium and palladium between spinel and silicate melt implications for platinum group element fractionation trends. *Chemical Geology*, *113*, 23-43.

Caricchi, L., Petrelli, M., Bali, E., Sheldrake, T., Pioli, L., & Simpson, G. (2020). A Data Driven Approach to Investigate the Chemical Variability of Clinopyroxenes From the 2014–2015 Holuhraun–Bárdarbunga Eruption (Iceland). *Frontiers in Earth Science*, *8*, 18.

Carroll, M. R., & Rutherford, M. J. (1985). Sulfide and sulfate saturation in hydrous silicate melts. *Journal of Geophysical Research: Solid Earth*, *90*(S02), C601-C612.

Casalbore, D., Romagnoli, C., Bosman, A., De Astis, G., Lucchi, F., Tranne, C. A., & Chiocci, F. L. (2019). Multi-stage formation of La Fossa Caldera (Vulcano Island, Italy) from an integrated subaerial and submarine analysis. *Marine Geophysical Research*, *40*(4), 479-492.

Cashman, K., & Blundy, J. (2013). Petrological cannibalism: the chemical and textural consequences of incremental magma body growth. *Contributions to Mineralogy and Petrology*, *166*(3), 703-729.

Cashman, K. V., Sparks, R. S. J., & Blundy, J. D. (2017). Vertically extensive and unstable magmatic systems: a unified view of igneous processes. *Science*, *355*(6331).

Chang, J., & Audétat, A. (2018). Petrogenesis and metal content of hornblende-rich xenoliths from two Laramide-age magma systems in southwestern USA: insights into the metal budget of arc magmas. *Journal of Petrology*, *59*(10), 1869-1898.

Charrad, M., Ghazzali, N., Boiteau, V., Niknafs, A., & Charrad, M. M. (2014). Package 'nbclust'. *Journal of statistical software*, *61*, 1-36.

Chen, K., Tang, M., Lee, C. T. A., Wang, Z., Zou, Z., Hu, Z., & Liu, Y. (2020). Sulfide-bearing cumulates in deep continental arcs: The missing copper reservoir. *Earth and Planetary Science Letters*, *531*, 115971.

Cheng, L., & Costa, F. (2019). Statistical analysis of crystal populations and links to volcano deformation for more robust estimates of magma replenishment volumes. *Geology*, *47*(12), 1171-1175.

Cheng, L., Costa, F., & Bergantz, G. (2020). Linking fluid dynamics and olivine crystal scale zoning during simulated magma intrusion. *Contributions to Mineralogy and Petrology*, *175*(6).

Cheng, L., Costa, F., & Carniel, R. (2017). Unraveling the presence of multiple plagioclase populations and identification of representative two-dimensional sections using a statistical and numerical approach. *American Mineralogist*, *102*(9), 1894-1905.

Chiarabba, C., De Gori, P., & Speranza, F. (2008). The southern Tyrrhenian subduction zone: deep geometry, magmatism and Plio-Pleistocene evolution. *Earth and Planetary Science Letters*, *268*(3-4), 408-423.

Chiaradia, M., Pujol-Solà, N., Farré-de-Pablo, J., Aiuppa, A., Paonita, A., Rizzo, A. L., & Brusca, L. (2018). Geochemistry and isotope composition (Sr, Pb, □66Zn) of Vulcano fumaroles (Aeolian Islands, Italy). *Chemical Geology*, 493, 153-171.

Chiodini, G., Cioni, R., Marini, L., & Panichi, C. (1995). Origin of the fumarolic fluids of Vulcano Island, Italy and implications for volcanic surveillance. *Bulletin of Volcanology*, *57*(2), 99-110.

Cioni, R., Bertagnini, A., Santacroce, R., & Andronico, D. (2008). Explosive activity and eruption scenarios at Somma-Vesuvius (Italy): towards a new classification scheme. *Journal of Volcanology and Geothermal Research*, *178*(3), 331-346.

Clocchiatti, R., Del Moro, A., Gioncada, A., Joron, J. L., Mosbah, M., Pinarelli, L., & Sbrana, A. (1994). Assessment of a shallow magmatic system: the 1888–90 eruption, Vulcano Island, Italy. *Bulletin of Volcanology*, *56*(6-7), 466-486.

Cocker, H. A., Valente, D. L., Park, J. W., & Campbell, I. H. (2016). Using platinum group elements to identify sulfide saturation in a porphyry Cu system: the El Abra porphyry Cu deposit, Northern Chile. *Journal of Petrology*, *56*(12), 2491-2514.

Cortés, J. A., Palma, J. L., & Wilson, M. (2007). Deciphering magma mixing: the application of cluster analysis to the mineral chemistry of crystal populations. *Journal of Volcanology and Geothermal Research*, *165*(3-4), 163-188.

Costa, F., & Morgan, D. (2011). Time constraints from chemical equilibration in magmatic crystals. *Timescales of magmatic processes: from core to atmosphere. Wiley, Chichester*, 125-159.

Costa, F., Shea, T., & Ubide, T. (2020b). Diffusion chronometry and the timescales of magmatic processes. *Nature Reviews Earth & Environment*, 1-14.

Costa, S. (2017). Indagini petrografiche e geochimiche sui prodotti piroclastici di Pietre Cotte (Vulcano, Isole Eolie). Considerazioni sulla genesi delle rioliti e degli inclusi magmatici mafici. Tesi di Laurea, Università di Pisa.

Costa, S., Fulignati, P., Gioncada, A., Pistolesi, M., Bosch, D., & Bruguier, O. (2021). Tracking metal evolution in arc magmas: Insights from the active volcano of La Fossa, Italy. *Lithos*, 105851

Costa, S., Masotta, M., Gioncada, A., Pistolesi, M., Bosch, D., & Scarlato, P. (2020). Magma evolution at La Fossa volcano (Vulcano Island, Italy) in the last 1000 years: evidence from eruptive products and temperature gradient experiments. *Contributions to Mineralogy and Petrology*, *175*(4), 1-22.

Cox, D., Watt, S. F., Jenner, F. E., Hastie, A. R., & Hammond, S. J. (2019). Chalcophile element processing beneath a continental arc stratovolcano. *Earth and Planetary Science Letters*, *522*, 1-11.

Crisci, G. M., De Rosa, R., Esperanca, S., Mazzuoli, R., & Sonnino, M. (1991). Temporal evolution of a three component system: the island of Lipari (Aeolian Arc, southern Italy). *Bulletin of Volcanology*, *53*(3), 207-221.

Crocket, J. H. (2000). PGE in fresh basalt, hydrothermal alteration products, and volcanic incrustations of Kilauea volcano, Hawaii. *Geochimica et Cosmochimica Acta*, *64*(10), 1791-1807.

Dale, C. W., Macpherson, C. G., Pearson, D. G., Hammond, S. J., & Arculus, R. J. (2012). Inter-element fractionation of highly siderophile elements in the Tonga Arc due to flux melting of a depleted source. *Geochimica et Cosmochimica Acta*, *89*, 202-225.

Davì, M., De Rosa, R., Donato, P., Vetere, F., Barca, D., & Cavallo, A. (2009). Magmatic Evolution and plumbing system of ring-fault volcanism: the Vulcanello Peninsula (Aeolian Islands, Italy). *European Journal of Mineralogy*, *21*(5), 1009-1028.

Davì, M., De Rosa, R., & Holtz, F. (2010). Mafic enclaves in the rhyolitic products of Lipari historical eruptions; relationships with the coeval Vulcano magmas (Aeolian Islands, Italy). *Bulletin of volcanology*, *72*(8), 991-1008.

Davidson, J., & De Silva, S. (2000). Composite volcanoes. *Encyclopedia of volcanoes*, *1*, 663-681.

De Astis, G., La Volpe, L., Peccerillo, A., & Civetta, L. (1997). Volcanological and petrological evolution of Vulcano island (Aeolian Arc, southern Tyrrhenian Sea). *Journal of Geophysical Research: Solid Earth*, *102*(B4), 8021-8050.

De Astis, G., Lucchi, F., Dellino, P., La Volpe, L., Tranne, C. A., Frezzotti, M. L., & Peccerillo, A. (2013). Geology, volcanic history and petrology of Vulcano (central Aeolian archipelago). *Geological Society, London, Memoirs*, *37*(1), 281-349.

De Astis, G., Peccerillo, A., Kempton, P. D., La Volpe, L., & Wu, T. W. (2000). Calcalkaline to potassium-rich magmatism in the Aeolian Arc: geochemical and Sr, Nd, Pb isotopic constraints from the Island of Vulcano (Aeolian arc). *Contributions to Mineralogy and Petrology*, *139*, 684-703.

De Fino, M., La Volpe, L., & Piccarreta, G. (1991). Role of magma mixing during the recent activity of La Fossa di Vulcano (Aeolian Islands, Italy). *Journal of volcanology and geothermal research*, *48*(3-4), 385-398.

Dellino, P. (1997). Scenario eruttivo ed eruzione massima attesa a La Fossa. *Progetto Vulcano Risultati*.

Dellino, P., De Astis, G., La Volpe, L., Mele, D., & Sulpizio, R. (2011). Quantitative hazard assessment of phreatomagmatic eruptions at Vulcano (Aeolian Islands, Southern Italy) as obtained by combining stratigraphy, event statistics and physical modelling. *Journal of Volcanology and Geothermal Research*, *201*(1-4), 364-384.

Del Moro, A., Gioncada, A., Pinarelli, L., Sbrana, A., & Joron, J. L. (1998). Sr, Nd, and Pb isotope evidence for open system evolution at Vulcano, Aeolian Arc, Italy. *Lithos*, *43*(2), 81-106.

DePaolo, D. J. (1981). Trace element and isotopic effects of combined wallrock assimilation and fractional crystallization. *Earth and planetary science letters*, *53*(2), 189-202.

De Rita, D., Giordano, G., & Milli, S. (1998). Forestepping-backstepping stacking pattern of volcaniclastic successions: Roccamonfina volcano, Italy. *Journal of Volcanology and Geothermal Research*, *80*(1-2), 155-178.

De Ritis, R., Blanco Montenegro, I., Ventura, G., & Chiappini, M. (2005). Aeromagnetic data provide new insights on the volcanism and tectonics of Vulcano Island and offshore areas (southern Tyrrhenian Sea, Italy). *Geophysical research letters*, *32*(15).

Deering, C. D., Cole, J. W., & Vogel, T. A. (2011). Extraction of crystal-poor rhyolite from a hornblende-bearing intermediate mush: a case study of the caldera-forming Matahina eruption, Okataina volcanic complex. *Contributions to Mineralogy and Petrology*, *161*(1), 129-151.

Di Martino, R. M., Capasso, G., Camarda, M., De Gregorio, S., & Prano, V. (2020). Deep CO2 release revealed by stable isotope and diffuse degassing surveys at Vulcano (Aeolian Islands) in 2015–2018. *Journal of Volcanology and Geothermal Research*, *401*, 106972.

D'Oriano, C., Bertagnini, A., & Pompilio, M. (2011). Ash erupted during normal activity at Stromboli (Aeolian Islands, Italy) raises questions on how the feeding system works. *Bulletin of Volcanology*, *73*(5), 471-477.

Di Traglia, F. (2011). The last 1000 years of eruptive activity at the Fossa Cone (Island of Vulcano, Southern Italy). PhD Thesis, University of Pisa.

Di Traglia, F., Pistolesi, M., Rosi, M., Bonadonna, C., Fusillo, R., & Roverato, M. (2013). Growth and erosion: The volcanic geology and morphological evolution of La Fossa (Island of Vulcano, Southern Italy) in the last 1000 years. *Geomorphology*, *194*, 94-107.

Di Stefano, F., Mollo, S., Ubide, T., Petrone, C. M., Caulfield, J., Scarlato, P., & Del Bello, E. (2020). Mush cannibalism and disruption recorded by clinopyroxene phenocrysts at Stromboli volcano: New insights from recent 2003–2017 activity. *Lithos*, *360*, 105440.

Downes, M. J. (1974). Sector and oscillatory zoning in calcic augites from M. Etna, Sicily. *Contributions to Mineralogy and Petrology*, *47*(3), 187-196.

Du, J., & Audétat, A. (2020). Early sulfide saturation is not detrimental to porphyry Cu-Au formation. *Geology*, *48*(5), 519-524.

Dufek, J., & Bachmann, O. (2010). Quantum magmatism: Magmatic compositional gaps generated by melt-crystal dynamics. *Geology*, *38*(8), 687-690.

Edmonds, M., Cashman, K. V., Holness, M., & Jackson, M. (2019). Architecture and dynamics of magma reservoirs.

Edmonds, M., & Mather, T. A. (2017). Volcanic sulfides and outgassing. *Elements*, *13*(2), 105-110.

Ellam, R. M., & Harmon, R. S. (1990). Oxygen isotope constraints on the crustal contribution to the subduction-related magmatism of the Aeolian Islands, southern Italy. *Journal of Volcanology and Geothermal Research*, *44*(1-2), 105-122.

Ellam, R. M., Menzies, M. A., Hawkesworth, C. J., Leeman, W. P., Rosi, M., & Serri, G. (1988). The transition from calc-alkaline to potassic orogenic magmatism in the Aeolian Islands, Southern Italy. *Bulletin of Volcanology*, *50*(6), 386-398.

Esperança, S., Crisci, G. M., De Rosa, R., & Mazzuoli, R. (1992). The role of the crust in the magmatic evolution of the island of Lipari (Aeolian Islands, Italy). *Contributions to Mineralogy and Petrology*, *112*(4), 450-462.

Faraone, D., Silvano, A., & Verdiani, G. (1986). The monzogabbroic intrusion in the island of Vulcano, Aeolian Archipelago, Italy. *Bulletin of volcanology*, *48*(5), 299-307.

Folzani, F. (2019). Studio delle sequenze cineritiche di Palizzi (Vulcano, Isole Eolie): implicazioni sulle dinamiche eruttive e messa in posto. Tesi di laurea, Università di Pisa.

Fonseca, R. O., Campbell, I. H., O'Neill, H. S. C., & Allen, C. M. (2009). Solubility of Pt in sulphide mattes: Implications for the genesis of PGE-rich horizons in layered intrusions. *Geochimica et Cosmochimica Acta*, *73*(19), 5764-5777.

Forni, F., Degruyter, W., Bachmann, O., De Astis, G., & Mollo, S. (2018a). Long-term magmatic evolution reveals the beginning of a new caldera cycle at Campi Flegrei. *Science advances*, *4*(11), eaat9401.

Forni, F., Ellis, B. S., Bachmann, O., Lucchi, F., Tranne, C. A., Agostini, S., & Dallai, L. (2015). Erupted cumulate fragments in rhyolites from Lipari (Aeolian Islands). *Contributions to Mineralogy and Petrology*, *170*(5-6), 49.

Forni, F., Petricca, E., Bachmann, O., Mollo, S., De Astis, G., & Piochi, M. (2018b). The role of magma mixing/mingling and cumulate melting in the Neapolitan Yellow Tuff caldera-forming eruption (Campi Flegrei, Southern Italy). *Contributions to Mineralogy and Petrology*, *173*(6), 45.

Fortin, M. A., Riddle, J., Desjardins-Langlais, Y., & Baker, D. R. (2015). The effect of water on the sulfur concentration at sulfide saturation (SCSS) in natural melts. *Geochimica et Cosmochimica Acta*, *160*, 100-116.

Francalanci, L., Avanzinelli, R., Petrone, C. M., & Santo, A. (2004). Petrochemical and magmatological characteristics of the Aeolian Arc volcanoes, southern Tyrrhenian Sea, Italy: inferences on shallow level processes and magma source variations. *Periodico di Mineralogia*, *73*(Special issue 1), 75-104.

Francalanci, L., Avanzinelli, R., Tommasini, S., & Heuman, A. (2007). A west-east geochemical and isotopic traverse along the volcanism of the Aeolian Island arc, southern Tyrrhenian Sea, Italy: Inferences on mantle source processes. *SPECIAL PAPERS-GEOLOGICAL SOCIETY OF AMERICA*, *418*, 235.

Frazzetta, G. (1991). Volcanic history and maximum expected eruption at" La Fossa di Vulcano"(Aeolian Islands, Italy). *Acta Vulcanologica*, *1*, 107-113.

Frazzetta, G., Gillot, P. Y., La Volpe, L., & Sheridan, M. F. (1984). Volcanic hazards at Fossa of Vulcano: data from the last 6,000 years. *Bulletin volcanologique*, *47*(1), 105-124.

Frazzetta, G., Lanzafame, G., & Villari, L. (1982). Deformazioni e tettonica a Lipari e Vulcano (Eolie). *Memorie della Società Geologica Italiana*, *24*, 293-297.

Frazzetta, G., La Volpe, L., & Sheridan, M. F. (1983). Evolution of the Fossa cone, Vulcano. *Journal of Volcanology and Geothermal Research*, *17*(1-4), 329-360.

Frezzotti, M. L., Peccerillo, A., Zanon, V., & Nikogosian, I. (2004). Silica-rich melts in quartz xenoliths from Vulcano Island and their bearing on processes of crustal anatexis and crust–magma interaction beneath the Aeolian Arc, Southern Italy. *Journal of petrology*, *45*(1), 3-26.

Fulignati, P., Gioncada, A., Costa, S., Di Genova, D., Di Traglia, F., & Pistolesi, M. (2018). Magmatic sulfide immiscibility at an active magmatic-hydrothermal system: The case of La Fossa (Vulcano, Italy). *Journal of Volcanology and Geothermal Research*, *358*, 45-57.

Fulignati, P., Gioncada, A., & Sbrana, A. (1998). Geologic model of the magmatichydrothermal system of vulcano (Aeolian Islands, Italy). *Mineralogy and Petrology*, *62*(3-4), 195-222.

Fusillo, R., Di Traglia, F., Gioncada, A., Pistolesi, M., Wallace, P. J., & Rosi, M. (2015). Deciphering post-caldera volcanism: insight into the Vulcanello (Island of Vulcano, Southern Italy) eruptive activity based on geological and petrological constraints. *Bulletin of Volcanology*, *77*(9), 76.

Garuti, G., Pushkarev, E. V., & Zaccarini, F. (2002). Composition and paragenesis of Pt alloys from chromitites of the Uralian–Alaskan-type Kytlym and Uktus complexes, northern and central Urals, Russia. *The Canadian Mineralogist*, *40*(4), 1127-1146.

Garuti, G., Pushkarev, E. V., Zaccarini, F., Cabella, R., & Anikina, E. (2003). Chromite composition and platinum-group mineral assemblage in the Uktus Uralian-Alaskan-type complex (Central Urals, Russia). Mineralium Deposita, 38(3), 312-326.

Gelman, S. E., Deering, C. D., Bachmann, O., Huber, C., & Gutierrez, F. J. (2014). Identifying the crystal graveyards remaining after large silicic eruptions. *Earth and Planetary Science Letters*, *403*, 299-306.

Georgatou, A., & Chiaradia, M. (2020). Magmatic sulfides in high-potassium calc-alkaline to shoshonitic and alkaline rocks. *Solid Earth*, *11*(1), 1-21.

Georgatou, A., Chiaradia, M., Rezeau, H., & Wälle, M. (2018). Magmatic sulphides in Quaternary Ecuadorian arc magmas. *Lithos*, *296*, 580-599.

Giacomoni, P. P., Coltorti, M., Bryce, J. G., Fahnestock, M. F., & Guitreau, M. (2016). Mt. Etna plumbing system revealed by combined textural, compositional, and thermobarometric studies in clinopyroxenes. *Contributions to Mineralogy and Petrology*, 171(4), 34.

Gioncada, A. (1997). *L'attività eruttiva degli ultimi 50000 anni di Vulcano (Eolie): aspetti vulcanologici e magmatologici"* (Doctoral dissertation, Tesi di Dottorato, Università degli Studi di Pisa).

Gioncada, A., Clocchiatti, R., Sbrana, A., Bottazzi, P., Massare, D., & Ottolini, L. (1998). A study of melt inclusions at Vulcano (Aeolian Islands, Italy): insights on the primitive magmas and on the volcanic feeding system. *Bulletin of Volcanology*, *60*(4), 286-306.

Gioncada, A., Mazzuoli, R., Bisson, M., & Pareschi, M. T. (2003). Petrology of volcanic products younger than 42 ka on the Lipari–Vulcano complex (Aeolian Islands, Italy): an example of volcanism controlled by tectonics. *Journal of Volcanology and Geothermal Research*, *122*(3-4), 191-220.

Gioncada, A., & Sbrana, A. (1991). "La Fossa caldera", Vulcano: inferences from deep drillings.

Granieri, D., Carapezza, M. L., Chiodini, G., Avino, R., Caliro, S., Ranaldi, M., & Tarchini, L. (2006). Correlated increase in CO2 fumarolic content and diffuse emission from La Fossa crater (Vulcano, Italy): Evidence of volcanic unrest or increasing gas release from a stationary deep magma body?. *Geophysical Research Letters*, *33*(13).

Gurioli, L., Zanella, E., Gioncada, A., & Sbrana, A. (2012). The historic magmatic-hydrothermal eruption of the Breccia di Commenda, Vulcano, Italy. *Bulletin of volcanology*, *74*(5), 1235-1254.

Halter, W. E., Heinrich, C. A., & Pettke, T. (2005). Magma evolution and the formation of porphyry Cu–Au ore fluids: evidence from silicate and sulfide melt inclusions. *Mineralium Deposita*, *39*(8), 845-863.

Halter, W. E., Pettke, T., & Heinrich, C. A. (2002). The origin of Cu/Au ratios in porphyry-type ore deposits. *Science*, *296*(5574), 1844-1846.

Hao, H., Campbell, I. H., Park, J. W., & Cooke, D. R. (2017). Platinum-group element geochemistry used to determine Cu and Au fertility in the Northparkes igneous suites, New South Wales, Australia. *Geochimica et Cosmochimica Acta*, *216*, 372-392.

Hao, H., Campbell, I. H., Richards, J. P., Nakamura, E., & Sakaguchi, C. (2019). Platinum-group element geochemistry of the Escondida igneous suites, Northern Chile: implications for ore formation. *Journal of Petrology*, *60*(3), 487-514.

Hartung, E., Weber, G., & Caricchi, L. (2019). The role of H2O on the extraction of melt from crystallising magmas. *Earth and Planetary Science Letters*, *508*, 85-96.

Hedenquist, J. W., & Lowenstern, J. B. (1994). The role of magmas in the formation of hydrothermal ore deposits. *Nature*, *370*(6490), 519-527.

Huang, F., Lundstrom, C. C., Glessner, J., Ianno, A., Boudreau, A., Li, J.,& DeFrates, J. (2009). Chemical and isotopic fractionation of wet andesite in a temperature gradient: experiments and models suggesting a new mechanism of magma differentiation. *Geochimica et Cosmochimica Acta*, *73*(3), 729-749.

Huang, M. L., Gao, J. F., Bi, X. W., Xu, L. L., Zhu, J. J., & Wang, D. P. (2020). The role of early sulfide saturation in the formation of the Yulong porphyry Cu-Mo deposit: Evidence from mineralogy of sulfide melt inclusions and platinum-group element geochemistry. *Ore Geology Reviews*, 103644.

Huebner, J. S., & Sato, M. (1970). The oxygen fugacity-temperature relationships of manganese oxide and nickel oxide buffers. *American Mineralogist: Journal of Earth and Planetary Materials*, *55*(5-6), 934-952.

Inguaggiato, S., Diliberto, I. S., Federico, C., Paonita, A., & Vita, F. (2018). Review of the evolution of geochemical monitoring, networks and methodologies applied to the volcanoes of the Aeolian Arc (Italy). *Earth-Science Reviews*, *176*, 241-276.

Inguaggiato, S., Mazot, A., Diliberto, I. S., Inguaggiato, C., Madonia, P., Rouwet, D., & Vita, F. (2012). Total CO2 output from Vulcano island (Aeolian Islands, Italy). *Geochemistry, Geophysics, Geosystems*, *13*(2).

Ireland, T. J., Walker, R. J., & Garcia, M. O. (2009). Highly siderophile element and ^{187}Os isotope systematics of Hawaiian picrites: implications for parental melt composition and source heterogeneity. *Chemical Geology*, *260*(1-2), 112-128.

Itano, K., Ueki, K., Iizuka, T., & Kuwatani, T. (2020). Geochemical discrimination of monazite source rock based on machine learning techniques and multinomial logistic regression analysis. *Geosciences*, *10*(2), 63.

Jarosewich, E., Nelen, J. A., & Norberg, J. A. (1980). Reference samples for electron microprobe analysis. *Geostandards Newsletter*, *4*(1), 43-47.

Jenner, F. E., Hauri, E. H., Bullock, E. S., König, S., Arculus, R. J., Mavrogenes, J. A., & Goddard, C. (2015). The competing effects of sulfide saturation versus degassing on the behavior of the chalcophile elements during the differentiation of hydrous melts. *Geochemistry, Geophysics, Geosystems*, *16*(5), 1490-1507.

Jenner, F. E., O'Neill, H. S. C., Arculus, R. J., & Mavrogenes, J. A. (2010). The magnetite crisis in the evolution of arc-related magmas and the initial concentration of Au, Ag and Cu. *Journal of Petrology*, *51*(12), 2445-2464.

Jugo, P. J., Wilke, M., & Botcharnikov, R. E. (2010). Sulfur K-edge XANES analysis of natural and synthetic basaltic glasses: Implications for S speciation and S content as function of oxygen fugacity. *Geochimica et Cosmochimica Acta*, *74*(20), 5926-5938.

Kahl, M., Chakraborty, S., Costa, F., & Pompilio, M. (2011). Dynamic plumbing system beneath volcanoes revealed by kinetic modeling, and the connection to monitoring data: An example from Mt. Etna. *Earth and Planetary Science Letters*, *308*(1-2), 11-22.

Kamenetsky, V., & Clocchiatti, R. (1996). Primitive magmatism of Mt. Etna: insights from mineralogy and melt inclusions. *Earth and Planetary Science Letters*, *142*(3-4), 553-572.

Keays, R. R., & Tegner, C. (2015). Magma chamber processes in the formation of the low-sulphide magmatic Au–PGE mineralization of the Platinova Reef in the Skaergaard Intrusion, East Greenland. *Journal of Petrology*, 56(12), 2319-2340.

Keith, J. D., Whitney, J. A., Hattori, K., Ballantyne, G. H., Christiansen, E. H., Barr, D. L., & Hook, C. J. (1997). The role of magmatic sulfides and mafic alkaline magmas in the Bingham and Tintic mining districts, Utah. *Journal of Petrology*, *38*(12), 1679-1690.

Keller, J. (1980). The island of Vulcano.

Lanzo, G., Di Carlo, I., Pichavant, M., Rotolo, S. G., & Scaillet, B. (2016). Origin of primitive ultra-calcic arc melts at crustal conditions—Experimental evidence on the La Sommata basalt, Vulcano, Aeolian Islands. *Journal of Volcanology and Geothermal Research*, *321*, 85-101.

Laumonier, M., Laporte, D., Faure, F., Provost, A., Schiano, P., & Ito, K. (2019). An experimental study of dissolution and precipitation of forsterite in a thermal gradient: implications for cellular growth of olivine phenocrysts in basalt and melt inclusion formation. *Contributions to Mineralogy and Petrology*, *174*(11), 94.

La Volpe L., Dellino P., Nuccio M., Privitera E., S. A. (1997). "Progetto Vulcano. Risultati delle attività di ricerca 1993-1995." CNR- Gruppo Nazionale per La Vulcanologia. Felici Editore, 214–237.

Lezzerini, M., Tamponi, M., & Bertoli, M. (2013). Reproducibility, precision and trueness of X-ray fluorescence data for mineralogical and/or petrographic purposes. *Atti Società Toscana Scienze Naturali Memorie, Serie A*, *120*, 67-73.

Le Voyer, M., Asimow, P. D., Mosenfelder, J. L., Guan, Y., Wallace, P. J., Schiano, P., & Eiler, J. M. (2014). Zonation of H2O and F concentrations around melt inclusions in olivines. *Journal of Petrology*, *55*(4), 685-707.

Li, X., Zhang, C., Almeev, R. R., & Holtz, F. (2020a). GeoBalance: An Excel VBA program for mass balance calculation in geosciences. *Geochemistry*, 125629.

Li, X., Zhang, C., Behrens, H., & Holtz, F. (2020b). Calculating amphibole formula from electron microprobe analysis data using a machine learning method based on principal components regression. *Lithos*, 105469.

Li, Y., & Audétat, A. (2015). Effects of temperature, silicate melt composition, and oxygen fugacity on the partitioning of V, Mn, Co, Ni, Cu, Zn, As, Mo, Ag, Sn, Sb, W, Au, Pb, and Bi between sulfide phases and silicate melt. *Geochimica et Cosmochimica Acta*, *162*, 25-45.

Lofgren, G. E., Huss, G. R., & Wasserburg, G. J. (2006). An experimental study of trace-element partitioning between Ti-Al-clinopyroxene and melt: Equilibrium and kinetic effects including sector zoning. *American Mineralogist*, *91*(10), 1596-1606.

Lowczak, J. N., Campbell, I. H., Cocker, H., Park, J. W., & Cooke, D. R. (2018). Platinum-group element geochemistry of the Forest Reef Volcanics, southeastern Australia: Implications for porphyry Au-Cu mineralisation. *Geochimica et Cosmochimica Acta*, *220*, 385-406.

Magee, R., Ubide, T., & Kahl, M. (2020). The lead-up to Mount Etna's most destructive historic eruption (1669). Cryptic recharge recorded in clinopyroxene. *Journal of Petrology*.

Mandarano, M., Paonita, A., Martelli, M., Viccaro, M., Nicotra, E., & Millar, I. L. (2016). Revealing magma degassing below closed-conduit active volcanoes: geochemical features of volcanic rocks versus fumarolic fluids at Vulcano (Aeolian Islands, Italy). *Lithos*, *248*, 272-287.

Mannini, S., Harris, A. J., Jessop, D. E., Chevrel, M. O., & Ramsey, M. S. (2019). Combining Ground- and ASTER-Based Thermal Measurements to Constrain Fumarole Field Heat Budgets: The Case of Vulcano Fossa 2000–2019. *Geophysical Research Letters*, *46*(21), 11868-11877.

Marsh, B. D. (2002). On bimodal differentiation by solidification front instability in basaltic magmas, part 1: basic mechanics. *Geochimica et Cosmochimica Acta*, *66*(12), 2211-2229.

Marsh, B. D. (1996). Solidification fronts and magmatic evolution. *Mineralogical Magazine*, *60*(398), 5-40.

Marshall, A. S., Hinton, R. W., & MacDonald, R. (1998). Phenocrystic fluorite in peralkaline rhyolites, Olkaria, Kenya rift valley. *Mineralogical Magazine*, *62*(4), 477-486.

Masotta, M., Freda, C., Paul, T. A., Moore, G. M., Gaeta, M., Scarlato, P., & Troll, V. R. (2012a). Low pressure experiments in piston cylinder apparatus: Calibration of newly designed 25 mm furnace assemblies to P= 150 MPa. *Chemical geology*, *312*, 74-79.

Masotta, M., Freda, C., & Gaeta, M. (2012b). Origin of crystal-poor, differentiated magmas: insights from thermal gradient experiments. *Contributions to Mineralogy and Petrology*, *163*(1), 49-65.

Masotta, M., & Mollo, S. (2019). A new plagioclase-liquid hygrometer specific to trachytic systems. *Minerals*, *9*(6), 375.

Masotta, M., Mollo, S., Freda, C., Gaeta, M., & Moore, G. (2013). Clinopyroxene–liquid thermometers and barometers specific to alkaline differentiated magmas. *Contributions to Mineralogy and Petrology*, *166*(6), 1545-1561.

Masotta, M., Mollo, S., Nazzari, M., Tecchiato, V., Scarlato, P., Papale, P., & Bachmann, O. (2018). Crystallization and partial melting of rhyolite and felsite rocks at Krafla volcano: A comparative approach based on mineral and glass chemistry of natural and experimental products. *Chemical Geology*, *483*, 603-618.

Masotta, M., Pontesilli, A., Mollo, S., Armienti, P., Ubide, T., Nazzari, M., & Scarlato, P. (2020). The role of undercooling during clinopyroxene growth in trachybasaltic magmas: Insights on magma decompression and cooling at Mt. Etna volcano. *Geochimica et Cosmochimica Acta*, *268*, 258-276.

Mazzuoli, R., Tortorici, L., & Ventura, G. (1995). Oblique rifting in Salina, Lipari and Vulcano islands (Aeolian islands, southern Italy). *Terra Nova*, *7*(4), 444-452.

Meisel, T., Fellner, N., & Moser, J. (2003). A simple procedure for the determination of platinum group elements and rhenium (Ru, Rh, Pd, Re, Os, Ir and Pt) using ID-ICP-MS with an inexpensive on-line matrix separation in geological and environmental materials. *Journal of Analytical Atomic Spectrometry*, *18*(7), 720-726.

Mercalli, G., & Silvestri, O. (1891). Le eruzioni dell'Isola di Vulcano incominciate il 3 agosto 1888 e terminate il 22 marzo 1890, relazione scientifica. *Ann Ufficio Centrale Metereol Geodin Ital*, *10*, 1-213.

Meschiari, S., Albert, P. G., Lucchi, F., Sulpizio, R., Smith, V. C., Kearney, R., & Tranne, C. A. (2020). Frequent activity on Vulcano (Italy) spanning the last 80 ky: New insights from the chemo-stratigraphy of the Brown Tuffs. *Journal of Volcanology and Geothermal Research*, 406, 107079.

Metrich, N., & Clocchiatti, R. (1996). Sulfur abundance and its speciation in oxidized alkaline melts. *Geochimica et Cosmochimica Acta*, *60*(21), 4151-4160.

Mollo, S., Blundy, J. D., Iezzi, G., Scarlato, P., & Langone, A. (2013b). The partitioning of trace elements between clinopyroxene and trachybasaltic melt during rapid cooling and crystal growth. *Contributions to Mineralogy and Petrology*, *166*(6), 1633-1654.

Mollo, S., Blundy, J., Scarlato, P., De Cristofaro, S. P., Tecchiato, V., Di Stefano, F., & Bachmann, O. (2018). An integrated PT-H2O-lattice strain model to quantify the role of clinopyroxene fractionation on REE+ Y and HFSE patterns of mafic alkaline magmas: Application to eruptions at Mt. Etna. *Earth-Science Reviews*, *185*, 32-56.

Mollo, S., Del Gaudio, P., Ventura, G., Iezzi, G., & Scarlato, P. (2010). Dependence of clinopyroxene composition on cooling rate in basaltic magmas: implications for thermobarometry. *Lithos*, *118*(3-4), 302-312.

Mollo, S., & Hammer, J. E. (2017). Dynamic crystallization in magmas. *EMU Notes in Mineralogy*, *16*, 373-418.

Mollo, S., & Masotta, M. (2014). Optimizing pre-eruptive temperature estimates in thermally and chemically zoned magma chambers. *Chemical Geology*, *368*, 97-103.

Mollo, S., Masotta, M., Forni, F., Bachmann, O., De Astis, G., Moore, G., & Scarlato, P. (2015). A K-feldspar–liquid hygrometer specific to alkaline differentiated magmas. *Chemical Geology*, *392*, 1-8.

Mollo, S., Putirka, K., Misiti, V., Soligo, M., & Scarlato, P. (2013a). A new test for equilibrium based on clinopyroxene–melt pairs: Clues on the solidification temperatures of Etnean alkaline melts at post-eruptive conditions. *Chemical Geology*, *352*, 92-100.

Morgan, D. J., & Blake, S. (2006). Magmatic residence times of zoned phenocrysts: introduction and application of the binary element diffusion modelling (BEDM) technique. *Contributions to Mineralogy and Petrology*, *151*(1), 58-70.

Morgavi, D., Perugini, D., De Campos, C. P., Ertel-Ingrisch, W., & Dingwell, D. B. (2013). Time evolution of chemical exchanges during mixing of rhyolitic and basaltic melts. *Contributions to Mineralogy and Petrology*, *166*(2), 615-638.

Morimoto, N., Fabries, J., & Ferguson, A. K. (1988). Pyroxene nomenclature. *Mineral. Petrol*, *39*, 55-76.

Mungall, J. E., & Brenan, J. M. (2014). Partitioning of platinum-group elements and Au between sulfide liquid and basalt and the origins of mantle-crust fractionation of the chalcophile elements. *Geochimica et Cosmochimica Acta*, *125*, 265-289.

Mungall, J. E., Brenan, J. M., Godel, B., Barnes, S. J., & Gaillard, F. (2015). Transport of metals and sulphur in magmas by flotation of sulphide melt on vapour bubbles. *Nature Geoscience*, *8*(3), 216-219.

Nadeau, O. (2015). Economic geology: Ore metals beneath volcanoes. *Nature Geoscience*, *8*(3), 168-170.

Nadeau, O., Williams-Jones, A. E., & Stix, J. (2010). Sulphide magma as a source of metals in arc-related magmatic hydrothermal ore fluids. *Nature Geoscience*, *3*(7), 501-505.

Nadeau, O., Stix, J., & Williams-Jones, A. E. (2016). Links between arc volcanoes and porphyry-epithermal ore deposits. *Geology*, *44*(1), 11-14.

Neave, D. A., & Putirka, K. D. (2017). A new clinopyroxene-liquid barometer, and implications for magma storage pressures under Icelandic rift zones. *American Mineralogist*, *102*(4), 777-794.

Németh, K., & Cronin, S. J. (2008). Volcanic craters, pit craters and high-level magma-feeding systems of a mafic island-arc volcano: Ambrym, Vanuatu, South Pacific. *Geological Society, London, Special Publications*, *302*(1), 87-102.

Németh, K., Cronin, S. J., Stewart, R. B., & Charley, D. (2009). Intra-and extra-caldera volcaniclastic facies and geomorphic characteristics of a frequently active mafic island–arc volcano, Ambrym Island, Vanuatu. *Sedimentary Geology*, *220*(3-4), 256-270.

Neri, A., Aspinall, W. P., Cioni, R., Bertagnini, A., Baxter, P. J., Zuccaro, G., & Hincks, T. K. (2008). Developing an event tree for probabilistic hazard and risk assessment at Vesuvius. *Journal of volcanology and geothermal research*, *178*(3), 397-415.

Newman, S., & Lowenstern, J. B. (2002). VolatileCalc: a silicate melt–H2O–CO2 solution model written in Visual Basic for excel. *Computers & Geosciences*, *28*(5), 597-604.

Nicotra, E., Giuffrida, M., Viccaro, M., Donato, P., D'Oriano, C., Paonita, A., & De Rosa, R. (2018). Timescales of pre-eruptive magmatic processes at Vulcano (Aeolian Islands, Italy) during the last 1000 years. *Lithos*, *316*, 347-365.

Nicotra, E., Minniti, M., Donato, P., & De Rosa, R. (2020). Insights into the eruptive dynamics of small caldera-forming eruptions: the case study of the welded scoriae of Vulcano (Aeolian Islands, Italy). *Frontiers in Earth Science*, *8*, 223.

O'Neill, H. S. C., & Mavrogenes, J. A. (2002). The sulfide capacity and the sulfur content at sulfide saturation of silicate melts at 1400 C and 1 bar. *Journal of Petrology*, *43*(6), 1049-1087.

Oppenheimer, J., Rust, A. C., Cashman, K. V., & Sandnes, B. (2015). Gas migration regimes and outgassing in particle-rich suspensions. *Frontiers in Physics*, *3*, 60.

Palummo, F., Mollo, S., De Astis, G., Di Stefano, F., Nazzari, M., & Scarlato, P. (2020). Petrological and geochemical modeling of magmas erupted at Vulcano Island in the period 54–8 ka: Quantitative constraints on the sub-volcanic architecture of the plumbing system. *Lithos*, *374*, 105715.

Paonita, A., Federico, C., Bonfanti, P., Capasso, G., Inguaggiato, S., Italiano, F., & Sortino, F. (2013). The episodic and abrupt geochemical changes at La Fossa fumaroles (Vulcano Island, Italy) and related constraints on the dynamics, structure, and compositions of the magmatic system. *Geochimica et cosmochimica acta*, *120*, 158-178.

Parat, F., Holtz, F., & Streck, M. J. (2011). Sulfur-bearing magmatic accessory minerals. *Reviews in Mineralogy and Geochemistry*, *73*(1), 285-314.

Park, J. W., & Campbell, I. (2021). Platinum-group element geochemistry of the volcanic rocks associated with the Jaguar and Bentley Cu–Zn volcanogenic massive sulfide (VMS) deposits, Western Australia: implications for the role of chalcophile element fertility on VMS mineralization. *Mineralium Deposita*, 1-18.

Park, J. W., Campbell, I. H., & Arculus, R. J. (2013b). Platinum-alloy and sulfur saturation in an arc-related basalt to rhyolite suite: Evidence from the Pual Ridge lavas, the Eastern Manus Basin. *Geochimica et Cosmochimica Acta*, *101*, 76-95.

Park, J. W., Campbell, I. H., & Eggins, S. M. (2012b). Enrichment of Rh, Ru, Ir and Os in Cr spinels from oxidized magmas: evidence from the Ambae volcano, Vanuatu. *Geochimica et Cosmochimica Acta*, *78*, 28-50.

Park, J. W., Campbell, I. H., Ickert, R. B., & Allen, C. M. (2013a). Chalcophile element geochemistry of the Boggy Plain zoned pluton, southeastern Australia: a S-saturated barren compositionally diverse magmatic system. *Contributions to Mineralogy and Petrology*, *165*(2), 217-236.

Park, J. W., Campbell, I. H., Kim, J., & Moon, J. W. (2015). The role of late sulfide saturation in the formation of a Cu-and Au-rich magma: Insights from the platinum group element geochemistry of Niuatahi–Motutahi lavas, Tonga rear arc. *Journal of Petrology*, *56*(1), 59-81.

Park, J. W., Campbell, I. H., Malaviarachchi, S. P., Cocker, H., Hao, H., & Kay, S. M. (2019). Chalcophile element fertility and the formation of porphyry Cu±Au deposits. *Mineralium Deposita*, *54*(5), 657-670.

Park, J. W., Hu, Z., Gao, S., Campbell, I. H., & Gong, H. (2012a). Platinum group element abundances in the upper continental crust revisited–New constraints from analyses of Chinese loess. *Geochimica et Cosmochimica Acta*, *93*, 63-76.

Parmigiani, A., Huber, C., & Bachmann, O. (2014). Mush microphysics and the reactivation of crystal-rich magma reservoirs. *Journal of Geophysical Research: Solid Earth*, *119*(8), 6308-6322.

Peccerillo, A. (2005). *Plio-quaternary volcanism in Italy* (Vol. 365). New York: Springer-Verlag Berlin Heidelberg.

Peccerillo, A., Frezzotti, M. L., De Astis, G., & Ventura, G. (2006). Modeling the magma plumbing system of Vulcano (Aeolian Islands, Italy) by integrated fluid-inclusion geobarometry, petrology, and geophysics. *Geology*, *34*(1), 17-20.

Peccerillo, A., De Astis, G., Faraone, D., Forni, F., & Frezzotti, M. L. (2013). Compositional variations of magmas in the Aeolian arc: implications for petrogenesis and geodynamics. *Geological Society, London, Memoirs*, *37*(1), 491-510.

Peccerillo, A., & Taylor, S. R. (1976). Geochemistry of Eocene calc-alkaline volcanic rocks from the Kastamonu area, northern Turkey. *Contributions to mineralogy and petrology*, *58*(1), 63-81.

Perinelli, C., Mollo, S., Gaeta, M., De Cristofaro, S. P., Palladino, D. M., Armienti, P., & Putirka, K. D. (2016). An improved clinopyroxene-based hygrometer for Etnean magmas and implications for eruption triggering mechanisms. *American Mineralogist*, *101*(12), 2774-2777.

Perugini, D., De Campos, C. P., Dingwell, D. B., & Dorfman, A. (2013). Relaxation of concentration variance: a new tool to measure chemical element mobility during mixing of magmas. *Chemical Geology*, *335*, 8-23.

Perugini, D., De Campos, C. P., Petrelli, M., & Dingwell, D. B. (2015). Concentration variance decay during magma mixing: a volcanic chronometer. *Scientific reports*, *5*, 14225.

Perugini, D., Valentini, L., & Poli, G. (2007). Insights into magma chamber processes from the analysis of size distribution of enclaves in lava flows: A case study from Vulcano Island (Southern Italy). *Journal of Volcanology and Geothermal Research*, *166*(3-4), 193-203.

Petford, N., Koenders, M. A., & Clemens, J. D. (2020). Igneous differentiation by deformation. *Contributions to Mineralogy and Petrology*, *175*(5), 1-21.

Petrelli, M., Bizzarri, R., Morgavi, D., Baldanza, A., & Perugini, D. (2017). Combining machine learning techniques, microanalyses and large geochemical datasets for tephrochronological studies in complex volcanic areas: New age constraints for the Pleistocene magmatism of central Italy. *Quaternary Geochronology*, *40*, 33-44.

Petrelli, M., Caricchi, L., & Perugini, D. (2020). Machine Learning Thermo□Barometry: Application to Clinopyroxene□Bearing Magmas. *Journal of Geophysical Research: Solid Earth*, *125*(9), e2020JB020130.

Petrelli, M., & Perugini, D. (2016). Solving petrological problems through machine learning: the study case of tectonic discrimination using geochemical and isotopic data. *Contributions to Mineralogy and Petrology*, *171*(10), 81.

Petrone, C. M., Braschi, E., Francalanci, L., Casalini, M., & Tommasini, S. (2018). Rapid mixing and short storage timescale in the magma dynamics of a steady-state volcano. *Earth and Planetary Science Letters*, *492*, 206-221.

Pinarelli, L., Gioncada, A., Capaccioni, B., Vaselli, O., & Downes, H. (2019). Mantle source heterogeneity in subduction zones: constraints from elemental and isotope (Sr, Nd, and Pb) data on Vulcano Island, Aeolian Archipelago, Italy. *Mineralogy and Petrology*, *113*(1), 39-60.

Pichavant, M., Scaillet, B., Pommier, A., Iacono-Marziano, G., & Cioni, R. (2014). Nature and evolution of primitive Vesuvius magmas: an experimental study. *Journal of Petrology*, 55(11), 2281-2310.

Piochi, M., De Astis, G., Petrelli, M., Ventura, G., Sulpizio, R., & Zanetti, A. (2009). Constraining the recent plumbing system of Vulcano (Aeolian Arc, Italy) by textural, petrological, and fractal analysis: The 1739 AD Pietre Cotte lava flow. *Geochemistry, Geophysics, Geosystems*, *10*(1).

Pistone, M., Arzilli, F., Dobson, K. J., Cordonnier, B., Reusser, E., Ulmer, P., ... & Blundy, J. D. (2015). Gas-driven filter pressing in magmas: Insights into in-situ melt segregation from crystal mushes. *Geology*, *43*(8), 699-702.

Pistone, M., Blundy, J., & Brooker, R. A. (2017). Water transfer during magma mixing events: Insights into crystal mush rejuvenation and melt extraction processes. *American Mineralogist*, *102*(4), 766-776.

Pistone, M., Caricchi, L., Ulmer, P., Reusser, E., & Ardia, P. (2013). Rheology of volatile-bearing crystal mushes: mobilization vs. viscous death. *Chemical Geology*, *345*, 16-39.
Pitcher, L., Helz, R. T., Walker, R. J., & Piccoli, P. (2009). Fractionation of the platinum-group elments and Re during crystallization of basalt in Kilauea Iki Lava Lake, Hawaii. *Chemical Geology*, *260*(3-4), 196-210.

Pokrovski, G. S., Borisova, A. Y., & Bychkov, A. Y. (2013). Speciation and transport of metals and metalloids in geological vapors. *Reviews in Mineralogy and Geochemistry*, *76*(1), 165-218.

Pontesilli, A., Masotta, M., Nazzari, M., Mollo, S., Armienti, P., Scarlato, P., & Brenna, M. (2019). Crystallization kinetics of clinopyroxene and titanomagnetite growing from a trachybasaltic melt: New insights from isothermal time-series experiments. *Chemical Geology*, *510*, 113-129.

Probst, L. C., Sheldrake, T. E., Gander, M. J., Wallace, G., Simpson, G., & Caricchi, L. (2018). A cross correlation method for chemical profiles in minerals, with an application to zircons of the Kilgore Tuff (USA). *Contributions to Mineralogy and Petrology*, *173*(3), 23.

Pushkarev, E. V., Kamenetsky, V., Gottman, I., & Yaxley, G. (2014). The PGM-bearing volcanic ankaramite (Urals, Russia): bridging ankaramite parental magmas and the Ural-Alaskan-type intrusions. In *Proceedings of the 12th International Platinum Symposium, Yekaterinburg, Russia: Institute of Geology and Geochemistry UB RAS* (pp. 204-205).

Putirka, K. D. (2008). Thermometers and barometers for volcanic systems. *Reviews in mineralogy and geochemistry*, *69*(1), 61-120.

Putirka, K. D., Johnson, M., Kinzler, R., Longhi, J., & Walker, D. (1996). Thermobarometry of mafic igneous rocks based on clinopyroxene-liquid equilibria, 0–30 kbar. *Contributions to Mineralogy and Petrology*, 123(1), 92-108.

Ren, Q., Li, M., Han, S., Zhang, Y., Zhang, Q., & Shi, J. (2019). Basalt Tectonic Discrimination Using Combined Machine Learning Approach. *Minerals*, *9*(6), 376.

Richards, J. P. (2015). The oxidation state, and sulfur and Cu contents of arc magmas: implications for metallogeny. *Lithos*, *233*, 27-45.

Richards, J. P. (2011). Magmatic to hydrothermal metal fluxes in convergent and collided margins. *Ore Geology Reviews*, *40*(1), 1-26.

Richards, J. P. (2009). Postsubduction porphyry Cu-Au and epithermal Au deposits: Products of remelting of subduction-modified lithosphere. *Geology*, *37*(3), 247-250.

Righter, K., Campbell, A. J., Humayun, M., & Hervig, R. L. (2004). Partitioning of Ru, Rh, Pd, Re, Ir, and Au between Cr-bearing spinel, olivine, pyroxene and silicate melts. *Geochimica et Cosmochimica Acta*, *68*(4), 867-880.

Ripley, E. M., Brophy, J. G., & Li, C. (2002). Copper solubility in a basaltic melt and sulfide liquid/silicate melt partition coefficients of Cu and Fe. *Geochimica et Cosmochimica Acta*, *66*(15), 2791-2800.

Rodríguez, C., & Castro, A. (2017). Silicic magma differentiation in ascent conduits. Experimental constraints. *Lithos*, *272*, 261-277.

Rodríguez, C., Geyer, A., Castro, A., & Villaseñor, A. (2015). Natural equivalents of thermal gradient experiments. *Journal of Volcanology and Geothermal Research*, *298*, 47-58.

Romagnoli, C. (2013). Characteristics and morphological evolution of the Aeolian volcanoes from the study of submarine portions. *Geological Society, London, Memoirs*, *37*(1), 13-26.

Rosi, M., Di Traglia, F., Pistolesi, M., Ongaro, T. E., Vitturi, M. D. M., & Bonadonna, C. (2018). Dynamics of shallow hydrothermal eruptions: new insights from Vulcano's Breccia di Commenda eruption. *Bulletin of Volcanology*, *80*(12), 83.

Rossi, S., Petrelli, M., Morgavi, D., Vetere, F. P., Almeev, R. R., Astbury, R. L., & Perugini, D. (2019). Role of magma mixing in the pre-eruptive dynamics of the Aeolian Islands volcanoes (Southern Tyrrhenian Sea, Italy). *Lithos*, *324*, 165-179.

Rottier, B., Audétat, A., Kodera, P., & Lexa, J. (2020). Magmatic evolution of the mineralized Stiavnica volcano (Central Slovakia): evidence from thermobarometry, melt inclusions, and sulfide inclusions. *Journal of Volcanology and Geothermal Research*, *401*, 106967.

Ruch, J., Vezzoli, L., De Rosa, R., Di Lorenzo, R., & Acocella, V. (2016). Magmatic control along a strike-slip volcanic arc: The central Aeolian arc (Italy). *Tectonics*, *35*(2), 407-424.

Scaillet, B., & Macdonald, R. (2006). Experimental and thermodynamic constraints on the sulphur yield of peralkaline and metaluminous silicic flood eruptions. *Journal of Petrology*, *47*(7), 1413-1437.

Scaillet, B., & Pichavant, M. (2005). A model of sulphur solubility for hydrous mafic melts: application to the determination of magmatic fluid compositions of Italian volcanoes. *Annals of Geophysics*.

Scaillet, B., Pichavant, M., & Cioni, R. (2008). Upward migration of Vesuvius magma chamber over the past 20,000 years. *Nature*, *455*(7210), 216-219.

Selva, J., Bonadonna, C., Branca, S., De Astis, G., Gambino, S., Paonita, A., & Ricciardi, A. (2020). Multiple hazards and paths to eruptions: A review of the volcanic system of Volcano (Aeolian Islands, Italy). *Earth-Science Reviews*, 103186.

Setiabudi, B. T., Campbell, I. H., Martin, C. E., & Allen, C. M. (2007). Platinum group element geochemistry of andesite intrusions of the Kelian region, East Kalimantan, Indonesia: implications of gold depletion in the intrusions associated with the Kelian gold deposit. *Economic Geology*, 102(1), 95-108.

Shaw, D. M. (1970). Trace element fractionation during anatexis. *Geochimica et Cosmochimica Acta*, *34*(2), 237-243.

Shea, T., & Hammer, J. E. (2013). Kinetics of cooling-and decompression-induced crystallization in hydrous mafic-intermediate magmas. *Journal of Volcanology and Geothermal research*, *260*, 127-145.

Sillitoe, R. H. (2010). Porphyry copper systems. *Economic geology*, *105*(1), 3-41.

Sisson, T. W., & Bacon, C. R. (1999). Gas-driven filter pressing in magmas. *Geology*, *27*(7), 613-616.

Skulski, T., Minarik, W., & Watson, E. B. (1994). High-pressure experimental trace-element partitioning between clinopyroxene and basaltic melts. *Chemical Geology*, *117*(1-4), 127-147.

Spandler, C. J., Arculus, R. J., Eggins, S. M., Mavrogenes, J. A., Price, R. C., & Reay, A. J. (2003). Petrogenesis of the Greenhills Complex, Southland, New Zealand: magmatic differentiation and cumulate formation at the roots of a Permian island-arc volcano. *Contributions to Mineralogy and Petrology*, *144*(6), 703-721.

Spandler, C. J., Eggins, S. M., Arculus, R. J., & Mavrogenes, J. A. (2000). Using melt inclusions to determine parent-magma compositions of layered intrusions: Application to the Greenhills Complex (New Zealand), a platinum group minerals–bearing, island-arc intrusion. *Geology*, *28*(11), 991-994.

Sparks, R. S. J., Annen, C., Blundy, J. D., Cashman, K. V., Rust, A. C., & Jackson, M. D. (2019). Formation and dynamics of magma reservoirs. *Philosophical Transactions of the Royal society A*, *377*(2139), 20180019.

Sparks, R. S. J., Bursik, M. I., Carey, S. N., Gilbert, J., Glaze, L. S., Sigurdsson, H., & Woods, A. W. (1997). *Volcanic plumes*. Wiley.

Sun, C., & Liang, Y. (2017). A REE-in-plagioclase–clinopyroxene thermometer for crustal rocks. *Contributions to Mineralogy and Petrology*, *172*(4), 24.

Sun, S. S., & McDonough, W. F. (1989). Chemical and isotopic systematics of oceanic basalts: implications for mantle composition and processes. *Geological Society, London, Special Publications*, *42*(1), 313-345.

Taddeucci, J., Pompilio, M., & Scarlato, P. (2004). Conduit processes during the July–August 2001 explosive activity of Mt. Etna (Italy): inferences from glass chemistry and crystal size distribution of ash particles. *Journal of Volcanology and Geothermal Research*, *137*(1-3), 33-54.

Timm, C., de Ronde, C. E., Leybourne, M. I., Layton-Matthews, D., & Graham, I. J. (2012). Sources of chalcophile and siderophile elements in Kermadec arc lavas. *Economic Geology*, *107*(8), 1527-1538.

Turner, S., & Costa, F. (2007). Measuring timescales of magmatic evolution. *Elements*, *3*(4).

Ubide, T., Caulfield, J., Brandt, C., Bussweiler, Y., Mollo, S., Di Stefano, F., & Scarlato, P. (2019b). Deep magma storage revealed by multi-method elemental mapping of clinopyroxene megacrysts at Stromboli volcano. *Frontiers in Earth Science*, *7*, 239.

Ubide, T., & Kamber, B. S. (2018). Volcanic crystals as time capsules of eruption history. *Nature communications*, *9*(1), 1-12.

Ubide, T., Mollo, S., Zhao, J. X., Nazzari, M., & Scarlato, P. (2019a). Sector-zoned clinopyroxene as a recorder of magma history, eruption triggers, and ascent rates. *Geochimica et Cosmochimica Acta*, *251*, 265-283.

Ueki, K., Kuwatani, T., Okamoto, A., Akaho, S., & Iwamori, H. (2020). Thermodynamic modeling of hydrous-melt–olivine equilibrium using exhaustive variable selection. *Physics of the Earth and Planetary Interiors*, *300*, 106430.

Ventura, G. (2013). Kinematics of the Aeolian volcanism (Southern Tyrrhenian Sea) from geophysical and geological data. *Geological Society, London, Memoirs*, *37*(1), 3-11.

Ventura, G., Vilardo, G., Milano, G., & Pino, N. A. (1999). Relationships among crustal structure, volcanism and strike–slip tectonics in the Lipari–Vulcano volcanic complex (Aeolian Islands, Southern Tyrrhenian Sea, Italy). *Physics of the Earth and Planetary Interiors*, *116*(1-4), 31-52.

Vetere, F., Behrens, H., Misiti, V., Ventura, G., Holtz, F., De Rosa, R., & Deubener, J. (2007). The viscosity of shoshonitic melts (Vulcanello Peninsula, Aeolian Islands, Italy): insight on the magma ascent in dikes. *Chemical Geology*, *245*(1-2), 89-102.

Vetere, F., Petrelli, M., Morgavi, D., & Perugini, D. (2015). Dynamics and time evolution of a shallow plumbing system: the 1739 and 1888–90 eruptions, Vulcano Island, Italy. *Journal of Volcanology and Geothermal Research*, *306*, 74-82.

Wallace, G. S., & Bergantz, G. W. (2002). Wavelet-based correlation (WBC) of zoned crystal populations and magma mixing. *Earth and Planetary Science Letters*, *202*(1), 133-145.

Wang, C. Y., Hwang, W. T., & Shi, Y. (1989). Thermal evolution of a rift basin: the Tyrrhenian Sea. *Journal of Geophysical Research: Solid Earth*, *94*(B4), 3991-4006.

Ward Jr, J. H. (1963). Hierarchical grouping to optimize an objective function. *Journal of the American statistical association*, *58*(301), 236-244.

Weber, G., Caricchi, L., Arce, J. L., & Schmitt, A. K. (2020). Determining the current size and state of subvolcanic magma reservoirs. *Nature communications*, 11(1), 1-14.

Welsch, B., Hammer, J., Baronnet, A., Jacob, S., Hellebrand, E., & Sinton, J. (2016). Clinopyroxene in postshield Haleakala ankaramite: 2. Texture, compositional zoning and supersaturation in the magma. *Contributions to Mineralogy and Petrology*, *171*(1), 6.

Wilkinson, J. J. (2013). Triggers for the formation of porphyry ore deposits in magmatic arcs. *Nature Geoscience*, *6*(11), 917-925.

Wolff, J. A., Ellis, B. S., Ramos, F. C., Starkel, W. A., Boroughs, S., Olin, P. H., & Bachmann, O. (2015). Remelting of cumulates as a process for producing chemical zoning in silicic tuffs: A comparison of cool, wet and hot, dry rhyolitic magma systems. *Lithos*, *236*, 275-286.

Wolff, J. A. (1985). The effect of explosive eruption processes on geochemical patterns within pyroclastic deposits. *Journal of Volcanology and Geothermal Research*, *26*(3-4), 189-201.

Wolff, J. A., Forni, F., Ellis, B. S., & Szymanowski, D. (2020). Europium and barium enrichments in compositionally zoned felsic tuffs: A smoking gun for the origin of chemical and physical gradients by cumulate melting. *Earth and Planetary Science Letters*, *540*, 116251.

Wood, B. J., & Blundy, J. D. (1997). A predictive model for rare earth element partitioning between clinopyroxene and anhydrous silicate melt. *Contributions to Mineralogy and Petrology*, *129*(2-3), 166-181.

Zaccarini, F., Garuti, G., & Pushkarev, E. V. (2011). Unusually PGE-rich chromitite in the Butyrin vein of the Kytlym Uralian–Alaskan complex, Northern Urals, Russia. *The Canadian Mineralogist*, *49*(6), 1413-1431.

Zajacz, Z., Candela, P. A., Piccoli, P. M., Wälle, M., & Sanchez-Valle, C. (2012). Gold and copper in volatile saturated mafic to intermediate magmas: Solubilities, partitioning, and implications for ore deposit formation. *Geochimica et Cosmochimica Acta*, *91*, 140-159.

Zajacz, Z., Halter, W. E., Pettke, T., & Guillong, M. (2008). Determination of fluid/melt partition coefficients by LA-ICPMS analysis of co-existing fluid and silicate melt inclusions: Controls on element partitioning. *Geochimica et Cosmochimica Acta*, *72*(8), 2169-2197.

Zanon, V., Frezzotti, M. L., & Peccerillo, A. (2003). Magmatic feeding system and crustal magma accumulation beneath Vulcano Island (Italy): evidence from CO2 fluid inclusions in quartz xenoliths. *Journal of Geophysical Research: Solid Earth*, *108*(B6).

Zelenski, M., Kamenetsky, V. S., Mavrogenes, J. A., Gurenko, A. A., & Danyushevsky, L. V. (2018). Silicate-sulfide liquid immiscibility in modern arc basalt (Tolbachik volcano, Kamchatka): Part I. Occurrence and compositions of sulfide melts. *Chemical Geology*, *478*, 102-111.

Zhang, D., & Audétat, A. (2017). What caused the formation of the giant Bingham Canyon porphyry Cu-Mo-Au deposit? Insights from melt inclusions and magmatic sulfides. *Economic Geology*, *112*(2), 221-244.

Zou, B., & Ma, C. (2020). Crystal mush rejuvenation induced by heat and water transfer: Evidence from amphibole analyses in the Jialuhe Composite Pluton, East Kunlun Orogen, northern Tibet Plateau. *Lithos*, *376*, 105722.

Appendix A: List of collected and employed samples

sample name	Eruptive center	Informal name	lithology	Stratigraphy (De Astis et al., 2013)	Stratigraphy (Di Traglia et al., 2013)	latitude and longitude
SC-18-5	La Sommata	La Sommata	Scoriaceous lapilli	so	-	38°22'42"N 14°58'53"E
VUL-06	Spiaggia Lunga	Spiaggia Lunga	Welded Scoriae	sl	-	38°24'04"N 14°56'28"E
SC-18-4	Mt Saraceno	Mt Saraceno	Scoriaceous lapilli	sa1	-	38°23'03"N 14°57'47"E
SC-18-8	Quadrara	Quadrara	Scoriaceous lapilli	qd	-	38°22'40"N 14°58'16"E
SC-18-12	Vulcanello	Vulcanello 1	Scoriaceous lapilli	vu1a	Vulcanello 1	38°25'35"N 14°58'02"E
SC-18-13	Vulcanello	Vulcanello 1	Scoriaceous lapilli	vu1a	Vulcanello 1	38°25'35"N 14°58'02"E
SC-20-28	Vulcanello	Vulcanello 1	Lava flow	vu1b	Vulcanello 1	38°25'33"N 14°58'07"E
Vul 17 T-21	La Fossa	Pal A	Tephra layer	gp2a	Pal A	38°23'47"N 14°58'11"E
Vul 17 T-18	La Fossa	Pal A	Tephra layer	gp2a	Pal A	38°23'47"N 14°58'11"E
Pal-L 18-01	La Fossa	Pal B	Pumiceous lapilli	gp2a	Pal B	38°24'19"N 14°56'57"E
Pal-L 18-02	La Fossa	Pal B	Pumiceous lapilli	gp2a	Pal B	38°24'19"N 14°56'57"E
Pal-L	La Fossa	Pal B	Pumiceous lapilli	gp2a	Pal B	38°24'19"N 14°56'57"E
Vul 17 B3	La Fossa	Pal B	Pumiceous lapilli	gp2a	Pal B	38°23'47"N 14°58'11"E
Vul 17 T-17	La Fossa	Pal C1	Tephra layer	gp2a	Pal C	38°23'47"N 14°58'11"E
Vul 17 T-11	La Fossa	Pal C1	Tephra layer	gp2a	Pal C	38°23'47"N 14°58'11"E
Vul 17 T-10	La Fossa	Pal C2	Tephra layer	gp2a	Pal C	38°23'47"N 14°58'11"E
Vul 17 T-08	La Fossa	Pal C2	Tephra layer	gp2a	Pal C	38°23'47"N 14°58'11"E
Vul 17 T-05	La Fossa	Pal C2	Tephra layer	gp2a	Pal C	38°23'47"N 14°58'11"E
Vul 17 T-04	La Fossa	Pal C3	Tephra layer	gp2a	Pal C	38°23'47"N 14°58'11"E
Vul 17 T-01	La Fossa	Pal C3	Tephra layer	gp2a	Pal C	38°23'47"N 14°58'11"E
SC-18-20	La Fossa	Pal D	Scoriaceous lapilli	gp2a	Pal D	38°23'57"N 14°57'41"E

SC-18-21	La Fossa	Pal D	Scoriaceous lapilli	gp2a	Pal D	38°23'56"N 14°57'40"E
SC-20-31	La Fossa	Pal D	Pumiceous lapilli	gp2a	PAL D	38°23'47"N 14°57'41"E
SC-20-31b	La Fossa	Pal D	Pumiceous lapilli	gp2a	PAL D	38°23'47"N 14°57'41"E
S33b 15-40	La Fossa	Pal D	Pumiceous lapilli	gp2a	PAL D	38°23'47"N 14°57'51"E
S33b 60-90	La Fossa	Pal D	Pumiceous lapilli	gp2a	PAL D	38°23'47"N 14°57'51"E
S33b 90-110	La Fossa	Pal D	Pumiceous lapilli	gp2a	PAL D	38°23'47"N 14°57'51"E
Vul 17 Pal D	La Fossa	Pal D	Pumiceous lapilli	gp2a	Pal D	38°23'47"N 14°58'11"E
SC-15-1	La Fossa	Palizzi lava	Lava flow	gp3b	Pal E	38°23'47"N 14°57'41"E
SC-18-24	La Fossa	Palizzi lava	Lava flow	gp3b	Pal E	38°23'47"N 14°57'41"E
VGPL3	La Fossa	Palizzi lava	Lava flow	gp3b	Pal E	38°23'47"N 14°57'41"E
SC-20-30	La Fossa	Pietre Cotte lava	Lava flow	pc2	Pietre Cotte Lava	38°24'37"N 14°27'56"E
VPCl8i*	La Fossa	Pietre Cotte lava	Enclaves	pc2	Pietre Cotte Lava	38°24'37"N 14°27'56"E
SC-20-29B	La Fossa	AD 1888-1890	Spatter	gc2	1888-1890 AD	38°24'07"N 14°57'45"E

* used as starting material for experiments

Appendix B: Analytical and quality control standards

Appendix B.1 – Glass standards analyzed by mean of Electron Microprobe.

	wt.% SiO_2	TiO_2	Al_2O_3	FeO_t	MnO	MgO	CaO	Na_2O	K_2O	P_2O_5		sum
reference VG-2[a]	*50.81*	*1.85*	*14.06*	*11.81*	*0.22*	*6.95*	*11.12*	*2.62*	*0.19*	*0.20*		*99.83*
#1	48.86	1.78	13.46	11.62	0.20	6.73	10.71	2.60	0.18	0.25		96.40
#2	48.86	1.69	13.52	11.61	0.21	6.77	10.67	2.78	0.19	0.20		96.50
	SiO_2	TiO_2	Al_2O_3	Fe_2O_{3t}	MnO	MgO	CaO	Na_2O	K_2O	P_2O_5	Cl	sum
reference SMN49[b]	*74.17*	*0.17*	*10.89*	*4.42*	*0.06*	*0*	*0.29*	*5.81*	*4.34*			*100.15*
#1	71.15	0.20	10.76	3.85	0.10	0.03	0.04	5.34	4.38	0.00	0.46	96.32
#2	70.80	0.15	10.45	3.89	0.02	0.01	0.05	5.53	4.12	0.02	0.47	95.50

[a]*Jarosewich, E., Nelen, J. A., and Norberg, J. A. (1980) Reference Samples for Electron Microprobe Analysis. Geostandards Newsletter 4, p. 43-47.*

[b]*Marshall, A. S., Hinton, R. W., & MacDonald, R. (1998). Phenocrystic fluorite in peralkaline rhyolites, Olkaria, Kenya rift valley. Mineralogical Magazine, 62(4), 477-486.*

Appendix B.2- Quality control standards for ICP-OES analyses provided by Actalabs.

	wt.% SiO_2	Al_2O_3	Fe_2O_{3tot}	MnO	MgO	CaO	Na_2O	K_2O	TiO_2	P_2O_5
Detection Limit (ppm)	0.01	0.01	0.01	0.001	0.01	0.01	0.01	0.01	0.001	0.01
Analysis Method	FUS-ICP	FUS-ICP	FUS-ICP	FUS-ICP	FUS-ICP	FUS-ICP	FUS-ICP	FUS-ICP	FUS-ICP	FUS-ICP
DNC-1 Meas	46.56	18.62	9.66	0.143	9.92	11.27	1.92	0.23	0.476	0.07
DNC-1 Cert	47.15	18.34	9.97	0.15	10.13	11.49	1.89	0.234	0.48	0.07
W-2a Meas	52.79	15.33	10.78	0.17	6.28	11.18	2.21	0.63	1.08	0.13
W-2a Cert	52.4	15.4	10.7	0.163	6.37	10.9	2.14	0.626	1.06	0.14
BIR-1a Meas	47.61	15.98	11.14	0.17	9.41	13.39	1.82	0.02	0.97	0.03
BIR-1a Cert	47.96	15.5	11.3	0.175	9.7	13.3	1.82	0.03	0.96	0.021
Method Blank	0.01	< 0.01	< 0.01	0.004	< 0.01	< 0.01	< 0.01	< 0.01	< 0.001	< 0.01

	ppm Ba	Sr	Y	Sc	Zr	Be	V
Detection Limit (ppm)	2	2	1	1	2	1	5
Analysis Method	FUS-ICP	FUS-ICP	FUS-ICP	FUS-ICP	FUS-ICP	FUS-ICP	FUS-ICP
DNC-1 Meas	108	146	15	31	30		153
DNC-1 Cert	118	144	18	31	38		148
W-2a Meas	180	197	19	36	77	1	282
W-2a Cert	182	190	24	36	94	1.3	262
BIR-1a Meas	12	110	13	43	13	< 1	338
BIR-1a Cert	6	110	16	44	18	0.58	310
Method Blank	< 2	< 2	< 1	< 1	2	< 1	< 5

Appendix B.3 – Geochemical reference sample WS-E

ppm	***WS-E_Ref****	Analytical session #1	Analytical session #2	Analytical session #3
Li	13.5	14.0	13.73	14.2
Be	1.10	1.10	1.16	1.07
V	336	328	338	326
Cr	97	90	96	93
Co	45	42	45	44
Ni	54	54	56	56
Cu	66	nd	56	63
Zn	113	117	112	118
Ga	21.6	21.2	21.4	21.4
Rb	25.8	25.6	17.9	27.3
Sr	407	402	391	422
Y	31.8	32.2	29.6	33.1
Zr	204	209	210	216
Nb	17.9	18.1	18.3	18.7
Mo	3.5	3.4	3.4	3.5
Cs	0.47	0.48	0.27	0.49
Ba	335	343	347	344
La	26.6	26.86	27.3	27.0
Ce	60	60	62	58
Pr	7.7	7.8	8.0	7.9
Nd	32.8	32.9	34.0	33.4
Sm	8.8	8.5	9.0	8.8
Eu	2.20	2.24	2.25	2.25
Gd	7.2	7.5	7.3	7.4
Tb	1.08	1.12	1.11	1.09
Dy	6.1	6.2	6.3	6.113
Ho	1.18	1.17	1.17	1.17
Er	3.07	3.15	3.09	3.153
Tm	0.42	0.42	0.413	0.42
Yb	2.51	2.62	2.435	2.47
Lu	0.40	0.36	0.34	0.36
Hf	5.2	5.39	5.5	5.3
Ta	1.12	1.12	1.17	1.15
Pb	12.3	12.9	18.4	21
Th	2.99	3.3	3.23	3.30
U	0.62	0.62	0.64	0.63
Sc	28	nd	34	37

*Govindaraju, K. (1995). Working values with confidence limits for twenty□six CRPG, ANRT and IWG□GIT geostandards. *Geostandards Newsletter*, *19*, 1-32.

Appendix B.4 – Procedural blanks analyses and reference material analyses (TDB-1, Oreas30a) for PGE geochemistry

procedural blanks	ppb Ir	2σ	Ru	2σ	Rh	2σ	Pt	2σ	Pd	2σ	Au	2σ	Re	2σ
#1	0.0062	0.0003	0.0036	0.0008	0.0117	0.0014	0.7400	0.7592	0.3127	0.0134	0.0103	0.0009	0.0199	0.0017
#2	0.0009	0.0001	0.0048	0.0002	0.0032	0.0004	0.0805	0.0044	0.1012	0.0050	0.0098	0.0004	0.0309	0.0010
#3	0.0063	0.0004	0.0544	0.0045	0.0016	0.0002	0.5806	0.0852	0.3179	0.0132	0.0274	0.0012	0.1509	0.0070
average	0.0044		0.0209		0.0055		0.4670		0.2439		0.0158		0.0673	
SD	0.0031		0.0290		0.0054		0.3441		0.1236		0.0100		0.0727	
3 SD (m.d.l.)	0.0093		0.0870		0.0163		1.0323		0.3709		0.0300		0.2180	

TDB-1 analyses	ppb Ir	2σ	Ru	2σ	Rh	2σ	Pt	2σ	Pd	2σ	Au	2σ	Re	2σ
#1	0.0780	0.0023	0.2002	0.0129	0.2942	0.0342	5.4322	0.3964	21.8677	2.8615	0.4298	0.0104	0.8301	0.0248
#2	0.0570	0.0018	0.1895	0.0188	1.0082	0.1179	3.9253	0.2124	20.4677	5.7379	1.4237	0.0253	0.7757	0.0240
#3	0.0870	0.0023	0.2339	0.0159	1.0268	0.1222	4.2689	0.5640	23.5604	14.3237	0.8223	0.0256	0.8294	0.0328
Average	0.0740		0.2079		0.7764		4.5421		21.9653		0.8919		0.8118	
SD	0.0154		0.0232		0.4177		0.7897		1.5486		0.5006		0.0312	
TDB value range*	0.08~0.15		0.2~0.33		0.33~0.7		3.7~5.8		20~25		4~4.75		0.74~0.79	

* Plessen and Erzinger (1998), Tagle and Claeys (2005), Meisel et al. (2001), Peucker-Ehrenbrink et al. (2003)

Oreas30a analyses	ppb Ir	2σ	Ru	2σ	Rh	2σ	Pt	2σ	Pd	2σ	Au	2σ	Re	2σ
#1	0.0186	0.0013	0.0272	0.0065	0.0251	0.0037	0.2208	0.0532	0.5887	0.0406	0.0408	0.0024	0.2577	0.0055
#2	0.0169	0.0011	0.0323	0.0043	0.0291	0.0040	0.1925	0.0525	0.8495	0.0481	0.0431	0.0019	0.2598	0.0112
#3	0.0222	0.0016	0.0708	0.0103	0.0248	0.0037	0.5078	0.0655	0.6636	0.0386		0.0011	0.3323	0.0149
Average	0.0193		0.0434		0.0263		0.3070		0.7006		0.0419		0.2832	
SD	0.0027		0.0238		0.0024		0.1744		0.1343		0.0016		0.0425	
Certified Values (Pb fire assay) https://www.ore.com.au/crm/oreas-30a/							<5 ppb		<2 ppb		<2 ppb			

Appendix B.5 – Average and standard deviation (SD) of trace elements analyses of reference materials NIST 610, NIST 612, BIR 1 and MASS1 by LA-ICP-MS and reference values from GeOReM.

	NIST 610		GeOReM preferred values		NIST 612		GeOReM preferred values		BIR 1		GeOReM preferred values	
ppm	av. (26)	SD (26)	Compiled value	Uncertainty 95% CL	av. (25)	SD (25)	Compiled value	Uncertainty 95%CL	av. (27)	SD (27)	Compiled value	Uncertainty 95% CL
V	443.163	13.619	450	9	39.205	0.516	39	1	303.843	37.142	321	3
Cr	407.480	42.356	408	10	39.759	0.738	36	2	386.587	41.346	393	4
Ni	441.380	18.206	459	4	38.425	0.636	39	0	171.910	15.342	169	2
Cu	432.242	20.363	441	15	36.681	0.606	38	2	120.122	7.067	121	2
Zn	453.585	31.624	460	18	37.963	0.605	39	2	75.339	21.416	70	1
Rb	433.330	18.466	426	1	31.624	0.359	31	0	0.221	0.094	0	0
Sr	494.014	21.734	516	1	76.062	1.540	78	0	94.258	9.286	109	1
Y	448.977	23.166	462	11	38.488	1.075	38	1	12.391	1.265	16	0
Zr	437.708	18.109	448	9	36.162	0.816	38	1	11.814	1.018	15	0
Nb	418.730	17.280	465	34	38.128	0.562	39	2	0.438	0.089	1	0
Cs	363.249	15.792	366	9	41.652	0.680	43	2	0.086	0.301	0	0
Ba	422.285	24.078	452	9	37.745	0.729	39	1	5.802	0.626	7	0
La	454.676	23.493	440	10	35.836	0.725	36	1	0.585	0.135	1	0
Ce	446.398	23.092	453	8	38.342	0.732	38	1	1.702	0.327	2	0
Pr	427.039	20.561	448	7	37.200	0.768	38	1	0.312	0.054	0	0
Nd	427.536	19.817	430	8	35.298	0.572	36	1	2.171	0.471	2	0
Sm	447.190	24.411	453	11	36.834	0.845	38	1	0.896	0.252	1	0
Eu	458.748	21.784	447	12	34.509	0.664	36	1	0.474	0.073	1	0
Gd	416.328	23.522	449	12	37.139	0.973	37	1	1.789	0.721	2	0
Tb	439.068	22.287	437	9	36.123	0.984	38	1	0.316	0.077	0	0
Dy	423.588	19.323	437	11	36.119	0.864	36	1	2.123	0.402	3	0
Ho	446.868	23.014	449	12	38.067	0.967	38	1	0.475	0.082	1	0
Er	422.415	24.349	455	14	37.618	0.920	38	1	1.444	0.232	2	0
Tm	417.208	18.112	435	10	37.762	0.965	37	1	0.233	0.067	0	0
Yb	457.483	25.133	450	9	40.172	1.205	39	1	1.469	0.191	2	0
Lu	430.624	24.330	439	8	37.942	1.114	37	1	0.221	0.039	0	0
Hf	413.664	20.121	435	12	34.980	1.011	37	1	0.467	0.109	1	0
Ta	375.402	19.728	446	33	39.968	1.092	38	2	0.032	0.016	0	0
Pb	413.788	10.082	426	1	38.976	0.922	39	0	3.513	0.390	3	0
Th	446.136	25.527	457	1	37.430	1.127	38	0	0.032	0.014	0	0
U	456.046	23.408	462	1	37.212	1.274	37	0	0.018	0.006	0	0

Appendix C: Whole-rock major and trace element composition

Appendix C.1 – Whole-rock major element by XRF and ICP-OES. Starting material for HP-HT experimental petrology.*

Eruptive Unit	La Sommata	Spiaggia Lunga	Mt Saraceno	Vulcanello 1	Vulcanello 1	Pietre Cotte Lava	AD 1888-1890	Quadrara	Palizzi Lava
Sample	SC-18-5	VUL-06	SC-18-4	SC-20-28	SC-18-13	VPCl8i*	SC-20-29B	SC-18-08	SC-18-24
Composition	Basalt	Shoshonite	Shoshonite	Shoshonite	Shoshonite	Latite	Latite	Trachyte	Trachyte
Lithology	Scoriae	Welded Scoriae	Scoriae	Lava	Scoriae	Enclave	Spatter	Scoriae	Lava
Type	XRF	ICP-OES	ICP-OES	ICP-OES	ICP-OES	XRF	ICP-OES	ICP-OES	ICP-OES
wt.% SiO_2	48.25	50.74	51.87	52.21	53.38	57.21	57.93	57.82	60.89
TiO_2	0.81	0.81	0.76	0.64	0.66	0.70	0.51	0.45	0.48
Al_2O_3	13.09	16.53	15.83	14.70	14.89	18.40	15.34	18.17	16.08
Fe_2O_3	11.22	10.38	9.92	8.50	9.17	5.53	6.56	4.74	6.22
MnO	0.19	0.21	0.20	0.16	0.17	0.13	0.13	0.14	0.12
MgO	8.50	4.08	3.57	4.14	4.62	1.83	2.97	1.19	2.08
CaO	12.91	9.58	7.71	7.91	8.80	4.18	5.79	3.10	4.60
Na_2O	1.99	2.98	3.09	4.42	3.45	4.23	3.57	4.33	4.03
K_2O	2.18	2.81	4.46	3.19	4.77	5.63	5.15	4.88	5.72
P_2O_5	0.34	0.33	0.50	0.47	0.46	0.31	0.38	0.17	0.32
Total	99.48	98.45	97.92	96.34	100.37	98.15	98.33	95.00	100.54
L.O.I.	0.52	1.55	2.33	2.65	0.26	1.85	0.52	5.48	0.09

Eruptive Unit	Palizzi Lava	Pal D	Pal D	Pal D	Pal D	Pal D	Pal B	Pal B	Pietre Cotte Lava
Sample	VGPl3	S33b 60-90	S33b 90-110	SC-18-20	SC-20-31	SC-20-31b	Pal-L 18-01	Pal-L 18-02	SC-20-30
Composition	Trachyte	K-rich Trachyte	K-rich Trachyte	K-rich Trachyte	K-rich Trachyte	K-rich Trachyte	Rhyolite	Rhyolite	Rhyolite
Lithology	Lava	Pumice	Pumice	Scoriae	Pumice	Pumice	Pumice	Pumice	Lava
Type	XRF	XRF	XRF	ICP-OES	ICP-OES	ICP-OES	XRF	XRF	
wt.% SiO_2	60.70	57.58	59.52	60.00	59.15	61.10	69.21	70.03	72.68
TiO_2	0.50	0.66	0.69	0.64	0.55	0.56	0.17	0.19	0.12
Al_2O_3	16.73	18.27	18.52	18.22	17.75	18.04	13.06	13.36	13.68
Fe_2O_3*	4.80	5.89	4.25	4.37	4.99	4.70	2.33	2.31	2.54
MnO	0.15	0.11	0.10	0.09	0.10	0.11	0.07	0.07	0.08
MgO	1.77	1.50	1.13	1.00	1.06	0.95	0.51	0.51	0.28
CaO	4.20	3.63	2.68	2.27	2.60	2.38	1.40	1.44	1.20
Na_2O	4.39	4.41	4.37	4.40	4.25	4.50	3.98	3.94	4.04
K_2O	5.60	6.65	7.22	7.34	7.23	7.58	5.07	5.04	5.24
P_2O_5	0.30	0.43	0.32	0.26	0.28	0.25	0.09	0.10	0.04
Total	99.14	99.13	98.80	98.59	97.96	100.16	95.89	96.99	99.90
L.O.I.	0.86	0.87	1.2	1.41	1.32	0.46	4.11	3.01	0.33

Appendix C.2 – Whole-rock trace elements by ICP-MS. Nd= not determined.

Eruptive unit	La Sommata	Spiaggia Lunga	Mt. Saraceno	Vulcanello 1	Vulcanello 1	AD 1888-1890	Quadrara	Palizzi Lava
Composition	Basalt	Shoshonite	Shoshonite	Shoshonite	Shoshonite	Latite	Trachyte	Trachyte
Lithology	Scoriaceous lapilli	Welded Scoriae	Scoriaceous lapilli	Scoriaceous lapilli	Lava flow	Spatter	Scoriaceous lapilli	Lava flow
Sample	SC-18-5	VUL-06	SC-18-04	SC-18-13	SC-20-28	SC-20-29B	SC-18-08	SC-18-24
ICP-MS analytical session	#3	#3	#3	#2	#3	#3	#3	#3
Li	11.05	19.17	31.38	30.78	31.14	41.70	38.54	49.75
Be	1.45	1.70	3.09	3.56	3.87	4.70	3.32	4.38
V	294.46	304.45	261.65	197.94	176.60	135.75	57.38	118.98
Cr	207.69	12.68	7.31	68.28	47.98	57.37	<8	19.40
Co	40.72	39.07	34.77	27.23	24.33	18.66	6.41	14.20
Ni	48.67	25.28	17.94	23.99	19.81	18.19	1.80	10.26
Cu	88.27	354.57	250.66	100.30	109.74	74.50	58.53	68.34
Zn	75.66	114.69	98.44	65.25	68.78	64.82	70.41	52.62
Ga	14.39	17.71	18.34	16.89	17.35	17.74	17.26	18.44
Rb	57.25	60.66	144.87	150.38	150.67	201.12	152.50	210.22
Sr	1060.44	1314.84	1263.30	1163.41	1240.63	1029.31	921.02	863.89
Y	18.48	26.96	27.56	22.78	23.72	26.88	25.99	29.65
Zr	79.18	109.66	151.14	158.23	173.24	217.87	194.92	254.56
Nb	6.38	8.36	19.48	18.81	20.89	25.96	19.67	28.28
Mo	1.49	1.27	2.50	3.34	2.75	4.23	2.61	5.51
Cs	1.83	0.57	5.48	6.79	7.24	9.39	6.94	3.51
Ba	590.54	778.83	1055.91	1046.45	1074.02	910.10	1005.61	806.59
La	29.37	36.26	52.58	58.24	58.57	64.53	51.10	82.25
Ce	58.47	66.10	96.47	107.91	103.46	111.80	93.43	146.93
Pr	7.10	8.55	11.59	11.97	12.00	12.76	10.78	15.26
Nd	28.47	34.57	43.64	43.96	43.70	44.48	39.09	51.95
Sm	6.00	6.91	8.11	7.96	7.76	7.64	6.92	8.65
Eu	1.61	1.91	1.91	1.77	1.76	1.42	1.61	1.39
Gd	5.15	6.28	6.74	6.13	6.04	5.94	5.44	6.49
Tb	0.69	0.85	0.91	0.83	0.80	0.84	0.78	0.92
Dy	3.72	4.64	4.88	4.35	4.13	4.48	4.25	5.00
Ho	0.68	0.91	0.92	0.77	0.76	0.86	0.84	1.00
Er	1.91	2.53	2.57	2.18	2.15	2.47	2.42	2.91
Tm	0.26	0.36	0.36	0.31	0.31	0.38	0.37	0.43
Yb	1.63	2.18	2.20	1.99	1.96	2.39	2.27	2.78
Lu	0.24	0.34	0.35	0.30	0.31	0.37	0.36	0.44
Hf	2.23	2.85	3.92	4.02	4.24	5.49	4.96	6.33
Ta	0.37	0.47	1.07	1.07	1.17	1.51	1.17	1.68
Pb	7.40	8.96	19.84	18.47	23.19	24.77	20.96	31.64
Th	6.77	8.54	20.38	24.09	25.98	35.76	22.15	41.74
U	1.83	2.39	5.82	6.59	7.08	9.22	5.49	11.14
Sc	52.53	30.62	23.95	28.55	25.45	20.18	7.08	14.93

Eruptive unit	Pal D	Pal D	Pal D	Pal D	Pal D	Pal B	Pal B	Pietre Cotte Lava
Composition	Trachyte	Trachyte	Trachyte	Trachyte	Trachyte	Rhyolite	Rhyolite	Rhyolite
Lithology	Scoriaceous lapilli	Pumiceous lapilli	Pumiceous lapilli	Pumiceous lapilli	Pumiceous lapilli	Pumiceous lapilli	Pumiceous lapilli	Lava flow
Sample	SC-18-20	SC-20-31b	SC-20-31	S33b 90-110	S33b 60-90	PAL-L 18-01	PAL-L 18-02	SC-20-30
ICP-MS analytical session	#3	#2	#2	#2	#2	#1	#1	#3
Li	50.91	46.01	43.98	43.99	42.97	78.45	84.75	96.28
Be	5.04	4.94	4.86	4.78	4.62	7.14	7.38	7.96
V	50.98	52.24	68.64	59.05	94.32	13.95	17.85	11.57
Cr	<8	<1	1.64	1.05	4.17	2.02	2.81	<8
Co	5.01	5.35	6.80	6.32	10.51	2.39	2.84	1.96
Ni	1.59	0.91	1.50	1.26	2.53	1.86	2.32	1.24
Cu	33.32	20.26	42.13	42.66	73.75	nd	nd	14.82
Zn	64.13	56.71	55.02	54.19	83.40	58.34	57.07	43.80
Ga	17.57	18.16	18.14	17.93	17.94	15.83	16.70	17.76
Rb	241.37	233.87	223.09	224.59	205.68	270.36	270.03	305.37
Sr	778.37	772.31	1032.56	936.23	1404.20	110.39	134.36	114.35
Y	21.02	22.98	23.78	25.09	24.17	37.49	38.95	42.59
Zr	229.18	232.87	208.75	220.42	201.11	171.22	175.63	220.47
Nb	28.51	31.63	27.76	28.17	24.96	32.35	32.94	36.83
Mo	4.47	4.76	4.79	4.45	4.17	5.65	5.82	6.58
Cs	10.43	11.28	10.80	10.38	9.49	15.48	15.68	18.30
Ba	1452.48	1528.66	2165.52	1909.28	3101.87	110.35	129.64	105.63
La	63.55	71.40	74.33	68.08	67.80	60.47	63.61	73.27
Ce	107.80	125.57	128.22	120.51	121.03	113.56	118.98	136.54
Pr	11.66	12.87	13.05	12.34	12.69	12.15	12.69	14.37
Nd	38.63	43.24	43.71	41.88	43.68	40.64	42.33	47.62
Sm	6.24	7.27	7.45	7.02	7.63	7.83	8.08	8.56
Eu	1.43	1.59	1.64	1.60	1.79	0.28	0.31	0.28
Gd	4.49	5.30	5.50	5.49	5.73	6.39	6.57	6.63
Tb	0.65	0.77	0.80	0.80	0.84	1.04	1.07	1.10
Dy	3.55	4.14	4.37	4.34	4.46	6.18	6.34	6.66
Ho	0.69	0.79	0.83	0.84	0.83	1.24	1.29	1.36
Er	2.03	2.30	2.43	2.44	2.37	3.73	3.85	4.19
Tm	0.31	0.34	0.37	0.37	0.36	0.59	0.60	0.66
Yb	1.99	2.24	2.40	2.43	2.33	3.83	3.94	4.34
Lu	0.32	0.34	0.36	0.36	0.35	0.58	0.61	0.67
Hf	5.35	5.58	5.26	5.33	4.81	6.03	6.18	7.28
Ta	1.60	1.91	1.66	1.67	1.48	2.23	2.31	2.53
Pb	30.04	26.95	38.53	25.67	24.83	34.57	34.09	30.96
Th	35.11	36.96	34.74	35.05	32.36	45.74	47.87	60.16
U	9.39	10.13	9.49	9.60	8.84	13.18	13.74	16.08
Sc	6.28	6.41	7.02	6.61	8.89	nd	nd	3.34

Appendix D: Major element composition of experimental glasses and mineral phases

Appendix D – Major element composition of starting experimental material, experimental glasses, feldspars, clinopyroxene and biotite.

Starting glass			wt.% SiO_2	TiO_2	Al_2O_3	FeO_{tot}	MnO	MgO	CaO	Na_2O	K_2O	total	type
Sample VPCl8i			56.60	0.40	19.98	5.95	0.12	1.90	4.48	3.92	5.32	98.67	EPMA
Pietre Cotte enclave		σ (10)	0.47	0.04	0.49	0.22	0.02	0.07	0.21	0.12	0.22		

Experimental glasses

Sample	MPa	H_2O wt.%	Distance from bottom (µm)	wt.% SiO_2	TiO_2	Al_2O_3	FeO_{tot}	MnO	MgO	CaO	Na_2O	K_2O	total	type
LTG2	150	0	100	56.80	0.64	17.78	4.95	0.17	1.80	3.90	4.46	6.01	96.51	EPMA
LTG2	150	0	200	56.85	0.47	17.94	4.90	0.15	1.55	3.65	4.63	6.08	96.21	EPMA
LTG2	150	0	300	56.18	0.54	18.28	5.15	0.13	1.62	3.65	4.54	6.10	96.20	EPMA
LTG2	150	0	400	56.65	0.57	17.65	6.00	0.08	1.64	3.74	4.60	5.93	96.86	EPMA
LTG2	150	0	500	56.13	0.49	17.86	5.70	0.09	1.65	3.77	4.51	5.94	96.14	EPMA
LTG2	150	0	600	55.96	0.56	17.76	6.25	0.09	1.65	3.63	4.42	5.90	96.21	EPMA
LTG2	150	0	700	56.31	0.59	18.07	6.04	0.10	1.54	3.49	4.50	5.92	96.56	EPMA
LTG2	150	0	800	56.19	0.58	17.67	6.09	0.08	1.48	3.54	4.65	5.98	96.26	EPMA
LTG2	150	0	900	56.52	0.56	17.72	6.04	0.16	1.56	3.44	4.45	5.99	96.43	EPMA
LTG2	150	0	1000	56.62	0.54	17.93	6.07	0.09	1.50	3.41	4.58	6.03	96.77	EPMA
LTG2	150	0	1100	56.41	0.50	18.26	5.74	0.15	1.49	3.42	4.35	6.04	96.35	EPMA
LTG2	150	0	1200	56.63	0.57	18.20	6.06	0.12	1.42	3.31	4.53	5.98	96.82	EPMA
LTG2	150	0	1300	56.44	0.55	18.19	5.89	0.03	1.42	3.39	4.45	6.01	96.37	EPMA
LTG2	150	0	1400	56.58	0.52	18.15	5.93	0.14	1.40	3.32	4.43	5.93	96.39	EPMA
LTG2	150	0	1500	56.52	0.56	18.10	6.09	0.11	1.35	3.26	4.38	6.00	96.36	EPMA
LTG2	150	0	1600	56.87	0.56	18.39	6.07	0.12	1.26	3.30	4.47	6.01	97.05	EPMA
LTG2	150	0	1700	56.67	0.51	18.07	5.96	0.13	1.34	3.24	4.40	6.16	96.47	EPMA
LTG2	150	0	1800	57.16	0.48	18.42	6.06	0.08	1.22	3.23	4.26	6.18	97.10	EPMA
LTG2	150	0	1900	56.99	0.49	18.48	5.99	0.13	1.22	3.13	4.37	6.14	96.94	EPMA
LTG2	150	0	2000	56.64	0.57	18.50	6.10	0.13	1.20	3.11	4.56	6.12	96.92	EPMA

LTG2	150	0	2100	56.83	0.53	18.26	6.22	0.11	1.24	3.03	4.53	6.20	96.95	EPMA
LTG2	150	0	2200	56.92	0.51	18.30	5.98	0.03	1.16	2.98	4.13	6.26	96.27	EPMA
LTG2	150	0	2300	56.85	0.49	18.53	5.86	0.12	1.11	2.75	4.61	6.51	96.84	EPMA
LTG2	150	0	2400	56.77	0.56	18.10	6.02	0.07	1.17	2.58	4.78	6.56	96.62	EPMA
LTG2	150	0	2500	56.33	0.49	17.87	6.90	0.10	1.24	2.67	4.46	6.36	96.42	EPMA
LTG2	150	0	2600	57.10	0.57	17.77	6.51	0.12	1.14	2.50	4.52	6.48	96.71	EPMA
LTG2	150	0	2700	56.11	0.60	17.36	7.16	0.11	1.23	2.63	4.66	6.31	96.17	EPMA
LTG2	150	0	2800	56.50	0.55	17.45	6.79	0.11	1.13	2.57	4.64	6.49	96.23	EPMA
LTG2	150	0	2900	56.69	0.54	17.00	6.67	0.19	1.14	2.54	4.48	6.50	95.75	EPMA
LTG2	150	0	3000	57.00	0.49	16.73	6.97	0.16	1.15	2.67	4.45	6.44	96.05	EPMA
LTG2	150	0	3100	59.64	0.53	15.84	7.82	0.04	1.40	3.46	4.17	7.09	100.00	EDS
LTG2	150	0	3200	60.45	0.58	17.18	5.80	0.00	1.07	2.99	3.82	8.11	100.00	EDS
LTG2	150	0	3300	59.08	0.25	16.78	7.10	0.55	1.23	3.20	4.49	7.32	100.00	EDS
LTG2	150	0	3400	59.87	0.43	17.00	7.17	0.52	0.95	2.92	4.10	7.03	100.00	EDS
LTG2	150	0	3500	58.38	1.24	16.94	7.98	0.00	0.84	3.02	4.26	7.36	100.00	EDS

Experimental glasses

Sample	MPa	H_2O wt.%	Distance from bottom (µm)	wt.% SiO_2	TiO_2	Al_2O_3	FeO_{tot}	MnO	MgO	CaO	Na_2O	K_2O	total	type
LTG1	150	2	225	56.39	0.55	17.16	5.31	0.11	1.83	3.98	3.89	5.62	94.83	EPMA
LTG1	150	2	375	56.12	0.45	17.55	5.36	0.07	1.87	3.93	4.24	5.64	95.23	EPMA
LTG1	150	2	525	55.74	0.55	17.65	5.51	0.13	1.90	4.02	4.16	5.57	95.24	EPMA
LTG1	150	2	675	55.83	0.56	17.75	5.51	0.08	1.80	3.95	4.22	5.54	95.24	EPMA
LTG1	150	2	825	56.27	0.51	17.63	5.81	0.06	1.80	3.89	4.12	5.70	95.79	EPMA
LTG1	150	2	975	56.28	0.52	17.66	5.75	0.11	1.78	3.83	4.22	5.62	95.76	EPMA
LTG1	150	2	1125	55.93	0.48	17.69	5.53	0.13	1.66	3.77	4.20	5.63	95.02	EPMA
LTG1	150	2	1275	56.01	0.52	17.45	5.54	0.08	1.75	3.85	4.07	5.63	94.90	EPMA
LTG1	150	2	1425	56.01	0.51	17.91	5.65	0.10	1.61	3.70	4.22	5.81	95.52	EPMA
LTG1	150	2	1575	56.09	0.47	17.88	5.20	0.13	1.45	3.61	4.21	5.78	94.82	EPMA
LTG1	150	2	1725	56.45	0.56	18.01	5.57	0.14	1.59	3.58	4.11	5.83	95.85	EPMA
LTG1	150	2	1875	56.34	0.47	17.90	5.11	0.12	1.40	3.44	4.32	5.90	95.00	EPMA
LTG1	150	2	2025	56.69	0.51	18.08	5.10	0.14	1.44	3.37	4.06	5.87	95.26	EPMA

LTG1	150	2	2175	56.83	0.44	18.05	4.85	0.12	1.36	3.25	4.02	6.03	94.95	EPMA
LTG1	150	2	2325	57.24	0.41	18.17	4.54	0.13	1.25	3.21	4.34	5.95	95.23	EPMA
LTG1	150	2	2475	57.32	0.41	18.32	4.56	0.13	1.15	3.21	4.45	6.09	95.64	EPMA
LTG1	150	2	2625	57.62	0.39	18.22	4.20	0.12	1.16	3.03	4.22	6.16	95.12	EPMA
LTG1	150	2	2775	57.22	0.37	18.45	4.24	0.16	1.15	2.96	4.32	6.07	94.94	EPMA
LTG1	150	2	2925	57.15	0.38	18.47	4.15	0.06	0.99	2.88	4.15	6.25	94.48	EPMA
LTG1	150	2	3075	57.60	0.32	18.45	3.98	0.07	1.02	2.90	4.08	6.29	94.70	EPMA
LTG1	150	2	3225	57.81	0.40	18.82	3.70	0.10	1.02	2.78	4.47	6.25	95.34	EPMA
LTG1	150	2	3375	58.00	0.30	18.72	3.80	0.12	0.91	2.81	4.36	6.30	95.32	EPMA
LTG1	150	2	3525	58.66	0.36	18.44	3.77	0.07	0.87	2.71	4.24	6.35	95.47	EPMA
LTG1	150	2	3675	58.50	0.24	18.73	3.56	0.07	0.80	2.67	4.36	6.38	95.31	EPMA
LTG1	150	2	3825	58.67	0.29	18.65	3.45	0.07	0.71	2.66	4.34	6.34	95.18	EPMA
LTG1	150	2	3975	59.05	0.18	18.64	3.43	0.11	0.71	2.56	4.23	6.38	95.29	EPMA
LTG1	150	2	4125	59.02	0.19	18.61	3.36	0.08	0.67	2.51	4.31	6.31	95.06	EPMA
LTG1	150	2	4275	59.12	0.15	18.75	3.25	0.10	0.65	2.65	4.25	6.31	95.23	EPMA
LTG1	150	2	4425	59.61	0.24	18.64	3.27	0.12	0.60	2.54	4.41	6.41	95.85	EPMA

Experimental glasses

Sample	**MPa**	**H_2O wt.%**	**Distance from bottom (µm)**	**wt.% SiO_2**	**TiO_2**	**Al_2O_3**	**FeO_{tot}**	**MnO**	**MgO**	**CaO**	**Na_2O**	**K_2O**	**total**	**type**
LTG3	150	4	150	62.47	0.09	20.82	1.53	0.17	1.20	3.50	4.52	5.70	100.00	EDS
LTG3	150	4	250	62.64	0.23	20.56	1.78	0.48	1.13	3.20	4.18	5.80	100.00	EDS
LTG3	150	4	350	63.64	0.26	20.74	1.18	0.26	0.30	3.54	4.37	5.70	100.00	EDS
LTG3	150	4	450	63.63	0.20	21.13	1.09	0.02	0.32	3.11	4.91	5.60	100.00	EDS
LTG3	150	4	550	65.36	0.53	17.96	1.39	0.39	1.20	3.40	3.89	5.87	100.00	EDS
LTG3	150	4	650	64.54	0.33	19.23	1.55	0.00	0.88	3.70	4.15	5.62	100.00	EDS
LTG3	150	4	750	64.86	0.02	20.45	1.04	0.09	0.27	2.44	5.01	5.81	100.00	EDS
LTG3	150	4	850	64.80	0.46	20.55	0.69	0.01	0.36	2.30	4.75	6.08	100.00	EDS
LTG3	150	4	950	64.61	0.39	18.82	1.70	0.07	0.89	3.80	3.71	6.02	100.00	EDS
LTG3	150	4	1050	63.98	0.32	20.00	1.11	0.00	0.53	4.10	4.21	5.75	100.00	EDS
LTG3	150	4	1150	64.13	0.40	20.13	1.15	0.14	0.27	3.43	4.56	5.79	100.00	EDS
LTG3	150	4	1250	64.60	0.41	20.79	0.65	0.00	0.24	2.46	4.86	5.99	100.00	EDS

LTG3	150	4	1350	64.40	0.40	19.41	1.91	0.11	0.06	3.87	4.12	5.72	100.00	EDS
LTG3	150	4	1450	65.60	0.33	19.81	1.19	0.00	0.00	3.62	3.75	5.70	100.00	EDS
LTG3	150	4	1550	65.08	0.00	20.77	1.09	0.00	0.09	2.56	4.55	5.86	100.00	EDS
LTG3	150	4	1650	65.69	0.00	20.79	0.53	0.12	0.04	2.40	4.92	5.51	100.00	EDS
LTG3	150	4	1750	64.96	0.22	19.65	1.09	0.00	0.65	3.70	4.29	5.45	100.00	EDS
LTG3	150	4	1850	65.89	0.00	20.24	0.82	0.06	0.11	2.24	4.61	6.03	100.00	EDS
LTG3	150	4	1950	65.85	0.29	20.40	0.62	0.00	0.25	2.01	4.78	5.79	100.00	EDS
LTG3	150	4	2050	65.04	0.27	20.56	0.65	0.02	0.01	2.75	4.81	5.90	100.00	EDS
LTG3	150	4	2150	65.13	0.14	20.40	0.53	0.26	0.30	2.12	5.18	5.94	100.00	EDS
LTG3	150	4	2250	65.57	0.18	20.39	0.62	0.17	0.06	1.99	4.92	6.12	100.00	EDS
LTG3	150	4	2350	65.37	0.00	20.70	0.71	0.00	0.38	1.83	5.29	5.71	100.00	EDS
LTG3	150	4	2450	65.52	0.26	20.31	0.70	0.00	0.32	1.71	5.15	6.02	100.00	EDS
LTG3	150	4	2550	65.40	0.63	19.20	1.16	0.00	1.09	3.25	3.58	5.70	100.00	EDS
LTG3	150	4	2650	65.20	0.18	18.77	1.80	0.15	1.19	3.60	3.61	5.50	100.00	EDS
LTG3	150	4	2750	66.37	0.28	20.50	0.50	0.04	0.01	1.63	5.26	5.41	100.00	EDS
LTG3	150	4	2850	66.34	0.16	19.95	1.10	0.07	0.02	2.35	4.60	5.41	100.00	EDS
LTG3	150	4	2950	67.23	0.24	19.26	1.15	0.00	0.00	2.16	4.06	5.90	100.00	EDS

Experimental Feldspar

Sample	LTG1	LTG1	LTG1	LTG1	LTG1	LTG1	LTG1	LTG1	LTG1	LTG1
P MPa	150	150	150	150	150	150	150	150	150	150
H_2O wt.%	2	2	2	2	2	2	2	2	2	2
Analyses	EDS	EDS	EDS	EDS	EDS	EDS	EDS	EDS	EDS	EDS
wt.% SiO_2	59.76	64.65	64.15	64.96	59.25	66.29	65.32	58.56	64.94	65.98
TiO_2	0.54	0.03	0.31	0.05	0.13	0.00	0.24	0.00	0.05	0.02
Al_2O_3	22.91	19.39	20.14	19.77	21.86	17.72	18.00	22.85	17.62	19.27
FeO	0.00	0.34	0.00	0.67	0.93	0.68	0.00	0.00	0.62	0.80
MnO	0.00	0.23	0.34	0.02	0.31	0.00	0.00	0.01	0.00	0.02
MgO	0.02	0.00	0.00	0.00	0.27	0.00	0.00	0.00	0.01	0.07
CaO	7.37	3.06	1.68	3.10	6.38	2.00	0.93	5.83	0.91	0.52
Na_2O	7.02	3.84	3.28	4.44	7.72	3.76	3.43	7.61	4.87	3.16
K_2O	2.39	8.46	10.10	6.99	3.14	9.55	12.08	5.13	10.98	10.17
total	100.00	100.00	100.00	100.00	100.00	100.00	100.00	100.00	100.00	100.00
8 oxygens formula										
Si	2.67	2.95	2.93	2.96	2.64	3.03	2.98	2.59	2.93	3.02
Ti	0.02	0.00	0.01	0.00	0.00	0.00	0.01	0.00	0.00	0.00
Al	1.21	1.04	1.08	1.06	1.15	0.95	0.97	1.19	0.94	1.04
Fe^{3+}	0.00	0.00	0.00	0.00	0.03	0.00	0.00	0.00	0.02	0.00
Fe^{2+}	0.00	0.01	0.00	0.03	0.00	0.03	0.00	0.00	0.00	0.03
Mn	0.00	0.01	0.01	0.00	0.01	0.00	0.00	0.00	0.00	0.00
Mg	0.00	0.00	0.00	0.00	0.02	0.00	0.00	0.00	0.00	0.00
Ca	0.35	0.15	0.08	0.15	0.30	0.10	0.05	0.28	0.04	0.03
Na	0.61	0.34	0.29	0.39	0.67	0.33	0.30	0.65	0.43	0.28
K	0.14	0.49	0.59	0.41	0.18	0.56	0.70	0.29	0.63	0.59
An	32.14	15.21	8.57	15.93	26.48	9.89	4.32	22.67	3.98	2.84
Ab	55.43	34.62	30.21	41.32	57.99	33.76	28.84	53.55	38.67	31.13
Or	12.43	50.17	61.22	42.75	15.53	56.35	66.84	23.77	57.36	66.03

Experimental Feldspar

Sample	LTG2	LTG2	LTG2	LTG2	LTG2	LTG2	LTG2	LTG2	LTG2	LTG2
P MPa	150	150	150	150	150	150	150	150	150	150
H_2O wt.%	0	0	0	0	0	0	0	0	0	0
Analyses	EDS	EDS	EDS	EDS	EDS	EPMA	EPMA	EPMA	EPMA	EPMA
wt.% SiO_2	64.27	65.85	63.66	62.70	64.31	61.00	63.58	61.08	59.05	60.91
TiO_2	0.24	0.24	0.25	0.77	0.00	0.13	0.25	0.56	0.21	0.13
Al_2O_3	19.58	18.64	19.67	18.16	16.63	20.91	19.86	17.91	20.99	19.03
FeO	0.29	0.00	0.00	1.17	0.73	0.57	0.53	2.64	2.87	1.99
MnO	0.00	0.04	0.12	0.00	0.00	0.06	0.00	0.04	0.13	0.03
MgO	0.17	0.00	0.21	0.22	0.00	0.00	0.05	0.30	0.55	1.06
CaO	2.72	2.40	3.69	2.22	2.66	3.19	2.03	1.59	4.99	4.31
Na_2O	4.67	4.89	5.24	4.74	5.31	4.29	3.72	3.38	5.02	4.24
K_2O	8.07	7.94	7.15	10.03	10.37	7.22	9.11	9.52	4.14	6.83
total	100.00	100.00	100.00	100.00	100.00	97.37	99.13	97.03	97.94	98.53
8 oxygens formula										
Si	2.91	2.99	2.88	2.84	2.90	2.84	2.92	2.89	2.74	2.81
Ti	0.01	0.01	0.01	0.03	0.00	0.00	0.01	0.02	0.01	0.00
Al	1.05	1.00	1.05	0.97	0.88	1.15	1.08	1.00	1.15	1.04
Fe^{3+}	0.00	0.00	0.00	0.04	0.03	0.00	0.00	0.10	0.11	0.08
Fe^{2+}	0.01	0.00	0.00	0.00	0.00	0.02	0.02	0.00	0.00	0.00
Mn	0.00	0.00	0.00	0.00	0.00	0.00	0.00	0.00	0.00	0.00
Mg	0.01	0.00	0.01	0.01	0.00	0.00	0.00	0.02	0.04	0.07
Ca	0.13	0.12	0.18	0.11	0.13	0.16	0.10	0.08	0.25	0.21
Na	0.41	0.43	0.46	0.42	0.46	0.39	0.33	0.31	0.45	0.38
K	0.47	0.46	0.41	0.58	0.60	0.43	0.53	0.57	0.25	0.40
An	13.09	11.61	17.01	9.78	10.80	16.32	10.35	8.35	26.26	21.43
Ab	40.66	42.71	43.72	37.70	39.03	39.71	34.33	32.12	47.80	38.14
Or	46.25	45.68	39.28	52.52	50.17	43.97	55.32	59.53	25.94	40.43

Experimental Feldspar

Sample	LTG2	LTG2	LTG2	LTG2	LTG2	LTG2	LTG2	LTG2	LTG2	LTG2
P MPa	150	150	150	150	150	150	150	150	150	150
H_2O wt.%	0	0	0	0	0	0	0	0	0	0
Analyses	EPMA	EPMA	EPMA	EPMA	EPMA	EPMA	EPMA	EPMA	EDS	EDS
wt.% SiO_2	59.64	62.32	60.01	62.43	61.67	60.49	60.67	60.64	64.35	60.77
TiO_2	0.00	0.08	0.14	0.17	0.12	0.13	0.14	0.16	0.40	0.67
Al_2O_3	19.84	20.61	20.45	20.48	19.03	21.30	21.06	21.50	19.26	19.91
FeO	0.86	0.59	1.05	0.54	0.98	0.51	0.55	0.50	0.96	0.62
MnO	0.01	0.01	0.04	0.00	0.08	0.00	0.00	0.00	0.00	0.51
MgO	0.08	0.00	0.37	0.07	0.23	0.01	0.03	0.01	0.02	0.09
CaO	5.50	2.91	3.39	2.88	2.89	2.81	2.68	2.76	2.50	4.82
Na_2O	4.30	4.67	4.50	4.85	4.21	4.38	4.10	4.26	4.05	5.36
K_2O	6.79	7.20	6.15	7.00	8.04	7.31	7.96	7.28	8.45	7.26
total	97.03	98.38	96.11	98.42	97.24	96.94	97.18	97.11	100.00	100.00
8 oxygens formula										
Si	2.79	2.87	2.83	2.87	2.88	2.83	2.83	2.83	2.94	2.75
Ti	0.00	0.00	0.01	0.01	0.00	0.00	0.00	0.01	0.01	0.02
Al	1.10	1.12	1.14	1.11	1.05	1.17	1.16	1.18	1.04	1.06
Fe^{3+}	0.03	0.00	0.00	0.00	0.04	0.00	0.02	0.00	0.00	0.02
Fe^{2+}	0.00	0.02	0.04	0.02	0.00	0.02	0.00	0.02	0.04	0.00
Mn	0.00	0.00	0.00	0.00	0.00	0.00	0.00	0.00	0.00	0.02
Mg	0.01	0.00	0.03	0.00	0.02	0.00	0.00	0.00	0.00	0.01
Ca	0.28	0.14	0.17	0.14	0.14	0.14	0.13	0.14	0.12	0.23
Na	0.39	0.42	0.41	0.43	0.38	0.40	0.37	0.39	0.36	0.47
K	0.41	0.42	0.37	0.41	0.48	0.44	0.47	0.43	0.49	0.42
An	25.74	14.60	17.98	14.41	14.39	14.45	13.69	14.42	12.58	20.82
Ab	36.42	42.39	43.19	43.90	37.94	40.77	37.90	40.28	36.83	41.86
Or	37.84	43.01	38.84	41.69	47.67	44.77	48.41	45.30	50.59	37.33

Experimental Clinopyroxene

Sample	LTG1	LTG1	LTG1	LTG1	LTG1	LTG1	LTG1	LTG1	LTG1	LTG1
P MPa	150	150	150	150	150	150	150	150	150	150
H_2O wt.%	2	2	2	2	2	2	2	2	2	2
Analyses	EPMA	EPMA	EPMA	EPMA	EDS	EDS	EDS	EDS	EDS	EDS
wt.% SiO_2	47.75	47.84	47.47	47.07	46.32	49.51	47.42	49.48	48.61	47.22
TiO_2	0.61	0.77	0.90	0.74	1.14	1.17	1.64	0.48	0.90	0.46
Al_2O_3	5.93	6.16	6.65	6.75	6.98	6.60	7.49	4.98	7.01	6.36
FeO	8.77	8.97	9.02	9.75	8.85	9.82	8.93	10.17	10.71	12.81
MnO	0.18	0.25	0.23	0.25	0.00	0.00	0.00	0.00	0.00	0.00
MgO	12.80	12.45	12.31	12.21	11.12	11.55	12.52	11.17	10.76	11.11
CaO	21.22	21.11	21.05	20.59	24.96	21.08	21.17	23.16	21.35	21.30
Na_2O	0.46	0.45	0.41	0.43	0.47	0.25	0.71	0.39	0.55	0.62
total	97.72	98.01	98.08	97.82	100.01	100.00	100.01	100.01	100.02	100.01
6 oxygens formula										
Si	1.81	1.81	1.80	1.79	1.73	1.86	1.76	1.86	1.83	1.78
Ti	0.02	0.02	0.03	0.02	0.03	0.03	0.05	0.01	0.03	0.01
Al^{IV}	0.19	0.19	0.20	0.21	0.27	0.14	0.24	0.14	0.17	0.22
Al^{VI}	0.08	0.09	0.10	0.10	0.04	0.15	0.09	0.08	0.14	0.06
Fe^{3+}	0.11	0.08	0.08	0.10	0.20	-0.05	0.11	0.06	0.03	0.19
Fe^{2+}	0.17	0.20	0.21	0.21	0.08	0.36	0.17	0.26	0.31	0.22
Mn	0.01	0.01	0.01	0.01	0.00	0.00	0.00	0.00	0.00	0.00
Mg	0.72	0.70	0.70	0.69	0.62	0.65	0.69	0.63	0.60	0.62
Ca	0.86	0.86	0.86	0.84	1.00	0.85	0.84	0.93	0.86	0.86
Na	0.03	0.03	0.03	0.03	0.03	0.02	0.05	0.03	0.04	0.05
Wo	46.25	46.46	46.55	45.56	52.72	47.04	46.46	49.66	47.78	45.55
En	38.83	38.13	37.88	37.60	32.69	35.86	38.24	33.33	33.51	33.06
Fs	14.92	15.41	15.57	16.84	14.59	17.10	15.30	17.02	18.71	21.38

Experimental Clinopyroxene

Sample	LTG2	LTG2	LTG2	LTG2	LTG2	LTG2	LTG2	LTG2	LTG2	LTG2
P MPa	150	150	150	150	150	150	150	150	150	150
H_2O wt.%	0	0	0	0	0	0	0	0	0	0
Analyses	EPMA	EPMA	EPMA	EPMA	EPMA	EPMA	EPMA	EPMA	EPMA	EPMA
wt.% SiO_2	47.71	47.58	47.52	49.54	49.33	52.44	49.59	49.39	49.73	50.70
TiO_2	0.86	0.65	0.86	0.54	0.36	0.45	0.38	0.58	0.76	0.79
Al_2O_3	6.56	5.94	6.76	3.91	3.03	5.32	3.24	3.91	7.31	9.25
FeO	8.33	8.48	8.24	6.89	7.36	7.18	8.66	8.47	7.65	8.61
MnO	0.24	0.22	0.22	0.06	0.18	0.10	0.12	0.17	0.14	0.24
MgO	13.16	12.80	12.96	13.61	13.77	9.74	13.47	13.16	10.50	9.12
CaO	20.44	20.30	20.26	20.83	21.07	16.16	19.96	20.19	16.45	14.75
Na_2O	0.42	0.48	0.40	0.48	0.49	1.97	0.49	0.34	1.40	1.67
total	97.75	96.49	97.27	95.86	95.67	95.13	95.96	96.27	95.29	96.98
6 oxygens formula										
Si	1.81	1.83	1.81	1.91	1.91	2.08	1.92	1.91	1.96	1.98
Ti	0.02	0.02	0.02	0.02	0.01	0.01	0.01	0.02	0.02	0.02
Al^{IV}	0.19	0.17	0.19	0.09	0.09	-0.08	0.08	0.09	0.04	0.02
Al^{VI}	0.10	0.10	0.11	0.08	0.04	0.33	0.06	0.09	0.30	0.41
Fe^{3+}	0.07	0.07	0.06	0.01	0.07	-0.29	0.03	0.00	-0.20	-0.31
Fe^{2+}	0.19	0.20	0.21	0.21	0.17	0.52	0.25	0.27	0.45	0.60
Mn	0.01	0.01	0.01	0.00	0.01	0.00	0.00	0.01	0.00	0.01
Mg	0.74	0.73	0.74	0.78	0.79	0.58	0.78	0.76	0.62	0.53
Ca	0.83	0.84	0.83	0.86	0.87	0.69	0.83	0.84	0.70	0.62
Na	0.03	0.04	0.03	0.04	0.04	0.15	0.04	0.03	0.11	0.13
Wo	45.17	45.38	45.30	46.14	45.83	45.76	43.90	44.75	44.42	43.18
En	40.47	39.82	40.32	41.95	41.68	38.38	41.23	40.59	39.46	37.15
Fs	14.37	14.80	14.38	11.91	12.49	15.87	14.87	14.65	16.12	19.67

Experimental biotite

Sample	LTG1	LTG1
MPa	150	150
H2O	2	2
type	EDS	EDS
wt.% SiO2	39.38	39.70
TiO2	4.55	3.85
Al2O3	16.94	13.92
FeO	14.67	19.88
MnO	0.00	0.00
MgO	14.99	12.67
CaO	0.21	0.22
Na2O	0.66	0.53
K2O	8.60	9.22
total	100.00	99.99
Ions number on a 24 oxygens basis		
Si	5.54	5.75
Al iv	2.46	2.25
Al vi	0.34	0.12
Ti	0.48	0.42
Fe3+	0.00	0.00
Fe2+	1.72	2.41
Mn	0.00	0.00
Mg	3.14	2.73
Ca	0.03	0.03
Na	0.18	0.15
K	1.54	1.70
Mg/(Mg+Fe)	0.65	0.53
Fe/(Fe+Mg)	0.35	0.47

Appendix E: Major and trace element composition of natural mineral phases

Appendix E.1 – Major element composition of clinopyrxene

Unit	Pal D	Pal D	Pal D	Pal D	Pal D	Pal D	Pal D	Pal D	Pal D
Lithology	Pumiceous lapilli	Pumiceous lapilli	Pumiceous lapilli	Pumiceous lapilli	Pumiceous lapilli	Pumiceous lapilli	Pumiceous lapilli	Pumiceous lapilli	Pumiceous lapilli
Sample	Pal 15	Pal 15	Pal 15	Pal 15	Pal 15	Pal 15	Pal 15	Pal 15	Pal 15
Type	EPMA	EPMA	EPMA	EPMA	EPMA	EPMA	EPMA	EPMA	EPMA
label	px1core	px1rim	px1rims1	px2core	px2rim	px2rims2	px3core	px3rims5s6	px3rims8
core/rim	core	rim	rim	core	rim	rim	core	rim	rim
wt.% SiO_2	52.18	51.84	51.04	50.24	50.37	50.90	50.96	50.57	50.91
TiO_2	0.51	0.55	0.62	0.58	0.69	0.54	0.60	0.61	0.72
Al_2O_3	2.15	2.20	3.01	3.16	3.14	2.71	3.08	2.97	3.06
FeO_{tot}	8.23	8.33	8.59	8.69	9.02	8.52	9.13	9.77	8.72
MnO	0.35	0.37	0.30	0.34	0.31	0.36	0.46	0.49	0.31
MgO	14.32	14.42	13.71	13.76	13.61	13.98	13.25	12.97	13.69
CaO	21.83	21.91	21.89	21.85	21.67	22.07	21.90	21.85	21.84
Na_2O	0.37	0.45	0.46	0.50	0.45	0.40	0.43	0.45	0.34
K_2O	0.00	0.00	0.00	0.00	0.00	0.00	0.00	0.00	0.00
Cr_2O_3	0.01	0.00	0.00	0.00	0.00	0.07	0.01	0.00	0.00
Total	99.95	100.07	99.63	99.11	99.26	99.55	99.82	99.68	99.59
6 oxygens formula									
Si	1.94	1.92	1.90	1.88	1.89	1.90	1.90	1.90	1.90
Ti	0.01	0.02	0.02	0.02	0.02	0.02	0.02	0.02	0.02
Al^{IV}	0.06	0.08	0.10	0.12	0.11	0.10	0.10	0.10	0.10
Al^{VI}	0.03	0.02	0.04	0.02	0.03	0.02	0.04	0.03	0.04
Fe^{3+}	0.03	0.06	0.06	0.10	0.08	0.08	0.06	0.08	0.05
Fe^{2+}	0.23	0.19	0.21	0.17	0.20	0.18	0.23	0.23	0.23
Mn	0.01	0.01	0.01	0.01	0.01	0.01	0.01	0.02	0.01
Mg	0.79	0.80	0.76	0.77	0.76	0.78	0.74	0.72	0.76
Ca	0.87	0.87	0.87	0.88	0.87	0.88	0.88	0.88	0.87
Na	0.03	0.03	0.03	0.04	0.03	0.03	0.03	0.03	0.02
K	0.00	0.00	0.00	0.00	0.00	0.00	0.00	0.00	0.00
Cr	0.00	0.00	0.00	0.00	0.00	0.00	0.00	0.00	0.00
Wo	45.31	45.20	45.92	45.73	45.48	45.81	46.14	45.98	45.79
En	41.36	41.39	40.02	40.07	39.75	40.38	38.85	37.98	39.94
Fs	13.33	13.41	14.06	14.20	14.78	13.80	15.01	16.05	14.27

clinopyroxene

Unit	Pal D	Pal D	Pal D	Pal D	Pal D	Pal D	Pal D	Pal D	Pal D
Lithology	Pumiceous lapilli	Pumiceous lapilli	Pumiceous lapilli	Pumiceous lapilli	Pumiceous lapilli	Pumiceous lapilli	Pumiceous lapilli	Pumiceous lapilli	Pumiceous lapilli
Sample	Pal 15	Pal 15	Pal 15	Pal 15	Pal 15	Pal 90	Pal 90	Pal 90	Pal 90
Type	EPMA	EPMA	EPMA	EPMA	EPMA	EPMA	EPMA	EPMA	EPMA
label	px4core	px4rim1	px4rim2	px5core	px5rim	px2core	px2rims2	px3core	px4core
core/rim	core	rim	rim	core	rim	core	rim	core	core
wt.% SiO_2	51.40	51.18	51.67	50.08	50.67	51.85	50.16	49.88	50.98
TiO_2	0.53	0.46	0.53	0.68	0.60	0.40	0.57	0.53	0.61
Al_2O_3	2.43	2.25	2.41	3.45	3.03	1.76	2.47	2.53	2.67
FeO_{tot}	8.41	7.97	8.43	9.20	8.81	8.95	8.38	9.28	9.00
MnO	0.37	0.35	0.29	0.31	0.30	0.44	0.36	0.48	0.36
MgO	13.77	14.40	14.14	13.73	13.83	14.13	14.20	13.60	13.73
CaO	22.14	21.91	22.04	21.86	21.97	21.96	22.13	21.74	21.84
Na_2O	0.46	0.39	0.41	0.42	0.40	0.34	0.47	0.43	0.42
K_2O	0.00	0.00	0.00	0.00	0.00	0.00	0.00	0.00	0.00
Cr_2O_3	0.00	0.00	0.00	0.04	0.03	0.00	0.04	0.04	0.00
Total	99.51	98.90	99.92	99.75	99.64	99.82	98.78	98.50	99.61
6 oxygens formula									
Si	1.92	1.92	1.92	1.87	1.89	1.93	1.88	1.88	1.90
Ti	0.01	0.01	0.01	0.02	0.02	0.01	0.02	0.02	0.02
Al^{IV}	0.08	0.08	0.08	0.13	0.11	0.07	0.12	0.12	0.10
Al^{VI}	0.03	0.02	0.02	0.02	0.02	0.01	-0.01	0.00	0.02
Fe^{3+}	0.06	0.07	0.06	0.11	0.08	0.06	0.13	0.12	0.07
Fe^{2+}	0.20	0.18	0.21	0.18	0.19	0.22	0.13	0.18	0.21
Mn	0.01	0.01	0.01	0.01	0.01	0.01	0.01	0.02	0.01
Mg	0.77	0.80	0.78	0.76	0.77	0.79	0.79	0.77	0.76
Ca	0.89	0.88	0.88	0.87	0.88	0.88	0.89	0.88	0.87
Na	0.03	0.03	0.03	0.03	0.03	0.02	0.03	0.03	0.03
K	0.00	0.00	0.00	0.00	0.00	0.00	0.00	0.00	0.00
Cr	0.00	0.00	0.00	0.00	0.00	0.00	0.00	0.00	0.00
Wo	46.25	45.49	45.63	45.40	45.68	45.18	45.69	45.38	45.53
En	40.03	41.60	40.74	39.68	40.02	40.45	40.80	39.50	39.83
Fs	13.71	12.91	13.62	14.91	14.30	14.37	13.51	15.12	14.64

clinopyroxene

Unit	Pal D	Pal D	Pal D	Pal D	Pal D	Palizzi lava	Palizzi lava	Palizzi lava	Palizzi lava
Lithology	Pumiceous lapilli	Pumiceous lapilli	Pumiceous lapilli	Pumiceous lapilli	Pumiceous lapilli	Lava	Lava	Lava	Lava
Sample	Pal 90	Pal 90	Pal 90	Pal 90	Pal 90	VGPL3	VGPL3	VGPL3	VGPL3
Type	EPMA	EPMA	EPMA	EPMA	EPMA	EPMA	EPMA	EPMA	EPMA
label	px4rim	px5core	px5rims13	px6core	px6rim	px7	px7	px8	px8
core/rim	rim	core	rim	core	rim	core	rim	core	rim
wt.% SiO_2	51.26	52.90	52.90	50.49	52.03	50.46	50.56	50.32	49.63
TiO_2	0.61	0.42	0.42	0.74	0.46	0.69	0.58	0.63	0.66
Al_2O_3	2.91	1.71	1.71	3.73	2.13	3.63	3.40	3.52	4.22
FeO_{tot}	9.31	9.06	9.06	8.99	7.95	9.21	8.76	8.23	9.15
MnO	0.38	0.46	0.46	0.35	0.32	0.36	0.22	0.35	0.29
MgO	13.60	13.97	13.97	13.85	14.59	13.23	13.13	13.51	13.35
CaO	21.88	22.08	22.08	21.67	21.85	21.56	21.41	21.55	21.60
Na_2O	0.45	0.43	0.43	0.43	0.36	0.43	0.42	0.44	0.39
K_2O	0.00	0.00	0.00	0.00	0.00	0.00	0.00	0.00	0.00
Cr_2O_3	0.00	0.00	0.00	0.02	0.00	0.01	0.02	0.01	0.00
Total	100.40	101.03	101.03	100.27	99.69	99.57	98.51	98.55	99.29
6 oxygens formula									
Si	1.90	1.95	1.95	1.87	1.93	1.89	1.91	1.90	1.86
Ti	0.02	0.01	0.01	0.02	0.01	0.02	0.02	0.02	0.02
Al^{IV}	0.10	0.05	0.05	0.13	0.07	0.11	0.09	0.10	0.14
Al^{VI}	0.03	0.02	0.02	0.03	0.03	0.05	0.06	0.05	0.04
Fe^{3+}	0.07	0.03	0.03	0.09	0.04	0.06	0.03	0.05	0.09
Fe^{2+}	0.22	0.25	0.25	0.19	0.21	0.23	0.25	0.21	0.20
Mn	0.01	0.01	0.01	0.01	0.01	0.01	0.01	0.01	0.01
Mg	0.75	0.77	0.77	0.77	0.81	0.74	0.74	0.76	0.75
Ca	0.87	0.87	0.87	0.86	0.87	0.86	0.87	0.87	0.87
Na	0.03	0.03	0.03	0.03	0.03	0.03	0.03	0.03	0.03
K	0.00	0.00	0.00	0.00	0.00	0.00	0.00	0.00	0.00
Cr	0.00	0.00	0.00	0.00	0.00	0.00	0.00	0.00	0.00
Wo	45.52	45.44	45.44	45.18	45.18	45.71	46.03	46.07	45.65
En	39.37	40.01	40.01	40.19	41.98	39.05	39.27	40.19	39.26
Fs	15.12	14.55	14.55	14.63	12.83	15.24	14.70	13.74	15.10

clinopyroxene

Unit	Palizzi lava	Palizzi lava	Palizzi lava	Palizzi lava	Palizzi lava	Palizzi lava	Palizzi lava	Palizzi lava	Palizzi lava
Lithology	Lava	Lava	Lava	Lava	Lava	Lava	Lava	Lava	Lava
Sample	VGPL3	VGPL3	SC-15-1	SC-15-1	SC-15-1	SC-15-1	SC-15-1	SC-15-1	SC-15-1
Type	EPMA	EPMA	EPMA	EPMA	EPMA	EPMA	EPMA	EPMA	EPMA
label	px1	px1	px1core	px1rim	px2core	px2rim	px3core	px3rim	px4core
core/rim	core	rim	core	rim	core	rim	core	rim	core
wt.% SiO_2	50.87	50.73	51.39	50.82	52.58	50.26	50.77	50.84	50.81
TiO_2	0.67	0.63	0.68	0.61	0.38	0.55	0.62	0.62	0.65
Al_2O_3	3.55	4.06	3.60	3.56	1.69	4.23	3.21	3.63	4.00
FeO_{tot}	8.75	8.28	7.30	9.05	10.47	8.47	8.86	8.69	7.54
MnO	0.25	0.28	0.17	0.27	0.47	0.22	0.27	0.27	0.15
MgO	13.36	13.33	14.13	13.58	14.04	13.72	13.68	13.80	14.59
CaO	21.62	22.09	22.86	21.92	20.44	22.15	21.87	21.97	22.44
Na_2O	0.38	0.45	0.37	0.49	0.45	0.36	0.46	0.53	0.36
K_2O	0.00	0.00	0.00	0.00	0.00	0.00	0.00	0.00	0.00
Cr_2O_3	0.00	0.05	0.13	0.02	0.06	0.00	0.00	0.00	0.05
Total	99.46	99.90	100.63	100.31	100.58	99.96	99.74	100.35	100.58
6 oxygens formula									
Si	1.90	1.89	1.89	1.88	1.95	1.86	1.89	1.88	1.87
Ti	0.02	0.02	0.02	0.02	0.01	0.02	0.02	0.02	0.02
Al^{IV}	0.10	0.11	0.11	0.12	0.05	0.14	0.11	0.12	0.13
Al^{VI}	0.06	0.06	0.05	0.04	0.03	0.05	0.03	0.04	0.04
Fe^{3+}	0.03	0.05	0.05	0.08	0.03	0.08	0.07	0.09	0.08
Fe^{2+}	0.25	0.21	0.17	0.20	0.29	0.18	0.20	0.18	0.15
Mn	0.01	0.01	0.01	0.01	0.01	0.01	0.01	0.01	0.00
Mg	0.75	0.74	0.77	0.75	0.78	0.76	0.76	0.76	0.80
Ca	0.87	0.88	0.90	0.87	0.81	0.88	0.87	0.87	0.88
Na	0.03	0.03	0.03	0.04	0.03	0.03	0.03	0.04	0.03
K	0.00	0.00	0.00	0.00	0.00	0.00	0.00	0.00	0.00
Cr	0.00	0.00	0.00	0.00	0.00	0.00	0.00	0.00	0.00
Wo	45.97	46.90	47.41	45.78	42.45	46.29	45.73	45.81	46.15
En	39.51	39.37	40.78	39.47	40.58	39.90	39.81	40.04	41.75
Fs	14.52	13.72	11.82	14.75	16.97	13.82	14.46	14.14	12.10

clinopyroxene

Unit	Palizzi lava	Palizzi lava	Palizzi lava	Palizzi lava	Palizzi lava	Palizzi lava	Palizzi lava	Palizzi lava	Palizzi lava
Lithology	Lava	Lava	Lava	Lava	Lava	Lava	Lava	Lava	Lava
Sample	SC-15-1	SC-15-1	SC-15-1	SC-15-1	SC-15-1	SC-15-1	SC-15-1	SC-15-1	SC-15-1
Type	EPMA	EPMA	EPMA	EPMA	EPMA	EPMA	EPMA	EPMA	EPMA
label	px4rim	px5core	px5rim	px6core	px6rim	px7core	px7rim	px8core	px8rim
core/rim	rim	core	rim	core	rim	core	rim	core	rim
wt.% SiO_2	52.46	50.71	51.42	50.93	51.17	52.39	50.63	50.81	52.04
TiO_2	0.38	0.69	0.56	0.49	0.63	0.38	0.56	0.50	0.41
Al_2O_3	2.32	3.88	3.38	3.41	3.79	2.76	3.32	3.73	2.65
FeO_{tot}	8.39	8.96	8.61	8.46	8.70	5.61	9.47	7.97	8.33
MnO	0.39	0.31	0.27	0.21	0.23	0.13	0.43	0.23	0.33
MgO	14.70	13.28	13.98	14.08	13.97	15.62	13.94	14.17	14.47
CaO	21.73	22.04	22.17	22.16	22.29	22.90	21.25	22.56	21.85
Na_2O	0.44	0.50	0.42	0.46	0.45	0.22	0.48	0.35	0.30
K_2O	0.00	0.00	0.00	0.00	0.00	0.00	0.00	0.00	0.00
Cr_2O_3	0.00	0.01	0.00	0.02	0.00	0.32	0.00	0.08	0.00
Total	100.80	100.38	100.81	100.23	101.23	100.34	100.08	100.40	100.38
6 oxygens formula									
Si	1.93	1.88	1.89	1.88	1.87	1.92	1.88	1.87	1.92
Ti	0.01	0.02	0.02	0.01	0.02	0.01	0.02	0.01	0.01
Al^{IV}	0.07	0.12	0.11	0.12	0.13	0.08	0.12	0.13	0.08
Al^{VI}	0.03	0.05	0.04	0.03	0.04	0.04	0.03	0.04	0.04
Fe^{3+}	0.06	0.07	0.07	0.09	0.08	0.03	0.10	0.09	0.04
Fe^{2+}	0.20	0.21	0.20	0.17	0.18	0.14	0.20	0.16	0.22
Mn	0.01	0.01	0.01	0.01	0.01	0.00	0.01	0.01	0.01
Mg	0.81	0.73	0.77	0.78	0.76	0.85	0.77	0.78	0.80
Ca	0.86	0.88	0.87	0.88	0.88	0.90	0.85	0.89	0.86
Na	0.03	0.04	0.03	0.03	0.03	0.02	0.03	0.03	0.02
K	0.00	0.00	0.00	0.00	0.00	0.00	0.00	0.00	0.00
Cr	0.00	0.00	0.00	0.00	0.00	0.01	0.00	0.00	0.00
Wo	44.59	46.39	45.86	45.83	45.94	46.72	44.23	46.52	45.06
En	41.97	38.89	40.24	40.52	40.07	44.35	40.38	40.66	41.53
Fs	13.44	14.72	13.90	13.66	14.00	8.93	15.39	12.83	13.41

clinopyroxene

Unit	Palizzi lava	Palizzi lava	Palizzi lava	Palizzi lava	Palizzi lava	Palizzi lava	Palizzi lava	Palizzi lava	Palizzi lava
Lithology	Lava	Lava	Lava	Lava	Lava	Lava	Lava	Lava	Lava
Sample	SC-15-1	SC-15-1	SC-18-24	SC-18-24	SC-18-24	SC-18-24	SC-18-24	SC-18-24	SC-18-24
Type	EPMA	EPMA	EPMA	EPMA	EPMA	EPMA	EPMA	EPMA	EPMA
label	px9core	px9rim	px1core	px1rim	px2core	px2rim	px3core	px3rim	px4core
core/rim	core	rim	core	rim	core	rim	core	rim	core
wt.% SiO_2	49.72	50.38	50.47	49.54	50.32	50.83	50.28	49.83	50.38
TiO_2	0.92	0.60	0.58	0.67	0.75	0.60	0.54	0.72	0.54
Al_2O_3	4.78	4.34	4.02	4.04	3.86	3.27	3.90	4.20	3.59
FeO_{tot}	8.78	8.75	8.10	8.21	8.86	8.02	8.48	9.03	8.45
MnO	0.28	0.23	0.26	0.18	0.23	0.25	0.28	0.23	0.26
MgO	13.44	13.79	14.19	13.60	13.69	14.14	13.75	13.28	13.72
CaO	22.05	22.03	21.90	21.93	21.61	21.55	21.85	21.80	21.69
Na_2O	0.41	0.43	0.45	0.46	0.51	0.44	0.45	0.48	0.42
K_2O	0.00	0.00	0.00	0.00	0.00	0.00	0.00	0.00	0.00
Cr_2O_3	0.01	0.00	0.03	0.01	0.00	0.06	0.06	0.02	0.00
Total	100.39	100.55	100.00	98.63	99.83	99.16	99.60	99.59	99.06
6 oxygens formula									
Si	1.84	1.86	1.87	1.86	1.87	1.90	1.87	1.86	1.89
Ti	0.03	0.02	0.02	0.02	0.02	0.02	0.02	0.02	0.02
Al^{IV}	0.16	0.14	0.13	0.14	0.13	0.10	0.13	0.14	0.11
Al^{VI}	0.05	0.05	0.04	0.04	0.04	0.04	0.04	0.04	0.04
Fe^{3+}	0.09	0.09	0.09	0.09	0.08	0.06	0.09	0.09	0.07
Fe^{2+}	0.18	0.18	0.16	0.16	0.19	0.19	0.18	0.19	0.20
Mn	0.01	0.01	0.01	0.01	0.01	0.01	0.01	0.01	0.01
Mg	0.74	0.76	0.78	0.76	0.76	0.79	0.76	0.74	0.77
Ca	0.87	0.87	0.87	0.88	0.86	0.86	0.87	0.87	0.87
Na	0.03	0.03	0.03	0.03	0.04	0.03	0.03	0.03	0.03
K	0.00	0.00	0.00	0.00	0.00	0.00	0.00	0.00	0.00
Cr	0.00	0.00	0.00	0.00	0.00	0.00	0.00	0.00	0.00
Wo	46.32	45.85	45.66	46.40	45.42	45.38	45.90	46.06	45.78
En	39.29	39.94	41.17	40.04	40.04	41.44	40.20	39.05	40.30
Fs	14.40	14.21	13.18	13.56	14.54	13.18	13.90	14.89	13.92

clinopyroxene

Unit	Palizzi lava	Palizzi lava	Palizzi lava	Palizzi lava	Palizzi lava	Palizzi lava	Palizzi lava	Palizzi lava	Palizzi lava
Lithology	Lava	Lava	Lava	Lava	Lava	Lava	Lava	Lava	Lava
Sample	SC-18-24	SC-18-24	SC-18-24	SC-18-24	SC-18-24	SC-18-24	SC-18-24	SC-18-24	SC-18-24
Type	EPMA	EPMA	EPMA	EPMA	EPMA	EPMA	EPMA	EPMA	EPMA
label	px4rim	px5core	px5rim	px6core	px6rim	px7core	px7rim	px8core	px8rim
core/rim	rim	core	rim	core	rim	core	rim	core	rim
wt.% SiO_2	49.77	50.10	49.78	49.95	49.61	50.88	51.09	51.05	49.85
TiO_2	0.68	0.50	0.69	0.61	0.56	0.45	0.39	0.52	0.67
Al_2O_3	4.17	4.10	4.13	3.76	3.97	2.89	2.64	3.60	4.03
FeO_{tot}	8.41	7.54	8.48	8.98	8.51	8.17	7.96	7.45	8.65
MnO	0.22	0.22	0.24	0.22	0.19	0.26	0.27	0.20	0.22
MgO	13.59	14.36	13.54	13.70	13.59	14.41	14.53	14.61	13.58
CaO	22.08	22.10	21.59	21.56	21.88	21.73	21.59	22.21	21.91
Na_2O	0.43	0.36	0.47	0.54	0.39	0.35	0.36	0.40	0.41
K_2O	0.00	0.00	0.00	0.00	0.00	0.00	0.00	0.00	0.00
Cr_2O_3	0.00	0.00	0.03	0.00	0.00	0.00	0.00	0.08	0.00
Total	99.35	99.28	98.95	99.32	98.70	99.14	98.83	100.11	99.33
6 oxygens formula									
Si	1.86	1.86	1.87	1.87	1.86	1.90	1.91	1.88	1.86
Ti	0.02	0.01	0.02	0.02	0.02	0.01	0.01	0.01	0.02
Al^{IV}	0.14	0.14	0.13	0.13	0.14	0.10	0.09	0.12	0.14
Al^{VI}	0.04	0.04	0.05	0.03	0.04	0.03	0.03	0.04	0.04
Fe^{3+}	0.09	0.09	0.08	0.11	0.09	0.07	0.06	0.08	0.09
Fe^{2+}	0.17	0.14	0.19	0.17	0.17	0.18	0.19	0.15	0.18
Mn	0.01	0.01	0.01	0.01	0.01	0.01	0.01	0.01	0.01
Mg	0.76	0.80	0.76	0.76	0.76	0.80	0.81	0.80	0.76
Ca	0.88	0.88	0.87	0.86	0.88	0.87	0.87	0.88	0.88
Na	0.03	0.03	0.03	0.04	0.03	0.03	0.03	0.03	0.03
K	0.00	0.00	0.00	0.00	0.00	0.00	0.00	0.00	0.00
Cr	0.00	0.00	0.00	0.00	0.00	0.00	0.00	0.00	0.00
Wo	46.43	46.07	45.89	45.26	46.13	45.12	44.96	45.93	46.07
En	39.77	41.66	40.05	40.02	39.87	41.64	42.10	42.04	39.73
Fs	13.80	12.27	14.07	14.71	14.00	13.24	12.94	12.03	14.20

clinopyroxene

Unit	Pietre Cotte	Pietre Cotte	Pietre Cotte	Pietre Cotte	Pietre Cotte	Pietre Cotte	Pietre Cotte	Pietre Cotte	Pietre Cotte
Lithology	Enclave	Enclave	Enclave	Enclave	Enclave	Enclave	Enclave	Enclave	Enclave
Sample	VPCL8i	VPCL8i	VPCL8i	VPCL8i	VPCL8i	VPCL8i	VPCL8i	VPCL8i	VPCL8i
Type	EPMA	EPMA	EPMA	EPMA	EPMA	EPMA	EPMA	EPMA	EPMA
label	cpx1 core	cpx1 rim	cpx 5 core	cpx 5 rim	cpx1 core	cpx1 core	cpx core	cpx1 rim	cpx rim
core/rim	core	rim	core	rim	core	core	core	rim	rim
wt.% SiO_2	51.04	51.98	50.57	51.31	50.38	51.04	50.57	51.98	51.31
TiO_2	0.78	0.55	0.69	0.54	0.66	0.78	0.69	0.55	0.54
Al_2O_3	3.95	2.79	3.88	2.79	3.91	3.95	3.88	2.79	2.79
FeO_{tot}	8.71	9.33	9.26	9.50	8.84	8.71	9.26	9.33	9.50
MnO	0.24	0.42	0.29	0.45	0.27	0.24	0.29	0.42	0.45
MgO	13.92	14.20	13.92	14.43	13.94	13.92	13.92	14.20	14.43
CaO	21.99	21.24	21.44	21.11	21.91	21.99	21.44	21.24	21.11
Na_2O	0.46	0.47	0.44	0.48	0.51	0.46	0.44	0.47	0.48
K_2O	0.00	0.00	0.00	0.00	0.00	0.00	0.00	0.00	0.00
Cr_2O_3	0.00	0.00	0.00	0.00	0.00	0.00	0.00	0.00	0.00
Total	101.09	100.99	100.50	100.61	100.42	101.09	100.50	100.99	100.61
6 oxygens formula									
Si	1.87	1.91	1.87	1.89	1.86	1.87	1.87	1.91	1.89
Ti	0.02	0.02	0.02	0.01	0.02	0.02	0.02	0.02	0.01
Al^{IV}	0.13	0.09	0.13	0.11	0.14	0.13	0.13	0.09	0.11
Al^{VI}	0.04	0.03	0.04	0.01	0.03	0.04	0.04	0.03	0.01
Fe^{3+}	0.07	0.06	0.09	0.10	0.11	0.07	0.09	0.06	0.10
Fe^{2+}	0.20	0.23	0.20	0.20	0.16	0.20	0.20	0.23	0.20
Mn	0.01	0.01	0.01	0.01	0.01	0.01	0.01	0.01	0.01
Mg	0.76	0.78	0.77	0.79	0.77	0.76	0.77	0.78	0.79
Ca	0.86	0.84	0.85	0.83	0.87	0.86	0.85	0.84	0.83
Na	0.03	0.03	0.03	0.03	0.04	0.03	0.03	0.03	0.03
K	0.00	0.00	0.00	0.00	0.00	0.00	0.00	0.00	0.00
Cr	0.00	0.00	0.00	0.00	0.00	0.00	0.00	0.00	0.00
Wo	45.65	44.00	44.64	43.44	45.45	45.65	44.64	44.00	43.44
En	40.23	40.92	40.31	41.30	40.23	40.23	40.31	40.92	41.30
Fs	14.12	15.08	15.05	15.26	14.32	14.12	15.05	15.08	15.26

clinopyroxene

Unit	Pal B	Pal B	Pal B	Pal B	Pal B	Pal B	Pal B	Pal B	Pal B
Lithology	Pumiceous lapilli	Pumiceous lapilli	Pumiceous lapilli	Pumiceous lapilli	Pumiceous lapilli	Pumiceous lapilli	Pumiceous lapilli	Pumiceous lapilli	Pumiceous lapilli
Sample	Pal-L	Pal-L	Pal-L	Pal-L	Pal-L	Pal-L	Pal-L	Pal-L	Pal-L
Type	EDS	EDS	EDS	EDS	EDS	EDS	EDS	EDS	EDS
label	Pal-L px1	Pal-L px u112	Pal-L px u112	Pal-L px u112	Pal-L px u113	Pal-L px u113	Pal-L px u113	Pal-L px u114	Pal-L px u114
core/rim	core	core	rim	rim	core	rim	rim	core	rim
wt.% SiO_2	49.38	50.59	52.62	50.03	50.38	51.92	50.74	51.65	52.06
TiO_2	0.79	0.65	0.31	0.58	0.60	0.45	0.73	0.40	0.34
Al_2O_3	4.20	3.43	1.60	3.64	3.62	2.22	3.63	3.28	1.76
FeO_{tot}	8.99	8.80	5.77	9.02	8.57	7.57	8.47	6.31	7.84
MnO	0.22	0.48	0.25	0.35	0.41	0.24	0.26	0.09	0.39
MgO	13.28	14.12	16.29	13.65	13.69	14.99	14.18	15.29	15.09
CaO	22.61	21.92	23.03	22.51	22.54	22.51	21.79	22.98	22.51
Na_2O	0.51	0.00	0.14	0.23	0.17	0.11	0.19	0.00	0.00
K_2O	0.01	0.00	0.00	0.00	0.00	0.00	0.00	0.00	0.00
Cr_2O_3	0.01	0.00	0.00	0.00	0.00	0.00	0.00	0.00	0.00
Total	100.00	99.99	100.01	100.01	99.98	100.01	99.99	100.00	99.99
6 oxygens formula									
Si	1.83	1.88	1.93	1.86	1.87	1.92	1.88	1.90	1.93
Ti	0.02	0.02	0.01	0.02	0.02	0.01	0.02	0.01	0.01
Al^{IV}	0.17	0.12	0.07	0.14	0.13	0.08	0.12	0.10	0.07
Al^{VI}	0.02	0.03	0.00	0.02	0.03	0.02	0.04	0.04	0.01
Fe^{3+}	0.14	0.05	0.06	0.10	0.07	0.04	0.05	0.03	0.04
Fe^{2+}	0.14	0.23	0.11	0.18	0.20	0.19	0.22	0.16	0.20
Mn	0.01	0.02	0.01	0.01	0.01	0.01	0.01	0.00	0.01
Mg	0.74	0.78	0.89	0.76	0.76	0.83	0.79	0.84	0.83
Ca	0.90	0.87	0.91	0.90	0.90	0.89	0.87	0.91	0.89
Na	0.04	0.00	0.01	0.02	0.01	0.01	0.01	0.00	0.00
K	0.00	0.00	0.00	0.00	0.00	0.00	0.00	0.00	0.00
Cr	0.00	0.00	0.00	0.00	0.00	0.00	0.00	0.00	0.00
Wo	46.99	45.25	45.87	46.37	46.69	45.68	45.27	46.72	45.36
En	38.42	40.57	45.15	39.13	39.46	42.33	41.00	43.26	42.31
Fs	14.59	14.18	8.97	14.50	13.85	11.99	13.73	10.01	12.33

clinopyroxene

Unit	Pal B	Pal B	Pal B	Pal B	Pal B
Lithology	Pumiceous lapilli	Pumiceous lapilli	Pumiceous lapilli	Pumiceous lapilli	Pumiceous lapilli
Sample	Pal-L	Pal-L	Pal-L	Pal-L	Pal-L
Type	EDS	EDS	EDS	EDS	EDS
label	Pal-L px 114 bd	Pal-L px u115 nc	Pal-L px u115 bd	Pal-L px u69 nc	Pal-L px u69 bd
core/rim	rim	core	rim	core	rim
wt.% SiO_2	50.36	50.69	50.28	50.75	51.90
TiO_2	0.56	0.64	0.61	0.52	0.25
Al_2O_3	4.19	3.58	3.60	3.02	1.02
FeO_{tot}	8.89	8.75	8.64	8.60	14.28
MnO	0.29	0.19	0.28	0.34	0.67
MgO	13.64	13.92	13.95	14.21	12.31
CaO	21.92	22.23	22.48	22.43	19.58
Na_2O	0.14	0.00	0.16	0.14	0.00
K_2O	0.00	0.00	0.00	0.00	0.00
Cr_2O_3	0.00	0.00	0.00	0.00	0.00
Total	99.99	100.00	100.00	100.01	100.01
6 oxygens formula					
Si	1.87	1.89	1.87	1.89	1.97
Ti	0.02	0.02	0.02	0.01	0.01
Al^{IV}	0.13	0.11	0.13	0.11	0.03
Al^{VI}	0.06	0.04	0.03	0.02	0.02
Fe^{3+}	0.05	0.03	0.08	0.08	-0.01
Fe^{2+}	0.23	0.24	0.19	0.19	0.46
Mn	0.01	0.01	0.01	0.01	0.02
Mg	0.76	0.77	0.77	0.79	0.70
Ca	0.87	0.89	0.90	0.89	0.80
Na	0.01	0.00	0.01	0.01	0.00
K	0.00	0.00	0.00	0.00	0.00
Cr	0.00	0.00	0.00	0.00	0.00
Wo	45.82	45.90	46.22	45.85	40.91
En	39.68	40.00	39.91	40.42	35.80
Fs	14.50	14.10	13.87	13.72	23.29

Appendix E.2 – Selected clinopyroxene core to rim profiles and assigned cluster (Appendix to chapter 8, the complete data set is available upon request to the author).

core (0) to rim (µm)	Sample	Unit	label	wt.% SiO_2	TiO_2	Al_2O_3	FeO_{tot}	MnO	MgO	CaO	Na_2O	K_2O	Cr_2O_3	Sum	DiHd	EnFs	Jd	CaTs	CaTi	Cluster
0	Vul 17 T-21	Pal A	O6	50.66	0.66	3.60	8.76	0.29	13.73	21.93	0.52	0.01	0.00	100.16	0.82	0.11	0.04	0.01	0.05	1
20	Vul 17 T-21	Pal A	O6	50.07	0.62	3.89	8.85	0.30	13.69	22.10	0.48	0.00	0.00	100.01	0.82	0.11	0.03	0.01	0.06	1
40	Vul 17 T-21	Pal A	O6	49.89	0.70	4.18	8.83	0.22	13.60	22.08	0.38	0.00	0.02	99.90	0.81	0.11	0.03	0.03	0.05	1
60	Vul 17 T-21	Pal A	O6	49.84	0.68	4.35	8.73	0.20	13.55	22.33	0.35	0.01	0.02	100.06	0.81	0.11	0.03	0.03	0.05	2
80	Vul 17 T-21	Pal A	O6	49.84	0.66	4.38	8.60	0.24	13.52	22.23	0.43	0.01	0.00	99.90	0.81	0.11	0.03	0.03	0.05	2
100	Vul 17 T-21	Pal A	O6	50.46	0.66	3.66	8.65	0.27	13.81	21.96	0.51	0.01	0.02	100.01	0.82	0.11	0.04	0.01	0.05	1
120	Vul 17 T-21	Pal A	O6	50.68	0.67	3.71	8.70	0.25	13.81	22.00	0.39	0.01	0.00	100.21	0.81	0.11	0.03	0.02	0.04	1
140	Vul 17 T-21	Pal A	O6	50.03	0.70	4.25	9.05	0.29	13.44	21.88	0.43	0.00	0.00	100.08	0.80	0.12	0.03	0.03	0.05	2
160	Vul 17 T-21	Pal A	O6	50.41	0.62	3.50	9.14	0.30	13.49	21.67	0.55	0.01	0.00	99.70	0.81	0.11	0.04	0.01	0.05	1
180	Vul 17 T-21	Pal A	O6	50.34	0.61	3.46	9.06	0.25	13.66	21.77	0.46	0.01	0.00	99.62	0.82	0.12	0.03	0.01	0.05	1
0	Vul 17 T B3	Pal B	D8	52.40	0.32	2.56	4.28	0.13	16.28	22.69	0.34	0.00	0.95	99.95	0.84	0.09	0.02	0.01	0.03	3
20	Vul 17 T B3	Pal B	D8	52.67	0.34	2.43	4.18	0.06	16.55	22.57	0.32	0.00	1.19	100.30	0.83	0.10	0.02	0.01	0.04	3
40	Vul 17 T B3	Pal B	D8	52.26	0.42	2.85	4.96	0.11	15.96	22.70	0.29	0.00	0.47	100.01	0.84	0.10	0.02	0.02	0.03	3
60	Vul 17 T B3	Pal B	D8	51.71	0.47	3.02	6.33	0.15	15.31	22.56	0.35	0.00	0.24	100.13	0.84	0.10	0.02	0.02	0.04	3
80	Vul 17 T B3	Pal B	D8	49.98	0.66	4.51	8.40	0.18	13.72	22.27	0.37	0.01	0.03	100.11	0.80	0.11	0.03	0.04	0.05	3
100	Vul 17 T B3	Pal B	D8	50.53	0.66	3.78	9.19	0.28	13.58	21.89	0.52	0.00	0.00	100.42	0.81	0.12	0.04	0.01	0.05	1
120	Vul 17 T B3	Pal B	D8	51.15	0.64	3.70	8.90	0.24	13.64	21.74	0.50	0.03	0.00	100.54	0.80	0.11	0.04	0.03	0.04	1
0	Vul 17 T-17	Pal C1	N8	52.05	0.35	2.52	5.33	0.09	15.67	23.11	0.32	0.00	0.42	99.86	0.86	0.08	0.02	0.01	0.04	3
20	Vul 17 T-17	Pal C1	N8	52.53	0.37	2.15	5.17	0.12	15.86	23.14	0.25	0.01	0.28	99.88	0.87	0.08	0.02	0.01	0.03	3
40	Vul 17 T-17	Pal C1	N8	51.53	0.43	2.66	6.79	0.11	15.13	22.68	0.31	0.00	0.16	99.79	0.85	0.10	0.02	0.01	0.04	3
60	Vul 17 T-17	Pal C1	N8	50.63	0.71	3.56	8.41	0.24	14.05	22.26	0.43	0.00	0.00	100.30	0.83	0.11	0.03	0.01	0.05	1
80	Vul 17 T-17	Pal C1	N8	50.01	0.65	4.04	8.74	0.24	13.67	22.24	0.45	0.00	0.03	100.07	0.82	0.11	0.03	0.02	0.06	1
100	Vul 17 T-17	Pal C1	N8	48.98	0.77	4.78	9.04	0.25	13.28	22.02	0.53	0.00	0.00	99.67	0.80	0.11	0.04	0.02	0.07	2
120	Vul 17 T-17	Pal C1	N8	50.53	0.51	3.52	7.70	0.17	14.56	22.48	0.35	0.00	0.13	99.95	0.83	0.11	0.03	0.01	0.05	3
140	Vul 17 T-17	Pal C1	N8	49.94	0.61	4.11	8.27	0.20	14.01	22.46	0.36	0.01	0.07	100.04	0.82	0.11	0.03	0.02	0.06	3
160	Vul 17 T-17	Pal C1	N8	50.03	0.73	3.71	8.51	0.28	13.94	22.20	0.45	0.00	0.00	99.85	0.83	0.11	0.03	0.01	0.06	1

180	Vul 17 T-17	Pal C1	N8	49.48	0.74	4.46	9.11	0.24	13.38	22.20	0.41	0.01	0.03	100.05	0.81	0.11	0.03	0.02	0.06	2
200	Vul 17 T-17	Pal C1	N8	50.26	0.69	3.65	8.87	0.24	13.78	22.14	0.44	0.00	0.04	100.11	0.82	0.11	0.03	0.01	0.06	1
240	Vul 17 T-17	Pal C1	N8	50.13	0.74	3.83	8.90	0.23	13.51	22.21	0.41	0.00	0.00	99.96	0.82	0.11	0.03	0.02	0.05	1
260	Vul 17 T-17	Pal C1	N8	49.94	0.73	3.94	8.97	0.27	13.51	22.01	0.47	0.00	0.00	99.85	0.82	0.11	0.03	0.01	0.06	1
280	Vul 17 T-17	Pal C1	N8	49.98	0.72	4.13	9.20	0.22	13.42	22.08	0.43	0.00	0.00	100.20	0.81	0.11	0.03	0.02	0.05	2
300	Vul 17 T-17	Pal C1	N8	50.29	0.60	4.00	8.24	0.22	13.90	22.37	0.39	0.00	0.03	100.05	0.82	0.11	0.03	0.02	0.05	1
320	Vul 17 T-17	Pal C1	N8	50.16	0.65	3.93	8.76	0.21	13.69	22.14	0.42	0.01	0.03	100.00	0.82	0.11	0.03	0.02	0.05	1
340	Vul 17 T-17	Pal C1	N8	50.33	0.67	3.54	9.08	0.30	13.66	21.94	0.50	0.01	0.00	100.06	0.82	0.11	0.04	0.01	0.05	1
0	Vul 17 T-10	Pal C2	B13	51.02	0.57	3.12	8.78	0.29	13.67	21.77	0.48	0.00	0.00	99.71	0.82	0.11	0.04	0.01	0.04	4
20	Vul 17 T-10	Pal C2	B13	51.34	0.52	3.06	8.52	0.25	13.79	22.07	0.45	0.00	0.02	100.02	0.83	0.10	0.03	0.02	0.03	4
40	Vul 17 T-10	Pal C2	B13	51.41	0.56	3.13	8.80	0.25	13.75	21.70	0.42	0.00	0.00	100.02	0.81	0.11	0.03	0.02	0.03	4
60	Vul 17 T-10	Pal C2	B13	51.53	0.45	2.84	8.27	0.23	14.02	22.24	0.38	0.01	0.00	99.98	0.84	0.10	0.03	0.02	0.03	4
80	Vul 17 T-10	Pal C2	B13	51.29	0.49	2.79	8.91	0.28	13.64	21.62	0.47	0.00	0.00	99.50	0.82	0.11	0.03	0.01	0.03	4
100	Vul 17 T-10	Pal C2	B13	51.78	0.47	2.64	8.63	0.27	13.74	21.87	0.39	0.00	0.00	99.81	0.83	0.10	0.03	0.02	0.02	4
120	Vul 17 T-10	Pal C2	B13	51.36	0.53	2.92	8.77	0.27	13.56	21.75	0.41	0.00	0.00	99.57	0.82	0.10	0.03	0.02	0.03	4
140	Vul 17 T-10	Pal C2	B13	51.15	0.56	3.12	8.92	0.28	13.47	21.87	0.46	0.01	0.00	99.84	0.82	0.10	0.03	0.02	0.03	4
160	Vul 17 T-10	Pal C2	B13	51.52	0.51	2.88	8.41	0.23	13.73	22.04	0.41	0.00	0.00	99.74	0.83	0.10	0.03	0.02	0.03	4
180	Vul 17 T-10	Pal C2	B13	53.19	0.32	1.70	5.80	0.18	15.63	23.00	0.25	0.00	0.07	100.15	0.88	0.08	0.02	0.01	0.02	3
200	Vul 17 T-10	Pal C2	B13	50.80	0.52	3.54	8.18	0.19	13.72	22.32	0.39	0.01	0.00	99.67	0.83	0.10	0.03	0.03	0.04	1
220	Vul 17 T-10	Pal C2	B13	50.91	0.59	3.56	9.04	0.24	13.30	21.81	0.47	0.02	0.00	99.93	0.81	0.11	0.03	0.03	0.03	1
0	Vul 17 T-08	Pal C2	A13	50.73	0.59	3.93	7.30	0.15	14.59	22.55	0.33	0.01	0.05	100.22	0.82	0.11	0.02	0.03	0.05	3
20	Vul 17 T-08	Pal C2	A13	50.55	0.55	3.71	7.08	0.25	14.95	22.41	0.42	0.00	0.10	100.01	0.82	0.11	0.03	0.01	0.05	3
40	Vul 17 T-08	Pal C2	A13	51.08	0.50	3.63	6.88	0.15	14.80	22.53	0.28	0.00	0.07	99.91	0.82	0.10	0.02	0.03	0.04	3
60	Vul 17 T-08	Pal C2	A13	50.63	0.51	3.60	6.62	0.12	14.97	22.50	0.32	0.00	0.10	99.37	0.83	0.10	0.02	0.02	0.04	3
80	Vul 17 T-08	Pal C2	A13	49.96	0.77	4.13	7.12	0.13	14.35	22.47	0.44	0.00	0.11	99.48	0.82	0.10	0.03	0.02	0.06	3
100	Vul 17 T-08	Pal C2	A13	49.86	0.66	4.08	7.39	0.16	14.24	22.40	0.39	0.00	0.03	99.22	0.82	0.10	0.03	0.02	0.05	3
120	Vul 17 T-08	Pal C2	A13	49.67	0.64	4.26	8.27	0.15	13.67	22.23	0.40	0.00	0.00	99.31	0.82	0.11	0.03	0.03	0.05	3
140	Vul 17 T-08	Pal C2	A13	49.71	0.61	3.57	8.69	0.30	13.57	21.95	0.49	0.02	0.00	98.90	0.83	0.11	0.04	0.01	0.06	1
160	Vul 17 T-08	Pal C2	A13	50.43	0.59	3.68	8.66	0.21	13.50	21.77	0.51	0.00	0.02	99.37	0.81	0.11	0.04	0.02	0.04	1

180	Vul 17 T-08	Pal C2	A13	49.67	0.63	3.66	8.69	0.26	13.48	21.96	0.43	0.00	0.00	98.78	0.83	0.11	0.03	0.01	0.05	1
0	Vul 17 T-01	Pal C3	l10	50.65	0.54	3.38	7.38	0.16	14.60	22.97	0.31	0.00	0.09	100.09	0.85	0.09	0.02	0.01	0.05	3
20	Vul 17 T-01	Pal C3	l10	50.31	0.60	3.94	8.07	0.21	13.89	22.80	0.37	0.01	0.05	100.25	0.84	0.09	0.03	0.02	0.05	3
40	Vul 17 T-01	Pal C3	l10	50.64	0.66	3.71	8.52	0.23	13.84	22.34	0.39	0.00	0.00	100.35	0.82	0.10	0.03	0.02	0.05	1
60	Vul 17 T-01	Pal C3	l10	50.45	0.65	3.64	8.78	0.21	13.70	22.41	0.45	0.01	0.03	100.33	0.83	0.10	0.03	0.01	0.05	1
80	Vul 17 T-01	Pal C3	l10	50.30	0.66	3.68	8.91	0.27	13.63	22.29	0.43	0.01	0.00	100.18	0.83	0.11	0.03	0.01	0.05	1
100	Vul 17 T-01	Pal C3	l10	48.21	0.89	4.44	9.34	0.27	12.89	22.14	0.47	0.01	0.00	98.68	0.82	0.10	0.03	0.01	0.08	2
120	Vul 17 T-01	Pal C3	l10	50.47	0.72	3.85	8.65	0.22	13.68	22.35	0.48	0.00	0.00	100.44	0.83	0.10	0.03	0.01	0.05	1
0	Vul 17 Pal D	Pal D	g12	51.59	0.42	2.21	8.92	0.45	13.70	22.12	0.44	0.01	0.00	99.86	0.85	0.10	0.03	0.00	0.03	4
20	Vul 17 Pal D	Pal D	g12	51.24	0.49	2.66	9.17	0.50	13.45	22.08	0.54	0.00	0.00	100.14	0.85	0.10	0.04	0.00	0.04	4
40	Vul 17 Pal D	Pal D	g12	51.39	0.47	2.43	9.00	0.53	13.51	22.04	0.52	0.02	0.00	99.91	0.85	0.09	0.03	0.00	0.04	4
60	Vul 17 Pal D	Pal D	g12	50.87	0.60	3.09	9.46	0.49	13.11	21.94	0.52	0.02	0.00	100.10	0.83	0.10	0.04	0.01	0.04	4
80	Vul 17 Pal D	Pal D	g12	51.14	0.51	2.65	8.99	0.41	13.50	22.08	0.56	0.00	0.00	99.86	0.85	0.10	0.04	0.00	0.04	4
100	Vul 17 Pal D	Pal D	g12	51.05	0.52	2.66	8.67	0.43	13.78	22.06	0.45	0.00	0.00	99.62	0.84	0.10	0.03	0.00	0.04	4
120	Vul 17 Pal D	Pal D	g12	51.48	0.50	2.49	8.45	0.39	13.95	22.02	0.48	0.00	0.00	99.77	0.85	0.10	0.03	0.00	0.04	4
140	Vul 17 Pal D	Pal D	g12	51.42	0.56	2.63	8.11	0.28	14.47	22.11	0.43	0.00	0.00	100.02	0.84	0.11	0.03	0.00	0.04	4
160	Vul 17 Pal D	Pal D	g12	51.07	0.63	2.87	8.29	0.31	13.92	21.95	0.45	0.00	0.00	99.48	0.83	0.10	0.03	0.01	0.04	4
180	Vul 17 Pal D	Pal D	g12	51.36	0.65	2.89	8.22	0.35	14.03	22.04	0.46	0.00	0.00	100.00	0.83	0.10	0.03	0.01	0.04	4
200	Vul 17 Pal D	Pal D	g12	51.22	0.60	3.04	8.01	0.30	14.25	22.02	0.41	0.00	0.00	99.87	0.83	0.11	0.03	0.01	0.04	4
220	Vul 17 Pal D	Pal D	g12	50.90	0.68	3.38	8.16	0.33	14.01	21.99	0.33	0.00	0.00	99.78	0.82	0.11	0.02	0.03	0.04	4
240	Vul 17 Pal D	Pal D	g12	50.60	0.67	3.19	8.54	0.36	14.10	22.12	0.44	0.00	0.00	100.02	0.83	0.11	0.03	0.00	0.05	1
260	Vul 17 Pal D	Pal D	g12	50.67	0.59	3.05	8.47	0.22	14.16	22.08	0.45	0.00	0.00	99.69	0.84	0.11	0.03	0.00	0.05	1
280	Vul 17 Pal D	Pal D	g12	51.38	0.59	2.87	8.64	0.26	14.20	22.10	0.34	0.00	0.00	100.39	0.83	0.11	0.02	0.01	0.04	4
300	Vul 17 Pal D	Pal D	g12	50.43	0.66	3.22	8.67	0.30	14.10	21.92	0.45	0.00	0.00	99.75	0.83	0.12	0.03	0.00	0.05	1
320	Vul 17 Pal D	Pal D	g12	50.78	0.56	2.96	8.79	0.31	14.00	22.01	0.41	0.01	0.00	99.84	0.83	0.11	0.03	0.00	0.05	4

Appendix E.3 – Major element composition of plagioclase

Unit	Palizzi Lava	Palizzi Lava	Palizzi Lava	Palizzi Lava	Palizzi Lava	Palizzi Lava	Palizzi Lava	Palizzi Lava	Palizzi Lava
Lithology	Lava	Lava	Lava	Lava	Lava	Lava	Lava	Lava	Lava
Sample	VGPL3	VGPL3	VGPL3	VGPL3	VGPL3	VGPL3	VGPL3	VGPL3	VGPL3
Type	EPMA	EPMA	EPMA	EPMA	EPMA	EPMA	EPMA	EPMA	EPMA
label	feld7	feld7	feld7	feld7	feld7	feld9	feld9	feld9	feld1
core/rim	rim	rim	rim	core	core	rim	rim	core	core
wt.% SiO_2	52.88	54.24	55.07	54.14	53.50	56.95	54.40	55.70	54.75
TiO_2	0.05	0.04	0.04	0.04	0.03	0.03	0.03	0.03	0.08
Al_2O_3	29.17	27.93	27.92	27.79	28.31	27.39	28.92	28.13	27.60
FeO_{tot}	0.83	0.57	0.52	0.71	0.59	0.26	0.24	0.36	0.50
MnO	0.00	0.00	0.03	0.02	0.05	0.04	0.00	0.05	0.00
MgO	0.09	0.05	0.07	0.04	0.05	0.00	0.01	0.05	0.04
CaO	12.01	10.42	9.93	10.56	11.04	9.04	10.84	9.91	10.08
Na_2O	3.85	4.51	4.64	4.62	4.44	5.43	4.66	5.32	4.93
K_2O	0.97	0.80	0.87	0.85	0.66	0.89	0.48	0.64	0.69
total	99.86	98.57	99.08	98.78	98.67	100.03	99.60	100.22	98.66
8 oxygens formula									
Si	2.41	2.49	2.51	2.48	2.46	2.56	2.46	2.51	2.51
Al	1.57	1.51	1.50	1.50	1.53	1.45	1.54	1.49	1.49
Fe	0.03	0.02	0.02	0.03	0.02	0.01	0.01	0.01	0.02
Ca	0.59	0.51	0.48	0.52	0.54	0.44	0.53	0.48	0.49
Na	0.34	0.40	0.41	0.41	0.40	0.47	0.41	0.46	0.44
K	0.06	0.05	0.05	0.05	0.04	0.05	0.03	0.04	0.04
An	59.67	53.35	51.28	52.97	55.55	45.36	54.61	48.83	50.85
Ab	34.61	41.79	43.38	41.96	40.48	49.34	42.50	47.39	45.00
Or	5.72	4.86	5.34	5.07	3.97	5.30	2.89	3.78	4.15

plagioclase

Unit	Palizzi Lava	Palizzi Lava	Palizzi Lava	Palizzi Lava	Palizzi Lava	Palizzi Lava	Palizzi lava	Palizzi lava	Palizzi lava
Lithology	Lava	Lava	Lava	Lava	Lava	Lava	Lava	Lava	Lava
Sample	VGPL3	VGPL3	VGPL3	VGPL3	VGPL3	VGPL3	SC-15-1	SC-15-1	SC-15-1
Type	EPMA	EPMA	EPMA	EPMA	EPMA	EPMA	EPMA	EPMA	EPMA
label	feld1	feld1	feld1	feld13	feld13	feld13	feld1core	feld1rim	feld2rim
core/rim	core	core	rim	core	core	rim	core	rim	rim
wt.% SiO_2	56.09	55.31	56.67	55.84	53.15	53.07	53.83	53.46	55.28
TiO_2	0.05	0.08	0.02	0.05	0.02	0.05	0.00	0.00	0.04
Al_2O_3	27.43	27.79	26.88	27.56	28.34	28.39	27.50	28.09	27.07
FeO_{tot}	0.54	0.70	0.56	0.56	0.62	0.56	0.81	0.63	0.64
MnO	0.00	0.00	0.03	0.00	0.01	0.02	0.02	0.01	0.00
MgO	0.05	0.05	0.04	0.05	0.08	0.08	0.07	0.08	0.06
CaO	9.65	9.99	9.10	9.74	11.12	11.10	11.44	11.64	10.01
Na_2O	5.17	4.97	5.33	4.20	4.45	4.32	4.23	4.11	4.60
K_2O	0.77	0.76	0.95	0.97	0.75	0.71	0.77	0.81	1.11
total	99.78	99.64	99.58	98.98	98.56	98.32	98.67	98.83	98.80
8 oxygens formula									
Si	2.54	2.51	2.56	2.54	2.45	2.45	2.48	2.46	2.53
Al	1.46	1.49	1.43	1.48	1.54	1.54	1.49	1.52	1.46
Fe	0.02	0.03	0.02	0.02	0.02	0.02	0.03	0.02	0.02
Ca	0.47	0.49	0.44	0.47	0.55	0.55	0.56	0.57	0.49
Na	0.45	0.44	0.47	0.37	0.40	0.39	0.38	0.37	0.41
K	0.04	0.04	0.05	0.06	0.04	0.04	0.05	0.05	0.06
An	48.45	50.22	45.80	52.66	55.42	56.18	57.15	58.08	50.93
Ab	46.94	45.25	48.54	41.07	40.12	39.52	38.24	37.11	42.36
Or	4.60	4.54	5.67	6.27	4.46	4.30	4.60	4.82	6.71

plagioclase

Unit	Palizzi lava	Palizzi lava	Palizzi lava	Palizzi lava	Palizzi lava	Palizzi lava	Palizzi lava	Palizzi lava	Pal D
Lithology	Lava	Lava	Lava	Lava	Lava	Lava	Lava	Lava	Scoriaceous lapilli
Sample	SC-15-1	SC-15-1	SC-15-1	SC-15-1	SC-15-1	SC-15-1	SC-18-24	SC-18-24	SC-18-20
Type	EPMA	EPMA	EPMA	EPMA	EPMA	EPMA	EPMA	EPMA	EPMA
label	feld2	feld3	feld3	feld4	feld4	feld4	feld2	feld2	feld1
core/rim	core	rim	core	core	rim	rim	core	rim	core
wt.% SiO_2	55.22	58.30	54.29	55.12	55.64	58.50	52.18	53.45	53.34
TiO_2	0.01	0.03	0.06	0.05	0.05	0.02	0.06	0.02	0.04
Al_2O_3	27.20	25.23	27.28	27.12	26.84	25.32	28.67	27.81	26.56
FeO_{tot}	0.64	0.61	0.62	0.64	0.62	0.50	0.75	0.62	0.67
MnO	0.03	0.00	0.02	0.03	0.00	0.01	0.00	0.00	0.00
MgO	0.05	0.06	0.07	0.07	0.05	0.01	0.08	0.06	0.06
CaO	10.38	7.87	10.87	10.67	9.79	7.91	12.03	11.27	10.78
Na_2O	4.80	5.62	4.40	4.37	4.87	5.31	3.81	4.09	4.35
K_2O	0.65	1.65	0.91	0.97	0.93	1.52	0.61	0.71	0.99
total	98.98	99.37	98.51	99.04	98.79	99.11	98.18	98.02	96.78
8 oxygens formula									
Si	2.52	2.64	2.50	2.52	2.54	2.65	2.42	2.47	2.50
Al	1.46	1.35	1.48	1.46	1.45	1.35	1.57	1.52	1.47
Fe	0.02	0.02	0.02	0.02	0.02	0.02	0.03	0.02	0.03
Ca	0.51	0.38	0.54	0.52	0.48	0.38	0.60	0.56	0.54
Na	0.42	0.49	0.39	0.39	0.43	0.47	0.34	0.37	0.40
K	0.04	0.10	0.05	0.06	0.05	0.09	0.04	0.04	0.06
An	52.31	39.34	54.57	54.06	49.66	40.92	61.23	57.76	54.38
Ab	43.77	50.84	39.97	40.07	44.70	49.71	35.09	37.93	39.71
Or	3.92	9.82	5.45	5.87	5.64	9.36	3.68	4.31	5.92

plagioclase

Unit	Pal D	Pal D	Pal D	Pal D	Pal D	Pal D	Pal D	Pal D	Pal D
Lithology	Scoriaceous lapilli	Scoriaceous lapilli	Pumiceous lapilli	Pumiceous lapilli	Pumiceous lapilli	Pumiceous lapilli	Pumiceous lapilli	Pumiceous lapilli	Pumiceous lapilli
Sample	SC-18-20	SC-18-20	S33b 90-110	S33b 90-110	S33b 90-110	S33b 90-110	S33b 90-110	S33b 90-110	S33b 90-110
Type	EPMA	EPMA	EPMA	EPMA	EPMA	EPMA	EPMA	EPMA	EPMA
label	feld1	feld1	feld1	feld1	feld2	feld2	feld2	feld3	feld3
core/rim	rim	rim	core	rim	rim	core	rim	core	rim
wt.% SiO_2	53.23	54.58	55.49	56.10	56.12	55.79	56.42	55.24	55.43
TiO_2	0.01	0.03	0.07	0.00	0.02	0.02	0.04	0.01	0.06
Al_2O_3	26.79	25.53	26.51	26.33	26.03	26.08	25.96	26.65	26.16
FeO_{tot}	0.58	0.47	0.45	0.46	0.39	0.51	0.62	0.46	0.37
MnO	0.02	0.01	0.00	0.03	0.02	0.01	0.01	0.00	0.05
MgO	0.06	0.06	0.06	0.02	0.05	0.05	0.05	0.04	0.05
CaO	10.79	9.59	8.94	8.89	8.49	8.59	8.62	8.74	7.85
Na_2O	4.25	4.74	4.80	4.91	5.15	4.87	4.95	4.93	5.00
K_2O	0.95	1.21	1.68	1.64	1.75	1.81	1.78	1.80	2.12
total	96.69	96.21	98.01	98.38	98.03	97.74	98.45	97.87	97.09
8 oxygens formula									
Si	2.50	2.56	2.56	2.57	2.58	2.58	2.59	2.55	2.58
Al	1.48	1.41	1.44	1.42	1.41	1.42	1.40	1.45	1.43
Fe	0.02	0.02	0.02	0.02	0.02	0.02	0.02	0.02	0.01
Ca	0.54	0.48	0.44	0.44	0.42	0.43	0.42	0.43	0.39
Na	0.39	0.43	0.43	0.44	0.46	0.44	0.44	0.44	0.45
K	0.06	0.07	0.10	0.10	0.10	0.11	0.10	0.11	0.13
An	55.01	48.91	45.55	45.06	42.68	43.92	43.76	44.13	40.42
Ab	39.21	43.74	44.26	45.04	46.85	45.06	45.48	45.05	46.59
Or	5.77	7.35	10.19	9.90	10.47	11.02	10.76	10.82	13.00

plagioclase

Unit	Pal D	Pal D	PAL B	PAL B	PAL B	PAL B	PAL B	PAL B	PAL B
Lithology	Pumiceous lapilli	Pumiceous lapilli	Pumiceous lapilli	Pumiceous lapilli	Pumiceous lapilli	Pumiceous lapilli	Pumiceous lapilli	Pumiceous lapilli	Pumiceous lapilli
Sample	S33b 90-110	S33b 90-110	Pal-L	Pal-L	Pal-L	Pal-L	Pal-L	Pal-L	Pal-L
Type	EPMA	EPMA	EDS	EDS	EDS	EDS	EDS	EDS	EDS
label	feld4	feld4	Pal-L pl	Pal-L pl	Pal-L plg	Pal-L pl	Pal-L pl	Pal-L pl	Pal-L pl
core/rim	core	rim	core	rim	core	rim	core	rim	core
wt.% SiO_2	55.38	54.68	59.62	60.78	53.30	54.30	53.80	57.70	54.19
TiO_2	0.00	0.10							
Al_2O_3	26.18	26.57	25.36	24.73	29.44	28.61	28.99	25.99	28.74
FeO_{tot}	0.51	0.49	0.37	0.27	0.40	0.78	0.45	0.62	0.52
MnO	0.03	0.00							
MgO	0.05	0.07							
CaO	9.31	9.62	6.55	5.66	11.93	10.26	11.18	7.73	10.60
Na_2O	4.90	4.75	6.98	7.19	3.70	4.40	4.35	6.00	4.40
K_2O	1.44	1.44	1.12	1.37	1.22	1.65	1.22	1.96	1.55
total	97.80	97.72	100.00	100.00	99.99	100.00	99.99	100.00	100.00
8 oxygens formula									
Si	2.56	2.53	2.67	2.71	2.42	2.47	2.44	2.60	2.46
Al	1.43	1.45	1.34	1.30	1.58	1.53	1.55	1.38	1.54
Fe	0.02	0.02	0.01	0.01	0.02	0.03	0.02	0.02	0.02
Ca	0.46	0.48	0.31	0.27	0.58	0.50	0.54	0.37	0.52
Na	0.44	0.43	0.61	0.62	0.33	0.39	0.38	0.53	0.39
K	0.08	0.09	0.06	0.08	0.07	0.10	0.07	0.11	0.09
An	46.80	48.27	31.93	27.88	59.42	50.83	54.52	36.95	51.94
Ab	44.58	43.13	61.57	64.09	33.35	39.44	38.39	51.90	39.02
Or	8.62	8.60	6.50	8.03	7.23	9.73	7.08	11.15	9.04

plagioclase

Unit	PAL B	PAL B	PAL B	PAL B	PAL B	PAL B	PAL B	Pietre Cotte	Pietre Cotte
Lithology	Pumiceous lapilli	Pumiceous lapilli	Pumiceous lapilli	Pumiceous lapilli	Pumiceous lapilli	Pumiceous lapilli	Pumiceous lapilli	Enclave	Enclave
Sample	Pal-L	Pal-L	Pal-L	Pal-L	Pal-L	Pal-L	Pal-L	VPCL8i	VPCL8i
Type	EDS	EDS	EDS	EDS	EDS	EDS	EDS	EPMPA	EPMPA
label	Pal-L pl	Pal-L (B3	Pal-L (B) 4pl	Pal-L (B) 10	Pal-L (B) 13	Pal-L (B) 14	Pal-L u117pl	plg1 core	plg1core
core/rim	rim	core	rim	core	rim	core	core	core	core
wt.%									
SiO_2	54.39	53.50	53.97	58.84	61.25	55.44	59.96	57.74	54.96
TiO_2								0.00	0.04
Al_2O_3	28.66	29.26	28.93	25.70	23.89	28.30	25.49	27.18	28.56
FeO_{tot}	0.69	0.69	0.65	0.37	0.31	0.26	0.21	0.59	0.61
MnO								0.00	0.00
MgO								0.04	0.06
CaO	10.46	10.85	10.60	7.04	5.30	9.87	6.78	8.94	10.96
Na_2O	4.41	4.05	4.31	6.97	7.73	5.61	6.69	5.17	4.56
K_2O	1.40	1.25	1.44	1.04	1.48	0.52	0.88	1.74	1.06
total	100.01	99.60	99.90	99.96	99.96	100.00	100.01	101.40	100.80
8 oxygens formula									
Si	2.47	2.44	2.45	2.64	2.74	2.50	2.67	2.57	2.47
Al	1.53	1.57	1.55	1.36	1.26	1.50	1.34	1.43	1.52
Fe	0.03	0.03	0.02	0.01	0.01	0.01	0.01	0.02	0.02
Ca	0.51	0.53	0.52	0.34	0.25	0.48	0.32	0.43	0.53
Na	0.39	0.36	0.38	0.61	0.67	0.49	0.58	0.45	0.40
K	0.08	0.07	0.08	0.06	0.08	0.03	0.05	0.10	0.06
An	52.02	55.17	52.70	33.70	25.18	47.82	34.01	43.91	53.50
Ab	39.69	37.26	38.78	60.37	66.45	49.18	60.73	45.91	40.34
Or	8.29	7.57	8.52	5.93	8.37	3.00	5.26	10.18	6.16

plagioclase

Unit	Pietre Cotte	Pietre Cotte	Pietre Cotte	Pietre Cotte	Pietre Cotte	Pietre Cotte	Pietre Cotte	Pietre Cotte	Pietre Cotte
Lithology	Enclave	Enclave	Enclave	Enclave	Enclave	Enclave	Enclave	Enclave	Enclave
Sample	VPCL8i	VPCL8i	VPCL8i	VPCL8i	VPCL8i	VPCL8i	VPCL8i	VPCL8i	VPCL8i
Type	EPMPA	EPMPA	EPMPA	EPMPA	EPMPA	EPMPA	EPMPA	EPMPA	EPMPA
label	plg1 rim	plg1 rim	plg1 core	plg1 rim	plg1 rim	plg1 core	1cum1	1cum2 rim	1cum2 core
core/rim	rim	rim	core	rim	rim	core	core	rim	core
wt.% SiO_2	57.14	57.50	56.77	57.15	57.01	55.84	57.19	57.44	56.60
TiO_2	0.08	0.04	0.00	0.04	0.04	0.10	0.02	0.06	0.06
Al_2O_3	27.12	26.87	27.82	26.97	27.18	28.03	27.45	27.02	27.58
FeO_{tot}	0.65	0.62	0.57	0.56	0.63	0.68	0.60	0.65	0.60
MnO	0.03	0.02	0.02	0.02	0.03	0.02	0.00	0.00	0.01
MgO	0.07	0.07	0.07	0.07	0.05	0.09	0.05	0.03	0.04
CaO	9.01	8.74	9.47	8.82	9.15	10.05	9.16	8.54	9.54
Na_2O	5.10	5.14	4.91	5.17	4.88	4.86	5.18	5.26	5.00
K_2O	1.81	1.86	1.51	1.80	1.73	1.26	1.69	1.95	1.55
total	101.00	100.85	101.14	100.61	100.70	100.93	101.34	100.95	100.97
8 oxygens formula									
Si	2.56	2.58	2.54	2.57	2.56	2.51	2.55	2.57	2.54
Al	1.43	1.42	1.46	1.43	1.44	1.48	1.44	1.43	1.46
Fe	0.02	0.02	0.02	0.02	0.02	0.03	0.02	0.02	0.02
Ca	0.43	0.42	0.45	0.42	0.44	0.48	0.44	0.41	0.46
Na	0.44	0.45	0.43	0.45	0.43	0.42	0.45	0.46	0.43
K	0.10	0.11	0.09	0.10	0.10	0.07	0.10	0.11	0.09
An	44.18	43.14	46.97	43.39	45.62	49.37	44.60	41.89	46.72
Ab	45.25	45.91	44.09	46.03	44.09	43.25	45.63	46.70	44.27
Or	10.57	10.95	8.94	10.57	10.30	7.38	9.77	11.42	9.01

plagioclase

Unit	Pietre Cotte	Pietre Cotte	Pietre Cotte	Pietre Cotte	Pietre Cotte	Pietre Cotte	Pietre Cotte	Pietre Cotte
Lithology	Enclave	Enclave	Enclave	Enclave	Enclave	Enclave	Enclave	Enclave
Sample	VPCL8i	VPCL8i	VPCL8i	VPCL8i	VPCL8i	VPCL8i	VPCL8i	VPCL8i
Type	EPMPA	EPMPA	EPMPA	EPMPA	EPMPA	EPMPA	EPMPA	EPMPA
label	1cum rim	11 rim	11 rim	11 rim	11 core	11 rim	10 rim	10 rim
core/rim	rim	rim	rim	rim	core	rim	rim	rim
wt.% SiO_2	55.46	55.29	53.99	54.74	53.84	57.69	57.19	55.44
TiO_2	0.05	0.09	0.05	0.05	0.07	0.09	0.08	0.04
Al_2O_3	28.39	28.97	29.31	28.95	29.08	26.73	26.72	28.13
FeO_{tot}	0.61	0.59	0.71	0.48	0.62	0.58	0.64	0.61
MnO	0.00	0.00	0.01	0.00	0.00	0.01	0.05	0.02
MgO	0.06	0.07	0.06	0.06	0.05	0.05	0.06	0.07
CaO	10.41	10.66	11.36	11.00	11.51	8.35	8.55	10.20
Na_2O	4.58	4.53	4.13	4.39	4.19	5.22	5.07	4.77
K_2O	1.21	1.14	0.93	1.10	0.92	2.05	1.94	1.37
total	100.77	101.32	100.52	100.76	100.28	100.77	100.29	100.65
8 oxygens formula								
Si	2.49	2.47	2.44	2.46	2.44	2.59	2.58	2.50
Al	1.50	1.53	1.56	1.54	1.55	1.41	1.42	1.49
Fe	0.02	0.02	0.03	0.02	0.02	0.02	0.02	0.02
Ca	0.50	0.51	0.55	0.53	0.56	0.40	0.41	0.49
Na	0.40	0.39	0.36	0.38	0.37	0.45	0.44	0.42
K	0.07	0.06	0.05	0.06	0.05	0.12	0.11	0.08
An	51.67	52.76	56.99	54.32	57.04	41.27	42.66	49.86
Ab	41.16	40.54	37.48	39.24	37.54	46.67	45.80	42.17
Or	7.17	6.70	5.53	6.44	5.42	12.06	11.53	7.97

Appendix E.4 – Major element composition of K-feldspar

Unit	Palizzi Lava	Palizzi Lava	Palizzi Lava	Palizzi Lava	Palizzi Lava	Palizzi Lava	Palizzi Lava	Palizzi lava	Palizzi lava
Lithology	Lava	Lava	Lava	Lava	Lava	Lava	Lava	Lava	Lava
Sample	VGPL3	VGPL3	VGPL3	VGPL3	VGPL3	VGPL3	VGPL3	SC-15-1	SC-15-1
Type	EPMA	EPMA	EPMA	EPMA	EPMA	EPMA	EPMA	EPMA	EPMA
label	feld9	feld9	feld10	feld10	feld12	feld12	feld12	feld5core	feld5rim
core/rim	rim	core	core	rim	core	core	rim	core	rim
wt.% SiO_2	66.29	66.33	66.62	65.46	66.11	66.55	65.53	65.62	66.29
TiO_2	0.03	0.03	0.03	0.03	0.05	0.03	0.01	0.00	0.06
Al_2O_3	19.17	19.62	19.35	20.52	20.12	19.34	19.22	19.48	18.98
FeO_{tot}	0.10	0.16	0.10	0.32	0.33	0.16	0.10	0.16	0.39
MnO	0.01	0.05	0.02	0.00	0.03	0.02	0.03	0.00	0.00
MgO	0.00	0.01	0.00	0.00	0.00	0.00	0.00	0.00	0.00
CaO	0.38	0.64	0.49	1.19	1.01	0.45	0.62	0.64	0.68
Na_2O	4.04	4.29	3.88	4.35	4.50	3.71	4.04	3.77	4.26
K_2O	10.06	9.01	10.03	8.39	8.60	10.43	9.77	10.60	9.82
total	100.13	100.14	100.53	100.26	100.74	100.68	99.31	100.28	100.47
8 oxygens formula									
Si	2.99	2.98	2.99	2.94	2.95	2.99	2.98	2.97	2.99
Al	1.02	1.04	1.02	1.09	1.06	1.02	1.03	1.04	1.01
Fe	0.00	0.01	0.00	0.01	0.01	0.01	0.00	0.01	0.01
Ca	0.02	0.03	0.02	0.06	0.05	0.02	0.03	0.03	0.03
Na	0.35	0.37	0.34	0.38	0.39	0.32	0.36	0.33	0.37
K	0.58	0.52	0.57	0.48	0.49	0.60	0.57	0.61	0.56
An	1.93	3.34	2.54	6.24	5.22	2.32	3.18	3.19	3.40
Ab	37.17	40.59	36.07	41.33	41.99	34.29	37.35	33.97	38.38
Or	60.90	56.08	61.40	52.43	52.80	63.39	59.47	62.84	58.22

K-feldspar

Unit	Palizzi lava	Palizzi lava	Palizzi lava	Palizzi lava	Pal D Scoriaceous lapilli	Pal D Scoriaceous lapilli	Pal D Scoriaceous lapilli	Pal D Scoriaceous lapilli	Pal D Scoriaceous lapilli	Pal D Scoriaceous lapilli
Lithology	Lava	Lava	Lava	Lava						
Sample	SC-15-1	SC-15-1	SC-18-24	SC-18-24	SC-18-20	SC-18-20	SC-18-20	SC-18-20	SC-18-20	SC-18-20
Type	EPMA	EPMA	EPMA	EPMA	EPMA	EPMA	EPMA	EPMA	EPMA	EPMA
label	feld6core	feld6rim	sa1core	sa1rim	feld2nc	feld2rim	feld3core	feld3rim	feld4core	feld4
core/rim	core	rim	core	rim	core	rim	core	rim	core	rim
wt.% SiO_2	66.62	66.58	65.47	65.07	61.89	61.84	62.12	61.87	63.64	63.07
TiO_2	0.03	0.04	0.07	0.08	0.12	0.06	0.04	0.14	0.09	0.06
Al_2O_3	18.62	18.68	18.72	18.49	18.54	18.60	18.58	18.58	18.50	18.56
FeO_{tot}	0.12	0.13	0.35	0.73	0.17	0.23	0.20	0.24	0.18	0.18
MnO	0.00	0.06	0.00	0.00	0.02	0.00	0.00	0.01	0.00	0.00
MgO	0.00	0.00	0.02	0.06	0.01	0.00	0.01	0.00	0.04	0.00
CaO	0.61	0.48	0.88	0.91	0.84	0.72	0.72	0.77	0.79	0.71
Na_2O	4.19	4.05	4.74	4.54	2.68	2.58	2.65	2.62	2.68	2.50
K_2O	10.14	10.46	8.40	8.65	11.89	11.93	11.94	11.66	12.41	12.30
total	100.33	100.47	98.65	98.53	96.16	95.96	96.26	95.89	98.33	97.39
8 oxygens formula										
Si	3.00	3.00	2.99	2.99	2.95	2.95	2.95	2.95	2.97	2.97
Al	0.99	0.99	1.01	1.00	1.04	1.05	1.04	1.05	1.02	1.03
Fe	0.00	0.00	0.01	0.03	0.01	0.01	0.01	0.01	0.01	0.01
Ca	0.03	0.02	0.04	0.04	0.04	0.04	0.04	0.04	0.04	0.04
Na	0.37	0.35	0.42	0.40	0.25	0.24	0.24	0.24	0.24	0.23
K	0.58	0.60	0.49	0.51	0.72	0.73	0.72	0.71	0.74	0.74
An	3.00	2.37	4.50	4.70	4.25	3.69	3.65	3.98	3.89	3.59
Ab	37.42	36.17	44.09	42.29	24.43	23.82	24.30	24.44	23.75	22.75
Or	59.58	61.46	51.41	53.01	71.32	72.48	72.05	71.57	72.36	73.66

K-feldspar

Unit	Pal D	Pal D	Pal D	Pal D	Pal D	Pal D	Pal D	Pal D	Pal D	Pal D
Lithology	Scoriaceous lapilli	Scoriaceous lapilli	Scoriaceous lapilli	Scoriaceous lapilli	Scoriaceous lapilli	Scoriaceous lapilli	Scoriaceous lapilli	Scoriaceous lapilli	Pumiceous lapilli	Pumiceous lapilli
Sample	SC-18-20	SC-18-20	SC-18-20	SC-18-20	SC-18-20	SC-18-20	SC-18-20	SC-18-20	S33b 15-40	S33b 15-40
Type	EPMA	EPMA	EPMA	EPMA	EPMA	EPMA	EPMA	EPMA	EPMA	EPMA
label	feld4rim	feld5core	feld5	feld5rim	feld6core	feld6rim	feld7core	feld7rim	feld1core	feld1
core/rim	rim	core	rim	rim	core	rim	core	rim	core	rim
wt.% SiO_2	61.78	63.86	63.27	61.95	61.10	62.55	62.92	62.60	62.54	61.00
TiO_2	0.09	0.04	0.07	0.11	0.11	0.16	0.09	0.14	0.13	0.19
Al_2O_3	18.91	18.36	18.69	19.01	18.82	18.98	18.23	18.75	18.69	19.13
FeO_{tot}	0.19	0.14	0.18	0.19	0.29	0.26	0.20	0.23	0.11	0.21
MnO	0.00	0.03	0.00	0.00	0.00	0.00	0.00	0.00	0.00	0.00
MgO	0.02	0.00	0.00	0.02	0.00	0.00	0.00	0.00	0.01	0.00
CaO	0.78	0.74	0.86	0.85	0.73	0.77	0.68	0.80	0.77	0.82
Na_2O	2.57	2.85	2.74	2.63	2.71	2.66	2.72	2.63	2.52	2.70
K_2O	11.76	12.68	12.11	11.58	11.41	11.84	12.19	11.68	11.94	11.54
total	96.10	98.71	97.92	96.34	95.17	97.22	97.04	96.83	96.71	95.59
8 oxygens formula										
Si	2.94	2.97	2.96	2.94	2.94	2.95	2.97	2.96	2.96	2.92
Al	1.06	1.01	1.03	1.06	1.07	1.05	1.02	1.04	1.04	1.08
Fe	0.01	0.01	0.01	0.01	0.01	0.01	0.01	0.01	0.00	0.01
Ca	0.04	0.04	0.04	0.04	0.04	0.04	0.03	0.04	0.04	0.04
Na	0.24	0.26	0.25	0.24	0.25	0.24	0.25	0.24	0.23	0.25
K	0.71	0.75	0.72	0.70	0.70	0.71	0.73	0.70	0.72	0.71
An	4.03	3.52	4.24	4.40	3.81	3.93	3.40	4.12	3.92	4.22
Ab	23.93	24.57	24.50	24.53	25.51	24.45	24.46	24.45	23.34	25.12
Or	72.04	71.92	71.26	71.07	70.68	71.61	72.14	71.44	72.75	70.65

K-feldspar

Unit	Pal D	PAL B	PAL B	PAL B	PAL B	PAL B	PAL B	PAL B	PAL B	PAL B
Lithology	Pumiceous lapilli	Pumiceous lapilli	Pumiceous lapilli	Pumiceous lapilli	Pumiceous lapilli	Pumiceous lapilli	Pumiceous lapilli	Pumiceous lapilli	Pumiceous lapilli	Pumiceous lapilli
Sample	S33b 15-40	Pal-L	Pal-L	Pal-L	Pal-L	Pal-L	Pal-L	Pal-L	Pal-L	Pal-L
Type	EPMA	EDS	EDS	EDS	EDS	EDS	EDS	EDS	EDS	EDS
label	feld1rim	Pal-L sa core	Pal-L sa rim	Pal-L sa2	Pal-L sa2	Pal-L (B) 8sa	Pal-L (B) 9	Pal-L (B) sa	u117 san	Pal-L sa core
core/rim	rim	core	rim	core	rim	core	rim	core	core	core
wt.% SiO_2	60.78	65.20	65.05	64.92	65.45	65.27	65.07	64.81	65.95	65.26
TiO_2	0.05									
Al_2O_3	19.28	19.52	19.40	19.47	19.23	19.67	19.34	19.48	19.35	19.53
FeO_{tot}	0.22	0.23	0.33	0.29	0.14	0.11	0.34	0.22	0.12	0.22
MnO	0.01									
MgO	0.01									
CaO	0.89	0.46	0.31	0.35	0.26	0.49	0.41	0.30	0.35	0.26
Na_2O	2.66	3.90	3.67	3.73	3.51	3.76	3.59	3.67	3.40	3.51
K_2O	11.27	10.69	11.23	11.24	11.42	10.70	11.18	11.02	10.81	11.23
total	95.17	100.00	99.99	100.00	100.01	100.00	99.93	99.50	99.98	100.01
8 oxygens formula										
Si	2.92	2.96	2.96	2.96	2.98	2.96	2.96	2.96	2.98	2.96
Al	1.09	1.04	1.04	1.05	1.03	1.05	1.04	1.05	1.03	1.05
Fe	0.01	0.01	0.01	0.01	0.01	0.00	0.01	0.01	0.00	0.01
Ca	0.05	0.02	0.02	0.02	0.01	0.02	0.02	0.01	0.02	0.01
Na	0.25	0.34	0.32	0.33	0.31	0.33	0.32	0.33	0.30	0.31
K	0.69	0.62	0.65	0.65	0.66	0.62	0.65	0.64	0.62	0.65
An	4.66	2.27	1.53	1.71	1.29	2.45	2.03	1.50	1.81	1.30
Ab	25.17	34.86	32.68	32.95	31.43	33.96	32.13	33.10	31.76	31.79
Or	70.17	62.87	65.79	65.34	67.28	63.59	65.84	65.40	66.44	66.91

Appendix E.5 – Trace element composition of clinopyroxene by LA-ICP-MS. 1σerror estimates on the signal and background counts; det lim= detection limit at the 99% confidence level.

Unit	PAL A			PAL A			PAL A			PAL A		
Sample	T-18			T-18			T-18			T-18		
Position	core			rim			core			rim		
label	eb_37	1σ	det lim	eb_38	1σ	det lim	eb_39	1σ	det lim	eb_40	1σ	det lim
ppm V	322.20	12.98	0.0072	258.95	10.61	0.0076	295.00	12.15	0.0067	254.53	10.55	0.0065
Cr	35.06	1.73	0.1680	84.12	4.24	0.1710	62.25	3.17	0.1560	45.58	2.34	0.1510
Ni	44.39	1.93	0.0913	47.13	2.09	0.0912	46.19	2.06	0.0839	45.44	2.04	0.0792
Cu	3.68	0.15	0.0062	3.14	0.13	0.0067	3.74	0.16	0.0060	3.36	0.14	0.0059
Zn	63.26	3.24	0.0341	53.89	2.82	0.0341	57.10	3.01	0.0308	57.65	3.06	0.0295
Rb	0.01	0.00	0.0062	0.00	0.00	0.0065	0.01	0.00	0.0059	0.10	0.01	0.0056
Sr	189.76	10.88	0.0036	226.61	13.35	0.0035	188.29	11.19	0.0032	183.84	11.03	0.0032
Y	36.87	1.91	0.0004	26.36	1.39	0.0004	32.51	1.73	0.0004	27.42	1.47	0.0004
Zr	105.76	5.02	0.0039	72.79	3.53	0.0033	95.44	4.66	0.0036	67.69	3.33	0.0032
Nb	0.45	0.02	0.0004	0.30	0.01	0.0004	0.40	0.02	0.0002	0.25	0.01	0.0002
Cs	bdl	0.00	0.0030	bdl	0.00	0.0032	bdl	0.00	0.0029	bdl	0.00	0.0028
Ba	0.12	0.01	0.0034	0.10	0.01	0.0034	0.11	0.01	0.0031	1.02	0.07	0.0026
La	19.82	0.92	0.0005	14.35	0.68	0.0004	17.70	0.85	0.0005	14.69	0.71	0.0004
Ce	66.85	3.85	0.0007	48.46	2.86	0.0006	58.60	3.49	0.0006	48.94	2.94	0.0005
Pr	10.39	0.64	0.0003	7.64	0.48	0.0002	9.32	0.59	0.0002	7.54	0.49	0.0002
Nd	50.12	2.24	0.0017	37.03	1.69	0.0016	44.69	2.05	0.0015	36.66	1.69	0.0015
Sm	12.64	0.72	0.0005	9.21	0.54	0.0005	11.44	0.67	0.0000	9.34	0.56	0.0008
Eu	2.71	0.14	0.0003	2.15	0.11	0.0003	2.47	0.13	0.0000	2.03	0.11	0.0002
Gd	10.91	0.63	0.0030	8.10	0.48	0.0025	9.88	0.59	0.0025	7.77	0.47	0.0025
Tb	1.42	0.09	0.0004	1.06	0.07	0.0005	1.27	0.09	0.0003	1.04	0.07	0.0003
Dy	7.93	0.45	0.0005	5.84	0.34	0.0007	7.16	0.42	0.0004	5.93	0.35	0.0008
Ho	1.44	0.08	0.0000	1.03	0.06	0.0001	1.26	0.07	0.0001	1.06	0.06	0.0000
Er	3.77	0.20	0.0004	2.68	0.15	0.0004	3.24	0.18	0.0004	2.72	0.15	0.0005
Tm	0.53	0.03	0.0001	0.36	0.02	0.0002	0.46	0.03	0.0002	0.38	0.02	0.0001
Yb	3.31	0.21	0.0000	2.24	0.15	0.0004	2.96	0.19	0.0006	2.43	0.16	0.0006
Lu	0.48	0.03	0.0001	0.34	0.02	0.0002	0.41	0.03	0.0002	0.36	0.03	0.0001
Hf	4.54	0.36	0.0004	3.26	0.27	0.0004	4.30	0.35	0.0006	2.96	0.25	0.0005
Ta	0.10	0.01	0.0002	0.06	0.00	0.0003	0.09	0.01	0.0002	0.05	0.00	0.0002
Pb	0.38	0.03	0.0023	0.31	0.03	0.0021	0.35	0.03	0.0021	0.33	0.03	0.0019
Th	0.67	0.05	0.0002	0.47	0.04	0.0001	0.63	0.05	0.0001	0.41	0.04	0.0001
U	0.10	0.01	0.0000	0.07	0.01	0.0001	0.09	0.01	0.0000	0.06	0.01	0.0000

clinopyroxene

Unit	PAL A			PAL A			PAL C			PAL C		
Sample	T-18			T-18			T-08			T-08		
Position	core			rim			core			core		
label	eb_41	1σ	det lim	eb_42	1σ	det lim	eb_43	1σ	det lim	eb_45	1σ	det lim
ppm V	253.37	10.56	0.0069	259.14	10.86	0.0066	298.22	12.57	0.0072	272.55	11.63	0.0068
Cr	35.54	1.84	0.1540	48.29	2.53	0.1510	52.76	2.78	0.1660	50.44	2.71	0.1590
Ni	43.18	1.95	0.0805	44.08	2.00	0.0796	50.18	2.29	0.0859	40.97	1.90	0.0826
Cu	3.47	0.15	0.0055	3.98	0.17	0.0058	3.50	0.15	0.0065	4.50	0.20	0.0061
Zn	62.78	3.36	0.0311	60.48	3.26	0.0296	58.97	3.21	0.0322	62.39	3.45	0.0309
Rb	0.02	0.00	0.0056	0.46	0.02	0.0055	0.07	0.01	0.0058	0.10	0.01	0.0056
Sr	252.12	15.26	0.0033	210.47	12.86	0.0032	177.61	10.95	0.0037	171.01	10.74	0.0035
Y	39.43	2.13	0.0004	34.98	1.91	0.0004	32.90	1.81	0.0004	30.58	1.71	0.0004
Zr	64.07	3.17	0.0027	69.28	3.45	0.0030	83.34	4.18	0.0031	72.60	3.70	0.0031
Nb	0.28	0.01	0.0003	0.35	0.01	0.0003	0.33	0.01	0.0004	0.30	0.01	0.0003
Cs	0.00	0.00	0.0027	0.02	0.00	0.0027	0.00	0.00	0.0029	0.00	0.00	0.0028
Ba	1.56	0.10	0.0025	2.69	0.18	0.0031	0.45	0.03	0.0027	0.65	0.05	0.0037
La	37.55	1.82	0.0004	23.98	1.17	0.0005	17.48	0.86	0.0005	16.34	0.81	0.0005
Ce	99.97	6.07	0.0005	71.75	4.39	0.0005	57.93	3.58	0.0007	54.55	3.43	0.0007
Pr	13.58	0.88	0.0002	10.48	0.69	0.0002	9.18	0.61	0.0002	8.60	0.58	0.0002
Nd	60.30	2.80	0.0013	48.56	2.27	0.0014	44.07	2.07	0.0018	40.85	1.95	0.0014
Sm	13.68	0.82	0.0008	11.77	0.71	0.0000	11.02	0.67	0.0007	10.02	0.62	0.0008
Eu	2.57	0.14	0.0003	2.30	0.13	0.0004	2.30	0.13	0.0002	2.18	0.12	0.0003
Gd	11.67	0.71	0.0022	10.22	0.63	0.0023	9.64	0.60	0.0025	8.91	0.56	0.0026
Tb	1.47	0.10	0.0003	1.31	0.09	0.0004	1.27	0.09	0.0003	1.16	0.08	0.0003
Dy	8.40	0.50	0.0003	7.47	0.45	0.0000	7.11	0.43	0.0005	6.77	0.42	0.0008
Ho	1.51	0.09	0.0000	1.35	0.08	0.0000	1.29	0.08	0.0001	1.20	0.07	0.0001
Er	3.98	0.22	0.0000	3.57	0.20	0.0000	3.33	0.19	0.0006	3.07	0.18	0.0008
Tm	0.54	0.03	0.0001	0.49	0.03	0.0001	0.46	0.03	0.0001	0.42	0.03	0.0000
Yb	3.45	0.23	0.0006	3.17	0.21	0.0006	2.98	0.20	0.0000	2.75	0.19	0.0004
Lu	0.51	0.04	0.0001	0.47	0.03	0.0000	0.44	0.03	0.0002	0.41	0.03	0.0001
Hf	2.92	0.25	0.0007	3.18	0.27	0.0003	3.69	0.32	0.0004	3.17	0.28	0.0006
Ta	0.05	0.00	0.0001	0.06	0.00	0.0002	0.06	0.00	0.0003	0.05	0.00	0.0003
Pb	0.44	0.04	0.0020	0.41	0.03	0.0020	0.37	0.03	0.0022	0.38	0.03	0.0020
Th	1.89	0.16	0.0002	1.02	0.09	0.0000	0.51	0.05	0.0001	0.46	0.04	0.0001
U	0.38	0.04	0.0001	0.19	0.02	0.0001	0.08	0.01	0.0001	0.08	0.01	0.0000

clinopyroxene

Unit	PAL C			PAL C			PAL C			PAL C		
Sample	T-08			T-08			T-08			T-08		
Position	rim			core			rim			core		
label	eb_46	1σ	det lim	eb_47	1σ	det lim	eb_48	1σ	det lim	eb_49	1σ	det lim
ppm V	306.84	13.17	0.0072	296.83	12.81	0.0074	287.14	12.55	0.0070	302.89	13.31	0.0072
Cr	40.17	2.18	0.1690	45.96	2.51	0.1690	41.09	2.29	0.1600	41.77	2.35	0.1630
Ni	43.88	2.05	0.0871	45.93	2.16	0.0854	45.57	2.17	0.0800	45.27	2.17	0.0835
Cu	4.28	0.19	0.0069	3.42	0.15	0.0065	3.50	0.16	0.0066	3.74	0.17	0.0063
Zn	61.49	3.43	0.0339	60.60	3.40	0.0333	63.32	3.61	0.0308	59.81	3.44	0.0321
Rb	bdl	0.00	0.0059	bdl	0.00	0.0058	0.06	0.01	0.0055	0.01	0.00	0.0056
Sr	190.35	12.07	0.0038	198.56	12.70	0.0040	197.06	12.84	0.0036	195.63	12.86	0.0038
Y	33.35	1.87	0.0004	31.60	1.79	0.0005	33.10	1.90	0.0004	31.48	1.82	0.0004
Zr	86.59	4.44	0.0029	82.92	4.28	0.0033	77.00	4.03	0.0028	78.63	4.14	0.0035
Nb	0.36	0.02	0.0003	0.35	0.02	0.0003	0.33	0.01	0.0003	0.33	0.02	0.0003
Cs	bdl	0.00	0.0030	bdl	0.00	0.0029	0.00	0.00	0.0028	bdl	0.00	0.0028
Ba	0.11	0.01	0.0030	0.12	0.01	0.0038	0.41	0.03	0.0030	0.12	0.01	0.0032
La	17.77	0.89	0.0005	17.35	0.88	0.0005	17.86	0.92	0.0004	16.85	0.87	0.0004
Ce	60.36	3.83	0.0007	58.64	3.76	0.0006	60.30	3.93	0.0006	57.39	3.78	0.0006
Pr	9.39	0.64	0.0003	9.27	0.64	0.0002	9.44	0.66	0.0002	9.03	0.64	0.0002
Nd	44.74	2.15	0.0018	44.22	2.14	0.0016	44.82	2.20	0.0015	42.47	2.10	0.0014
Sm	11.14	0.70	0.0007	11.03	0.70	0.0000	11.26	0.72	0.0000	10.70	0.69	0.0000
Eu	2.47	0.14	0.0002	2.40	0.14	0.0003	2.28	0.13	0.0002	2.34	0.14	0.0003
Gd	9.79	0.62	0.0025	9.64	0.62	0.0019	9.60	0.63	0.0021	9.27	0.61	0.0030
Tb	1.28	0.09	0.0004	1.24	0.09	0.0004	1.28	0.09	0.0004	1.22	0.09	0.0004
Dy	7.28	0.45	0.0011	6.94	0.43	0.0004	7.25	0.46	0.0008	6.83	0.44	0.0000
Ho	1.30	0.08	0.0001	1.22	0.08	0.0002	1.30	0.08	0.0001	1.22	0.08	0.0001
Er	3.37	0.20	0.0006	3.22	0.19	0.0009	3.24	0.19	0.0000	3.10	0.19	0.0004
Tm	0.47	0.03	0.0002	0.44	0.03	0.0001	0.47	0.03	0.0002	0.42	0.03	0.0001
Yb	3.01	0.21	0.0008	2.93	0.21	0.0009	3.00	0.21	0.0004	2.81	0.20	0.0004
Lu	0.45	0.03	0.0001	0.42	0.03	0.0002	0.44	0.03	0.0001	0.42	0.03	0.0001
Hf	3.87	0.34	0.0000	3.65	0.32	0.0004	3.39	0.31	0.0006	3.42	0.31	0.0005
Ta	0.07	0.01	0.0002	0.07	0.01	0.0001	0.06	0.01	0.0002	0.06	0.01	0.0002
Pb	0.38	0.03	0.0024	0.38	0.03	0.0021	0.40	0.04	0.0021	0.40	0.04	0.0021
Th	0.54	0.05	0.0000	0.54	0.05	0.0001	0.55	0.05	0.0000	0.50	0.05	0.0000
U	0.09	0.01	0.0001	0.08	0.01	0.0001	0.09	0.01	0.0001	0.08	0.01	0.0001

clinopyroxene

Unit	PAL C			Pal D			Pal D			Pal D		
Sample	T-08			S33b90-110			S33b90-110			S33b90-110		
Position	rim			core			rim			rim		
label	eb_50	1σ	det lim	ca_5	1σ	det lim	ca_6	1σ	det lim	ca_7	1σ	det lim
ppm V	292.32	12.93	0.0070	130.65	5.09	0.0074	171.93	6.79	0.0076	150.93	6.27	0.0070
Cr	63.99	3.63	0.1580	2.67	0.13	0.1410	2.84	0.13	0.1440	5.17	0.20	0.1350
Ni	46.91	2.26	0.0799	bdl	0.16	0.1970	bdl	0.14	0.1980	bdl	0.13	0.1830
Cu	3.45	0.16	0.0061	0.37	0.02	0.0231	0.72	0.04	0.0232	3.18	0.13	0.0202
Zn	59.07	3.42	0.0321	99.82	3.47	0.0590	94.48	3.29	0.0594	103.45	3.65	0.0533
Rb	0.01	0.00	0.0053	0.00	0.00	0.0139	0.02	0.01	0.0142	0.06	0.01	0.0132
Sr	204.45	13.57	0.0038	93.02	4.74	0.0131	113.89	5.95	0.0131	98.90	5.59	0.0124
Y	32.07	1.87	0.0004	48.37	3.28	0.0014	58.16	4.06	0.0014	61.74	4.71	0.0014
Zr	85.11	4.52	0.0029	63.29	3.66	0.0084	101.66	6.04	0.0078	96.76	6.25	0.0073
Nb	0.37	0.02	0.0003	0.20	0.01	0.0005	0.35	0.02	0.0007	0.41	0.02	0.0005
Cs	bdl	0.00	0.0027	0.01	0.00	0.0068	0.00	0.00	0.0070	bdl	0.00	0.0065
Ba	0.16	0.01	0.0032	0.10	0.02	0.0240	0.14	0.02	0.0232	0.81	0.04	0.0178
La	17.53	0.91	0.0004	23.05	1.26	0.0036	27.52	1.54	0.0036	44.48	2.69	0.0034
Ce	57.66	3.83	0.0006	75.67	3.29	0.0039	91.15	4.04	0.0039	129.62	6.13	0.0036
Pr	9.10	0.65	0.0002	12.26	0.52	0.0015	14.65	0.64	0.0015	19.32	0.89	0.0014
Nd	44.12	2.20	0.0017	59.24	2.43	0.0094	71.17	2.97	0.0099	88.02	3.88	0.0087
Sm	11.21	0.73	0.0008	15.45	0.86	0.0041	18.18	1.04	0.0037	21.46	1.33	0.0041
Eu	2.44	0.14	0.0004	2.84	0.13	0.0025	3.37	0.16	0.0022	3.62	0.19	0.0019
Gd	9.55	0.63	0.0025	13.21	0.86	0.0214	16.12	1.08	0.0218	17.62	1.29	0.0210
Tb	1.23	0.09	0.0003	1.80	0.12	0.0026	2.22	0.16	0.0026	2.42	0.19	0.0024
Dy	6.92	0.45	0.0004	10.46	0.64	0.0039	12.90	0.81	0.0042	13.79	0.94	0.0039
Ho	1.25	0.08	0.0002	1.95	0.12	0.0008	2.32	0.15	0.0010	2.48	0.17	0.0008
Er	3.18	0.19	0.0000	4.97	0.30	0.0024	6.12	0.38	0.0027	6.41	0.43	0.0020
Tm	0.45	0.03	0.0002	0.70	0.04	0.0008	0.88	0.06	0.0007	0.88	0.06	0.0005
Yb	2.91	0.21	0.0004	4.61	0.35	0.0032	5.67	0.44	0.0035	5.83	0.50	0.0032
Lu	0.43	0.03	0.0001	0.65	0.05	0.0006	0.80	0.06	0.0007	0.84	0.07	0.0006
Hf	3.73	0.34	0.0006	2.93	0.19	0.0036	4.82	0.33	0.0028	4.38	0.32	0.0028
Ta	0.07	0.01	0.0002	0.04	0.00	0.0006	0.07	0.00	0.0008	0.07	0.01	0.0005
Pb	0.44	0.04	0.0023	0.40	0.02	0.0039	0.50	0.02	0.0040	0.58	0.03	0.0036
Th	0.59	0.06	0.0001	0.45	0.03	0.0003	0.52	0.04	0.0003	1.72	0.13	0.0002
U	0.08	0.01	0.0000	0.10	0.01	0.0002	0.10	0.01	0.0003	0.35	0.02	0.0000

clinopyroxene

Unit	Pal D			Pal D			Pal D			Pal D		
Sample	S33b90-110			S33b90-110			S33b90-110			S33b90-110		
Position	core			core			rim			core		
label	ca_8	1σ	det lim	ca_9	1σ	det lim	ca_10	1σ	det lim	ca_11	1σ	det lim
ppm V	152.14	6.43	0.0073	155.28	6.69	0.0079	181.38	7.97	0.0079	106.30	4.86	0.0079
Cr	4.92	0.20	0.1370	14.77	0.54	0.1500	5.44	0.22	0.1510	3.57	0.16	0.1490
Ni	bdl	0.12	0.1830	bdl	0.13	0.1980	bdl	0.13	0.1980	0.22	0.12	0.1940
Cu	0.46	0.03	0.0205	7.11	0.30	0.0221	0.28	0.02	0.0215	1.60	0.08	0.0217
Zn	100.16	3.55	0.0527	88.40	3.15	0.0566	96.23	3.44	0.0600	147.31	5.32	0.0558
Rb	0.00	0.01	0.0130	1.97	0.07	0.0141		0.01	0.0142	0.02	0.01	0.0139
Sr	72.75	4.23	0.0126	119.03	7.11	0.0136	104.34	6.41	0.0137	40.32	2.62	0.0135
Y	53.80	4.24	0.0012	49.17	3.99	0.0015	58.86	4.92	0.0014	60.00	5.32	0.0015
Zr	95.74	6.36	0.0078	77.37	5.29	0.0079	94.85	6.67	0.0077	91.32	6.79	0.0074
Nb	0.37	0.02	0.0005	0.53	0.03	0.0005	0.37	0.02	0.0005	0.26	0.01	0.0006
Cs	0.00	0.00	0.0065	0.08	0.01	0.0070	bdl	0.00	0.0071	0.01	0.00	0.0068
Ba	0.01	0.01	0.0179	2.55	0.12	0.0186	0.04	0.01	0.0171	0.10	0.02	0.0175
La	24.45	1.52	0.0033	21.43	1.37	0.0036	26.76	1.76	0.0036	26.10	1.82	0.0035
Ce	84.40	4.08	0.0037	73.77	3.65	0.0040	92.82	4.70	0.0041	93.92	4.99	0.0040
Pr	13.70	0.65	0.0015	11.92	0.58	0.0016	14.64	0.72	0.0016	15.58	0.81	0.0015
Nd	66.23	2.98	0.0089	58.10	2.67	0.0097	70.87	3.32	0.0097	77.38	3.78	0.0087
Sm	17.05	1.09	0.0034	15.03	0.99	0.0036	18.40	1.24	0.0043	20.26	1.44	0.0044
Eu	2.92	0.16	0.0018	2.91	0.16	0.0019	3.34	0.19	0.0019	2.92	0.17	0.0012
Gd	14.91	1.13	0.0201	13.11	1.02	0.0209	16.02	1.28	0.0222	17.24	1.46	0.0211
Tb	2.07	0.16	0.0022	1.86	0.15	0.0026	2.24	0.19	0.0026	2.36	0.21	0.0026
Dy	12.04	0.84	0.0035	10.85	0.78	0.0041	13.08	0.97	0.0039	13.42	1.05	0.0037
Ho	2.21	0.16	0.0009	1.98	0.15	0.0008	2.36	0.18	0.0009	2.40	0.19	0.0010
Er	5.75	0.39	0.0023	5.01	0.35	0.0025	6.07	0.44	0.0030	6.22	0.48	0.0029
Tm	0.79	0.06	0.0006	0.71	0.05	0.0007	0.85	0.06	0.0008	0.87	0.07	0.0007
Yb	5.30	0.47	0.0027	4.74	0.43	0.0033	5.77	0.54	0.0031	5.73	0.57	0.0028
Lu	0.76	0.06	0.0006	0.68	0.06	0.0006	0.79	0.07	0.0007	0.91	0.09	0.0007
Hf	4.29	0.33	0.0025	3.52	0.28	0.0031	4.43	0.36	0.0023	4.14	0.35	0.0027
Ta	0.07	0.01	0.0006	0.07	0.01	0.0005	0.08	0.01	0.0007	0.04	0.00	0.0007
Pb	0.52	0.03	0.0039	1.09	0.05	0.0040	0.48	0.03	0.0038	0.60	0.03	0.0040
Th	0.41	0.03	0.0002	0.73	0.06	0.0003	0.52	0.04	0.0003	0.25	0.02	0.0001
U	0.09	0.01	0.0002	0.23	0.02	0.0002	0.10	0.01	0.0002	0.07	0.01	0.0003

clinopyroxene

Unit	Pal D			Pal D			Pal D			Pal D		
Sample	S33b90-110			S33b90-110			S33b90-110			S33b15-40		
Position	rim			core			rim			core		
label	ca_12	1σ	det lim	ca_13	1σ	det lim	ca_14	1σ	det lim	cc_1	1σ	det lim
ppm V	176.95	8.25	0.0081	265.88	12.66	0.0082	276.57	13.44	0.0087	177.32	5.87	0.0083
Cr	3.54	0.17	0.1530	18.73	0.73	0.1560	7.22	0.30	0.1630	4.44	0.25	0.1540
Ni	0.21	0.12	0.1960	3.47	0.28	0.2000	3.16	0.26	0.2080	1.46	0.13	0.1820
Cu	0.34	0.02	0.0216	0.68	0.04	0.0223	22.78	1.07	0.0235	0.38	0.02	0.0178
Zn	84.20	3.06	0.0572	78.18	2.86	0.0576	83.98	3.09	0.0598	84.64	3.09	0.0500
Rb	bdl	0.01	0.0142	0.02	0.01	0.0145	0.16	0.01	0.0152	bdl	0.01	0.0140
Sr	153.66	10.26	0.0137	190.54	13.08	0.0141	206.48	14.57	0.0149	158.37	5.25	0.0158
Y	43.14	3.94	0.0015	52.53	4.94	0.0014	59.38	5.74	0.0015	42.93	1.35	0.0014
Zr	57.58	4.41	0.0075	103.14	8.11	0.0078	121.90	9.84	0.0089	58.73	1.84	0.0086
Nb	0.22	0.01	0.0005	0.47	0.03	0.0005	0.63	0.04	0.0006	0.22	0.01	0.0007
Cs	0.00	0.00	0.0070	bdl	0.00	0.0072	0.02	0.00	0.0074	bdl	0.00	0.0069
Ba	0.07	0.01	0.0159	0.10	0.01	0.0168	1.93	0.10	0.0180	0.03	0.01	0.0157
La	18.44	1.32	0.0036	21.96	1.62	0.0037	30.80	2.33	0.0039	17.86	0.64	0.0038
Ce	64.36	3.50	0.0039	78.53	4.38	0.0041	102.98	5.88	0.0042	63.82	2.17	0.0042
Pr	10.31	0.55	0.0015	12.43	0.67	0.0016	15.71	0.87	0.0017	10.49	0.38	0.0016
Nd	50.15	2.50	0.0096	60.83	3.10	0.0099	74.12	3.85	0.0103	50.78	1.64	0.0102
Sm	13.14	0.96	0.0033	16.11	1.21	0.0041	18.65	1.44	0.0056	13.69	0.43	0.0053
Eu	2.76	0.17	0.0017	3.45	0.21	0.0017	3.94	0.25	0.0022	2.78	0.10	0.0021
Gd	11.93	1.04	0.0214	14.41	1.29	0.0218	16.43	1.51	0.0223	11.99	0.39	0.0230
Tb	1.62	0.15	0.0026	2.01	0.19	0.0026	2.20	0.21	0.0028	1.60	0.05	0.0028
Dy	9.40	0.76	0.0040	11.42	0.95	0.0046	12.91	1.10	0.0039	9.39	0.31	0.0041
Ho	1.70	0.14	0.0010	2.09	0.18	0.0009	2.41	0.21	0.0011	1.70	0.06	0.0008
Er	4.48	0.35	0.0010	5.41	0.44	0.0033	6.06	0.50	0.0030	4.62	0.17	0.0035
Tm	0.63	0.05	0.0007	0.77	0.07	0.0008	0.83	0.07	0.0007	0.61	0.02	0.0007
Yb	4.08	0.42	0.0032	4.98	0.52	0.0032	5.44	0.59	0.0030	4.10	0.14	0.0030
Lu	0.58	0.06	0.0007	0.72	0.07	0.0007	0.77	0.08	0.0007	0.59	0.02	0.0007
Hf	2.51	0.22	0.0030	4.75	0.43	0.0025	6.05	0.56	0.0027	2.58	0.09	0.0021
Ta	0.04	0.00	0.0006	0.10	0.01	0.0006	0.14	0.01	0.0008	0.04	0.00	0.0009
Pb	0.38	0.02	0.0041	0.43	0.02	0.0039	2.55	0.13	0.0041	0.43	0.02	0.0037
Th	0.30	0.03	0.0003	0.59	0.05	0.0003	1.36	0.13	0.0003	0.30	0.01	0.0002
U	0.06	0.01	0.0003	0.11	0.01	0.0003	0.37	0.03	0.0003	0.06	0.00	0.0001

clinopyroxene

Unit	Pal D			Pal D			Pal D			Pal D		
Sample	S33b-15-40			S33b-15-40			S33b-15-40			S33b-15-40		
Position	rim			core			rim			core		
label	cc 2	1σ	det lim	cc 3	1σ	det lim	cc 4	1σ	det lim	cc 5	1σ	det lim
ppm V	192.00	6.37	0.0086	209.83	6.98	0.0081	167.09	5.57	0.0081	266.53	8.92	0.0085
Cr	1.44	0.13	0.1640	7.66	0.42	0.1510	11.15	0.61	0.1530	68.18	3.72	0.1550
Ni	1.32	0.13	0.1950	2.09	0.14	0.1770	1.25	0.14	0.1820	7.51	0.28	0.1850
Cu	0.28	0.02	0.0202	7.81	0.26	0.0181	0.72	0.04	0.0183	0.45	0.02	0.0187
Zn	80.70	2.96	0.0536	73.99	2.72	0.0490	86.55	3.20	0.0505	69.31	2.57	0.0512
Rb	0.01	0.01	0.0147	0.08	0.01	0.0134	2.68	0.09	0.0138	bdl	0.01	0.0141
Sr	166.97	5.54	0.0170	189.49	6.30	0.0155	144.91	4.84	0.0158	197.90	6.63	0.0162
Y	43.45	1.37	0.0017	49.80	1.57	0.0014	49.82	1.58	0.0014	42.95	1.36	0.0016
Zr	62.02	1.94	0.0092	79.38	2.48	0.0078	82.83	2.60	0.0086	84.27	2.64	0.0087
Nb	0.25	0.01	0.0006	0.37	0.01	0.0007	0.59	0.02	0.0004	0.36	0.01	0.0006
Cs	bdl	0.00	0.0073	bdl	0.00	0.0067	0.10	0.01	0.0068	bdl	0.00	0.0069
Ba	0.07	0.01	0.0164	6.82	0.26	0.0146	11.05	0.42	0.0163	0.07	0.01	0.0155
La	18.65	0.67	0.0040	22.51	0.81	0.0038	23.24	0.85	0.0038	17.29	0.63	0.0038
Ce	66.16	2.25	0.0045	77.45	2.65	0.0042	81.30	2.79	0.0043	62.33	2.15	0.0043
Pr	10.48	0.38	0.0018	12.38	0.45	0.0016	13.23	0.48	0.0017	bdl	0.37	0.0018
Nd	51.19	1.66	0.0110	59.15	1.92	0.0101	63.35	2.06	0.0108	48.22	1.58	0.0110
Sm	13.67	0.43	0.0040	15.61	0.49	0.0031	16.10	0.51	0.0046	12.81	0.40	0.0055
Eu	2.73	0.10	0.0018	3.24	0.12	0.0016	3.20	0.12	0.0015	2.77	0.11	0.0016
Gd	11.72	0.38	0.0239	13.37	0.43	0.0217	13.99	0.45	0.0220	11.54	0.37	0.0226
Tb	1.61	0.05	0.0030	1.90	0.06	0.0028	1.90	0.07	0.0029	1.56	0.05	0.0028
Dy	9.23	0.30	0.0052	11.13	0.36	0.0051	10.95	0.36	0.0041	9.28	0.30	0.0054
Ho	1.75	0.06	0.0008	1.98	0.06	0.0007	2.05	0.07	0.0011	1.68	0.05	0.0010
Er	4.56	0.16	0.0028	5.12	0.18	0.0035	5.26	0.19	0.0028	4.55	0.17	0.0037
Tm	0.64	0.02	0.0008	0.70	0.03	0.0008	0.72	0.03	0.0007	0.64	0.02	0.0007
Yb	4.18	0.15	0.0031	4.63	0.16	0.0030	4.76	0.17	0.0031	4.06	0.14	0.0032
Lu	0.59	0.02	0.0009	0.66	0.02	0.0008	0.70	0.03	0.0007	0.57	0.02	0.0008
Hf	2.69	0.09	0.0025	3.62	0.12	0.0025	3.83	0.13	0.0028	3.79	0.13	0.0028
Ta	0.04	0.00	0.0007	0.06	0.00	0.0006	0.08	0.00	0.0007	0.08	0.00	0.0006
Pb	0.40	0.02	0.0041	4.31	0.16	0.0039	0.80	0.04	0.0034	0.37	0.02	0.0038
Th	0.36	0.01	0.0003	0.59	0.02	0.0004	0.73	0.03	0.0004	0.48	0.02	0.0004
U	0.07	0.00	0.0003	0.17	0.01	0.0002	0.19	0.01	0.0003	0.10	0.00	0.0003

clinopyroxene

Unit	Pal D			Pal D			Pal D			Palizzi Lava		
Sample	S33b-15-40			S33b-15-40			S33b-15-40			SC-18-24		
Position	rim			core			rim			core		
label	cc_6	1σ	det lim	cc_7	1σ	det lim	cc_8	1σ	det lim	cc_9	1σ	det lim
ppm V	263.92	8.95	0.0084	171.81	5.86	0.0082	140.32	4.81	0.0087	265.85	9.17	0.0083
Cr	6.50	0.39	0.1520	3.40	0.22	0.1490	1.43	0.13	0.1530	271.80	16.53	0.1480
Ni	3.65	0.17	0.1820	0.88	0.12	0.1740	0.82	0.12	0.1810	64.21	2.21	0.1720
Cu	0.50	0.03	0.0186	0.53	0.03	0.0180	0.45	0.03	0.0184	2.75	0.10	0.0180
Zn	74.25	2.80	0.0500	80.03	3.04	0.0494	78.83	3.02	0.0495	50.89	1.97	0.0484
Rb	bdl	0.01	0.0138	0.01	0.01	0.0133	bdl	0.01	0.0136	bdl	0.01	0.0130
Sr	192.64	6.54	0.0155	162.80	5.56	0.0153	140.66	4.83	0.0155	197.73	6.84	0.0149
Y	52.12	1.66	0.0014	51.16	1.63	0.0014	41.19	1.32	0.0014	27.19	0.87	0.0014
Zr	100.99	3.18	0.0087	84.88	2.68	0.0082	57.70	1.83	0.0086	65.76	2.09	0.0086
Nb	0.46	0.02	0.0007	0.33	0.01	0.0006	0.21	0.01	0.0006	0.29	0.01	0.0005
Cs	0.01	0.00	0.0067	bdl	0.00	0.0064	bdl	0.00	0.0067	bdl	0.00	0.0062
Ba	0.09	0.01	0.0146	0.04	0.01	0.0146	0.04	0.01	0.0145	0.11	0.01	0.0141
La	21.16	0.79	0.0036	23.85	0.90	0.0035	18.15	0.69	0.0037	13.48	0.52	0.0035
Ce	75.36	2.64	0.0040	81.28	2.87	0.0040	63.26	2.25	0.0040	44.63	1.60	0.0038
Pr	12.09	0.46	0.0016	13.25	0.51	0.0016	10.14	0.39	0.0017	7.29	0.28	0.0015
Nd	58.76	1.94	0.0106	63.43	2.10	0.0102	49.11	1.64	0.0103	35.98	1.21	0.0099
Sm	15.53	0.49	0.0038	16.41	0.52	0.0036	13.04	0.41	0.0043	9.03	0.29	0.0051
Eu	3.24	0.13	0.0016	3.24	0.13	0.0016	2.64	0.11	0.0016	1.96	0.08	0.0017
Gd	14.13	0.46	0.0221	14.39	0.47	0.0211	11.51	0.38	0.0215	8.16	0.27	0.0216
Tb	1.94	0.07	0.0028	1.94	0.07	0.0027	1.54	0.05	0.0028	1.04	0.04	0.0025
Dy	11.39	0.37	0.0048	11.26	0.37	0.0039	9.02	0.30	0.0046	5.86	0.20	0.0047
Ho	2.02	0.07	0.0009	2.07	0.07	0.0009	1.59	0.05	0.0010	1.06	0.04	0.0008
Er	5.57	0.20	0.0024	5.39	0.20	0.0019	4.37	0.16	0.0032	2.76	0.11	0.0032
Tm	0.76	0.03	0.0007	0.76	0.03	0.0009	0.59	0.02	0.0008	0.38	0.01	0.0007
Yb	4.99	0.18	0.0031	5.00	0.18	0.0035	3.97	0.14	0.0030	2.38	0.09	0.0035
Lu	0.69	0.02	0.0007	0.70	0.03	0.0007	0.56	0.02	0.0007	0.34	0.01	0.0006
Hf	4.54	0.15	0.0019	4.16	0.14	0.0025	2.48	0.09	0.0026	2.97	0.10	0.0025
Ta	0.10	0.00	0.0008	0.06	0.00	0.0006	0.03	0.00	0.0008	0.06	0.00	0.0006
Pb	0.39	0.02	0.0038	0.48	0.02	0.0042	0.40	0.02	0.0034	0.31	0.02	0.0038
Th	0.59	0.02	0.0003	0.44	0.02	0.0002	0.29	0.01	0.0002	0.48	0.02	0.0003
U	0.12	0.01	0.0000	0.08	0.00	0.0003	0.06	0.00	0.0002	0.08	0.00	0.0001

clinopyroxene

Unit	Palizzi Lava			Palizzi Lava			Palizzi Lava			Palizzi Lava		
Sample	SC-18-24			SC-18-24			SC-18-24			SC-18-24		
Position	rim			core			rim			core		
label	cc_10	1σ	det lim	cc_11	1σ	det lim	cc_12	1σ	det lim	cc_13	1σ	det lim
ppm V	288.38	10.02	0.0088	323.59	11.40	0.0085	286.27	10.17	0.0085	209.49	7.50	0.0086
Cr	169.50	10.54	0.1590	90.14	5.86	0.1510	123.76	8.24	0.1520	701.57	47.79	0.1520
Ni	53.31	1.85	0.1900	46.63	1.64	0.1810	44.70	1.58	0.1780	50.02	1.78	0.1830
Cu	2.71	0.10	0.0202	3.49	0.13	0.0190	3.51	0.13	0.0180	13.26	0.47	0.0191
Zn	57.89	2.26	0.0534	66.42	2.64	0.0498	63.25	2.55	0.0491	51.93	2.12	0.0509
Rb	1.96	0.07	0.0143	bdl	0.01	0.0139	bdl	0.01	0.0134	0.42	0.02	0.0137
Sr	190.81	6.64	0.0166	190.47	6.73	0.0161	182.53	6.50	0.0155	168.99	6.07	0.0160
Y	30.24	0.98	0.0016	33.70	1.10	0.0015	29.91	0.98	0.0014	22.78	0.75	0.0015
Zr	71.80	2.28	0.0095	84.98	2.72	0.0086	82.30	2.64	0.0080	65.90	2.12	0.0091
Nb	0.51	0.02	0.0007	0.36	0.01	0.0005	0.35	0.01	0.0006	0.46	0.02	0.0005
Cs	0.08	0.01	0.0070	bdl	0.00	0.0068	bdl	0.00	0.0065	0.09	0.01	0.0067
Ba	0.14	0.02	0.0154	0.12	0.01	0.0137	0.20	0.02	0.0140	2.47	0.11	0.0142
La	16.74	0.65	0.0038	19.30	0.77	0.0037	16.58	0.67	0.0035	11.93	0.49	0.0036
Ce	52.94	1.91	0.0044	63.81	2.35	0.0040	55.31	2.06	0.0039	39.83	1.50	0.0040
Pr	8.22	0.32	0.0017	9.95	0.40	0.0016	8.71	0.36	0.0016	6.40	0.27	0.0015
Nd	40.21	1.35	0.0111	47.53	1.62	0.0096	42.40	1.45	0.0097	31.53	1.09	0.0107
Sm	10.15	0.32	0.0037	11.27	0.36	0.0047	10.47	0.34	0.0039	8.26	0.27	0.0043
Eu	2.13	0.09	0.0018	2.44	0.10	0.0015	2.29	0.10	0.0016	1.77	0.08	0.0016
Gd	8.65	0.29	0.0236	9.99	0.33	0.0215	9.03	0.30	0.0210	7.03	0.24	0.0223
Tb	1.13	0.04	0.0031	1.28	0.05	0.0028	1.17	0.04	0.0026	0.90	0.03	0.0027
Dy	6.28	0.21	0.0038	7.12	0.24	0.0046	6.72	0.23	0.0047	5.00	0.17	0.0045
Ho	1.14	0.04	0.0010	1.29	0.04	0.0010	1.20	0.04	0.0008	0.93	0.03	0.0010
Er	2.95	0.11	0.0033	3.33	0.13	0.0036	3.09	0.12	0.0029	2.34	0.10	0.0024
Tm	0.44	0.02	0.0006	0.46	0.02	0.0007	0.43	0.02	0.0008	0.31	0.01	0.0009
Yb	2.81	0.11	0.0032	2.98	0.11	0.0029	2.70	0.10	0.0031	2.02	0.08	0.0024
Lu	0.39	0.02	0.0009	0.44	0.02	0.0007	0.40	0.02	0.0007	0.29	0.01	0.0007
Hf	3.02	0.11	0.0027	3.63	0.13	0.0025	3.60	0.13	0.0026	3.16	0.11	0.0027
Ta	0.06	0.00	0.0007	0.06	0.00	0.0009	0.07	0.00	0.0007	0.10	0.01	0.0006
Pb	0.52	0.02	0.0037	0.41	0.02	0.0037	0.34	0.02	0.0034	0.35	0.02	0.0036
Th	0.73	0.03	0.0004	0.56	0.02	0.0002	0.51	0.02	0.0000	0.59	0.02	0.0002
U	0.16	0.01	0.0003	0.09	0.00	0.0003	0.08	0.00	0.0001	0.11	0.01	0.0002

clinopyroxene

Unit	Palizzi Lava			Palizzi Lava			Palizzi Lava			Palizzi Lava		
Sample	SC-18-24			SC-18-24			SC-18-24			SC-18-24		
Position	rim			rim			rim			rim		
label	cc_14	1σ	det lim	cc_15	1σ	det lim	cc_16	1σ	det lim	cc_18	1σ	det lim
ppm V	249.40	9.00	0.0087	267.02	9.73	0.0087	277.28	10.19	0.0086	218.27	8.34	0.0082
Cr	368.65	25.72	0.1500	35.65	2.55	0.1540	48.00	3.51	0.1500	494.35	39.80	0.1430
Ni	45.91	1.65	0.1760	44.28	1.61	0.1820	46.90	1.71	0.1790	70.46	2.66	0.1710
Cu	4.07	0.15	0.0184	3.93	0.15	0.0186	4.96	0.18	0.0187	2.44	0.10	0.0182
Zn	59.04	2.43	0.0494	57.99	2.41	0.0517	60.63	2.55	0.0501	47.65	2.11	0.0484
Rb	0.06	0.01	0.0132	0.02	0.01	0.0135	0.00	0.01	0.0132	0.16	0.01	0.0128
Sr	186.64	6.76	0.0154	190.18	6.96	0.0156	201.01	7.42	0.0155	193.58	7.44	0.0146
Y	29.76	0.98	0.0013	26.54	0.88	0.0013	29.46	0.98	0.0014	23.93	0.81	0.0012
Zr	73.06	2.36	0.0076	66.40	2.15	0.0091	69.59	2.26	0.0090	63.50	2.10	0.0084
Nb	0.41	0.02	0.0005	0.27	0.01	0.0004	0.29	0.01	0.0005	0.29	0.01	0.0005
Cs	0.00	0.00	0.0063	bdl	0.00	0.0075	bdl	0.00	0.0065	0.00	0.00	0.0062
Ba	0.47	0.03	0.0146	2.81	0.13	0.0145	0.09	0.01	0.0147	0.12	0.02	0.0136
La	15.79	0.66	0.0034	14.45	0.61	0.0034	15.80	0.68	0.0036	13.34	0.61	0.0032
Ce	52.13	1.98	0.0039	48.30	1.85	0.0040	52.80	2.05	0.0041	43.59	1.78	0.0037
Pr	8.20	0.34	0.0015	7.72	0.33	0.0016	8.29	0.36	0.0015	6.89	0.32	0.0014
Nd	39.85	1.39	0.0095	36.95	1.29	0.0101	41.26	1.46	0.0103	33.77	1.23	0.0091
Sm	10.06	0.32	0.0035	9.33	0.30	0.0036	10.47	0.34	0.0043	8.41	0.28	0.0042
Eu	2.11	0.09	0.0014	2.00	0.09	0.0016	2.20	0.10	0.0016	1.91	0.09	0.0014
Gd	8.96	0.30	0.0209	8.20	0.28	0.0209	8.74	0.30	0.0210	7.47	0.26	0.0191
Tb	1.15	0.04	0.0027	1.02	0.04	0.0027	1.15	0.04	0.0026	0.96	0.04	0.0025
Dy	6.59	0.23	0.0045	5.70	0.20	0.0041	6.38	0.22	0.0036	5.14	0.18	0.0043
Ho	1.10	0.04	0.0010	1.04	0.04	0.0010	1.12	0.04	0.0008	0.96	0.03	0.0008
Er	2.93	0.12	0.0026	2.74	0.11	0.0027	2.93	0.12	0.0029	2.33	0.10	0.0026
Tm	0.42	0.02	0.0007	0.36	0.01	0.0007	0.42	0.02	0.0006	0.33	0.01	0.0006
Yb	2.63	0.10	0.0034	2.29	0.09	0.0024	2.60	0.10	0.0036	2.07	0.09	0.0031
Lu	0.38	0.02	0.0005	0.34	0.01	0.0007	0.36	0.01	0.0008	0.30	0.01	0.0005
Hf	3.35	0.12	0.0025	2.83	0.10	0.0028	2.99	0.11	0.0024	2.89	0.11	0.0026
Ta	0.08	0.00	0.0007	0.04	0.00	0.0008	0.05	0.00	0.0006	0.06	0.00	0.0007
Pb	0.33	0.02	0.0031	0.36	0.02	0.0032	0.35	0.02	0.0035	0.29	0.02	0.0031
Th	0.58	0.02	0.0002	0.39	0.02	0.0002	0.44	0.02	0.0002	0.46	0.02	0.0002
U	0.07	0.00	0.0001	0.06	0.00	0.0003	0.08	0.00	0.0002	0.06	0.00	0.0003

clinopyroxene

Unit	Palizzi Lava			Palizzi Lava			Palizzi Lava			Palizzi Lava		
Sample	SC-18-24			SC-18-24			SC-18-24			SC-18-24		
Position	rim			core			core			rim		
label	cc_19	1σ	det lim	cc_20	1σ	det lim	cc_21	1σ	det lim	cc_22	1σ	det lim
ppm V	273.53	10.56	0.0096	210.05	8.19	0.0088	283.05	11.16	0.0091	229.65	9.15	0.0095
Cr	4.35	0.37	0.1650	5.18	0.45	0.1560	7.81	0.68	0.1580	214.87	19.00	0.1610
Ni	28.13	1.08	0.1950	76.07	2.93	0.1810	20.97	0.83	0.1850	62.55	2.46	0.1890
Cu	25.11	0.93	0.0205	3126.65	116.40	0.0190	2.71	0.11	0.0189	3.21	0.13	0.0195
Zn	75.93	3.40	0.0553	75.29	3.41	0.0507	49.95	2.30	0.0525	52.26	2.43	0.0552
Rb	1.12	0.05	0.0144	6.10	0.25	0.0134	0.51	0.02	0.0136	0.00	0.01	0.0138
Sr	177.43	6.89	0.0170	180.17	7.07	0.0155	223.43	8.86	0.0157	192.64	7.73	0.0163
Y	43.13	1.47	0.0015	26.36	0.90	0.0014	28.56	0.99	0.0014	22.82	0.79	0.0015
Zr	109.70	3.63	0.0096	63.72	2.12	0.0087	74.76	2.50	0.0081	54.87	1.85	0.0085
Nb	0.69	0.03	0.0007	0.96	0.04	0.0005	0.32	0.01	0.0006	0.23	0.01	0.0006
Cs	0.15	0.01	0.0070	0.33	0.02	0.0063	0.01	0.00	0.0065	bdl	0.00	0.0067
Ba	1.26	0.07	0.0136	2.23	0.12	0.0142	1.24	0.07	0.0143	0.09	0.01	0.0148
La	21.03	0.97	0.0037	14.30	0.67	0.0035	13.65	0.65	0.0035	12.32	0.59	0.0037
Ce	69.78	2.88	0.0042	44.58	1.86	0.0040	47.18	2.00	0.0039	41.25	1.77	0.0041
Pr	11.22	0.52	0.0017	7.06	0.34	0.0015	7.69	0.37	0.0015	6.63	0.33	0.0017
Nd	54.69	2.01	0.0112	34.28	1.27	0.0099	38.60	1.45	0.0098	32.45	1.23	0.0109
Sm	13.34	0.43	0.0038	8.52	0.28	0.0034	10.05	0.33	0.0033	8.06	0.27	0.0047
Eu	2.50	0.12	0.0017	1.80	0.09	0.0018	2.34	0.12	0.0013	1.82	0.09	0.0016
Gd	11.65	0.40	0.0227	7.88	0.27	0.0211	8.91	0.31	0.0208	6.86	0.24	0.0212
Tb	1.58	0.06	0.0027	1.00	0.04	0.0026	1.14	0.04	0.0027	0.88	0.04	0.0028
Dy	8.89	0.32	0.0050	5.65	0.20	0.0045	6.48	0.23	0.0041	5.04	0.19	0.0046
Ho	1.74	0.06	0.0010	1.04	0.04	0.0009	1.14	0.04	0.0009	0.87	0.03	0.0010
Er	4.62	0.20	0.0030	2.75	0.12	0.0023	2.83	0.13	0.0033	2.26	0.10	0.0024
Tm	0.65	0.03	0.0008	0.37	0.02	0.0006	0.39	0.02	0.0008	0.31	0.01	0.0007
Yb	4.17	0.17	0.0027	2.57	0.11	0.0035	2.41	0.10	0.0025	1.97	0.09	0.0031
Lu	0.60	0.02	0.0008	0.36	0.02	0.0006	0.34	0.01	0.0008	0.31	0.01	0.0006
Hf	4.85	0.18	0.0025	2.73	0.10	0.0024	3.43	0.13	0.0032	2.32	0.09	0.0029
Ta	0.12	0.01	0.0009	0.08	0.00	0.0008	0.06	0.00	0.0007	0.04	0.00	0.0007
Pb	1.11	0.05	0.0038	7.33	0.34	0.0038	0.31	0.02	0.0037	0.30	0.02	0.0036
Th	1.17	0.04	0.0003	1.35	0.05	0.0002	0.48	0.02	0.0003	0.35	0.01	0.0003
U	0.26	0.01	0.0002	0.34	0.02	0.0001	0.09	0.01	0.0002	0.05	0.00	0.0003

Appendix E.6 – Trace element composition of plagioclase by LA-ICP-MS. 1σerror estimates on the signal and background counts; det lim= detection limit at the 99% confidence level.

Unit	Pal B			Pal B			Pal B			Pal B		
Sample	Pal-L			Pal-L			Pal-L			Pal-L		
Position	core			rim			core			rim		
label	eb_69	1σ	det lim	eb_70	1σ	det lim	eb_71	1σ	det lim	eb_72	1σ	det lim
ppm V	1.36	0.07	0.0155	1.33	0.07	0.0154	0.07	1.34	0.0137	1.25	0.07	0.0138
Cr	6.14	0.48	0.3530	3.41	0.33	0.3600	0.42	5.19	0.3280	4.42	0.37	0.3210
Ni	bdl	0.10	0.1650	bdl	0.11	0.1700	0.10	bdl	0.1540	bdl	0.09	0.1510
Cu	2.44	0.13	0.0138	2.65	0.14	0.0138	0.13	2.46	0.0121	2.62	0.14	0.0123
Zn	6.68	0.47	0.0688	6.61	0.47	0.0700	0.49	6.86	0.0641	7.18	0.52	0.0645
Rb	4.32	0.25	0.0100	4.08	0.24	0.0100	0.25	4.26	0.0091	5.56	0.33	0.0088
Sr	5110.58	415.88	0.0183	5084.66	417.29	0.0194	393.52	4754.69	0.0181	4830.79	403.19	0.0186
Y	0.24	0.02	0.0010	0.23	0.02	0.0012	0.02	0.29	0.0011	0.23	0.02	0.0010
Zr	0.19	0.02	0.0052	0.11	0.01	0.0059	0.01	0.10	0.0057	0.10	0.01	0.0062
Nb	0.04	0.00	0.0006	0.01	0.00	0.0006	0.00	0.01	0.0007	0.01	0.00	0.0005
Cs	0.01	0.00	0.0049	bdl	0.00	0.0051	0.00	0.01	0.0045	0.01	0.00	0.0043
Ba	995.99	86.34	0.0189	1047.25	91.54	0.0185	80.42	912.50	0.0181	1153.50	102.50	0.0190
La	13.20	0.81	0.0011	13.42	0.83	0.0012	0.97	15.47	0.0010	14.42	0.91	0.0010
Ce	15.85	1.28	0.0015	16.08	1.31	0.0013	1.55	18.83	0.0012	17.07	1.42	0.0012
Pr	1.25	0.11	0.0005	1.24	0.11	0.0005	0.13	1.44	0.0004	1.30	0.12	0.0005
Nd	3.46	0.21	0.0032	3.55	0.21	0.0037	0.24	4.07	0.0030	3.58	0.22	0.0034
Sm	0.27	0.03	0.0021	0.30	0.03	0.0015	0.04	0.38	0.0010	0.27	0.03	0.0019
Eu	0.91	0.07	0.0015	1.01	0.07	0.0014	0.07	0.96	0.0010	1.04	0.08	0.0015
Gd	0.17	0.02	0.0054	0.15	0.02	0.0057	0.02	0.21	0.0051	0.18	0.02	0.0036
Tb	0.01	0.00	0.0009	0.01	0.00	0.0009	0.00	0.02	0.0007	0.01	0.00	0.0008
Dy	0.05	0.01	0.0008	0.04	0.01	0.0016	0.01	0.06	0.0010	0.04	0.01	0.0012
Ho	0.01	0.00	0.0002	0.01	0.00	0.0003	0.00	0.01	0.0003	0.01	0.00	0.0002
Er	0.02	0.00	0.0012	0.01	0.00	<0,00000	0.00	0.01	<0,00000	0.01	0.00	<0,00000
Tm	0.00	0.00	<0,00000	0.00	0.00	0.0002	0.00	0.00	<0,00000	0.00	0.00	0.0003
Yb	0.01	0.00	0.0012	0.00	0.00	0.0009	0.00	0.01	0.0013	0.01	0.00	0.0011
Lu	0.00	0.00	0.0001	0.00	0.00	0.0002	0.00	0.00	0.0001	0.00	0.00	<0,00000
Hf	0.00	0.00	0.0013	0.00	0.00	0.0011	0.00	0.00	0.0011	0.00	0.00	0.0014
Ta	0.00	0.00	0.0007	0.00	0.00	0.0005	0.00	0.00	0.0005	0.00	0.00	0.0004
Pb	5.72	0.64	0.0043	5.97	0.68	0.0047	0.75	6.61	0.0044	6.88	0.79	0.0041
Th	0.03	0.00	0.0002	0.01	0.00	<0,00000	0.00	0.01	0.0001	0.01	0.00	<0,00000
U	0.01	0.00	0.0002	0.00	0.00	0.0001	0.00	0.00	<0,00000	0.00	0.00	0.0002

plagioclase

Unit	Pal B			Pal B			Pal D			Pal D		
Sample	Pal-L			Pal-L			S33b90-110			S33b90-110		
Position	core			rim			core			rim		
label	eb 73	1σ	det lim	eb 74	1σ	det lim	ca 15	1σ	det lim	ca 16	1σ	det lim
ppm V	1.28	0.07	0.0142	5.39	0.29	0.0134	0.71	0.04	0.0166	0.63	0.04	0.0159
Cr	4.71	0.40	0.3340	3.65	0.33	0.3150	3.58	0.24	0.3120	3.66	0.23	0.2980
Ni	0.26	0.10	0.1540	0.13	0.09	0.1470	bdl	0.25	0.3990	0.02	0.23	0.3840
Cu	2.07	0.12	0.0129	4.15	0.22	0.0112	2.00	0.11	0.0431	1.68	0.09	0.0422
Zn	6.06	0.44	0.0647	9.51	0.69	0.0617	8.59	0.36	0.1160	8.98	0.37	0.1090
Rb	3.48	0.21	0.0090	14.47	0.87	0.0085	7.01	0.26	0.0290	6.95	0.26	0.0279
Sr	4701.36	395.68	0.0191	4559.10	386.91	0.0185	5724.51	415.14	0.0290	5519.38	411.22	0.0293
Y	0.31	0.02	0.0010	1.14	0.08	0.0010	0.22	0.02	0.0028	0.25	0.03	0.0029
Zr	0.06	0.01	0.0056	8.23	0.53	0.0057	0.47	0.05	0.0156	0.54	0.05	0.0149
Nb	0.01	0.00	0.0006	1.31	0.06	0.0006	0.08	0.01	0.0010	0.08	0.01	0.0010
Cs	bdl	0.00	0.0044	0.48	0.04	0.0041	0.02	0.01	0.0143	0.04	0.01	0.0138
Ba	808.78	72.46	0.0182	950.21	85.83	0.0178	2126.54	102.15	0.0338	2408.94	117.99	0.0341
La	12.20	0.77	0.0011	16.68	1.06	0.0009	18.65	1.45	0.0075	17.91	1.43	0.0070
Ce	15.01	1.25	0.0013	21.57	1.82	0.0012	21.15	1.24	0.0082	20.39	1.22	0.0077
Pr	1.23	0.11	0.0005	1.77	0.16	0.0004	1.45	0.08	0.0031	1.42	0.08	0.0031
Nd	3.43	0.21	0.0031	5.39	0.33	0.0032	3.73	0.21	0.0203	3.63	0.20	0.0194
Sm	0.37	0.03	0.0025	0.64	0.06	0.0016	0.29	0.03	0.0077	0.31	0.03	0.0091
Eu	0.94	0.07	0.0013	0.99	0.07	0.0011	1.79	0.12	0.0033	1.78	0.12	0.0033
Gd	0.19	0.02	0.0048	0.36	0.03	0.0046	0.08	0.03	0.0442	0.15	0.03	0.0427
Tb	0.02	0.00	0.0008	0.05	0.00	0.0007	0.00	0.00	0.0056	0.01	0.00	0.0053
Dy	0.07	0.01	0.0014	0.24	0.02	0.0015	0.06	0.01	0.0079	0.06	0.01	0.0080
Ho	0.01	0.00	<0,00000	0.04	0.00	0.0002	0.00	0.00	0.0015	0.00	0.00	0.0018
Er	0.02	0.00	<0,00000	0.13	0.01	0.0011	0.01	0.00	0.0044	0.01	0.01	0.0061
Tm	0.00	0.00	0.0003	0.02	0.00	<0,00000	0.00	0.00	0.0013	0.00	0.00	0.0015
Yb	0.01	0.00	0.0015	0.11	0.01	0.0016	0.01	0.01	0.0071	0.01	0.00	0.0055
Lu	0.00	0.00	0.0003	0.02	0.00	0.0002	0.00	0.00	0.0011	0.00	0.00	0.0015
Hf	0.00	0.00	0.0009	0.22	0.03	0.0015	0.01	0.00	0.0048	0.01	0.00	0.0053
Ta	bdl	0.00	0.0006	0.08	0.01	0.0005	0.00	0.00	0.0014	0.00	0.00	0.0012
Pb	6.40	0.74	0.0042	7.71	0.90	0.0040	9.46	0.49	0.0078	8.99	0.47	0.0080
Th	0.01	0.00	0.0002	1.70	0.20	0.0001	0.04	0.00	0.0006	0.08	0.01	0.0009
U	0.00	0.00	0.0002	0.51	0.08	<0,00000	0.0170	0.0024	0.0005	0.0345	0.0040	0.0004

plagioclase

Unit	Pal D S33b90-			Pal D S33b90-			Pal D S33b90-			Pal D S33b90-		
Sample	110			110			110			110		
Position	core			rim			core			rim		
label	ca_17	1σ	det lim	ca_18	1σ	det lim	ca_19	1σ	det lim	ca_20	1σ	det lim
ppm V	0.55	0.03	0.0142	0.80	0.05	0.0143	0.39	0.03	0.0144	0.40	0.03	0.0135
Cr	2.61	0.20	0.2700	3.80	0.23	0.2690	3.51	0.23	0.2700	2.84	0.21	0.2560
Ni	bdl	0.22	0.3480	bdl	0.22	0.3440	0.10	0.21	0.3340	bdl	0.21	0.3190
Cu	1.45	0.08	0.0366	6.31	0.33	0.0373	1.02	0.07	0.0353	1.00	0.07	0.0344
Zn	8.25	0.34	0.0973	9.19	0.38	0.0988	6.54	0.28	0.0981	6.93	0.30	0.0934
Rb	4.98	0.19	0.0257	6.05	0.23	0.0255	5.66	0.23	0.0253	5.51	0.22	0.0241
Sr	5538.47	423.79	0.0273	6136.68	482.10	0.0278	4303.94	365.13	0.0268	4358.17	379.03	0.0265
Y	0.21	0.02	0.0026	0.36	0.04	0.0023	0.19	0.02	0.0025	0.19	0.02	0.0022
Zr	0.08	0.02	0.0136	0.26	0.03	0.0128	0.05	0.01	0.0122	0.05	0.01	0.0114
Nb	0.01	0.00	0.0009	0.06	0.01	0.0009	0.01	0.00	0.0011	0.00	0.00	0.0011
Cs	0.01	0.01	0.0126	0.01	0.01	0.0126	0.01	0.01	0.0124	bdl	0.01	0.0120
Ba	1809.65	90.39	0.0324	2303.60	117.34	0.0323	1138.27	61.46	0.0311	1139.77	62.74	0.0278
La	17.19	1.41	0.0065	16.90	1.42	0.0063	18.29	1.65	0.0062	19.74	1.82	0.0059
Ce	20.23	1.24	0.0072	19.03	1.20	0.0073	21.20	1.43	0.0067	22.20	1.53	0.0066
Pr	1.41	0.09	0.0028	1.39	0.09	0.0029	1.47	0.10	0.0027	1.54	0.10	0.0025
Nd	3.71	0.21	0.0169	3.61	0.21	0.0175	3.81	0.23	0.0162	3.94	0.25	0.0155
Sm	0.36	0.04	0.0072	0.34	0.04	0.0074	0.32	0.04	0.0087	0.37	0.04	0.0058
Eu	1.75	0.12	0.0031	1.77	0.12	0.0034	2.07	0.15	0.0031	1.98	0.15	0.0026
Gd	0.16	0.03	0.0381	0.15	0.03	0.0380	0.10	0.03	0.0376	0.13	0.03	0.0353
Tb	0.01	0.00	0.0045	0.02	0.00	0.0046	0.01	0.00	0.0045	0.01	0.00	0.0044
Dy	0.05	0.01	0.0065	0.05	0.01	0.0082	0.05	0.01	0.0068	0.04	0.01	0.0070
Ho	0.00	0.00	0.0012	0.01	0.00	0.0015	0.00	0.00	0.0016	0.00	0.00	0.0015
Er	0.01	0.00	0.0056	0.02	0.01	0.0046	0.01	0.00	0.0048	0.00	0.00	0.0041
Tm	0.00	0.00	0.0013	0.00	0.00	0.0015	0.00	0.00	0.0011	0.00	0.00	0.0012
Yb	0.00	0.00	0.0053	0.02	0.01	0.0064	0.00	0.00	0.0054	0.00	0.00	0.0048
Lu	0.00	0.00	0.0013	0.00	0.00	0.0010	0.00	0.00	0.0011	0.00	0.00	0.0009
Hf	0.00	0.00	0.0045	0.01	0.00	0.0047	bdl	0.00	0.0051	bdl	0.00	0.0035
Ta	bdl	0.00	0.0014	0.00	0.00	0.0011	0.00	0.00	0.0010	0.00	0.00	0.0008
Pb	8.57	0.46	0.0072	8.63	0.47	0.0067	9.47	0.55	0.0059	9.18	0.54	0.0066
Th	0.01	0.00	0.0006	0.02	0.00	0.0003	0.00	0.00	0.0004	0.00	0.00	0.0007
U	0.0030	0.0008	0.0004	0.0328	0.0039	0.0004	bdl	0.0001	0.0003	0.0008	0.0004	<0,00000

plagioclase

Unit	Pal D			Pal D		
Sample	S33b90-110			S33b90-110		
Position	core			rim		
label	ca_21	1σ	det lim	ca_22	1σ	det lim
ppm V	0.77	0.05	0.0153	0.73	0.05	0.0155
Cr	3.39	0.24	0.2920	4.45	0.27	0.2930
Ni	bdl	0.23	0.3640	0.08	0.23	0.3640
Cu	3.93	0.23	0.0390	1.86	0.12	0.0384
Zn	10.39	0.44	0.1060	9.34	0.40	0.1060
Rb	4.59	0.19	0.0276	4.48	0.19	0.0279
Sr	6869.78	612.26	0.0306	6662.16	608.23	0.0317
Y	0.27	0.03	0.0026	0.22	0.03	0.0027
Zr	0.20	0.03	0.0155	0.07	0.02	0.0144
Nb	0.04	0.00	0.0013	0.01	0.00	0.0010
Cs	0.03	0.01	0.0135	0.02	0.01	0.0136
Ba	2536.25	142.29	0.0328	2510.65	143.55	0.0357
La	15.42	1.46	0.0067	15.78	1.53	0.0067
Ce	18.27	1.28	0.0073	18.82	1.35	0.0076
Pr	1.34	0.09	0.0030	1.35	0.09	0.0029
Nd	3.51	0.22	0.0185	3.44	0.22	0.0175
Sm	0.28	0.03	0.0087	0.29	0.03	0.0078
Eu	1.52	0.12	0.0031	1.47	0.12	0.0035
Gd	0.17	0.03	0.0381	0.15	0.03	0.0385
Tb	0.01	0.00	0.0046	0.01	0.00	0.0047
Dy	0.03	0.01	0.0074	0.06	0.01	0.0080
Ho	0.00	0.00	0.0019	0.01	0.00	0.0015
Er	0.00	0.00	0.0050	0.01	0.00	0.0042
Tm	0.00	0.00	0.0011	0.00	0.00	0.0011
Yb	0.01	0.00	0.0045	0.00	0.00	0.0060
Lu	bdl	0.00	0.0013	0.00	0.00	0.0011
Hf	0.00	0.00	0.0057	0.01	0.00	0.0048
Ta	bdl	0.00	0.0014	bdl	0.00	0.0012
Pb	7.92	0.48	0.0064	7.78	0.48	0.0070
Th	0.02	0.00	0.0004	0.00	0.00	0.0005
U	0.0206	0.0030	0.0004	0.0010	0.0005	0.0003

Appendix F: Melt inclusions major and trace element composition

Appendix F.1 – Major element composition of melt inclusions, data from literature and this work; Ol: olivine; Cpx: clinopyroxene;Pl: plagioclase; Bt: biotite; San:sanidine.

Unit	La Sommata	La Sommata	La Sommata	La Sommata	La Sommata	La Sommata	La Sommata	La Sommata	La Sommata
Sample	IV28	IV13	IV30	N1-4	N1-6	N1-9	SOM1A	SOM1B	SOM2A
Comp.	Basalt	Basalt	Basalt	Basalt	Basalt	Basalt	Basalt	Basalt	Basalt
reference	Gioncada et al. 1998	Gioncada et al. 1998	Gioncada et al. 1998	Gioncada et al. 1998	Gioncada et al. 1998	Gioncada et al. 1998	Le Voyer et al. 2014	Le Voyer et al. 2014	Le Voyer et al. 2014
Host	Ol	Ol	Ol	Ol	Ol	Ol	Ol	Ol	Ol
Analysis type	EPMA	EPMA	EPMA	EPMA	EPMA	EPMA	EPMA	EPMA	EPMA
wt.% SiO_2	46.46	45.28	46.05	44.71	45.56	44.44	46.09	47.41	46.28
TiO_2	0.52	0.54	0.67	0.59	0.64	0.59	0.53	0.64	0.65
Al_2O_3	10.42	11.06	11.65	10.64	10.29	11.31	10.78	10.88	10.87
FeO_{tot}	8.35	7.85	9.21	8.68	8.99	9.60	8.36	8.51	9.20
MnO	0.18	0.18	0.16	0.17	0.20	0.17	0.17	0.16	0.17
MgO	9.08	8.53	7.43	11.80	11.53	10.27	8.44	8.03	8.30
CaO	15.12	14.45	14.49	13.59	13.22	14.20	14.60	14.86	14.27
Na_2O	1.85	2.03	2.18	1.91	1.89	1.51	1.93	1.93	2.10
K_2O	1.53	1.94	1.86	1.80	1.46	2.69	1.97	2.09	1.76
P_2O_5	0.26	1.02	0.27	0.25	0.21	0.28	0.29	0.30	0.26
Cl	0.31	0.31	0.40	0.30	0.35	0.22	0.24	0.22	0.28
total	94.08	93.19	94.37	94.44	94.34	95.28	93.40	95.03	94.14
Mg#	45.76	45.74	38.49	51.33	49.87	45.35	43.92	42.26	41.17

Unit	La Sommata	La Sommata	La Sommata	La Sommata	La Sommata	La Sommata	Vulcanello1	Vulcanello1	Vulcanello1
Sample	SOM2B	SOM3A	SOM4A	SOM4B	SOM5A	SOM6A	V1B	V1B	V1B
Comp.	Basalt	Basalt	Basalt	Basalt	Basalt	Basalt	Shoshonite	Shoshonite	Shoshonite
reference	Le Voyer et al. 2014	Le Voyer et al. 2014	Le Voyer et al. 2014	Le Voyer et al. 2014	Le Voyer et al. 2014	Le Voyer et al. 2014	Fusillo et al. 2015	Fusillo et al. 2015	Fusillo et al. 2015
Host	Ol	Ol	Ol	Ol	Ol	Ol	Ol	Ol	Ol
Analysis type	EPMA	EPMA	EPMA	EPMA	EPMA	EPMA	EPMA	EPMA	EPMA
wt.% SiO_2	45.29	46.42	45.67	45.89	45.92	47.13	53.35	54.94	53.75
TiO_2	0.69	0.69	0.64	0.71	0.66	0.53	0.64	0.58	0.65
$Al2O_3$	10.75	11.62	10.93	11.01	11.41	11.29	18.16	17.84	17.77
FeO_{tot}	9.02	9.59	9.06	9.31	9.20	9.07	7.37	6.69	7.46
MnO	0.18	0.18	0.17	0.14	0.20	0.12	0.16	0.15	0.15
MgO	8.24	8.01	8.21	7.97	7.45	8.11	2.17	1.92	2.22
CaO	14.24	14.02	14.44	14.60	14.17	14.85	4.91	4.00	5.12
Na_2O	1.99	2.26	2.03	2.08	2.10	2.03	4.79	5.23	4.74
K_2O	1.79	1.89	1.69	1.71	1.93	1.69	6.71	7.09	6.63
P_2O_5	0.23	0.28	0.24	0.24	0.25	0.25	0.60	0.59	0.57
Cl	0.32	0.31	0.29	0.28	0.27	0.33	0.31	0.29	0.32
total	92.74	95.27	93.37	93.94	93.56	95.40	99.17	99.32	99.38
Mg#	41.48	39.32	41.28	39.91	38.58	40.96	18.59	18.21	18.76

Unit	Vulcanello1	Vulcanello1	Vulcanello1	Vulcanello1	Vulcanello1	Vulcanello1	Vulcanello1	Vulcanello1	Vulcanello1
Sample	V1B	V1B	V1C	V1C	V1C	SC-18-12	SC-18-12	SC-18-12	SC-18-12
Comp.	Shoshonite	Shoshonite	Shoshonite	Shoshonite	Shoshonite	Shoshonite	Shoshonite	Shoshonite	Shoshonite
reference	Fusillo et al. 2015	Fusillo et al. 2015	Fusillo et al. 2015	Fusillo et al. 2015	Fusillo et al. 2015	This work	This work	This work	This work
Host	Ol	Ol	Ol	Ol	Ol	Cpx	Cpx	Cpx	Cpx
Analysis type	EPMA	EPMA	EPMA	EPMA	EPMA	EPMA	EPMA	EPMA	EPMA
wt.% SiO_2	55.44	55.87	52.10	52.61	51.12	55.71	55.56	55.09	53.47
TiO_2	0.58	0.71	0.66	0.63	0.64	0.66	0.70	0.63	0.54
Al_2O_3	17.74	17.16	17.12	18.02	16.34	17.29	16.97	16.80	18.55
FeO_{tot}	6.81	6.62	8.49	7.77	9.32	6.48	6.36	6.75	6.42
MnO	0.15	0.16	0.17	0.15	0.19	0.07	0.13	0.16	0.11
MgO	1.71	1.80	2.91	2.82	4.26	1.64	1.49	1.57	1.87
CaO	3.62	3.77	6.52	6.05	5.55	3.73	3.75	3.80	3.84
Na_2O	5.14	4.96	4.15	4.57	4.25	4.52	4.60	4.68	4.75
K_2O	7.11	7.00	5.77	6.10	5.70	7.02	7.01	6.89	7.41
P_2O_5	0.55	0.78	0.81	0.56	0.81	nd	nd	nd	nd
Cl	0.33	0.33	0.31	0.30	0.31	0.32	0.33	0.34	0.33
total	99.18	99.16	99.01	99.58	98.49	97.44	96.89	96.72	97.30
Mg#	16.30	17.42	21.01	21.97	26.18	16.40	15.34	15.30	18.43

Unit	Vulcanello1	Vulcanello1	Vulcanello1	Vulcanello1	Vulcanello1	Vulcanello1	Vulcanello1	Vulcanello1	Vulcanello1
Sample	SC-18-12	SC-18-12	SC-18-12	SC-18-12	SC-18-12	SC-18-12	SC-18-12	SC-18-13	SC-18-13
Comp.	Shoshonite	Shoshonite	Shoshonite	Shoshonite	Shoshonite	Shoshonite	Shoshonite	Shoshonite	Shoshonite
reference	This work	This work	This work	This work	This work	This work	This work	This work	This work
Host	Cpx	Cpx	Cpx	Cpx	Cpx	Cpx	Cpx	Cpx	Cpx
Analysis type	EPMA	EPMA	EPMA	EPMA	EPMA	EPMA	EPMA	EPMA	EPMA
wt.% SiO_2	52.62	54.37	55.04	56.55	54.00	54.43	55.69	55.19	55.23
TiO_2	0.57	0.58	0.65	0.59	0.65	0.62	0.64	0.65	0.63
Al_2O_3	18.38	18.34	17.63	17.60	17.61	17.82	17.42	17.30	17.43
FeO_{tot}	6.61	6.00	6.59	6.13	6.66	6.49	6.58	6.51	6.41
MnO	0.18	0.13	0.17	0.24	0.16	0.14	0.09	0.13	0.12
MgO	1.99	1.79	1.87	1.60	1.90	1.85	1.48	1.94	1.90
CaO	4.02	3.65	4.13	3.44	4.13	4.16	3.59	4.12	4.05
Na_2O	5.10	4.81	4.60	4.52	4.82	4.90	4.44	4.69	4.68
K_2O	7.16	8.05	7.28	7.22	7.17	7.15	7.51	7.22	7.29
P_2O_5	nd	nd	nd	nd	nd	nd	nd	nd	nd
Cl	0.31	0.33	0.34	0.31	0.28	0.29	0.30	0.27	0.29
total	96.94	98.05	98.29	98.20	97.38	97.85	97.74	98.01	98.03
Mg#	18.93	18.79	18.04	16.81	18.12	18.11	14.86	18.78	18.70

Unit	Vulcanello1	Vulcanello1	Vulcanello1	Vulcanello1	Vulcanello1	Vulcanello1	Vulcanello1	Vulcanello1	Vulcanello1
Sample	SC-18-13	SC-18-13	SC-18-13	SC-18-13	SC-18-13	SC-18-13	SC-18-13	SC-18-13	SC-18-13
Comp.	Shoshonite	Shoshonite	Shoshonite	Shoshonite	Shoshonite	Shoshonite	Shoshonite	Shoshonite	Shoshonite
reference	This work	This work	This work	This work	This work	This work	This work	This work	This work
Host	Cpx	Cpx	Cpx	Cpx	Cpx	Cpx	Cpx	Cpx	Cpx
Analysis type	EPMA	EPMA	EPMA	EPMA	EPMA	EPMA	EPMA	EPMA	EPMA
wt.% SiO_2	55.77	55.38	54.27	52.35	52.37	52.46	55.85	52.55	53.34
TiO_2	0.61	0.63	0.32	0.74	0.67	0.70	0.64	0.95	0.64
Al_2O_3	17.44	17.45	16.26	17.13	16.49	17.01	16.43	16.44	16.81
FeO_{tot}	6.43	6.52	8.94	7.94	9.22	7.72	6.59	7.86	7.63
MnO	0.12	0.13	0.19	0.18	0.20	0.19	0.11	0.16	0.15
MgO	1.82	1.91	2.51	2.89	2.36	2.87	2.44	2.93	2.85
CaO	3.92	4.19	5.71	5.56	4.71	5.67	4.82	6.04	5.79
Na_2O	4.76	4.44	3.98	4.04	4.43	4.35	3.70	4.43	4.34
K_2O	7.49	7.34	4.98	5.94	6.68	6.01	6.69	5.91	6.51
P_2O_5	nd	nd	nd	nd	nd	nd	nd	nd	nd
Cl	0.27	0.28	0.41	0.26	0.28	0.29	0.27	0.27	0.29
total	98.63	98.27	97.58	97.03	97.42	97.26	97.54	97.54	98.35
Mg#	18.01	18.52	17.89	22.02	16.57	22.39	22.31	22.43	22.47

Unit	Vulcanello1	Vulcanello1	Vulcanello1	Pal C	Pal C	Pal C	Pal C	Pal C	Pal D
Sample	SC-18-13	SC-18-13	SC-18-13	T-08	T-08	T-08	T-08	T-08	S33b15-40
Comp.	Shoshonite	Shoshonite	Shoshonite	Latite	Latite	Latite	Latite	Latite	Trachyte
reference	This work	This work	This work	This work	This work	This work	This work	This work	Fulignati et al. 2018
Host	Cpx	Cpx	Cpx	Cpx	Cpx	Cpx	Cpx	Cpx	Cpx
Analysis type	EPMA	EPMA	EPMA	EDS	EDS	EDS	EDS	EDS	EPMA
wt.% SiO_2	56.03	55.53	55.11	56.45	56.24	58.42	56.01	55.62	58.55
TiO_2	0.59	0.62	0.60	0.75	0.75	0.79	1.09	0.94	0.82
Al_2O_3	17.12	16.19	17.19	18.18	18.75	18.80	17.81	16.86	17.45
FeO_{tot}	6.38	6.29	6.48	7.19	4.89	4.07	7.20	7.55	5.42
MnO	0.10	0.13	0.13	0.10	0.08	0.35	0.12	0.03	0.18
MgO	1.78	2.48	1.74	1.40	1.19	0.74	1.07	1.11	1.41
CaO	3.71	4.84	3.81	4.16	3.68	2.15	3.22	3.74	2.68
Na_2O	4.67	4.08	4.59	4.76	5.39	5.22	4.96	4.40	5.49
K2O	7.45	6.53	7.40	6.37	7.95	8.70	7.72	8.92	6.38
P_2O_5	nd	nd	nd	0.24	0.55	0.23	0.45	0.51	0.00
Cl	0.27	0.30	0.28	0.39	0.51	0.53	0.36	0.32	0.43
total	98.09	96.99	97.33	100.00	100.00	100.00	100.00	100.00	98.80
Mg#	17.79	23.42	17.24	13.13	15.91	12.33	10.31	10.23	16.83

Unit	Pal D	Pal D	Pal D	Pal D	Pal D	Pal D	Pal D	Pal D	Pal D
Sample	S33b15-40	S33b15-40	S33b15-40	S33b15-40	S33b15-40	S33b15-40	S33b60-90	S33b60-90	S33b60-90
Comp.	Trachyte	Trachyte	Trachyte	Trachyte	Trachyte	Trachyte	Trachyte	Trachyte	Trachyte
reference	Fulignati et al. 2018	Fulignati et al. 2018	Fulignati et al. 2018	Fulignati et al. 2018	Fulignati et al. 2018	Fulignati et al. 2018	Fulignati et al. 2018	Fulignati et al. 2018	Fulignati et al. 2018
Host	Pl	Cpx	Cpx	Cpx	Cpx	Bt	Cpx	Ol	Ol
Analysis type	EPMA	EPMA	EPMA	EPMA	EPMA	EPMA	EPMA	EPMA	EPMA
wt.% SiO_2	59.54	58.33	60.50	58.21	59.60	60.27	60.16	60.20	59.84
TiO_2	0.39	0.52	0.78	0.85	0.67	0.54	0.67	0.60	0.61
Al_2O_3	17.50	17.66	17.68	17.19	17.91	17.78	17.87	17.30	17.34
FeO_{tot}	4.72	5.34	4.18	5.68	4.49	4.63	4.73	4.11	4.08
MnO	0.21	0.04	0.11	0.29	0.24	0.08	0.15	0.15	0.13
MgO	1.16	0.89	0.78	1.04	0.79	0.93	0.86	0.91	0.86
CaO	2.65	2.39	2.11	2.76	2.19	2.03	2.18	2.14	2.26
Na_2O	5.74	5.31	4.72	3.99	4.23	5.74	4.14	4.44	4.42
K_2O	7.02	5.73	4.76	5.11	4.65	6.90	5.11	7.61	7.77
P_2O_5	0.38	0.27	0.12	0.16	0.29	0.10	0.12	0.23	0.25
Cl	0.23	0.41	bdl	bdl	bdl	0.52	bdl	0.38	0.34
total	99.56	96.89	95.74	95.29	95.06	99.50	96.00	98.07	97.88
Mg#	16.06	11.48	12.62	12.40	12.03	13.42	12.32	14.59	14.00

Unit	Pal D	Pal D	Pal D	Pal D	Pal D	Pal D	Pal D	Pal D	Pal D
Sample	S33b60-90	S33b60-90	S33b60-90	S33b60-90	S33b60-90	S33b60-90	S33b60-90	S33b60-90	S33b60-90
Comp.	Trachyte	Trachyte	Trachyte	Trachyte	Trachyte	Trachyte	Trachyte	Trachyte	Trachyte
reference	Fulignati et al. 2018	Fulignati et al. 2018	Fulignati et al. 2018	Fulignati et al. 2018	Fulignati et al. 2018	Fulignati et al. 2018	Fulignati et al. 2018	Fulignati et al. 2018	Fulignati et al. 2018
Host	Ol	Ol	Pl	Cpx	Cpx	Cpx	Cpx	Cpx	Cpx
Analysis type	EPMA	EPMA	EPMA	EPMA	EPMA	EPMA	EPMA	EPMA	EPMA
wt.% SiO_2	59.94	61.57	60.42	60.04	60.18	61.62	61.04	60.38	60.18
TiO_2	0.54	0.55	0.40	0.45	0.46	0.57	0.50	0.54	0.50
Al_2O_3	17.46	17.62	18.68	15.93	17.03	17.57	17.21	17.40	17.22
FeO_{tot}	4.19	3.92	3.27	4.07	3.79	4.18	3.72	4.75	4.23
MnO	0.11	0.13	0.05	0.20	0.10	0.09	0.14	0.10	0.17
MgO	0.94	0.82	0.68	1.90	0.87	0.88	0.81	0.94	0.97
CaO	2.17	2.19	2.97	4.06	2.16	2.08	2.23	2.41	2.44
Na_2O	4.60	4.58	4.56	4.29	4.32	3.67	4.39	4.41	4.44
K_2O	7.60	7.67	6.99	7.04	7.45	7.49	7.47	7.61	7.41
P_2O_5	0.19	0.24	0.19	0.20	0.23	0.20	0.17	0.24	0.15
Cl	0.39	0.41	0.37	0.36	0.40	0.39	0.41	0.35	0.38
total	98.13	99.70	98.57	98.53	96.98	98.74	98.08	99.15	98.10
Mg#	14.75	14.02	13.81	26.55	15.07	14.00	14.52	13.35	15.12

Unit	Pal D	Pal D	Pal D	Pal B	Pal B	Pal B	Pal B	Pal B	Pal B
Sample	S33b60-90	S33b60-90	S33b60-90	PAL-L	PAL-L	PAL-L	PAL-L	PAL-L	PAL-L
Comp.	Trachyte	Trachyte	Trachyte	Rhyolite	Rhyolite	Rhyolite	Rhyolite	Rhyolite	Rhyolite
reference	Fulignati et al. 2018	Fulignati et al. 2018	Fulignati et al. 2018	This work	This work	This work	This work	This work	This work
Host	Cpx	Cpx	Bt	San	San	San	San	San	San
Analysis type	EPMA	EPMA	EPMA	EDS	EDS	EDS	EDS	EDS	EDS
wt.% SiO_2	59.79	59.93	59.77	69.69	70.97	71.02	71.49	69.45	70.89
TiO_2	0.61	0.52	0.60	bdl	bdl	bdl	bdl	bdl	bdl
$Al2O_3$	16.16	17.10	17.31	14.78	14.81	14.76	14.11	15.57	14.80
FeO_{tot}	4.49	4.59	4.33	2.48	2.12	2.39	1.97	1.76	1.86
MnO	0.13	0.08	0.09	bdl	bdl	bdl	bdl	bdl	bdl
MgO	1.88	0.91	1.01		0.23	0.00	0.23	0.08	0.23
CaO	3.88	2.55	2.19	bdl	1.38	bdl	bdl	0.85	1.05
Na_2O	4.13	4.45	4.84	4.50	3.46	4.59	4.86	5.72	4.28
K_2O	7.19	7.50	7.56	7.96	6.62	6.73	6.69	6.10	6.39
P_2O_5	0.19	0.26	0.25	bdl	bdl	bdl	bdl	bdl	bdl
Cl	0.33	0.40	bdl	0.60	0.43	0.51	0.64	0.47	0.50
total	98.78	98.29	97.95	100.00	100.00	100.00	100.00	100.00	100.00
Mg#	24.49	13.32	15.27		7.71	0.00	8.30	3.31	8.87

Unit	Pal B	Pal B	Pal B	Pal B	Pal B	Pal B	Pal B	Pal B	Pal B
Sample	PAL-L	PAL-L	PAL-L	PAL-L	PAL-L	PAL-L	PAL-L	PAL-L	PAL-L
Comp.	Rhyolite	Rhyolite	Rhyolite	Rhyolite	Rhyolite	Rhyolite	Rhyolite	Rhyolite	Rhyolite
reference	This work	This work	This work	This work	This work	This work	This work	This work	This work
Host	San	San	San	San	San	San	San	San	San
Analysis type	EDS	EDS	EDS	EDS	EDS	EDS	EDS	EDS	EDS
wt.% SiO_2	69.87	71.55	70.76	70.67	70.22	71.02	70.83	69.32	70.71
TiO_2	bdl	bdl	bdl	bdl	bdl	bdl	bdl	0.21	0.11
Al_2O_3	15.09	14.42	14.08	15.17	14.20	14.72	14.25	15.81	15.03
FeO_{tot}	2.51	1.79	2.10	1.60	1.44	1.81	2.21	1.90	2.20
MnO	bdl	bdl	bdl	bdl	bdl	bdl	bdl	0.12	0.07
MgO	0.07	0.12	0.00	0.00	0.12	0.03	0.00	0.11	0.37
CaO	0.97	0.77	1.03	0.81	0.88	0.90	1.03	0.82	0.80
Na_2O	4.50	4.50	4.24	4.55	5.08	5.06	4.33	4.59	3.99
K_2O	6.54	6.29	7.29	6.73	7.46	6.14	6.91	6.57	6.19
P_2O_5	bdl	bdl	bdl	bdl	bdl	bdl	bdl	0.06	bdl
Cl	0.45	0.56	0.50	0.47	0.60	0.32	0.43	0.49	0.53
total	100.00	100.00	100.00	100.00	100.00	100.00	100.00	100.00	100.00
Mg#	2.06	5.02			5.87	1.17		4.30	11.54

Unit	Pal B	Pal B	Pal B
Sample	PAL-L	PAL-L	PAL-L
Comp.	Rhyolite	Rhyolite	Rhyolite
reference	This work	This work	This work
Host	San	San	San
Analysis type	EDS	EDS	EDS
wt.% SiO_2	69.05	71.04	69.32
TiO_2	0.07	0.14	0.13
Al_2O_3	15.94	14.23	15.91
FeO_{tot}	2.04	2.30	1.96
MnO	0.10	0.20	0.08
MgO	0.27	0.22	0.12
CaO	1.04	1.11	0.84
Na_2O	4.36	4.21	4.65
K_2O	6.61	5.99	6.36
P_2O_5	0.06	bdl	bdl
Cl	0.46	0.56	0.63
total	100.00	100.00	100.00
Mg#	9.31	6.91	4.53

Appendix F.2 - Trace element composition of melt inclusions by LA-ICP-MS. 1σerror estimates on the signal and background counts; det lim= detection limit at the 99% confidence level. Bdl: below detection limit; nd: not determined. Abbreviation of mineral phases as in Appendix F.1.

Comp.	Basalt			Basalt			Basalt			Basalt		
Unit	La Sommata			La Sommata			La Sommata			La Sommata		
Sample	SC-18-05			SC-18-05			SC-18-05			SC-18-05		
Host	Ol			Ol			Ol			Ol		
label	dc_1	1σ	det lim	dc_4	1σ	det lim	dc_7	1σ	det lim	dc_10	1σ	det lim
ppm V	285.19	9.30	0.1610	143.80	4.76	0.1890	234.25	7.87	0.2860	213.65	7.32	0.2280
Cr	6.68	2.27	3.5500	259.95	10.37	4.2600	501.40	20.50	6.5000	17.93	3.40	5.1900
Ni	13.35	2.05	3.0700	405.52	17.78	3.6000	32.97	3.28	5.4700	2.70	2.72	4.2500
Cu	39.54	1.35	0.1520	7.62	0.39	0.1870	31.29	1.14	0.2560	132.36	4.32	0.2020
Zn	106.53	5.16	0.9450	79.49	4.11	1.1000	54.66	3.13	1.6300	104.17	5.94	1.3000
Rb	62.73	2.14	0.0941	31.77	1.12	0.1110	35.58	1.29	0.1750	45.01	1.66	0.1390
Sr	1047.46	43.62	0.1120	516.29	22.26	0.1350	949.58	43.54	0.2140	1417.46	68.75	0.1720
Y	13.61	0.50	0.0143	7.20	0.29	0.0140	9.91	0.40	0.0258	7.22	0.31	0.0184
Zr	65.99	2.32	0.1080	28.86	1.19	0.1250	55.62	2.08	0.1350	21.43	1.00	0.1420
Nb	5.60	0.21	0.0089	2.26	0.10	0.0091	3.11	0.13	0.0122	2.97	0.13	0.0083
Cs	1.73	0.11	0.0435	0.68	0.06	0.0531	0.91	0.08	0.0806	0.46	0.06	0.0661
Ba	571.75	25.47	0.0852	243.28	11.38	0.1030	355.22	17.71	0.1260	442.37	23.44	0.1390
La	28.24	0.87	0.0205	12.34	0.40	0.0224	19.11	0.60	0.0396	21.28	0.67	0.0300
Ce	53.95	2.27	0.0245	23.08	1.02	0.0304	38.45	1.79	0.0419	39.91	1.96	0.0367
Pr	6.37	0.29	0.0090	2.67	0.13	0.0106	4.51	0.23	0.0160	4.27	0.23	0.0130
Nd	25.34	0.94	0.0760	12.65	0.54	0.0838	20.04	0.81	0.1230	16.53	0.72	0.0931
Sm	4.47	0.27	0.0287	2.53	0.21	0.0305	3.70	0.27	0.0393	2.55	0.23	0.0266
Eu	1.22	0.08	0.0075	0.74	0.06	0.0115	1.00	0.08	0.0186	0.65	0.06	0.0154
Gd	4.16	0.27	0.1150	1.89	0.20	0.1510	3.03	0.26	0.2030	1.62	0.21	0.1800
Tb	0.52	0.04	0.0190	0.24	0.03	0.0227	0.39	0.04	0.0324	0.24	0.03	0.0219
Dy	3.01	0.19	0.0187	1.73	0.14	0.0192	2.29	0.18	0.0402	1.64	0.15	0.0271
Ho	0.59	0.04	0.0059	0.39	0.03	0.0081	0.29	0.03	0.0158	0.27	0.03	0.0080
Er	1.33	0.11	0.0146	0.80	0.10	0.0122	1.18	0.12	0.0000	0.99	0.12	0.0000
Tm	0.22	0.02	0.0000	0.08	0.02	0.0000	0.12	0.02	0.0091	0.10	0.02	0.0000
Yb	1.68	0.13	0.0143	0.82	0.10	0.0120	0.79	0.10	0.0377	0.77	0.10	0.0208
Lu	0.14	0.02	0.0057	0.08	0.01	0.0059	0.13	0.02	0.0062	0.08	0.01	0.0072
Hf	1.61	0.12	0.0223	0.72	0.08	0.0160	1.35	0.12	0.0291	0.74	0.09	0.0241
Ta	0.22	0.02	0.0056	0.10	0.01	0.0052	0.17	0.02	0.0063	0.13	0.02	0.0064
Pb	9.46	0.39	0.0559	3.74	0.20	0.0626	3.50	0.19	0.0981	9.16	0.43	0.0711
Th	6.13	0.22	0.0000	2.70	0.11	0.0000	2.64	0.11	0.0037	3.50	0.15	0.0062
U	2.08	0.11	0.0016	0.85	0.05	0.0019	0.94	0.06	0.0035	1.55	0.10	0.0023

Comp.	Basalt			Basalt			Basalt			Basalt		
Unit	La Sommata			La Sommata			La Sommata			La Sommata		
Sample	SC-18-05			SC-18-05			SC-18-05			SC-18-05		
Host	Ol			Ol			Ol			Ol		
label	dc_12	1σ	det lim	dc_13	1σ	det lim	dc_14	1σ	det lim	dc_17	1σ	det lim
ppm V	109.28	4.00	0.1900	268.92	9.54	0.4120	297.31	10.62	0.2010	259.27	9.54	0.1480
Cr	359.40	17.08	4.3300	346.23	16.36	9.3500	15.68	2.55	4.5900	378.00	19.00	3.4800
Ni	518.22	27.78	3.4900	bdl	2.92	7.6500	23.68	2.36	3.6300	25.72	2.42	2.7300
Cu	16.49	1.00	0.1760	33.11	1.18	0.4150	18.57	0.70	0.1840	135.39	4.43	0.1470
Zn	97.63	6.55	1.0300	91.63	5.71	2.3200	111.19	6.96	1.1100	162.38	10.77	0.8030
Rb	17.35	0.79	0.1170	115.44	4.41	0.2580	63.00	2.44	0.1220	28.95	1.19	0.0964
Sr	294.15	15.61	0.1440	705.20	38.02	0.3260	1151.62	63.46	0.1540	860.05	50.73	0.1200
Y	4.17	0.25	0.0188	12.71	0.55	0.0416	14.81	0.64	0.0166	12.50	0.58	0.0137
Zr	18.23	1.31	0.1420	52.29	1.98	0.2470	67.67	2.49	0.1460	44.19	1.76	0.1010
Nb	1.31	0.11	0.0084	3.91	0.16	0.0144	5.77	0.23	0.0080	3.59	0.16	0.0071
Cs	0.76	0.11	0.0532	19.11	1.40	0.1290	1.68	0.14	0.0570	1.29	0.12	0.0436
Ba	141.01	8.67	0.0956	973.16	57.51	0.2740	586.24	35.50	0.1220	330.73	21.60	0.1060
La	9.21	0.37	0.0246	20.20	0.63	0.0636	30.68	0.94	0.0270	19.87	0.62	0.0206
Ce	20.48	1.14	0.0302	37.55	2.04	0.0739	57.56	3.19	0.0311	36.38	2.16	0.0249
Pr	1.99	0.15	0.0105	4.78	0.28	0.0237	6.48	0.38	0.0117	4.32	0.27	0.0077
Nd	8.17	0.61	0.0766	20.81	0.86	0.1840	27.87	1.11	0.0753	17.58	0.77	0.0593
Sm	2.07	0.34	0.0240	4.50	0.30	0.0000	5.67	0.35	0.0258	3.91	0.29	0.0247
Eu	0.58	0.10	0.0112	1.32	0.08	0.0363	1.55	0.09	0.0060	1.25	0.09	0.0129
Gd	1.19	0.30	0.1400	3.44	0.26	0.2990	3.70	0.25	0.1330	3.19	0.25	0.1200
Tb	0.20	0.05	0.0195	0.45	0.04	0.0451	0.53	0.04	0.0208	0.49	0.04	0.0170
Dy	1.32	0.23	0.0243	2.53	0.18	0.0000	3.04	0.20	0.0000	2.51	0.19	0.0153
Ho	0.18	0.04	0.0064	0.46	0.03	0.0207	0.59	0.04	0.0060	0.48	0.04	0.0062
Er	0.60	0.16	0.0000	1.18	0.11	0.1080	1.48	0.11	0.0254	1.16	0.11	0.0140
Tm	0.10	0.03	0.0056	0.17	0.02	0.0000	0.25	0.02	0.0000	0.16	0.02	0.0000
Yb	0.33	0.12	0.0228	0.91	0.10	0.0602	1.18	0.10	0.0000	1.17	0.12	0.0166
Lu	0.11	0.03	0.0038	0.16	0.02	0.0000	0.24	0.02	0.0052	0.16	0.02	0.0027
Hf	0.66	0.15	0.0177	1.47	0.11	0.0000	1.75	0.12	0.0095	1.21	0.11	0.0157
Ta	0.03	0.02	0.0079	0.18	0.02	0.0087	0.26	0.02	0.0036	0.18	0.02	0.0052
Pb	0.49	0.12	0.0702	1.73	0.12	0.1230	9.43	0.44	0.0651	6.47	0.34	0.0492
Th	1.49	0.11	0.0000	4.55	0.18	0.0000	6.52	0.25	0.0042	3.79	0.16	0.0028
U	0.69	0.08	0.0021	0.78	0.06	0.0135	2.09	0.13	0.0032	1.43	0.10	0.0015

Comp.	Shoshonite			Shoshonite			Shoshonite			Shoshonite		
Unit	Vulcanello 1			Vulcanello 1			Vulcanello 1			Vulcanello 1		
Sample	SC-18-12			SC-18-12			SC-18-12			SC-18-12		
Host	Cpx			Cpx			Cpx			Cpx		
label	ea_1	1σ	det lim	ea_2	1σ	det lim	ea_3	1σ	det lim	ea_4	1σ	det lim
ppm V	130.42	4.18	0.0444	223.92	7.18	0.0390	113.73	3.66	0.0452	194.90	6.29	0.1510
Cr	1.06	0.63	1.0200	29.85	1.18	0.9160		0.66	1.0500	155.88	5.68	3.4200
Ni	4.21	0.54	0.8360	27.06	1.13	0.7410	1.91	0.55	0.8570	48.68	2.53	2.8300
Cu	176.85	6.29	0.0423	89.20	3.20	0.0373	209.57	7.50	0.0443	41.57	1.58	0.1420
Zn	107.63	7.81	0.2780	86.82	6.34	0.2450	109.68	8.05	0.2810	62.03	4.71	0.9150
Rb	209.10	6.76	0.0278	100.65	3.27	0.0246	233.61	7.58	0.0292	45.37	1.50	0.0970
Sr	692.04	31.10	0.0296	440.68	19.93	0.0258	769.43	35.07	0.0303	327.79	15.09	0.1010
Y	25.25	1.02	0.0040	27.92	1.14	0.0029	23.94	0.98	0.0040	20.21	0.85	0.0112
Zr	186.02	8.09	0.0244	139.25	6.10	0.0262	202.68	8.93	0.0280	77.60	3.56	0.0853
Nb	23.19	0.89	0.0020	11.66	0.45	0.0017	25.37	0.98	0.0022	4.79	0.20	0.0059
Cs	9.28	0.31	0.0132	4.55	0.15	0.0120	10.46	0.35	0.0137	1.87	0.08	0.0470
Ba	878.38	36.31	0.0234	451.01	18.77	0.0251	951.82	39.84	0.0306	242.03	10.32	0.0990
La	77.15	3.36	0.0048	45.00	1.97	0.0047	78.12	3.44	0.0051	24.19	1.09	0.0151
Ce	134.91	5.58	0.0061	89.90	3.74	0.0053	138.17	5.79	0.0059	53.76	2.28	0.0205
Pr	14.05	0.64	0.0025	10.97	0.51	0.0021	13.82	0.64	0.0023	7.01	0.34	0.0077
Nd	51.54	2.40	0.0148	46.39	2.18	0.0121	48.85	2.32	0.0162	32.88	1.61	0.0514
Sm	9.04	0.47	0.0063	9.67	0.50	0.0080	7.78	0.41	0.0065	8.36	0.49	0.0108
Eu	1.69	0.08	0.0039	2.23	0.10	0.0030	1.65	0.08	0.0025	1.84	0.11	0.0097
Gd	5.87	0.33	0.0295	7.63	0.43	0.0244	5.44	0.32	0.0265	6.08	0.40	0.0821
Tb	0.88	0.05	0.0045	1.08	0.06	0.0040	0.84	0.05	0.0044	0.77	0.05	0.0142
Dy	4.85	0.24	0.0060	5.73	0.28	0.0039	4.40	0.22	0.0078	4.67	0.27	0.0280
Ho	0.91	0.05	0.0014	1.07	0.05	0.0013	0.86	0.05	0.0015	0.78	0.05	0.0042
Er	2.56	0.16	0.0044	2.64	0.16	0.0037	2.22	0.14	0.0045	1.92	0.15	0.0171
Tm	0.39	0.02	0.0006	0.40	0.02	0.0010	0.39	0.02	0.0000	0.24	0.02	0.0036
Yb	2.48	0.15	0.0024	2.90	0.17	0.0041	2.69	0.16	0.0050	1.67	0.13	0.0166
Lu	0.39	0.03	0.0008	0.39	0.03	0.0010	0.39	0.03	0.0009	0.26	0.02	0.0024
Hf	4.93	0.25	0.0050	4.51	0.24	0.0031	5.37	0.28	0.0042	2.86	0.18	0.0113
Ta	1.23	0.06	0.0014	0.61	0.03	0.0011	1.34	0.06	0.0014	0.26	0.02	0.0039
Pb	26.59	0.95	0.0171	13.20	0.48	0.0161	29.13	1.05	0.0173	5.55	0.24	0.0565
Th	32.48	1.68	0.0008	15.34	0.80	0.0006	35.16	1.85	0.0006	5.49	0.30	0.0020
U	10.10	0.44	0.0000	5.11	0.22	0.0005	11.36	0.50	0.0008	1.75	0.09	0.0014

Comp.	Shoshonite			Shoshonite			Shoshonite			Shoshonite		
Unit	Vulcanello 1			Vulcanello 1			Vulcanello 1			Vulcanello 1		
Sample	SC-18-12			SC-18-12			SC-18-12			SC-18-12		
Host	Cpx			Cpx			Cpx			Cpx		
label	ea_5	1σ	det lim	ea_6	1σ	det lim	ea_7	1σ	det lim	ea_8	1σ	det lim
ppm V	124.48	4.04	0.1560	146.44	4.75	0.0430	153.11	4.98	0.0425	118.06	3.85	0.0430
Cr	237.73	8.38	3.5900	5.25	0.63	1.0000	3.13	0.61	0.9620	2.71	0.60	0.9660
Ni	28.92	2.16	2.9900	1.77	0.52	0.8470	6.32	0.57	0.8170	1.51	0.52	0.8300
Cu	83.55	3.11	0.1600	157.89	5.78	0.0440	142.64	5.26	0.0408	189.01	7.01	0.0434
Zn	65.53	5.03	0.9630	107.17	8.20	0.2550	104.95	8.14	0.2460	101.47	7.99	0.2540
Rb	117.05	3.84	0.1040	223.31	7.32	0.0291	197.95	6.51	0.0297	221.78	7.32	0.0310
Sr	493.17	22.93	0.1070	965.13	45.88	0.0308	900.03	43.35	0.0296	959.45	46.86	0.0303
Y	13.61	0.58	0.0127	19.82	0.84	0.0037	20.51	0.88	0.0040	16.79	0.73	0.0031
Zr	86.58	4.00	0.0932	178.57	8.18	0.0292	163.99	7.61	0.0282	159.75	7.51	0.0307
Nb	11.91	0.48	0.0073	24.34	0.97	0.0017	21.96	0.88	0.0021	22.56	0.91	0.0019
Cs	5.03	0.18	0.0495	9.24	0.31	0.0145	8.27	0.28	0.0144	9.17	0.31	0.0146
Ba	574.28	24.55	0.0920	1166.10	50.62	0.0297	1045.62	45.92	0.0271	1136.72	50.53	0.0273
La	35.02	1.58	0.0185	74.66	3.42	0.0049	68.28	3.17	0.0047	66.53	3.13	0.0052
Ce	63.22	2.70	0.0220	128.68	5.59	0.0059	119.01	5.23	0.0058	115.23	5.13	0.0061
Pr	6.94	0.34	0.0086	12.61	0.61	0.0022	12.18	0.60	0.0022	11.42	0.57	0.0021
Nd	27.03	1.36	0.0585	45.07	2.23	0.0183	45.20	2.27	0.0133	39.93	2.03	0.0123
Sm	5.51	0.35	0.0230	7.65	0.42	0.0065	8.08	0.45	0.0054	6.96	0.40	0.0063
Eu	1.39	0.09	0.0117	1.75	0.09	0.0038	1.70	0.09	0.0024	1.48	0.08	0.0032
Gd	4.36	0.31	0.0940	5.03	0.30	0.0241	5.24	0.32	0.0307	4.67	0.29	0.0264
Tb	0.57	0.04	0.0135	0.70	0.04	0.0046	0.76	0.04	0.0040	0.61	0.04	0.0042
Dy	3.04	0.20	0.0117	3.93	0.21	0.0057	4.00	0.21	0.0067	3.26	0.18	0.0051
Ho	0.57	0.04	0.0054	0.80	0.04	0.0013	0.74	0.04	0.0015	0.64	0.04	0.0012
Er	1.01	0.10	0.0129	2.11	0.14	0.0037	2.02	0.14	0.0000	1.57	0.11	0.0044
Tm	0.21	0.02	0.0049	0.28	0.02	0.0009	0.30	0.02	0.0006	0.24	0.02	0.0009
Yb	1.40	0.12	0.0089	2.00	0.13	0.0025	2.08	0.13	0.0000	1.72	0.11	0.0049
Lu	0.22	0.02	0.0039	0.30	0.02	0.0010	0.29	0.02	0.0011	0.25	0.02	0.0011
Hf	2.73	0.18	0.0209	4.55	0.25	0.0034	4.11	0.23	0.0040	3.85	0.22	0.0028
Ta	0.69	0.04	0.0033	1.24	0.06	0.0008	1.12	0.05	0.0013	1.07	0.05	0.0015
Pb	15.26	0.59	0.0635	28.98	1.06	0.0163	26.03	0.96	0.0166	28.52	1.06	0.0165
Th	15.56	0.84	0.0026	30.41	1.68	0.0009	27.67	1.55	0.0004	27.81	1.58	0.0004
U	5.56	0.26	0.0025	9.64	0.44	0.0000	8.76	0.40	0.0004	8.79	0.41	0.0006

Comp.	Shoshonite			Shoshonite			Shoshonite			Shoshonite		
Unit	Vulcanello 1			Vulcanello 1			Vulcanello 1			Vulcanello 1		
Sample	SC-18-12			SC-18-12			SC-18-13			SC-18-13		
Host	Cpx			Cpx			Cpx			Cpx		
label	ea_9	1σ	det lim	ea_10	1σ	det lim	ea_11	1σ	det lim	ea_12	1σ	det lim
ppm V	126.66	4.14	0.0451	208.08	6.82	0.0416	172.81	5.76	0.0405	126.62	4.24	0.0437
Cr	3.49	0.63	0.9880	70.43	2.53	0.9340	7.70	0.63	0.9010	1.67	0.62	0.9800
Ni	3.29	0.55	0.8500	17.65	0.86	0.7920	9.76	0.62	0.7470	1.22	0.52	0.8190
Cu	144.13	5.40	0.0431	126.96	4.79	0.0418	185.51	7.26	0.0406	203.00	8.03	0.0411
Zn	108.51	8.68	0.2530	131.54	10.68	0.2510	102.16	8.90	0.2280	104.64	9.29	0.2460
Rb	201.59	6.68	0.0332	160.43	5.34	0.0307	178.35	6.05	0.0304	205.50	7.01	0.0346
Sr	1053.89	52.23	0.0316	667.97	33.62	0.0298	1284.39	69.15	0.0291	838.65	45.98	0.0320
Y	18.33	0.81	0.0037	26.34	1.17	0.0032	17.00	0.80	0.0032	18.37	0.88	0.0038
Zr	156.09	7.45	0.0293	163.95	7.93	0.0267	140.77	7.26	0.0245	180.26	9.45	0.0306
Nb	20.83	0.85	0.0027	19.59	0.81	0.0025	17.90	0.78	0.0023	23.89	1.05	0.0027
Cs	7.63	0.26	0.0149	6.30	0.22	0.0140	7.37	0.26	0.0143	7.84	0.28	0.0167
Ba	1212.45	54.60	0.0292	828.02	37.81	0.0296	1056.25	51.22	0.0255	1150.56	56.71	0.0314
La	65.42	3.12	0.0051	75.23	3.64	0.0049	59.99	3.10	0.0048	68.52	3.60	0.0052
Ce	112.29	5.07	0.0068	136.78	6.25	0.0061	104.77	5.09	0.0059	117.68	5.81	0.0065
Pr	11.05	0.56	0.0025	14.77	0.76	0.0021	10.72	0.59	0.0022	11.57	0.65	0.0021
Nd	41.08	2.13	0.0143	58.34	3.06	0.0139	39.71	2.24	0.0159	41.58	2.39	0.0179
Sm	6.76	0.39	0.0073	10.35	0.60	0.0069	6.85	0.43	0.0051	6.97	0.45	0.0084
Eu	1.73	0.09	0.0019	2.23	0.11	0.0033	1.63	0.09	0.0030	1.67	0.09	0.0042
Gd	4.59	0.29	0.0263	7.60	0.48	0.0251	4.55	0.32	0.0273	4.84	0.34	0.0281
Tb	0.65	0.04	0.0042	1.03	0.06	0.0036	0.63	0.04	0.0043	0.66	0.04	0.0039
Dy	3.51	0.19	0.0047	5.25	0.29	0.0059	3.43	0.20	0.0077	3.51	0.21	0.0075
Ho	0.64	0.04	0.0020	1.00	0.06	0.0010	0.62	0.04	0.0010	0.63	0.04	0.0015
Er	1.76	0.12	0.0037	2.30	0.16	0.0000	1.55	0.12	0.0034	1.77	0.14	0.0044
Tm	0.24	0.02	0.0014	0.37	0.02	0.0006	0.25	0.02	0.0010	0.27	0.02	0.0014
Yb	1.91	0.13	0.0056	2.51	0.16	0.0053	1.73	0.12	0.0046	1.79	0.13	0.0035
Lu	0.29	0.02	0.0009	0.36	0.03	0.0012	0.24	0.02	0.0010	0.28	0.02	0.0013
Hf	3.56	0.21	0.0048	4.55	0.26	0.0028	3.52	0.22	0.0034	4.18	0.26	0.0023
Ta	1.02	0.05	0.0016	0.97	0.05	0.0014	0.93	0.05	0.0014	1.17	0.06	0.0013
Pb	25.36	0.95	0.0157	21.10	0.80	0.0146	23.98	0.94	0.0133	28.89	1.14	0.0154
Th	26.53	1.53	0.0000	24.27	1.43	0.0009	23.36	1.48	0.0007	28.53	1.85	0.0007
U	8.39	0.39	0.0006	7.59	0.36	0.0000	7.29	0.37	0.0005	9.27	0.48	0.0004

Comp.	Shoshonite			Shoshonite			Shoshonite			Shoshonite		
Unit	Vulcanello 1			Vulcanello 1			Vulcanello 1			Vulcanello 1		
Sample	SC-18-13			SC-18-13			SC-18-13			SC-18-13		
Host	Cpx			Cpx			Cpx			Cpx		
label	ea_13	1σ	det lim	ea_14	1σ	det lim	ea_15	1σ	det lim	ea_16	1σ	det lim
ppm V	117.45	3.95	0.0439	155.85	5.29	0.1500	168.92	5.74	0.0379	179.51	6.16	0.0424
Cr	3.92	0.64	1.0100	15.17	2.18	3.3900	24.12	1.05	0.8610	18.33	0.90	0.9390
Ni	0.99	0.51	0.8330	5.94	1.76	2.7800	26.69	1.23	0.7050	21.67	1.07	0.7640
Cu	195.35	7.81	0.0439	64.67	2.70	0.1490	131.72	5.39	0.0382	110.32	4.63	0.0398
Zn	100.29	9.06	0.2490	91.97	8.54	0.8460	107.46	10.07	0.2100	89.41	8.69	0.2270
Rb	226.71	7.78	0.0353	160.13	5.55	0.1230	111.69	3.88	0.0312	124.39	4.38	0.0341
Sr	779.28	43.51	0.0332	1041.22	59.25	0.1120	557.19	32.30	0.0288	577.40	34.77	0.0315
Y	17.92	0.87	0.0038	16.55	0.83	0.0148	26.03	1.30	0.0030	25.05	1.29	0.0037
Zr	180.86	9.65	0.0310	126.38	6.96	0.0957	123.06	6.81	0.0282	129.99	7.46	0.0308
Nb	24.56	1.09	0.0027	16.58	0.76	0.0074	12.11	0.56	0.0022	13.88	0.66	0.0021
Cs	8.97	0.32	0.0163	6.67	0.25	0.0546	4.79	0.17	0.0140	5.43	0.20	0.0157
Ba	1145.59	57.41	0.0361	938.58	47.93	0.1190	520.14	26.99	0.0301	657.74	35.34	0.0321
La	66.51	3.56	0.0057	54.50	2.97	0.0188	54.53	3.02	0.0043	48.00	2.76	0.0048
Ce	114.39	5.75	0.0066	95.36	4.88	0.0219	103.18	5.36	0.0055	95.49	5.14	0.0061
Pr	11.09	0.64	0.0022	9.53	0.56	0.0077	11.64	0.69	0.0018	11.08	0.69	0.0021
Nd	39.59	2.32	0.0156	35.69	2.16	0.0522	47.99	2.91	0.0140	44.40	2.81	0.0143
Sm	6.73	0.44	0.0057	6.38	0.47	0.0110	9.78	0.65	0.0070	9.30	0.65	0.0109
Eu	1.54	0.09	0.0040	1.30	0.09	0.0134	1.98	0.11	0.0029	1.95	0.11	0.0028
Gd	4.76	0.34	0.0304	4.51	0.38	0.0956	7.16	0.53	0.0215	6.52	0.50	0.0277
Tb	0.63	0.04	0.0044	0.58	0.05	0.0132	0.95	0.06	0.0039	0.95	0.07	0.0036
Dy	3.53	0.22	0.0053	3.03	0.22	0.0176	5.31	0.33	0.0029	5.12	0.33	0.0074
Ho	0.65	0.04	0.0011	0.64	0.05	0.0037	1.05	0.07	0.0008	0.99	0.07	0.0010
Er	1.68	0.13	0.0026	1.52	0.15	0.0088	2.48	0.20	0.0000	2.56	0.21	0.0044
Tm	0.24	0.02	0.0013	0.22	0.02	0.0056	0.38	0.03	0.0014	0.34	0.02	0.0009
Yb	1.82	0.14	0.0000	1.44	0.14	0.0189	2.39	0.18	0.0031	2.36	0.18	0.0034
Lu	0.27	0.02	0.0010	0.21	0.02	0.0046	0.34	0.03	0.0012	0.36	0.03	0.0010
Hf	4.36	0.28	0.0045	3.09	0.23	0.0099	3.77	0.25	0.0033	3.79	0.26	0.0036
Ta	1.20	0.06	0.0017	0.82	0.05	0.0047	0.62	0.04	0.0010	0.70	0.04	0.0016
Pb	29.27	1.17	0.0167	23.71	0.99	0.0535	13.59	0.56	0.0145	16.60	0.70	0.0138
Th	30.03	1.98	0.0000	20.24	1.37	0.0000	17.28	1.19	0.0005	17.30	1.24	0.0004
U	9.52	0.50	0.0006	6.88	0.37	0.0014	5.12	0.28	0.0004	5.54	0.31	0.0000

Comp.	Shoshonite			Latite			Latite			Latite		
Unit	Vulcanello 1			PAL A			PAL A			PAL A		
Sample	SC-18-13			T-18			T-18			T-18		
Host	Cpx			Cpx			Cpx			Cpx		
label	ea_17	1σ	det lim	dd_2	1σ	det lim	dd_3	1σ	det lim	dd_4	1σ	det lim
ppm V	291.95	10.08	0.0432	117.74	8.64	0.1860	114.85	8.48	0.1750	96.04	7.17	0.1730
Cr	2.54	0.61	0.9660	bdl	2.83	4.1900	42.75	3.53	3.9900	4.10	2.59	3.9300
Ni	7.43	0.59	0.7750	7.39	2.29	3.3200	3.31	1.92	3.1900	3.65	2.06	3.1100
Cu	50.35	2.15	0.0410	248.57	13.12	0.1740	160.23	8.51	0.1680	207.13	11.08	0.1600
Zn	103.84	10.28	0.2240	100.93	8.31	0.9610	82.23	6.80	0.9710	103.63	8.63	0.9140
Rb	173.63	6.15	0.0349	218.95	11.67	0.1160	206.17	11.05	0.1120	237.25	12.81	0.1130
Sr	1258.14	77.24	0.0326	845.37	50.13	0.1490	618.59	36.90	0.1440	734.97	44.17	0.1400
Y	18.77	0.99	0.0032	19.34	1.23	0.0147	19.68	1.26	0.0142	19.98	1.29	0.0170
Zr	159.71	9.33	0.0307	175.23	11.44	0.1360	169.57	11.11	0.1180	179.12	11.86	0.1220
Nb	20.50	0.98	0.0020	24.60	1.53	0.0088	21.18	1.32	0.0072	24.46	1.54	0.0086
Cs	7.30	0.27	0.0158	9.63	0.61	0.0541	8.75	0.56	0.0534	10.04	0.64	0.0518
Ba	1097.68	60.02	0.0351	1160.52	88.23	0.1230	837.85	64.17	0.1130	1089.66	84.22	0.1160
La	63.28	3.71	0.0055	72.13	4.35	0.0267	62.34	3.78	0.0250	72.45	4.43	0.0246
Ce	110.42	6.05	0.0062	124.14	9.74	0.0299	108.15	8.55	0.0292	122.21	9.76	0.0287
Pr	11.28	0.71	0.0022	12.43	0.83	0.0115	10.91	0.73	0.0104	12.19	0.82	0.0113
Nd	40.22	2.59	0.0148	44.34	2.52	0.0743	40.26	2.29	0.0729	42.94	2.47	0.0683
Sm	7.24	0.52	0.0079	7.02	0.54	0.0244	7.69	0.56	0.0234	7.43	0.56	0.0323
Eu	1.72	0.10	0.0032	1.59	0.12	0.0195	1.62	0.11	0.0136	1.56	0.11	0.0139
Gd	4.86	0.39	0.0216	4.85	0.41	0.1290	4.92	0.39	0.1160	4.78	0.40	0.1220
Tb	0.71	0.05	0.0039	0.69	0.07	0.0217	0.70	0.07	0.0193	0.65	0.06	0.0199
Dy	3.55	0.24	0.0046	3.70	0.38	0.0202	4.05	0.40	0.0194	3.88	0.40	0.0231
Ho	0.64	0.05	0.0020	0.78	0.07	0.0066	0.68	0.06	0.0037	0.75	0.06	0.0067
Er	1.85	0.16	0.0000	1.63	0.18	0.0114	2.01	0.20	0.0109	2.10	0.21	0.0185
Tm	0.28	0.02	0.0012	0.33	0.04	0.0046	0.35	0.04	0.0044	0.28	0.03	0.0075
Yb	1.90	0.15	0.0049	1.80	0.19	0.0158	1.88	0.18	0.0186	2.42	0.23	0.0209
Lu	0.28	0.03	0.0010	0.33	0.03	0.0048	0.28	0.03	0.0055	0.32	0.03	0.0042
Hf	4.06	0.29	0.0044	4.53	0.38	0.0074	4.69	0.38	0.0158	4.82	0.40	0.0194
Ta	1.08	0.06	0.0010	1.20	0.08	0.0067	1.13	0.07	0.0071	1.27	0.08	0.0047
Pb	25.55	1.08	0.0151	29.06	1.67	0.0616	24.75	1.42	0.0532	29.56	1.71	0.0576
Th	26.17	1.92	0.0000	31.71	2.47	0.0000	29.43	2.31	0.0031	34.61	2.74	0.0030
U	8.03	0.46	0.0006	10.09	0.69	0.0000	9.08	0.62	0.0023	11.24	0.78	0.0043

Comp.	Latite			Latite			Latite			Latite		
Unit	PAL A			PAL A			PAL A			PAL C		
Sample	T-18			T-18			T-18			T-08		
Host	Cpx			Cpx			Cpx			Ol		
label	dd_5	1σ	det lim	dd_6	1σ	det lim	dd_7	1σ	det lim	dd_17	1σ	det lim
ppm V	195.90	14.76	0.1940	190.24	14.96	0.1790	119.96	9.60	0.1870	97.52	9.87	0.1970
Cr	65.71	4.81	4.3800	3.96	2.59	4.0400	64.93	4.98	4.1700	10.12	3.56	4.4200
Ni	24.84	2.46	3.4900	16.25	2.24	3.1900	bdl	2.08	3.2900	116.31	7.95	3.4500
Cu	101.45	5.51	0.1760	244.87	13.63	0.1770	185.21	10.47	0.1740	150.83	10.43	0.1950
Zn	83.66	7.07	1.0200	97.72	8.56	0.9150	97.41	8.67	0.9500	231.00	25.65	1.0100
Rb	104.70	5.72	0.1250	158.78	8.97	0.1150	222.02	12.71	0.1170	151.70	10.64	0.1300
Sr	567.66	34.43	0.1580	659.75	41.49	0.1460	830.52	52.98	0.1530	650.71	51.07	0.1700
Y	23.71	1.54	0.0162	24.48	1.66	0.0192	17.74	1.22	0.0150	14.78	1.28	0.0210
Zr	124.81	8.38	0.1380	165.47	11.52	0.1380	178.33	12.60	0.1390	130.01	11.57	0.1590
Nb	12.03	0.77	0.0095	17.65	1.17	0.0102	23.51	1.57	0.0104	16.53	1.38	0.0107
Cs	4.49	0.30	0.0595	6.67	0.45	0.0526	8.32	0.57	0.0574	6.29	0.54	0.0630
Ba	568.46	44.47	0.1230	801.45	65.36	0.1180	1109.32	91.97	0.1280	839.48	87.95	0.1390
La	44.69	2.76	0.0280	58.78	3.77	0.0250	65.86	4.29	0.0256	53.90	4.36	0.0273
Ce	88.73	7.17	0.0322	108.85	9.18	0.0293	108.58	9.31	0.0300	93.88	10.21	0.0339
Pr	10.33	0.71	0.0114	11.77	0.84	0.0102	11.08	0.80	0.0107	9.43	0.86	0.0119
Nd	43.86	2.54	0.0895	47.79	2.86	0.0739	40.49	2.47	0.0849	31.85	2.43	0.0981
Sm	8.97	0.66	0.0284	8.68	0.66	0.0384	7.24	0.57	0.0345	5.56	0.59	0.0487
Eu	1.87	0.13	0.0122	2.19	0.15	0.0150	1.67	0.12	0.0124	0.91	0.10	0.0144
Gd	7.18	0.56	0.1450	6.77	0.55	0.1540	4.53	0.40	0.1350	3.46	0.42	0.1450
Tb	0.86	0.08	0.0216	0.94	0.09	0.0188	0.75	0.08	0.0185	0.47	0.07	0.0234
Dy	5.01	0.50	0.0234	4.86	0.51	0.0168	3.71	0.40	0.0142	2.73	0.40	0.0247
Ho	1.04	0.08	0.0044	0.94	0.08	0.0058	0.84	0.07	0.0038	0.48	0.06	0.0071
Er	2.16	0.22	0.0000	2.76	0.27	0.0190	1.78	0.19	0.0000	0.93	0.16	0.0123
Tm	0.35	0.04	0.0031	0.33	0.04	0.0036	0.25	0.03	0.0053	0.16	0.03	0.0058
Yb	2.10	0.20	0.0259	2.45	0.24	0.0239	1.95	0.20	0.0157	1.36	0.20	0.0294
Lu	0.32	0.03	0.0042	0.32	0.03	0.0043	0.30	0.03	0.0051	0.26	0.03	0.0034
Hf	3.38	0.29	0.0148	4.49	0.39	0.0212	4.13	0.36	0.0194	3.07	0.36	0.0179
Ta	0.65	0.05	0.0075	0.92	0.07	0.0059	1.13	0.08	0.0059	0.87	0.08	0.0065
Pb	14.62	0.87	0.0721	21.50	1.31	0.0508	27.60	1.70	0.0521	35.44	2.69	0.0574
Th	14.78	1.19	0.0105	22.83	1.91	0.0000	27.50	2.34	0.0000	21.84	2.36	0.0029
U	4.83	0.34	0.0040	6.87	0.50	0.0029	8.82	0.66	0.0024	6.77	0.63	0.0000

Comp.	Latite			Latite			Latite			Latite		
Unit	PAL C			PAL C			PAL C			PAL C		
Sample	T-08			T-08			T-08			T-08		
Host	Cpx			Cpx			Cpx			Cpx		
label	dd_20	1σ	det lim	dd_21	1σ	det lim	dd_22	1σ	det lim	dd_23	1σ	det lim
ppm V	90.05	9.77	0.1900	81.18	9.44	0.1880	149.28	17.75	0.2450	113.09	13.75	0.2060
Cr	29.12	3.69	4.1900	bdl	2.79	4.1500	74.46	7.71	5.3900	21.55	3.45	4.4600
Ni	3.28	2.07	3.1800	12.43	2.29	3.1300	24.06	3.08	4.1000	1.49	2.07	3.3400
Cu	180.54	13.18	0.1670	95.64	7.45	0.1860	78.39	6.25	0.2120	230.79	18.61	0.1880
Zn	96.60	11.50	0.9570	97.89	12.45	0.9290	75.30	9.83	1.2100	106.56	14.13	1.0000
Rb	233.92	17.43	0.1200	239.08	18.96	0.1190	158.17	12.81	0.1550	249.88	20.65	0.1280
Sr	936.00	78.19	0.1590	950.16	84.48	0.1580	573.13	52.03	0.2080	787.90	73.00	0.1700
Y	13.87	1.27	0.0163	14.83	1.45	0.0180	17.29	1.73	0.0188	18.82	1.92	0.0178
Zr	161.80	15.27	0.1480	166.51	16.80	0.1530	138.05	14.26	0.2200	184.84	19.47	0.1460
Nb	24.12	2.13	0.0086	25.30	2.39	0.0110	16.09	1.55	0.0130	25.22	2.48	0.0096
Cs	9.58	0.86	0.0553	9.31	0.89	0.0563	6.72	0.66	0.0732	10.24	1.02	0.0586
Ba	1295.22	145.29	0.1420	1244.82	149.56	0.1330	719.48	88.45	0.1550	1156.83	145.38	0.1270
La	66.62	5.74	0.0268	71.09	6.54	0.0252	45.92	4.32	0.0360	75.79	7.28	0.0292
Ce	106.71	12.45	0.0325	113.73	14.22	0.0314	80.65	10.32	0.0401	128.96	16.88	0.0337
Pr	9.96	0.96	0.0123	10.64	1.10	0.0105	8.57	0.90	0.0141	12.16	1.31	0.0105
Nd	34.51	2.75	0.0859	35.64	3.03	0.0863	33.38	2.90	0.1170	44.74	3.95	0.0907
Sm	5.06	0.53	0.0476	5.57	0.61	0.0317	6.06	0.67	0.0265	7.29	0.80	0.0349
Eu	1.23	0.11	0.0170	1.38	0.13	0.0140	1.34	0.13	0.0204	1.41	0.13	0.0198
Gd	3.65	0.41	0.1220	3.52	0.42	0.1430	4.64	0.54	0.1730	4.73	0.55	0.1470
Tb	0.53	0.07	0.0232	0.42	0.06	0.0226	0.61	0.09	0.0313	0.63	0.09	0.0229
Dy	2.80	0.41	0.0178	2.12	0.34	0.0176	3.68	0.58	0.0300	3.71	0.59	0.0274
Ho	0.50	0.06	0.0076	0.49	0.06	0.0027	0.62	0.07	0.0061	0.74	0.09	0.0041
Er	1.39	0.19	0.0000	1.56	0.23	0.0159	1.78	0.26	0.0258	2.28	0.32	0.0248
Tm	0.23	0.04	0.0038	0.19	0.03	0.0053	0.24	0.04	0.0071	0.29	0.05	0.0051
Yb	1.23	0.17	0.0158	1.28	0.18	0.0269	2.03	0.27	0.0411	2.20	0.29	0.0270
Lu	0.21	0.03	0.0041	0.24	0.03	0.0040	0.23	0.03	0.0067	0.24	0.03	0.0066
Hf	3.70	0.42	0.0211	3.45	0.42	0.0233	3.83	0.48	0.0239	4.76	0.59	0.0244
Ta	1.26	0.11	0.0053	1.20	0.11	0.0053	0.84	0.08	0.0096	1.33	0.13	0.0055
Pb	33.52	2.69	0.0604	32.72	2.80	0.0578	17.61	1.56	0.0736	31.48	2.81	0.0605
Th	31.52	3.64	0.0027	32.13	3.98	0.0019	21.34	2.70	0.0025	33.09	4.29	0.0041
U	10.03	0.99	0.0000	9.99	1.05	0.0017	6.40	0.69	0.0045	10.52	1.16	0.0042

Comp.	Latite			Latite			Latite			Trachyte		
Unit	Pal C			Pal C			Pal C			Pal D		
Sample	T-17			T-17			T-17			Sr33b60-90		
Host	Cpx			Cpx			Ol			Ol		
label	dd_10	1σ	det lim	dd_11	1σ	det lim	dd_16	1σ	det lim	cb_3	1σ	det lim
ppm V	107.17	9.08	0.2180	101.69	8.98	0.2110	164.26	16.23	0.2040	80.02	3.23	0.8680
Cr	bdl	2.99	4.8900	41.04	4.10	4.6200	39.03	4.25	4.4900	7.36	13.58	14.9100
Ni	bdl	2.36	3.8600	bdl	2.29	3.6100	bdl	2.25	3.4700	8.51	18.93	20.7700
Cu	214.80	12.71	0.1950	200.83	12.31	0.2080	108.94	7.38	0.1870	20.05	2.73	2.1800
Zn	105.33	9.91	1.1400	111.66	10.92	1.0900	65.77	7.23	1.0100	89.71	11.26	7.7100
Rb	244.35	14.67	0.1420	245.73	15.28	0.1370	251.65	17.26	0.1310	246.56	8.63	1.6500
Sr	1040.26	69.73	0.1840	1036.52	72.08	0.1740	741.78	57.01	0.1720	834.98	28.29	1.8700
Y	18.77	1.36	0.0218	18.12	1.37	0.0190	18.29	1.53	0.0181	19.87	1.49	0.1740
Zr	197.34	14.71	0.1820	201.38	15.61	0.1560	220.88	19.05	0.1670	200.42	11.69	1.0700
Nb	25.51	1.80	0.0085	28.47	2.08	0.0108	29.17	2.37	0.0077	27.66	1.25	0.0548
Cs	9.86	0.71	0.0671	9.73	0.73	0.0639	10.80	0.89	0.0612	12.70	1.08	0.7960
Ba	1279.20	112.23	0.1380	1325.59	121.24	0.1370	805.08	82.39	0.1460	1963.36	166.45	2.0400
La	80.31	5.50	0.0307	83.77	5.97	0.0283	75.09	5.93	0.0277	63.07	4.05	0.4740
Ce	137.55	12.50	0.0363	140.64	13.33	0.0348	124.65	13.24	0.0348	109.49	5.10	0.4960
Pr	13.20	1.00	0.0130	13.99	1.11	0.0128	11.71	1.03	0.0113	10.23	0.70	0.2010
Nd	48.13	3.07	0.0893	48.82	3.23	0.0956	42.34	3.10	0.0896	35.41	2.69	1.2400
Sm	8.14	0.67	0.0544	7.81	0.67	0.0285	7.44	0.70	0.0350	8.14	1.53	0.6910
Eu	1.78	0.13	0.0161	1.47	0.12	0.0122	1.16	0.10	0.0090	0.75	0.32	0.2420
Gd	3.99	0.38	0.1670	4.87	0.46	0.1670	4.31	0.45	0.1380	5.28	2.63	2.6200
Tb	0.65	0.07	0.0234	0.66	0.07	0.0211	0.60	0.07	0.0242	0.85	0.37	0.3630
Dy	3.57	0.41	0.0246	3.42	0.41	0.0264	3.58	0.48	0.0275	2.63	0.79	0.5050
Ho	0.70	0.07	0.0092	0.58	0.06	0.0054	0.64	0.07	0.0072	0.54	0.18	0.1100
Er	1.95	0.22	0.0276	1.70	0.20	0.0125	1.41	0.19	0.0125	2.13	0.67	0.2820
Tm	0.31	0.04	0.0056	0.24	0.03	0.0054	0.33	0.05	0.0042	0.35	0.15	0.1000
Yb	2.16	0.23	0.0331	1.94	0.21	0.0129	1.72	0.21	0.0324	3.34	0.89	0.4260
Lu	0.28	0.03	0.0031	0.27	0.03	0.0060	0.31	0.03	0.0049	0.03	0.08	0.0869
Hf	4.94	0.45	0.0127	4.81	0.46	0.0171	5.30	0.55	0.0141	4.66	0.93	0.4110
Ta	1.31	0.10	0.0075	1.48	0.11	0.0061	1.37	0.11	0.0072	1.31	0.20	0.0818
Pb	32.20	2.08	0.0717	33.42	2.24	0.0710	36.53	2.70	0.0628	34.88	2.16	0.4120
Th	33.63	3.03	0.0032	34.86	3.27	0.0038	37.21	3.91	0.0021	30.17	1.41	0.0414
U	10.59	0.83	0.0036	10.47	0.85	0.0028	11.75	1.06	0.0047	11.41	0.94	0.0418

Comp.	Trachyte			Trachyte			Trachyte			Trachyte		
Unit	Pal D			Pal D			Pal D			Pal D		
Sample	Sr33b60-90			Sr33b60-90			S33b15-40			S33b15-40		
Host	Ol			Cpx			Cpx			Cpx		
label	cb_4	1σ	det lim	cb_6	1σ	det lim	da_1	1σ	det lim	da_2	1σ	det lim
ppm V	59.76	2.64	0.8200	34.12	1.87	0.7880	45.01	3.34	0.4540	77.34	6.07	0.5730
Cr	bdl	14.01	14.0400	79.40	15.23	13.9500	14.26	12.92	11.8100	8.99	13.51	14.6400
Ni	18.65	19.31	19.3700	bdl	19.13	18.3900	bdl	10.33	9.7600	7.97	11.08	12.1500
Cu	23.52	3.02	2.0900	8.91	2.42	1.9400	16.76	2.04	0.4340	63.95	7.25	0.5520
Zn	169.39	16.78	7.1600	49.49	9.67	6.8200	70.02	12.27	3.7700	91.08	16.67	4.5200
Rb	198.29	7.20	1.5200	212.12	7.84	1.4700	256.80	28.12	0.2300	246.25	29.58	0.2940
Sr	760.11	26.06	1.7600	450.96	16.39	1.7300	711.69	59.62	0.3330	935.98	85.55	0.4270
Y	15.01	1.23	0.1620	17.83	1.61	0.1570	16.41	1.80	0.0416	16.45	1.96	0.0538
Zr	136.96	9.08	1.0500	194.32	13.11	0.9040	179.81	14.41	0.3040	168.96	14.66	0.2640
Nb	18.80	0.98	0.0673	20.83	1.09	0.0612	22.31	2.14	0.0227	23.56	2.45	0.0295
Cs	7.77	0.94	0.7410	7.79	1.00	0.7310	10.29	1.14	0.1080	10.44	1.26	0.1330
Ba	1893.95	166.13	1.8000	865.60	89.49	1.7500	1578.24	181.48	0.2890	1699.23	215.13	0.3330
La	48.36	3.28	0.4500	45.03	3.53	0.4410	56.67	5.77	0.0645	67.34	7.48	0.0835
Ce	83.05	4.06	0.4640	86.88	4.66	0.4420	98.53	10.04	0.0754	111.88	12.47	0.0958
Pr	8.94	0.66	0.1840	7.76	0.66	0.1840	8.67	0.76	0.0255	10.76	1.01	0.0330
Nd	30.01	2.62	1.2000	29.85	2.70	1.1300	30.85	3.11	0.2420	34.65	3.72	0.2840
Sm	6.73	1.43	0.5160	5.86	1.46	0.5820	4.11	0.75	0.0815	6.75	1.11	0.0645
Eu	2.29	0.47	0.1920	0.95	0.35	0.1890	1.27	0.24	0.0335	1.34	0.25	0.0403
Gd	7.72	2.80	2.4200	6.90	3.02	2.5300	4.26	0.84	0.3360	2.11	0.65	0.4670
Tb	0.33	0.34	0.3180	0.69	0.37	0.3160	0.33	0.10	0.0558	0.54	0.13	0.0845
Dy	1.83	0.75	0.4940	3.77	1.01	0.4980	3.28	0.51	0.0480	4.52	0.63	0.0935
Ho	0.67	0.22	0.1290	0.38	0.17	0.1020	0.59	0.12	0.0218	0.54	0.12	0.0126
Er	1.56	0.63	0.3000	2.80	0.88	0.3040	1.41	0.36	0.0618	1.99	0.45	0.1000
Tm	bdl	0.06	0.0978	0.50	0.19	0.0916	0.17	0.06	0.0088	0.23	0.07	0.0225
Yb	1.41	0.69	0.4200	1.81	0.77	0.3810	0.84	0.26	0.0467	2.64	0.51	0.0638
Lu	0.05	0.08	0.0754	0.27	0.13	0.0800	0.21	0.06	0.0118	0.26	0.06	0.0137
Hf	3.37	0.82	0.3130	2.97	0.83	0.3350	3.95	0.62	0.0417	3.48	0.58	0.0506
Ta	1.11	0.18	0.0519	1.22	0.21	0.0726	1.18	0.17	0.0160	1.46	0.21	0.0196
Pb	24.80	1.83	0.3800	24.12	1.87	0.3460	26.94	1.75	0.1680	45.15	2.91	0.2100
Th	20.51	1.11	0.0317	26.13	1.38	0.0353	28.45	2.75	0.0047	29.83	3.14	0.0064
U	6.43	0.64	0.0296	7.95	0.83	0.0251	9.71	0.99	0.0082	10.90	1.20	0.0113

Comp.	Trachyte			Trachyte			Trachyte			Trachyte		
Unit	Pal D			Pal D			Pal D			Pal D		
Sample	S33b15-40			S33b15-40			S33b15-40			S33b15-40		
Host	Cpx			Cpx			Cpx			Cpx		
label	da_3	1σ	det lim	da_4	1σ	det lim	da_5	1σ	det lim	da_6	1σ	det lim
ppm V	66.66	5.50	0.5260	44.22	3.94	0.3500	63.80	6.48	0.4140	58.45	6.53	0.4160
Cr	10.44	12.88	3.4200	bdl	18.66	8.8700	41.97	17.45	10.0900	36.91	15.98	10.0000
Ni	bdl	10.56	11.2700	bdl	10.22	7.4800	bdl	9.99	8.7500	bdl	8.63	8.7500
Cu	32.66	4.05	0.4690	13.28	2.05	0.3260	17.49	2.83	0.3870	23.21	3.97	0.4050
Zn	108.84	20.49	4.0000	85.79	17.46	2.6600	81.59	18.84	2.9700	85.15	21.11	2.9200
Rb	225.56	28.62	0.2790	215.98	29.07	0.1930	228.84	36.69	0.2340	208.31	37.35	0.2410
Sr	886.60	85.39	0.3860	695.30	70.83	0.2620	855.66	103.13	0.3250	766.95	102.93	0.3250
Y	23.81	2.96	0.0422	16.16	2.17	0.0317	16.29	2.54	0.0349	22.30	3.82	0.0378
Zr	157.16	14.32	0.3060	182.90	17.73	0.1900	179.14	19.96	0.2060	193.58	23.58	0.2480
Nb	19.46	2.14	0.0241	20.25	2.38	0.0150	20.65	2.82	0.0216	17.95	2.70	0.0154
Cs	9.02	1.15	0.1230	9.07	1.24	0.0889	9.40	1.48	0.1020	7.84	1.36	0.1040
Ba	1768.68	236.99	0.3230	1561.16	222.31	0.2180	1879.63	320.68	0.2030	1658.10	317.54	0.2490
La	63.81	7.48	0.0737	62.70	7.79	0.0474	54.54	8.00	0.0593	57.16	9.29	0.0582
Ce	118.17	13.89	0.0862	105.69	13.17	0.0557	90.27	13.30	0.0722	104.52	17.10	0.0731
Pr	12.21	1.19	0.0318	10.27	1.08	0.0216	8.86	1.07	0.0270	10.49	1.38	0.0248
Nd	43.40	4.79	0.2700	39.22	4.70	0.1780	31.76	4.38	0.2180	37.83	5.64	0.2140
Sm	8.11	1.31	0.1010	5.49	1.11	0.0816	6.86	1.36	0.0917	6.94	1.41	0.0338
Eu	1.60	0.29	0.0274	1.56	0.33	0.0300	1.23	0.27	0.0186	1.63	0.34	0.0334
Gd	7.34	1.21	0.3940	6.54	1.26	0.2450	3.72	0.88	0.3230	5.14	1.06	0.3450
Tb	0.49	0.12	0.0761	0.39	0.12	0.0482	0.36	0.11	0.0603	0.79	0.16	0.0540
Dy	4.30	0.61	0.0729	3.75	0.66	0.0341	3.08	0.55	0.0746	4.69	0.69	0.0740
Ho	1.34	0.22	0.0080	0.57	0.14	0.0166	0.43	0.11	0.0138	0.77	0.17	0.0064
Er	2.22	0.48	0.0125	1.39	0.43	0.0501	0.81	0.29	0.0375	3.01	0.66	0.0125
Tm	0.47	0.10	0.0133	0.35	0.10	0.0134	0.32	0.08	0.0085	0.40	0.09	0.0140
Yb	1.38	0.35	0.0739	2.34	0.56	0.0873	2.31	0.52	0.0894	2.67	0.55	0.0757
Lu	0.30	0.07	0.0182	0.30	0.08	0.0089	0.37	0.09	0.0137	0.33	0.08	0.0162
Hf	4.76	0.73	0.0599	3.96	0.74	0.0364	6.27	1.05	0.0390	4.68	0.84	0.0360
Ta	1.03	0.16	0.0154	1.37	0.23	0.0106	1.02	0.19	0.0099	1.06	0.21	0.0160
Pb	24.52	1.75	0.1840	26.43	2.04	0.1270	24.58	2.07	0.1470	23.05	2.06	0.1490
Th	25.79	2.86	0.0128	28.45	3.35	0.0125	28.10	3.88	0.0125	23.61	3.60	0.0045
U	8.86	1.03	0.0089	9.69	1.20	0.0034	8.42	1.22	0.0041	7.86	1.26	0.0060

Comp.	Trachyte			Rhyolite			Rhyolite			Rhyolite		
Unit	Pal D			Pal B			Pal B			Pal B		
Sample	S33b15-40			Pal L			Pal L			Pal L		
Host	Cpx			Sa			Sa			Sa		
label	da_7	1σ	det lim	ca1	1σ	det lim	ca2	1σ	det lim	ca3	1σ	det lim
ppm V	45.01	5.52	0.4180	1.79	0.57	0.6370	1.87	0.50	0.5530	1.22	0.40	0.4340
Cr	33.14	15.38	9.8800	nd	nd	nd	16.31	7.54	10.0700	bdl	6.08	7.7700
Ni	bdl	7.79	8.6200	nd	nd	nd	9.98	6.18	8.4500	20.24	5.97	6.6900
Cu	21.69	4.09	0.4070	27.60	4.79	1.3800	67.43	11.16	1.0700	51.56	8.67	0.8090
Zn	87.71	23.34	2.7500	nd	nd	nd	nd	nd	nd	nd	nd	nd
Rb	234.42	46.69	0.2470	454.31	68.29	0.2100	372.51	56.24	0.1900	298.02	45.35	0.1470
Sr	669.38	99.39	0.3230	5.46	0.86	0.5340	9.21	1.28	0.4750	6.93	0.99	0.3860
Y	25.36	4.78	0.0436	37.53	5.02	0.0592	31.28	4.20	0.0670	25.28	3.42	0.0492
Zr	177.25	23.70	0.2520	228.43	28.43	0.6640	181.54	22.71	0.6260	151.05	19.11	0.4480
Nb	22.06	3.63	0.0209	38.39	5.13	0.0310	29.58	3.97	0.0202	24.64	3.33	0.0220
Cs	9.91	1.88	0.1050	24.17	3.22	0.0931	17.81	2.38	0.0917	15.90	2.14	0.0717
Ba	1272.97	271.75	0.2360	1.39	0.52	0.4580	2.21	0.55	0.3850	nd	nd	nd
La	82.81	14.81	0.0567	130.93	16.67	0.0524	104.89	13.40	0.0477	85.15	10.96	0.0364
Ce	140.46	25.32	0.0716	207.93	27.66	0.0450	168.92	22.54	0.0434	140.30	18.85	0.0334
Pr	14.41	2.07	0.0250	19.46	2.45	0.0218	15.26	1.93	0.0189	13.34	1.70	0.0131
Nd	48.71	7.90	0.1910	65.99	7.98	0.1110	49.81	6.05	0.1160	42.15	5.18	0.0738
Sm	7.41	1.61	0.0920	9.36	1.34	0.0651	8.31	1.17	0.0996	6.16	0.91	0.0000
Eu	1.55	0.34	0.0342	0.26	0.09	0.0521	0.32	0.09	0.0538	0.09	0.05	0.0370
Gd	5.70	1.20	0.3470	5.79	1.01	0.3340	5.49	0.90	0.2050	5.22	0.87	0.1870
Tb	0.66	0.15	0.0603	1.43	0.21	0.0558	1.00	0.15	0.0424	0.72	0.12	0.0380
Dy	5.04	0.75	0.0509	6.94	1.10	0.0971	5.30	0.84	0.0640	4.24	0.69	0.0514
Ho	0.83	0.19	0.0158	1.51	0.25	0.0190	1.05	0.17	0.0199	0.92	0.16	0.0105
Er	2.86	0.67	0.0748	3.76	0.61	0.0353	2.92	0.47	0.0000	2.16	0.37	0.0000
Tm	0.45	0.09	0.0129	0.63	0.11	0.0117	0.47	0.09	0.0000	0.43	0.08	0.0000
Yb	2.89	0.59	0.0474	3.87	0.65	0.1300	3.40	0.55	0.0597	3.11	0.51	0.0390
Lu	0.38	0.09	0.0160	0.68	0.12	0.0352	0.47	0.09	0.0310	0.38	0.07	0.0268
Hf	4.03	0.78	0.0519	8.10	1.10	0.0395	6.32	0.85	0.0000	5.61	0.77	0.0000
Ta	1.07	0.22	0.0148	2.76	0.37	0.0000	1.77	0.24	0.0000	1.64	0.23	0.0079
Pb	28.73	2.74	0.1690	46.25	6.16	0.1310	36.18	4.82	0.1290	29.68	3.99	0.0980
Th	35.79	5.98	0.0046	76.08	9.72	0.0000	58.18	7.43	0.0000	52.55	6.74	0.0000
U	10.36	1.82	0.0044	21.99	3.06	0.0000	17.64	2.46	0.0000	14.88	2.08	0.0000

Comp.	Rhyolite			Rhyolite			Rhyolite			Rhyolite		
Unit	Pal B			Pal B			Pal B			Pal B		
Sample	Pal L			Pal L			Pal L			Pal L		
Host	Sa			Sa			Sa			Sa		
label	ca5	1σ	det lim	ca6	1σ	det lim	ca7	1σ	det lim	ca9	1σ	det lim
ppm V	0.84	0.40	0.6100	bdl	0.57	0.4560	0.73	0.37	0.3690	2.10	0.52	0.5920
Cr	bdl	6.63	10.7100	bdl	9.92	7.8800	13.78	6.39	6.5700	bdl	6.43	10.5900
Ni	bdl	5.96	9.7700	bdl	9.03	7.2100	bdl	5.61	6.1400	bdl	6.33	10.0700
Cu	44.35	7.69	1.1300	39.75	7.57	0.7830	37.79	7.06	0.6280	42.55	8.22	0.9480
Zn	nd	nd	nd	nd	nd	nd	nd	nd	nd	nd	nd	nd
Rb	345.70	53.88	0.2170	353.03	56.96	0.1630	342.45	56.25	0.1420	326.59	55.91	0.2210
Sr	7.79	1.13	0.5650	25.84	3.72	0.4190	21.28	3.06	0.3480	21.44	3.20	0.5700
Y	25.99	3.59	0.0671	33.40	4.82	0.0484	31.75	4.61	0.0443	26.70	4.03	0.0670
Zr	168.25	21.77	0.7380	311.54	42.23	0.5500	303.29	41.49	0.4660	413.39	58.87	0.8260
Nb	26.55	3.66	0.0361	32.38	4.67	0.0276	30.76	4.47	0.0209	28.81	4.34	0.0287
Cs	16.92	2.33	0.0998	17.69	2.56	0.0724	14.05	2.04	0.0619	15.93	2.39	0.0956
Ba	2.53	0.56	0.4200	7.81	1.73	0.3500	7.61	1.42	0.2960	8.38	1.51	0.4640
La	97.77	12.84	0.0615	110.90	15.07	0.0414	102.59	14.15	0.0314	90.35	12.95	0.0584
Ce	158.38	21.73	0.0507	202.74	28.72	0.0337	168.00	24.19	0.0335	153.90	23.03	0.0591
Pr	13.86	1.80	0.0205	19.41	2.63	0.0188	16.15	2.20	0.0148	14.27	2.01	0.0240
Nd	46.55	5.82	0.1350	68.12	9.04	0.0859	53.12	7.05	0.0681	50.00	6.86	0.1070
Sm	7.92	1.11	0.0455	9.41	1.67	0.0699	9.21	1.42	0.0417	5.00	0.81	0.1070
Eu	0.14	0.05	0.0513	0.52	0.18	0.0335	0.52	0.12	0.0000	0.59	0.13	0.0606
Gd	3.87	0.68	0.3100	6.98	1.44	0.2000	3.52	0.70	0.1170	5.51	0.97	0.2600
Tb	0.64	0.11	0.0596	0.96	0.20	0.0386	1.11	0.18	0.0292	0.73	0.12	0.0545
Dy	4.23	0.68	0.0450	6.98	1.32	0.0647	5.79	1.00	0.0000	4.34	0.76	0.1250
Ho	0.82	0.14	0.0168	1.13	0.24	0.0091	1.14	0.20	0.0000	1.11	0.20	0.0125
Er	2.91	0.45	0.0852	4.21	0.86	0.0462	2.74	0.50	0.0000	3.18	0.52	0.0515
Tm	0.42	0.07	0.0082	0.35	0.11	0.0167	0.52	0.10	0.0106	0.57	0.10	0.0212
Yb	2.93	0.47	0.1310	6.20	1.17	0.0868	4.08	0.70	0.0000	3.61	0.59	0.0000
Lu	0.46	0.08	0.0347	0.86	0.18	0.0280	0.65	0.12	0.0143	0.54	0.10	0.0350
Hf	5.95	0.79	0.0000	10.71	1.65	0.0000	10.16	1.40	0.0000	10.32	1.41	0.0000
Ta	1.88	0.26	0.0077	2.08	0.33	0.0092	2.06	0.30	0.0000	1.74	0.26	0.0000
Pb	35.44	4.84	0.1280	34.86	5.04	0.1180	36.12	5.20	0.0943	31.37	4.67	0.1410
Th	56.25	7.33	0.0000	71.17	9.59	0.0000	58.30	7.95	0.0000	49.38	6.97	0.0000
U	18.17	2.58	0.0000	18.98	2.82	0.0000	16.11	2.41	0.0000	15.77	2.43	0.0000

Comp.	Rhyolite			Rhyolite			Rhyolite			Rhyolite		
Unit	Pal B			Pal B			Pal B			Pal B		
Sample	Pal L			Pal L			Pal L			Pal L		
Host	Sa			Sa			Sa			Sa		
label	ca12	1σ	det lim	ca13	1σ	det lim	ca14	1σ	det lim	ca16	1σ	det lim
ppm V	0.63	0.32	0.4610	1.79	0.50	0.5800	1.37	0.46	0.4220	0.65	0.38	0.5800
Cr	bdl	5.12	8.0600	bdl	6.56	10.1100	bdl	5.92	7.2500	v	6.16	9.8600
Ni	11.60	5.30	7.7600	bdl	5.95	9.8900	bdl	5.88	7.0800	bdl	6.01	9.7800
Cu	52.78	11.24	0.7440	56.73	12.41	0.9840	41.22	9.34	0.6850	41.29	10.31	1.0200
Zn	nd	nd	nd	nd	nd	nd	nd	nd	nd	nd	nd	nd
Rb	309.79	58.08	0.1710	354.32	67.99	0.2200	308.30	60.56	0.1590	330.35	71.05	0.2190
Sr	17.88	2.91	0.4390	16.25	2.72	0.5560	28.29	4.81	0.3940	11.33	2.13	0.5680
Y	31.00	5.09	0.0421	32.72	5.50	0.0698	28.49	4.91	0.0481	26.50	4.97	0.0751
Zr	367.87	57.67	0.6040	402.46	64.66	0.8310	283.20	46.75	0.6260	343.62	62.22	0.8630
Nb	28.60	4.70	0.0224	30.34	5.10	0.0271	31.85	5.48	0.0201	27.55	5.17	0.0368
Cs	15.63	2.56	0.0812	17.23	2.89	0.1050	14.98	2.57	0.0760	14.45	2.71	0.1000
Ba	3.79	0.80	0.3420	2.60	0.63	0.4170	8.86	1.84	0.3290	1.90	0.54	0.4050
La	106.36	16.59	0.0459	111.06	17.72	0.0588	94.38	15.40	0.0376	86.94	15.46	0.0619
Ce	173.20	28.23	0.0409	179.81	29.96	0.0533	158.32	26.98	0.0383	141.79	26.34	0.0568
Pr	16.81	2.57	0.0143	17.48	2.74	0.0244	14.46	2.32	0.0192	13.27	2.32	0.0187
Nd	56.10	8.41	0.0966	57.23	8.79	0.1290	46.57	7.37	0.0990	43.80	7.56	0.1310
Sm	9.11	1.48	0.0376	8.28	1.39	0.0000	8.41	1.49	0.0479	7.24	1.36	0.1050
Eu	0.28	0.08	0.0491	0.26	0.08	0.0547	0.33	0.10	0.0411	0.39	0.10	0.0544
Gd	6.27	1.16	0.2470	7.18	1.36	0.2260	4.70	0.99	0.1780	5.16	1.11	0.2760
Tb	0.91	0.15	0.0426	0.98	0.17	0.0481	0.82	0.16	0.0366	0.71	0.14	0.0527
Dy	5.62	1.03	0.0584	5.08	0.97	0.0563	5.21	1.04	0.0575	4.67	0.99	0.0647
Ho	1.13	0.21	0.0120	1.07	0.21	0.0193	1.06	0.22	0.0062	1.18	0.25	0.0122
Er	2.46	0.44	0.0403	3.57	0.62	0.0355	2.76	0.54	0.0363	3.44	0.66	0.0611
Tm	0.43	0.08	0.0152	0.46	0.09	0.0294	0.43	0.09	0.0087	0.44	0.09	0.0240
Yb	3.44	0.59	0.0740	3.51	0.62	0.0650	3.18	0.62	0.0663	3.48	0.67	0.0000
Lu	0.56	0.10	0.0184	0.72	0.13	0.0273	0.62	0.12	0.0216	0.45	0.09	0.0322
Hf	9.06	1.33	0.0000	10.56	1.58	0.0000	7.65	1.22	0.0000	8.71	1.44	0.0000
Ta	1.75	0.27	0.0000	1.92	0.31	0.0000	1.88	0.31	0.0054	1.72	0.30	0.0073
Pb	32.94	5.33	0.0794	34.27	5.67	0.1360	33.16	5.62	0.0937	31.80	5.84	0.1200
Th	53.41	8.15	0.0000	58.63	9.13	0.0000	53.56	8.52	0.0000	48.05	8.27	0.0000
U	16.78	2.80	0.0000	17.28	2.95	0.0000	15.62	2.73	0.0000	14.17	2.68	0.0000

Comp.	Rhyolite			Rhyolite			Rhyolite		
Unit	Pal B			Pal B			Pal B		
Sample	Pal L			Pal L			Pal L		
Host	Sa			Sa			Sa		
label	ca17	1σ	det lim	ca18	1σ	det lim	ca19	1σ	det lim
ppm V	bdl	0.43	0.7140	bdl	0.45	0.7200	bdl	0.42	0.6550
Cr	bdl	7.18	12.3100	bdl	7.07	12.1300	bdl	9.06	11.5000
Ni	bdl	6.95	11.9100	bdl	8.33	11.9700	bdl	7.19	11.2200
Cu	54.42	13.92	1.0500	59.68	15.63	1.1300	43.60	11.74	1.1500
Zn	nd	nd	nd	nd	nd	nd	nd	nd	nd
Rb	343.97	75.63	0.2720	360.78	81.05	0.2700	328.14	75.30	0.2590
Sr	6.69	1.34	0.6870	13.18	2.59	0.6960	20.05	3.98	0.6510
Y	24.95	4.79	0.0821	27.52	5.39	0.0845	26.93	5.38	0.0738
Zr	206.74	38.38	1.1800	199.33	37.84	1.1600	222.16	43.10	0.9420
Nb	26.15	5.01	0.0390	29.33	5.74	0.0389	29.19	5.83	0.0359
Cs	15.15	2.90	0.1170	19.27	3.76	0.1300	18.29	3.65	0.1220
Ba	3.74	0.94	0.4670	3.48	0.90	0.5040	8.50	2.00	0.5240
La	85.49	15.53	0.0665	104.79	19.43	0.0740	95.83	18.14	0.0728
Ce	143.40	27.21	0.0688	171.37	33.19	0.0696	154.70	30.57	0.0693
Pr	13.70	2.44	0.0308	16.13	2.93	0.0261	14.20	2.63	0.0236
Nd	46.74	8.25	0.1570	51.19	9.22	0.1570	45.97	8.46	0.1370
Sm	7.24	1.41	0.1660	8.02	1.57	0.1150	7.54	1.52	0.0554
Eu	0.27	0.09	0.0652	0.24	0.08	0.0429	0.20	0.08	0.0740
Gd	4.73	1.07	0.3190	5.05	1.15	0.3730	4.67	1.09	0.3270
Tb	0.74	0.15	0.0614	0.80	0.16	0.0616	0.75	0.16	0.0593
Dy	4.62	1.01	0.0809	5.20	1.15	0.0685	4.96	1.12	0.0000
Ho	0.96	0.21	0.0000	1.17	0.26	0.0149	0.96	0.22	0.0102
Er	2.86	0.58	0.0988	2.93	0.60	0.0432	2.94	0.61	0.0589
Tm	0.30	0.07	0.0301	0.46	0.10	0.0208	0.36	0.09	0.0174
Yb	2.74	0.56	0.0796	2.86	0.59	0.0448	2.77	0.58	0.0964
Lu	0.51	0.11	0.0358	0.52	0.11	0.0411	0.54	0.12	0.0335
Hf	6.59	1.13	0.0000	7.38	1.28	0.0000	6.43	1.15	0.0000
Ta	1.32	0.24	0.0158	2.02	0.37	0.0109	2.28	0.42	0.0104
Pb	30.45	5.71	0.1710	35.73	6.83	0.1170	37.42	7.29	0.1410
Th	46.72	8.19	0.0000	61.05	10.90	0.0000	62.18	11.31	0.0000
U	15.07	2.90	0.0000	18.53	3.63	0.0000	18.97	3.79	0.0000

Appendix G: Major and trace elements composition of sulfide inclusions.

Appendix G.1 – Major element composition of type 1 and type 2 sulfide inclusions. Calc refers to reconstructed bulk composition of type 1 sulfides by image analysis (Chapter 4). Bdl: below detection limit.*

Unit	Sample	Host	Max diameter (µm)	Sulfide id	Type	Analysis type	Phase %	N° spots (EPMA or FE SEM)	reference	Fe	S	Co	Mn	Ni	Zn	Cu	total
PAL D	S33b90-110	Sa	40	PAL-90 sulf1	Type 2	EPMA		1	Fulignati et al., 2018	58.48	37.19	0.09	0.08	0.06	bdl	1.44	97.33
PAL D	S33b90-110	Cpx	35	PAL-90 sulf2	Type 2	EPMA		2	Fulignati et al., 2018	59.12	38.05	0.03	0.09	0.03	0.10	1.19	98.60
"	"	"	"	PAL-90 sulf2	Type 2	EPMA		\	Fulignati et al., 2018	59.89	38.08	0.07	0.12	0.05	0.03	0.42	98.65
PAL D	S33b90-110	Ol	10	pal90solf3	Type 2	EPMA		1	Fulignati et al., 2018	57.19	37.24	0.14	0.18	0.07	0.07	1.62	96.52
PAL D	S33b90-110	Gl	15	pal90solf4	Type 2	EPMA		1	Fulignati et al., 2018	58.01	37.24	0.16	0.11	0.09	bdl	2.32	97.93
PAL D	S33b90-110	Ol	30	pal90solf5	Type 2	EPMA		2	Fulignati et al., 2018	58.94	37.60	0.10	0.12	0.10	bdl	1.67	98.53
"	"	"	"	pal90solf5	Type 2	EPMA		\	Fulignati et al., 2018	59.19	38.08	0.09	0.18	0.04	bdl	1.29	98.88
PAL D	S33b90-110	Gl	20	pal90sulf8	Type 2	EPMA		1	Fulignati et al., 2018	57.09	38.05	0.07	0.10	0.04	0.11	1.34	96.80
PAL D	S33b90-110	Ti-Mt	40	pal90sulf10	Type 2	EPMA		1	Fulignati et al., 2018	58.72	38.24	0.05	0.16	0.05	0.05	0.97	98.23
PAL D	S33b90-110	Cpx	25	pal90sulf13	Type 2	EPMA		2	Fulignati et al., 2018	58.38	37.99	0.13	0.12	0.00	0.03	1.54	98.18
"	"	"	"	pal90sulf13	Type 2	EPMA		\	Fulignati et al., 2018	58.25	37.70	0.07	0.04	0.01	0.06	1.46	97.58
PAL D	S33b90-110	Cpx	20	pal90sulf14, 14a	Type 2	EPMA		1	Fulignati et al., 2018	53.30	39.64	0.14	0.09	0.06	bdl	2.16	95.39
PAL D	S33b90-110	Ti-Mt	60	PAL90 u293sulf17	Type 2	EPMA		2	Fulignati et al., 2018	58.15	37.73	0.09	0.08	0.01	bdl	1.31	97.37
"	"	"	"	PAL90 u293sulf17	Type 2	EPMA		\	Fulignati et al., 2018	58.60	38.26	0.07	0.12	0.09	0.02	1.39	98.54
PAL D	S33b90-110	Pl	15	PAL90U297 sulf18	Type 2	EPMA		1	Fulignati et al., 2018	56.63	37.48	0.03	0.10	0.08	0.10	1.55	95.95
PAL D	S33b15-40	Cpx	20	PAL-15D sulf1	Type 2	EPMA		1	Fulignati et al. 2018	56.33	37.35	0.11	0.11	0.04	bdl	1.34	95.28
PAL D	S33b15-40	Cpx	25	PAL-15D sulf2	Type 2	EPMA		1	Fulignati et al., 2018	57.60	37.53	0.12	0.13	0.05	bdl	1.32	96.75
PAL D	S33b15-40	Ti-Mt	10	PAL-15D sulf3	Type 2	EPMA		1	Fulignati et al., 2018	56.48	37.45	0.13	0.12	0.05	0.04	1.34	95.60
PAL D	S33b15-40	gl	5	PAL-15D sulf4	Type 2	EPMA		1	Fulignati et al., 2018	56.85	37.61	0.09	0.11	0.05	0.11	1.30	96.12
PAL D	S33b15-40	Cpx	20	sulf5	Type 2	EPMA		1	Fulignati et al., 2018	56.06	37.68	0.06	0.14	0.06	bdl	1.84	95.84
PAL D	S33b15-40	Cpx	30	pal15sulf8.spc	Type 2	EPMA		1	Fulignati et al., 2018	57.15	37.63	0.04	0.13	bdl	0.04	1.02	96.00
PAL D	S33b15-40	Cpx	60	Pal 15 D sulf 6	Type 2	EPMA		3	Fulignati et al., 2018	56.28	37.64	0.08	0.10	0.05	0.06	2.51	96.71
"	"	"	"	Pal 15 D sulf 6	Type 2	EPMA		\	Fulignati et al., 2018	56.35	37.64	0.14	0.12	0.11	0.11	2.54	97.01
"	"	"	"	Pal 15 D sulf 6	Type 2	EPMA		\	Fulignati et al., 2018	56.40	37.67	0.15	0.01	0.07	0.07	2.72	97.09
PAL D	S33b15-40	Ti-Mt	20	Pal 15 D sulf 7	Type 2	EPMA		1	Fulignati et al., 2018	57.99	37.64	0.03	0.10	0.05	0.04	1.21	97.06
PAL D	S33b15-40	Ti-Mt	15	Pal 15 D sulf 8	Type 2	EPMA		1	Fulignati et al., 2018	57.96	37.57	0.12	0.11	0.08	0.04	1.58	97.46
Palizzi lava	SC-15-1	Pl	5	SC15-1_1	Type 1	EDS	35%	2	This work	24.05	32.12	bdl	bdl	bdl	bdl	43.83	100.00
"	"	"	"	SC15-1_1	Type 1	EDS	65%	\	This work	38.65	33.84	bdl	bdl	bdl	bdl	27.51	100.00
"	*"*	*"*	*"*	*calc*SC15-1_1*	*Type 1*	EDS		*recalculated*	*This work*	*33.54*	*33.24*	bdl	bdl	bdl	bdl	*33.22*	*100.00*
Palizzi lava	SC-15-1	Pl	10	SC15-1_2	Type 1	EDS	44%	2	This work	21.84	31.58	bdl	bdl	bdl	bdl	46.58	100.00
"	"	"	"	SC15-1_2	Type 1	EDS	56%	\	This work	33.72	34.57	bdl	bdl	bdl	bdl	31.70	100.00

″	*″*	*″*	*″*	*calc*SC15-1_2*	*Type 1*	EDS		*recalculated*	*This work*	*28.50*	*33.25*	bdl	bdl	bdl	bdl	*38.25*	*100.00*
Palizzi lava	SC-15-1	Cpx	4	SC15-1_3	Type 1	EDS	6%	3	This work	20.92	28.88	bdl	bdl	bdl	bdl	50.20	100.00
"	"	"	"	SC15-1_3	Type 1	EDS	30%	\	This work	5.09	22.51	bdl	bdl	bdl	bdl	72.40	100.00
"	"	"	"	SC15-1_3	Type 1	EDS	64%	\	This work	20.74	30.62	bdl	bdl	bdl	bdl	48.64	100.00
″	*″*	*″*	*″*	*calc*SC15-1_3*	*Type 1*	EDS		*recalculated*	*This work*	*16.05*	*28.08*	bdl	bdl	bdl	bdl	*55.86*	*99.99*
Palizzi lava	SC-15-1	Cpx	1	SC15-1_3b	Type 1	EDS		2	This work	21.60	23.91	bdl	bdl	bdl	bdl	54.49	100.00
"	"	"	"	SC15-1_3b	Type 1	EDS		\	This work	12.40	21.58	bdl	bdl	bdl	bdl	66.02	100.00
Palizzi lava	SC-15-1	Cpx	2	SC15-1_4	Type 1	EDS		2	This work	37.20	29.81	bdl	bdl	bdl	bdl	32.99	100.00
"	"	"	"	SC15-1_4	Type 1	EDS		\	This work	30.91	31.85	bdl	bdl	bdl	bdl	37.24	100.00
Palizzi lava	SC-15-1	Pl	4	SC15-1_5	Type 1	EDS	15%	2	This work	10.02	25.69	bdl	bdl	bdl	bdl	64.29	100.00
"	"	"	"	SC15-1_5	Type 1	EDS	85%	\	This work	22.46	29.18	bdl	bdl	bdl	bdl	48.36	100.00
″	*″*	*″*	*″*	*calc*SC15-1_5*	*Type 1*	*EDS*		*recalculated*	*This work*	*20.64*	*28.67*	bdl	bdl	bdl	bdl	*50.69*	*100.00*
Palizzi lava	SC-15-1	Pl	4	SC15-1_6	Type 1	EDS	29%	2	This work	18.07	30.59	bdl	bdl	bdl	bdl	51.35	100.00
"	"	"	"	SC15-1_6	Type 1	EDS	71%	\	This work	9.64	24.69	bdl	bdl	bdl	bdl	65.66	100.00
″	*″*	*″*	*″*	*calc*SC15-1_6*	*Type 1*	*EDS*		*recalculated*	*This work*	*15.62*	*28.88*	bdl	bdl	bdl	bdl	*55.50*	*100.00*
PAL_D	SC-18-20	Sa	15	SC_18_20c1	Type 2	EDS		1	This work	62.38	37.48	bdl	bdl	bdl	bdl	0.14	100.00
PAL_D	SC-18-20	Sa	15	SC_18_20c2	Type 2	EDS		1	This work	62.83	36.85	bdl	bdl	bdl	bdl	0.32	100.00
PAL_D	SC-18-20	Sa	12	SC_18_20c3	Type 2	EDS		1	This work	62.18	37.21	bdl	bdl	bdl	bdl	0.60	100.00
PAL_D	SC-18-20	Sa	20	SC_18_20c4	Type 2	EDS		1	This work	63.61	36.11	bdl	bdl	bdl	bdl	0.28	100.00
PAL_D	SC-18-20	Pl	8	SC_18_20c5	Type 2	EDS		1	This work	63.70	36.20	bdl	bdl	bdl	bdl	0.10	100.00
Palizzi lava	SC-18-24	Ti-Mt	8	sc1824 11-12	Type 1	EDS		2	This work	24.18	28.79	bdl	bdl	bdl	bdl	47.04	100.00
"	"	"	"	sc1824 11-12	Type 1	EDS		\	This work	31.37	29.73	bdl	bdl	bdl	bdl	38.91	100.00
Palizzi lava	SC-18-24	Cpx	20	sc1824 4-5-6	Type 1	EDS	52%	2	This work	20.42	28.20	bdl	bdl	bdl	bdl	51.38	100.00
"	"	"	"	sc1824 4-5-6	Type 1	EDS	48%	\	This work	2.27	18.68	bdl	bdl	bdl	bdl	79.05	100.00
″	*″*	*″*	*″*	*calc*sc1824 4-5-6*	*Type 1*	*EDS*		*recalculated*	*This work*	*10.89*	*23.21*	bdl	bdl	bdl	bdl	*65.90*	*100.00*
Palizzi lava	SC-18-24	Cpx	15	sc1824 7-8	Type 1	EDS	32%	2	This work	29.89	29.63	bdl	bdl	bdl	bdl	40.48	100.00
"	"	"	"	sc1824 7-8	Type 1	EDS	68%	\	This work	22.97	28.30	bdl	bdl	bdl	bdl	48.73	100.00
"	"	"	"	*calc*sc1824 7-8*	*Type1*			*recalculated*	*This work*	*25.18*	*28.73*	bdl	bdl	bdl	bdl	*46.09*	100.00
Pal C	T-08	Ti-Mt	5	sulf n4	Type 1	EDS	60%	2	This work	28.65	32.34	bdl	bdl	bdl	bdl	39.01	100.00
"	"	"	"	solf n4	Type 1	EDS	40%	\	This work	11.75	25.37	bdl	bdl	bdl	bdl	62.88	100.00
″	*″*	*″*	*″*	*calc*solfn4*	*Type 1*	*EDS*		*recalculated*	*This work*	*18.51*	*28.15*	bdl	bdl	bdl	bdl	*53.34*	*100.00*
PAL B	PAL-L	Sa	30	pallentiasulf1	Type 2	EPMA		2	Fulignati et al., 2018	59.58	36.72	0.03	0.03	0.04	0.09	0.33	96.81
"	"	"	"	pallentiasulf1	Type 2	EPMA		\	Fulignati et al., 2018	58.57	36.56	0.04	0.07	0.01	bdl	0.42	95.67

Appendix G.2 – Trace element composition of sulfide inclusions by LA-ICP-MS. 1σerror estimates on the signal and background counts; det lim= detection limit at the 99% confidence level. Bdl: below detection limit; nd: not determined

Unit	Pal D			Pal D			Pal D			Pal D		
Sample	S33b90-110			S33b90-110			S33b90-110			S33b90-110		
sulfide id	PAL-90 sulf1			sulf2			pal90solf5			pal90sulf10		
label	cc_1	1σ	det lim	cc_2	1σ	det lim	cc_3	1σ	det lim	cc_4	1σ	det lim
ppm S^{33}	371918.69	14918.91	2049.1400	380657.94	17981.74	6340.0300	378389.75	13770.99	1659.5100	382459.19	16812.47	2986.2500
S^{34}	433597.13	33029.76	605.5100	327148.41	26646.61	1923.6800	385534.84	31539.64	497.6300	394503.97	34744.79	899.5700
V	bdl	0.56	0.3710	8.80	1.47	1.1500	1.39	0.41	0.2920	170.38	13.38	0.5100
Mn	670.99	100.85	4.9300	275.07	46.95	16.0800	493.02	83.05	4.2900	762.43	138.41	8.0500
Fe	676628.63	25772.61	47.7800	249571.66	10572.42	153.5600	454061.06	16760.21	39.9000	690365.31	28510.04	73.7400
Co	823.13	95.23	0.6970	362.31	45.00	2.3100	1405.69	182.72	0.6220	593.07	83.56	1.1700
Ni	269.49	82.79	7.4000	110.62	43.52	24.1500	689.86	234.44	6.3900	85.44	35.83	11.9400
Cu	17047.72	2398.99	1.2300	6626.26	982.61	3.9000	35368.78	5457.09	1.0700	17666.47	2900.71	1.9000
Zn	241.12	25.02	3.6200	377.83	41.40	11.4900	149.66	16.50	2.9900	313.87	37.23	5.5000
As	bdl	1.06	0.7120	bdl	2.13	2.1900	bdl	0.71	0.5640	34.08	4.65	0.9750
Se	25.84	391.52	253.4800	2.21	550.64	534.9900	183.55	347.83	105.1100	bdl	233.16	154.0400
Mo	0.47	0.81	0.5110	bdl	1.51	1.6000	1.67	0.66	0.4210	26.79	3.46	0.7180
Ag	3.98	0.56	0.2150	3.46	0.88	0.7080	3.43	0.41	0.1850	2.21	0.62	0.3290
Cd	1.16	0.70	0.3610	bdl	1.27	1.2700	3.85	0.81	0.3520	1.16	1.15	0.6790
Sn	2.05	0.94	0.5620	3.47	1.93	1.7700	bdl	0.57	0.4620	bdl	1.22	0.8590
Sb	0.18	0.28	0.1750	bdl	0.52	0.5620	0.06	0.19	0.1450	0.12	0.39	0.2580
Te	bdl	0.99	0.7120	bdl	2.79	2.8600	bdl	0.30	0.7000	1.67	2.33	1.2100
Ba	1954.32	2328.80	1.5800	6.24	9.16	4.6000	5.38	7.06	1.1300	373.78	496.47	2.0600
W	bdl	0.02	0.0586		0.18	0.2230	0.05	0.08	0.0523	5.89	0.96	0.0962
Pt	0.08	0.16	0.0849	0.48	0.35	0.2120	0.02	0.09	0.0656	0.51	0.33	0.0958
Au	0.01	0.09	0.0565	bdl	0.18	0.1920	0.14	0.10	0.0454	bdl	0.14	0.1070
Tl	0.07	0.07	0.0298	0.01	0.10	0.0984	60.27	5.58	0.0266	4.06	0.66	0.0561
Pb	3.90	1.06	0.1340	4.38	1.35	0.4580	4.50	1.31	0.1160	193.81	58.39	0.2060
Bi	bdl	0.06	0.0426	0.08	0.14	0.1230	0.13	0.06	0.0333	78.40	5.95	0.0652

Unit	Pal D			Pal D			Pal D			Pal D		
Sample	S33b90-110			S33b90-110			S33b90-110			S33b90-110		
sulfide id	pal90sulf13			pal90sulf14a			u293sulf17			u293sulf17		
label	cc 5	1σ	det lim	cc 6	1σ	det lim	cc 7	1σ	det lim	cc 8	1σ	det lim
ppm S^{33}	378456.44	15528.71	2977.6100	396401.97	15311.79	2519.6600	379924.13	16181.09	2020.0100	379924.13	14605.22	1700.7600
S^{34}	547823.63	56411.20	936.3000	412358.25	44819.83	800.1500	437705.13	50775.61	634.2000	342123.47	41773.93	543.9700
V	24.98	2.45	0.4900	6.23	0.85	0.4110	85.56	8.57	0.3130	32.83	3.45	0.2580
Mn	1202.07	272.69	8.8400	795.19	195.64	7.8600	796.56	213.36	6.4100	745.92	217.06	5.6100
Fe	533044.38	22223.76	76.7300	695233.19	28751.34	65.9200	445303.06	19684.01	52.3100	459803.56	19893.04	44.6300
Co	1701.08	302.29	1.3000	1334.13	257.67	1.1800	1106.62	233.51	0.9540	868.94	199.79	0.8560
Ni	380.40	171.90	12.8200	354.11	172.32	11.3400	153.41	82.10	9.1200	185.19	105.55	7.9000
Cu	20826.16	4112.85	2.0300	29342.07	6182.36	1.7400	11737.91	2648.65	1.3600	10466.67	2520.96	1.1200
Zn	157.41	22.90	5.8200	229.99	32.36	4.8000	293.92	44.20	3.8400	243.26	37.70	3.2500
As	3.19	1.46	0.9770	bdl	0.97	0.8460	3.32	1.50	0.6800	8.76	1.84	0.5470
Se	bdl	132.69	95.6700	bdl	140.15	73.2800	78.58	116.87	51.2300	bdl	129.91	39.3300
Mo	2.78	1.19	0.7520	3.81	1.12	0.6510	2.31	1.15	0.5010	7.57	1.46	0.4080
Ag	4.13	0.65	0.3370	3.22	0.53	0.2920	2.28	0.58	0.2360	2.19	0.44	0.2070
Cd	0.46	1.02	0.7550	0.50	0.83	0.6360	0.16	1.02	0.5640	3.60	1.28	0.5120
Sn	1.41	1.12	0.8400	1.07	0.92	0.7280	2.77	1.15	0.5670	0.94	0.78	0.4910
Sb	1.00	0.40	0.2500	bdl	0.25	0.2190	bdl	0.30	0.1700		0.20	0.1390
Te	1.23	1.81	1.1500	bdl	1.04	0.9870	bdl	0.34	0.6930	0.37	0.96	0.5440
Ba	5.79	9.19	1.8300	bdl	1.95	1.5200	7.78	13.08	1.1300	42.51	72.84	0.9420
W	0.05	0.12	0.0798	bdl	0.03	0.0764	0.24	0.19	0.0565	0.60	0.22	0.0380
Pt	bdl	0.12	0.1170	0.08	0.13	0.0794	bdl	0.03	0.0689	bdl	0.02	0.0518
Au	0.26	0.23	0.1130	0.10	0.14	0.0903	0.04	0.15	0.0796	bdl	0.09	0.0630
Tl	1.35	0.33	0.0580	0.07	0.09	0.0493	1.09	0.36	0.0469	0.49	0.19	0.0352
Pb	3.27	1.37	0.2320	3.08	1.38	0.2100	35.01	16.22	0.1580	19.60	9.90	0.1320
Bi	0.14	0.11	0.0630	0.17	0.10	0.0536	0.71	0.20	0.0417	10.80	1.21	0.0365

Unit	Pal D			Pal D			Pal D			Pal D		
Sample	S33b15-40			S33b15-40			S33b15-40			S33b15-40		
sulfide id	sulf1			sulf2			sulf5			sulf 6		
label	db_1	1σ	det lim	db_2	1σ	det lim	db_3	1σ	det lim	db_4	1σ	det lim
ppm S^{33}	149585.17	34083.68	1127.020	341033.88	52968.88	2126.5100	346343.53	55124.00	14199.16	370083.03	58421.16	2476.9700
S^{34}	81933.63	15097.77	437.9300	366578.44	52830.35	826.9900	307791.63	44915.19	5552.3400	409054.59	59989.34	953.0900
V	1068.14	63.00	0.3540	119.17	7.12	0.6490	205.91	12.82	4.5500	1.66	0.50	0.7670
Mn	39727.54	28713.66	15.9700	6799.54	4855.14	27.1700	12951.49	9181.82	220.3300	3026.10	2139.09	36.6600
Fe	582983.25	19101.63	24.5900	582983.25	18511.66	45.2200	582983.25	18626.38	319.4900	582983.25	18467.91	54.6400
Co	1437.87	271.66	0.5440	2627.21	495.16	0.9760	2412.34	460.45	7.5200	4247.78	822.71	1.2200
Ni	1145.43	1217.79	27.5200	2917.33	2809.28	51.3300	374.58	410.03	348.4800	3495.00	3553.90	59.6000
Cu	6334.13	715.86	0.3210	13900.15	1576.41	0.5880	10978.81	1274.04	4.9600	24755.34	2941.46	0.7230
Zn	1663.72	666.81	5.4400	603.13	237.44	9.5500	1444.97	578.18	74.1300	432.75	176.18	12.5300
As	bdl	8.40	0.4150	2.11	1.31	0.7700	bdl	2.61	5.4000	bdl	0.54	0.9130
Se	84.77	325.85	15.1300	4.71	45.07	27.3800	107.58	112.30	200.7400	48.50	31.10	33.8100
Mo	0.20	4.68	0.2210	2.09	0.90	0.3900	2.36	1.84	2.9000	1.68	0.49	0.4920
Ag	17.52	3.09	0.0702	3.68	0.48	0.1320	9.86	1.22	0.9440	1.87	0.22	0.1630
Cd	bdl	4.09	0.2340	4.18	1.38	0.4320	10.95	3.53	3.1400	1.31	0.53	0.4720
Sn	16.35	8.21	0.3640	0.48	1.06	0.6640	4.96	2.54	4.5900	0.93	0.51	0.7830
Sb	bdl	2.37	0.1320		0.35	0.2410	0.99	0.90	1.7200	bdl	0.16	0.2850
Te	2.31	6.00	0.2460	2.00	1.35	0.5210	bdl	0.45	2.9500	0.48	0.49	0.5220
Ba	20.51	36.80	0.3730	1.51	2.89	0.5990	1.76	3.92	5.2500	1.42	2.51	0.8320
W	0.50	0.62	0.0202	0.05	0.07	0.0355	bdl	0.02	0.1700	bdl	0.01	0.0289
Pt	bdl	0.12	0.0214	0.13	0.13	0.0674	0.29	0.33	0.3470	0.18	0.09	0.0561
Au	bdl	0.41	0.0291	0.18	0.12	0.0583	0.04	0.20	0.3200	0.18	0.07	0.0614
Tl	bdl	0.08	0.0153	0.03	0.05	0.0242	0.20	0.14	0.1720	0.35	0.08	0.0278
Pb	12.81	3.32	0.0881	4.15	0.73	0.1630	6.64	1.34	1.1700	14.51	2.03	0.1980
Bi	0.85	0.68	0.0294	0.30	0.12	0.0533	0.38	0.24	0.3340	7.60	0.99	0.0646

Unit	Pal D			Pal D			Pal D			Pal B		
Sample	S33b15-40			S33b15-40			S33b15-40			PAL-L		
sulfide id	sulf 6			sulf 7			sulf 8			pallsulf1		
label	db_5	1σ	det lim	db_6	1σ	det lim	db_7	1σ	det lim	db_8	1σ	det lim
ppm S^{33}	232690.66	38624.79	4837.0400	422053.28	70793.69	1644.9900	349260.28	59640.85	1696.3600	362456.09	63099.36	1827.3400
S^{34}	203222.59	30942.53	1894.5700	334437.03	51556.42	656.5300	379239.31	59308.05	670.2500	411510.59	65361.74	731.2900
V	132.39	8.65	1.5100	712.04	46.20	0.5250	314.46	21.12	0.5420	bdl	0.80	0.5840
Mn	2413.03	1725.88	70.6300	3501.14	2525.71	21.4600	2604.97	1899.02	21.6900	1616.47	1192.64	22.6900
Fe	582983.25	18507.86	107.9700	582983.25	18496.22	37.0200	582983.25	18488.09	37.4700	582983.25	18500.15	40.2500
Co	1549.72	320.71	2.4000	3247.86	689.32	0.7630	3376.53	735.92	0.7850	1215.58	272.35	0.8430
Ni	2144.53	2419.21	118.9600	2661.20	3117.83	42.0200	3396.89	4138.70	43.0000	1979.09	2510.68	46.9900
Cu	12372.95	1615.80	1.4600	15932.26	2153.49	0.4780	16454.81	2303.98	0.5380	8003.40	1161.68	0.5690
Zn	643.92	285.11	24.0300	1006.08	458.09	7.8200	830.46	390.26	8.1100	44.44	25.14	8.1700
As	50.61	4.85	1.7900	bdl	0.87	0.6100	bdl	0.77	0.6140	bdl	0.91	0.6680
Se	15.36	39.20	66.6500	bdl	31.95	21.9600	11.01	29.62	22.3700	45.77	42.57	24.0300
Mo	22.58	3.56	1.0500	2.12	0.78	0.3440	1.72	0.68	0.3500	76.36	11.84	0.3950
Ag	13.36	0.99	0.3230	6.36	0.59	0.1100	3.74	0.42	0.1190	1.85	0.34	0.1320
Cd	6.27	1.74	1.0600	1.07	0.69	0.3390	1.60	0.72	0.3210	2.14	0.92	0.3630
Sn	bdl	0.91	1.5600	1.29	0.85	0.5450	3.16	0.90	0.5580	1.83	0.91	0.5910
Sb	1.82	0.48	0.5550	bdl	0.27	0.1980	bdl	0.24	0.1950	bdl	0.27	0.2040
Te	1.52	1.20	1.3400	bdl	0.50	0.3570	bdl	0.44	0.4010	3.41	1.47	0.4300
Ba	308.04	545.62	1.4800	1.66	3.15	0.5020	1.16	2.29	0.4740	21.02	39.56	0.4770
W	1.59	0.37	0.0743	0.26	0.13	0.0279	0.18	0.10	0.0255	bdl	0.01	0.0325
Pt	0.34	0.20	0.1370	0.10	0.10	0.0421	0.12	0.11	0.0505	bdl	0.02	0.0503
Au	0.46	0.17	0.1290	0.11	0.09	0.0435	0.07	0.08	0.0494	0.03	0.08	0.0521
Tl	7.18	1.32	0.0620	0.45	0.13	0.0182	0.32	0.10	0.0221	0.12	0.06	0.0203
Pb	384.56	57.02	0.3750	4.66	0.84	0.1320	3.72	0.70	0.1400	0.80	0.29	0.1450
Bi	166.29	23.34	0.1230	0.23	0.09	0.0420	0.12	0.07	0.0429	0.23	0.10	0.0459

Unit	Palizzi lava			Palizzi lava		
Sample	SC-18-24			SC-18-24		
sulfide id	sc1824 7-8			sc1824 4-5-6		
label	db_9	1σ	det lim	db_10	1σ	det lim
ppm S^{33}	148141.20	27353.18	446.7200	595242.75	151541.36	4620.5400
S^{34}	139416.58	23287.32	180.1500	684828.35	156862.34	1844.7200
V	0.05	0.21	0.1400	117.27	13.05	1.4100
Mn	681.79	523.46	5.0600	1504.64	1578.71	49.9800
Fe	108823.55	3459.38	9.6700	173262.62	7554.23	98.2700
Co	131.45	31.99	0.1900	58.68	20.29	1.8800
Ni	493.09	707.02	11.3700	46.99	195.56	115.8300
Cu	248441.20	40071.19	0.1400	1193582.42	268243.34	1.4100
Zn	607.19	322.92	1.9500	1145.25	846.85	18.8700
As	0.47	0.28	0.1670	397.31	57.84	1.7000
Se	15.66	12.91	5.5700	208.42	197.76	56.6500
Mo	0.02	0.15	0.0957	6.46	2.73	0.8760
Ag	9.07	0.59	0.0313	354.05	27.57	0.3220
Cd	16.64	3.66	0.0896	0.64	1.42	0.8360
Sn	3.95	0.59	0.1400	14.27	3.78	1.4900
Sb	0.11	0.09	0.0517	4.93	1.41	0.4920
Te	1.14	0.42	0.0774	0.50	1.35	0.6540
Ba	4.71	9.43	0.1030	43.87	120.49	1.2000
W	0.03	0.02	0.0068	0.80	0.47	0.0934
Pt	bdl	0.01	0.0128	0.07	0.30	0.1810
Au	0.04	0.03	0.0125	bdl	0.12	0.1390
Tl	0.03	0.02	0.0059	0.03	0.10	0.0583
Pb	2019.88	368.49	0.0346	34.41	9.01	0.3460
Bi	32.60	5.87	0.0113	3.31	0.99	0.1150

Appendix H: Mass balance calculations with major elements.

Appendix H – Examples of mass balance calculation obtained using whole-rock and mineral phases major elements. SSR is the sum of squared deviations of predicted values (predicted using regression) from the mean value, and SSE is the sum of squared deviations of actual values from predicted values. Calculation made with GeoBalance di Li et al. 2020 (left column).

1 - Pietre Cotte Latite to Pal D K-rich Trachyte					
Phases	**Prop.(%)**	**Prop.(%)**	**Std.**	**Comp.**	**Residual**
Melt	70.07	70.24	4.34	SiO_2	-0.01
Cpx	7.34	7.36	4.42	TiO_2	-0.03
Pl	16.79	16.83	8.14	Al_2O_3	0.00
Sa	2.96	2.97	4.27	FeO_{tot}	0.00
Ti-Mt	2.34	2.35	1.46	MnO	0.00
Ol	0.07	0.07	2.94	MgO	0.01
Bt	0.20	0.20	4.06	CaO	0.01
SUM	99.77	100.00		Na_2O	0.05
				K_2O	0.03
				SSE	**0.0038**

1 - Pietre Cotte Latite to Pal D K-rich Trachyte					
	Difference	**Deviation^2**	**Phases**		
SiO_2	3.00	0.00	Cpx	-7.37	0.25
TiO_2	-0.03	0.00	Plag	-16.98	0.57
Al_2O_3	-0.38	0.00	San	-2.61	0.09
FeO_{tot}	-1.34	0.00	TiMt	-2.34	0.08
MnO	0.00	0.00	Bt	-0.61	0.02
MgO	-0.81	0.00	% removed	-29.92	
CaO	-2.33	0.00			
Na_2O	0.37	0.00			
K_2O	1.43	0.00			
	SSR	**0.0129**			

2 - Pietre Cotte Latite to Palizzi Lava Trachyte					
Phases	**Prop.(%)**	**Prop.(%)**	**Std.**	**Comp.**	**Residual**
Melt	61.79	61.85	4.35	SiO_2	-0.04
Cpx	4.36	4.36	4.41	TiO_2	-0.04
Pl	15.12	15.13	7.48	Al_2O_3	-0.02
Sa	12.60	12.61	4.81	FeO_{tot}	0.00
Ti-Mt	2.20	2.20	1.34	MnO	0.01
Bt	3.25	3.25	4.04	MgO	0.01
Ol	0.59	0.59	2.96	CaO	0.08
SUM	99.92	100.00		Na_2O	0.32
				K_2O	0.16
				SSE	**0.1409**

2 - Pietre Cotte Latite to Palizzi Lava Trachyte					
	Difference	**Deviation^2**	**Phases**		
SiO_2	3.32	0.02	Cpx	-4.49	0.12
TiO_2	-0.21	0.01	Pl	-15.44	0.40
Al_2O_3	-1.12	0.01	Sa	-12.60	0.32
FeO_{tot}	-0.86	0.01	Ti-Mt	-2.22	0.06
MnO	0.01	0.00	Bt	-4.06	0.10
MgO	-0.75	0.01	% removed	-38.81	
CaO	-0.96	0.00			
Na_2O	0.47	0.10			
K_2O	0.16	0.02			
	SSR	**0.1824**			

3 - Pal D K-rich Trachyte to Pal B Rhyolite					
Phases	**Prop.(%)**	**Prop.(%)**	**Std.**	**Comp.**	**Residual**
Melt	24.51	24.82	7.78	SiO_2	-0.03
Cpx	3.36	3.40	2.76	TiO_2	0.07
Pl	18.57	18.81	6.92	Al_2O_3	-0.15
Sa	43.75	44.31	5.81	FeO_{tot}	0.01
Ti-Mt	4.13	4.18	1.15	MnO	0.06
Bt	4.41	4.46	2.68	MgO	-0.02
SUM	98.71	100.00		CaO	0.10
				Na_2O	0.68
				K_2O	0.30
				SSE	**0.5910**

3 - Pal D K-rich Trachyte to Pal B Rhyolite					
	Difference	**Deviation^2**	**Phases**		
SiO_2	11.13	0.08	Cpx	-3.26	0.05
TiO_2	-0.46	0.00	Pl	-17.23	0.24
$Al2O_3$	-4.30	0.22	Sa	-42.08	0.58
FeO_{tot}	-2.88	0.05	Ti-Mt	-3.74	0.05
MnO	0.01	0.00	Bt	-6.02	0.08
MgO	-1.19	0.09	% removed	-72.34	
CaO	-1.31	0.00			
Na_2O	0.49	0.67			
K_2O	-1.55	0.06			
	SSR	**1.1738**			

4 - Palizzi Lava Trachyte to Pal B Rhyolite					
Phases	**Prop.(%)**	**Prop.(%)**	**Std.**	**Comp.**	**Residual**
Melt	34.55	34.54	6.30	SiO_2	-0.01
Cpx	5.86	5.86	2.44	TiO_2	-0.06
Pl	21.29	21.28	3.29	Al_2O_3	-0.05
Sa	32.02	32.01	4.30	FeO_{tot}	0.01
Ti-Mt	4.12	4.12	0.75	MnO	0.03
Bt	2.20	2.20	2.83	MgO	0.03
SUM	100.04	100.00		CaO	0.00
				Na_2O	0.24
				K_2O	0.06
				SSE	**0.0681**

4 - Palizzi Lava Trachyte to Pal B Rhyolite					
	Difference	**Deviation^2**	**Phases**		
SiO_2	10.84	0.03	Cpx	-8.36	0.12
TiO_2	-0.28	0.00	Olig	-21.74	0.32
Al_2O_3	-3.46	0.08	San	-31.81	0.47
FeO_{tot}	-3.33	0.02	Ox	-4.48	0.07
MnO	0.00	0.00	Bt	-1.41	0.02
MgO	-1.22	0.04	% removed	-67.80	
CaO	-2.61	0.00			
Na_2O	0.29	0.19			
K_2O	-0.28	0.01			
	SSR	**0.3881**			

Appendix I: Trace elements geochemical modelling

Appendix I.1- Partition coefficient employed in trace elements geochemical modelling. (Appendix to Chapter 6).

$kd^{min/melt}$		Ba	ref.	Rb	ref.	Sr	ref.
Olivine	max	0.103	[1]	0.095	[1]	0.242	[1]
	min	0.03	[2]	0.04	[2]	0.02	[2]
Clinopyroxene	max	0.065	[1]	0.065	[1]	0.36	[6]
	min	0.02	[3]	0.02	[3]	0.22	[3]
Plagioclase	max	1.088	[1]	0.09	[3]	5.825	[1]
	min	0.4	[4]	0.041	[1]	1.3	[3]
Biotite	max	5.66	[3]	1.52	[3]	0.587	[1]
	min	4.04	[3]	1.072	[1]	0.2	[3]
Sanidine	max	7.882	[1]	0.664	[1]	5.236	[1]
	min	1.7	[5]	0.21	[5]	1.48	[5]
Ti-Magnetite		0.014	[1]	0.057	[1]	0.087	[1]

[1]Gioncada, A., (1997). L'attività eruttiva degli ultimi 50000 anni di Vulcano (Eolie): aspetti vulcanologici e magmatologici, PhD thesis, University of Pisa

[2]Villemant, B., Jaffrezic, H., Joron, J. L., & Treuil, M. (1981). Distribution coefficients of major and trace elements; fractional crystallization in the alkali basalt series of Chaine des Puys (Massif Central, France). Geochimica et Cosmochimica Acta, 45(11), 1997-2016.

[3]Villemant, B. (1988). Trace element evolution in the Phlegrean Fields (Central Italy): fractional crystallization and selective enrichment. Contributions to Mineralogy and Petrology, 98(2), 169-183.

[4]Calc. with Blundy, J. D., & Wood, B. J. (1991). Crystal-chemical controls on the partitioning of Sr and Ba between plagioclase feldspar, silicate melts, and hydrothermal solutions. Geochimica et Cosmochimica Acta, 55(1), 193-209.

[5]Ewart, A., & Griffin, W. L. (1994). Application of proton-microprobe data to trace-element partitioning in volcanic rocks. Chemical Geology, 117(14), 251-284.

[6]Piochi, M., De Astis, G., Petrelli, M., Ventura, G., Sulpizio, R., & Zanetti, A. (2009). Constraining the recent plumbing system of Vulcano (Aeolian Arc, Italy) by textural, petrological, and fractal analysis: The 1739 AD Pietre Cotte lava flow. Geochemistry, Geophysics, Geosystems, 10(1).

Appendix I.2 – Fractional crystallization and Assimilation and fractional crystallization models. Min D and Max D are the bulk partition coefficient calculated with the selected kd and calculated modal proportions. (Appendix to Chapter 6).

FC-AFC model	Phase	Ol	Cpx	Pl	Ti-Mt	Bt	Sa	Sum		Min D		Max D
Latite to K-rich trachyte	Proportion from mass balance	0.50%	7.00%	17.00%	2.00%	0.50%	2.50%	29.50%	Rb	0.07	Rb	0.15
	Normalized proportion	1.69%	23.73%	57.63%	6.78%	1.69%	8.47%	100.00%	Ba	0.45	Ba	1.41
									Sr	0.94	Sr	3.03
Latite to trachyte	Proportion from mass balance	0.50%	5.00%	13.00%	3.00%	2.00%	12.00%	35.50%	Rb	0.15	Rb	0.36
	Normalized proportion	1.41%	14.08%	36.62%	8.45%	5.63%	33.80%	100.00%	Ba	0.95	Ba	3.39
									Sr	1.03	Sr	2.98
Trachyte (Lava and Mush) to Rhyolite	Proportion from mass balance	0.00%	6.00%	21.00%	4.00%	3.00%	31.00%	65.00%	Rb	0.17	Rb	0.43
	Normalized proportion	0.00%	9.23%	32.31%	6.15%	4.62%	47.69%	100.00%	Ba	1.13	Ba	4.38
									Sr	1.16	Sr	4.44

Assimilant average*	**Sr**	**Ba**	**Rb**	Calabrian Arc metapelites
ppm	205.62	104.67	683.19	

*Frezzotti, M. L., Peccerillo, A., Zanon, V., & Nikogosian, I. (2004). Silica-rich melts in quartz xenoliths from Vulcano Island and their bearing on processes of crustal anatexis and crust–magma interaction beneath the Aeolian Arc, Southern Italy. *Journal of petrology*, *45*(1), 3-26.

Appendix I.4 – Calculated composition of extracted melt and residual cumulates with the model of Gelman et al. (2014). (Appendix to Chapter 6)

Starting point 1 (green in Fig. 6.19)

	ppm Rb	Ba	Sr	Rb	Ba	Sr
Starting point	212.03	342.39	398.7			
V fraction of extracted melt	**Extracted melt**			**Cumulate composition**		
0.1	328.1	43.05	36.34	193.2	394.6	428.2
0.2	341	41.8	35.04	173.1	438.8	477.5
0.3	359.8	40.67	34.14	141	496	541.1

Starting point 2 (pink in Fig. 6.19)

	ppm Rb	Ba	Sr	Rb	Ba	Sr
Starting point	231.93	982.58	951.6			
V fraction of extracted melt	**Extracted melt**			**Cumulate composition**		
0.1	358.2	102.6	82.28	210.9	1064	1007
0.2	372.2	98.99	79.2	188.9	1185	1123
0.3	392.7	96.35	77.17	154	1341	1273

Starting point 3 (blue in Fig. 6.19)

	ppm Rb	Ba	Sr	Rb	Ba	Sr
Starting point	200	700	600			
V fraction of extracted melt	**Extracted melt**			**Cumulate composition**		
0.1	313.3	74.58	55.06	185.4	769.1	651.8
0.2	326.5	71.7	52.86	166.1	856.7	726.9
0.3	345.3	69.61	51.35	135	969.7	823.8

* Values from Clocchiatti, R., Del Moro, A., Gioncada, A. N. N. A., Joron, J. L., Mosbah, M., Pinarelli, L., & Sbrana, A. (1994). Assessment of a shallow magmatic system: the 1888–90 eruption, Vulcano Island, Italy. Bulletin of Volcanology, 56(6-7), 466-486.

Appendix I.5 - Calculation of Bulk Partition Coefficient D calculated using selected partition coefficient (kd) from the GERM database earthref.com and normalized mineral % in the solid pahse from Gioncada, 1997 and this work; % of fractionated phases (from Gioncada, 1997, for Basalt to Latite; Mass Balance of this work for Latite to Trachyte and Rhyolite) (Appendix to chapter 8).

Fractionation steps	**Ol**	**Cpx**	**Ti-Mt**	**Pl**	**Bt**	**Sa**	**Sum**
Basalt - Trachy Basalt	0.5%	24.3%	5.5%	8.1%	0.0%	0.0%	38.4%
Trachy Basalt - Shoshonite	4.6%	15.7%	2.0%	26.5%	0.0%	0.0%	48.8%
Shoshonite - Latite	2.5%	11.1%	2.3%	5.7%	0.0%	0.0%	21.6%
Latite - Trachyte	0.5%	7.0%	2.0%	17.0%	0.5%	2.5%	29.5%
Trachyte - Rhyolite	0.0%	6.0%	4.0%	21.0%	3.0%	31.0%	65.0%

Basalt - Trachy Basalt		**Ol**	**Cpx**	**Ti-Mt**	**Pl**	**Bt**	**Sa**	**Sulf**		
		1.3%	63.3%	14.3%	21.1%	0.0%	0.0%	0.0%		
	Kd Cu	0.02	0.07	0.42	0.00				**DCu**	0.11
	Kd Zr	0.00	0.11	0.02	0.13				**DZr**	0.10
	Kd Pb	0.00	0.01	0.00	0.36				**DPb**	0.08
Trachy Basalt - Shoshonite		9.4%	32.2%	4.1%	54.3%	0.0%	0.0%	0.0%		
	Kd Cu	0.02	0.07	0.42	0.00				**DCu**	0.04
	Kd Zr	0.00	0.11	0.02	0.13				**DZr**	0.11
	Kd Pb	0.00	0.01	0.00	0.36				**DPb**	0.20
Shoshonite - Latite		11.6%	51.4%	10.6%	26.4%	0.0%	0.0%	0.0%		
	Kd Cu	0.05	0.36	0.39	0.08				**DCu**	0.25
	Kd Zr	0.07	0.30	0.31	0.02				**DZr**	0.20
	Kd Pb	0.00	0.01	0.00	0.19				**DPb**	0.06
Latite - Trachyte		1.7%	23.7%	6.8%	57.6%	1.7%	8.5%	0.0%		
	Kd Cu	0.05	0.36	0.31	0.08	20.03	0.24		**DCu**	0.51
	Kd Zr	0.07	0.30	0.31	0.02	0.19	0.01		**DZr**	0.11
	Kd Pb	0.00	0.32	0.38	0.19	0.10	0.98		**DPb**	0.29
		1.69	23.73	6.78	57.63	1.69	8.47			
Latite - Trachyte (Sulfide saturation)		1.7%	23.7%	6.8%	57.6%	1.7%	8.5%	0.2%		
	Kd Cu	0.05	0.36	0.31	0.08	20.03	0.24	5600[a]	**DCu**	11.7
	Kd Zr	0.07	0.30	0.31	0.02	0.19	0.01	0.00	**DZr**	0.10
Trachyte - Rhyolite (Sulfide saturation)		0.0%	8.0%	6.0%	38.9%	5.0%	41.9%	0.2%		
	Kd Cu	0.05	0.36	0.31	0.08	20.03	0.24	5600[a] - 1200[b]	**DCu**	12.3- 3.5
	Kd Zr	0.07	0.30	0.31	0.02	0.19	0.01	0.00	**DZr**	0.06
	Kd Pb	0.00	0.32	0.38	0.19	0.10	0.98	48.5[c]	**DPb**	0.64

[a]Kd Cu SL/SM Calculated with the model of Li and Audetat, 2015; [b]Kd Cu MSS/SM calculated with the model of Li and Audetat, 2015; [c]Kd Pb SL/SM Calculated with the model of Li and Audetat, 2015. All Kd calculated with a T of 950°C, DFMQ = - 0.77 and FeO in the melt = 4.4wt%, estimated for La Fossa trachyte by Fulignati et al., 2018.